The Structure of Massive Star-forming Clumps

Dissertation
zur
Erlangung des Doktorgrades (Dr. rer. nat.)
der
Mathematisch-Naturwissenschaftlichen Fakultät
der
Rheinischen Friedrich-Wilhelms-Universität Bonn

vorgelegt von
Yuxin Lin
aus
Liaoning, China

Bonn 2021

Angefertigt mit Genehmigung der Mathematisch-Naturwissenschaftlichen Fakultät der Rheinischen Friedrich-Wilhelms-Universität Bonn

1. Gutachter:	Prof. Dr. Karl Menten
2. Gutachter:	Prof. Dr. Pavel Kroupa
Tag der Promotion:	08.09.2021
Erscheinungsjahr:	2021

Contents

Abstract

Among many other critical questions in astrophysics, the high-mass star formation process is a matter of heated debate; so far a comprehensive understanding is lacking. Star formation takes place in cold molecular clouds. It also has been long known that massive stars form almost exclusively in star clusters. Galactic-scale surveys from millimeter to infrared wavelengths in the last decades have identified numerous massive molecular clumps (~1 pc in size, $\gtrsim$500 $M_\odot$ in mass), which are believed to be the nurseries for massive proto-clusters. Studying the physical structure and the evolution of these massive clumps is therefore an important prerequisite for understanding the process of massive star formation. In this thesis, we report intermediate spatial resolution (~0.1 pc) observations towards selected samples of massive clumps, aiming at revealing their underlying physical structures, including fragmentation properties, as well as density and temperature profiles and their variations, along the evolutionary track of massive proto-cluster formation. Throughout the thesis, we discuss dust continuum and molecular line data of the clumps, relying on various radiative transfer modeling methods to derive their physical properties, with an attempt to achieve stringent estimates. In Chapter 2, using ground-based 350 μm continuum imaging, we analyse observations of >200 massive clumps and obtain high-angular resolution ($10''$) dust temperature and hydrogen column density maps based on an image combination technique and iterative spectral energy distribution fitting procedure. We reveal the clump fragmentation properties at intermediate scales (~0.1 pc), and show that a large clump mass reservoir is essential for the mass accumulation into massive cores. In Chapters 3 and 4, with wide-band interferometric and single-dish spectroscopic observations, we utilize multiple molecular lines sensitive to a wide range of physical conditions to obtain a continuous mapping of the temperature and hierarchical density structures of a sample of massive clumps, which spans an evolutionary sequence from sources in the earliest infrared-dark stage to active OB cluster forming regions. In Chapter 3, we study the evolutionary variations of radial profiles of the temperature, density, linewidth, and dynamical state of massive clumps. We find that the temperature structure of massive clumps on scales of 0.1 pc in general follows predictions of simple central heating models with notable deviations that can be attributed to a particular source geometry, indicating significant central merging of protostars within massive clumps, which strongly shapes the temperature structure at >0.1 pc. The gas density profile becomes steeper with clump evolution, which, together with the variations of the radial profile of the virial parameter, suggests a gravo-turbulent picture of clump gas dynamics and evolution. By adopting single-dish multi-wavelength dust continuum which trace the density of the bulk gas, and molecular line densitometers which selectively probe the dense gas regimes, we reveal the hierarchical gas structures and the gas condensation process of massive clumps. The different radial profiles of the dense gas fraction may indicate different modes of the star formation process, which is either dominated by global contraction or exhibiting significant secondary fragmentation and structure formation around the global potential center. We corroborate the clump evolutionary sequence by comparing the abundance ratios of several molecules that have

been suggested as evolutionary indicators. This line of work of Chapter 3 is extended to more massive clumps in Chapter 4, in which a detailed study is presented of 5 early-stage massive clumps residing in W43-main, an extreme Galactic OB cluster forming complex representative of a highly turbulent cloud environment. In addition to revealing the temperature and density structures of these clumps, we further investigate the relation between cloud-scale dynamics, specifically the cloud collision activities, and the formation and fragmentation of early-stage cores and the enhancement of more processed dense gas.

CHAPTER 1

Introduction

Understanding the star formation process is fundamental in the realm of astrophysics and astronomy. Stars and star clusters make an essential contribution to the mass and energy budget of galaxies. The matter cycling over their lifetimes has profound impact on galaxy evolution and dynamics. The view that star formation takes place in molecular clouds is long established and well accepted. However, there are still unresolved important questions concerning the star formation process, one of which, the detailed physical mechanisms and their interplay that lead to the universal stellar initial mass function (IMF), is a highly debated and acute problem. Moreover, the processes determining the formation of massive stars are less clear compared to the case of low-mass stars. Molecular clouds encompass the birth and life cycle of stars and star clusters, imprinted with various feedback activities. Investigating the formation and evolution of molecular clouds is essential for understanding the star formation process.

1.1 Molecular clouds: structure and physical properties

The interstellar medium (ISM) consists of highly hierarchical gas structures, spanning several density and temperature regimes, often called "phases" (Hollenbach, Werner and Salpeter 1971). Stars are formed in the densest regions within molecular clouds. In the classical Jeans scenario (Jeans 1902), these regions are where self-gravity dominates over the outward thermal pressure. Considering a system following the equations of hydrodynamics and gas gravitational potential through the Poisson equation, the length scale of these regions, L, must meet the criterion:

$$L \gtrsim \lambda_{\mathrm{J}} = \sqrt{\frac{\pi c_{\mathrm{s}}^2}{G\rho_0}} \tag{1.1}$$

where $c_{\mathrm{s}} = \sqrt{\frac{k_{\mathrm{B}}T}{\mu}}$ is the sound speed and G is the gravitational constant, ρ_0 the gas density, k_{B} the Boltzmann constant, T the temperature of the gas and μ the molecular weight. Therefore based on the assumption that the only opposing force of gravity is the thermal pressure, this relation introduces a critical scale, the Jeans length, λ_{J}, and correspondingly a critical mass scale, $M_{\mathrm{J}} = \rho_0\lambda_{\mathrm{J}}^3$, beyond which the dense gas is prone to gravitational collapse to form a star. In reality, besides thermal pressure, there are other mechanisms in molecular clouds that affect the gas dynamics, among which the important ones are turbulence, magnetic fields and radiation feedback.

The importance of turbulence in shaping the ISM and molecular cloud structure was recognised decades ago: its supersonic and compressible nature is suggested to be at the origin of the hierarchy of the interstellar medium (Elmegreen 1999, Hennebelle and Falgarone 2012) and the physical properties' scaling relations (Larson 1981, Elmegreen and Scalo 2004), and of the general form of the IMF (Padoan, Nordlund and Jones 1997, Hennebelle and Chabrier 2008).

The compressibility of supersonic turbulence introduces a dual effect on cloud structure: on large scales, turbulence stabilises the clouds against gravitational collapse with the strong random distortions of the velocity field (Chabrier and Hennebelle 2011, Mac Low and Klessen 2004), while it also creates and enhances localised over-densities, which may be seeds of gravitationally collapsing regions for subsequent star formation (e.g Krumholz and McKee 2005, Robertson and Goldreich 2018). If seen as an additional component opposing gravity, the influence of turbulence can be generalised into the classical Jeans scenario by (quadratically) adding the 'turbulent line-width' ($\sigma_{\rm rms}$) to the thermal line-width, replacing the $c_{\rm s}^2$ by a sum of both:

$$\sigma_{\rm s}^2 = \sigma_{\rm rms}^2 + c_{\rm s}^2 \ . \tag{1.2}$$

In this formalisation, the inclusion of turbulent support effectively raises the critical length and mass scales for star formation. Note that this modification does not indicate that the role of turbulence is static and pressure-like since the dissipation of turbulence causes dynamical variations with the process of core formation (Elmegreen and Scalo 2004). It is usually convenient to adopt the virial parameter α (hereafter $\alpha_{\rm vir}$) to describe the relative importance of kinetic (T) and gravitational energy (W), following

$$\alpha = a_1 \frac{2T}{|W|} = \frac{5\sigma_{\rm s}^2 R}{M_{\rm enc} G} \tag{1.3}$$

which is valid for a spherical gas structure of enclosed mass, $M_{\rm enc}$ with a radius of R, with density profile of power-law slope q ($\rho \propto r^{-q}$) (Bertoldi and McKee 1992). In this equation, $a_1 = \frac{1+q/3}{1+2/5q}$ corresponds to the critical virial parameter indicating equilibrium, and $\alpha_{\rm vir}/a_1 = 2$ suggests energy equipartition. In terms of the density enhancement induced by turbulence, a typical rms density fluctuation of $\rho_{\rm rms} = \mathscr{M}_{\rm s}^2 \rho$ resulted from compressive turbulence (Padoan, Nordlund and Jones 1997, Passot and Vázquez-Semadeni 1998a), where the sonic Mach number ($\mathscr{M}_{\rm s}$) is defined as,

$$\mathscr{M}_{\rm s} = \frac{\sigma_{\rm rms}}{c_{\rm s}} \ . \tag{1.4}$$

This multiplicative nature of the density enhancement is at the origin of the log-normal distribution of the molecular cloud gas density probability distribution function (ρ-PDF) (Passot and Vázquez-Semadeni 1998b, Federrath et al. 2010, Hopkins 2013), the features of which depend on $\mathscr{M}_{\rm s}$. In Eq. 1.3 to characterize the dynamical state of molecular clouds, two energy sources are effectively ignored: one from the surface pressure due to bulk flows of mass across the cloud boundary, and the other from magnetic fields. Magnetic fields can provide additional support against fragmentation and gravitational collapse (Basu and Mouschovias 1995, Heitsch, Mac Low and Klessen 2001); they can also limit the turbulent compression by altering the shock conditions (Padoan and Nordlund 2002a, Burkhart et al. 2009, Mocz and Burkhart 2018).

There are other intricacies to the classical Jeans scenario. For example, the initial condition for gravitational contraction is taken to be a uniform isothermal medium at rest. The isothermality assumption relies on the efficient cooling of dense gas ($\gtrsim 10^5$ cm^{-3}) during contraction: heating from compression (PdV) is completely radiated away as long as the gas is optically thin to thermal dust emission. However, at even higher densities, due to the increasing heating rate, i.e. increased collapsing rate at high density, the balance might breaks down, which remains so until a point where gas can be described by adiabatic process. This phenomenon is usually generalised by polytropic equation of state (EOS) (see also e.g. Nolan, Federrath and Sutherland (2015) for the EOS of adiabatic gas), where the relation of gas pressure (P), temperature (T) and density (ρ) follows:

$$P \sim \rho^{\Gamma}, T \sim \rho^{\Gamma-1} \tag{1.5}$$

where Γ is polytropic exponent. Γ characterises deviations of the gas physical state from isothermality. In different gas density regimes, Γ has values of less or larger than 1 (Spaans and Silk 2000). As previously shown, the critical scale for gravitational contraction is determined by a combination of gas temperature and density ($M_\mathrm{J} \propto \rho^{\frac{3\Gamma-4}{2}}$), the value of Γ thus has critical impact on the density distribution and fragmentation process of molecular clouds (Li, Klessen and Mac Low 2003, Jappsen et al. 2005, Federrath and Banerjee 2015), and further in settling the peak mass of the IMF (Larson 2005, Lee and Hennebelle 2019). With $\Gamma < 4/3$, the Jeans mass decreases with increasing density. An isothermal cloud of fixed mass ($\Gamma = 1$) evolves as follows: while contracting and becoming denser, the number of Jeans mass it contains grows, and more and more lower mass objects become unstable and collapse at sequential time (e.g. Vázquez-Semadeni et al. 2019). $\Gamma = 4/3$ is a critical state, separating regimes that are unstable or stable against gravity. For adiabatic gas that is not able to radiate anymore, Γ approaches 5/3 or 7/3, depending on whether the gas is monoatomic (with three degrees of freedom) or diatomic (with five degrees of freedom). In reality, in addition to internal heating mechanisms, also the effects of radiative feedback must be considered; this feedback is dependent on the detailed structure of gas and dust grain properties, which cannot be fully incorporated by a piece-wise EOS (Masunaga and Inutsuka 2000, Stamatellos et al. 2007). Some works have pointed out the dominant role of the stellar radiation feedback in determining the gas temperature structures (Bate 2009, Offner et al. 2009, Krumholz, Klein and McKee 2011, 2012): the gas at very high density, i.e. 10^{8-10} cm^{-3}, is significantly heated, such that the Jeans mass in this regime only weakly depends on density (e.g. Guszejnov, Krumholz and Hopkins 2016a).

It is generally believed that the fragmentation process of molecular clouds leads to dense *cores* that are the basic entities (~0.1 pc) out of which stars form (Shu, Adams and Lizano 1987, Andre, Ward-Thompson and Barsony 2000, Ward-Thompson et al. 2007). A well known phenomenon, especially found for nearby (low-mass) star-forming clouds, is that the core mass function (CMF) resembles the IMF (Offner et al. 2014). Their power-law tails have similar slopes, while in absolute scales the CMF is shifted to larger masses (Testi and Sargent 1998, André et al. 2010, Könyves et al. 2015). This provides important evidence for the hypothesis that the IMF is set at an early stage of star formation. The similar power-law tails of CMF and IMF can result from two scenarios, (1) the star formation efficiency of individual cores is constant and it fulfills that either the mass reservoir of a single star (or a star system) is confined to its parental core structure, or the fragmentation of cores happens self-similarly, which is a one-to-one mapping picture (Padoan and Nordlund 2002b, Hennebelle and Chabrier 2008), or (2) the accretion happens self-similarly as $\dot{M} \propto M^{\eta}$ from the core to the protostellar scale. For example, for Bondi-Hoyle accretion a point mass forms from an infinitely uniform medium as $\dot{M} \propto M^2$. The final stellar mass may not have a tight correlation with the initial core mass, but might rather be determined by the subsequent accretion and distribution of accretion stopping times for a cluster of objects (Bate and Bonnell 2005, Myers 2011). In this latter view, the CMF is measured *instantly* during a highly dynamical mass accumulation process, and the resemblance of CMF and IMF can be coincidental (Bonnell et al. 2001a). These two scenarios have both been invoked for understanding the origin of the IMF. In relation to the definition of *core*, *clumps* refer to larger scale gas pockets (~1 pc) (Williams, Blitz and McKee 2000, Fall, Krumholz and Matzner 2010) that contain multiple cores and will form a cluster of stars eventually. Understanding of the morphology and physical structure of the very unit of *clumps* is crucial especially for the second scenario, since clumps are the gas environment where the extended accretions beyond core scale take place (Wang et al. 2010, Smith, Longmore and Bonnell 2009).

Most theories concerning the origin of CMF are built on the role of turbulence on molecular cloud structure. Essentially two features of CMF have to be explained by theories: the power-law tail and the peak position. In the framework of turbulent fragmentation, the power-law tail is produced by the scale-free nature of turbulence, and the peak position is determine by the turnover of the lognormal ρ-PDF below which density fluctuations (number distribution of Jeans mass) are damped to produce the peak position (Padoan and Nordlund 2002a; Padoan, Nordlund and Jones 1997). In such solutions, the Jeans critical length scale can be quite uncertain. Incorporating multi-scale methods to better describe the hierarchical structure of the clouds (Hennebelle and Chabrier 2008), the counting bias can be mitigated, as such theories also consider large-scale kinematics, such as galactic rotational motions (Hopkins 2012a,b). In essence, the critical scale in this framework depends on the sound speed c_s and the linewidth-size relation introduced by supersonic turbulence. Starting from the classical definition of Jeans length and mass, $M_\mathrm{J} \propto {\rho_0}^{-1/2} c_\mathrm{s}^3$ (Eq. 1.1), and replacing the density ρ_0 with the post-shock density $\rho = \mathscr{M}_\mathrm{s} \rho_0$ without considering the turbulence at local scale as additional support against gravity, the relation between the gravo-turbulent critical length scale ($L_\mathrm{J,\,turb}$) and mass scale ($M_\mathrm{J,\,turb}$) and the classical Jeans predictions of (L_J, M_J) are,

$$L_\mathrm{J,\,turb} \propto L_\mathrm{J}/\mathscr{M}_\mathrm{s}, M_\mathrm{J,\,turb} \propto M_\mathrm{J}/\mathscr{M}_\mathrm{s} \tag{1.6}$$

or equivalently $M_\mathrm{J,\,turb} \propto \sigma_\mathrm{rms}^{-1} \rho^{-1} T^2$ (e.g. Gong and Ostriker 2011). On the other hand, if turbulence works as an additional support against collapse (whose energy is dissipated on a crossing time $t_\mathrm{crossing} = \frac{L}{\mathscr{M}_\mathrm{s} c_\mathrm{s}}$ with L denoting the size of the cloud under consideration), then the critical mass $M_\mathrm{J,\,turb,\,non-thermal} \propto \sigma_\mathrm{rms}^3 \rho^{-1/2} T^{1/2}$ (e.g. Mac Low and Klessen 2004). Compared to the classical Jeans fragmentation scenario, now the Jeans critical scales depend additionally on the linewidth. With the supersonic linewidth (σ_rms) and size (L) scaling relation, i.e. $\sigma_\mathrm{rms} \propto L^{1/2}$, a characteristic mass can be defined, generally referred to as the sonic mass (e.g. Hopkins 2012b), as

$$M_\mathrm{sonic} \propto \frac{c_\mathrm{s}^2 \lambda_\mathrm{s}}{G} \quad , \tag{1.7}$$

which is the minimum mass required for a sphere of radius λ_s to collapse. λ_s is commonly referred to as the sonic scale, as $\lambda_\mathrm{s} = \frac{L}{\mathscr{M}_\mathrm{s}^2}$ in which L denotes the cloud size. Following the turbulent fragmentation theory, the resultant CMF has a peak mass at $\sim M_\mathrm{sonic}$ and a power-law form beyond M_sonic, resembling the shape of IMF. However, since the turnover scale is determined by λ_s, i.e. where turbulence kinetic energy is equivalent to thermal energy, the extrapolation of this relation to different gas dynamics, especially that in highly turbulent environments ($\alpha_\mathrm{vir} \gg 1$), can be critical. In fact, there are works showing that with large $\alpha_{\rm vir}$ ($\gtrsim$3), i.e. excessive kinetic energy, at initial stage of the cloud, the mass distribution of the cores/clumps can appear top-heavy (e.g. Bertelli Motta et al. 2016). Turbulence enhancement on smaller scale, i.e. a flatter turbulence power spectrum, is also shown to induce an IMF with a flatter power-law tail (Padoan and Nordlund 2002a, Nam, Federrath and Krumholz 2021).

With the development of numerical methods, more sophisticated magneto-hydrodynamic simulations, which in some cases include also radiative feedback, have been conducted. The existence of magnetic fields and stellar feedback can effectively reduce fragmentation (Price and Bate 2009). It is shown that magnetic field can reduce the secondary fragmentation of the accretion flows, while facilitate the formation of the central massive stars by transporting the angular momentum (Commerçon, Hennebelle and Henning 2011, Peters et al. 2011). A similar picture is shown by Li et al. (2010) in which magnetic fields modify the proportion of low-mass and intermediate-mass stars formed in the filamentary clouds by inhibiting their collapse (see also Lee, Hennebelle and Chabrier 2017). Compared to other mechanisms, the effect of magnetic field on IMF can be minor (e.g. Chen and Ostriker 2015), but the interplay of magnetic field and turbulence as well as feedback in many forms, can play a significant role (Nakamura and Li 2008, Cunningham et al. 2018, Krumholz and Federrath 2019).

Apart from diagnosing the effect of the global physical mechanisms, it is crucial to understand the collective impact from the cluster members on the formation process of individual stars. For example, the presence of multiple accreting centers results in a competitive environment for mass accumulation (Bonnell et al. 2001b, more in Sect. 1.2). Dynamical interactions between members can diminish accretion, by ejecting stars out of the gas environment or increasing the relative speed to lower down accretion rate (e.g. Price and Podsiadlowski 1995, Myers 2011). As mentioned before, radiative feedback also has a significant effect on the fragmentation process. Particularly, since radiative feedback is localised, the effect is more prominent in dense clumps, which may effectively erase the influence of the cloud initial condition on the IMF (Bate 2009, Guszejnov, Krumholz and Hopkins 2016b) and prevent over-fragmentation so that massive star formation is favored (Offner et al. 2009, Urban, Martel and Evans 2010). Radiative hydrodynamic simulations usually adopt a simple approximation of radiative transfer to describe the heating of gas in the vicinity of stars. To fully account for the effect of radiative feedback on the fragmentation process, it is important for theoretical works to implement accurate full radiative transfer modeling as well as for observations to measure and dissect the thermal properties of clump gas which is immersed in enhanced radiation. Kinematic feedback including ionisation fronts and outflows, by contribution to the turbulence and disrupting accretion flows (e.g. Wang et al. 2010, Dale and Bonnell 2011, Offner and Arce 2014), can also be important mechanisms regulating fragmentation. Outflows may play a key role in setting the star formation efficiency (Federrath et al. 2014, Tanaka, Tan and Zhang 2017). Particularly, the existence of outflow cavities, in addition to an accretion disk help reduce the excessive feedback of radiative heating (Yorke and Sonnhalter 2002, Krumholz, Klein and McKee 2011), by tunneling out the radiation power through the non-uniform optically thin subregions (Cunningham et al. 2011).

With the availability of unbiased FIR/submm galactic surveys of massive clumps, it becomes possible to constrain the gas temperature by building full spectral energy distributions (SEDs) that result in more accurate mass estimates (more in Sect. 1.3). This is an important aspect to link the observations of cores and clumps to theoretical works. For massive star-forming regions, which are generally quite distant ($\gtrsim$4 kpc), pursuit of high angular resolution observations is indispensable. Observations of massive star-forming clouds by state-of-art interferometry typically can achieve thousands of AU resolution to resolve the Jeans length (more in Sect. 1.5). To distinguish the physical mechanisms at work in the fragmentation process, observations towards large sample of massive clumps which span wide evolutionary stages are necessary. Meanwhile, characterising the physical environment with high dynamical range to map the density, temperature, and kinematics (of both ordered and turbulent motions) is a prerequisite. The major part of this thesis is based on observations of moderate angular resolution (0.1-0.2 pc) towards samples of massive clumps to probe the extended gas structures and intermediate-scale fragmentation properties, which aims at establishing a comprehensive understanding of clump fragmentation and physical conditions along their evolutionary tracks.

In the next sections of this chapter, massive star-formation scenarios (Sect. 1.2) and the general view of the evolution of massive star-forming regions (Sect. 1.3) are summarised. The dust continuum and molecular lines used as tools for diagnosing physical properties of molecular clouds are introduced in Sect. 1.4. Finally, Sect. 1.5 summarises recent observational results of massive star-forming clumps.

1.2 Formation processes of massive stars

Our understanding of the formation process of massive stars has not yet reached a consensus. Over the last few decades, many theoretical scenarios have been put forward, among which the most well received ones include the *turbulent core-collapse* and the *competitive accretion* model.

The *turbulent core-collapse* model provides a relatively static view of massive star formation (McKee and Tan 2003): the precursors of massive star(s), generally referred to as the pre-stellar cores, are massive and supported by turbulent motions, with virial parameter $\alpha_{\rm vir}\simeq1$; the formation timescale of massive stars is on the order of the free-fall timescale of these pre-stellar cores. This is a scale-up view of the framework of low-mass star formation, in which turbulence is playing the dominant role in stablising the core structures, than the thermal support. Indeed, a higher level of turbulence is commonly observed in massive star-forming regions (e.g. Plume et al. 1997, Caselli and Myers 1995). The physical structure of the core follows the logatropic model of McLaughlin and Pudritz (1997) and the temporal evolution of accretion rate is dependent on the slope of the density profile of the core on the verge of singularity formation. The turbulent surface pressure is at the origin of the high accretion rate necessary for the formation of massive stars.

The *competitive accretion* model suggests that star clusters originate from seeds of local over-densities that are continuously accreting from larger scale mass reservoirs in a more dynamic manner (Zinnecker 1982, Bonnell, Vine and Bate 2004). The accretion happens in two channels: Bondi-Hoyle type accretion and that related to tidal fields. The over-densities located close to the center of a global potential well preferentially acquire more gas, gradually becoming more massive. The accretion rate increases with the stellar mass (since the accretion is driven by the gravity of the forming star), in both the early-phase gas dominated potentials and the late-phase stellar dominated potentials (Bonnell et al. 2001b, Bonnell, Larson and Zinnecker 2007). The accretion process introduces an initial mass segregation and stellar masses of a wide range. In this scenario, the formation timescale of massive stars is longer than that in *turbulent core-collapse* model. The initial mass scale of the over-densities is controlled by Jeans fragmentation. However, it has been demonstrated that in this framework, for the initial seeds to obtain significant mass, the virial parameter $\alpha_{\rm vir}$ must be $\ll1$ (Krumholz, McKee and Klein 2005). There are similar frameworks which emphasise the extended accretion beyond core scales from less dense gas (than cores) that constitutes the majority of the mass of the massive cluster members; these are usually referred to as clump-fed scenarios (Smith, Longmore and Bonnell 2009,

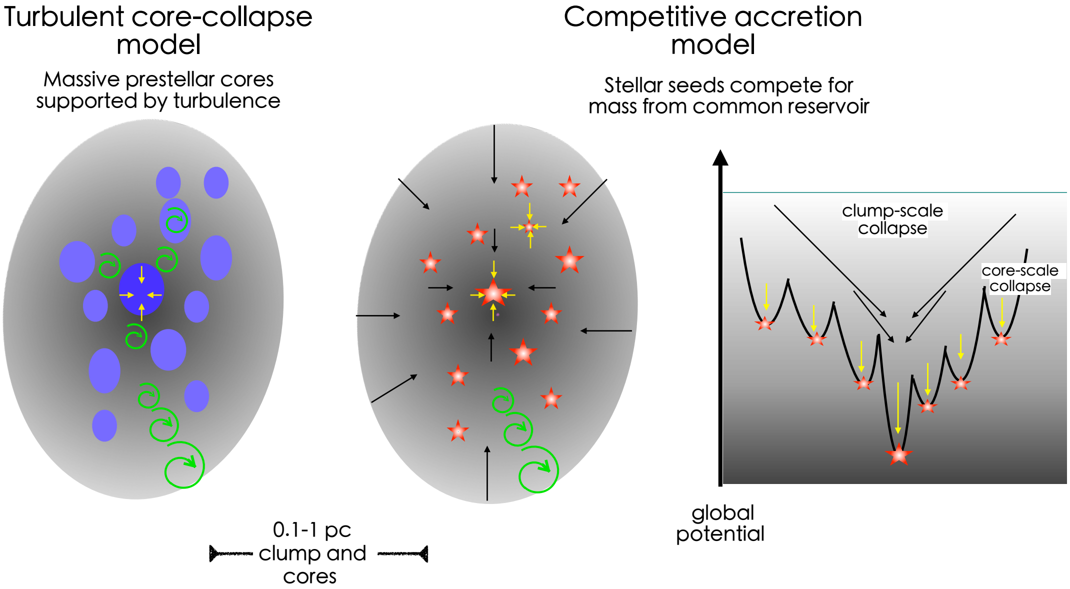

Figure 1.1: Schematic views of the *turbulent-core* model and *competitive accretion* model (left and middle panels). Large gray ellipses indicate the massive clump, as the parental structure that envelopes small ellipses and stars that represent cores and young stellar objects (stellar seeds). Arrows indicate the direction of gas flows, and green swirls represent turbulent motions. Particularly, in *turbulent-core* model, the pre-stellar cores are sufficiently massive at early stage, which are supported by turbulent motions and will undergo monolithic collapse to form massive stars. While in *competitive accretion* model, stars of all masses are initially low-mass objects and the continuous accretion onto the existing stellar seeds produce massive stars. The accretion is mainly driven by the stellar mass (Bondi-Hoyle accretion) except that at the very early stage, while stellar seeds located in the clump center preferentially acquire more masses owing to the clump-scale collapse which tunnels gas down to the center of the global potential (of gas and star clusters). The accretion process is illustrated in the right panel in which local and global potential wells are marked (adapted from Bonnel, Larson & Zinnecker 2007).

Wang et al. 2010). One notable difference is that while the *competitive accretion* model predicts run-away accretion onto the central stars which limits the growth of secondary stars, the fragmentation induced starvation scenario suggests that gas flows fragmenting into low-mass objects limit the growth of massive cluster members and henceforth put a limit on the mass of the most massive stars (Peters et al. 2010, Peters et al. 2011). This picture, in contrast to *competitive accretion*, corresponds to a decreasing mass accretion rate along the evolution of massive star formation. We illustrate the general picture of massive star formation process predicted by *turbulent core-collapse* and *competitive accretion* model in Figure 1.1.

Recent years have witnessed development of a few other massive star formation scenarios. The *global hierarchical collapse* model puts a special emphasis on the evolution and impact of large-scale giant molecular cloud (GMC) structure: the global contraction and convergent flows tunnel gas into the smaller scale structures continuously (Vázquez-Semadeni et al. 2019). At pc scale this scenario has similarities with the *competitive accretion* model. An important argument of this scenario is that molecular clouds are not necessarily in equilibrium and are contracting instead. On large scales, clouds are dominated by gravity and the turbulent motions are fed by gravitational collapse, while turbulent motions do not resist the collapse. Due to the highly hierarchical density structure of molecular clouds, the localised over-dense substructures terminate their collapse earlier with a shorter free-fall timescale. The feedback of massive stars then significantly disrupts the cloud structure: the gas at large scale far from the infall front likely ends up dispersing before falling onto the accreting centers. This keeps the overall SFR low in this framework. The evolution of the GMC-systems spans a few Myrs (few times the free-fall timescale) before gas dispersal driven by stellar feedback. The infalling gas has virial parameter $\alpha_{\rm vir}{\sim}1$ while gas being dispersed has $\alpha_{\rm vir}{\gg}1$. For a pre-stellar core, its external regions show an inside-out collapse, while its inner region collapses in an outside-in manner. The mass accretion rate increases with stellar mass generally in a Bondi-Hoyle manner, which is modified by the position of the accretion center and temporal variations of the environment (Ballesteros-Paredes et al. 2015).

The *inertial inflow* model also stresses the important role of large-scale gas dynamics in forming the massive stars (Padoan et al. 2020). However, contrary to the assumption that large-scale gas reservoirs are undergoing gravitational collapse, the gas is highly compressive and turbulent. It is the turbulent flows in the inertial range that feed the localised cores. In this scenario, the supersonic turbulence controls the timescale and the stellar accretion rate. Particularly, the timescale of star formation correlates tightly with the size scale of the inflow region, concomitant with the turbulent linewidth-size scaling relation. The pc-scale region around the pre-stellar cores has $\alpha_{\rm vir}{>}1$. Although with large stochastic fluctuations, the mass accretion rate is approximately constant along the evolutionary track, in contrast to the *competitive accretion* model. Compared to the *turbulent core-collapse* model, in this scenario the mass of the pre-stellar core does not play the deterministic role on the final stellar mass: for the most massive stars, the inflow region, from where most of the stellar mass comes from, can have a size of up to ~10 pc. The inflow velocity is in general much smaller than the turbulent velocity, which is also contrary to other models for which infall velocity is comparable to the turbulent velocity (gravo-turbulent models, e.g. Murray et al. 2017). Due to the highly supersonic turbulence at pc-scale, the inflow region is highly fragmented, showing a configuration of a network of filaments feeding multiple stars. A comparison between *global hierarchical collapse* model and *inertial inflow* model is shown in Figure 1.2. A similar paradigm is followed by *cloud-cloud collision* models (e.g. Inoue and Fukui 2013, Fukui et al. 2021), in which shock compressed dense gas layers from colliding supersonic flows are shaped into filamentary structures at pc scale. The formation of filaments is more rapid than the free-fall time (of the cloud initial density) and further gas is accumulated by inflows. In both paradigms, the high mass accretion rate ($>10^{-4}$ M$_\odot$ yr^{-1}) (e.g. Inoue et al. 2018) is achieved due to the supersonic sound speed. It seems the *cloud-cloud collision* model can explain the observed top-heavy core mass distribution functions in some extreme star formation sites, since it preferentially predicts that more massive stars in a short timescale, before the gas mass is consumed by low-mass stars. The age of the O stars peaks around 0.1 Myr after the collisions, while low-mass stars have an age spread determined by the mean free-fall time of the cloud. Numerically, it has been shown that a higher cloud collision speed and initial cloud density, together with lower turbulence yield a higher overall star formation rate and produce more massive clusters (Liow and Dobbs 2020). Moreover, the cloud structure preceding cloud collisions can also play a role, with more clumpy clouds favoring massive star formation regardless of collision velocities (Balfour, Whitworth and Hubber 2017). The *cloud-cloud collision* model can therefore explain the birth of the young massive clusters from giant molecular clouds in the Milky Way.

We summarize the features and predictions of the aforementioned formation scenarios in Table 1.1.

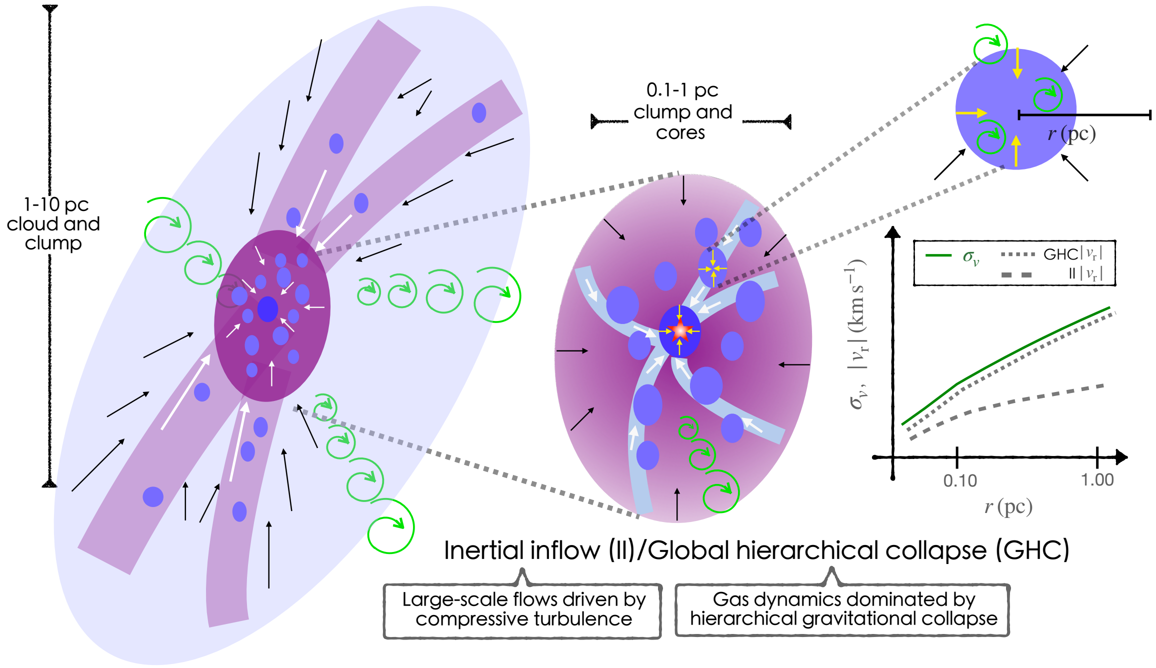

Figure 1.2: Schematic views of the *inertial inflow* model and *global hierarchical collapse* model (left and middle panels, with the middle one a zoom-in view on the central massive massive clump). The general configurations of cloud structures in the two models do not differ from each other. Markers at clump scale follow the same definitions as in Figure 1.1. At scale larger than the massive clump, elongated thick structures indicate filametary gas flows feeding the central clump, and the larger ellipse indicates the parental cloud structure. For these two models, the driving source of the large-scale (larger than core scale) gas flows feeding the central clump or core(s) is different: in the *inertial inflow* model, compressive turbulent motions are at the origin of the inflows, while in the *global hierarchical collapse* model cloud-scale gravitational collapse is playing the dominant role. One essential difference between the two models is the different relation between the velocity dispersion ($\sigma_{\rm v}$) and the radial velocity ($v_{\rm r}$) around the pre-stellar core: in the *global hierarchical collapse* model, $v_{\rm r}$ is comparable to $\sigma_{\rm v}$, as the turbulent motions result from gravitational collapse which dominates at all scales. While in the *inertial inflow* model, $v_{\rm r}$ are much less than $\sigma_{\rm v}$ at all radii, as inflow motions are mainly caused by compressive turbulence and beyond the pre-stellar core, the gas volumes are always gravitationally unbound ($\alpha_{\rm vir}>1$). This comparison is shown in right panel, in which the x-axis and y-axis sample the distance (radius) to the center of an arbitrary pre-stellar core and the corresponding velocity profiles of $v_{\rm r}$ and $\sigma_{\rm v}$. $v_{\rm r}$ of the *global hierarchical collapse* and *inertial inflow* model are shown in dotted and dashed lines in gray, respectively; $\sigma_{\rm v}$ is shown as green line.

1.3 Evolutionary sequence of massive star formation

Galaxy-wide surveys have provided large unbiased samples of massive star-forming clumps, and allowed a detailed diagnosis of their infrared properties. *Spitzer* imaging surveys at near-infrared to mid-infrared wavelengths (4 μm to 70 μm) identified a sample of infrared dark clouds (IRDC), seen as silhouettes against the bright, diffuse galactic background of mid-infrared emission (see, e.g. Menten, Pillai and Wyrowski 2005). They are cold and dense, believed to be representing the early stage of massive star-forming regions. The far-infrared and submm wavelengths emission of the clumps are further covered by the *Herschel* space telescope (70-500 μm), which enables a full establishment of the cloud SEDs. The SED constitutes an important evolutionary indicator (Molinari et al. 2016). Meanwhile, ground-based submillimeter bolometer cameras such as the Large APEX Bolometer Camera (Siringo et al. 2009) working at longer wavelength (870 μm) provide a two-fold better angular resolution (18$''$) than *Herschel* at 500 μm; the ATLASGAL survey (Schuller et al. 2009) revealed more than 10 000 star-forming dusty clumps in the galaxy (Contreras et al. 2013, Csengeri et al. 2014), which have relatively well-determined distances (Wienen et al. 2015, Urquhart et al. 2018). These large surveys, which enable statistical studies, allowed selecting representative targets for follow-up high-angular resolution sample/case studies; for most of the massive star-forming sites located farther away than 5 kpc, to reach below the typical core size (0.1 pc), <4$''$ angular resolution observations are mandatory for investigating the core populations and their associated gas flows.

The SED constructed from multi-wavelength observations of the dust continuum enables a quantitative evolutionary diagnosis towards large samples of massive clumps. If considered as isolated objects, the star formation process within massive clumps proceeds, roughly speaking, in two phases. The first phase is characterised by the conversion of a fraction of the clump gas mass into stellar objects, which results in an increasing bolometric luminosity. The luminosity during clump evolution is initially dominated by kinetic energy converted from gravitational collapse of gas. This accretion luminosity is given by (Stahler, Shu and Taam 1980):

$$L_{\rm acc} = f_{\rm acc}\frac{M_\star \dot{M}}{R_\star} \quad , \tag{1.8}$$

where $M_\star$ and $R_\star$ are the stellar mass and radius, and $\dot{M}$ is the accretion rate. $f_{\rm acc}$ is a factor quantifying the efficiency of this radiation, which is not a well-constrained, yet critical in protostellar evolution (Hosokawa, Offner and Krumholz 2011). At later stages (second phase) the luminosity is contributed mostly from the stellar radiation and is rather fixed. massive stars start nuclear burning while still actively accreting, but the stellar luminosity well exceeds the accretion luminosity even if the accretion rate is considerable $\sim 10^{-4}$ M$_\odot$ yr^{-1} (Krumholz et al. 2009). The second phase also features a significant dispersal of (remaining) gas due to the strong and diverse stellar feedback at work, i.e. the pressure from photonized gas and (proto)stellar winds, outflows, and radiation pressure. Based on the *turbulent core-collapse* model and assuming that massive clumps will collapse to form single massive stars, Molinari et al. (2008) put forward an evolutionary sequence following these two phases through changes in their SEDs: the luminosity to mass ratio (L/M) increases as an efficient evolutionary indicator. In this view, massive star formation is essentially seen as a scaled-up version of the formation of low-mass stars. The different evolutionary phases are correspondingly analogues to Class 0/I/II objects (Andre, Ward-Thompson and Barsony 1993, Adams, Lada and Shu 1987). This simple framework is further expanded by considering instead of single objects, the formation of a stellar cluster in Veneziani et al. (2017) and Molinari et al. (2019). Molinari et al. (2019) further incorporate the gas mass contained in core structures within massive clumps and a mid-IR color index ([24-70]) as two additional parameters to characterise the evolution of massive clumps. In addition to increasing L/M, it is shown that the dense core mass fraction increases along clump evolution.

The qualitative classification of clump evolutionary stages is also important. The empirical picture is that massive clumps initially harbour (mostly) pre-stellar cores which are dim at near- and mid-IR wavelengths, generally referred to as starless clumps or IRDCs (e.g. Carey et al. 2000, Peretto and Fuller 2009). With the continuing accretion and gravitational contraction, the pre-stellar cores evolve to be proto-stellar objects, emerging as hot-core structures. The hot-core stage is unique chemically since it shows significant line emission of complex organic molecules (COMs) as diagnostic signatures (Blake et al. 1987, Wyrowski et al. 1999, more in Sect. 1.5). Subsequent to the hot (massive) core (HMC) phase, the UV irradiation from the yound hot star creates an embedded ultra-compact Hii region (Churchwell 2002), which eventually expands, which together with a stellar wind and an outflow leads to the the dispersal of envelope gas. These processes are marked by several observational tracers: lack of near-IR and/or mid-IR emission, near-IR compact source, abundant molecular line emission of COMs, and appearance of radio continuum (centimeter emission) from Hii regions. The distinctive tracers of star-formation activities include also H_2O and Class II CH_3OH masers. H_2O masers, which are collisionally pumped in dense hot shocked material, are found in outflows, while radiatively pumped Class II CH_3OH masers arise from the dense, warm material close to the young stellar objects (e.g. Codella et al. 2004, Torrelles et al. 2003, Brogan et al. 2018). Particularly, strongly variable maser emission has been found to be associated with accretion bursts of massive young stellar objects (e.g. Goedhart, Gaylard and van der Walt 2003, Burns et al. 2020). The gas jet and outflow activities also cause near-IR ro-vibrational H_2 line emission (e.g. Varricatt et al. 2010, Caratti o Garatti et al. 2015) and radio emission (e.g. Purser et al. 2016). The shocks accompanying accretion and outflows/jets cause the formation of many molecules, e.g., SiO, sulfur-bearing species, COMs (more in Sect. 1.5). All these observational signposts can be used to characterize the evolutionary stages of massive clumps. Due to the more turbulent and intense dynamics (as compared to low-mass star-forming sites), massive clumps usually exhibit more clumpy structures with dynamical timescale changing drastically from one sub-region to another. The clumps might contain several cores in different evolutionary stages. This often makes results derived from a single diagnostic ambiguous.

The picture described above is a highly simplified description of the evolutionary sequence for massive clumps. In reality, sources in different evolutionary stages can co-exist in a certain clump, e.g. IRDCs are not completely infrared-dark but also commonly host localised embedded protostellar objects or young stars.

With the development of wide-band receivers for both single dish and interferometry, line surveys, covering wide frequency ranges in an unbiased way, become powerful tools to establish evolutionary indicators, as the chemical content is sensitive to both the cold collapse and heating processes (more in Sect. 1.5).

1.4 Molecular line and dust continuum emission: probing the physical properties of molecular clouds

Molecular lines carry important information on the physical properties of the ISM. Through molecular line excitation calculations, the volume density, temperature, and column density (abundance) of the

Table 1.1: Comparisons between scenarios of massive star formation

Model	Cloud status	Relation of HM and LM^a stars	Mass origin and accretion rate	Predictions
turbulent core-collapse	cores and clumps in hydrostatic equilibrium, supported by turbulence		mostly from localised cores $\dot{M}\propto$ M^s, s depends on clump density profile (if $\rho\,\propto r^{-1.5}$, $\dot{M}\propto t$)	supersonic, massive pre-stellar cores in a turbulent parental clump
competitive accretion	gravitationally bound clump	HM seeds locate early and grow in the center	core and clump Bondi-Hoyle, tidal-lobe $\dot{M}\propto M^2$, $\dot{M}\propto M^{2/3}$	pre-existing low-mass proto-systems of Jeans mass objects, mass segregation, no isolated massive stars
global hierarchical collapse	pressureless gravitational contraction in a hierarchical manner	LM stars form early HM stars form late	large-scale cloud *continuously*, Bondi-Hoyle, $\dot{M}\propto M^2$ with large scatter at lower M	large-scale infall motions, time-delay of Jeans fragmentation, new generation of fragments locate *within* preceding ones comparable infall and turbulent velocity
inertial inflow	turbulent and gravitationally unbound	HM stars can have an in flow region of ~10 pc, $t_{\rm form}\propto R_{\rm inflow}$	pc-scale supersonic inflow approximately constant $\dot{M}$ with fluctuations	inflow velocity less than the turbulent linewidth, mass-inflow rate increase with scale

^{a}: HM–massive stars; LM–low-mass stars.

gas (H_2), which are essential physical properties quantifying molecular clouds, can be constrained. Particularly, the variety of molecular species and multiple transitions involving different energy levels can provide diagnosis of a wide range of physical conditions. For the definitions and formulas used in this section, and more detailed discussions of the topic of radiative transfer, we refer to the textbooks of Rybicki and Lightman (1985), Draine (2011) and Hubeny and Mihalas (2014) in general if not stated otherwise.

1.4.1 The level population of molecular lines and radiative transfer

The population of the energy levels of a molecule is governed by radiation and collision processes. The de-excitation of molecule by radiation is through stimulated and spontaneous emission. Collisions between the molecule and collisional partners (in dense clouds mainly H_2) can cause both de-excitation and excitation. Considering a two-level energy system with populations of n_1 and n_2, the populations of the two levels change, in statistical equilibrium, as

$$\begin{aligned}\frac{dn_1}{dt} &= -n_1(B_{12}\bar{J} + C_{12}) + n_2(A_{21} + B_{21}\bar{J} + C_{21})\\ \frac{dn_2}{dt} &= n_1(B_{12}\bar{J} + C_{12}) - n_2(A_{21} + B_{21}\bar{J} + C_{21})\ .\end{aligned} \tag{1.9}$$

In this expression, $\bar{J}$ stands for the integrated radiation field averaged over all directions,

$$\bar{J} = \frac{1}{4\pi}\int I_\nu d\Omega \int_0^\infty \phi_\nu d\nu \tag{1.10}$$

while ϕ_ν is the line profile. I_ν is the specific intensity at frequency ν. $A_{\rm ij}$ and $B_{\rm ij}$ are the Einstein A and B coefficients. $C_{\rm ij}$ is the collisional rate of the two levels, defined by:

$$C_{ij} = \Sigma n_{\rm colp} K_{ij} \tag{1.11}$$

where $n_{\rm colp}$ denotes the density of a certain collisional partner that contributes by an coefficient of $K_{\rm ij}$; $K_{\rm ij}$ and $K_{\rm ij}$ fulfill the detailed balance relation,

$$K_{ji} = K_{ij}\frac{g_j}{g_i}e^{(\frac{h\nu_{ij}}{kT_{\rm kin}})} \tag{1.12}$$

where $g_{\rm i}$ is the statistical weight of the respective level and k is the Boltzmann coefficient, $T_{\rm kin}$ is the kinetic temperature, ν_{ij} is the frequency of the transition. $K_{\rm ij}$ is independent of $n_{\rm colp}$, but depends on the temperature via the distribution of velocity (u) of the collisional partners; it is defined as,

$$K_{ij} = \langle u\sigma_{ij}\rangle = \int u\sigma_{ij} f(u) d^3u \tag{1.13}$$

where the integral is done over velocity space with $f(u)d^3u$ as the velocity distribution function. σ_{ij} is the cross section. The Maxwellian velocity distribution follows,

$$f(u)d^3u = (\frac{m}{2\pi kT})^{3/2} e^{-\frac{mu^2}{2kT}} 4\pi u^2 du \tag{1.14}$$

$$\sigma_{ij} = \frac{\pi}{g_i}(\frac{h}{2\pi mu})^2 \Omega_{ij} = \frac{\pi}{g_i}(\frac{\hbar}{mu})^2 \Omega_{ij} \tag{1.15}$$

where m is the mass of the colliding particles. Ω_{ij} is a dimensionless factor quantifying the deviation of the cross section from that having a radius close to De Broglie wavelength. Substituting this velocity distribution in Eq. (1.13), one obtains (after integration),

$$K_{ij} = \frac{\hbar^2}{g_i m^{3/2}} \sqrt{\frac{2\pi}{kT}} \Omega_{ij} \quad . \tag{1.16}$$

The Einstein coefficients are related by

$$g_1 B_{12} = g_2 B_{21} \tag{1.17}$$

$$A_{21} = \frac{2h\nu^3}{c^2} B_{21} \tag{1.18}$$

where ν is the frequency of the transition under consideration, h is Planck constant and c the speed of light. With these definitions, we now return to specific intensity I_ν, which is the core variable in the radiative transfer equation. I_ν changes due to primarily two aspects: absorption and emission. The equation is written as:

$$\frac{dI_\nu}{ds} = j_\nu(r) - \alpha_\nu(r) I_\nu \tag{1.19}$$

where j_ν(r) is the position-dependent emission coefficient, and α_ν(r) the absorption coefficient. These are determined by:

$$\begin{aligned} j_\nu &= \frac{h\nu}{4\pi} n_2 A_{21} \phi_\nu \\ \alpha_\nu &= \frac{h\nu}{4\pi} (n_1 B_{12} - n_2 B_{21}) \phi_\nu \quad . \end{aligned} \tag{1.20}$$

The optical depth is defined as the absorption coefficients along the path:

$$\tau_\nu(s) = \int_0^s \alpha(s') ds' \quad . \tag{1.21}$$

The radiative transfer equation can be expressed with τ_ν instead,

$$\frac{dI_\nu}{d\tau_\nu} = -I_\nu + S_\nu(\tau_\nu) \tag{1.22}$$

which is a first-order differential equation in which $S_\nu(\tau_\nu)$ is the source function, defined as the ratio of the emission and absorption coefficients, j_ν/α_ν. The solution to Eq. (1.22) is

$$I_\nu(\tau_\nu) = I_\nu(0)e^{-\tau_\nu} + \int_0^{\tau_\nu} S_\nu e^{-(\tau_\nu - \tau'_\nu)} d\tau'_\nu \ . \tag{1.23}$$

As seen from Eq. (1.9), (1.20), and (1.22), the radiation field and level populations are mutually dependent. Moreover the radiative transfer problem is a non-local one, as a photon emitted in one position in the cloud can affect the level population in another through the radiation field. In the following, we look at the solutions of radiative transfer equation based on simple assumptions. These assumptions essentially decouple the effect of level populations and the radiation field and/or make the problem a much simpler local excitation problem. In Sect. 1.4.3 we summarise briefly the non-local solutions.

For the ISM, statistical equilibrium can often be assumed, i.e. for all the levels Eq. (1.9) fulfills, $dn_i/dt = 0$, Eq. (1.9) becomes

$$n_1(C_{12} + B_{12}\bar{J}) = n_2(C_{21} + B_{21}\bar{J} + A_{21}) \ . \tag{1.24}$$

Further, to describe the relative level populations, the two levels denoted as u and l it holds

$$\frac{n_u}{n_l} = \frac{g_u}{g_l} e^{-\frac{h\nu}{kT_{\mathrm{ex}}}} \ . \tag{1.25}$$

This equation defines the excitation temperature T_{ex}, which in thermal equilibrium is equal to the kinetic temperature. T_{ex} can also be defined with Planck function, assuming an infinite large uniform medium in which the radiation field is described as blackbody radiation, such that $I_\nu = B_\nu\ (T_{\mathrm{ex}}) = S_\nu$. The condition is generally referred to as "local thermodynamic equilibrium" (LTE). From Eq. (1.24) it can be gauged when LTE is met, i.e. when the collisional de-excitation dominates over radiative decay in setting the statistical equilibrium. For a multi-level energy system, in general, it must be that

$$\Sigma_{j<i} A_{ij} \ll \Sigma\, C_{ik} \tag{1.26}$$

where k runs over all collision-related energy levels with level i. This relation defines a critical density,

$$n_{\mathrm{crit}} = \frac{\Sigma_{j<i} A_{ij}}{\Sigma\, K_{ik}} \ . \tag{1.27}$$

Correspondingly, when the density of a collisional partner n_{colp} is lower than n_{crit}, the population of excited energy levels is lower than in the thermodynamic limit, i.e. lower than that predicted from a Boltzmann distribution, due to insufficient collisional excitation. When the LTE condition is met, T_{kin} is equal to T_{ex}. In general, T_{ex} is a sigmoid function that varies between background radiation temperature at low density and T_{kin} at high density (e.g. Shirley 2015). Assuming no ambient radiation field ($\bar{J} = 0$), considering again a two-level system, for T_{ex} and T_{kin} it holds

$$\frac{T_{\mathrm{kin}}}{T_{\mathrm{ex}}} = 1 + \frac{kT_{\mathrm{kin}}}{E_{21}} \ln\left(1 + \frac{n_{\mathrm{crit}}}{n_{\mathrm{colp}}}\right) \tag{1.28}$$

with E_{u} denotes the upper energy level, which is derived from Eq. (1.24), (1.12) and (1.25). It can be seen from this relation that when $n_{\mathrm{colp}} < n_{\mathrm{crit}}$, that $T_{\mathrm{ex}} \sim \mathrm{T}_{\mathrm{kin}}$ can still be met if the energy level of the transition under consideration E_{u} is much larger than kT_{kin}, although this is hard to fulfill since the line emission is likely weak under such conditions. Under the LTE assumption, using level population calculations, commonly referred to as population diagram analysis, the gas temperature (T_{rot}) and molecular column density (N_{mol}) can be estimated (Goldsmith and Langer 1999). The temperature calculated this way is the rotational temperature. The two quantities T_{rot} and N_{mol} are connected with a certain level population, denoted as u, through,

$$\frac{N_{\mathrm{mol}}}{N_u} = \frac{Q_{\mathrm{rot}}}{g_u}\exp(\frac{E_u}{kT_{\mathrm{ex}}}) \tag{1.29}$$

$$N_u = \frac{8\pi\nu^3}{A_{ul}c^3}[exp(\frac{h\nu}{kT_{\mathrm{ex}}}) - 1]^{-1}\int \tau_\nu d\nu \tag{1.30}$$

where $T_{\mathrm{ex}} = T_{\mathrm{rot}}$, E_{u} denotes the upper energy level, and $Q_{\mathrm{rot}}(T_{\mathrm{rot}}$ is the “rotational partition function", the sum over all Boltzmann factors, $\sum_i g_i\, e^{-E_i/kT_{\mathrm{rot}}}$. For a determination of T_{ex} and N_{mol}, at least two transitions must be observed, which link $\int \tau_\nu d\nu$ to the observed integrated intensities W, as

$$W = \int T_{\mathrm{B}} d\nu$$

$$T_{\mathrm{B}} = f(J(T_{\mathrm{ex}}) - J(T_{\mathrm{bg}}))(1 - \exp(-\tau_\nu)) \tag{1.31}$$

where T_{B} denotes the measured main-beam brightness temperature, and f the beam filling factor of the emission. Substituting for $\int \tau_\nu d\nu$ to Eq.(1.31), yields,

$$ln\frac{8\pi k\nu^2}{A_{ul}hc^3}\frac{W}{g_u} = ln\,N_{\mathrm{mol}} - ln\,C_\tau - ln\,Q_{\mathrm{rot}} - \frac{E_u}{kT} \tag{1.32}$$

$$C_\tau = \frac{\tau}{1 - e^{-\tau}} \tag{1.33}$$

in which C_τ is referred to as optical depth correction factor (Goldsmith and Langer 1999), which indicates the difference between this general form to derive N_{mol} and the form when the optically thin assumption is made.

With the optically thin assumption and with Eq.(1.33), N_{mol} and T_{ex} can be fitted with a linear function, where $1/T_{\mathrm{ex}}$ is the negative slope and N_{mol} is related to the intercept. In order to account for C_τ, on the other hand, an iterative procedure is required.

We can see that the LTE condition decouples the level population and radiation field in the radiative transfer equation as the Boltzmann equation solely determines the level population through the gas temperature T_{ex}. For gas densities lower than n_{crit}, the LTE assumption does not hold. To reduce the radiative transfer problem to a local process, two assumptions have to be made: (1) the excitation conditions within the cloud in consideration are uniform, (2) if a radiated photon is to be absorbed, it gets absorbed at the position of its emission. With (1) and no background radiation, Eq. 1.10 and Eq. 1.23 simplify to

$$\bar{J} = S(1 - \langle e^{-\tau} \rangle)\ , \tag{1.34}$$

where the brackets indicate averaging over all directions; S is the source function derived by profile averaged S_ν. We can define the escape probability β as,

$$\beta = \langle e^{-\tau} \rangle \ . \tag{1.35}$$

With this relation, the statistical equilibrium relation, Eq. 1.24 takes the simpler form,

$$n_1 C_{12} - n_2 C_{21} - \beta n_2 A_{21} = 0 \ . \tag{1.36}$$

Hence, the level populations can be solved independently with the assumption that β is independent of the radiation field. β depends on the geometry and velocity structure of the cloud in consideration. If the cloud has a velocity gradient in its flow field that is large than the fluctuation of velocity distribution at a certain point, as generally referred to as the large velocity gradient (LVG) approximation, then,

$$\beta = \frac{1 - e^{-\tau}}{\tau} \ . \tag{1.37}$$

Similarly, there are expressions of β calculated for other typical geometries of clouds. With β defined as a function of optical depth, solving Eq. 1.36 becomes an iterative problem: one can start with an initial guess of β and derive the level populations (through τ); a modified β can be updated and one iterates on this process till the self-consistent level population and optical depth are found. This is the calculation method adopted by the widely used non-LTE RADEX modeling program (van der Tak et al. 2007).

1.4.2 Dust emission and dust grain properties

Although comprising only 1% of the mass budget of the ISM, dust is a major coolant of dense molecular clouds (10^4-10^5 cm^{-3}) and thus has an important role in the ISM thermodynamics, and henceforth in the formation process of stars. The continuum emission of dust is therefore another vital probe of physical properties of interstellar medium and molecular clouds. The emission results from irradiation of mainly starlight that emits originally at high frequencies, i.e. optical wavelengths. The emission has the form of thermal radiation at infrared (IR) wavelength. This heating process of dust can be formulated as,

$$(\frac{dE}{dt})_{\rm abs} = \int \frac{u_\nu d\nu}{h\nu} h\nu c Q_{\rm abs}(\nu)\pi a^2 \tag{1.38}$$

where the number density of photons in the frequency range ν, $\nu + d\nu$ is denoted as $\frac{u_\nu d\nu}{h\nu}$, each having energy of $h\nu$, and the dust grain has a mass absorption cross section of $C_{\rm abs} = Q_{\rm abs}(\nu)\pi a^2$. Here, a stands for the radius of an equal-volume sphere for the dust grain, and $Q_{\rm abs}$ the absorption coefficient. Another heating avenue of dust is through collisions with gas. The energy transfer of this process is

$$(\frac{dE}{dt})_{\rm col} = \Sigma n_i (\frac{8kT_{\rm g}}{\pi m_i})^{1/2} \pi a^2 \alpha_i 2k(T_{\rm g} - T_{\rm d}) \tag{1.39}$$

where $n_{\rm i}$ and $m_{\rm i}$ are, respectively, the number density and mass of a certain gas species contributing to the sum. $\alpha_{\rm i}$ denotes the efficiency of energy transfer in the range of [0, 1]: for full elastic collision α_i = 0. $T_{\rm g}$ and $T_{\rm d}$ are gas and dust temperature, respectively. It can be seen that the energy transfer rate is proportional to the temperature difference of gas and dust. At high gas densities, thermal equilibrium of gas and dust is established quickly from sufficient collisions. The energy rate of thermal radiation of dust follows,

$$(\frac{dE}{dt})_{\rm emi} = \int d\nu 4\pi B_\nu(T_{\rm d})C_{\rm abs}(\nu) = 4\pi a^2\langle Q_{\rm abs}\rangle\sigma T_{\rm d}^4 \tag{1.40}$$

in which σ is the Stefan-Boltzmann constant. $\langle Q_{\rm abs}\rangle$ is Planck averaged of $Q_{\rm abs}$. Equating Eq. (1.38) and (1.40) gives the thermal equilibrium of dust grains with the radiation field. It is usually established in the presence of large grains (a $\gtrsim$ 0.02 μm) that have larger enthalpy than the incident photons. The smaller size grains are prone to stochastic heating and are subject to time-varying temperature jumps. It is the equilibrium temperature of dust ($T_{\rm d}$) that is used in quantifying physical conditions of molecular clouds, since the larger size grains in equilibrium dominate the mass budget of dust. Instead of using $C_{\rm abs}$, the literature refers commonly to the dust opacity: $\kappa(\nu)$ is defined as $C_{\rm abs}(\nu)$ normalized by the mass of a dust grain. Dust opacity changes with physical conditions and grain composition. It increases with gas density and the carbon content (with respect to silicate) in dust composition. It has been shown that κ_ν can be described by a power-law form at far-IR and sub-millimeter wavelengths,

$$\kappa_\nu = \kappa_0(\frac{\nu}{\nu_0})^\beta \tag{1.41}$$

where β is referred to as the dust emissivity index or opacity index, and κ_0 is a reference dust opacity value at frequency ν_0. A smaller β corresponds to lower dust opacities. Observations have shown that dust in the Galactic plane has typically β~1.7-2.0. A smaller β may indicate grain growth in a dense environment, by accretion and coagulation processes. Variations in β are observed particularly in dense cores and proto-planetary disks, by FIR-submm observations that establish an SED or/and IR spectroscopic diagnosis (e.g. Roy et al. 2013, Natta et al. 2007, Pérez et al. 2012). The timescale of dust growth in molecular clouds is primarily dependent on the gas density (Draine 1990) and also turbulent motions (for large size of grains, e.g. Ossenkopf 1993). The coagulation timescale is generally larger than the dynamical timescale of typical molecular clouds of $\lesssim 10^7$ cm^{-3} (e.g. Ormel et al. 2009), while long-term stabilization of a cloud can boost the amount of grain growth.

From Eq (1.40), it can be seen that the cooling rate of dust emission is proportional to $T^{4+\beta}$. Following the general solution of the radiative transfer equation Eq (1.23), assuming no emitting source in the background and a single, uniform cloud, it becomes,

$$I_\nu = S_\nu(1 - e^{-\tau_\nu}) \tag{1.42}$$

in which τ_ν, following Eq (1.21), is described as,

$$\tau_\nu = \int_0^s \kappa_\nu\rho ds' = \frac{1}{R}\kappa_\nu\mu_{\rm H_2}m_{\rm H}\int n_{\rm H_2}ds' = \frac{1}{R}\kappa_\nu\mu_{\rm H_2}m_{\rm H}N_{\rm H_2} \tag{1.43}$$

where R stands for the gas-to-dust mass ratio. $\mu_{\rm H_2}$ is the relative molecular weight and $m_{\rm H}$ the mass of a proton. $n_{\rm H_2}$ and $N_{\rm H_2}$ are the volume density and column density of hydrogen. Eq (1.42) and (1.43) are commonly adopted for estimating cloud mass from dust emission from far-IR to millimeter wavelengths, by constructing the SED, which yields simultaneously molecular gas mass, and dust temperature $T_{\rm d}$, which is determined, according to Wien's law, from the peak frequency of the modified

Planck function fitted to the SED. When longer wavelengths millimeter data is available, β can also be simultaneously constrained. An anti-correlation between β and T_d is observed in the general ISM and in molecular clouds (Dupac et al. 2003, Planck Collaboration et al. 2011) as predicted by dust opacity modeling (e.g. Boudet et al. 2005). This indicates different grain properties, although mixing of physical conditions, e.g. temperature gradients, as well as observational uncertainties can bias the estimate. From a technical side, least-square fitting can introduce a false anti-correlation of β-T_d (e.g. Shetty et al. 2009); Bayesian inference and hierarchical models can mitigate the issue (e.g. Galliano 2018). For shorter wavelength emission ($\lambda \lesssim 70\mu$m), stochastic heating (Draine and Li 2001) may cause unknown contribution from grains of smaller sizes. The ideal settings for measuring β is the diffuse ISM, where the interstellar radiation field is more uniform, and also cold dense cores.

T_d estimated from a single-component SED can be regarded as a line-of-sight *mass-weighted average* temperature that represents the condition for the bulk gas component. Temperature gradients caused by nearby heating sources are better probed by more sophisticated full radiative transfer calculations (Sect. 1.4.3). The assumptions on κ are the main source of uncertainty in estimating cloud mass using dust continuum: they are degenerate with each other. To constrain κ, an independent estimate of dust mass is needed, e.g. from optical measurements, which is only possible for the diffuse ISM. For typical physical conditions associated with dense molecular clouds, κ at submillimeter to millimeter wavelength can have a factor 2-3 times variation (Ossenkopf and Henning 1994), which is a major source uncertainty.

1.4.3 Solving the radiative transfer equation: a brief overview

There are two main strategies to solve the radiative transfer problem: Monte Carlo (MC) and deterministic approaches. They are adopted individually or in a hybrid manner by current state-of-art solvers for radiative transfer modeling. In this section, a brief summary of the methods is given, together with an overview of two state-of-art radiative transfer solvers, `LIME` (Brinch and Hogerheijde 2010) and `RADMC-3D` (Dullemond et al. 2012), which are used in this thesis (Chapter 3). We refer to the original papers of the two solvers for more details. For a thorough review of the Monte Carlo radiative transfer method and its development we refer to the recent paper of Noebauer and Sim (2019).

MC methods employ simulations to address the radiative transfer problem: the propagation of photons, absorption or scattering, through the medium is followed stochastically; when a sufficiently large population of test particles, which mimic photons, is in consideration, it collectively represents the transfer process and radiation field in an accurate way. One of the features for MC methods is that since the photon packages are followed explicitly, the location where the carried energy is deposited can be determined directly. For radiative transfer emission for dust, assuming radiation equilibrium, the dust temperature and spectral shape can be obtained together. Given the nature of MC methods, the programs can be implemented in a simple manner and easily parallelized to ease the computational time. The disadvantages of MC models include that the predicted physical quantities are subject to stochastic fluctuations which can be alleviated by involvement of large number of test photons, and that in conditions of high optical depth, the computational cost increases drastically; this is due to the more frequent interactions between the medium and photons, and because their interaction in MC methods has to be followed explicitly.

`RADMC-3D` is a pure MC solver, which is mainly used for continuum radiative transfer problems (Dullemond et al. 2012). It can self-consistently calculate dust temperatures with thermal MC simulations based on the assumption of radiative equilibrium. In the high optical depth limit, to reduce the computational time, it adopts a strategy of modified random walk, in which the analytical solution of the diffusion equation is used to predict the path of the photon package trapped in optically thick regions. The MC framework is based on the adaptive MC technique (Bjorkman and Wood (2001)), which is a temperature correction procedure that predicts the frequency distribution of the reemitted photons under the condition that opacity is temperature-independent. It is essentially a method relying on sampling photon absorption. `RADMC-3D` also incorporates a photon density sampling method, based on Lucy (1999), by summing up the path length of all photons passing through (not only those that are absorbed) a cell, yielding a more accurate temperature determination in the optically thin regime.

The deterministic solvers rely on an iterative method to compute the radiation field in a ray-tracing manner. The major problem these solvers face is known as the Lambda-iteration problem, in which optical depth effects cause slow convergence of the iterative procedure. Different techniques are employed to tackle this, among which the accelerated Lambda iteration (ALI) technique is commonly adopted (Rybicki and Hummer 1991). In a simple Lambda iteration framework, an approximate operator Λ-*operator* is used to describe the relation between the specific radiation intensity I_ν and level populations so that the radiative transfer equations can be solved iteratively. In order to achieve faster convergence, ALI goes a step further to separate the operator Λ-*operator* to an approximate part and a residual part: the former can be inverted directly given the current level populations, when used for the molecular line problems, while the former can be evaluated by level populations of previous iteration.

The core of ALI describes the radiative transfer equation as an iterative form,

$$J_\nu^{k+1} = \Lambda[S_\nu(J_\nu^k] \tag{1.44}$$

where Λ is a matrix with elements in the diagonal representing the radiative contribution from the cell, and non-diagonal elements the coupling between it with its neighbors. The separation of the Λ-*operator* follows,

$$J_\nu^{k+1} = \Lambda_{\text{ext}}[S_\nu(J_\nu^k)] + \Lambda_{\text{loc}}[S_\nu(J_\nu^{k+1})] \tag{1.45}$$

where Λ_{loc} represents the radiative interaction from the local neighborhood, which will dominate the external term Λ_{ext} in high opacity conditions. In the implementation of ALI (or similar to ALI) in the state-of-art `LIME` software, instead of constructing Λ, J_ν is splitted to a local and an external term, leading to a form similar to Eq. 1.23 in which the second term S_ν does not depend on τ_ν (Brinch and Hogerheijde 2010).

To simulate the ray-tracing process, `LIME` adopts a source model on a grid of cells, in which density, temperature, molecular abundance, velocity, radiation field and level population are kept constant. Photon packages are traced with directions randomly from random points of absorption; the random points can represent physical models in three-dimensional space. In this realisation, the molecular gas density profile is used as a probability distribution of grid points: the distance between a point to its neighbor is inversely proportional to the local density, to mimic the radiative trapping process which is determined by the mean free path. The mean free path l follows,

$$l = \frac{1}{\alpha_\nu \rho} = \frac{s}{\tau} \tag{1.46}$$

in which s denotes the travelled path length. Note that in line radiative transfer, α_ν is dependent on the level population (Eq. 1.20), so l no longer only depends on density. Nevertheless, using the density distribution to describe the spatial distribution of the random points is still a reasonable approach.

1.5 The observational quest for the massive star formation process

The massive star-formation scenarios, as presented in Sect. 1.2, can be broadly classified into two categories: the more dynamical view, in which most of the gas mass ending up in massive stars originates from the accumulation process, and the more static view, where the level of initial core mass matters. For distinguishing these two views, systematic searches for massive pre-stellar cores ($\gtrsim$30 $M_{\odot}$, $\lesssim$0.1 pc, hereafter MPCs, McKee and Tan 2003) are critical. Recent interferometric observations have identified several candidate MPCs (Duarte-Cabral et al. 2013, Kong et al. 2018, Cyganowski et al. 2017, Liu et al. 2017, Nony et al. 2018) but the number remains low even though increasingly large samples are observed. Interestingly, these MPC candidates all reside in relatively evolved massive clumps, i.e. those with IR counterparts/hosting confirmed massive protostellar objects. Towards the massive starless clumps/candidates (IRDCs), recent ALMA observations reveal only low-mass core populations (Sanhueza et al. 2019, Svoboda et al. 2019) at $\sim$ 3000 -5000 au scales. On the other hand, observations over a continuous scale of massive star-formation sites have revealed a picture showing multi-scale gas inflow and collapse: in fact, many of the most extreme massive star-forming clumps (in terms of mass scale and density) are ridge or hub-like structures, which are interconnected regions of multiple filamentary structures, akin to rivers (e.g. Schneider et al. 2010, Liu, Zhang and Ho 2011, Peretto et al. 2013, Treviño-Morales et al. 2019, Chen et al. 2019). Such geometrical configurations of the gas may favor the scenario of *global hierarchical collapse* or similarly the paradigm of convergent flow models, in which initial cores are only seeds of subsequent accretion and fed by gas flows from much larger scales.

Illuminating the fragmentation process of massive clumps is critical to understand the OB cluster formation. The mass of the cores and core mass distribution is one aspect of quantifying fragmentation properties. In addition to the considerable uncertainties of core mass estimation, there is an observational ambiguity that higher angular resolution observations might resolve the core mass into multiple objects, while coarser resolution observations may tend to resolve over-massive cores, much larger than Jeans fragmentation prediction. The length scale of the core spatial distribution might be a more robust measure of fragmentation, as the clustering scales can be distinguished hierarchically and linked to the key physical properties (density, temperature and velocity dispersion) of each hierarchy resolved at a certain physical scale. In light of this, observations towards early-stage massive clumps with better than thousands of AU physical resolution seem to reveal consistently a pure thermal Jeans fragmentation scenario to explain the spatial distribution of most cores/YSO objects (Palau et al. 2018, Sanhueza et al. 2019, Svoboda et al. 2019), i.e. the characteristic separations are close to the thermal Jeans length.

Fragmentation of clumps at a more evolved stage sometimes shows a spatial distribution whose characteristic scale is smaller than the critical thermal Jeans scale, which is suggested to be due to dynamical evolution after the initial fragmentation (Beuther et al. 2018). On the other hand, global collapse of gas with much smaller bulk density, may be at the origin of the seemingly over-massive cores: the cores may actually originate from a gas environment of higher Jeans mass (Csengeri et al. 2017). These results, based on high angular resolution observations and increased mass sensitivities, have revealed a picture that is in contrast to previous results that discovered over-massive cores in early-stage massive clumps and attribute their existence to turbulence support (e.g. Zhang and Wang 2011, Wang et al. 2014). However, due to the evolution and layering of the different gas densities within massive clumps and their larger embedding environment that participates in the mass accumulation, the fragmentation processes are expected to be hierarchical. In this sense, these results together may instead indicate a fragmentation process that is spatially and temporarily variable (e.g. Vázquez-Semadeni et al. 2019), reflecting different dominant physics that change over scales and with evolution. In light of this, high dynamical range measurements of gas physical properties towards massive clumps over multiple scales and analysis of fragmentation on scales larger than the typical Jeans length ($\gtrsim$ 6000 au -0.1 pc, for gas density of $\sim 10^{4.5}$-10^{6} cm^{-3} and temperature of 20 K) are important avenues to understand the multi-scale fragmentation process. Particularly, the existence of MPCs in environments where feedback is already at work may hint at the importance of heating mechanisms in shaping the core masses, which offset the trend of more fragmentation in increasingly denser gas environment as clouds evolve. This is highlighted in numerical simulations that include radiative feedback (e.g. Krumholz, Klein and McKee 2012, Offner et al. 2009, Hennebelle et al. 2020). Combined observations of localised cores and extended gas structures of massive clumps along evolutionary tracks are critical to shed light on the massive star-formation scenario and the origin of the multiplicity of OB clusters.

To distinguish between different formation scenarios, measurements of the infall/accretion rates and their evolution are important proofs. Direct measurements of infall motions are possible by observing lines showing red-shifted absorption against background continuum sources, which mostly avoid confusion with other motions compared to observations of emission lines. Traditionally cm-wavelength red-shifted absorption lines of ammonia have been used to probe the infall motions associated with HCHII regions (Keto, Ho and Haschick 1988, Sollins et al. 2005). Wyrowski et al. (2012, 2016) use ammonia absorption lines in the THz regime to probe the infall motions around massive star-forming sites which include evolutionary stages prior to appearance of HII regions, and derive infall rates on the clump scale of 3 $\times 10^{-4}$ -2 $\times 10^{-2}$ M$_\odot$ yr^{-1}. They found no systematic variations of infall rates of different evolutionary stages.

Close to the hot core and disk, rotational lines of molecules in the submillimeter wavelengths range can also turn into absorption against the bright optical thick dust continuum. Observations by Zapata et al. (2008) and Beltrán et al. (2011, 2018) similarly suggest mass accretion rates up to 1 -7$\times$ 10^{-2} M$_\odot$ yr^{-1}. These results are usually based on modeling of localized absorption lines in the foreground of the continuum and the spatial change of infall rates may not be hinted, so that the modelling has to rely on the assumption of infall velocity profiles. Also, spherical accretion is usually assumed. By mapping the large-scale gas kinematics, velocity gradients along the gas streams can give another inflow rate measurement. The longitudal inflows along filamentary structures are frequently resolved, indicating the importance of highly elongated geometries in the mass accumulation process (e.g. Peretto et al. 2014, Tackenberg et al. 2014). As a reference, Lu et al. (2018) derive an inflow rate of 10^{-4} M$_\odot$ along massive filaments of 1-2 pc length, which are feeding protostellar cores (see also Chen et al. 2019). A caveat is that all these measurements are quantifying the infall rates from ambient gas to the star-forming cores/disks which may not be equal to the accretion rates onto the stars themselves. An indirect measure of the latter has to assume a ratio between the outflow mass loss and accretion rate (Shu et al. 1999, Frank et al. 2014), and then yield a characteristic accretion rate from observing outflow/jet activities (e.g. Beuther et al. 2002). The spatially and temporally varying infall rates, if probed, can be critical evidence to distinguish between different massive star formation scenarios (Sect. 1.2).

With the physical evolution of massive clumps, chemical processes leading to the formation and destruction of different molecular species are taking place. Molecular abundances, varying with changes in, e.g., the gas density, temperature and radiative processes, can be used as an effective diagnosis of the clump evolution, and constrain the timescales of physical phases. Although massive star-forming regions undergo more complex dynamics that are prone to stronger interplay between different physical processes, they share some general similarities of chemical evolution to low-mass stars due to the prevailing, if scaled-up physics at each stage (Jørgensen, Belloche and Garrod 2020). The evolution of low-mass cores follows relatively well-known phases. The initial stage as pre-stellar cores is characterised by low temperature (<10 K) and dense gas (10^3 -10^4 cm^{-3}). At this stage, most gaseous molecules freeze out onto the dust grain surface which form icy mantles, including the most abundant CO molecule. During collapse, the gas is heated by the conversion of gravitational energy to thermal energy, and also becomes denser ($\gtrsim 10^8$ cm^{-3}). When the temperature reaches 100 K, the icy mantles start to sublimate, which release the molecules formed on the grain surface into the gas phase. Subsequently, gas-phase chemical reactions produce more complex molecules, resulting in the so-called hot corino stage for low-mass cores. At this stage, abundant complex organic molecules (COMs) can be observed through multiple rotational lines. Throughout the evolution, processes accompanying the star formation activities, such as jets/outflows, and infall motions, can create shocks in the ambient gas, which also invoke chemical complexity in the gas phase through shock chemistry (Kaufman and Neufeld 1996).

Massive clumps usually host cores that are in different evolutionary stages, but the bulk gas environment may follow a similar physical evolution as evolution as that of low-mass cores, which starts from cold collapse (globally) and undergoes progressively intense gas heating. It is natural to expect massive clumps keep track of a qualitatively similar chemical evolution, especially before the the intense UV radiation kicks in to introduce an active UV photochemistry. For example, as scaled-up counterparts to starless and pre-stellar cores, massive starless clumps (e.g. Molet et al. 2019) are also observed to have emission of both saturated and unsaturated COMs (CH_3OH, CH_3CN), which sometimes appear offset from the peak of dust emission, showing similar picture as that of low-mass cores (e.g. Soma et al. 2015, Punanova et al. 2018). Emission from SiO and sulfur-bearing species are present in massive clumps in their early evolutionary phases. This indicates outflowing shocked gas (Feng et al. 2016, Jiménez-Serra et al. 2010). Elevated SiO abundances are the results of the destruction of silicate grains in fast shocks (Schilke et al. 1997). The abundance ratios of some sulfur-bearing molecules (OCS, SO_2, SO) have been suggested to be chemical clocks for IRDCs (Herpin et al. 2009, Esplugues et al. 2014). But there are also unique shock features of massive star-forming regions. For example, very extended SiO emission ($\gtrsim$1-5 pc) with narrow linewidths is frequently observed towards young massive clouds, which may be signatures of low-velocity cloud collisions (Louvet et al. 2016, Cosentino et al. 2020), or fossil records of outflows from preceding epoch of star formation (López-Sepulcre et al. 2016).

The kinematics of various tracers can be used to investigate the dynamical history of massive clump formation. Along the evolutionary track of massive clumps, it is found that a series of organic molecules including CH_3CN, CH_3CCH and CH_3OH can trace the progressively heated gas temperature profiles, showing continuously varying temperatures from the central region to the outer envelopes (Giannetti et al. 2017). The HMCs may be roughly regarded as a scaled-up version of hot corinos, as abundance ratios of many oxygen- and nitrogen-bearing species show tight correlations between the two types of sources (Jørgensen, Belloche and Garrod 2020). This may suggest that the preceding physical state, the cold collapse, is the dominant factor controlling the formation of COMs. In fact, with rather different excitation temperatures, COMs associated with massive clumps are classified into two categories, tracing either the relatively cold gas of <100 K or the hot gas (Bisschop et al. 2007). The prevalence of COMs at various stages of massive clumps, their numerous transitions due to complex energy level structure, and the dependence of their abundance on both thermal and non-thermal processes make them ideal tracers of clump physical properties. The chemical similarities and differentiation between massive clumps and low-mass cores require further investigations, before a comprehensive understanding of the relation between environment effects and chemical inventories can be attained.

1.6 Outline of thesis

Following the observational efforts in Sect. 1.5, in this thesis we investigate the physical structure of massive star-forming clumps with a special emphasis on the intermediate-scale ($\gtrsim$0.1-1 pc) gas structures which are connecting the core ($\lesssim$ 0.1 pc) and cloud ($\gtrsim$ 10 pc) scales. Particularly, we are interested in how the fragmentation process shapes the core populations in the early stages and along massive clump evolution, and whether the thermal properties and density structures of massive clumps follow a comprehensive evolution track towards OB cluster formation. A thorough understanding with stringent measurement of the physical structure of massive clumps is a pre-requisite for establishing the massive star-formation scenario. The thesis work is based on extensive radiative transfer modeling of high angular resolution dust continuum and various molecular lines data obtained from state-of-art wide-band spectroscopic survey. Chapter 2 of this thesis focuses on a large sample (>200) of massive star-forming clumps and investigations of their fragmentation properties using dust continuum emission (0.1-0.2 pc) from ground-based bolometers having best achievable angular resolution. In Chapter 3, utilising line surveys from the Submillimeter Array and APEX telescope, we conduct detailed modelings to probe the hierarchical density structure and temperature distribution of a representative sample of massive clumps that span an evolutionary sequence. Chapter 4 is a parallel study of Chapter 3 in which we target several massive clumps in the extreme cloud environment of W43-main molecular complex, to investigate the gas assembly process induced by cloud collisions and the influence of such gas dynamics on smaller scale structure formation and dense gas conversion, including both early-stage quiescent core structures and warm dense gas pockets which are likely shock processed. Finally, in Chapter 5 we summarise and discuss the results we obtained in the context of the current understanding of massive star formation process, and highlight several aspects to extend our line of works in the future.

References

Adams, Fred C., Charles J. Lada and Frank H. Shu (1987), *Spectral Evolution of Young Stellar Objects*, Astrophys. J. **312** 788 (cit. on p. 12).

Andre, P., D. Ward-Thompson and M. Barsony (2000), "From Prestellar Cores to Protostars: the Initial Conditions of Star Formation", *Protostars and Planets IV*, ed. by V. Mannings, A. P. Boss and S. S. Russell 59, arXiv: `astro-ph/9903284 [astro-ph]` (cit. on p. 5).

Andre, Philippe, Derek Ward-Thompson and Mary Barsony (1993), *Submillimeter Continuum Observations of rho Ophiuchi A: The Candidate Protostar VLA 1623 and Prestellar Clumps*, Astrophys. J. **406** 122 (cit. on p. 12).

André, P. et al. (2010), *From filamentary clouds to prestellar cores to the stellar IMF: Initial highlights from the Herschel Gould Belt Survey*, Astron. Astrophys. **518**, L102 L102, arXiv: `1005.2618` (cit. on p. 5).

Balfour, S. K., A. P. Whitworth and D. A. Hubber (2017), *Star formation triggered by non-head-on cloud-cloud collisions, and clouds with pre-collision sub-structure*, Mon. Not. R. Astron. Soc. **465** 3483 (cit. on p. 10).

Ballesteros-Paredes, Javier et al. (2015), *Bondi-Hoyle-Littleton accretion and the upper-mass stellar initial mass function*, Mon. Not. R. Astron. Soc. **452** 566, arXiv: `1506.02591 [astro-ph.GA]` (cit. on p. 10).

Basu, Shantanu and Telemachos Ch. Mouschovias (1995), *Magnetic Braking, Ambipolar Diffusion, and the Formation of Cloud Cores and Protostars. III. Effect of the Initial Mass-to-Flux Ratio*, Astrophys. J. **453** 271 (cit. on p. 4).

Bate, Matthew R. (2009), *The importance of radiative feedback for the stellar initial mass function*, Mon. Not. R. Astron. Soc. **392** 1363, arXiv: `0811.1035 [astro-ph]` (cit. on pp. 5, 7).

Bate, Matthew R. and Ian A. Bonnell (2005), *The origin of the initial mass function and its dependence on the mean Jeans mass in molecular clouds*, Mon. Not. R. Astron. Soc. **356** 1201, arXiv: `astro-ph/0411084 [astro-ph]` (cit. on p. 6).

Beltrán, M. T. et al. (2011), *Rotating toroids in G10.62-0.38, G19.61-0.23, and G29.96-0.02*, Astron. Astrophys. **525**, A151 A151, arXiv: `1010.0843 [astro-ph.GA]` (cit. on p. 24).

Beltrán, M. T. et al. (2018), *Accelerating infall and rotational spin-up in the hot molecular core G31.41+0.31*, Astron. Astrophys. **615**, A141 A141, arXiv: `1803.05300 [astro-ph.SR]` (cit. on p. 24).

Bertelli Motta, C. et al. (2016), *The IMF as a function of supersonic turbulence*, Mon. Not. R. Astron. Soc. **462** 4171, arXiv: `1608.01306 [astro-ph.GA]` (cit. on p. 7).

Bertoldi, Frank and Christopher F. McKee (1992), *Pressure-confined Clumps in Magnetized Molecular Clouds*, Astrophys. J. **395** 140 (cit. on p. 4).

Beuther, H. et al. (2002), *Massive molecular outflows*, Astron. Astrophys. **383** 892, arXiv: `astro-ph/0110372 [astro-ph]` (cit. on p. 24).

Beuther, H. et al. (2018), *Fragmentation and disk formation during high-mass star formation. IRAM NOEMA (Northern Extended Millimeter Array) large program CORE*, Astron. Astrophys. **617**, A100 A100, arXiv: `1805.01191 [astro-ph.GA]` (cit. on p. 23).

Bisschop, S. E. et al. (2007), *Testing grain-surface chemistry in massive hot-core regions*, Astron. Astrophys. **465** 913, arXiv: `astro-ph/0702066 [astro-ph]` (cit. on p. 26).

Bjorkman, J. E. and K. Wood (2001), *Radiative Equilibrium and Temperature Correction in Monte Carlo Radiation Transfer*, Astrophys. J. **554** 615, eprint: `astro-ph/0103249` (cit. on p. 22).

Blake, Geoffrey A. et al. (1987), *Molecular Abundances in OMC-1: The Chemical Composition of Interstellar Molecular Clouds and the Influence of Massive Star Formation*, Astrophys. J. **315** 621 (cit. on p. 13).

Bonnell, I. A., R. B. Larson and H. Zinnecker (2007), "The Origin of the Initial Mass Function", *Protostars and Planets V*, ed. by Bo Reipurth, David Jewitt and Klaus Keil 149, arXiv: `astro-ph/0603447 [astro-ph]` (cit. on p. 8).

Bonnell, I. A. et al. (2001a), *Accretion in stellar clusters and the initial mass function*, Mon. Not. R. Astron. Soc. **324** 573, arXiv: `astro-ph/0102121 [astro-ph]` (cit. on p. 6).

Bonnell, I. A. et al. (2001b), *Competitive accretion in embedded stellar clusters*, Mon. Not. R. Astron. Soc. **323** 785, arXiv: `astro-ph/0102074 [astro-ph]` (cit. on pp. 7, 8).

Bonnell, Ian A., Stephen G. Vine and Matthew R. Bate (2004), *Massive star formation: nurture, not nature*, Mon. Not. R. Astron. Soc. **349** 735, arXiv: `astro-ph/0401059 [astro-ph]` (cit. on p. 8).

Boudet, N. et al. (2005), *Temperature Dependence of the Submillimeter Absorption Coefficient of Amorphous Silicate Grains*, Astrophys. J. **633** 272 (cit. on p. 21).

Brinch, C. and M. R. Hogerheijde (2010), *LIME - a flexible, non-LTE line excitation and radiation transfer method for millimeter and far-infrared wavelengths*, Astron. Astrophys. **523**, A25 A25, arXiv: `1008.1492 [astro-ph.SR]` (cit. on pp. 21, 22).

Brogan, C. L. et al. (2018), *The Extraordinary Outburst in the Massive Protostellar System NGC 6334I-MM1: Flaring of the Water Masers in a North-South Bipolar Outflow Driven by MM1B*, Astrophys. J. **866**, 87 87, arXiv: `1809.04178 [astro-ph.SR]` (cit. on p. 13).

Burkhart, Blakesley et al. (2009), *Density Studies of MHD Interstellar Turbulence: Statistical Moments, Correlations and Bispectrum*, Astrophys. J. **693** 250, arXiv: `0811.0822 [astro-ph]` (cit. on p. 4).

Burns, R. A. et al. (2020), *A heatwave of accretion energy traced by masers in the G358-MM1 high-mass protostar*, Nature Astronomy **4** 506 (cit. on p. 13).

Caratti o Garatti, A. et al. (2015), *A near-infrared spectroscopic survey of massive jets towards extended green objects*, Astron. Astrophys. **573**, A82 A82, arXiv: `1410.4041 [astro-ph.SR]` (cit. on p. 13).

Carey, Sean J. et al. (2000), *Submillimeter Observations of Midcourse Space Experiment Galactic Infrared-Dark Clouds*, Astrophys. J. Letters **543** L157 (cit. on p. 13).

Caselli, P. and P. C. Myers (1995), *The Line Width–Size Relation in Massive Cloud Cores*, Astrophys. J. **446** 665 (cit. on p. 8).

Chabrier, G. and P. Hennebelle (2011), *Dimensional argument for the impact of turbulent support on the stellar initial mass function*, Astron. Astrophys. **534**, A106 A106, arXiv: `1109.2780 [astro-ph.SR]` (cit. on p. 4).

Chen, Che-Yu and Eve C. Ostriker (2015), *Anisotropic Formation of Magnetized Cores in Turbulent Clouds*, Astrophys. J. **810**, 126 126, arXiv: `1508.02710 [astro-ph.GA]` (cit. on p. 7).

Chen, Huei-Ru Vivien et al. (2019), *Filamentary Accretion Flows in the Infrared Dark Cloud G14.225–0.506 Revealed by ALMA*, Astrophys. J. **875**, 24 24, arXiv: `1903.04376 [astro-ph.GA]` (cit. on pp. 23, 24).

Churchwell, Ed (2002), *Ultra-Compact HII Regions and Massive Star Formation*, ARA&A **40** 27 (cit. on p. 13).

Codella, C. et al. (2004), *The association between masers and outflows in massive star forming regions*, Astron. Astrophys. **417** 615 (cit. on p. 13).

Commerçon, Benoît, Patrick Hennebelle and Thomas Henning (2011), *Collapse of Massive Magnetized Dense Cores Using Radiation Magnetohydrodynamics: Early Fragmentation Inhibition*, Astrophys. J. Letters **742**, L9 L9, arXiv: `1110.2955 [astro-ph.SR]` (cit. on p. 7).

Contreras, Y. et al. (2013), *ATLASGAL - compact source catalogue: 330° < ℓ < 21°*, Astron. Astrophys. **549**, A45 A45, arXiv: `1211.0741 [astro-ph.GA]` (cit. on p. 12).

Cosentino, G. et al. (2020), *SiO emission as a probe of cloud-cloud collisions in infrared dark clouds*, Mon. Not. R. Astron. Soc. **499** 1666, arXiv: `2009.13890 [astro-ph.GA]` (cit. on p. 25).

Csengeri, T. et al. (2014), *The ATLASGAL survey: a catalog of dust condensations in the Galactic plane*, Astron. Astrophys. **565**, A75 A75, arXiv: `1312.0937` (cit. on p. 12).

Csengeri, T. et al. (2017), *ALMA survey of massive cluster progenitors from ATLASGAL. Limited fragmentation at the early evolutionary stage of massive clumps*, Astron. Astrophys. **600**, L10 L10, arXiv: `1703.03273 [astro-ph.GA]` (cit. on p. 23).

Cunningham, Andrew J. et al. (2011), *Radiation-hydrodynamic Simulations of Massive Star Formation with Protostellar Outflows*, Astrophys. J. **740**, 107 107, arXiv: `1104.1218 [astro-ph.SR]` (cit. on p. 7).

Cunningham, Andrew J. et al. (2018), *The effects of magnetic fields and protostellar feedback on low-mass cluster formation*, Mon. Not. R. Astron. Soc. **476** 771, arXiv: `1709.01277 [astro-ph.GA]` (cit. on p. 7).

Cyganowski, C. J. et al. (2017), *Simultaneous low- and high-mass star formation in a massive protocluster: ALMA observations of G11.92-0.61*, Mon. Not. R. Astron. Soc. **468** 3694, arXiv: `1701.02802 [astro-ph.GA]` (cit. on p. 23).

Dale, James E. and Ian Bonnell (2011), *Ionizing feedback from massive stars in massive clusters: fake bubbles and untriggered star formation*, Mon. Not. R. Astron. Soc. **414** 321, arXiv: `1103.1532 [astro-ph.SR]` (cit. on p. 7).

Draine, B. T. and Aigen Li (2001), *Infrared Emission from Interstellar Dust. I. Stochastic Heating of Small Grains*, Astrophys. J. **551** 807, arXiv: `astro-ph/0011318 [astro-ph]` (cit. on p. 21).

Draine, Bruce T. (1990), "Evolution of interstellar dust.", *The Evolution of the Interstellar Medium*, ed. by Leo Blitz, vol. 12, Astronomical Society of the Pacific Conference Series 193 (cit. on p. 20).

– (2011), *Physics of the Interstellar and Intergalactic Medium* (cit. on p. 15).

Duarte-Cabral, A. et al. (2013), *CO outflows from high-mass Class 0 protostars in Cygnus-X*, Astron. Astrophys. **558**, A125 A125, arXiv: `1308.6490 [astro-ph.GA]` (cit. on p. 23).

Dullemond, C. P. et al. (2012), *RADMC-3D: A multi-purpose radiative transfer tool*, Astrophysics Source Code Library, ascl: `1202.015` (cit. on p. 21).

Dupac, X. et al. (2003), *Inverse temperature dependence of the dust submillimeter spectral index*, Astron. Astrophys. **404** L11, arXiv: `astro-ph/0304253 [astro-ph]` (cit. on p. 21).

Elmegreen, Bruce G. (1999), *Formation and Loss of Hierarchical Structure in Two-dimensional Magnetohydrodynamic Simulations of Wave-driven Turbulence in Interstellar Clouds*, Astrophys. J. **527** 266, arXiv: `astro-ph/9911156 [astro-ph]` (cit. on p. 4).

Elmegreen, Bruce G. and John Scalo (2004), *Interstellar Turbulence I: Observations and Processes*, ARA&A **42** 211, arXiv: `astro-ph/0404451 [astro-ph]` (cit. on p. 4).

Esplugues, G. B. et al. (2014), *Modelling the sulphur chemistry evolution in Orion KL*, Astron. Astrophys. **567**, A95 A95, arXiv: `1406.2278 [astro-ph.SR]` (cit. on p. 25).

Fall, S. M., M. R. Krumholz and C. D. Matzner (2010), *Stellar Feedback in Molecular Clouds and its Influence on the Mass Function of Young Star Clusters*, Astrophys. J. Letters **710** L142, arXiv: `0910.2238 [astro-ph.SR]` (cit. on p. 6).

Federrath, C. et al. (2010), *Comparing the statistics of interstellar turbulence in simulations and observations. Solenoidal versus compressive turbulence forcing*, Astron. Astrophys. **512**, A81 A81, arXiv: `0905.1060 [astro-ph.SR]` (cit. on p. 4).

Federrath, Christoph and Supratik Banerjee (2015), *The density structure and star formation rate of non-isothermal polytropic turbulence*, Mon. Not. R. Astron. Soc. **448** 3297, arXiv: `1412.2756 [astro-ph.GA]` (cit. on p. 5).

Federrath, Christoph et al. (2014), *Modeling Jet and Outflow Feedback during Star Cluster Formation*, Astrophys. J. **790**, 128 128, arXiv: `1406.3625 [astro-ph.SR]` (cit. on p. 7).

Feng, S. et al. (2016), *Outflow Detection in a 70 μm Dark High-Mass Core*, Astrophys. J. **828**, 100 100, arXiv: `1605.01736` (cit. on p. 25).

Frank, A. et al. (2014), "Jets and Outflows from Star to Cloud: Observations Confront Theory", *Protostars and Planets VI*, ed. by Henrik Beuther et al. 451, arXiv: `1402.3553 [astro-ph.SR]` (cit. on p. 24).

Fukui, Yasuo et al. (2021), *Rapid and efficient mass collection by a supersonic cloud-cloud collision as a major mechanism of high-mass star formation*, PASJ **73** S405, arXiv: `1909.08202 [astro-ph.GA]` (cit. on p. 10).

Galliano, Frédéric (2018), *A dust spectral energy distribution model with hierarchical Bayesian inference - I. Formalism and benchmarking*, Mon. Not. R. Astron. Soc. **476** 1445, arXiv: `1801.06660 [astro-ph.GA]` (cit. on p. 21).

Giannetti, A. et al. (2017), *ATLASGAL-selected massive clumps in the inner Galaxy. V. Temperature structure and evolution*, Astron. Astrophys. **603**, A33 A33, arXiv: `1703.08485 [astro-ph.GA]` (cit. on p. 25).

Goedhart, S., M. J. Gaylard and D. J. van der Walt (2003), *Periodic flares in the methanol maser source G9.62+0.20E*, Mon. Not. R. Astron. Soc. **339** L33 (cit. on p. 13).

Goldsmith, Paul F. and William D. Langer (1999), *Population Diagram Analysis of Molecular Line Emission*, Astrophys. J. **517** 209 (cit. on p. 18).

Gong, Hao and Eve C. Ostriker (2011), *Dense Core Formation in Supersonic Turbulent Converging Flows*, Astrophys. J. **729**, 120 120, arXiv: `1101.2650 [astro-ph.SR]` (cit. on p. 6).

Guszejnov, Dávid, Mark R. Krumholz and Philip F. Hopkins (2016a), *The necessity of feedback physics in setting the peak of the initial mass function*, Mon. Not. R. Astron. Soc. **458** 673, arXiv: `1510.05040 [astro-ph.SR]` (cit. on p. 5).

– (2016b), *The necessity of feedback physics in setting the peak of the initial mass function*, Mon. Not. R. Astron. Soc. **458** 673, arXiv: `1510.05040 [astro-ph.SR]` (cit. on p. 7).

Heitsch, Fabian, Mordecai-Mark Mac Low and Ralf S. Klessen (2001), *Gravitational Collapse in Turbulent Molecular Clouds. II. Magnetohydrodynamical Turbulence*, Astrophys. J. **547** 280, arXiv: `astro-ph/0009227 [astro-ph]` (cit. on p. 4).

Hennebelle, Patrick and Gilles Chabrier (2008), *Analytical Theory for the Initial Mass Function: CO Clumps and Prestellar Cores*, Astrophys. J. **684** 395, arXiv: `0805.0691 [astro-ph]` (cit. on pp. 4–6).

Hennebelle, Patrick and Edith Falgarone (2012), *Turbulent molecular clouds*, Astron. Astrophys. Rev. **20**, 55 55, arXiv: `1211.0637 [astro-ph.GA]` (cit. on p. 4).

Hennebelle, Patrick et al. (2020), *What is the role of stellar radiative feedback in setting the stellar mass spectrum?*, arXiv e-prints, arXiv:2010.03539 arXiv:2010.03539, arXiv: `2010.03539 [astro-ph.GA]` (cit. on p. 24).

Herpin, F. et al. (2009), *S-bearing molecules in massive dense cores*, Astron. Astrophys. **504** 853, arXiv: `0906.1122 [astro-ph.SR]` (cit. on p. 25).

Hollenbach, David J., Michael W. Werner and Edwin E. Salpeter (1971), *Molecular Hydrogen in H i Regions*, Astrophys. J. **163** 165 (cit. on p. 3).

Hopkins, Philip F. (2012a), *An excursion-set model for the structure of giant molecular clouds and the interstellar medium*, Mon. Not. R. Astron. Soc. **423** 2016, arXiv: `1111.2863 [astro-ph.GA]` (cit. on p. 6).

– (2012b), *An excursion-set model for the structure of giant molecular clouds and the interstellar medium*, Mon. Not. R. Astron. Soc. **423** 2016, arXiv: `1111.2863 [astro-ph.GA]` (cit. on p. 6).

– (2013), *A model for (non-lognormal) density distributions in isothermal turbulence*, Mon. Not. R. Astron. Soc. **430** 1880, arXiv: `1211.3119 [astro-ph.GA]` (cit. on p. 4).

Hosokawa, Takashi, Stella S. R. Offner and Mark R. Krumholz (2011), *On the Reliability of Stellar Ages and Age Spreads Inferred from Pre-main-sequence Evolutionary Models*, Astrophys. J. **738**, 140 140, arXiv: `1101.3599 [astro-ph.SR]` (cit. on p. 12).

Hubeny, Ivan and Dimitri Mihalas (2014), *Theory of Stellar Atmospheres* (cit. on p. 15).

Inoue, Tsuyoshi and Yasuo Fukui (2013), *Formation of Massive Molecular Cloud Cores by Cloud-Cloud Collision*, Astrophys. J. Letters **774**, L31 L31, arXiv: `1305.4655 [astro-ph.GA]` (cit. on p. 10).

Inoue, Tsuyoshi et al. (2018), *The formation of massive molecular filaments and massive stars triggered by a magnetohydrodynamic shock wave*, Pub. Astron. Soc. Japan **70**, S53 S53, arXiv: `1707.02035 [astro-ph.GA]` (cit. on p. 10).

Jappsen, A. -K. et al. (2005), *The stellar mass spectrum from non-isothermal gravoturbulent fragmentation*, Astron. Astrophys. **435** 611, arXiv: `astro-ph/0410351 [astro-ph]` (cit. on p. 5).

Jeans, J. H. (1902), *The Stability of a Spherical Nebula*, Philosophical Transactions of the Royal Society of London Series A **199** 1 (cit. on p. 3).

Jiménez-Serra, I. et al. (2010), *Parsec-scale SiO emission in an infrared dark cloud*, Mon. Not. R. Astron. Soc. **406** 187, arXiv: `1003.3463 [astro-ph.SR]` (cit. on p. 25).

Jørgensen, Jes K., Arnaud Belloche and Robin T. Garrod (2020), *Astrochemistry During the Formation of Stars*, ARA&A **58** 727, arXiv: `2006.07071 [astro-ph.SR]` (cit. on p. 25).

Kaufman, Michael J. and David A. Neufeld (1996), *Far-Infrared Water Emission from Magnetohydrodynamic Shock Waves*, Astrophys. J. **456** 611 (cit. on p. 25).

Keto, Eric R., Paul T. P. Ho and Aubrey D. Haschick (1988), *The Observed Structure of the Accretion Flow around G10.6-0.4*, Astrophys. J. **324** 920 (cit. on p. 24).

Kong, Shuo et al. (2018), *Zooming in to Massive Star Birth*, Astrophys. J. **867**, 94 94, arXiv: `1701.05953 [astro-ph.GA]` (cit. on p. 23).

Könyves, V. et al. (2015), *A census of dense cores in the Aquila cloud complex: SPIRE/PACS observations from the Herschel Gould Belt survey*, Astron. Astrophys. **584**, A91 A91, arXiv: `1507.05926 [astro-ph.GA]` (cit. on p. 5).

Krumholz, Mark R. and Christoph Federrath (2019), *The Role of Magnetic Fields in Setting the Star Formation Rate and the Initial Mass Function*, Frontiers in Astronomy and Space Sciences **6**, 7 7, arXiv: `1902.02557 [astro-ph.GA]` (cit. on p. 7).

Krumholz, Mark R., Richard I. Klein and Christopher F. McKee (2011), *Radiation-hydrodynamic Simulations of the Formation of Orion-like Star Clusters. I. Implications for the Origin of the Initial Mass Function*, Astrophys. J. **740**, 74 74, arXiv: `1104.2038 [astro-ph.GA]` (cit. on pp. 5, 7).

Krumholz, Mark R., Richard I. Klein and Christopher F. McKee (2012), *Radiation-hydrodynamic Simulations of the Formation of Orion-like Star Clusters. II. The Initial Mass Function from Winds, Turbulence, and Radiation*, Astrophys. J. **754**, 71 71, arXiv: `1203.2620 [astro-ph.SR]` (cit. on pp. 5, 24).

Krumholz, Mark R. and Christopher F. McKee (2005), *A General Theory of Turbulence-regulated Star Formation, from Spirals to Ultraluminous Infrared Galaxies*, Astrophys. J. **630** 250, arXiv: `astro-ph/0505177 [astro-ph]` (cit. on p. 4).

Krumholz, Mark R., Christopher F. McKee and Richard I. Klein (2005), *The formation of stars by gravitational collapse rather than competitive accretion*, Nature **438** 332 (cit. on p. 8).

Krumholz, Mark R. et al. (2009), *The Formation of Massive Star Systems by Accretion*, Science **323** 754, arXiv: `0901.3157 [astro-ph.SR]` (cit. on p. 12).

Larson, R. B. (1981), *Turbulence and star formation in molecular clouds.*, Mon. Not. R. Astron. Soc. **194** 809 (cit. on p. 4).

Larson, Richard B. (2005), *Thermal physics, cloud geometry and the stellar initial mass function*, Mon. Not. R. Astron. Soc. **359** 211, arXiv: `astro-ph/0412357 [astro-ph]` (cit. on p. 5).

Lee, Yueh-Ning and Patrick Hennebelle (2019), *Stellar mass spectrum within massive collapsing clumps. III. Effects of temperature and magnetic field*, Astron. Astrophys. **622**, A125 A125, arXiv: `1812.05508 [astro-ph.GA]` (cit. on p. 5).

Lee, Yueh-Ning, Patrick Hennebelle and Gilles Chabrier (2017), *Analytical Core Mass Function (CMF) from Filaments: Under Which Circumstances Can Filament Fragmentation Reproduce the CMF?*, Astrophys. J. **847**, 114 114, arXiv: `1709.01446 [astro-ph.GA]` (cit. on p. 7).

Li, Yuexing, Ralf S. Klessen and Mordecai-Mark Mac Low (2003), *The Formation of Stellar Clusters in Turbulent Molecular Clouds: Effects of the Equation of State*, Astrophys. J. **592** 975, arXiv: `astro-ph/0302606 [astro-ph]` (cit. on p. 5).

Li, Zhi-Yun et al. (2010), *Lowering the Characteristic Mass of Cluster Stars by Magnetic Fields and Outflow Feedback*, Astrophys. J. Letters **720** L26, arXiv: `1008.0409 [astro-ph.SR]` (cit. on p. 7).

Liow, Kong You and Clare L. Dobbs (2020), *The role of collision speed, cloud density, and turbulence in the formation of young massive clusters via cloud-cloud collisions*, Mon. Not. R. Astron. Soc. **499** 1099, arXiv: `2009.07857 [astro-ph.GA]` (cit. on p. 10).

Liu, Hauyu Baobab, Qizhou Zhang and Paul T. P. Ho (2011), *An Overall Picture of the Gas Flow in a Massive Cluster-forming Region: The Case of G10.6-0.4*, Astrophys. J. **729**, 100 100, arXiv: `1101.3459 [astro-ph.SR]` (cit. on p. 23).

Liu, Tie et al. (2017), *ALMA Reveals Sequential High-mass Star Formation in the G9.62+0.19 Complex*, Astrophys. J. **849**, 25 25, arXiv: `1705.04907 [astro-ph.GA]` (cit. on p. 23).

López-Sepulcre, Ana et al. (2016), *The Role of SiO as a Tracer of Past Star-formation Events: The Case of the High-mass Protocluster NGC 2264-C*, Astrophys. J. **822**, 85 85, arXiv: `1603.05885 [astro-ph.GA]` (cit. on p. 25).

Louvet, F. et al. (2016), *Tracing extended low-velocity shocks through SiO emission. Case study of the W43-MM1 ridge*, Astron. Astrophys. **595**, A122 A122, arXiv: `1607.08668 [astro-ph.GA]` (cit. on p. 25).

Lu, Xing et al. (2018), *Filamentary Fragmentation and Accretion in High-mass Star-forming Molecular Clouds*, Astrophys. J. **855**, 9 9, arXiv: `1801.05955 [astro-ph.GA]` (cit. on p. 24).

Lucy, L. B. (1999), *Computing radiative equilibria with Monte Carlo techniques*, Astron. Astrophys. **344** 282 (cit. on p. 22).

Mac Low, Mordecai-Mark and Ralf S. Klessen (2004), *Control of star formation by supersonic turbulence*, Reviews of Modern Physics **76** 125, arXiv: `astro-ph/0301093 [astro-ph]` (cit. on pp. 4, 6).

Masunaga, Hirohiko and Shu-ichiro Inutsuka (2000), *A Radiation Hydrodynamic Model for Protostellar Collapse. II. The Second Collapse and the Birth of a Protostar*, Astrophys. J. **531** 350 (cit. on p. 5).

McKee, Christopher F. and Jonathan C. Tan (2003), *The Formation of Massive Stars from Turbulent Cores*, Astrophys. J. **585** 850, arXiv: `astro-ph/0206037 [astro-ph]` (cit. on pp. 8, 23).

McLaughlin, Dean E. and Ralph E. Pudritz (1997), *Gravitational Collapse and Star Formation in Logotropic and Nonisothermal Spheres*, Astrophys. J. **476** 750, arXiv: `astro-ph/9609080 [astro-ph]` (cit. on p. 8).

Menten, K. M., T. Pillai and F. Wyrowski (2005), "Initial conditions for massive star birth-Infrared dark clouds", *Massive Star Birth: A Crossroads of Astrophysics*, ed. by R. Cesaroni et al., vol. 227 23, arXiv: `astro-ph/0508030 [astro-ph]` (cit. on p. 12).

Mocz, Philip and Blakesley Burkhart (2018), *Star formation from dense shocked regions in supersonic isothermal magnetoturbulence*, Mon. Not. R. Astron. Soc. **480** 3916, arXiv: `1805.11105 [astro-ph.GA]` (cit. on p. 4).

Molet, J. et al. (2019), *Molecular analysis of a high-mass prestellar core candidate in W43-MM1*, Astron. Astrophys. **626**, A132 A132, arXiv: `1905.12463 [astro-ph.GA]` (cit. on p. 25).

Molinari, S. et al. (2008), *The evolution of the spectral energy distribution in massive young stellar objects*, Astron. Astrophys. **481** 345 (cit. on p. 12).

Molinari, S. et al. (2016), *Calibration of Evolutionary Diagnostics in High-mass Star Formation*, Astrophys. J. Letters **826**, L8 L8, arXiv: `1604.06192 [astro-ph.GA]` (cit. on p. 12).

Molinari, Sergio et al. (2019), *Evolution of young protoclusters embedded in dense massive clumps. A new grid of population synthesis SED models and a new set of L/M evolutionary tracks*, Mon. Not. R. Astron. Soc. **486** 4508, arXiv: `1904.08140 [astro-ph.SR]` (cit. on p. 13).

Murray, Daniel W. et al. (2017), *Collapse in self-gravitating turbulent fluids*, Mon. Not. R. Astron. Soc. **465** 1316, arXiv: `1509.05910 [astro-ph.GA]` (cit. on p. 10).

Myers, Philip C. (2011), *Star Formation in Dense Clusters*, Astrophys. J. **743**, 98 98, arXiv: `1109.4137 [astro-ph.GA]` (cit. on pp. 6, 7).

Nakamura, Fumitaka and Zhi-Yun Li (2008), *Magnetically Regulated Star Formation in Three Dimensions: The Case of the Taurus Molecular Cloud Complex*, Astrophys. J. **687** 354, arXiv: `0804.4201 [astro-ph]` (cit. on p. 7).

Nam, Donghee G., Christoph Federrath and Mark R. Krumholz (2021), *Testing the turbulent origin of the stellar initial mass function*, Mon. Not. R. Astron. Soc. **503** 1138, arXiv: `2102.08564 [astro-ph.GA]` (cit. on p. 7).

Natta, A. et al. (2007), "Dust in Protoplanetary Disks: Properties and Evolution", *Protostars and Planets V*, ed. by Bo Reipurth, David Jewitt and Klaus Keil 767, arXiv: `astro-ph/0602041 [astro-ph]` (cit. on p. 20).

Noebauer, Ulrich M. and Stuart A. Sim (2019), *Monte Carlo radiative transfer*, Living Reviews in Computational Astrophysics **5**, 1 1, arXiv: `1907.09840 [astro-ph.IM]` (cit. on p. 21).

Nolan, C. A., C. Federrath and R. S. Sutherland (2015), *The density variance-Mach number relation in isothermal and non-isothermal adiabatic turbulence*, Mon. Not. R. Astron. Soc. **451** 1380, arXiv: `1504.04370 [astro-ph.GA]` (cit. on p. 5).

Nony, T. et al. (2018), *Detection of a high-mass prestellar core candidate in W43-MM1*, Astron. Astrophys. **618**, L5 L5, arXiv: `1810.01404 [astro-ph.GA]` (cit. on p. 23).

Offner, S. S. R. et al. (2014), “The Origin and Universality of the Stellar Initial Mass Function”, *Protostars and Planets VI*, ed. by Henrik Beuther et al. 53, arXiv: `1312.5326 [astro-ph.SR]` (cit. on p. 5).

Offner, Stella S. R. and Héctor G. Arce (2014), *Investigations of Protostellar Outflow Launching and Gas Entrainment: Hydrodynamic Simulations and Molecular Emission*, Astrophys. J. **784**, 61 61, arXiv: `1312.0951 [astro-ph.SR]` (cit. on p. 7).

Offner, Stella S. R. et al. (2009), *The Effects of Radiative Transfer on Low-Mass Star Formation*, Astrophys. J. **703** 131, arXiv: `0904.2004 [astro-ph.SR]` (cit. on pp. 5, 7, 24).

Ormel, C. W. et al. (2009), *Dust coagulation and fragmentation in molecular clouds. I. How collisions between dust aggregates alter the dust size distribution*, Astron. Astrophys. **502** 845, arXiv: `0906.1770 [astro-ph.SR]` (cit. on p. 20).

Ossenkopf, V. (1993), *Dust coagulation in dense molecular clouds : the formation of fluffy aggregates.*, Astron. Astrophys. **280** 617 (cit. on p. 20).

Ossenkopf, V. and T. Henning (1994), *Dust opacities for protostellar cores*, Astron. Astrophys. **291** 943 (cit. on p. 21).

Padoan, Paolo and Åke Nordlund (2002a), *The Stellar Initial Mass Function from Turbulent Fragmentation*, Astrophys. J. **576** 870, arXiv: `astro-ph/0011465 [astro-ph]` (cit. on pp. 4, 6, 7).

– (2002b), *The Stellar Initial Mass Function from Turbulent Fragmentation*, Astrophys. J. **576** 870, arXiv: `astro-ph/0011465 [astro-ph]` (cit. on p. 5).

Padoan, Paolo, Ake Nordlund and Bernard J. T. Jones (1997), *The universality of the stellar initial mass function*, Mon. Not. R. Astron. Soc. **288** 145, arXiv: `astro-ph/9703110 [astro-ph]` (cit. on pp. 4, 6).

Padoan, Paolo et al. (2020), *The Origin of Massive Stars: The Inertial-inflow Model*, Astrophys. J. **900**, 82 82, arXiv: `1911.04465 [astro-ph.GA]` (cit. on p. 10).

Palau, Aina et al. (2018), *Thermal Jeans Fragmentation within ∼1000 au in OMC-1S*, Astrophys. J. **855**, 24 24, arXiv: `1706.04623 [astro-ph.GA]` (cit. on p. 23).

Passot, Thierry and Enrique Vázquez-Semadeni (1998a), *Density probability distribution in one-dimensional polytropic gas dynamics*, PRE **58** 4501, arXiv: `physics/9802019 [physics.flu-dyn]` (cit. on p. 4).

– (1998b), *Density probability distribution in one-dimensional polytropic gas dynamics*, PRE **58** 4501, arXiv: `physics/9802019 [physics.flu-dyn]` (cit. on p. 4).

Peretto, N. and G. A. Fuller (2009), *The initial conditions of stellar protocluster formation. I. A catalogue of Spitzer dark clouds*, Astron. Astrophys. **505** 405, arXiv: `0906.3493 [astro-ph.GA]` (cit. on p. 13).

Peretto, N. et al. (2013), *Global collapse of molecular clouds as a formation mechanism for the most massive stars*, Astron. Astrophys. **555**, A112 A112, arXiv: `1307.2590 [astro-ph.GA]` (cit. on p. 23).

Peretto, N. et al. (2014), *SDC13 infrared dark clouds: Longitudinally collapsing filaments?*, Astron. Astrophys. **561**, A83 A83, arXiv: `1311.0203 [astro-ph.GA]` (cit. on p. 24).

Pérez, Laura M. et al. (2012), *Constraints on the Radial Variation of Grain Growth in the AS 209 Circumstellar Disk*, Astrophys. J. Letters **760**, L17 L17, arXiv: `1210.5252 [astro-ph.SR]` (cit. on p. 20).

Peters, Thomas et al. (2010), *Limiting Accretion onto Massive Stars by Fragmentation-induced Starvation*, Astrophys. J. **725** 134, arXiv: `1005.3271 [astro-ph.GA]` (cit. on p. 9).

Peters, Thomas et al. (2011), *The Interplay of Magnetic Fields, Fragmentation, and Ionization Feedback in High-mass Star Formation*, Astrophys. J. **729**, 72 72, arXiv: `1010.5905 [astro-ph.SR]` (cit. on pp. 7, 9).

Planck Collaboration et al. (2011), *Planck early results. XXIII. The first all-sky survey of Galactic cold clumps*, Astron. Astrophys. **536**, A23 A23, arXiv: `1101.2035 [astro-ph.GA]` (cit. on p. 21).

Plume, Rene et al. (1997), *Dense Gas and Star Formation: Characteristics of Cloud Cores Associated with Water Masers*, The Astrophysical Journal **476** 730, URL: `https://doi.org/10.1086%5C%2F303654` (cit. on p. 8).

Price, Daniel J. and Matthew R. Bate (2009), *Inefficient star formation: the combined effects of magnetic fields and radiative feedback*, Mon. Not. R. Astron. Soc. **398** 33, arXiv: `0904.4071 [astro-ph.SR]` (cit. on p. 7).

Price, Nigel M. and Ph. Podsiadlowski (1995), *Dynamical interactions between young stellar objects and a collisional model for the origin of the stellar mass spectrum*, Mon. Not. R. Astron. Soc. **273** 1041 (cit. on p. 7).

Punanova, Anna et al. (2018), *Seeds of Life in Space (SOLIS). III. Zooming Into the Methanol Peak of the Prestellar Core L1544*, Astrophys. J. **855**, 112 112, arXiv: `1802.00859 [astro-ph.GA]` (cit. on p. 25).

Purser, S. J. D. et al. (2016), *A search for ionized jets towards massive young stellar objects*, Mon. Not. R. Astron. Soc. **460** 1039, arXiv: `1605.01200 [astro-ph.GA]` (cit. on p. 13).

Robertson, Brant and Peter Goldreich (2018), *Dense Regions in Supersonic Isothermal Turbulence*, Astrophys. J. **854**, 88 88, arXiv: `1801.05440 [astro-ph.GA]` (cit. on p. 4).

Roy, Arabindo et al. (2013), *Changes of Dust Opacity with Density in the Orion A Molecular Cloud*, Astrophys. J. **763**, 55 55, arXiv: `1211.6475 [astro-ph.GA]` (cit. on p. 20).

Rybicki, G. B. and D. G. Hummer (1991), *An accelerated lambda iteration method for multilevel radiative transfer.*, Astron. Astrophys. **245** 171 (cit. on p. 22).

Rybicki, George B and Alan P Lightman (1985), *Radiative Processes in Astrophysics*, URL: `https://cds.cern.ch/record/847173` (cit. on p. 15).

Sanhueza, Patricio et al. (2019), *The ALMA Survey of 70 μm Dark High-mass Clumps in Early Stages (ASHES). I. Pilot Survey: Clump Fragmentation*, Astrophys. J. **886**, 102 102, arXiv: `1909.07985 [astro-ph.GA]` (cit. on p. 23).

Schilke, P. et al. (1997), *SiO production in interstellar shocks.*, Astron. Astrophys. **321** 293 (cit. on p. 25).

Schneider, N. et al. (2010), *The Herschel view of star formation in the Rosette molecular cloud under the influence of NGC 2244*, Astron. Astrophys. **518**, L83 L83, arXiv: `1005.3924 [astro-ph.GA]` (cit. on p. 23).

Schuller, F. et al. (2009), *ATLASGAL - The APEX telescope large area survey of the galaxy at 870 μm*, Astron. Astrophys. **504** 415, arXiv: `0903.1369` (cit. on p. 12).

Shetty, Rahul et al. (2009), *The Effect of Noise on the Dust Temperature-Spectral Index Correlation*, Astrophys. J. **696** 676, arXiv: `0902.0636 [astro-ph.GA]` (cit. on p. 21).

Shirley, Yancy L. (2015), *The Critical Density and the Effective Excitation Density of Commonly Observed Molecular Dense Gas Tracers*, PASP **127** 299, arXiv: `1501.01629 [astro-ph.IM]` (cit. on p. 17).

Shu, Frank H., Fred C. Adams and Susana Lizano (1987), *Star formation in molecular clouds: observation and theory.*, ARA&A **25** 23 (cit. on p. 5).

Shu, Frank H. et al. (1999), "Low-Mass Star Formation: Theory", *The Origin of Stars and Planetary Systems*, ed. by Charles J. Lada and Nikolaos D. Kylafis, vol. 540, NATO Advanced Study Institute (ASI) Series C 193 (cit. on p. 24).

Siringo, G. et al. (2009), *The Large APEX BOlometer CAmera LABOCA*, Astron. Astrophys. **497** 945, arXiv: `0903.1354 [astro-ph.IM]` (cit. on p. 12).

Smith, Rowan J., Steven Longmore and Ian Bonnell (2009), *The simultaneous formation of massive stars and stellar clusters*, Mon. Not. R. Astron. Soc. **400** 1775, arXiv: `0908.3910 [astro-ph.SR]` (cit. on pp. 6, 8).

Sollins, Peter K. et al. (2005), *Spherical Infall in G10.6-0.4: Accretion through an Ultracompact H II Region*, Astrophys. J. Letters **624** L49, arXiv: `astro-ph/0410604 [astro-ph]` (cit. on p. 24).

Soma, Tatsuya et al. (2015), *Methanol in the Starless Core, Taurus Molecular Cloud-1*, Astrophys. J. **802**, 74 74 (cit. on p. 25).

Spaans, Marco and Joseph Silk (2000), *The Polytropic Equation of State of Interstellar Gas Clouds*, Astrophys. J. **538** 115, arXiv: `astro-ph/0002483 [astro-ph]` (cit. on p. 5).

Stahler, S. W., F. H. Shu and R. E. Taam (1980), *The evolution of protostars. I - Global formulation and results*, Astrophys. J. **241** 637 (cit. on p. 12).

Stamatellos, D. et al. (2007), *Radiative transfer and the energy equation in SPH simulations of star formation*, Astron. Astrophys. **475** 37, arXiv: `0705.0127 [astro-ph]` (cit. on p. 5).

Svoboda, Brian E. et al. (2019), *ALMA Observations of Fragmentation, Substructure, and Protostars in High-mass Starless Clump Candidates*, Astrophys. J. **886**, 36 36, arXiv: `1908.10374 [astro-ph.GA]` (cit. on p. 23).

Tackenberg, J. et al. (2014), *Kinematic structure of massive star-forming regions. I. Accretion along filaments*, Astron. Astrophys. **565**, A101 A101, arXiv: `1402.0021 [astro-ph.GA]` (cit. on p. 24).

Tanaka, K. E. I., J. C. Tan and Y. Zhang (2017), *The Impact of Feedback During Massive Star Formation by Core Accretion*, Astrophys. J. **835**, 32 32, arXiv: `1610.08856 [astro-ph.SR]` (cit. on p. 7).

Testi, Leonardo and Anneila I. Sargent (1998), *Star Formation in Clusters: A Survey of Compact Millimeter-Wave Sources in the Serpens Core*, Astrophys. J. Letters **508** L91, arXiv: `astro-ph/9809323 [astro-ph]` (cit. on p. 5).

Torrelles, J. M. et al. (2003), *Evidence for Evolution of the Outflow Collimation in Very Young Stellar Objects*, Astrophys. J. Letters **598** L115 (cit. on p. 13).

Treviño-Morales, S. P. et al. (2019), *Dynamics of cluster-forming hub-filament systems. The case of the high-mass star-forming complex Monoceros R2*, Astron. Astrophys. **629**, A81 A81, arXiv: `1907.03524 [astro-ph.GA]` (cit. on p. 23).

Urban, Andrea, Hugo Martel and II Evans Neal J. (2010), *Fragmentation and Evolution of Molecular Clouds. II. The Effect of Dust Heating*, Astrophys. J. **710** 1343, arXiv: `0912.3819 [astro-ph.GA]` (cit. on p. 7).

Urquhart, J. S. et al. (2018), *ATLASGAL - properties of a complete sample of Galactic clumps*, Mon. Not. R. Astron. Soc. **473** 1059, arXiv: `1709.00392` (cit. on p. 12).

van der Tak, F. F. S. et al. (2007), *A computer program for fast non-LTE analysis of interstellar line spectra. With diagnostic plots to interpret observed line intensity ratios*, Astron. Astrophys. **468** 627, arXiv: `0704.0155 [astro-ph]` (cit. on p. 19).

Varricatt, Watson P. et al. (2010), *A near-IR imaging survey of intermediate- and high-mass young stellar outflow candidates*, Mon. Not. R. Astron. Soc. **404** 661, arXiv: `1001.2708 [astro-ph.SR]` (cit. on p. 13).

Vázquez-Semadeni, Enrique et al. (2019), *Global Hierarchical Collapse In Molecular Clouds. Towards a Comprehensive Scenario*, arXiv e-prints, arXiv:1903.11247 arXiv:1903.11247, arXiv: `1903.11247 [astro-ph.GA]` (cit. on pp. 5, 9, 24).

Veneziani, M. et al. (2017), *An analysis of star formation with Herschel in the Hi-GAL Survey. II. The tips of the Galactic bar*, Astron. Astrophys. **599**, A7 A7, arXiv: `1612.04995 [astro-ph.GA]` (cit. on p. 13).

Wang, Ke et al. (2014), *Hierarchical fragmentation and differential star formation in the Galactic 'Snake': infrared dark cloud G11.11-0.12*, Mon. Not. R. Astron. Soc. **439** 3275, arXiv: `1401.4157 [astro-ph.GA]` (cit. on p. 24).

Wang, Peng et al. (2010), *Outflow Feedback Regulated Massive Star Formation in Parsec-Scale Cluster-Forming Clumps*, Astrophys. J. **709** 27, arXiv: `0908.4129 [astro-ph.SR]` (cit. on pp. 6, 7, 9).

Ward-Thompson, D. et al. (2007), "An Observational Perspective of Low-Mass Dense Cores II: Evolution Toward the Initial Mass Function", *Protostars and Planets V*, ed. by Bo Reipurth, David Jewitt and Klaus Keil 33, arXiv: `astro-ph/0603474 [astro-ph]` (cit. on p. 5).

Wienen, M. et al. (2015), *ATLASGAL - Kinematic distances and the dense gas mass distribution of the inner Galaxy*, Astron. Astrophys. **579**, A91 A91, arXiv: `1503.00007 [astro-ph.SR]` (cit. on p. 12).

Williams, J. P., L. Blitz and C. F. McKee (2000), "The Structure and Evolution of Molecular Clouds: from Clumps to Cores to the IMF", *Protostars and Planets IV*, ed. by V. Mannings, A. P. Boss and S. S. Russell 97, arXiv: `astro-ph/9902246 [astro-ph]` (cit. on p. 6).

Wyrowski, F. et al. (2012), *Terahertz ammonia absorption as a probe of infall in high-mass star forming clumps*, Astron. Astrophys. **542**, L15 L15, arXiv: `1203.3406 [astro-ph.GA]` (cit. on p. 24).

Wyrowski, F. et al. (2016), *Infall through the evolution of high-mass star-forming clumps*, Astron. Astrophys. **585**, A149 A149, arXiv: `1510.08374 [astro-ph.SR]` (cit. on p. 24).

Wyrowski, Friedrich et al. (1999), *Hot Gas and Dust in a Protostellar Cluster near W3(OH)*, Astrophys. J. Letters **514** L43, arXiv: `astro-ph/9901261 [astro-ph]` (cit. on p. 13).

Yorke, Harold W. and Cordula Sonnhalter (2002), *On the Formation of Massive Stars*, Astrophys. J. **569** 846, arXiv: `astro-ph/0201041 [astro-ph]` (cit. on p. 7).

Zapata, L. A. et al. (2008), *Forming an early O-type star through gas accretion?*, Astron. Astrophys. **479** L25, arXiv: `0711.4941 [astro-ph]` (cit. on p. 24).

Zhang, Qizhou and Ke Wang (2011), *IRDC G030.88+00.13: A Tale of Two Massive Clumps*, Astrophys. J. **733**, 26 26, arXiv: `1103.5092 [astro-ph.GA]` (cit. on p. 24).

Zinnecker, H. (1982), *Prediction of the protostellar mass spectrum in the Orion near-infrared cluster*, Annals of the New York Academy of Sciences **395** 226 (cit. on p. 8).

CHAPTER 2

Fragmentation and filaments at the onset of star and cluster formation: a SABOCA 350 μm survey of ATLASGAL selected massive clumps

This chapter is published as Lin, Y., Csengeri, T., Wyrowski, F., Urquhart, J. S., Schuller, F., Weiss, A., Menten, K. M., 2019, *Astronomy & Astrophysics*, 631, A72

2.1 Introduction

Despite the significant influence of massive stars on their natal environment and the Galaxy as a whole, their formation process remains poorly constrained. Massive stars (M$\gtrsim$10 $M_{\odot}$) are considerably rarer than solar-mass stars. They constitute less than ~10% of the stellar initial mass function (IMF) in mass. The duration of their formation time is short, hence the deeply embedded early stages are difficult to identify. Adding to the complexity of the high-mass star-forming scenario is that massive stars form typically in clusters (Stahler, Palla and Ho 2000; Lada and Lada 2003), yet, the mass assembly and the fragmentation of massive clumps into cores is still not well understood (for recent reviews see Tan et al. 2014, Motte, Bontemps and Louvet 2018).

In the last decade, Galactic plane surveys in the far-infrared and submillimeter regime such as the APEX Telescope Large Area Survey of the Galaxy (ATLASGAL, Schuller et al. 2009; Csengeri et al. 2014), the Bolocam Galactic Plane Survey (BGPS, Aguirre et al. 2011), the Herschel infrared Galactic Plane Survey (*Hi-Gal*, Molinari et al. 2010) and the JCMT Plane Survey (JPS, Moore et al. 2015; Eden et al. 2017) have proven to be excellent finding charts for identifying large samples of massive clumps that exhibit typical physical characteristics of $>10^3-10^4\,M_{\odot}$, an extent up to ~1 pc and a temperature of ~20 K typically associated with giant molecular cloud complexes (e.g. Csengeri et al. 2016a; Svoboda et al. 2016; König et al. 2017; Elia et al. 2017; Urquhart et al. 2018). Massive clumps fragment into cores where star formation takes place (Motte, Bontemps and Louvet 2018). Investigating how the dense gas is structured within massive clumps, and how they fragment and form filaments and cores on a 0.1-0.3 pc scale (e.g. Motte et al. 2007; André et al. 2014) is, therefore, an important step to understand the mass assembly process to form stars and clusters.

Due to the typically large, several kilo-parsec distance of high-mass star-forming regions, investigating their structure and fragmentation requires high-angular resolution interferometric studies (e.g.

Bontemps et al. 2010; Palau et al., 2013, 2015; Csengeri et al. 2017a; Beuther et al. 2018). Reaching physical scales of a few thousands to tens of thousands of au is necessary to resolve the typical Jeans length in these objects, which is 0.1-0.3 pc, assuming a temperature of 20 K and a volume density of 10^4-10^5 cm^{-3}, characteristic of massive cores or clumps (e.g. Williams, Blitz and McKee 2000; Motte et al. 2007; Wienen et al. 2012; Urquhart et al. 2018). Mapping of large areas is not feasible with current interferometers in the (sub)millimetre wavelength range. However, ground-based telescopes with sensitive, large field-of-view bolometer arrays provide an efficient way to map large regions at a moderate resolution at short wavelengths (350 and 450 μm, i.e. $\sim$10.$''$ corresponding to a physical scale of 0.1 pc at d $\sim$2 kpc). This allows us to conduct a statistical study of fragmentation from clump to core scales (e. g. Motte, Schilke and Lis 2003; Minier et al. 2009; Ragan, Henning and Beuther 2013; Merello et al. 2015; André et al. 2016; Rayner et al. 2017, Heyer et al. 2018). We have, therefore, carried out observations towards more than 200 ATLASGAL selected sources at 350 μm with the Submillimetre APEX Bolometer array camera (SABOCA, Siringo et al. 2010) at the Atacama Pathfinder Experiment 12-meter telescope (APEX, Güsten et al. 2006). These observations achieve an angular resolution of 8.$''$5, a factor of > 2 improvement in terms of angular resolution compared to the ATLASGAL survey, allowing us to identify a population of cores with sizes of 0.1-0.2 pc embedded in clumps with distances $d \lesssim 5$ kpc. The angular resolution achieved corresponds to an intermediate physical scale to dissect structures of massive star-forming clumps, which is a missing gap to link with typical interferometric studies. The sample is twice that of Merello et al. (2015) who targeted a sample of BGPS sources with the SHARC-II camera on the Caltech Submillimeter Observatory (CSO). Combining our results with ancillary submillimeter and infrared data, we estimate the cores' physical parameters and compare them with the properties of clumps in order to constrain their fragmentation and structure formation. The higher angular resolution compared to ATLASGAL allows us to distinguish between quiescent and star-forming cores and deliver a sample of starless or pre-stellar massive cores.

This paper is organised as follows: in Section 2 we present the observations, data reduction, and the complementary data used. In Section 3 we present our results and the data analysis, including source extraction, and determination of physical properties of clumps and SABOCA compact sources. In Section 4 we discuss the statistics of the sample in terms of the fragmentation properties and the relation between clump and core properties. Our main results and conclusions are summarised in Section 5.

2.2 Observations and data reduction

2.2.1 Source selection

Over 10 000 compact sources have been identified in the ATLASGAL survey (Csengeri et al. 2014; Urquhart et al. 2014), and the majority of them (8007) have distance estimates allowing their physical parameters to be determined (Urquhart et al. 2018). In this study, we use 350 μm SABOCA observations to investigate small scale structure of the clumps. In comparison with the extensive follow-up observations of the brightest submillimetre clumps selected from the ATLASGAL survey using both single dish (Giannetti et al., 2014, 2017; Csengeri et al. 2016a; Kim et al., 2017, 2018), and interferometric observations (Csengeri et al., 2017a, 2018) this study focuses more on a population of massive, but lower surface density clumps (with typically lower submillimeter flux density). Our targets have been selected to be weak or in absorption at 24 μm based on the Spitzer MIPS GALactic

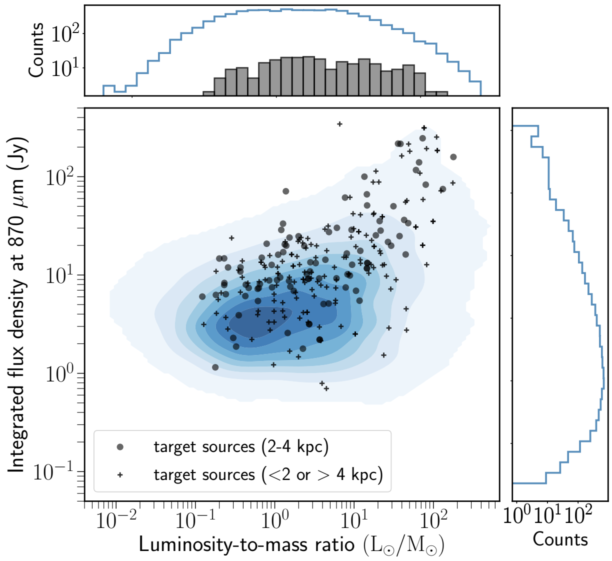

Figure 2.1: Distribution of the integrated flux density and bolometric luminosity-to-mass ratios (L/M) of all ATLASGAL sources (in blue filled contours, the darker region corresponds to higher density) (Urquhart et al. 2018), and the target sources observed with SABOCA (gray pluses and dots) at different distance ranges. The histograms in the right side and top panel show the 1-dimensional distributions of integrated flux density and L/M of all ATLASGAL sources (blue) and all target sources (gray), respectively.

plane survey (MIPSGAL; Carey et al. 2009). This initial sample of 95 clumps has been complemented with sources at different evolutionary stages based on their mid-infrared color selection at 24 and 70 μm mostly having a bolometric luminosity to mass ratio ($L_{\rm bol}/M$) less than 10. In addition, we include the data for the brightest 25 sources from ATLASGAL survey.

Altogether we targeted 204 ATLASGAL clumps, which is the largest number of clumps targeted with SABOCA. Since we obtained maps of the targets, there are 371 other ATLASGAL sources covered in the fields, on average we have 2-3 ATLASGAL clumps per field. The total number of observed clumps from the *GaussClump* compact source catalog of Csengeri et al. (2014) is, therefore, 575. In Fig. 2.1, we compare the integrated flux density and $L_{\rm bol}/M$ of our sample with the same quantities of the whole ATLASGAL sample where available (Urquhart et al. 2018). This shows that our sample is representative of the entire population of sub-millimetre sources, having a $L_{\rm bol}/M$ range of 0.1 to 100 $L_\odot/M_\odot$. Many of these sources are good candidates to host objects in early stages of high-mass star and cluster formation (see for example Csengeri et al. 2017a). The sample also comprises, however, massive clumps in more advanced stages of high-mass star formation that are associated with bright mid-infrared sources and ultra-compact Hɪɪ regions exhibiting $L/M >$ 100 $L_\odot/M_\odot$. In the following, we perform all the analysis on the entire sample homogeneously, and clarify in the discussion when only focusing on the mid-infrared dark sources.

We show the distance distribution of all sources in Fig. 2.2 for which a distance has been determined by Urquhart et al. (2018); these are primarily kinematic distances. Altogether, this provides us with a distance to 507 clumps, which corresponds to 88% of our sample.

The entire sample covers a distance range from 1 to 14.5 kpc (Fig. 2.2), corresponding to a physical

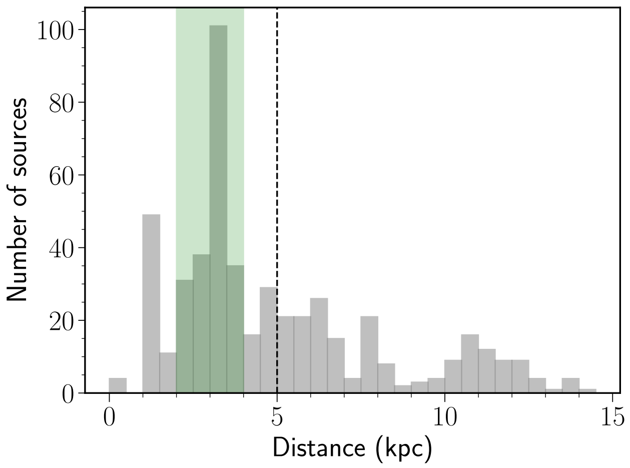

Figure 2.2: Distance distribution of the observed ATLASGAL clumps. The vertical dashed line indicates the 5 kpc distance. The filled green region indicates 2-4 kpc range.

resolution between 0.04 and 0.6 pc. The large range of linear scales (~ 10) has an impact the observed morphologies and derived physical properties. To mitigate any possible observational biases we restrict our statistical analysis to a distance limited sample ($d \lesssim$2-4 kpc); this corresponds to physical sizes of 0.07 and 0.15 pc, and thus, reducing the range of linear scales to a factor of 2. The majority of the clumps are located within 5 kpc (314 out of the 507 clumps corresponding to 62% of the sample), 205 of which are located in 2-4 kpc. The more distant sources are mostly luminous OB clusters that tend to be associated with very active star forming regions, which belong to the 25 strongest submillimeter sources with ATLASGAL survey, such as the W51, W43 complexes (e.g. Ginsburg et al. 2015; Motte et al. 2014).

2.2.2 SABOCA observations and data reduction

We targeted the selected ATLASGAL sources using the SABOCA instrument installed at the APEX telescope which offers ~8″ angular resolution at 350 μm. We used a raster spiral mapping strategy for each source that mapped a 4′ region centered on the source position. The observations were conducted in 2010 and 2012 with a median precipitable water vapor (PWV) of 0.3 mm and all less than 0.5 mm. The typical on-source integration time is ~5 minutes, which gives a better than ~160 mJy/beam noise level for most of the sources (Fig. 2.3). This corresponds to a mass sensitivity of 1.84 $M_{\odot}$ at 3 kpc, assuming a dust temperature of 20 K, $\kappa_{350\,\mu\mathrm{m}} = 0.076\,\mathrm{cm}^2\,\mathrm{g}^{-1}$, and a gas-to-dust ratio of 100 (Eqs. 1 and 2).

We used the BoA software (Schuller 2012) with standard procedures and iterative masking for the data reduction. The atmospheric zenith opacity determined from the radiometer in each science scan was used to correct for atmospheric opacity. These values were compared to the results of the `skydip` measurement and found to be consistent. Mars and standard calibrators, such as IRAS 13134-6264, were regularly observed and used as primary flux calibrators. Typical calibration uncertainties are within 20%. Pointing and focus were updated every 1-2 hours. The telescope pointing accuracy is within 2-3.″0.

We used the standard, iterative source-masking reduction procedures optimised for the faint and the bright sources, respectively. In the first step of the iterative processing, an initial map is obtained after opacity correction, and then the correlated noise and bad channels are removed. The resulting map is then smoothed by 2/3 of the beam size (yielding a resolution of 9.5″) to achieve a better signal-to-noise ratio. This is then used as an input model for the following iterations to represent the real source structure. The residual flux is modeled by subtracting the model image from the initial map, with a cut-off level at a signal-to-noise ratio of 3. After adding the model back to the image, the process is repeated until the peak flux level remains unchanged. For the final maps, we applied 3.″ smoothing which gives a resolution of 8.″5 (original beam size ~8″). We checked the convergence of the data reduction process by examining the relative change of the peak and integrated flux density around the brightest pixels during the iterative process. The pixel size is 1.″85 in the final map.

In order to have a uniform and consistent noise level estimation for all fields, we use a wavelet-based estimator implemented in the `skimage` python package; this assumes a Gaussian noise distribution and calculates the standard deviation in each map (Donoho and Johnstone 1994). Before this estimation, we trimmed the edge of the maps, because of the increased noise level due to the non-uniform sampling at the map edges caused by the scanning strategy. We selected several sources to check the derived values and found them to be consistent with measurements made of an emission-free region of the map. The achieved rms noise distribution of all the sources is shown in Fig. 2.3. The mean noise level for the relatively weak sources (from projects M-0085.F-0046-2010, M-0090.F-0026-2012) is 0.12 Jy/beam with a standard deviation of 0.07 Jy/beam, and for the brightest sources (M-0085.F-0055-2010) it is 0.21 Jy/beam with a standard deviation of 0.10 Jy/beam.

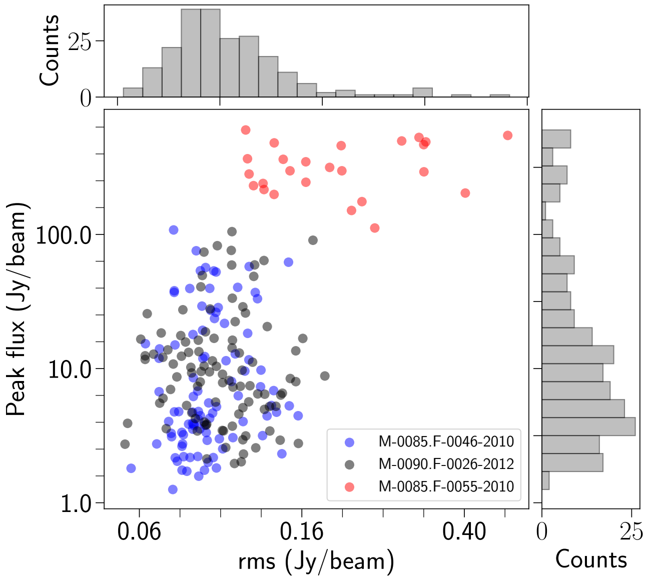

Figure 2.3: 350 μm peak flux density versus the 1σ rms noise level observed with SABOCA towards all fields. The histogram on the right side, and the top panel show the distribution of peak flux densities and the noise levels, respectively.

We find that the brightest sources, above 100 Jy/beam peak flux density, have up to a factor of 5 higher rms noise compared to the weaker sources (Fig. 2.3). Altogether the sources exhibit a large

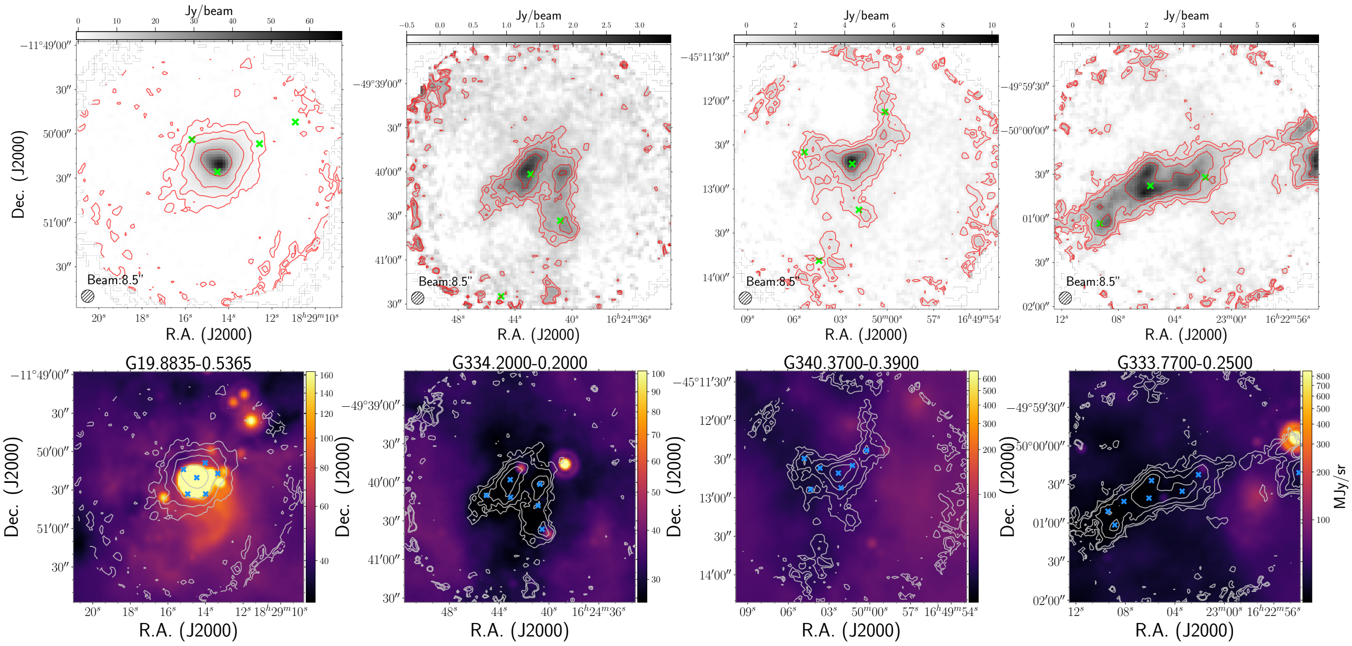

G19.8835-0.5365

G334.2000-0.2000

G340.3700-0.3900

G333.7700-0.2500

Figure 2.4: *Top panels*: Examples of 350 μm emission towards ATLASGAL selected massive clumps obtained with APEX/SABOCA. Contour levels start at 5σ and show 5 uniformly spaced intervals on a logarithmic scale up to the peak flux density in each field. The green crosses show the position of ATLASGAL sources. *Bottom panels*: Coloured images show the 24 μm emission from MIPSGAL on a logarithmic scale, contours are the same as in the top panel of the 350 μm emission. red crosses mark the positions of the compact sources identified in the SABOCA maps. The target name from the ATLASGAL Gaussclumps catalog is given in each plot.

range of peak flux density from as low as 1.25 Jy/beam up to 600.4 Jy/beam, with an average of 52.0 Jy/beam and a median of 9.0 Jy/beam at 350 μm. In agreement with our initial selection from ATLASGAL, this shows that we have a large number of relatively faint and a few extremely bright clumps.

2.2.3 Ancillary data

To be able to determine the physical properties of the clumps, we rely on the far-infrared emission of the dust. For this, we use level 2.5/3 archival data from Herschel PACS and SPIRE at 70/160 μm, 250/350 μm, respectively, from the Hi-Gal survey (Molinari et al. 2010, 2016). The zero point offsets of the SPIRE data have been corrected by *Planck*-HFI data via cross-calibration[1]; this accounts for the thermal background produced by the instrument itself. There are 6 fields not covered in Hi-Gal or at the edges of the maps that were excluded from the following analysis.

We complement the HiGAL data with the combined ATLASGAL and *Planck*-HFI 870 μm data (Csengeri et al. 2016b). This data product has a considerably larger spatial dynamic range than the ATLASGAL data alone allowing the recovery of large-scale structures, which can be directly compared with the emission probed by Herschel. To associate the sub-millimetre emission with mid-infrared

---

[1] The procedure is elaborated in `http://herschel.esac.esa.int/Docs/SPIRE/spire_handbook.pdf`

sources, we also make use of the MIPSGAL survey and its point source catalog (Gutermuth and Heyer 2015).

2.3 Results

2.3.1 The SABOCA 350 μm view of ATLAGSAL clumps: filaments and cores

We show examples of massive clumps at 350 μm observed by APEX/SABOCA in Fig. 2.4, where we also directly compare them with the 24 μm emission from the Spitzer/MIPSGAL survey probing their star formation activity at a comparable angular resolution of 6.″. We detect emission at 350 μm towards all fields, typically tracing emission from the ambient cloud material, as well as from compact sources. The images for all the targeted sources are shown in App. A.1.

The observed fields have a range of peak flux densities spanning two orders of magnitude at 350 μm with a typical dynamic range of ∼100, however, this is noticeably lower for fields containing brighter sources. The high dynamic range and improved resolution allows us to conduct a detailed analysis of the overall morphology of the sample in a homogeneous way for the majority of the sources; this is particularly true for the mid-infrared weak sources due to the better sensitivity and dynamic range.

As revealed in Fig. 2.4, the morphology of the 350 μm emission exhibits a large variety including isolated compact spherical structures (Fig. 2.4a) and prominent elongated structures, which are often referred to as filaments (Fig. 2.4b, c, d). The structure of the source presented in Fig. 2.4d reveals a relatively straight filamentary morphology, however, we also find a network of connecting filamentary-like and branches, which are illustrated in Fig. 2.4b, c, for example. These structures are reminiscent of the large-scale filamentary structure of the ISM (e.g. Li et al. 2016). Visual inspection of all the maps in App. A.1 indicates that the majority of the fields exhibit elongated, filamentary(-like) emission (67%). This either corresponds to low-intensity uniformly distributed material or consists of brighter emission with several compact sources associated with it. These sources are marked in Table 2.1 together with the properties of the identified substructures (see more detail in Sec. 2.4.3). In general, fields dominated by a single, bright source at 350 μm represent only a minor fraction of the sample.

2.3.2 Extraction of compact sources

We use the Gaussian decomposition algorithm `Gaussclumps` to identify compact structures embedded within the ATLASGAL clumps [2]. Originally developed for identifying structures in 3D, position-position-velocity data cubes, `Gaussclumps` assumes that the resolved structures are Gaussian-shaped and iteratively subtracts the fitted structures from the map (Stutzki and Guesten 1990). `Gaussclumps` is the same tool used to extract the compact sources from the ATLAGSAL survey (Csengeri et al. 2014).

We set the initial guesses of aperture cutoff and aperture $FWHM$ to 8.″5 and 1.1 times the angular resolution respectively. The initial guess for the source $FWHM$ is also set to 1.1 times the angular resolution, and we require the identified substructure by `Gaussclumps` to have a peak flux larger than 3 times the rms. There are several other control parameters in the least-square fitting algorithm. The stiffness parameters s_0, s_c and s_a adjust the tolerance between the observed intensity, maximum

---

[2] This is implemented in the GILDAS software package that can be found at http://www.iram.fr/IRAMFR/GILDAS

intensity and its position, respectively, with the corresponding fitted parameters. We performed a series of tests to see how the choices for the stiffness parameters affect the identified sources. We found that using 1, 1, 10 for s_0, s_c and s_a results in a more stringent constraint on the fitted peak flux position, and seems to more robustly recover the prominent structures while avoiding the detection of spurious sources at relatively low signal-to-noise levels.

In total, we identify 1120 structures with `Gaussclumps` within our SABOCA maps, yielding on average 4-5 compact sources within the 4′ maps. We list the parameters of the extracted compact sources in Table 2.1. In the following, we use the nomenclature commonly adopted in the literature (e.g., Williams, Blitz and McKee 2000, Motte et al. 2007, Zhang et al. 2009, Liu et al. 2012a,b), where clumps refer to structures with sizes of ~0.5-1 pc, and cores refer to ~0.1 pc structures embedded within a clump. Since most of our analysis and discussions are based on the distance limited sample, in the following we use the term *cores* to refer to the compact sources extracted from the SABOCA 350 μm observations, since the majority of them have a $FWHM$ size $\lesssim$0.2 pc. When discussing the properties of SABOCA 350 μm compact sources together with clumps, we use the term *fragments* instead, to indicate their relation.

2.4 Physical properties of clumps and cores

2.4.1 Dust temperature and H_2 column density maps on the clump-scale

We performed a pixel-by-pixel fitting of the far-infrared spectral energy distribution (SED) to compute maps of the dust temperature, T_d, and the H_2 column density, $N(H_2)$. For this, we used PACS 160 μm, SPIRE 250 μm, and 350 μm maps and the combined APEX/LABOCA-*Planck*-HFI 870 μm data. We first convolved the maps to a common resolution of ~25.″and then gridded the data on to the same pixel grid. We performed SED fit of each pixel, using a modified-blackbody model:

$$I_\nu = B_\nu(T_d)(1 - e^{-\tau_\nu}) \tag{2.1}$$

where in $\tau_\nu = \mu m_\mathrm{H} N(H_2)\kappa_\nu$, m_H is the mean molecular weight and we adopt a value of 2.8, $N(H_2)$ is the gas column density. We adopted a dust opacity law of $\kappa_\nu = \kappa_{300\,\mu m}(\frac{\nu}{1000\,GHz})^\beta$, where $\kappa_{300\,\mu m} = 0.1\,\mathrm{cm}^2\,\mathrm{g}^{-1}$ is the dust opacity per unit mass (gas and dust) at a reference wavelength 300 μm and β is fixed to 1.8, which is the average value found towards the Galactic plane (Planck Collaboration et al. 2011). These parameters have been used for the Herschel Gould Belt Survey (André et al. 2010), the HOBYS (Motte et al. 2010) and Hi-Gal (e.g. Elia et al. 2017) key programs. This dust emissivity relation yields $\kappa_{870\,\mu m} = 0.0147\,\mathrm{cm}^2\,\mathrm{g}^{-1}$, while the previous ATLASGAL studies, e.g. Csengeri et al. (2014), König et al. (2017) use a $\kappa_{870\,\mu m}$ of $0.0185\,\mathrm{cm}^2\,\mathrm{g}^{-1}$, which corresponds to a factor of 1.25 difference in the mass estimates. In addition, for the clumps which have a fitted temperature larger than 45 K we additionally include the PACS 70 μm measurements in the final fits since in this temperature regime inclusion of the shorter wavelength better constrains the fit. We note that there is emerging evidence that β and T_d are anti-correlated (e.g. Juvela et al. 2013), which means fixing β to a certain value will cause an uncertainty of T_d which propagates into the mass estimate. More sophisticated modelling methods are required to accurately recover this anti-correlation (Juvela et al. 2013; Galliano 2018) by properly taking into account observational uncertainties, line-of-sight mixing of different components, etc. In addition, the dust opacity (reference value) can also increase in dense and cold cloud, due to grain growth (dust coagulation, e.g. Ossenkopf and Henning 1994,

Table 2.1: Properties of SABOCA sources from *Gaussclumps* source extraction.

SABOCA name	RA (J2000) (h m s)	Dec (J2000) (d m s)	$FWHM_{\rm maj}$ ($''$)	$FWHM_{\rm min}$ ($''$)	PA ($^\circ$)	$FWHM_{\rm g}$ ($''$)	$S_{\rm peak}$ (Jy/beam)	$S_{\rm int}$ (Jy)	Filament flag
GS301.1338−0.2285	12:35:33.64	-63:02:41.2	25.2	13.7	147.4	18.6	28.1	138.8	–
GS301.1350−0.2220	12:35:34.51	-63:02:18.2	21.6	9.7	245.0	14.5	40.0	120.3	–
GS301.1364−0.2252	12:35:35.11	-63:02:29.7	13.0	11.9	55.4	12.4	236.5	521.6	–
GS301.1400−0.2233	12:35:37.00	-63:02:02.0	23.8	13.7	159.7	18.0	33.3	155.3	–
GS302.1493−0.9497	12:44:20.68	-63:48:38.5	12.2	11.2	65.7	11.7	5.2	10.1	–
GS303.1176−0.9717	12:53:07.36	-63:50:34.0	12.6	10.4	180.6	11.5	9.6	18.1	–
GS303.9991+0.2799	13:00:42.43	-62:34:21.3	11.5	9.7	60.6	10.6	4.5	7.1	–
GS304.7120+0.6001	13:06:43.36	-62:13:07.6	11.5	9.4	95.0	10.4	1.7	2.6	–
GS305.0947+0.2501	13:10:13.03	-62:32:33.7	20.2	10.4	101.9	14.5	3.1	9.3	Y
GS305.0997+0.2484	13:10:15.67	-62:32:38.7	13.0	10.1	129.8	11.4	2.0	3.8	–
GS305.2566+0.3162	13:11:34.34	-62:27:52.9	13.3	11.5	177.0	12.4	2.4	5.4	–
GS305.2589+0.3257	13:11:35.13	-62:27:1	19.1	11.5	149.9	14.8	4.6	14.6	Y
GS305.8169−0.1115	13:16:45.62	-62:50:28.6	15.5	9.4	130.1	12.0	8.3	17.2	–
GS309.1537−0.3509	13:45:51.16	-62:33:48.	13.0	10.4	184.4	11.6	4.2	8.1	Y
GS309.1560−0.3477	13:45:52.03	-62:33:35.6	12.6	12.2	183.8	12.4	2.1	4.7	Y
GS309.1629−0.3380	13:45:54.4	-62:32:56.	16.2	11.2	122.9	13.4	1.5	3.9	–
GS309.1727−0.3279	13:45:58.36	-62:32:13.	12.2	11.2	117.5	11.7	2.7	5.2	Y
GS309.1697−0.3442	13:45:58.63	-62:33:12.9	15.1	9.4	140.2	11.9	1.5	2.9	Y
GS309.1763−0.3487	13:46:02.47	-62:33:23.7	15.1	7.9	95.1	10.9	1.5	2.6	–
GS309.1826−0.3509	13:46:05.8	-62:33:26.6	10.4	9.4	223.3	9.9	3.3	4.6	–

Notes. The columns are defined as follows: Name: the SABOCA catalog source name. RA: Right ascension of the source center. Dec: Declination of the source center. $FWHM_{maj}$ and $FWHM_{min}$: Major and minor $FWHM$ size of the source. PA: Position angle of the Gaussian structure measured from north to east. $FWHM_g$: Geometrical mean of the source size calculated by $\sqrt{FWHM_{\rm maj} \times FWHM_{\rm min}}$. $S_{\rm peak}$: The fitted peak value of the Gaussian emission structure from SABOCA 350 μm map. $S_{\rm int}$: The integrated source flux assuming a Gaussian distribution of flux calculated by $S_{\rm peak}\times({\rm FWHM}_{\rm source}/{\rm FWHM}_{\rm beam})^2$. Filament flag: The SABOCA sources originate from filamentary(-like) clouds are marked with "Y".

Full table will be available on CDS.

Planck Collaboration et al. 2011,Ysard et al. 2013). In general, the mass estimates may have an uncertainty up to a factor of 2-3 due to possible variations of the dust opacity and emissivity index β.

Using ATLASGAL and Herschel data, König et al. (2017) determined the properties of 109 ATLASGAL selected massive clumps from SEDs of mid- to far-infrared data. That study is based on the clump averaged integrated properties, while here we map the spatial distribution of the physical properties (e.g. dust temperature and gas column density). Examples of the resulting dust temperature and column density maps on the 25″ grid are shown in the top panels of Fig. 2.5.

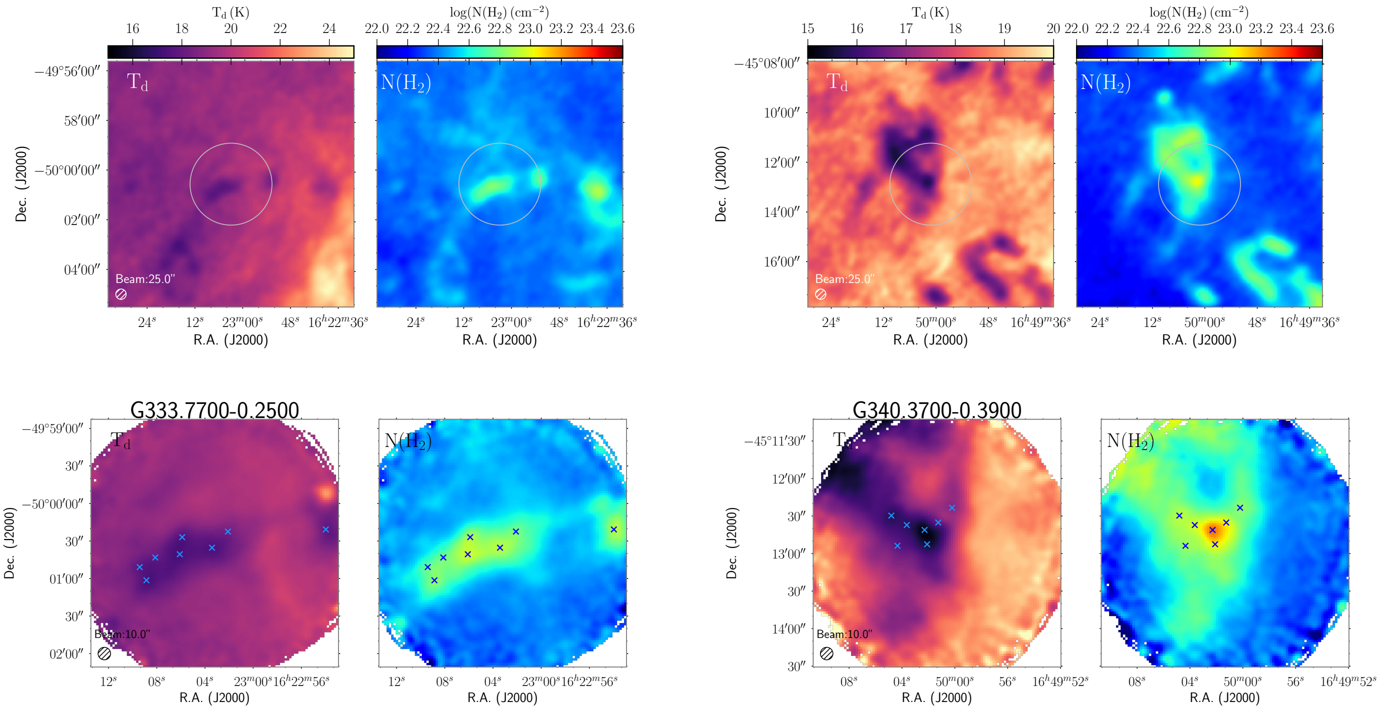

Figure 2.5: *Top panels*: Dust temperature (T_d) and H$_2$ column density (N_{H_2}) maps obtained with a pixel-by-pixel SED fitting of PACS 160 μm, SPIRE 250, 350 μm and combined LABOCA and *Planck* 870 μm data at 25.″ resolution. *Bottom panels*: As top panels but using the PACS 70 μm and the SABOCA and SPIRE 350 μm combined maps at 10.″ resolution. Top panel and lower panel are in same color-scale for dust temperature and column density maps, respectively. The circles in the top panel indicate the region mapped by SABOCA.

2.4.2 Dust temperature and H$_2$ column density maps on the core-scale

To obtain the same parameters at the scale of cores, we make use of the high-resolution SABOCA observations for the SED fitting. Since ground-based submillimeter observations are not sensitive to extended emission due to sky noise subtraction, the SABOCA maps do not recover emission from scales larger than ~0.9-1.0′ (~ 60-70% instrument's field-of-view of SABOCA) (Siringo et al. 2009). Since the Herschel SPIRE 350 μm covers a similar frequency range (Fig. 2.6) we can use these data to recover the extended emission. The sampled angular scales of the two data sets have an overlap between the ~25″ resolution Herschel 350 μm and the largest angular scales recovered by SABOCA.

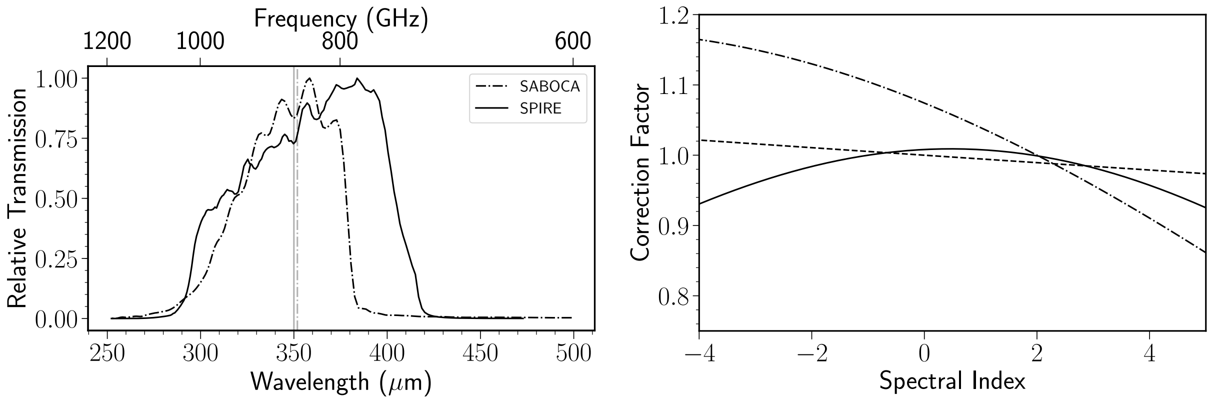

Figure 2.6: *Top panel*: Transmission of the *Herschel*/SPIRE and the APEX/SABOCA instruments. *Bottom panel*: Color correction factors for SABOCA (dashed line) and SPIRE (solid line) as a function of the spectral index of the source. The dash-dotted line shows the conversion factor to scale the SPIRE intensities to the nominal center wavelength of SABOCA.

For the combination of the SABOCA and the SPIRE 350 μm data, we first calculate the color corrections due to the different shape of the transmission curves and nominal frequencies of SABOCA and SPIRE instruments. Following a similar procedure described in Csengeri et al. (2016a), we determine the central wavelength correction factor from SPIRE to SABOCA (F = 0.97) and color correction factors for both instruments (C_{SPIRE} = 0.93, C_{SABOCA} = 0.86). These factors were applied to maps made with each instrument before the combination procedure. The transmission curves and the relation between the assumed spectral index and the correction factors are shown in Fig. 2.6.

An additional complication is that 10 of the brightest sources are saturated in the SPIRE 350 μm images. We correct for this by interpolating between the saturated pixels assuming a 2-dimensional Gaussian flux distribution around the center. We find that the interpolated images are, in general, consistent with the SABOCA images after they are smoothed to the SPIRE 350 μm resolution of 25″. Finally, for all sources, we linearly combine the SABOCA and SPIRE 350 μm images in the Fourier domain using the `immerge` task of the Miriad software package (Sault, Teuben and Wright 1995). Before the combination, we calculate a weighting factor from the overlapping spatial scales between the two dataset, which is then applied to scale the SABOCA flux to match that of the SPIRE 350 μm measurements. For more details on the procedure of the combination, we refer to Lin et al. (2016).

We use these combined maps together with the PACS 70 μm band, at a similarly high resolution of ~10″ after smoothing, to estimate the physical properties of the SABOCA sources, such as H_2 column density N_{H_2}, mass, and average dust temperatures T_{d}. We do this by fitting SEDs to each pixel in the maps to trace the local heating sources and estimate the core-scale temperature and column density. The formulations used are the same as when fitting the 4 bands at a coarser resolution (Sec. 2.4.1). Assuming that the 4-band SED fits, in general, describe the bulk of the cold component in the coarser resolution maps, we scaled the 70 μm flux densities in order to remove the contribution of a second, hotter gas component often seen towards deeply embedded protostars and massive young stellar objects (MYSO). The scaling factor is defined as the flux ratio of the observed 70 μm emission map and the extrapolated 70 μm flux based on the SED fit with the 4 bands. This step is necessary because the majority of our sources are mid-infrared weak, thus dominated by cold dust which mainly emits at wavelengths longer than ~100 μm. Hence our method of using only the 70 μm and the 350 μm data would lead to an underestimate of core masses, with flux at 70 μm predominantly originating from the deeply embedded heating sources.

We find that the scaling factors are generally less than 1.0 for most of our mid-infrared dark and relatively bright evolved sources. However, for the extremely bright OB cluster forming regions such as G10.6-0.4, G12.8-0.2 (ATLASGAL names: G010.6237-0.3833, G012.7914-0.1958) we find a ratio larger than one for the predicted 70 μm flux compared to the observed flux density. These sources are at the edge of prominent compact 70 μm emission features, and due to their more evolved nature, including the 70 μm flux in the SED fits without any scaling provides a better constraint on their temperature fit (e.g. Lin et al. 2016). Therefore, for those cases where the scaling factor exceeds 1, we use the original 70 μm fluxes. In the App. B we present two examples including one of these extremely bright OB clusters and the statistics of the scaling factors with the derived properties. The difference between the derived values using the original and scaled 70 μm flux density in the SED fits are generally within 20% for temperature and 50% for column density depending on the flux scaling factor, which are discussed in detail in Appendix B. The uncertainties of the fitted column density and dust temperature are within 20%. Examples of the 10.″ temperature and column density maps are shown in bottom panels of Fig. 2.5. Altogether we could perform a pixel-by-pixel SED fits for 198 of our maps, which includes 971 cores identified in the SABOCA maps.

2.4.3 Statistics of the physical properties of ATLASGAL clumps and SABOCA cores

We derive the physical properties, such as average dust temperature, mass, bolometric luminosity of the identified SABOCA compact sources, and their ATLAGSAL host clumps, from the pixel-by-pixel SED fitting described in Sec. 2.4.2.

The average dust temperature is calculated from the mean pixel values within the identified Gaussian structures based on the *FWHM*s reported in Csengeri et al. (2014). Similarly, we calculate the clump masses by summing up the column densities (N_{H_2}) of each pixel over the source area at distance, d (see Sec. 2.1),

$$M_{clump} = \mu m_H \overline{N_{\mathrm{H}_2}} A d^2 \tag{2.2}$$

where A stands for the clump area defined by πR^2. The radius is defined as $R = \sigma$, where $\sigma = \frac{FWHM}{2\sqrt{2ln2}}$. We estimate the total bolometric luminosity by integrating the fitted SEDs,

$$L_{\mathrm{bol}} = 4\pi d^2 \int_0^\infty S_\nu d\nu \tag{2.3}$$

where S_ν is derived by the fitted SED curve described in Sec. 3.3.1, and is summed up within $R = \sigma$, as well.

To estimate the physical properties of the 350 μm SABOCA compact sources we follow the same procedure as described above using the corresponding parameters fitted by *Gaussclumps* and using the high-resolution column density and dust temperature maps (10.″). The physical parameters of the individual ATLASGAL clumps and the SABOCA sources are listed in Table 2.2 and Table 2.3, respectively. We list the general statistics of the clump and core properties in Table 2.4 for all the sources and the distance limited sample.

The distribution of the physical properties of the clumps are shown in Fig. 2.7. The average mass of

Table 2.2: ATLASGAL clump properties.

ATLASGAL name	$FWHM_{maj}$ ($''$)	$FWHM_{min}$ ($''$)	S_{int} (870 μm) (Jy)	Distance (kpc)	Mass ($M_{\odot}$)	Luminosity ($L_{\odot}$)	Average $N(H_2)$ (cm^{-2})	Average T_{d} (K)
G300.9506+0.8944	70.0	22.0	4.2	3.3	308	297	4.5×10^{22}	15.1
G301.1292−0.2278	50.0	19.0	2.1	4.6	301	1.7×10^{4}	4.8×10^{22}	30.7
G301.1365−0.2256	26.0	23.0	34.5	4.6	494	3.9×10^{4}	1.0×10^{23}	33.9
G301.1438−0.2227	42.0	19.0	2.1	4.6	260	7.1×10^{3}	6.1×10^{22}	27.1
G302.1487−0.9494	29.0	26.0	1.8	11.1	474	5.3×10^{3}	1.5×10^{22}	22.9
G303.1169−0.9724	24.0	20.0	1.8	1.6	6	133	1.4×10^{22}	25.7
G303.9978+0.2804	28.0	19.0	0.8	11.6	417	3.2×10^{3}	1.9×10^{22}	21.5
G304.0209+0.2919	27.0	22.0	2.3	11.6	961	4.6×10^{3}	3.5×10^{22}	19.8
G304.7127+0.6005	29.0	22.0	0.8	2.3	24	30	2.1×10^{22}	15.7
G305.0943+0.2510	60.0	20.0	2.1	6.0	378	1.4×10^{3}	2.3×10^{22}	18.9
G305.2581+0.3275	55.0	19.0	2.2	6.1	489	1.9×10^{3}	3.3×10^{22}	19.2
G305.2608+0.3083	56.0	30.0	3.2	6.1	908	5.9×10^{3}	4.3×10^{22}	21.0
G305.7949−0.0965	45.0	25.0	4.0	6.3	750	1.1×10^{3}	4.0×10^{22}	16.1
G305.8040−0.0972	32.0	19.0	0.8	6.3	266	478	3.6×10^{22}	16.7
G309.1531−0.3517	36.0	21.0	1.5	3.2	80	299	3.2×10^{22}	19.0
G309.1721−0.3274	33.0	29.0	1.8	3.2	78	535	2.6×10^{22}	21.1

Notes. The columns are defined as follows: ATLASGAL name: clump name from the ATLASGAL catalog. $FWHM_{maj}$ and $FWHM_{min}$: Major and minor $FWHM$ size of the source from Csengeri et al. (2014). Distance: distance of the source from Urquhart et al (2018). S_{int}: the integrated flux density at 870 μm. Mass, luminosity, average $N(H_2)$ and T_{d} are based on the SED fitting in Sec. 2.4.1, calculated with 1σ source size.

Full table will be available on CDS.

Table 2.3: Properties of SABOCA sources, their 24 μm and 70 μm associations and parental clumps.

Name	Distance (kpc)	$M_{1\sigma}$ ($M_\odot$)	T_d (K)	$N(H_2)$ (cm^{-2})	$L_{1\sigma}$ ($L_\odot$)	MIR type	Parental clump
GS301.1350−0.2220	4.6	208.0	31.1	1.56×10^{23}	9.87×10^{3}	24sat	G301.1365−0.2256
GS301.1364−0.2252	4.6	162.3	38.9	1.66×10^{23}	2.40×10^{4}	22ct,70ct,24sat	G301.1365−0.2256
GS301.1400−0.2233	4.6	217.2	29.1	1.05×10^{23}	7.94×10^{3}	24sat	G301.1438−0.2227
GS302.1493−0.9497	11.1	96.0	26.0	1.90×10^{22}	2.23×10^{3}	22ct,70ct,24sat	G302.1487−0.9494
GS303.1176−0.9717	1.6	1.9	30.1	1.92×10^{22}	1.04×10^{2}	22ct,70ct,24sat	G303.1169−0.9724
GS303.9991+0.2799	11.6	182.2	21.1	4.04×10^{22}	1.23×10^{3}	22ct,70ct	G303.9978+0.2804
GS304.7120+0.6001	2.3	5.2	15.5	3.07×10^{22}	6.19×10^{0}	70ct	G304.7127+0.6005
GS305.0947+0.2501	6.0	115.7	18.1	5.10×10^{22}	3.17×10^{2}	70q	G305.0943+0.2510
GS305.0997+0.2484	6.0	54.4	18.9	3.86×10^{22}	1.95×10^{2}	70q	–
GS305.2566+0.3162	6.1	145.4	18.7	8.50×10^{22}	4.70×10^{2}	70q	–
GS305.8169−0.1115	6.3	257.7	17.0	1.50×10^{23}	4.56×10^{2}	22ct,70ct	–

Notes. The columns are defined as follows: Name: the SABOCA catalog source name. Distance: distance of the source in kpc. $M_{1\sigma}$: Mass of the source by summing up all the pixel values in the column density map according to Eq. 2.2, using a radius of 1σ. T_d: Average dust temperature of the source. $N(H_2)$: Average column density of the source. L_{sab}: Luminosity of the source by integrating the SED from 1μm to 1 mm according to Eq. 2.3. MIR type: Source mid-infrared association as described in Sec. 3.5. (24sat: associated with saturated 24 μm emission. 70ct: associated with PACS 70 μm compact source. 24ct:associated with MIPSGAL 24 μm compact source. 22ct: associated with WISE 22 μm compact source. HII: associated with (UC)HII regions. 70q: associated with extended 70μm emission or 70 μm quiet). Parental clump: The name of the ATLASGAL clump that the SABOCA core is associated with (Sec. 2.5.3).

Full table will be available on CDS.

Table 2.4: Physical properties of ATLASGAL clumps and SABOCA compact sources.

	All clumps (507)				Clumps at 2-4 kpc (205, 41%)			
	Max	Min	Mean	std	Max	Min	Mean	std
FWHM size (pc)	2.9	0.13	0.68	0.45	0.87	0.19	0.42	0.11
Mass ($M_\odot$)	9.71×10^3	0.05	598	1.03×10^3	1.42×10^3	3.0	172	156
T_d (K)	45.6	14.1	20.8	5.0	45.5	14.1	21.3	6.3
Σ (gcm^{-2})	3.6	0.004	0.33	0.32	1.8	0.005	0.4	0.4
	All SABOCA sources (971)				SABOCA sources at 2-4 kpc (405, 42%)			
	Max	Min	Mean	std	Max	Min	Mean	std
FWHM size (pc)	1.17	0.052	0.32	0.21	0.40	0.08	0.19	0.05
Mass ($M_\odot$)	5.43×10^3	0.017	198	374	435	5	52	50
T_d (K)	53.3	13.3	21.6	6.0	53.3	13.7	21.8	7.0
Σ (gcm^{-2})	4.3	0.05	0.4	0.3	2.0	0.06	0.4	0.3

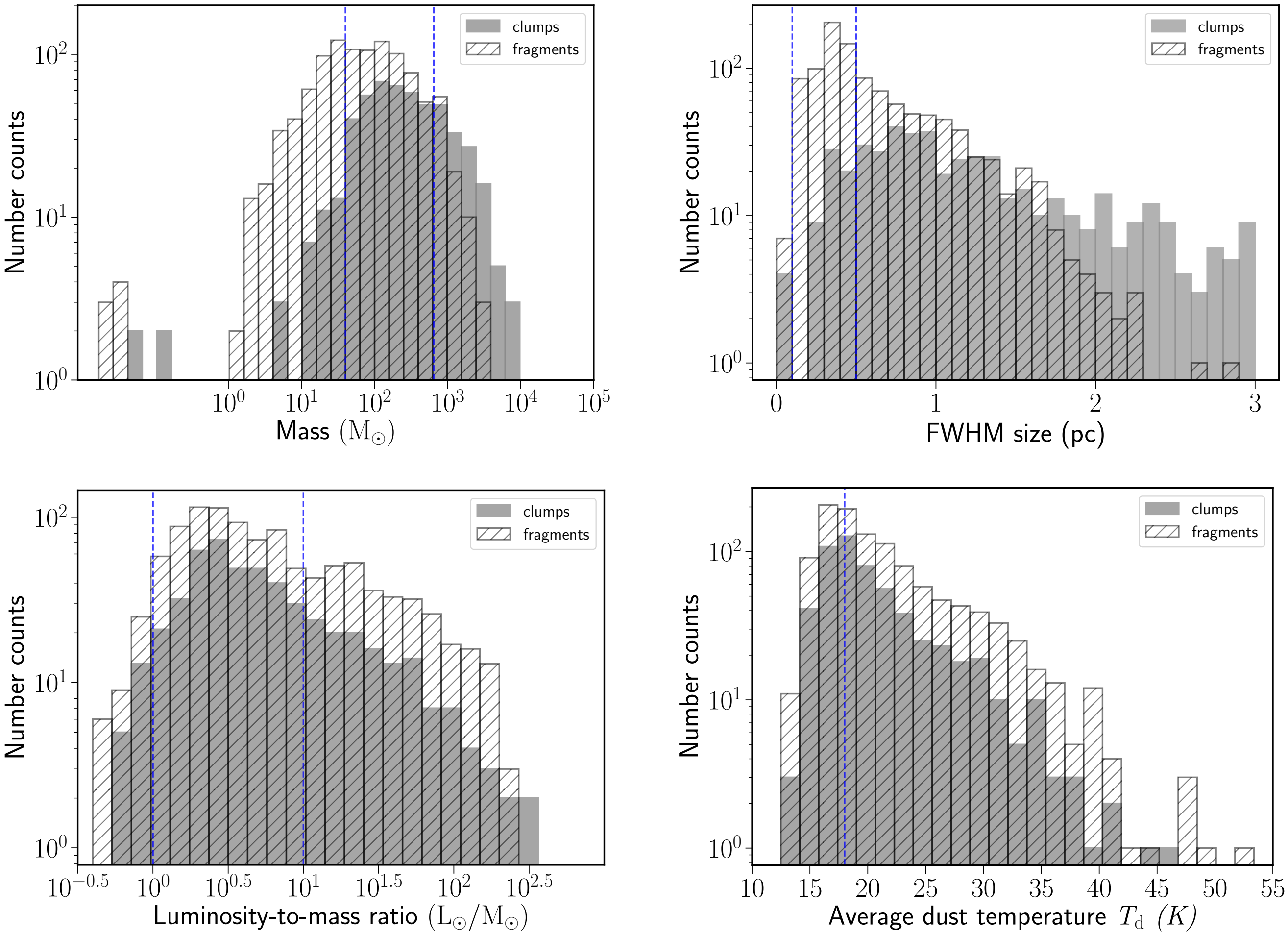

Figure 2.7: Distribution of the physical properties of all the observed ATLASGAL clumps and compact sources identified at 350 μm with SABOCA. *Top left*: The mass distribution of clumps and SABOCA compact sources. The vertical lines show mass limits of 40 $M_\odot$ and 650 $M_\odot$. *Top right*: Distribution of size which are the measured FWHM size from the *Gaussclumps* source extraction. Vertical lines show the 0.1 and 0.5 pc range for definition of cores and clumps. *Bottom left*: The luminosity-to-mass ratio distribution of the clumps and SABOCA compact sources. The vertical dotted lines indicate luminosity-to-mass ratios of 1 and 10, which are taken as empirical evolutionary boundaries in Molinari et al. (2016) for massive clumps. *Bottom right*: The temperature distribution with a vertical line showing 18 K, which is the average temperature for galactic background.

all of the clumps is 600 M$_\odot$. In total, 65% of the sources have > 100 M$_\odot$ and the most massive clump has a mass of 1×10^4 M$_\odot$, which is one of the more distant sources in our sample. In addition, there are 130 clumps above 650 $M_\odot$, which is a mass limit used by Csengeri et al. (2014) as a threshold for a massive clump to potentially form high-mass stars. The average mass of all the SABOCA sources is 198 $M_\odot$, and for the distance limited sample it is 50 M$_\odot$, which is ~3 times lower than the values of the clumps (Table 2.2).

The mean clump *FWHM* size of all the clumps and those in 2-4 kpc is 0.68 ± 0.45 pc and

0.42 ± 0.11 pc, corresponding to the typically observed scales for Galactic clumps. The mean $FWHM$ size is 0.31 ± 0.21 pc for all the SABOCA sources, and for the sources in 2-4 kpc the value is 0.19 ± 0.05 pc, corresponding to a typical core-scale.

We also calculate the surface density based on the average column density derived from SED fits, where $\Sigma = \mu m_H N(H_2)$ (g cm^{-2}). In Table 2.4, we can see that SABOCA sources have typically larger surface densities on average than the clumps, indicating a concentration of dense gas at smaller scales. The majority of the clumps (65%) and cores (78%) have a mass surface density larger than 0.2 g cm^{-2} which is used to identify promising massive star progenitors by Butler and Tan (2012).

We find dust temperatures between ~14 K and ~50 K for the clumps, and on average we find similar values for clumps and cores. This is expected from our SED fitting method which is mainly sensitive to the cold component. The most active star-forming clumps have an average dust temperature of > 40 K and correspond to the most massive OB cluster-forming regions in the Galaxy.

Due to our source selection strategy, we have a large fraction of clumps with low bolometric luminosity and a luminosity-to-mass ratio of less than 10 (74%). Since a low bolometric luminosity together with a large mass is indicative of an early evolutionary stage (e.g. Motte et al. 2007, Molinari et al. 2016), a large number of our targeted clumps are likely to be at early evolutionary stages. We indicate the $L_{\rm bol}/M = 1$ and $L_{\rm bol}/M = 10$ vertical lines in the luminosity-to-mass ratio distribution plot (Fig. 2.7); which show empirical limits from Molinari et al. 2016 for massive clumps in a starless or pre-stellar stage, and clumps hosting high-mass ZAMS stars, respectively. The $L_{\rm bol}/M > 10$ ratio can also correspond to a qualitatively different heating source reflecting the presence of deeply embedded UC-HII regions (see Sec. 2.4.4; see also Kim et al. 2018). The most evolved clumps, with luminosity-to-mass ratios above 100, e.g. G34.3+0.2, G10.6−0.4, G333.6+0.2 (Campbell et al. 2004; Liu, Ho and Zhang 2010; Lo et al. 2015, respectively), are clumps residing in well-known extreme Galactic massive star-forming regions.

2.4.4 Signposts of star-forming activity of the 350 μm SABOCA sources

We use the MIPSGAL point source catalog at 24 μm (~6″; Gutermuth and Heyer 2015) and the Herschel/Hi-GAL point source catalog at 70 μm (~8.″4; Molinari et al. (2016)) to assess the star formation activity of the SABOCA 350 μm compact sources. These catalogs have a comparable angular resolution to the SABOCA observations. We also make use of the WISE point source catalog (11.″ at 22 μm; Cutri et al. 2012) to complement the mid-infrared surveys as MIPSGAL is saturated at >2 Jy, while the WISE point source photometry is reliable to ~330.0 Jy flux density at 22 μm. We also used the existing RMS (Lumsden et al. 2013; Urquhart et al. 2013) and the CORNISH (UC-)HII region catalogs (Kalcheva et al. 2018) to identify the sources associated with HII regions that are likely to be saturated in mid-infrared images. These catalogs have a coordinate range that covers in total ~30% of our SABOCA (295 out of 971) cores. The higher angular resolution of the SABOCA data allows a better matching with these higher angular resolution ancillary catalogs compared to ATLASGAL, which is necessary to assess the star-forming activities in the cores.

We performed a cross-match between the position of the SABOCA sources and these catalogs with an angular separation limit of 8.″5 corresponding to the angular resolution of SABOCA maps. The distribution of the angular offsets between the SABOCA compact sources and their mid-infrared emission (Fig. 2.8, left panel) suggests a good positional correlation between the mid-infrared sources and the 350 μm SABOCA peak positions. The dispersion of offsets in the range of 2-4.″, which is consistent with the pointing accuracy of the telescope.

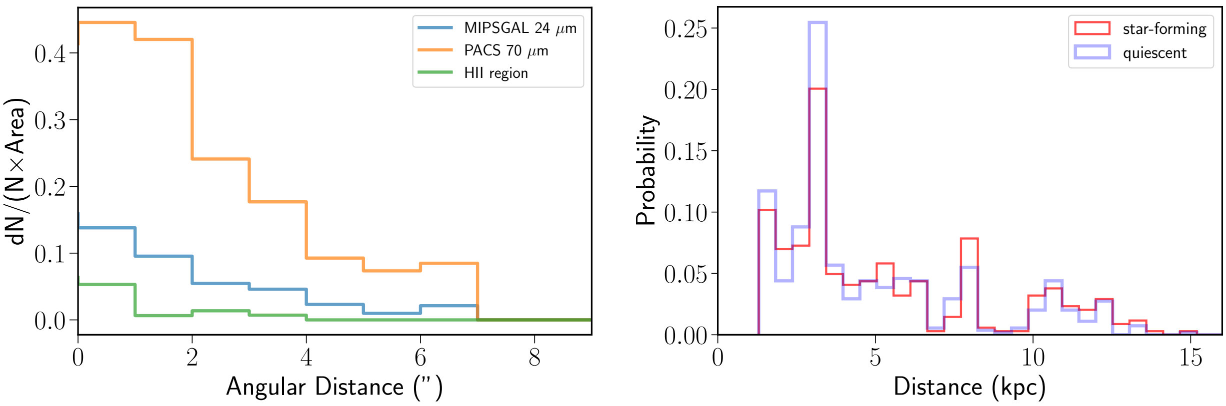

Figure 2.8: *Left*: Distribution of angular distances between SABOCA sources and their MIR compact source or/and HII region associations. In each bin, the probability of dN/N is normalised by the annular area defined by adjacent angular bins as dN/(N×Area); *Right*: Distribution of distances of star-forming and quiescent SABOCA compact sources.

We use the association with UC-HII regions, 24/22 μm or 70 μm point sources to distinguish between star-forming and quiescent cores and assess the statistics of their physical properties. Due to the varying diffuse mid-infrared background emission, the completeness of these catalogs is, however, not homogeneous. The sensitivity limit of the MIPSGAL 24 μm survey (5σ, ~10 mJy) can probe down to 18 $L_\odot$ protostars within 15 kpc following the calculation of Motte et al. (2007) based on IRAS colors from Wood and Churchwell (1989). This suggests that even intermediate-mass protostars could be revealed throughout our sample. However, as discussed in Gutermuth and Heyer (2015), the MIPSGAL catalog completeness is strongly dependent on the spatial variation of the local emission, therefore the sensitivity limit does not reflect the level of the completeness towards all sources. The sensitivity limit of the PACS 70 μm band of 0.2 Jy (Molinari et al. 2016) corresponds to a luminosity of ~25 $L_\odot$ at 5 kpc (Dunham et al. 2008). This similarly suggests that at least intermediate-mass protostars should be detected at 70 μm, if neglecting the spatial variation of the completeness level and source confusion.

In all the 1120 compact sources identified from the SABOCA maps, of which 971 have physical parameters based on their SED fitting, 13 (1.3%) have UCHII region counterparts. In the remaining sources, 184 (19.0%) are directly associated with 24/22 μm compact sources. In addition, we also have 87 (8.9%) sources that spatially coincide with regions of saturated 24 μm emission, but without 22 μm or 70 μm counterparts which are ignored in the following analysis. Of the 184 sources that have 24/22 μm compact sources, 18 do not have a 70 μm compact source counterpart. Visual inspection of these 18 sources shows that they are all associated with faint or extended 70 μm emission, and hence they are likely to be below the completeness limit of the PACS 70 μm catalog. Among the remaining sources, 142 (14.6%) have a compact source counterpart only at 70 μm. The remaining 545 (56.1%) sources are either dark at 24/22 μm or are associated with extended or diffuse 70 μm emission which is not included in the compact source catalog. To summarise, we have used the various surveys described above to classify 884 cores; 545 cores are found to be quiescent (64%) and 339 cores to be as star-forming (36%).

Dust extinction may prohibit detection of deeply embedded 24/70 μm compact sources. We calculate the dust opacities at 70 μm based on the derived column densities for quiescent cores with our assumed opacity law (see in Sec. 2.4.1). We find that 90% of the calculated opacities are lower than 1 with a 95% quartile level of opacity ~2.4, indicating that dust extinction does not significantly affect our classification. However, the effect of source geometry and the uncertainty of dust emissivity may also influence the actual extinction.

To check whether the non-uniform distances of our sources affect the classification, we show the distance distribution of the star-forming and quiescent cores in Fig. 2.8 (right panel). The two distributions are similar with a KS-test yielding p-value = 0.31 and D = 0.08 (p-value > 0.05 and $D < D_\alpha$ at a significance level of $\alpha = 0.05$), which means that there are not more quiescent cores appearing at nearer distances than star-forming cores, suggesting that the different distances do not bias our classification. However, we caution that this similarities in the distributions could be due to the presence of a mutual cancellation of two opposite biases: at larger distances, the objects identified will tend to be more massive and hence more likely to be star-forming already. This effect will be counteracting the decreasing likelihood of detecting mid-infrared compact sources. In the following, we restrict our analysis to distance-limited sample, or samples in certain distance bins, so that the results are less affected from the classification bias due to distance non-uniformity.

2.5 Discussion

In this section we compare the physical properties of the star-forming and quiescent SABOCA cores (Section 2.5.1), and investigate their capability of forming high-mass stars (Section 2.5.2). We study the fragmentation properties and the clump structure in Section 2.5.3 based on a distance limited sample of 2-4 kpc. In Section 2.5.4 we identify a sample of massive quiescent SABOCA cores at < 5 kpc that are potential high-mass pre-stellar core candidates.

2.5.1 Physical properties of star-forming and quiescent cores

In Sec. 2.4.4 we classify the SABOCA cores into two categories according to their radio, mid- and far-infrared compact source associations: star-forming and quiescent. As discussed in the following paragraphs, our approach is more sensitive to the deeply embedded low- to intermediate mass protostars than using a single wavelength.

A 24 μm point source associated with a compact 350 μm source suggests the presence of a local heating source, corresponding to one or more protostars. However, the absence of a 24 μm point-source does not necessarily mean that there is no star-forming activity, a high optical depth or mid-infrared confusion may inhibit the detection of compact 24 μm sources. In that case, being more sensitive to the outer regions of internally heated cores, the PACS 70 μm compact source association (e.g. Dunham et al. 2008; Ragan, Henning and Beuther 2013) is used to further pinpoint the star-formation activity. While it is clear that the absence of a 24-70 μm point source appears to exclude the presence of a massive YSO, early stage (even up to high-mass) protostars have been detected towards infrared quiet massive clumps (Bontemps et al. 2010; Feng et al. 2016; Csengeri et al. 2018), and dense cores with luminosities as low as 400 $L_\odot$ (Duarte-Cabral et al. 2013).

In Fig. 2.9 we show the distribution of the physical parameters of cores located at a distance of 2-4 kpc. This sample consists of 233 quiescent and 129 star-forming cores. We find that the star-forming cores have, in general, a modestly higher temperature (24.0 K±0.75 K) than the quiescent cores

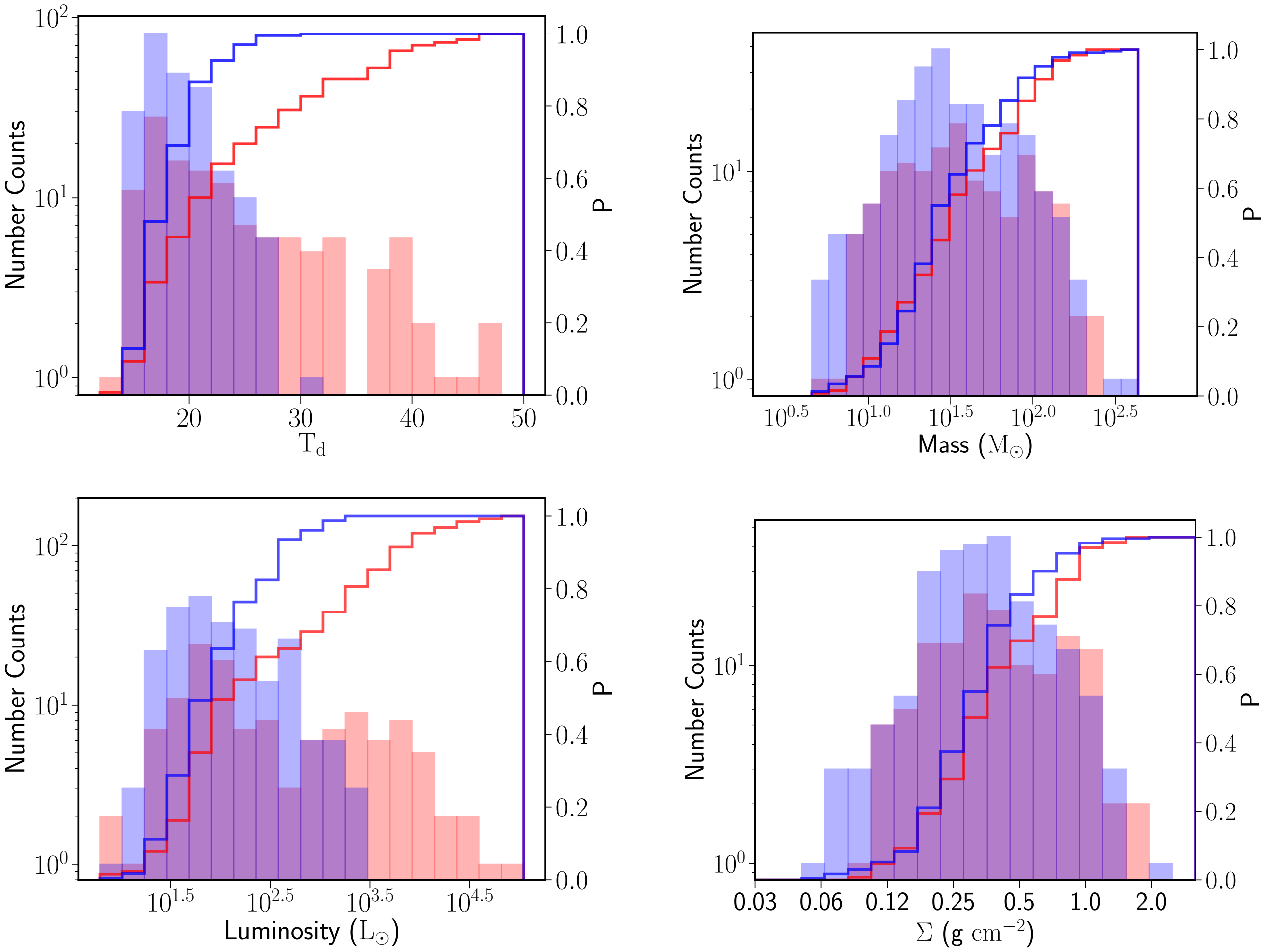

Figure 2.9: Distribution of the physical properties of star-forming and quiescent SABOCA compact sources in the 2-4 kpc distance bin, in red and blue color, respectively. *Top left*: The temperature distribution of two categories. *Top right*: The mass distribution. *Bottom left*: The luminosity distribution. *Bottom right*: The surface density distribution. In each plot, the cumulative probability distribution is drawn with respective colors according to the right y-axis.

(18.9 K±0.19 K). We obtain a p-value < 0.001 for a KS-test confirming that the temperatures of the two populations are statistically different. However, we also note that there is a large fraction (43%) of star-forming cores have a relatively low dust temperature (< 20 K). There is also a small number of quiescent cores with temperatures larger than 25 K (5%). Visual inspection of these cores reveals that they are located close to extended nebulosities at 70 μm; these cores may, therefore, be star-forming cores that remain undetected due to confusion from the nearby bright source or genuinely quiescent cores with the warmer temperature caused by external heating.

The luminosity distribution of the SABOCA cores is presented in the bottom left panel of Fig. 2.9. This plot shows a similar picture as the dust temperature with the star-forming cores having higher luminosities. The KS test results in p-value < 0.001, again indicating a distinct distribution. However, we find a large number of quiescent sources with high luminosities of $>10^3\ L_\odot$. The number of quiescent sources decreases to zero above $L_{\rm bol}{\sim}10^{3.5}\,L_\odot$, which is equivalent to the ZAMS luminosity of a B2-B4 star. As discussed in the previous paragraph, these large values of the bolometric luminosities towards quiescent cores are either due to external heating or to a higher level of confusion and blending with nearby sources. So it is possible that some of the quiescent cores might be protostellar, however, the lack of a corresponding bright 24 μm source suggests that the star formation is still at a very early stage.

The mass distribution of the quiescent and star-forming sources is remarkably similar. Together with their difference in bolometric luminosities, this may suggest that the cores classified as quiescent are in an earlier stage of star formation, and would follow the same evolutionary path as the star-forming cores (Csengeri et al. 2017b, see also discussion in Sec. 2.5.2). The range of typical core masses is between 10 and 320 $M_\odot$, with an average mass of star-forming and quiescent cores of $53.1{\pm}4.2\,M_\odot$ and $45.5{\pm}3.1\,M_\odot$, respectively. The KS test yields p-value = 0.26, indicating a similar mass distribution. The typical core masses for star-forming and quiescent cores are not significantly different. The star-forming cores have on average smaller size (0.15±0.002 pc in $FWHM$) compared to quiescent cores (0.16±0.003 pc in $FWHM$). The mean mass surface density of star-forming cores ($0.50{\pm}0.03\,{\rm g\,cm^{-2}}$) is higher than that of the quiescent cores ($0.40{\pm}0.02\,{\rm g\,cm^{-2}}$). The KS-test yields p-value ~ 0.012 (~1%), indicating that the two distributions are different, with star-forming cores having higher surface density.

The similar mass distribution and relatively different surface density distribution of quiescent and star-forming cores indicate that, at the typical scale of ~0.2 pc the quiescent cores have enough mass assembled to evolve into protostellar cores when contracting. Cores can be gravitationally contracting ever since they first appear, allowed by the presence of an unstable background (Naranjo-Romero, Vázquez-Semadeni and Loughnane 2015). In the framework of dynamical evolution cores are clump-fed (see also Wang et al. 2010), which is supported by growing observational evidence for gas replenishment beyond the core-scale (e.g. Galván-Madrid et al. 2009, Csengeri et al. 2011, Peretto et al. 2013, Liu et al. 2015, Chen et al. 2019). In this case cores prior to star formation may be expected to have a lower mass compared to star-forming cores, however, the fact that quiescent cores are relatively more extended, and their aspect ratio (from *Gaussclump*) showing them to be less roundish compared to star-forming cores, may indicate the similar mass distributions do not contradict with such dynamical evolution scenario. In addition, some of the star-forming cores may be in a state of gas dispersal (Fig. 2.11). Among the quiescent cores, the most luminous ones ($L > 10^{2.5}\,L_\odot$) have larger surface densities of $0.69{\pm}0.13\,{\rm g\,cm^{-2}}$ compared to their less luminous counterparts with $0.33{\pm}0.01\,{\rm g\,cm^{-2}}$. The number of quiescent cores decreases significantly above ${\sim}0.5\,{\rm g\,cm^{2}}$. This may suggest that when reaching a higher mass surface density regime the cores necessarily form high-mass stars, for which the formation time-scales are shorter than for low- and intermediate mass star-formation (Csengeri et al. 2014, Urquhart et al. 2018).

2.5.2 Fraction of massive star-forming cores

To estimate what fraction of the SABOCA cores are potential precursors or in the early stage of forming massive stars, we show the mass-radius plot and mass-luminosity diagram of all the samples in Fig. 2.10 and Fig. 2.11. Both of these plots show the distribution for the star-forming and quiescent cores in red and blue, respectively. For this analysis we only use sources located at 1-2 kpc, and 2-4 kpc distance ranges, which allows us to compare sources with similar size-scales. We briefly discuss sources more distant for comparison purposes.

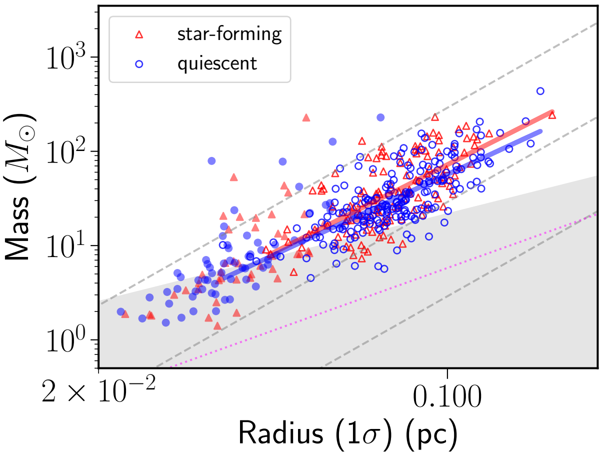

Figure 2.10: Mass-radius diagram of SABOCA compact sources. The quiescent cores and star-forming cores are indicated with blue and red colors, in 2-4 kpc (hollow markers) and 1-2 kpc (filled markers) distance bins. The dashed lines show the constant volume density of 10^4, 10^5 and 10^6 cm^{-3}. Magenta dotted line indicate Larson's third relation of approximately 10^{21} cm^{-2} column density. Gray filled region is below the empirical threshold of massive star-formation from Kauffmann & Pillai (2010) scaled to match the dust opacity values we used in this work. Red and blue lines indicate the fitted linear regression for the quiescent cores and star-forming cores in 2-4 kpc.

The mass-radius plot (Fig. 2.10) shows no clear difference between the star-forming and the quiescent cores in mass scale. A substantial number of the cores are found above the empirical threshold for massive star-formation introduced by Kauffmann and Pillai (2010) suggesting that a large fraction of them are capable of, or are already in the process of forming high-mass stars. In particular, we cover a large fraction of quiescent cores that have a radius of ~0.2 pc with masses of ~100 $M_\odot$ corresponding to a mass surface density of ~0.2 g cm^{-2}, thus representing potentially young regions where massive star formation could occur (e.g. Butler and Tan 2012).

The derived power-law relation of $M \propto r^\alpha$ gives $\alpha = 2.67 \pm 0.25$ and $\alpha = 2.60 \pm 0.16$ for star-forming and quiescent cores in a distance range of 2-4 kpc, respectively. For sources in 1-2 kpc, the indices are somewhat larger, with $\alpha = 3.00 \pm 0.62$ and $\alpha = 3.07 \pm 0.32$ for the star-forming and quiescent sample, respectively. Moving to sources at 4-8, 8-12 kpc, more shallower slopes of ~2.0 are found. These slopes are generally steeper than observed on the even larger clump-scale where a relation of $M \propto R^{1.4-1.7}$ is derived (e.g. Urquhart et al. 2018). The trend of a steepening mass-radius relation at small scale (or smaller distance range) is also seen in, e.g., Ragan, Henning and Beuther (2013) towards cores in infrared dark clouds, and in Beuther et al. (2018) towards young massive star-forming regions at thousands of au scale (as reflected in their Fig. 11).

Observationally, the Larson's density-size relation ($M \propto R^2$) could be due to a selection effect of a certain column density threshold, as frequently pointed out by previous works (e.g. Larson 1981, Ballesteros-Paredes and Mac Low 2002, Camacho et al. 2016). In our case, the more distant objects having smaller slope of power-law dependence on radius could be simply due to the fact that they correspond to larger physical sizes, and thus a larger contribution from their more diffuse envelope. The steepening of the mass-radius relation from slope~2 to ~3 correspond to a change from constant column density to constant volume density. Considering that cores are usually embedded in a gaseous

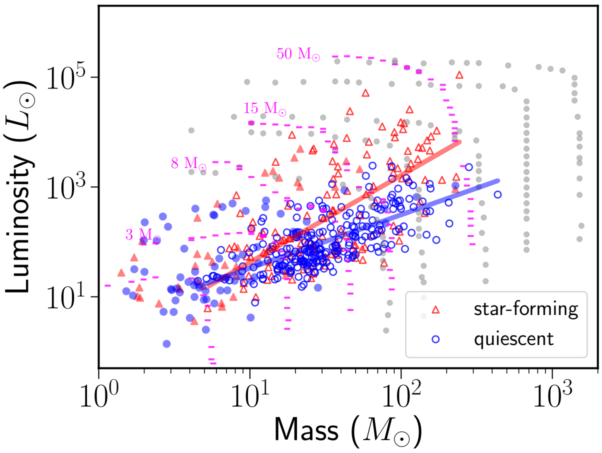

Figure 2.11: Luminosity-mass diagram of SABOCA compact sources. The quiescent cores and star-forming cores are indicated with blue and red colors, in 2-4 kpc (hollow markers) and 1-2 kpc (filled markers) distance bins. The empirical evolutionary tracks for massive clumps of envelope masses 80, 140, 350, 700, and 2000 $M_\odot$ in Molinari et al. (2008) are shown in grey dots. André et al. (2008) tracks for final stellar masses of 1, 3, 8, 15 and 50 $M_\odot$ are shown in magenta dashed lines. Red and blue lines indicate the fitted linear regression for the quiescent cores and star-forming cores in 2-4 kpc.

environment, the slopes of $\alpha = 3, 2, 1$ can result from different environments such as (spherically) uniform medium, a two-dimensional layer or a centrally concentrated filament, respectively (Myers 2009). This again indicates that at larger distances the amount of envelope gas might be influencing the slope, i.e. cores appear more "concentrated" if a diffuse layer is involved. On the other hand, the different power-law forms of $M \propto R^2$ or $M \propto R^3$ might indicate different modes of accretion (Hennebelle 2012), either dominated by turbulence from larger scale or the proto-cluster's self-gravity. Hence the steepening of the mass-radius relation may be reflective of the successively prevailing role of self-gravity at smaller scale (see also Camacho et al. 2016).

The luminosity and mass distribution for the star-forming versus quiescent cores is shown in Fig. 2.11. The evolutionary tracks for different final stellar masses and initial envelope masses (André et al. 2008; Molinari et al. 2008) are also included in this plot. These tracks have two main components, a vertical track that represents the main accretion phase and a horizontal track that indicates the clump gas dispersal phase. Where these lines join forms an apex that effectively defines the start of a star's zero-age main sequence (ZAMS) lifetime. The majority of the quiescent cores are below this apex and are, therefore, in the early stage of the evolution. Some of the star-forming cores, on the other hand, may be in a phase of gas dispersal. The brightest star-forming cores are clusters around or above the apex, indicating that many have reached the ZAMS stage and the envelope clean-up phase has probably begun (Molinari et al. 2008). Although scattered, the two distributions for quiescent and star-forming cores are clearly distinct for core masses larger than a few tens of $M_\odot$, with star-forming cores having larger luminosities. A linear regression fit between the log-log mass and luminosity give $L \propto M^{0.97\pm0.06}$ and $L \propto M^{1.58\pm0.16}$ for quiescent and star-forming cores in 2-4 kpc, respectively. Similarly drastic differences in power-law slopes for the sources in 1-2 kpc distance are found, with $L \propto M^{0.76\pm0.16}$ and $L \propto M^{1.37\pm0.23}$ for quiescent and star-forming cores. Moving further to sources at 4-8 kpc, the difference in slopes gets smaller, with quiescent cores having $L \propto M^{1.20\pm0.08}$ and star-forming cores $L \propto M^{1.40\pm0.13}$. Within the uncertainties, for clumps a consistent relationship is found between luminosity and mass with $L \propto M^{1.3}$ (e.g. Molinari et al. 2008; Urquhart et al. 2018). The less pronounced difference in the mass-luminosity scaling relation of these two populations with larger distances can be explained if the mid-infrared source association with the submillimeter compact source becomes less robust with increasing distance to distinguish genuine quiescent cores, but also because more distant sources have more ambient gas, as mentioned before, which contributes to the mass but not much to the luminosity. The latter case is consistent with the fact that for sources more distant than 8 kpc, shallower slopes are found for quiescent and star-forming cores as $L \propto M^{0.81\pm0.13}$ and $L \propto M^{0.91\pm0.20}$. In line with our previous results, i.e. the mass distribution and the mass-radius relation of the quiescent cores and star-forming cores, the luminosity and mass diagram with evolutionary tracks also suggests that a significant fraction of these cores can form a high-mass star, should they eventually collapse on a single object.

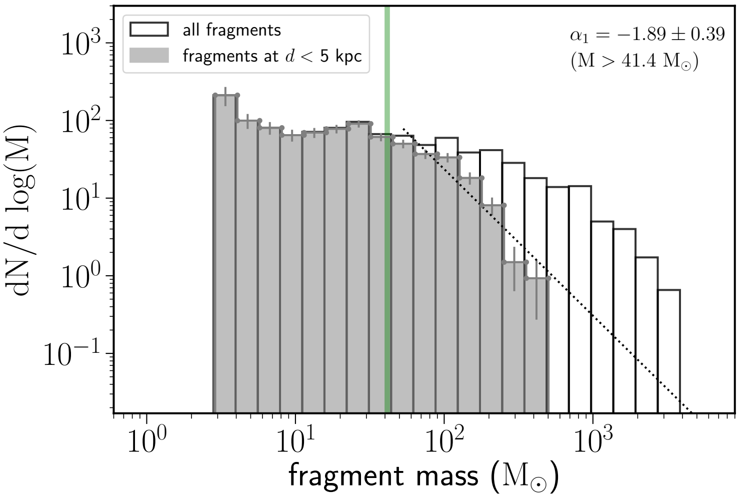

Figure 2.12: Fragment mass distribution of all SABOCA sources. The fitted power-law index of the all the sources at < 5 kpc above our mass completeness (> 41.4 $M_\odot$) is indicated by the green vertical line.

In Fig. 2.12 we show the mass distribution of the cores ($\Delta N/\Delta \log(M)$, André et al. 2014), of the SABOCA cores at < 5 kpc. The completeness level of our sample is not straightforward to assess due to the varying sensitivity, and the different dust temperatures in each field. We estimate the mass completeness use the largest noise level (0.18 Jy/beam) for sources at $d < 5$ kpc, and assume a dust temperature of 15 K, which is the lowest value we have for the core population. This allows us to obtain a conservative estimate of the mass completeness limit of cores in the sample. With a flux density of 3σ and a source size close to the beam size, the mass completeness limit is approximately 41.4 $M_\odot$. We fit a power-law to the cores at $d < 5$ kpc above 41.4 $M_\odot$, and find a power-law index of -1.89±0.39. Although the fit has large uncertainty, the slope is larger than the Salpeter IMF (−1.35), and is also steeper than recent findings of mass distribution of cores in higher angular-resolution studies of the early-stages of high-mass proto-clusters (e.g. Csengeri et al. 2017a; Motte, Bontemps and Louvet 2018). This could be explained by the fact that our study is more limited by confusion due to the poorer angular resolution; the slope is fitted in a higher mass range than these works suggesting that there could be intrinsically less massive cores at this larger scale (0.1-0.2 pc). On the other hand, the derived core mass distribution may be described better by a log-normal than a power-law distribution, as shown by previous studies (e.g. Peretto and Fuller 2010). Indeed we also find that moving the cutoff mass to a higher value would result in a steeper fitted slope. We also note that different source extraction methods may result in different core mass distributions (e.g. Cheng et al. 2018) and such results should be interpreted with caution.

2.5.3 Clump structure and fragmentation

Association of cores to clumps: fragmentation level

Here, we investigate the hierarchical structure of the clumps by assigning the SABOCA cores (child fragments) to their parent clumps in which they are embedded. We focus on the 971 SABOCA sources that have physical properties derived in the analysis here. Because the Jeans length is typically resolved up to 4 kpc, we again consider sample in 2-4 kpc distance range, while the sample located in 1-2 kpc are added in some plots for comparison purpose.

For each parent and child structure, we generate a mask based on their $FWHM$ size from `Gaussclumps` and assign the child fragments to their parental clumps based on their overlapping area as illustrated in Fig. 2.13. Clumps located at the edge of the SABOCA maps are omitted from this analysis since we may not cover the full extent of the clump. We calculate the fragmentation level in two ways: *exact* $N_{\rm mm}$ corresponds to the exact sum of the probability of overlapping areas of child fragments within the extent of the parent clump; the other is *rounding* $N_{\rm mm}$, which assigns each fragment to the clump with which it has the largest overlapping area. In short, the *exact* N_{mm} considers fragments overlapping with multiple clumps.For example, fragment 3 in Fig. 2.13, which overlaps with two clumps giving 0.20 and 0.33 to the two clumps' *exact* $N_{\rm mm}$ while it is counted to the central clump as 1 in *rounding* $N_{\rm mm}$. In this approach, the sum of *exact* $N_{\rm mm}$ equals that of *rounding* $N_{\rm mm}$ while for some clumps, *rounding* $N_{\rm mm}$ may be zero if a fragment overlapping with it has a larger proportion of area inside another clump.

We allocate 874 fragments to 444 clumps for the whole sample, with the remaining ~100 SABOCA sources lack of parental clump structure, and 353 fragments to 161 clumps in the 2-4 kpc distance bin, 77 fragments to 37 clumps in the 1-2 kpc distance bin; consequently, each clump average ~2 fragments. This is similar to what Merello et al. (2015) find going from 33.″ to 8.5.″ resolution. The thermal Jeans mass and Jeans length for a clump with a temperature of 20 K and a volume density of 10^4-10^5 cm^{-3}, is 2-6 $M_\odot$ and 0.1-0.3 pc, respectively (Bontemps et al. 2010; Palau et al. 2015). Even at a later stage with a typical temperature of 30 K, the Jeans mass is only a factor of two higher, and the Jeans length is only 20% larger. Therefore, we resolve the hierarchical fragmentation of clumps to cores, on the scales of 0.1-1.0 pc. Considering the typical clump properties of our sample, our results suggest that the number of fragments is broadly consistent with the Jeans length that we resolve here: the number of fragments is consistent with the number of predicted Jeans lengths within the clump's size. But the SABOCA cores have considerably larger masses compared to that of the thermal Jeans mass by a factor of 10-100. This has been found in similar studies of $\lesssim$0.1 pc cores or condensations (e.g. Motte et al. 2007, Wang et al. 2011, Csengeri et al. 2017a).

In Fig. 2.14 we investigate in detail the fragmentation level of the clumps as a function of their physical properties for sources in 2-4 kpc distance. For the analysis, we only take into consideration parental clumps that have at least one fragment lying entirely within the clump. The coloured points mark the fragment numbers according to the *rounding* $N_{\rm mm}$ criterion and gray points the *exact* $N_{\rm mm}$

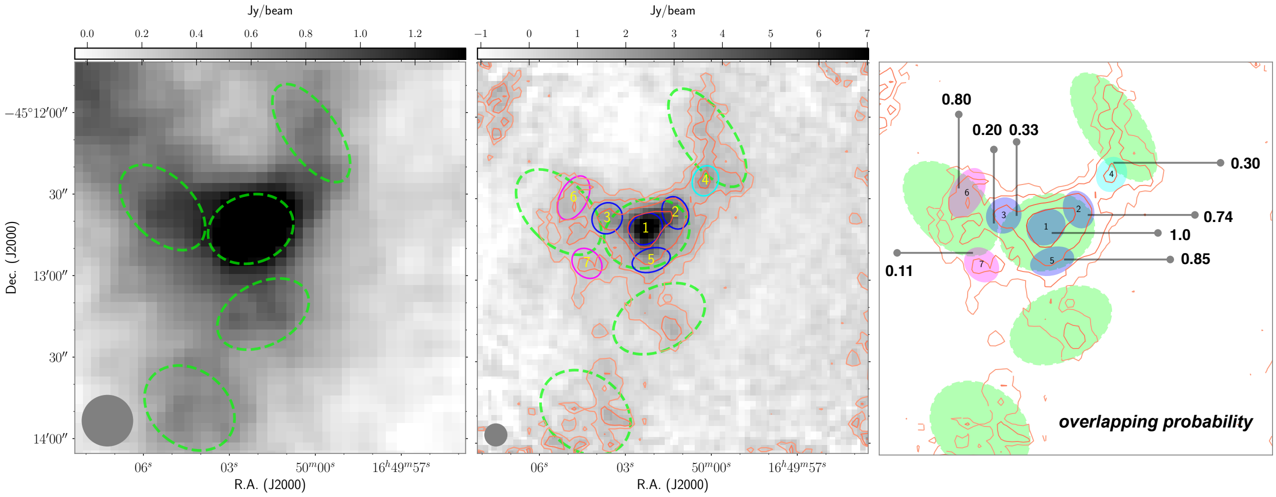

Figure 2.13: Example of fragment allocation criterion towards an example SABOCA mapping field. The left panel shows the 870 μm LABOCA emission in grayscale, overlaid with ATLASGAL clumps in green dashed ellipses. The middle panel shows the 350 μm SABOCA emission in grayscale with contour levels from 3σ to the peak flux with 5 linear logarithmic spacing. Each SABOCA core is labeled with a number and will be refered to as Nr. x. Green dashed ellipses mark the ATLASGAL clumps as identified in Csengeri et al. (2014). Blue, magenta and cyan ellipses mark the position of three sets of fragments belonging to several ATLASGAL clumps. In the right panel (slightly zoomed in compared to the middle panel), the overlapping possibilities of each fragment with the ATLASGAL clumps are indicated with arrows.

with each pair linked with dotted lines. We find that although the different fragment allocation methods may result in quantitatively different fragmentation levels, the general trend of fragmentation is similar. Therefore, both methods give a qualitatively similar picture.

Comparing the level of fragmentation, i.e. the number of fragments with clump mass, L/M and the predicted number of fragments with Jeans scenario, we find a generally significant scatter in the fragmentation levels, while the left panel of Fig. 2.14 suggests that the number of fragments increases slightly with clump mass. The Spearman correlation coefficient is 0.39 (*exact* $N_{\rm mm}$ vs. $M_{\rm clump}$, 0.38 of *rounding* $N_{\rm mm}$ vs. $M_{\rm clump}$, p-value<0.001), indicating a moderate correlation. We hereby define the specific fragmentation level as a number of fragments per unit clump size, as $\mathrm{N}_{mm}/\mathrm{R}_{clump}$. The normalisation by clump size is necessary given our limited angular resolution improvement in identifying fragments, such that one tends to pick up more fragments when the clump size is larger. The middle panel shows the specific fragmentation level as a function of the clumps' luminosity-to-mass ratio, a proxy of the evolutionary stage (e.g. Molinari et al. 2008; Csengeri et al. 2016a; Urquhart et al. 2018). There is a trend of subtle increase in the specific fragmentation as a function of L/M, with a Spearman correlation coefficient of 0.24 (*exact* $N_{\rm mm}/R_{\rm clump}$ vs. $L_{\rm clump}$, 0.29 of *rounding* $N_{\rm mm}/R_{\rm clump}$ vs. $L_{\rm clump}$, p-value~0.015). We caution that a higher $L_{\rm bol}/M$ ratio could also be due to that the most massive (proto)stars are forming within the clump (Ma, Tan and Barnes 2013) rather than an evolved stage characterised by gas dispersal. Finally, comparing the number of fragments with the thermal Jeans fragmentation prediction, we examine the correlation between specific fragment level with clump gas density (middle right panel of Fig. 2.14), and find a Spearman correlation coefficient of 0.41 (*exact* N_{mm}/R_{clump} vs. ρ_{clump}, 0.45 of *rounding* N_{mm}/R_{clump} vs.

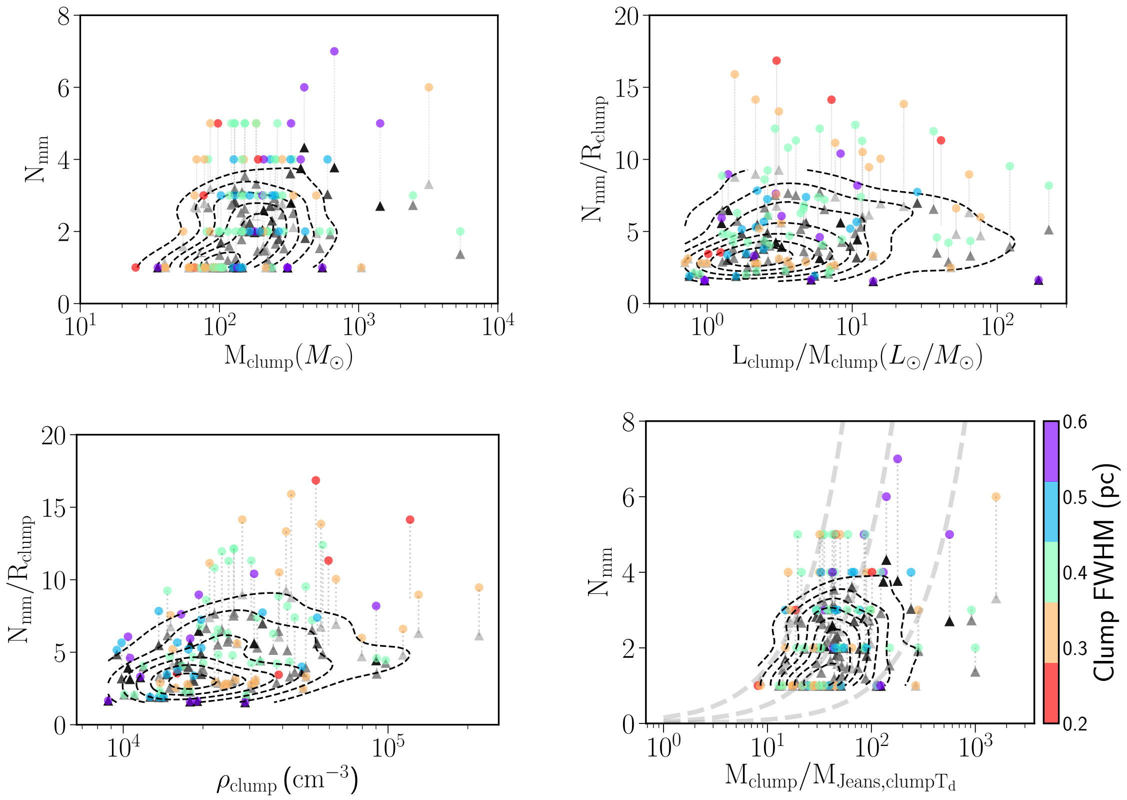

Figure 2.14: Fragmentation level as a function of clump properties of sources located at a distance in 2-4 kpc. In each plot, data points are color-coded according to the clump size. Gray triangles show the exact fragment number *exact* N_{mm}; colored dots show the rounding fragment number *rounding* N_{mm} (see definitions in Sec. 2.5.3). Dashed contours show the distribution of *exact* N_{mm} from Gaussian kernel density estimation. *Upper left*: Number of fragments as a function of clump mass. *Upper right*: Specific fragment level (N_{mm} normalised by clump radius) as a function of the clump's luminosity-to-mass ratio. *Lower left:* Specific fragment level as a function of the clump's density. *Lower right*: Number of fragments as a function of predicted number of fragments based on Jeans fragmentation scenario. Gray dashed lines mark the lines of N_{mm} = 0.15/0.05/0.01×$M_{\mathrm{clump}}/M_{\mathrm{Jeans\,clumpT_d}}$.

ρ_{clump}, p-value<0.001). Based on the clump's temperature and gas density, we also find a moderate correlation between the fragment level with the predicted Jeans number ($N_{Jeans} = M_{clump}/M_{Jeans}$), with a Spearman correlation coefficient of 0.31 (*exact* N_{mm} vs. N_{Jeans}, 0.32 of *rounding* N_{mm} vs. N_{Jeans}, p-value~0.001). We also notice that the clumps considered here have a positive correlation of their gas volume density and temperature ($T \propto \rho^{0.22}$), corresponding to the gas equation of state (EOS) having a polytropic exponent of $\gamma \sim 1.22$, close to the upper limit relevant for Galactic molecular clouds (Spaans and Silk 2000). The increase of temperature with density means that the Jeans mass decreases slowly with density than isothermal gas, favouring less fragmentation. If compared with an assumed initial temperature of 20 K, i.e. the clump temperature when fragmentation happened (e.g. Palau et al. 2015), a stronger correlation between observed fragmentation level with predicted Jeans number is found, with a Spearman correlation coefficient of 0.40 (*exact* N_{mm} vs. N_{Jeans}, 0.42 of *rounding* N_{mm}

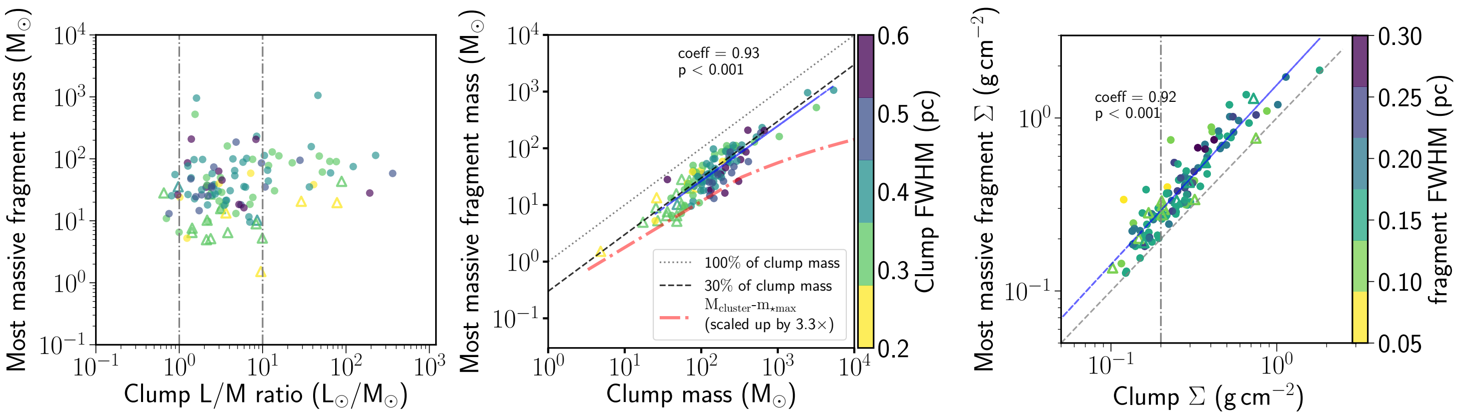

Figure 2.15: Most massive fragment mass as a function of clump properties for sources at a distance 2-4 kpc (dots) and 1-2 kpc (triangles). *Left*: Mass of the most massive fragment as a function of clump luminosity-to-mass ratio. Vertical lines mark the luminosity-to-mass ratio of 1 and 10. *Middle*: Mass of the most massive fragment mass as a function of clump mass. Gray lines show the 30% and 100% proportion of clump mass; blue dashed line shows the result of a linear fit on logarithmic scale to sources in 2-4 kpc distance range of $M_{\rm fragments}$ = 0.96log$M_{\rm clumps}$ − 1.18. The relation between cluster mass and maximum stellar mass in indicated in red dashed-dotted line, which is an analytical relation from Weidner, Kroupa and Pflamm-Altenburg (2013), and is scaled up by 3.3 assuming a 30% star-formation efficiency. Left and middle plots share the same color bar, with clumps color coded according to their sizes. *Right*: Surface density of the most massive fragment as a function of clump surface density. Vertical line marks the 0.2 g cm^{-2} empirical limit from Butler & Tan (2012). The blue dashed line shows the result of a linear fit to sources in 2-4 kpc distance range of log$\Sigma_{\rm fragments}$ = 1.03log$\Sigma_{\rm clumps}$+0.43.

vs. $N_{\rm Jeans}$, p-value<0.001). On smaller scales towards more evolved massive clumps, it seems Jeans fragmentation is at work (e.g. Palau et al. 2015, Beuther et al. 2018, Liu et al. 2019). It is possible that turbulence dominates the fragmentation process at larger scale (e.g. Zhang et al. 2009, Wang et al. 2014) to induce a larger critical mass. On the other hand, the time delay of fragments having Jeans mass may be explained within the global hierarchical collapse scenario (Vázquez-Semadeni et al. 2019), since the density of the fragments must grow to sufficiently high contrast, and while this happens, the Jeans mass in the contracting clump will have decreased. This implies that the fragment masses, especially in early stage clumps, will in general be larger than the average Jeans mass measured for the clump.

Since *Gaussclump* is a non-hierarchical source extraction method, the association of child structures to parental structures suffer from ambiguity, which introduces a source of uncertainty in the fragmentation level and the correlations with properties of the parental clumps. Here we provide two set of fragmentation levels as a first attempt to deal with the association uncertainties. As a further benchmark, we adopt a completely independent method of source extraction (`dendrogram`, Rosolowsky et al. 2008) which is not hampered by the association issue, and present the same correlations between fragmentation level with clump properties in Appendix C. We find that the moderate correlations we derive here are also present in the dendrogram analysis, with some of them showing slightly tighter correlations, i.e. $N_{\rm mm}$ vs. $M_{\rm clump}$ (Spearman correlation coefficient of 0.42), $N_{\rm mm}$ vs. $N_{\rm Jeans}$ (Spearman correlation coefficient of 0.48). These results help to solidify the analysis in this section.

Studies of smaller, but more homogeneous samples of massive cores and high-mass protostars based on higher angular resolution observations, e.g. thousands of au, did not find a clear correlation between the core properties and fragmentation level, except that a larger central volume density, a larger clump mass may lead to a larger number of fragments (Palau et al. 2015). Although we discuss here the core scale and a considerably larger sample, we can only conclude that there is no strong indication of Jeans fragmentation at work, or any trend of fragmentation level with clump evolution. It is, however, possible, that the overall sample covers a too wide range of Galactic clumps to reveal which clump properties could influence the fragmentation level. In addition, our source selection may not be homogeneous for massive clumps with luminosity-to-mass ratio range larger than 10 $L_{\odot}/M_{\odot}$.

In Fig. 2.15 we illustrate the relationship between the most massive fragment and clump properties for sources in 1-2 kpc (triangles) and 2-4 kpc (circles) distance bins. For these plots, we again only include cases in which the parental clump has at least one fragment lying entirely within the clump. Comparing the mass of the most massive fragment with the clump $L_{\rm bol}/M$ ratio, it seems that more evolved clumps with a larger $L_{\rm bol}/M$ ratio (Fig. 2.15, left panel) only host core masses above ~20 $M_{\odot}$. We hereby derive the correlations and regressions only for sources in 2-4 kpc distance range, and sources in 1-2 kpc distance range are shown in the figure for comparison purpose. We find a strong correlation between the clump mass and the mass of the most massive core. This correlation is statistically significant and has a Spearman coefficient of 0.92 and p-value less than 0.001. This clearly indicates more massive cores tend to form in more massive clumps. A linear fit in the logarithmic scale yields a relation of $\log M_{\rm mmf}$ = 0.96log $M_{\rm clump}$ - 1.18, which corresponds to $M_{\rm mmf}$ = 0.31 $M_{\rm clump}^{0.96}$. This relation is close to a fraction of 30% of the clump mass is assembled in the most massive fragment. In App. A.3 we demonstrate this strong correlation is preserved when `dendrogram` source extraction method is applied, regardless of the distinct concepts behind these algorithms in recognising cloud structures. As a comparison, Merello et al. (2015) find that 19% of the clump mass resides within the total dense substructures seen at 350 μm, when going from 30$''$ to 8.$''$5 resolution maps. We note that the exact values of this fraction depend primarily on the relative resolution differences in defining the parental structure and substructures. We also find that the surface density of the most massive fragment correlates well with the clump surface density, and has a fitted relation of $\log\Sigma_{\rm mmf}$ = 1.02log $\Sigma_{\rm clump}$ + 0.42, close to $\Sigma_{\rm mmf}$ ~1.5$\Sigma_{\rm clump}$. This indicates that the gas in the cores is denser compared to their parental clumps.

With the approximate relations between clump and its most massive fragment $\Sigma_{\rm mmf}$~1.5$\Sigma_{\rm clump}$ and $M_{\rm mmf}$~0.31$M_{\rm clump}$, assuming the clump density profile follows a power-law form as a function of radius $n(r) \propto {\rm r}^{-k_{\rho}}$, a density structure of $n(r) \propto {\rm r}^{-1.5}$ is obtained, equivalent to that the clump enclosed mass profile is $M(r) \propto {\rm r}^{1.5}$. The self-similar density profile of $n(r) \propto r^{-k_{\rho}}$ with k_{ρ} in range of 1.6-1.9 is obtained in gas spheres of high density from simulations of self-gravitating supersonic turbulence (Collins et al. 2012, Murray and Chang 2015). In particular, Murray and Chang (2015) suggests that the $n(r) \propto r^{-1.5}$ is an attractor solution at clump inner radii that is reached over clumps' self-similar gravitational collapse, when the density is then independent of time, i.e. $n(r,t) \rightarrow n(r)$. Furthermore, the clump density power-law forms can be directly linked with the power-law tails seen in molecular cloud column density probability distribution functions (N-PDF), lnN ~ N^{-s}, with s = 2/(k_{ρ}-1) (Federrath and Klessen 2013). k_{ρ}~1.5 thus corresponds to an N-PDF slope of -4. Lin et al. (2017) proposed a tentative critical value of the N-PDF power-law slope of -4 to separate massive star-forming cloud intermediate evolutionary stages, which have a shallower slope, with early or late stages, by analysis of 10 massive star-forming clouds from infrared dark stage to evolved stage with embedded luminous OB clusters. Since most of the clumps in consideration here are of $L/M < 10$, which are in relatively early evolutionary stage (Molinari et al. 2008), this small scale clump density distribution is in accord with the evolution trend of cloud N-PDF, which are compatible indirect observational evidence of cloud multi-scale collapse, as in global hierarchical collapse scenario (Vázquez-Semadeni et al. 2019).

In middle panel of Fig. 2.15 we also plot the mass of the most massive star in a cluster ($M_{\rm max}$) as a function of the cluster mass ($M_{\rm ecl}$) (Weidner, Kroupa and Pflamm-Altenburg 2013) scaled up by 3.3 times, together with the relation of masses between the most massive fragments and parental clumps. Here we make the simple assumption that the mass of most massive stellar member formed in the most massive fragment is proportional to the fragment mass with a constant SFE of 30% regardless of the mass-scale. The relation between $m_{\rm max}$ and $M_{\rm ecl}$ indicates that the mass of the most massive star systematically changes with the cluster mass in stars, and is incompatible with a scale-free IMF (Weidner, Kroupa and Pflamm-Altenburg 2013). The sampling procedure that introduces such a relation also suggests star formation is highly regulated, with low-mass stars forming until feedback from the massive stars is able to prevail against the gravity dominated formation process (Weidner and Kroupa 2006). The fact that the formation of low-mass stars starts early and continues until massive stars are formed is seen in the numerical simulations of cloud formation and collapse by converging flows, over a time span of a few Myr (Vázquez-Semadeni, Gonzalez-Samaniego and Colin 2017). The relation of the most massive fragment and clump mass is compatible with the $m_{\rm max} - M_{\rm ecl}$ relation, with the most massive core likely to be the progenitor of the most massive stellar member and perhaps fragmenting into somewhat less massive cores which may also remain unresolved at present, indicating the reservoir clump mass to be essential in regulating the mass distribution at smaller scales. The larger deviation of our observed most massive core-clump mass relation to $m_{\rm max} - M_{\rm ecl}$ in larger mass range is understandable since we do find more massive objects tend to have more fragments as discussed before. With higher angular resolution observations we might resolve the bending of the åmost massive core-clump mass relation. Numerical simulations of rotating massive cloud cores with radiative feedback have indicated that fragmentation-induced starvation could be a possible scenario that set the limit of the mass of the most massive stars (Peters et al. 2010).

2.5.4 Massive quiescent cores: candidate high-mass pre-stellar cores?

The higher resolution 350 μm observations with SABOCA compared to the 870 μm LABOCA maps of ATLASGAL offer the possibility to better distinguish between star-forming and quiescent cores. We take this opportunity to investigate in more detail the brightest SABOCA sources that are quiescent and lack embedded compact sources at 24 and 70 μm. To select the most massive cores, we use our mass estimates measured in a radius of 1σ, corresponding typically to a mass measurement within an $FWHM$ diameter of 0.17 pc for a 0.2 pc core. We select cores that are located at d<5 kpc and have $M_{1\sigma}$>100 $M_{\odot}$, assuming that they are capable of forming at least one early B or O-type star. Among all SABOCA cores, we find 87 sources that fulfil this distance and mass criteria, of which 34 (37%) are not associated with any embedded compact sources at 24 and 70 μm. The fraction of star-forming versus quiescent cores is higher in this high-mass regime than towards all sources within 5 kpc where 58% are found to be quiescent. Considering only the most massive cores the relative fraction of star-forming versus quiescent cores is significantly higher, which is consistent with other studies (e.g. Csengeri et al. 2014; Urquhart et al. 2018) suggesting shorter formation timescales for the most massive clumps.

Table 2.5: Candidate massive pre-stellar cores with >100 $M_\odot$ at < 5 kpc.

name	Distance (kpc)	v_{LSR} (km/s)	SiO (J=2–1) detection	HCO+/H^{13}CO+ lines	Outflow?$^+$	Infall?
GS327.2954−0.5787	2.8	-44.2±1.0	det.[a]	det.	–	y
GS327.2990−0.5735	2.8	-44.0±1.3	det.[ad]	det.	–	y
GS333.1274−0.5599	3.5	-54.9±1.7	det. [a,d]	det.	–	y
GS333.1294−0.5554	3.5	-57.9±2.1	no det.[a,d]	det.	–	y
GS333.1353−0.5645	3.5	-57.8±1.9	det.[a,d]	det.	–	y
GS333.1241−0.5594	3.5	-57.3±2.2	det.[a,e]	det.	–	y
GS333.1280−0.5520	3.5	-57.7±1.9	no det.[a,e]	det.	–	y
GS333.4641−0.1614	2.9	-43.1±1.4	no det.[a]	det.	–	–
GS333.6570+0.0587	5.0	−84.6±2.3	no det.[a]	det.	–	–
GS334.7438+0.5049	3.9	-62.2±5.8	no det.[a]	det.	–	–
GS336.8802−0.0079	4.6	-73.8±3.0	no det.[a]	det.	–	–
GS340.2403−0.3735	3.6	-50.1±0.9	det. [a]	det.	–	y
GS340.2504−0.3804	3.6	-50.3±0.8	det.[a,d]	det.	–	–
GS341.9324−0.1741	3.3	-43.6±0.7	no det. [a]	only HCO$^+$ [a]	–	–
GS344.5771+0.2166	4.8	-62.3±0.8	no det	no det.[a]	–	–
GS351.4378+0.6537	1.4	-4.2±0.4	det.	det.[a,c]	y	y
GS351.4416+0.6534	1.4	-4.2±0.4	det.	det.[a,c]	y	y
GS8.4009−0.2888	4.4	37.2±1.1	no det	det.[a]	–	y
GS8.4068−0.2995	4.4	37.0±1.4	no det	det.[a,d]	–	y
GS9.2098−0.2012	4.8	42.6±2.1	no det	det.[a]	–	–
GS19.0131−0.0268	4.2	59.8±0.5	–	–		
GS12.8796−0.2871	3.0	34.2±2.7	det. [b,c]	det.[a]	–	y
GS28.5585−0.2398	4.7	85.5±0.07	det.[b,d]	–		
GS28.5643−0.2313	4.7	85.5±0.07	det.[b,d]	–		
GS28.5665−0.2376	4.7	85.5±0.07	det.[b,d]	–		
GS35.5766+0.0068	3.2	54.2±0.18	det.[b]	–		
GS35.5816+0.0116	3.2	54.2±0.18	det.[b]	–		

[a]: MALT90 data, [b]: results from Csengeri et al. 2016a, [c]: possible contamination by a nearby bright source, [d]: within the same beam as the core above. In the last two columns, sources without observations are left blank; “y” stands for confirmation and “-” otherwise.

A quiescent massive core with $> 100\,M_\odot$ within a typical radius of 0.085 pc has a volume density $> 7.5 \times 10^5\,\mathrm{cm}^{-3}$, and a mass surface density of $0.92\,\mathrm{g\,cm}^{-2}$ assuming a uniform density distribution. However, most of these sources typically have non-flat flux distribution, suggesting a steeper density profile, as it is the case for their embedding clump. The bulk of the gas is cold with dust temperatures between 14 and 25 K, and on average of 18 K. Like the overall population of quiescent cores, the massive quiescent cores also exhibit lower bolometric luminosities between 60 and 2300 $L_\odot$.

To investigate whether these massive quiescent cores could qualify as candidates for extremely elusive and rare high-mass pre-stellar cores (Csengeri et al. 2017b; Motte, Bontemps and Louvet 2018), we visually inspected these candidates, and removed 7 cores from the final list that are too close to and blended with a bright source at 24 μm. This left us with a final list of 27 sources (Table 2.5). Being embedded in a larger scale clump, these sources are typically surrounded by other cores, some of which are lower mass and/or star-forming. We do not find any isolated or single candidate high-mass pre-stellar core above the $> 100\,M_\odot$ mass limit. An example of the massive quiescent core embedded in clump structure with lower-mass counterparts is shown in Fig. 2.16

We searched for available ancillary higher angular resolution archival data, that would help us to investigate the nature of these cores further, and found that G333.1298-0.5602 and G333.4659−0.1641 have been observed at high angular resolution as part of the SPARKS project using ALMA (Csengeri et al., 2017a, 2018). These studies suggest, however, that the brightest fragments on a 2000 au scale in these sources are high-mass protostellar objects rather than pre-stellar cores.

To further probe the star formation activity of these cores we examined ancillary data on molecular tracers obtained with the IRAM 30m telescope described in Csengeri et al. (2016a), and the MALT90 survey observed with the MOPRA telescope (Foster et al., 2013) which are available for all but one of the sources. These observations, however, have a coarser angular resolution than the SABOCA maps are, therefore, only indicative as an independent probe of their star formation activity.

Similarly to Motte et al. (2007), we first investigate here the velocity profiles of the SiO (2–1) line. SiO is a widely used tracer for shocks, in particular, it becomes abundant in fast shocks associated with jet activity (e.g. Schilke et al. 1997; Codella, Bachiller and Reipurth 1999). Therefore, high-velocity line wings could be indicative of the presence of jets and outflow activity related to embedded protostars, however, it might also originate from a nearby more evolved core if the resolution is lower than our SABOCA maps. We use here the pointed observations of Csengeri et al. (2016a) and the MALT90 maps (Foster et al., 2013), where we extracted and averaged the spectra towards the core position within the MOPRA beam (∼38″). For the MOPRA data, these figures are shown in App. C. Except for the cores GS351.4379+0.6537 and G351.4416+0.6534 we find no clear evidence of a broad velocity component in this line towards our candidate high-mass pre-stellar cores, however, the lack of SiO line-wings could also be due to sensitivity limitations. Where available (6 sources), we checked the IRAM 30m observations for the CO (1–0) line covered by our spectral survey described in Csengeri et al. (2016a) that could be a more sensitive probe for high-velocity outflowing gas. Although the line shape is strongly affected by absorption from the reference position, there is no clear evidence for high-velocity emission that could be related to outflowing gas in this tracer either. The observed line wings of the SiO (2-1) transitions towards GS351.4379+0.6537 and G351.4416+0.6534 are likely due to blending with a star-forming core within the beam of the MOPRA observations. From the remaining 24 sources, 13 (54%) have detections in the SiO (2–1) line showing a narrow SiO component and altogether 11 sources show no detection in the SiO (2–1) line at all. To conclude, the SiO (2–1) line does not provide an indication for deeply embedded ongoing star formation activity.

To make use of the available spectroscopic data, we also investigated whether infall signatures on the clump scale could be revealed towards our sample. While Csengeri et al. (2016b) suggests that most of the massive clumps are gravitationally unstable, spectroscopic signatures of infall (e.g. Myers et al. 1996; Mardones et al. 1997; Wu and Evans 2003) could provide an indication that the clump itself is collapsing (see, however, Smith et al. 2013). To search for an infall signature, i.e. red-shifted self-absorption of optically thick lines, we use the HCO^+ and $H^{13}CO^+$ (J=1–0) lines, and where detected, we used a single Gaussian fit to the $H^{13}CO^+$ line to extract the v_{lsr} of the clump. Although a proper interpretation of these line profiles would require dedicated modelling, visual inspection of the spectra suggests possible infall motions towards 16 sources (60%). The information obtained from molecular line data is listed in Table 2.5.

Considering a typical star formation efficiency of 20-40% (Tanaka, Tan and Zhang 2017), the SABOCA cores with $>100\,M_\odot$ are good candidates to form at least one massive star. The absence of 24-70 μm emission, together with the indications from SiO/HCO^+/$H^{13}CO^+$ tracers suggest that except for two cores, there is no further indication for star formation activity related to jets and outflows in the sample based on the SiO (2–1) line, while more than half of the clumps hosting half of the cores shows indications of the presence of global infall motions. We identify 7 sources where the SiO (2–1) line is not detected and there is no indication for infall. On the clump scale, these sources could be considered as starless massive sources. However, we cannot exclude on-going low-mass star-formation when the core would fragment and form only a low-mass cluster. What physical processes determine the possibility for a massive core to form high-mass stars is not yet clear.

We conclude that considering all of the available low angular-resolution data, our sample of candidate high-mass pre-stellar cores is robust, although deeply embedded high-mass protostars have been detected towards mid-infrared quiet massive cores and clumps (Bontemps et al. 2010; Wang et al. 2011; Ohashi et al. 2016; Csengeri et al. 2017a). High angular resolution observations are needed to confirm their nature.

2.6 Conclusions

We present the largest sample of Galactic clumps studied at a moderate resolution of 8.″5 at 350 μm studied with APEX/*SABOCA*. By combining with available *Herschel* and *LABOCA* observations from ATLASGAL, we analyze the core properties derived from SED fits and investigate the fragmentation as a function of the physical properties of clumps. Our major findings are as follows:

1. Our *SABOCA* observations detect the 350 μm emission towards all targeted ATLASGAL clumps and reveal a variety of morphology from compact, relatively isolated sources to complex filamentary structures with branches. We find that the majority of the targeted sources exhibit a filamentary structure emission. Fields dominated by a single, bright source at 350 μm represent only a minor fraction of the sample.

2. We identify 1120 compact sources at 350 μm using *Gaussclumps*. We estimate the physical properties towards 971 SABOCA sources from SED fits. The average $FWHM$ size is 0.32 pc, dust temperature is 21.6 K, average mass is 198 $M_\odot$ and average surface density is 0.40 g cm^{-2}. Among them, 405 cores are located in a distance range of 2-4 kpc; these have an average $FWHM$ size of 0.19 pc, an average dust temperature of 21.8 K, average mass of 52 $M_\odot$ and

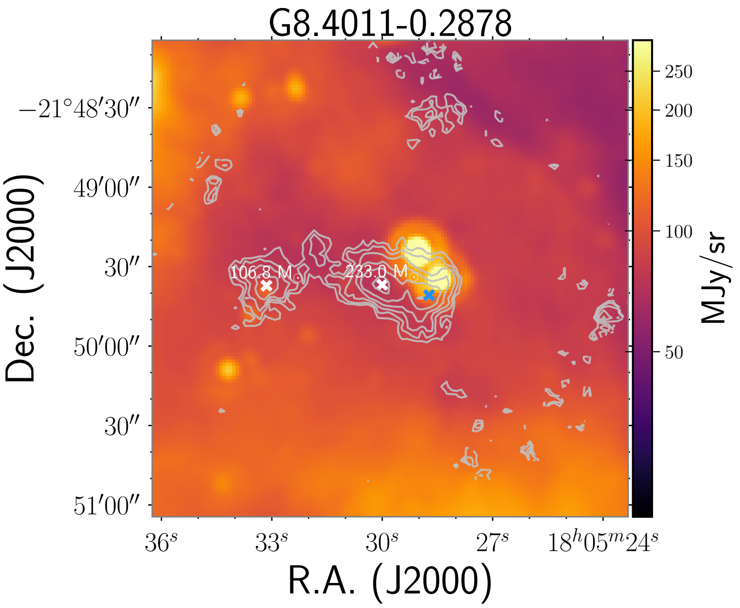

Figure 2.16: Example of a clump hosting massive quiescent cores. White crosses mark the >100 $M_{\odot}$ quiescent cores and blue cross marks the star-forming cores. The masses for quiescent cores are indicated in the figure. Contour levels are from 7σ to the peak flux with 6 logarithmic linear levels in-between.

average surface density of 0.40 g cm^{-2}. We find a systematic shallowing of slopes of the cores' mass-radius relation as a function of distance, from ~3 to ~2.

3. Using the presence of 22-24 μm and 70 μm point sources, we distinguish between star-forming and quiescent SABOCA sources. The majority of the sources lack mid- and far-infrared counterparts (56.1%) and are classified as quiescent cores. For the distance-limited sample (2-4 kpc), we find that the quiescent cores have a similar mass range as the star-forming cores but are somewhat more extended and hence less dense, and of lower dust temperature (0.16 pc, 0.40 g cm^{-2},18.9 K) than the star-forming cores (0.15 pc, 0.50 g cm^{-2}, 24.0 K).

4. We find on average each clump hosts two cores, which is broadly consistent with the length scale of thermal Jeans fragmentation. The core masses are, however, a factor of 10-100 times larger than what the thermal fragmentation would predict. The observed number of fragments is moderately correlated with the clump density and the number of fragments predicted by pure thermal Jeans fragmentation inferred from the clump properties (correlation coefficient of $\gtrsim$0.4, p-value~0.001). We do not find strong indication that a larger number of cores would form as the clumps evolve as traced by their increasing L_{bol}/M ratio.

5. We find a strong correlation between the clump mass and the mass of the most massive core, close to that ~30% of the clump mass is assembled in the most massive core. The surface density of the most massive fragment is increased compared to the parental clumps.

6. We identify 27 massive ($> 100\,M_\odot$) quiescent cores at $d < 5\,\mathrm{kpc}$ that represent promising candidates of massive star-forming progenitors at earliest stages. Further high-resolution observations are necessary to confirm the nature of these cores and settle whether they could host genuine high-mass pre-stellar cores.

References

Aguirre, James E. et al. (2011), *The Bolocam Galactic Plane Survey: Survey Description and Data Reduction*, The Astrophysical Journal Supplement Series **192**, 4 4, arXiv: `1011.0691 [astro-ph.GA]` (cit. on p. 39).

André, P. et al. (2008), *First 450 µm dust continuum mapping of the massive star-forming region NGC 3576 with the P-ArTéMiS bolometer camera*, Astron. Astrophys. **490** L27, arXiv: `0809.3968` (cit. on p. 61).

André, P. et al. (2010), *From filamentary clouds to prestellar cores to the stellar IMF: Initial highlights from the Herschel Gould Belt Survey*, Astron. Astrophys. **518**, L102 L102, arXiv: `1005.2618` (cit. on p. 46).

André, P. et al. (2014), *From Filamentary Networks to Dense Cores in Molecular Clouds: Toward a New Paradigm for Star Formation*, Protostars and Planets VI 27, arXiv: `1312.6232` (cit. on pp. 39, 62).

André, P. et al. (2016), *Characterizing filaments in regions of high-mass star formation: High-resolution submilimeter imaging of the massive star-forming complex NGC 6334 with ArTéMiS*, Astron. Astrophys. **592**, A54 A54, arXiv: `1605.07434` (cit. on p. 40).

Ballesteros-Paredes, J. and M.-M. Mac Low (2002), *Physical versus Observational Properties of Clouds in Turbulent Molecular Cloud Models*, Astrophys. J. **570** 734, eprint: `astro-ph/0108136` (cit. on p. 60).

Beuther, H. et al. (2018), *Fragmentation and disk formation during high-mass star formation. IRAM NOEMA (Northern Extended Millimeter Array) large program CORE*, Astron. Astrophys. **617**, A100 A100, arXiv: `1805.01191 [astro-ph.GA]` (cit. on pp. 40, 60, 66).

Bontemps, S. et al. (2010), *Fragmentation and mass segregation in the massive dense cores of Cygnus X*, Astron. Astrophys. **524**, A18 A18, arXiv: `0909.2315 [astro-ph.GA]` (cit. on pp. 40, 57, 63, 71).

Butler, M. J. and J. C. Tan (2012), *Mid-infrared Extinction Mapping of Infrared Dark Clouds. II. The Structure of Massive Starless Cores and Clumps*, Astrophys. J. **754**, 5 5, arXiv: `1205.2391 [astro-ph.SR]` (cit. on pp. 55, 60).

Camacho, Vianey et al. (2016), *Energy Budget of Forming Clumps in Numerical Simulations of Collapsing Clouds*, Astrophys. J. **833**, 113 113, arXiv: `1609.09112 [astro-ph.GA]` (cit. on pp. 60, 61).

Campbell, Murray F. et al. (2004), *High-Resolution Far-Infrared Observations and Models of the Star Formation Core of G34.3+0.2C*, Astrophys. J. **600** 254 (cit. on p. 55).

Carey, S. J. et al. (2009), *MIPSGAL: A Survey of the Inner Galactic Plane at 24 and 70 µm*, PASP **121** 76 (cit. on p. 41).

Chen, Huei-Ru Vivien et al. (2019), *Filamentary Accretion Flows in the Infrared Dark Cloud G14.225–0.506 Revealed by ALMA*, Astrophys. J. **875**, 24 24, arXiv: `1903.04376 [astro-ph.GA]` (cit. on p. 59).

Cheng, Y. et al. (2018), *The Core Mass Function in the Massive Protocluster G286.21+0.17 Revealed by ALMA*, Astrophys. J. **853**, 160 160, arXiv: `1706.06584` (cit. on p. 63).

Codella, C., R. Bachiller and B. Reipurth (1999), *Low and high velocity SiO emission around young stellar objects*, Astron. Astrophys. **343** 585 (cit. on p. 70).

Collins, David C. et al. (2012), *The Two States of Star-forming Clouds*, Astrophys. J. **750**, 13 13, arXiv: `1202.2594 [astro-ph.SR]` (cit. on p. 67).

Csengeri, T. et al. (2011), *Convergent Flows and Low-velocity Shocks in DR21(OH)*, Astrophys. J. Letters **740**, L5 L5, arXiv: `1108.4451 [astro-ph.GA]` (cit. on p. 59).

Csengeri, T. et al. (2014), *The ATLASGAL survey: a catalog of dust condensations in the Galactic plane*, Astron. Astrophys. **565**, A75 A75, arXiv: `1312.0937` (cit. on pp. 39–41, 45, 46, 50, 51, 54, 59, 68).

Csengeri, T. et al. (2016a), *ATLASGAL-selected massive clumps in the inner Galaxy. II. Characterisation of different evolutionary stages and their SiO emission*, Astron. Astrophys. **586**, A149 A149, arXiv: `1511.05138` (cit. on pp. 39, 40, 49, 64, 69, 70).

Csengeri, T. et al. (2016b), *The ATLASGAL survey: distribution of cold dust in the Galactic plane. Combination with Planck data*, Astron. Astrophys. **585**, A104 A104 (cit. on pp. 44, 71).

Csengeri, T. et al. (2017a), *ALMA survey of massive cluster progenitors from ATLASGAL. Limited fragmentation at the early evolutionary stage of massive clumps*, Astron. Astrophys. **600**, L10 L10, arXiv: `1703.03273` (cit. on pp. 40, 41, 62, 63, 70, 71).

Csengeri, T. et al. (2017b), *The ATLASGAL survey: The sample of young massive cluster progenitors*, Astron. Astrophys. **601**, A60 A60 (cit. on pp. 59, 70).

Csengeri, T. et al. (2018), *Search for high-mass protostars with ALMA revealed up to kilo-parsec scales (SPARKS). I. Indication for a centrifugal barrier in the environment of a single high-mass envelope*, Astron. Astrophys. **617**, A89 A89, arXiv: `1804.06482` (cit. on pp. 40, 57, 70).

Cutri, R. M. et al. (2012), *Explanatory Supplement to the WISE All-Sky Data Release Products*, tech. rep. (cit. on p. 55).

Donoho, David L and Iain M Johnstone (1994), *Ideal spatial adaptation by wavelet shrinkage*, Biometrika **81** 425, eprint: `/oup/backfile/content_public/journal/biomet/81/3/10.1093_biomet_81.3.425/1/81.3.425.pdf`, URL: `http://dx.doi.org/10.1093/biomet/81.3.425` (cit. on p. 43).

Duarte-Cabral, A. et al. (2013), *CO outflows from high-mass Class 0 protostars in Cygnus-X*, Astron. Astrophys. **558**, A125 A125, arXiv: `1308.6490` (cit. on p. 57).

Dunham, Michael M. et al. (2008), *Identifying the Low-Luminosity Population of Embedded Protostars in the c2d Observations of Clouds and Cores*, The Astrophysical Journal Supplement Series **179** 249, arXiv: `0806.1754 [astro-ph]` (cit. on pp. 56, 57).

Eden, D. J. et al. (2017), *The JCMT Plane Survey: first complete data release - emission maps and compact source catalogue*, Mon. Not. R. Astron. Soc. **469** 2163, arXiv: `1704.02982` (cit. on p. 39).

Elia, D. et al. (2017), *The Hi-GAL compact source catalogue - I. The physical properties of the clumps in the inner Galaxy (-71.0*deg $< \ell <$ *67.0*deg*)*, Mon. Not. R. Astron. Soc. **471** 100, arXiv: `1706.01046` (cit. on pp. 39, 46).

Federrath, Christoph and Ralf S. Klessen (2013), *On the Star Formation Efficiency of Turbulent Magnetized Clouds*, Astrophys. J. **763**, 51 51, arXiv: `1211.6433 [astro-ph.SR]` (cit. on p. 67).

Feng, S. et al. (2016), *Outflow Detection in a 70 μm Dark High-Mass Core*, Astrophys. J. **828**, 100 100, arXiv: `1605.01736` (cit. on p. 57).

Foster, J. B. et al. (2013), *Characterisation of the MALT90 Survey and the Mopra Telescope at 90 GHz*, PASA **30**, e038 e038, arXiv: `1306.0560 [astro-ph.IM]` (cit. on p. 70).

Galliano, Frédéric (2018), *A dust spectral energy distribution model with hierarchical Bayesian inference - I. Formalism and benchmarking*, Mon. Not. R. Astron. Soc. **476** 1445, arXiv: `1801.06660 [astro-ph.GA]` (cit. on p. 46).

Galván-Madrid, Roberto et al. (2009), *Formation of an O-Star Cluster by Hierarchical Accretion in G20.08-0.14 N*, Astrophys. J. **706** 1036, arXiv: `0910.2270 [astro-ph.GA]` (cit. on p. 59).

Giannetti, A. et al. (2014), *ATLASGAL-selected massive clumps in the inner Galaxy. I. CO depletion and isotopic ratios*, Astron. Astrophys. **570**, A65 A65, arXiv: `1407.2215` (cit. on p. 40).

Giannetti, A. et al. (2017), *ATLASGAL-selected massive clumps in the inner Galaxy. V. Temperature structure and evolution*, Astron. Astrophys. **603**, A33 A33, arXiv: `1703.08485 [astro-ph.GA]` (cit. on p. 40).

Ginsburg, Adam et al. (2015), *The dense gas mass fraction in the W51 cloud and its protoclusters*, Astron. Astrophys. **573**, A106 A106, arXiv: `1411.1756 [astro-ph.GA]` (cit. on p. 42).

Güsten, R. et al. (2006), *The Atacama Pathfinder EXperiment (APEX) - a new submillimeter facility for southern skies* -, Astron. Astrophys. **454** L13 (cit. on p. 40).

Gutermuth, R. A. and M. Heyer (2015), *A 24 μm Point Source Catalog of the Galactic Plane from Spitzer/MIPSGAL*, Astron. J. **149**, 64 64, arXiv: `1412.4751 [astro-ph.SR]` (cit. on pp. 45, 55, 56).

Hennebelle, P. (2012), *Formation of proto-clusters and star formation within clusters: apparent universality of the initial mass function?*, Astron. Astrophys. **545**, A147 A147, arXiv: `1207.6776 [astro-ph.GA]` (cit. on p. 61).

Heyer, M. et al. (2018), *Early science with the Large Millimetre Telescope: fragmentation of molecular clumps in the Galaxy*, Mon. Not. R. Astron. Soc. **473** 2222, arXiv: `1709.09059` (cit. on p. 40).

Juvela, M. et al. (2013), *The degeneracy between dust colour temperature and spectral index. Comparison of methods for estimating the β(T) relation*, Astron. Astrophys. **556**, A63 A63, arXiv: `1305.2130 [astro-ph.GA]` (cit. on p. 46).

Kalcheva, I. E. et al. (2018), *The coordinated radio and infrared survey for high-mass star formation. III. A catalogue of northern ultra-compact H II regions*, Astron. Astrophys. **615**, A103 A103, arXiv: `1803.09334` (cit. on p. 55).

Kauffmann, Jens and Thushara Pillai (2010), *How Many Infrared Dark Clouds Can form Massive Stars and Clusters?*, The Astrophysical Journal Letters **723** L7, URL: `http://stacks.iop.org/2041-8205/723/i=1/a=L7` (cit. on p. 60).

Kim, W.-J. et al. (2017), *ATLASGAL-selected massive clumps in the inner Galaxy. IV. Millimeter hydrogen recombination lines from associated H II regions*, Astron. Astrophys. **602**, A37 A37, arXiv: `1702.02062` (cit. on p. 40).

Kim, W.-J. et al. (2018), *New detections of (sub)millimeter hydrogen radio recombination lines towards high-mass star-forming clumps*, Astron. Astrophys. **616**, A107 A107, arXiv: `1804.06999` (cit. on pp. 40, 55).

König, C. et al. (2017), *ATLASGAL-selected massive clumps in the inner Galaxy. III. Dust continuum characterization of an evolutionary sample*, Astron. Astrophys. **599**, A139 A139 (cit. on pp. 39, 46, 48).

Lada, Charles J. and Elizabeth A. Lada (2003), *Embedded Clusters in Molecular Clouds*, Annual Review of Astronomy and Astrophysics **41** 57, arXiv: `astro-ph/0301540 [astro-ph]` (cit. on p. 39).

Larson, R. B. (1981), *Turbulence and star formation in molecular clouds*, Mon. Not. R. Astron. Soc. **194** 809 (cit. on p. 60).

Li, G.-X. et al. (2016), *ATLASGAL: A Galaxy-wide sample of dense filamentary structures*, Astron. Astrophys. **591**, A5 A5, arXiv: `1604.00544 [astro-ph.SR]` (cit. on p. 45).

Lin, Y. et al. (2016), *Cloud Structure of Galactic OB Cluster-forming Regions from Combining Ground- and Space-based Bolometric Observations*, Astrophys. J. **828**, 32 32, arXiv: `1606.07645` (cit. on pp. 49, 50).

Lin, Yuxin et al. (2017), *Cloud Structure of Three Galactic Infrared Dark Star-forming Regions from Combining Ground- and Space-based Bolometric Observations*, Astrophys. J. **840**, 22 22, arXiv: `1704.06448 [astro-ph.GA]` (cit. on p. 67).

Liu, H. B., P. T. P. Ho and Q. Zhang (2010), *The High-velocity Molecular Outflows in Massive Cluster-forming Region G10.6-0.4*, Astrophys. J. **725** 2190, arXiv: `1010.2785 [astro-ph.SR]` (cit. on p. 55).

Liu, H. B. et al. (2012a), *Fragmentation and OB Star Formation in High-mass Molecular Hub-Filament Systems*, Astrophys. J. **756**, 10 10, arXiv: `1206.1907 [astro-ph.SR]` (cit. on p. 46).

Liu, H. B. et al. (2012b), *The Origin of OB Clusters: From 10 pc to 0.1 pc*, Astrophys. J. **745**, 61 61, arXiv: `1110.1318 [astro-ph.SR]` (cit. on p. 46).

Liu, Hauyu Baobab et al. (2015), *ALMA Resolves the Spiraling Accretion Flow in the Luminous OB Cluster-forming Region G33.92+0.11*, Astrophys. J. **804**, 37 37, arXiv: `1505.04255 [astro-ph.SR]` (cit. on p. 59).

Liu, Hauyu Baobab et al. (2019), *Investigating Fragmentation of Gas Structures in OB Cluster-forming Molecular Clump G33.92+0.11 with 1000 au Resolution Observations of ALMA*, Astrophys. J. **871**, 185 185, arXiv: `1808.07702 [astro-ph.GA]` (cit. on p. 66).

Lo, N. et al. (2015), *Infall, outflow, and turbulence in massive star-forming cores in the G333 giant molecular cloud*, Mon. Not. R. Astron. Soc. **453** 3245, arXiv: `1509.03308` (cit. on p. 55).

Lumsden, S. L. et al. (2013), *The Red MSX Source Survey: The Massive Young Stellar Population of Our Galaxy*, Astrophys. J. Supp. **208**, 11 11, arXiv: `1308.0134` (cit. on p. 55).

Ma, B., J. C. Tan and P. J. Barnes (2013), *The Galactic Census of High- and Medium-mass Protostars. II. Luminosities and Evolutionary States of a Complete Sample of Dense Gas Clumps*, Astrophys. J. **779**, 79 79, arXiv: `1211.6492` (cit. on p. 64).

Mardones, D. et al. (1997), *A Search for Infall Motions toward Nearby Young Stellar Objects*, Astrophys. J. **489** 719, eprint: `astro-ph/9707011` (cit. on p. 71).

Merello, M. et al. (2015), *The Bolocam Galactic Plane Survey. XI. Temperatures and Substructure of Galactic Clumps Based On 350 μM Observations*, Astrophys. J. Supp. **218**, 1 1, arXiv: `1501.05965` (cit. on pp. 40, 63, 67).

Minier, V. et al. (2009), *Evidence of triggered star formation in G327.3-0.6. Dust-continuum mapping of an infrared dark cloud with P-ArTéMiS*, Astron. Astrophys. **501** L1, arXiv: `0907.3031 [astro-ph.GA]` (cit. on p. 40).

Molinari, S. et al. (2008), *The evolution of the spectral energy distribution in massive young stellar objects*, Astron. Astrophys. **481** 345 (cit. on pp. 61, 62, 64, 68).

Molinari, S. et al. (2010), *Clouds, filaments, and protostars: The Herschel Hi-GAL Milky Way*, Astron. Astrophys. **518**, L100 L100, arXiv: `1005.3317` (cit. on pp. 39, 44).

Molinari, S. et al. (2016), *Calibration of Evolutionary Diagnostics in High-mass Star Formation*, Astrophys. J. Letters **826**, L8 L8, arXiv: `1604.06192 [astro-ph.GA]` (cit. on pp. 44, 54–56).

Moore, T. J. T. et al. (2015), *The JCMT Plane Survey: early results from the $\ell = 30$deg field*, Mon. Not. R. Astron. Soc. **453** 4264, arXiv: `1509.00318` (cit. on p. 39).

Motte, F., P. Schilke and D. C. Lis (2003), *From Massive Protostars to a Giant H II Region: Submillimeter Imaging of the Galactic Ministarburst W43*, Astrophys. J. **582** 277, eprint: `astro-ph/0208519` (cit. on p. 40).

Motte, F. et al. (2007), *The earliest phases of high-mass star formation: a 3 square degree millimeter continuum mapping of Cygnus X*, Astron. Astrophys. **476** 1243, arXiv: `0708.2774` (cit. on pp. 39, 40, 46, 55, 56, 63, 70).

Motte, F. et al. (2010), *Initial highlights of the HOBYS key program, the Herschel imaging survey of OB young stellar objects*, Astron. Astrophys. **518**, L77 L77 (cit. on p. 46).

Motte, F. et al. (2014), *The formation of the W43 complex: constraining its atomic-to-molecular transition and searching for colliding clouds*, Astron. Astrophys. **571**, A32 A32, arXiv: `1404.4404 [astro-ph.GA]` (cit. on p. 42).

Motte, Frédérique, Sylvain Bontemps and Fabien Louvet (2018), *High-Mass Star and Massive Cluster Formation in the Milky Way*, ARA&A **56** 41, arXiv: `1706.00118 [astro-ph.GA]` (cit. on pp. 39, 62, 70).

Murray, N. and P. Chang (2015), *Star Formation in Self-gravitating Turbulent Fluids*, Astrophys. J. **804**, 44 44, arXiv: `1407.6373 [astro-ph.SR]` (cit. on p. 67).

Myers, P. C. (2009), *On the Distribution of Protostar Masses*, Astrophys. J. **706** 1341, arXiv: `0910.3120` (cit. on p. 61).

Myers, P. C. et al. (1996), *A Simple Model of Spectral-Line Profiles from Contracting Clouds*, Astrophys. J. Letters **465** L133 (cit. on p. 71).

Naranjo-Romero, R., E. Vázquez-Semadeni and R. M. Loughnane (2015), *Hierarchical Gravitational Fragmentation. I. Collapsing Cores within Collapsing Clouds*, Astrophys. J. **814**, 48 48, arXiv: `1510.05617` (cit. on p. 59).

Ohashi, S. et al. (2016), *Dense Core Properties in the Infrared Dark Cloud G14.225-0.506 Revealed by ALMA*, Astrophys. J. **833**, 209 209, arXiv: `1610.08581` (cit. on p. 71).

Ossenkopf, V. and T. Henning (1994), *Dust opacities for protostellar cores*, Astron. Astrophys. **291** 943 (cit. on p. 46).

Palau, A. et al. (2013), *Early Stages of Cluster Formation: Fragmentation of Massive Dense Cores down to* $\lesssim$*1000 AU*, Astrophys. J. **762**, 120 120, arXiv: `1211.2666` (cit. on p. 40).

Palau, A. et al. (2015), *Gravity or turbulence? - III. Evidence of pure thermal Jeans fragmentation at* $\sim$*0.1 pc scale*, Mon. Not. R. Astron. Soc. **453** 3785, arXiv: `1504.07644` (cit. on pp. 40, 63, 65–67).

Peretto, N. and G. A. Fuller (2010), *A Statistical Study of the Mass and Density Structure of Infrared Dark Clouds*, Astrophys. J. **723** 555, arXiv: `1009.0716` (cit. on p. 63).

Peretto, N. et al. (2013), *Global collapse of molecular clouds as a formation mechanism for the most massive stars*, Astron. Astrophys. **555**, A112 A112, arXiv: `1307.2590` (cit. on p. 59).

Peters, Thomas et al. (2010), *Limiting Accretion onto Massive Stars by Fragmentation-induced Starvation*, Astrophys. J. **725** 134, arXiv: `1005.3271 [astro-ph.GA]` (cit. on p. 68).

Planck Collaboration et al. (2011), *Planck early results. XXV. Thermal dust in nearby molecular clouds*, Astron. Astrophys. **536**, A25 A25, arXiv: `1101.2037` (cit. on pp. 46, 48).

Ragan, S. E., T. Henning and H. Beuther (2013), *APEX/SABOCA observations of small-scale structure of infrared-dark clouds . I. Early evolutionary stages of star-forming cores*, Astron. Astrophys. **559**, A79 A79, arXiv: `1308.6157` (cit. on pp. 40, 57, 60).

Rayner, T. S. M. et al. (2017), *Far-infrared observations of a massive cluster forming in the Monoceros R2 filament hub*, Astron. Astrophys. **607**, A22 A22, arXiv: `1712.00616` (cit. on p. 40).

Rosolowsky, E. W. et al. (2008), *Structural Analysis of Molecular Clouds: Dendrograms*, Astrophys. J. **679** 1338, arXiv: `0802.2944 [astro-ph]` (cit. on p. 66).

Sault, R. J., P. J. Teuben and M. C. H. Wright (1995), “A Retrospective View of MIRIAD”, *Astronomical Data Analysis Software and Systems IV*, ed. by R. A. Shaw, H. E. Payne and J. J. E. Hayes, vol. 77, Astronomical Society of the Pacific Conference Series 433, eprint: `astro-ph/0612759` (cit. on p. 49).

Schilke, P. et al. (1997), *SiO production in interstellar shocks.*, Astron. Astrophys. **321** 293 (cit. on p. 70).

Schuller, F. (2012), “BoA: a versatile software for bolometer data reduction”, *Millimeter, Submillimeter, and Far-Infrared Detectors and Instrumentation for Astronomy VI*, vol. 8452, Proceedings of the SPIE 84521T, arXiv: `1211.6485 [astro-ph.IM]` (cit. on p. 42).

Schuller, F. et al. (2009), *ATLASGAL - The APEX telescope large area survey of the galaxy at 870 μm*, Astron. Astrophys. **504** 415, arXiv: `0903.1369` (cit. on p. 39).

Siringo, G. et al. (2009), *The Large APEX BOlometer CAmera LABOCA*, Astron. Astrophys. **497** 945, arXiv: `0903.1354 [astro-ph.IM]` (cit. on p. 48).

Siringo, G. et al. (2010), *A New Facility Receiver on APEX: The Submillimetre APEX Bolometer Camera, SABOCA*, The Messenger **139** 20 (cit. on p. 40).

Smith, R. J. et al. (2013), *Line Profiles of Cores within Clusters. II. Signatures of Dynamical Collapse during High-mass Star Formation*, Astrophys. J. **771**, 24 24, arXiv: `1304.4950` (cit. on p. 71).

Spaans, Marco and Joseph Silk (2000), *The Polytropic Equation of State of Interstellar Gas Clouds*, Astrophys. J. **538** 115, arXiv: `astro-ph/0002483 [astro-ph]` (cit. on p. 65).

Stahler, S. W., F. Palla and P. T. P. Ho (2000), *The Formation of Massive Stars*, Protostars and Planets IV 327 (cit. on p. 39).

Stutzki, J. and R. Guesten (1990), *High spatial resolution isotopic CO and CS observations of M17 SW - The clumpy structure of the molecular cloud core*, Astrophys. J. **356** 513 (cit. on p. 45).

Svoboda, B. E. et al. (2016), *The Bolocam Galactic Plane Survey. XIV. Physical Properties of Massive Starless and Star-forming Clumps*, Astrophys. J. **822**, 59 59, arXiv: `1511.08810` (cit. on p. 39).

Tan, J. C. et al. (2014), *Massive Star Formation*, Protostars and Planets VI 149, arXiv: `1402.0919` (cit. on p. 39).

Tanaka, K. E. I., J. C. Tan and Y. Zhang (2017), *The Impact of Feedback During Massive Star Formation by Core Accretion*, Astrophys. J. **835**, 32 32, arXiv: `1610.08856 [astro-ph.SR]` (cit. on p. 71).

Urquhart, J. S. et al. (2013), *ATLASGAL – properties of compact Hii regions and their natal clumps*, Monthly Notices of the Royal Astronomical Society **435** 400, eprint: `/oup/backfile/content_public/journal/mnras/435/1/10.1093_mnras_stt1310/2/stt1310.pdf`, URL: `http://dx.doi.org/10.1093/mnras/stt1310` (cit. on p. 55).

Urquhart, J. S. et al. (2014), *ATLASGAL - towards a complete sample of massive star forming clumps*, Mon. Not. R. Astron. Soc. **443** 1555, arXiv: `1406.5078` (cit. on p. 40).

Urquhart, J. S. et al. (2018), *ATLASGAL - properties of a complete sample of Galactic clumps*, Mon. Not. R. Astron. Soc. **473** 1059, arXiv: `1709.00392` (cit. on pp. 39–41, 59, 60, 62, 64, 68).

Vázquez-Semadeni, Enrique, Alejandro Gonzalez-Samaniego and Pedro Colin (2017), *Hierarchical star cluster assembly in globally collapsing molecular clouds*, Mon. Not. R. Astron. Soc. **467** 1313, arXiv: `1611.00088 [astro-ph.GA]` (cit. on p. 68).

Vázquez-Semadeni, Enrique et al. (2019), *Global Hierarchical Collapse In Molecular Clouds. Towards a Comprehensive Scenario*, arXiv e-prints, arXiv:1903.11247 arXiv:1903.11247, arXiv: `1903.11247 [astro-ph.GA]` (cit. on pp. 66, 68).

Wang, K. et al. (2011), *Hierarchical Fragmentation and Jet-like Outflows in IRDC G28.34+0.06: A Growing Massive Protostar Cluster*, Astrophys. J. **735**, 64 64, arXiv: `1105.4559` (cit. on pp. 63, 71).

Wang, Ke et al. (2014), *Hierarchical fragmentation and differential star formation in the Galactic 'Snake': infrared dark cloud G11.11-0.12*, Mon. Not. R. Astron. Soc. **439** 3275, arXiv: `1401.4157 [astro-ph.GA]` (cit. on p. 66).

Wang, Peng et al. (2010), *Outflow Feedback Regulated Massive Star Formation in Parsec-Scale Cluster-Forming Clumps*, Astrophys. J. **709** 27, arXiv: `0908.4129 [astro-ph.SR]` (cit. on p. 59).

Weidner, C. and P. Kroupa (2006), *The maximum stellar mass, star-cluster formation and composite stellar populations*, Mon. Not. R. Astron. Soc. **365** 1333, eprint: `astro-ph/0511331` (cit. on p. 68).

Weidner, C., P. Kroupa and J. Pflamm-Altenburg (2013), *The* m_{max}-M_{ecl} *relation, the IMF and IGIMF: probabilistically sampled functions*, Mon. Not. R. Astron. Soc. **434** 84, arXiv: `1306.1229` (cit. on pp. 66, 68).

Wienen, M. et al. (2012), *Ammonia from cold high-mass clumps discovered in the inner Galactic disk by the ATLASGAL survey*, Astron. Astrophys. **544**, A146 A146, arXiv: `1208.4848` (cit. on p. 40).

Williams, J. P., L. Blitz and C. F. McKee (2000), "The Structure and Evolution of Molecular Clouds: from Clumps to Cores to the IMF", *Protostars and Planets IV*, ed. by V. Mannings, A. P. Boss and S. S. Russell 97, arXiv: `astro-ph/9902246 [astro-ph]` (cit. on pp. 40, 46).

Wood, Douglas O. S. and Ed Churchwell (1989), *Massive Stars Embedded in Molecular Clouds: Their Population and Distribution in the Galaxy*, Astrophys. J. **340** 265 (cit. on p. 56).

Wu, J. and N. J. Evans II (2003), *Indications of Inflow Motions in Regions Forming Massive Stars*, Astrophys. J. Letters **592** L79, eprint: `astro-ph/0306543` (cit. on p. 71).

Ysard, N. et al. (2013), *Variation in dust properties in a dense filament of the Taurus molecular complex (L1506)*, Astron. Astrophys. **559**, A133 A133, arXiv: `1309.6489` (cit. on p. 48).

Zhang, Qizhou et al. (2009), *Fragmentation at the Earliest Phase of Massive Star Formation*, Astrophys. J. **696** 268, arXiv: `0902.0647 [astro-ph.GA]` (cit. on pp. 46, 66).

CHAPTER 3

The evolution of temperature and density structures of OB cluster-forming molecular clumps

The content of this chapter was submitted to *Astronomy & Astrophysics*.

3.1 Introduction

Massive star-forming clumps are progenitors of OB clusters (Williams, Blitz and McKee 2000, Motte, Bontemps and Louvet 2018). They have masses of typically $\gtrsim$1000 $M_\odot$ over a spatial scale of ~1 pc. The evolution of the pc-scale clump gas, its physical structures of density, temperature, and dynamics critically influence the fragmentation and accretion process of star clusters (Girichidis et al. 2011, Lee and Hennebelle 2019, Padoan et al. 2020), and vice versa (Krumholz, Klein and McKee 2012, Offner et al. 2009). Particularly, the universality of the stellar initial mass function (IMF) indicates the formation of most massive stars is deterministic, favoring particular physical environment instead of randomly occurring in molecular clouds (Kroupa et al. 2013). This, together with dominant feedback caused by massive stars, may lead to a comprehensive evolutionary track of massive clumps. Accordingly, observational evidence can be collected by sampling a wide range of clumps at different evolutionary stages.

The process of gas collapse to form protostars has been studied since decades, among the first are the works by Larson (1969), Penston (1969) and Shu (1977) (hereafter LP69 and S77). These are commonly refered to as 'outside-in' and 'inside-out' models indicating the succession of the spherical collapse of isothermal clouds, which describe the gas flows (immediately) prior to and after development of a protostar (singularity), respectively. The density profiles of LP69 exhibits a relation of r^{-2} while the density profile of the inner free-falling and outer static envelopes of S77 model follow $\mathrm{r}^{-1.5}$ and r^{-2}, separately. Incorporating turbulent pressure to explain the observed line width-scale relation, the logatropic (nonisothermal) gas follows, on the other hand, a flatter profile of r^{-1} (e.g. McLaughlin and Pudritz 1997) in the outer region. Recently, the process of spherically symmetric cloud collapse has been revisited extensively: Coughlin (2017) present solutions for arbitrary initial density profiles, extending to non-self-similar regime; work by Murray and Chang (2015), Murray et al. (2017) considers turbulence energy generated from gravitational collapse and a highly dynamic system (as compared to hydrostatic equilibrium assumed by S77). Furthermore, due to significant heating sources and high opacities associated in massive star-formation clouds, the assumption of isothermality might break down when a polytropic equation of state (EOS) needs to be introduced which quantify the balance of gas cooling and heating and can incorporate turbulent pressure (Curry and McKee 2000). The polytropic index γ (with $T \propto \rho^{\gamma-1}$) has been shown to have a decisive effect on the dynamical evolution of molecular clouds (Passot and Vázquez-Semadeni 1998, Spaans and Silk 2000) and eventually the IMF (e.g. Klessen, Spaans and Jappsen 2007, Jappsen et al. 2005). Moreover, recent works have demonstrated that a simple EOS assumption for the gas evolution might fail to explain the invariability of the peak of the IMF, while (proto)stellar radiative heating , a process that is not fully captured by the EOS, seems to play a crucial role in setting the characteristic mass scale (e.g. Bate 2009, Krumholz, Klein and McKee 2011, Guszejnov, Hopkins and Ma 2017; Guszejnov, Krumholz and Hopkins 2016). Given these theoretical developments, it is timely to measure with observations the detailed gas temperature and density structure of massive clumps.

How the mass of massive clumps is distributed into different density regimes is fundamental to understanding the evolution of the star formation rate (SFR) and star formation efficiency (SFE) on larger physical scales (e.g. Lee, Chang and Murray 2015, Parmentier 2019). On cloud scales ($\gtrsim$10 pc), the gas column density distribution follows a probability function (N-PDF) of log-normal form in a turbulent medium while it develops a power-law tail(s) as significant gravitational collapse sets in high density regimes (e.g. Klessen 2000), which are readily resolved in nearby star-forming clouds and OB cluster forming regions (e.g. Kainulainen et al. 2009, Lin et al. 2017). The power-law shape is suggested to originate from power-law density profiles (Federrath and Klessen 2013a, Myers 2015). Hence, measurements of clump density profiles can test how the dense gas of molecular clouds lead to the power-law excess of N-PDFs.

Most previous works on the density structure of massive clumps are based on single dish observations, of both continuum and molecular lines. Works targeting at a sample of sources include but are not limited to, e.g. van der Tak et al. (2000), Mueller et al. (2002), Beuther et al. (2002), Hatchell and van der Tak 2003, Rolffs et al. (2011), Williams, Fuller and Sridharan (2005), Palau et al. (2014). With the advent of wide-band receivers, especially those equipping with interferometers, spatially resolved multi-line observations become efficient (e.g. Beuther et al. 2007, Li et al. 2019), which are indispensable to measure the broad density and temperature ranges associated with massive star formation.

We have conducted a pilot survey of massive clumps by observations with the Submillimeter Array (SMA) and the APEX telescope. The target sources are selected from ATLASGAL survey (Schuller et al. 2009) and located at a distance of 4-6 kpc. They cover different evolutionary stages, suggested by different luminosity-to-mass ratios (Figure 3.1) and different signposts of star-formation activities (more in Appendix A.5). In Figure 3.1, the distribution of luminosity and mass for ATLASGAL sources in a distance range of 4-8 kpc with a radius of <2 pc (Urquhart et al. (2018)), having masses over 300 $M_{\odot}$ and peak flux ~2 Jy/beam are shown. The mass lower limit of 300 $M_{\odot}$ corresponds to the mass of a massive clump in which at least one $> 8\ M_{\odot}$ star will form according to the normal IMF with an assumed star formation efficiency (SFE) of 30% (Kroupa, Tout and Gilmore 1993, Sanhueza et al. 2017). The peak flux density of 2 Jy/beam (~20″ beam FWHM) at 870 μm from ATLASGAL survey, considering a distance of 6 kpc, indicates a mass of >100 $M_{\odot}$ concentrated in the clump central ~0.5 pc region, assuming a dust temperature of 50 K and dust opacity of 1.8 cm^{2}g^{-1} with a gas-to-dust ratio of 100. The selection criterion therefore yields a sample of massive clumps with

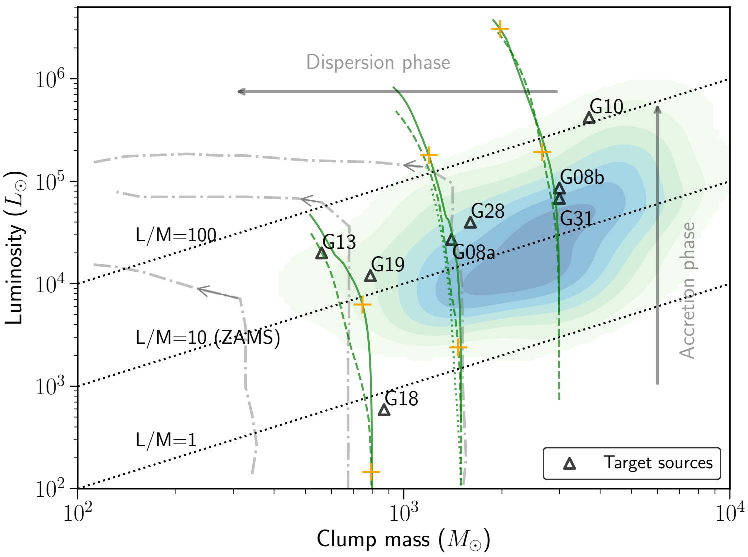

Figure 3.1: The luminosity-mass diagram of target sources (triangle markers). Greens lines indicate evolutionary tracks with accretion rate of 10^{-5} $M_\odot yr^{-1}$ (dotted), 10^{-4} $M_\odot yr^{-1}$ (dashed) and 10^{-3} $M_\odot yr^{-1}$ (solid), of the most massive star in the cluster . The other stellar members follow an equal accretion stopping probability, and with accretion rate $\propto M^{1.5}$. The orange pluses mark the time epoch of $2{\times}10^4$ yr for each accretion track. The SFE is assumed to be 30% and the underlying stellar population follows canonical IMF (Kroupa, Tout and Gilmore 1993). Accretion luminosities are estimated based on interpolating massive protostar models in Hosokawa and Omukai (2009). The background contours are showing the distribution of ATLASGAL sources in distance range of 4-8 kpc, having masses over 300 $M_\odot$ and peak flux $\gtrsim$2 Jy/beam with a radius of less than 2 pc.

moderate to high central concentration. Our selected sample is representative of the relatively more evolved sources among all that fulfills the criterion. These sources are easily detected with 1 mm lines given their likely excitation conditions, and we further complement the sample with an infrared dark source G18.

Main molecular lines of interest are listed in Table 3.3, which include multiple efficient thermometers and densitometers for massive clumps, as suggested by single dish observations towards a statistically large sample (Giannetti et al. 2017, Leurini et al. 2004, 2007). We use various modeling methods to quantify the clump density and temperature structure using these lines. The paper is organised as follows: in Sect. 3.2 we describe the observations and data reduction. Sect. 3.3.1 is dedicated to a general outline of the radiative modeling methods and procedures we adopted. In Section 3.2.1 the properties of the source extracted from SMA 1.2 mm continuum are shown. Section 3.3.3, Section 3.3.4, in addition to Section 3.3.7, 3.3.8 focus on the radiative transfer modeling procedures and results of continuum and molecular lines. Analysis of some complementary lines is presented in Section A.8. In Section 3.4 we discuss the outcome of the modeling results with a comparison between sources and make physical implications.

3.2 Observations and data reduction

3.2.1 SMA observations

We performed SMA observations in the ~1 mm band towards seven clumps in the subcompact array configuration on 2017 June 11, and in the compact array configuration on 2017 August 28 (Project 2017A-S030, PI: Yuxin Lin), which covered baseline lengths of 9.5-45 meters and 16-77 meters, respectively. The selected target sources are summarized in Table 3.2. Detailed information about each target source from previous studies is summarised in Appendix A.5. We used the dual receivers mode supported with the SMA Wideband Astronomical ROACH2 Machine (SWARM) backend: The RxA receivers covered the frequency ranges of 188.4-196.7 GHz and 204.4-212.7 GHz in the lower and upper sidebands, respectively; the RxB receivers covered the frequency ranges of 238.5-246.8 GHz and 254.5-262.8 GHz, respectively. The intrinsic spectral channel width was 140 kHz. The molecular line transitions we covered are summarized in Table 3.3.

In addition, we retrieved archival SMA data towards the luminous ultra compact (UC) Hɪɪ region G10.624-0.38, which remains deeply embedded in a $M_{\rm gas}$ =10^3-10^4 $M_\odot$ molecular clumps and harbors a cluster of OB stars. These observations covered the CH_3OH J=5-4 and J=7-6 and the CH_3CN J=19-18 line multiplets. We refer to Baobab Liu et al. (2010), Liu, Zhang and Ho (2011), and Liu et al. (2012) for details of these observations.

We followed the standard SMA data calibration strategy. The application of system temperature ($T_{\rm sys}$) information and the absolute flux, passband, and gain calibrations were carried out using the MIR IDL software package (Qi, 2003). The absolute flux scalings were derived by comparing the visibility amplitudes of the gain calibrators with those of the absolute flux standard sources of the SMA, which were Callisto and Neptune for the subcompact and compact array observations, respectively. After calibration, we performed zeroth-order fitting of continuum levels from line-free channels and the joint weighted imaging adopting robust weighting of all continuum data were performed using the Miriad software package (Sault, Teuben and Wright, 1995).

3.2.2 APEX observations

Single-dish observations at 1 mm towards our target sources were performed with the MPIfR principal investigator (PI) instrument PI230 on the the Atacama Pathfinder Experiment 12-meter telescope (APEX, Güsten et al. 2006), between March to September 2017 and July 2018 (Project M-099.F-9513A-2017, PI: Yuxin Lin). The PI230 receiver is a dual polarisation sideband separating heterodyne system with a total of 32 GHz bandwidth working at 230 GHz, and can cover the spectral range of 200-270 GHz. We conducted observations with two spectral setups, covering frequency ranges of 202.2-210.0 GHz, 218.0-225.8 GHz and 239.2-247.0 GHz, 255.0-262.8 GHz, respectively. For each target source a region of $3'\times3'$ centered at the source position was mapped in the On-The-Fly (OTF) mode with both setups.

During the observations, the typical precipitable water vapor (PWV) was ~1.5 to 2.5 mm. The pointing was determined by continuum observations on Saturn when available, or CO J=2-1 observations on bright nearby evolved stars (e.g. RAFGL2135, R-Dor). The pointing accuracy was found to be within $3''$. Focus was checked on Saturn every 2-4 hours. The main beam efficiency ($\eta_{\rm mb}$) for the PI230 instrument varies over the observing period, with a range of ~63%−72%[1]. The

---

[1] `http://www.apex-telescope.org/telescope/efficiency/`

Table 3.1: Source properties from 1.2 mm SMA continuum.

Source	$S_{1.2\mathrm{mm}}{}^{a}$ (Jy)	$R_{\mathrm{eff}}{}^{b}$ (pc)	$\bar{T}_{\mathrm{d}}{}^{c}$ (K)	M_{core} ($M_{\odot}$)	$M^{\mathrm{Abel}}_{\mathrm{core}}$ ($M_{\odot}$)	$\bar{\rho}^{d}$ (10^{4} cm^{-3})
G18	0.18	0.11	30	39.0	22.1	6.0
G28	0.69	0.12	49	93.5	103.7	19.5
G19	1.07	0.10	37	124.1	65.3	23.6
G08a	0.35	0.10	50	49.1	18.6	8.0
G31	5.12	0.17	94	943.8	914.0	61.0
G08b	1.91	0.16	56	223.2	188.1	15.0
G13	0.51	0.11	48	59.0	58.5	15.2
G10	1.85	0.04	132	102.0	67.8	210.0

a: Total flux above 5σ. For source G08b, G31 and G10, subtraction of free-free emission is considered (details in Appendix A.6).

b: Effective radius is defined as πR_{eff}^{2} = Area, where Area stands for the emission region above 5σ for each 1.2 mm map, i.e., non-deconvolved averaged size.

c: Dust temperature is assumed to be equal to gas temperature $T(r)$ obtained and refined in Sec 3.3.3, and the average temperature $\bar{T}_{\mathrm{d}}$ is calculated by averaging over pixels that have continuum emission above 5σ.

d: Average density calculated from $M^{\mathrm{Abel}}_{\mathrm{core}}$ and R_{eff}.

Table 3.2: Target sources

Source	R.A. (J2000)	Decl. (J2000)	Distance (kpc)	Gas mass (10^{2} $M_{\odot}$)	Luminosity (10^{3} $L_{\odot}$)	L/M ($L_{\odot}/M_{\odot}$)	Category
G18.606–00.074	$18^{h}25^{s}08^{s}.27$	$-12^{\circ}45'22.^{s}7$	4.3	8.7	0.59	0.68	IR weak
G28.397+00.080	$18^{h}42^{s}52^{s}.08$	$-03^{\circ}59'53.^{s}7$	4.8	33	26	8	IR bright
G19.882–00.534	$18^{h}29^{s}14^{s}.19$	$-11^{\circ}50'28.^{s}4$	3.7	7.9	12	15	IR bright
G08.684–00.367	$18^{h}06^{s}23^{s}.35$	$-21^{\circ}37'05.^{s}2$	4.8	14	27	19	IR weak
G31.412+00.307	$18^{h}47^{s}34^{s}.32$	$-01^{\circ}12'45.^{s}5$	6.9	30	68	23	HII
G08.671–00.356	$18^{h}06^{s}19^{s}.23$	$-21^{\circ}37'26.^{s}8$	4.8	30	86	29	HII
G13.658–00.599	$18^{h}17^{s}23^{s}.46$	$-17^{\circ}22'09.^{s}2$	4.5	5.6	20	36	IR bright
G10.624–00.380	$18^{h}10^{s}28^{s}.638$	$-19^{\circ}55'49.^{s}1$	4.95	50	460	92	HII

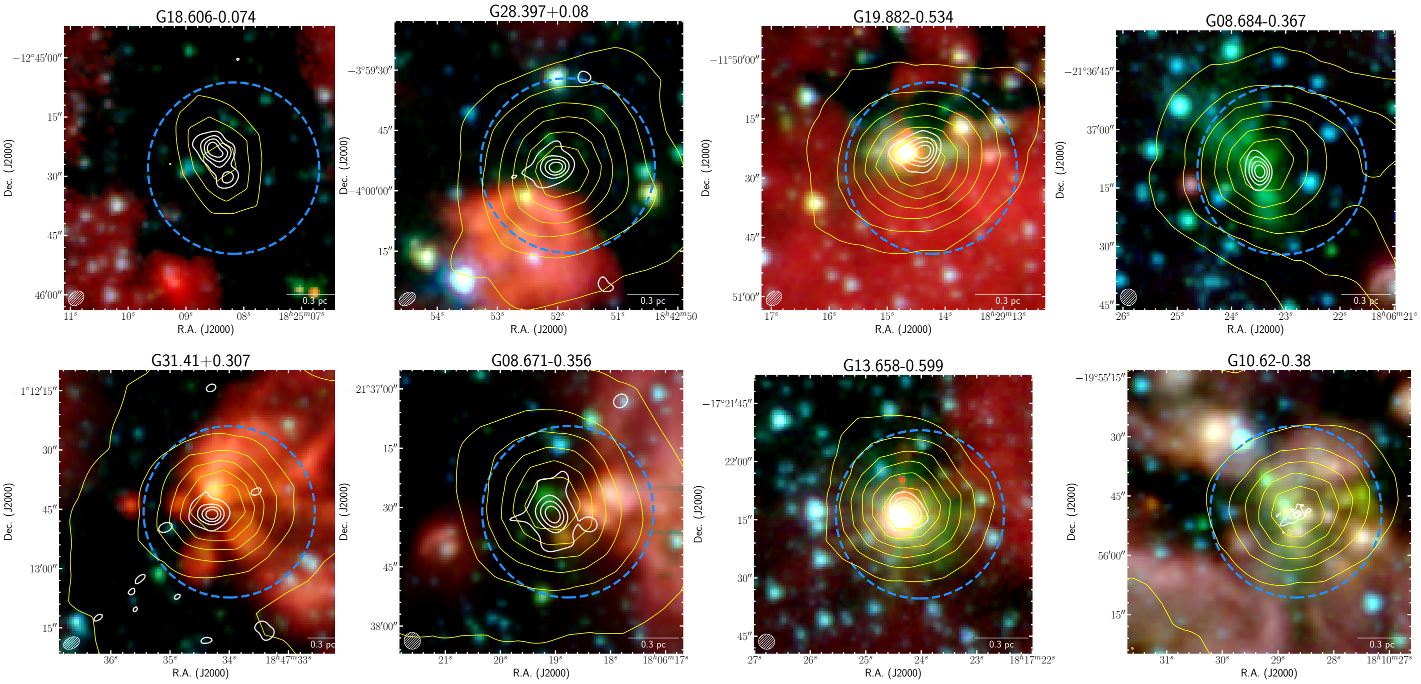

Figure 3.2: *SPITZER* IRAC RGBs (R: 8.0 μm; G: 4.5 μm B: 3.6 μm) maps of the target sources. Yellow contours show the ATLASGAL 870 μm emission from 1 Jy/beam to the peak flux for each source, using 7 levels with uniform spacing. White contours show SMA 1.2 mm emission from 2σ to the peak flux using 5 levels with uniform spacings. The primary beam size is shown in each plot as blue dashed circle.

Table 3.3: Molecular lines of interest covered by the SMA observations. Information is taken from CDMS database (Müller et al. 2001).

Transitions	Rest frequency (GHz)	$E_{\rm up}$ (K)
	(RxA lower sideband)	
$C^{34}S$ $J = 5$-4	241.016	27.8
CS $J = 5$-4	244.935	35.3
	(RxA upper sideband)	
CH_3CCH $J = 12$-11 K=0-5	205.046-205.081	64.0-178.2
H_2CS $J = 6$-5	205.988-206.002	34.6-245.1
	(RxB lower sideband)	
CH_3OH $v_t = 0$ $J = 5$-4	241.700-241.905	34.8-115.2
CH_3OH $v_t = 1$ $J = 5$-4	240.960-241.238	359.9-448.1
CH_3CN $J = 13$-12 $K = 0$-5	239.023-239.138	80.3-258.8
CH_3CCH $J = 14$-13 $K = 0$-4	239.179-239.252	86.1-201.3
H_2CS $J = 7$ -6	240.267-240.394	46.1-164.6
	(RxB upper sideband)	
C_2H $v_t = 0$ $N = 3$-2	262.006-262.079	25.2
CH_3CCH $J = 15$ -14 $K = 0$-4	256.258-256.337	98.4-213.6

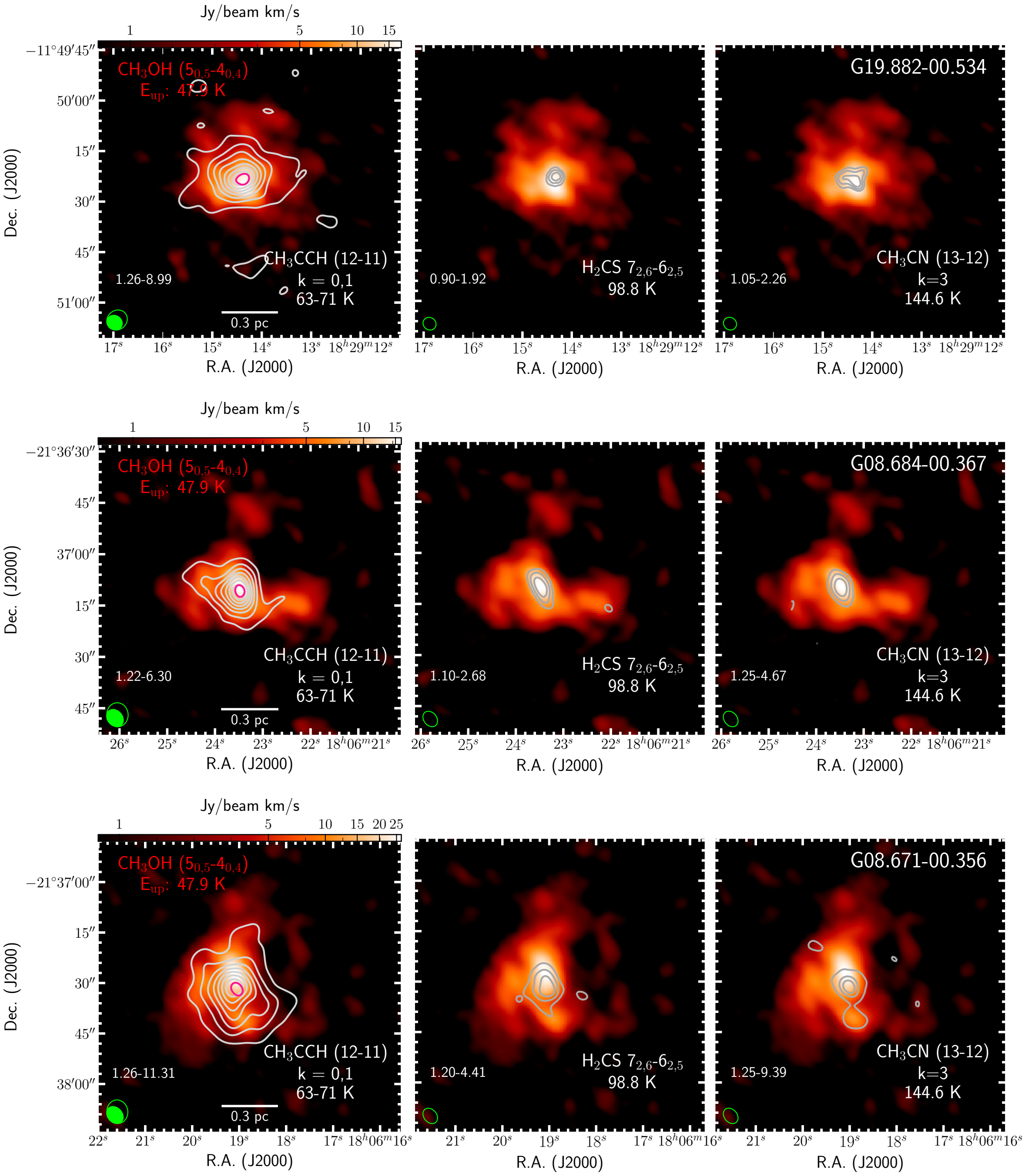

Figure 3.3: Intensity integrated maps (gray contours) of CH_3CCH, H_2CS and CH_3CN toward source G19.882−00.534 and G08.671−00.356. Intensity integrated CH_3OH 5(0,5)-4(0,4) ([v_{lsr} − 3, v_{lsr} + 3] km/s) in shown in color scale. Gray contours show the intensity levels with uniform intervals from 5σ up to the peak emission, with the range (Jy beam^{-1} km s^{-1}) indicated in the *lower left* of each panel. Magenta contour in the *right panel* shows the location of 0.8× peak emission of the 1.2 mm SMA continuum image. The green ellipses indicate beams of respective lines (void) and CH_3OH 5(0,5)-4(0,4) (filled).

calibration uncertainty is typically within 20%, estimated based on the flux measurement of the pointing sources.

Basic data reductions were done with the GILDAS software package [2], including flagging of bad spectra, baseline subtraction, unit conversion (T_A^* to $T_{\rm mb}$), and building spectral cubes. Final spectral cubes are re-sampled to 0.5 km/s spectral resolution for all lines.

3.2.3 SMA-APEX combination and imaging

For our primary target lines covered by both SMA and APEX, which have extended emission, namely CH_3CCH J=12-11, CH_3OH J=5-4, C_2H J=3-2, $H^{13}CO^+$ J=3-2, CS J=5-4, $C^{34}S$ J=5-4 and SO J = 4_5-3_4, we combined the two dataset in the Fourier domain (*uv*-domain) with MIRIAD. This combination is essentially imaging together the pseudo-visibilities generated from single-dish observations and interferometer measurements, so that the short-spacing information including zero baseline which is obtained with single dish can be complemented to interferometry data; the method is commonly referred to as joint deconvolution or joint reconstruction method (Kurono, Morita and Kamazaki 2009, Koda et al. 2011).

In the combination procedure, we first deconvolved the APEX data by the single-dish Gaussian beam (FWHM~30″) and then convolved the resultant image with the primary beam of the SMA observations. The obtained image is then used to generate the single-dish *uv* model, i.e. the pseudo-visibilities, by randomly sampling a visibility distribution to match that of the single-dish beam pattern, and the zero spacing visibility is additionally sampled and added to make sure it preserves in the produced pseudo-visibilities. Finally the pseudo- and interferometric visibilities are imaged together to produce the combined image. In the final imaging step, we apply a Gaussian taper function of FWHM~2″ to increase the detectability of extended emission. In the end we adopt a final step to linearly combine the product of this standard joint deconvolution method with the single-dish image in the Fourier domain, using `immerge` in the MIRIAD package. This step is necessary and found to be preserving the single-dish overall fluxes better than using solely the joint deconvolution method, due to the fact that the deconvolution method is not flux conserving; a similar procedure has been adopted in e.g. Monsch et al. (2018). The combined images have comparable total fluxes as the APEX data, within a difference of 15%.

For details on the proper weighting scheme in the joint deconvolution method and the impact of sensitivities of single-dish and interferometry data, we refer to Kurono, Morita and Kamazaki (2009).

3.3 Results and analysis

3.3.1 Outline of the modeling and analysis procedure

In this work, we aim to measure the gas density and temperature of massive clumps, which are made possible by radiative transfer calculations of molecular lines and multi-wavelength dust continuum. In this section we introduce the logic and overall workflow of the modeling efforts we made, starting by introducing basic definitions for molecular line excitations. The modeling steps (shown in Figure 3.4) are introduced further in Section 3.3.3 to Section 3.3.5 and Section 3.3.7 to 3.3.8. The results of the radiative transfer models are discussed in Section 3.4.

---

[2] `http://www.iram.fr/IRAMFR/GILDAS`

Table 3.4: Critical density for transitions of interest

Transitions	Critical density [a] (cm^{-3})
CS 5-4	$1.1{\times}10^6$
CH_3CCH 12(0)-11(0)	$2.7{\times}10^4$ [b]
H_2CS 6(0,6)-5(0,5)	$2.6{\times}10^5$
CH_3OH 5(1)-4(1)	$6.8{\times}10^5$
CH_3OH 5(4)-4(4)	$6.2{\times}10^7$
CH_3CN 13(0)-12(0)	$3.5{\times}10^6$
CH_3CCH 14(0)-13(0)	$4.3{\times}10^4$ [b]
H_2CS 7(0,7)-6(0,6)	$4.3{\times}10^5$
C_2H (N = 3-2, J=7/2-5/2, F=4-3)	$4.1{\times}10^5$
SO 4(5)-3(4)	$2.4{\times}10^5$
SO 6(6)-5(5)	$6.4{\times}10^5$
SO 7(6)-6(5)	$1.0{\times}10^6$
$H^{13}CO^+$ 3-2	$1.1{\times}10^6$
SO_2 14(0,14)-13(1,13)	$3.9{\times}10^5$
SO_2 3(2,2)-2(1,1)	$1.7{\times}10^5$
CH_3CCH 15(0)-14(0)	$5.3{\times}10^4$ [b]

a: Calculated following definition in Shirley (2015) in the optically thin limit ($\tau \sim 0.1$) at 50 K, considering a multi-level energy system whenever necessary.

b: Calculated using collisional coefficients of CH_3CN.

Massive clumps have molecular hydrogen densities of typically $\sim 10^4$ cm^{-3}; the collisional partner participating in the de- and excitation of molecular lines considered in this paper is primarily hydrogen gas. The critical density ($n_{\rm crit}$) defines the way in which a molecule in an excited state decays to ground state, referred to as the hydrogen density at which timescales of radiative decay and collisional de-excitation are comparable. With gas densites close to and well above $n_{\rm crit}$, the thermalisation of energy levels is achieved, such that the excitation temperature ($T_{\rm ex}$) can approximate the gas kinetic temperature ($T_{\rm kin}$), with the population of energy levels reaching Boltzmann prediction (local thermal equilibrium, LTE). On the other hand, if gas densities are below $n_{\rm crit}$ (sub-thermal excitation), then the population of the upper energy level is sensitive to varying gas densities. Observations of combination of multiple transitions with different $n_{\rm crit}$ can probe a range of gas densities, by showing rather different ratios of line intensities. Especially, if the energy levels associated with these transitions are of similar energy level, then the dependence of line ratios on temperature is minimised. This breaks the degeneracy of the mutual effect of gas temperature and density in determining the level populations. These properties of transitions of a certain molecule, thus, yield a useful 'densitometer'.

In a simple view, massive star-forming clumps may be considered as multi-layered gas structures showing centrally peaked gas density profiles. This is a natural outcome under self-gravity. From outermost layer to innermost region, transitions of higher and higher $n_{\rm crit}$ are thermalised progressively. Using a kit of thermometers of different $n_{\rm crit}$, based on LTE assumption, can constrain gas temperature over a continuous spatial scale (with respect to the clump center). Here a 'thermometer' is defined as, similarly as 'densitometer', a set of molecular lines of a certain species whose level population is only (or dominantly) sensitive to gas temperature, which arise from energy levels spanning a wide energy range and are connected ideally only through collisions, e.g. lines of symmetric top molecules.

Considering the gas density regime of massive star-forming clumps, and based on previous single-dish experiment (Giannetti et al. 2017) we have identified CH_3CCH, H_2CS and CH_3CN lines at 1 mm band as ideal tracers for measuring temperature profiles of massive clumps, which have $n_{\rm crit}$ of several 10^4, 10^5 and 10^6 cm^{-3}, respectively. On the other hand, the combination of distinct $n_{\rm crit}$ brings about a filtering effect, such that with each thermometer, the region it probes is limited to the gas density regimes ranging around its $n_{\rm crit}$. The emission then is negligibly contaminated by fore- and back-ground gas layers of lower density. This means that the line-of-sight effect is reduced to gas component of a limited density range.

In addition, considering typical abundance of these molecules and excitation condition, the optical depths (τ) are usually negligible: the line ratios probe the gas kinetic temperature at the inner location of the gas layer. With these properties in mind, we derive the rotational temperature ($T_{\rm rot}$) maps with LTE assumption using multiple thermometers in Section 3.3.3. We utilise the temperature measurement of the outer regions of the extended CH_3CCH and H_2CS emission, combining with that from CH_3CN emission which is confined to the central region of the clumps, to establish the clump radial temperature profile. We also use multi-wavelength single-dish dust emission (SD continuum, as in Figure 3.4) to derive dust temperature map by building spectral energy distribution (SED) of single-component modified black-body assumption. The dust temperatures at the outer layer of clumps, are used to complete the temperature profile at larger radii for the clumps. With the simple one-component LTE modeling and one-component dust SED construction, we derive and regard the azimuthal profile of the obtained multiple temperature maps as the radial profiles (denoted as $T(r)$, also in Figure 3.4). With this approximation, there is then naturally the difference caused by line-of-sight (LOS) (averaging) effect, i.e. the azimuthal averaged temperature is more closed to density/mass-weighted LOS temperature for each radius. However, as previously mentioned, due to the density-filtering effect by combination of multiple thermometers, the difference between the two profiles is largely minimised. Moreover, the azimuthal temperature profile used as radial temperature profile is further benchmarked and refined by SED construction from full radiative transfer modeling of dust based on adopting a density profile for the clump (Sect. 3.3.5, Section 3.3.7), and further shown to be able to produce the observed CH_3CCH lines and their spatial variation by full line radiative transfer models (Section 3.3.8).

To probe the gas density, we rely on CH_3OH line series at 1 mm band as a densitometer. We adopt one-component non-LTE model to derive the hydrogen volume density (n(H_2)) maps. and benchmark the results using full non-LTE radiative transfer modeling (Sect. 3.3.5, Section 3.3.8). The highest and lowest $n_{\rm crit}$ of its line series we adopted are listed in Table 3.4. Moreover, With measured radial temperature profiles, the degeneracy of temperature and density can be further reduced by introducing $T_{\rm kin}$ ($T(r)$) in the non-LTE modeling, to constrain solely n(H_2). We adopt this strategy as elaborated in Section 3.3.4 (see also Appendix A.7). In Section 3.3.4 we use the one-component non-LTE model of CH_3OH lines to constrain n(H_2). As aforementioned, the excitation of molecular lines has selective effect on gas densities. Since we are also interested in the bulk gas density structure of massive clumps, we complement the density measure with single-dish multi-wavelength dust emission. We conduct full radiative transfer modeling of dust to fit with these data (Section 3.3.7), again incorporating the $T(r)$ already measured from thermometers. To benchmark the one-component non-LTE model, as well as to understand the gas density results from modeling of dust emission and simple non-LTE modeling of CH_3OH, we utilise method of non-LTE full radiative transfer calculation of lines in Section 3.3.8, for CH_3OH and CH_3CCH lines. This also serves as examining the possibly spatially-varying abundance of these lines as an additional factor in affecting the line emission. In this effort, particularly, the modeling of CH_3CCH provides a sanity check of the measured radial temperature profile $T(r)$. The workflow of the whole procedure is shown graphically in Figure 3.4.

3.3.2 The distribution of the emission from CH_3CCH, H_2CS, CH_3CN, CH_3OH lines and 1.2 mm continuum

Figure 3.2 shows the 1.2 mm dust continuum images taken using the SMA (Figure 3.2). We resolved two compact sources (separated by ~7.″2, ~0.15 pc) in G18, and resolved isolated compact sources in the rest of the samples. Figure 3.3 shows the integrated intensity maps of CH_3CCH, H_2CS, and CH_3CN which are overlaid on the integrated intensity maps of CH_3OH. In general, the CH_3OH lines and the lower K ladders of CH_3CCH were resolved on 0.3-0.4 pc scales while the CH_3CN lines and higher K ladders of H_2CS were resolved on 0.1-0.2 pc scales. The results of our quantitative analyses are introduced in the following subsections.

3.3.3 Deriving the pixel-based gas rotational temperature maps with LTE models for multiple thermometers

Thermometers

CH_3CCH and CH_3CN are symmetric top molecules. Their K ladder populations at a certain J level are determined primarily through collisions. Therefore, they have been regarded as thermometers for molecular clouds (Kuiper et al. 1984, Bergin et al. 1994). Given their similar molecule geometry and molecular weight, CH_3CCH and CH_3CN are often assumed to have the same collisional coefficients, while CH_3CN has higher dipole moments than CH_3CCH. Due to this, a molecular clump can exhibit brighter CH_3CN line emission than CH_3CCH line emission even in the case that the excitation of the CH_3CN molecules is limited to small pockets of dense gas, e.g. confined hot core region.

The CH_3CN lines have been very commonly observed. They have been regarded as good tracers for the hot molecular cores owing to that they were typically only detected around significantly heated regions. On the other hand, CH_3CCH has been detected in the spatially more extended, lower temperature regions (e. g. Bergin et al. 1994, Öberg et al. 2014) therefore is particularly advantageous for probing sources which are in relatively early evolutionary stages (Molinari et al. 2016), prior to hot core formation. Giannetti et al. (2017) showed that among various thermometers, the kinetic temperature constrained by CH_3CCH is representative of bulk gas temperature of massive clumps.

The H_2CS molecule is a near-prolate rotor. Its transitions between levels at various K_p ladders are also excellent indicators of the gas kinetic temperature (Blake et al. 1994). As a sulfur-bearing species, the gas phase H_2CS abundance can be enhanced either by direct evaporation or by outflow/shock sputtering (e.g. Bachiller and Gutiérrez 1997, Minh et al. 2011). Previous observations have also revealed that the H_2CS emission is originated from extended warm regions surrounding compact hot cores (e.g. Helmich and van Dishoeck 1997).

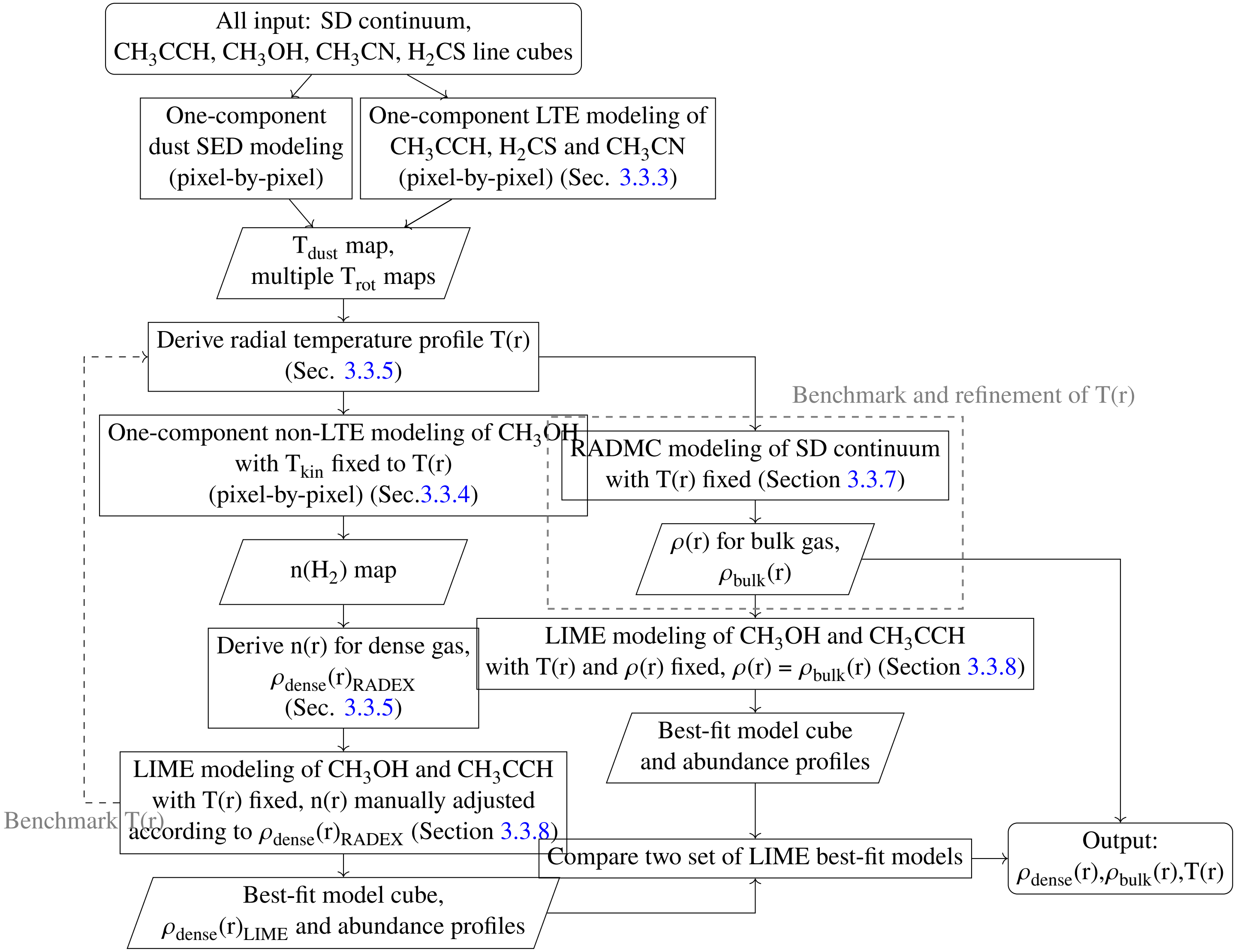

Figure 3.4: Overall work flow showing the radiative transfer modeling procedure in this work.

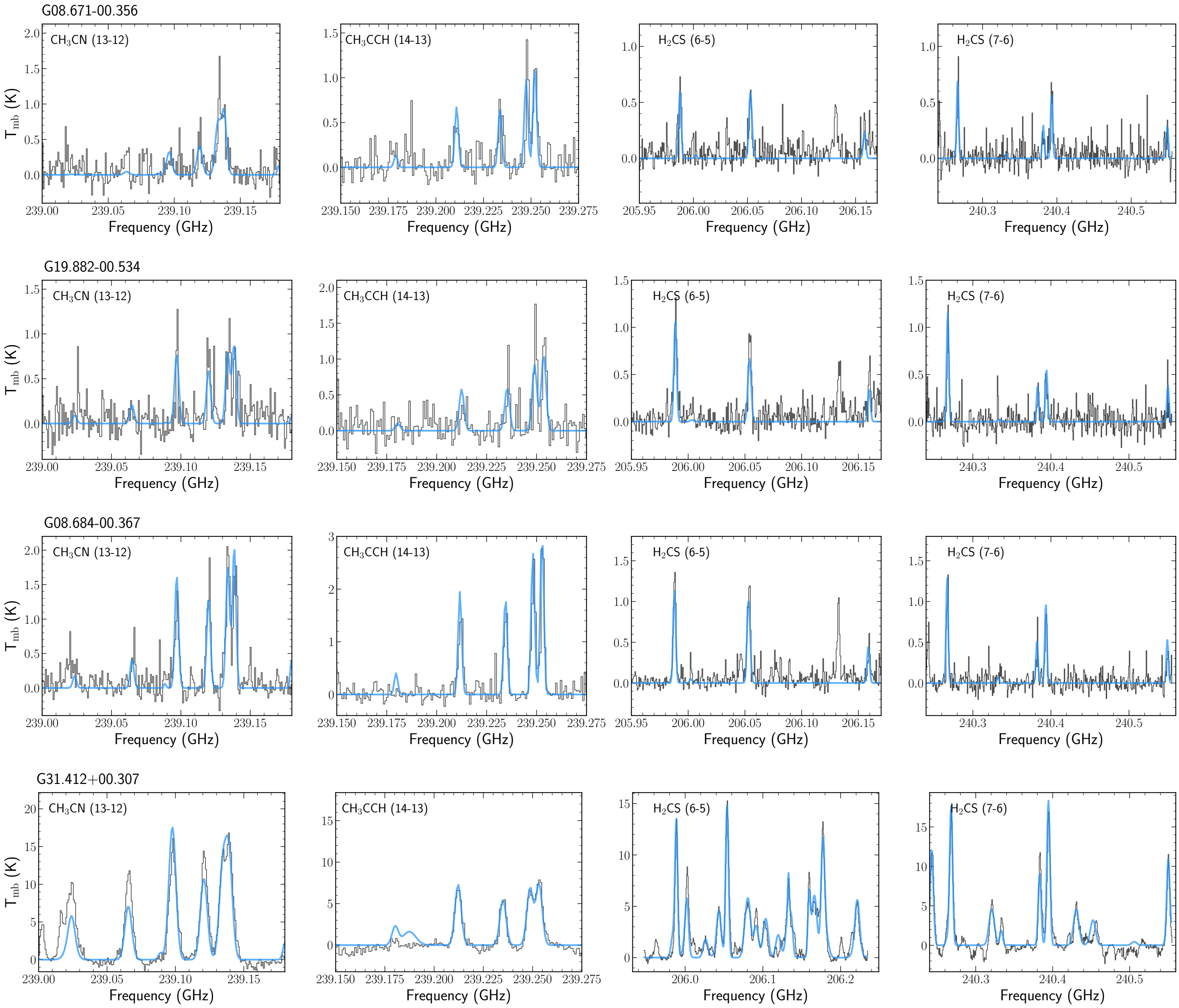

Figure 3.5: Example spectra of the thermometer lines CH$_3$CN (13-12), CH$_3$CCH (14-13), H$_2$CS (6-5), H$_2$CS (7-6) at the continuum peak of the target source; blue profiles show the XCLASS LTE fitted results. For source G31.412+0.307 which is very affected by line blending from other species in these frequency ranges, in the fits the possible blending transitions are also included.

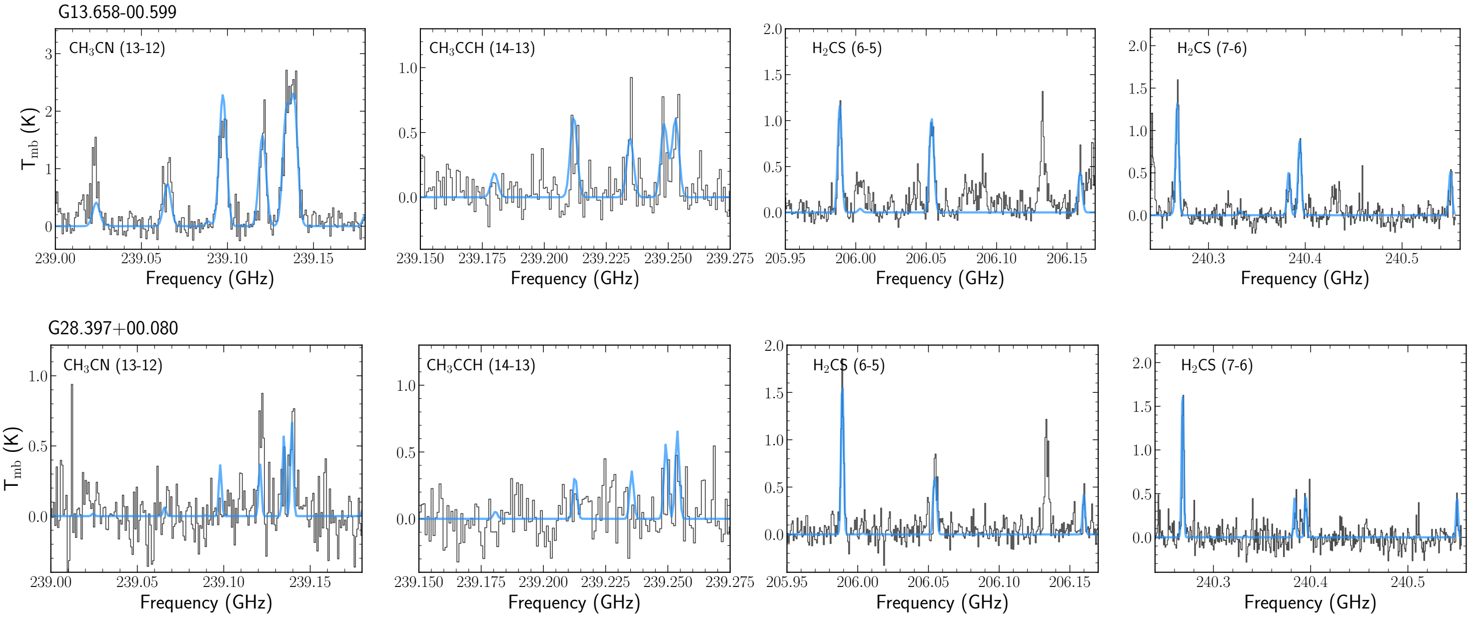

Figure 3.6: Same as Fig. 3.5, continued.

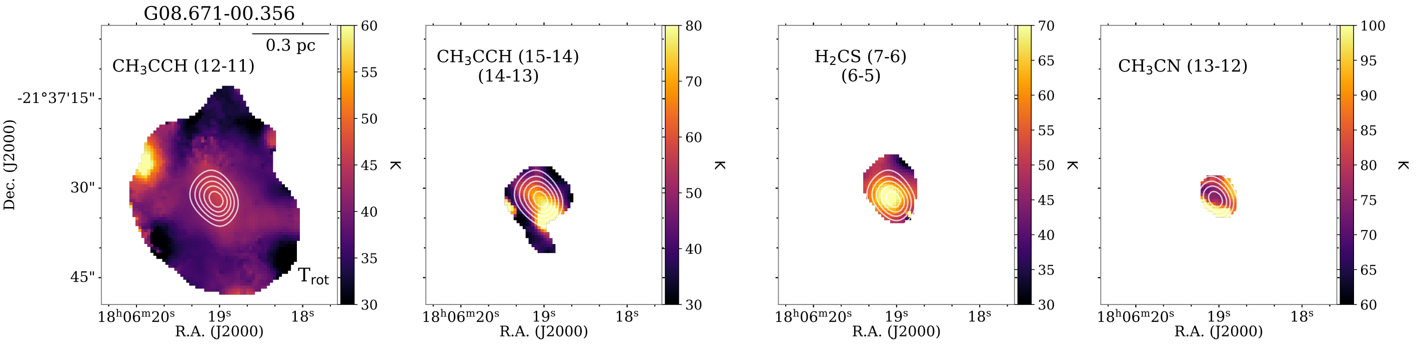

Figure 3.7: Rotational temperature maps derived from multiple lines using XCLASS pixel-by-pixel fit (Sec. 3.3.3), of source G08b. White contours indicate SMA 1.2 mm continuum levels from 0.3 to 0.9× peak flux by 5 levels of uniform interval.

Modeling procedure

Using the XCLASS package (Möller, Endres and Schilke 2017), we have established a pixel-by-pixel Local Thermodynamic Equilibrium (LTE) model-fittings procedure for the observed CH_3CCH, H_2CS, CH_3CN, and CH_3OH v_t =1 lines which returns the best fits of source size, rotational temperature (T_{rot}), molecular column density (N_{mol}), line width (ΔV) and the source velocity (V_{source}). In this specific implementation, we fixed the source size to the synthesized beam size (i.e., assuming beam filling factor of 1) and optimized the rest of free parameters. The optimization procedure employed an initial global parameter search using the bees algorithm (Pham et al. 2006) which was followed by the Levenberg-Marquardt iterations. Such working flow helps avoid trapping in local minima. Finally, for each target source, we selected a few characteristic spectra from the maps and performed the Markov chain Monte Carlo (MCMC) fittings to assess the typical uncertainties of the fit parameters. We fit the J = 15-14 and J = 14-13 ladders of CH_3CCH together, separately from the J = 12-11 ladders, given that the former lines show a less extended emission and appear to trace hotter gas. Examples of the fitted spectra are shown in Figure 3.5. Examples of the obtained rotational temperature maps are shown in Figure 3.7.

3.3.4 Deriving the pixel-based hydrogen volume density maps with non-LTE RADEX models

Methanol lines

Methanol (CH_3OH) is a slightly asymmetric top. It has three types of symmetry, which were denoted as A, E1 and E2, respectively. The E1 and E2 states can be considered as doubly degenerate states of the E symmetry where the quantum number of the angular momentum along the symmetry axis of the CH_3 group (K) can take either positive and negative values. The torsional ground state $E{-}CH_3OH$ $5_K - 4_K$, K = 0, ±1, ±2, ±3, ±4 (v_t = 0) transitions were found to be a good densitometer for gas denser than 10^4 cm^{-3} (Leurini et al., 2004, 2007).

The excitation of these K ladders is usually observed to be sub-thermal. These K=0 and K=±1 ladders occupy a rather narrow range of upper level energies (E_{up} ~40-55 K). At the same time, they cover a wide range of critical densities ($\sim 10^5$ to $\gtrsim 10^7$ cm^{-3}), such that the line ratios of two K components can be good density probes. The higher K components ($K \geq 3$, E_{up}>80 K) are generally excited in hot regions where the gas volume densities are close to or higher than the critical densities. Hence, ratios of the $K \geq 3$ components additionally provide constraints on kinetic temperature. In addition to the high enough abundance of CH_3OH, it is this property of the methanol energy system and the relatively low upper level energies of the $K < 3$ transitions that make this line series sensitive to gas density for a broad range of physical conditions in molecular clouds.

As can be seen from Figure 3.3, the CH_3OH emission appears clumpy and exhibits elongated structures, extending to up to 0.5 pc with respect to the continuum peak. The $K < 2$ transitions of $E{-}CH_3OH$ (5-4) (v_t = 0) are excited over an extended region, while the emission of the $K > 2$ lines are confined to the central region of the clumps.

Modeling procedure

We produced a series of large velocity gradients (LVG) RADEX models (van der Tak et al., 2007) to search for the best fits of n(H_2), molecular gas column density, N(CH_3OH-E)/N(CH_3OH-A) and

Table 3.5: Parameters of CH_3OH derived radial density $\rho_{\rm dense}(r)$ and multi-thermometer derived temperature profiles $T(r)$.

Source	$\rho_{0\,0.1\rm pc}$ $\times 10^6$ ($\rm cm^{-3}$)	Power-law slope $q_{\rm dense}$	$R^a_{\rm eff}$ (pc)	$R^b_{\rm max}$ (pc)	$T_{\rm in}$ (K)	$r_{\rm in}$ (pc)	$T_{\rm out}$ (K)	$r_{\rm out}$ (pc)
G18	2.96(0.246)	-0.26(0.073)	0.08	0.10	64.7(1.08)	0.016^e	19.2(0.07)	0.25(0.05)
G28	6.26(0.4000)	-0.83(0.070)	0.20	0.30	96.1(1.18)	0.02	21.5(0.10)	0.8(0.10)
G19	5.26(0.311)	-0.61(0.051)	0.20	0.25	119.5(2.5)	0.008^e	21.2(0.10)	0.25(0.03)
G08a	10.34(1.234)	-1.33(0.120)	0.30	0.50	128.6(1.76)	0.008^e	22.4(0.12)	1.1(0.14)
G31	8660 (3000)	-3.22(0.37)	0.34	0.42	400.0^d	0.01^e	18.35(1.46)	0.27(0.03)
G08b	22.93(0.681)	-1.35(0.022)	0.34	0.50	135.0(1.44)	0.02	22.3(0.07)	0.8(0.08)
G13	9.15(1.793)	-1.67(0.198)	0.20	0.40	229.6(23.14)	0.004^e	17.0(1.53)	0.2(0.07)
G10	51.64(2.590)	-1.07(0.033)	0.28	0.42	172.4(4.77)	0.02	24.7(0.57)	0.9(0.31)

[a]: Effective radius $R_{\rm eff}$ is defined as the $\pi\ R_{\rm eff}{}^2$ = A, in which the A is the CH_3OH emission area where reliable n(H_2) can be derived.

[b]: The largest radius (distance to the center) of CH_3OH derived n(H_2) map; this is due to the irregular shape of the emission area.

[c]: The density profile of source G31 is better described by a centrally slope~0 density profile plus a steep slope of $-5.22(0.045)$ in the outer region than the single power-law fit listed here.

[d]: Upper limit is set to 400 K in the fit.

[e]: For these source, $r_{\rm in}$ is a re-adjusted parameter based on SED calculation and comparison shown in Figure 3.10 (temperature profile shown as blue lines in Figure 3.22).

Table 3.6: Best fitted parameters of `RADMC-3D` models to the dust continuum of 350/450 μm and 870 μm.

Source	$\bar{\rho}^a$ (10^3 cm^{-3})	q^b	$R_{\rm clump}$ (pc)	$\rho^c_{0\,0.1\,\rm pc}$ (10^4 cm^{-3})	$M_{\rm tot}$ (10^3 $M_\odot$)	$L^d_{\rm bol}$ (10^4 $L_\odot$)	$M_{\rm tot}$ (< 0.5 pc)^e (10^3 $M_\odot$)
G18	14.80	-0.57	0.76	3.81	1.9	0.8	0.7
G28	12.30	-0.66	1.25	5.08	6.9	6.1	0.8
G19	7.76	-1.37	1.04	10.43	2.5	3.1	0.7
G08a	13.18	-1.19	1.00	12.31	3.8	3.5	1.1
G31	11.74	-1.22	2.18	29.93	35.3	57.0	2.6
G08b	3.55	-1.66	2.00	22.90	8.2	24.3	1.3
G13	9.54	-1.41	0.88	10.86	1.9	3.9	0.8
G10	7.76	-1.52	1.58	23.41	8.9	65.3	1.6

^{a}: Average density within clump radius of $R_{\rm clump}$.
^{b}: Density power-law slope.
^{c}: Density at 0.1 pc.
^{d}: Bolometric luminosity calculated by using the SED profile shown in Figure 3.10 (blue lines for source G19, G08a, G31 and G13).
^{e}: Total mass within 0.5 pc from clump center.

kinetic temperature ($T_{\rm kin}$) to the observed CH$_3$OH lines. We took the collisional rates from (Rabli and Flower, 2010) which were evaluated for temperatures from 10 to 200 K. We adopt the Markov Chains Monte Carlo (MCMCs) method to derive the parameters and estimate the associated uncertainties. The details of the modeling procedure are elaborated in Appendix A.7). In the fitting, for each pixel we enforce the posterior distribution of $T_{\rm kin}$ as a narrow Gaussian distribution centralised at $T(r)$ (more in Sect. 3.3.5) as measured from Section 3.3.3 from the multiple rotational temperature maps. Although the ratios between especially the lower k ladders of CH$_3$OH lines only weakly depend on the kinetic temperature, having a fixed term help to avoid randomly converged parameters, which is useful to ensure that resultant parameter maps are continuous. The obtained n(H$_2$) maps are shown in Figure 3.8. The CH$_3$OH column density maps are shown in Figure A.40).

3.3.5 Radial density and temperature profiles used in full radiative transfer models

In our full radiative transfer analyses (Figure 3.4; Section 3.3.1), we assumed that the gas density profile for the bulk gas ($\rho_{\rm bulk}(r)$) is described by the following functional form:

$$\rho_{\rm bulk}(r) = \begin{cases} \bar{\rho}\cdot(\frac{r}{r_{\rm c}})^q & (r \le R_{\rm clump}), \\ 0 & (r > R_{\rm clump}), \end{cases} \tag{3.1}$$

where $\bar{\rho}$ is the mean hydrogen gas number density, $r_{\rm c}$ is the radius where $\rho(r) = \bar{\rho}$, $R_{\rm clump}$ is the assumed outer radii of the clumps which were fixed to the FHWM measured from the ATLASGAL 870 μm maps (c.f., Contreras et al. 2013). When converting ρ to mass density, we assume that the mass per hydrogen molecule is 2.8 $m_{\rm H}$, where $m_{\rm H}$ is the hydrogen atom mass. We assumed that the gas-to-dust mass ratio is 100.

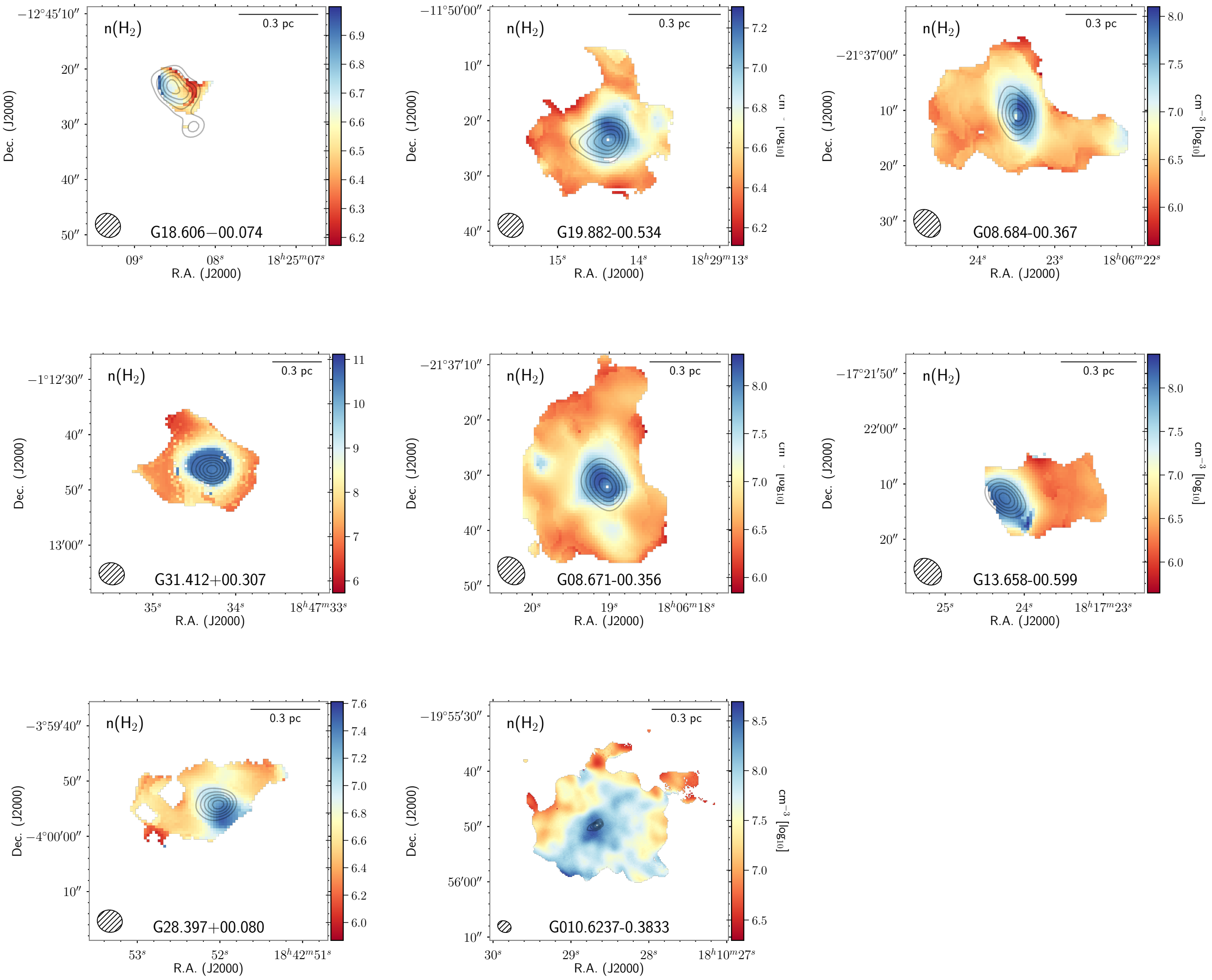

Figure 3.8: CH_3OH derived n(H_2) maps from RADEX modeling, of all target sources. Gray contours indicates the SMA 1.2 mm continuum level from 0.1 to 0.9×peak flux represented by 5 levels of uniform interval.

Table 3.7: Best-fit CH_3OH and CH_3CCH abundance results of `LIME` modeling based on density model from A: `RADMC` continuum modeling as listed in Table 3.6; B: manually-adjusted RADEX radial density profile as listed in Table 3.5.

	A							B						
	CH_3OH			CH_3CCH				CH_3OH			CH_3CCH			
Source	X_{out} ($\times10^{-10}$)	T_{jump} (K)	f_{inc} [a]	X_{out} ($\times10^{-10}$)	T_{jump} (K)	f_{inc}	f_{r} [b]	X_{out} ($\times10^{-10}$)	T_{jump} (K)	f_{inc}	X_{out} ($\times10^{-10}$)	T_{jump} (K)	f_{inc}	$f\,f_{\mathrm{dens}}$ [c]
G28	10	30	10	10	30	10	3	1.5	80	150	0.018	30	200	0.13
G19	15	80	10	75	–	1	3	1.5	80	100	5	80	30	0.19
G08a	10	80	20	100	80	20	3	0.84	80	35	6	–	1	0.06
G31	2.5	80	10	20	80	10	50	4.0	120	8	12	120	2	0.09
G08b	10	80	5	100	–	1	5	0.6	80	40	5	80	70	0.05
G13	10	80	5	20	80	10	3	0.67	80	4	1.9	80	3	0.28
G10	10	80	5	–	–	–	7.5	0.54	40, 100	4, 75	–	–	–	0.05

Marker "–" denotes parameter invalid or not available.

a: f_{inc} represents increase factor of the abundance jump model (Equation 3.4).

b: Reduction factor applied to RADEX density results in the modeling (Equation 3.5).

c: Dense gas volume filling factor defined in Section 3.3.8.

We parameterised the measured temperature profiles $T(r)$ by

$$T(r) = \omega T_{\rm in}(\frac{r}{r_{\rm in}})^{-0.5} + (1-\omega)T_{\rm out}, \tag{3.2}$$

where $\omega = e^{-\frac{r}{r_{\rm out}}}$ is an exponential tappering function characterized by outer radius $r_{\rm out}$; $T_{\rm in}$ and $T_{\rm out}$ are the characteristic temperatures at the radius $r_{\rm in}$ and at asymptotically large radii, respectively. In this equation, the first term describes radiative heating by the centrally embedded stars while the second term can be attributed to the ambient radiation fields of the massive clumps. The multiplicative factors ω and $(1-\omega)$ prescribe the transition from one heating regime to the other.

Based on the multiple rotational temperature maps, we derived the azimuthal averaged temperature profile and obtain best-fit parameters $T_{\rm in}$ and $T_{\rm out}$, while $r_{\rm in}$ is initially kept as a fiducial value of 0.02 pc. Figure 3.9 and 3.10 shows how the multi-wavelength radial intensity profiles and the SEDs evaluated from our best-fit models compare with those taken from the observations. Based on this comparison, we re-adjust the $r_{\rm in}$ in Equation 3.2 in the continuum radiative transfer modeling to obtain a SED consistent with observed one. The $T(r)$ is updated by the refined temperature profile. The parameters $T_{\rm in}$, $T_{\rm out}$, and $r_{\rm in}$ that define $T(r)$ are listed in Table 3.5. With $T(r)$ defined, we fix the dust temperature profile in the multi-wavelength continuum modeling for the bulk gas and obtain the $\rho_{\rm bulk}(r)$, the parameters $\bar{\rho}$ and q as in Equation 3.1 are listed in Table 3.6.

From RADEX modeling of CH_3OH lines we constrain the radial density profiles from the n(H_2) maps for the dense gas $\rho_{\rm dense}(r)$. Similarly, to obtain the n(H_2) maps (Figure 3.8) we fix the gas kinetic temperature in the modeling as $T(r)$ for each pixel. We adopt a single power-law form as Equation 3.1 to characterize the profiles extracted from n(H_2) maps, as

$$\rho_{\rm dense}(r) = \rho_{0\,0.1\rm pc}(\frac{r}{0.1pc})^{q_{\rm radex}}, \tag{3.3}$$

where $\rho_{0\,0.1\rm pc}$ is the reference gas density at 0.1 pc. The description is valid up to a maximum scale of $R_{\rm max}$, which is determined from the largest radius where n(H_2) can be robustly estimated. These parameters are listed in Table 3.5. Figure 3.11 shows the comparisons between the model fits and the observed radial profiles.

We then conduct full radiative transfer modeling to benchmark and refine these results. In the `LIME` modeling of CH_3OH and CH_3CCH lines, we first adopted the bulk gas density profile $\rho_{\rm bulk}(r)$ constrained from single-dish dust continuum modeling, and $T(r)$ with assumed abundance profiles to find the best-fit models. We parameterized the molecular abundance profiles ($X_{\rm mol}(r)$) as:

$$X_{\rm mol}(r) = \begin{cases} X_{\rm out} & (T(r) < T_{\rm jump}) \\ X_{\rm in} \equiv f_{\rm inc}X_{\rm out} & (T(r) > T_{\rm jump}), \end{cases} \tag{3.4}$$

where $T_{\rm jump}$ is a threshold temperature chosen to be either 30 or 80 K, $X_{\rm out}$ is the abundance at the outer radii, and $f_{\rm inc}$ is an increment factor to characterize the abundance enhancement over $X_{\rm out}$ in inner regions of higher temperature. This form is driven by published chemical modeling results of CH_3OH and CH_3CCH (more in Section 3.3.8). The best-fit model parameters $T_{\rm jump}$, $X_{\rm out}$ and $f_{\rm inc}$ for this model (hereafter model A) are listed in Table 3.7 (column A). For all sources, we find that with the assumed density profile of $\rho_{\rm bulk}(r)$ the models cannot reproduce the observed high ratios between the higher and lower K components of CH_3OH lines, which points to, as also indicated from the RADEX modeling results, a much higher gas density regime. Therefore, we updated the `LIME` modeling with gas density radial profiles based on $\rho_{\text{dense}}(r)$ (Equation 3.3), the RADEX results of n(H$_2$) radial profiles, following:

$$\rho_{\text{dense}}(r) = \begin{cases} \frac{1}{f_{\text{r}}}\rho_0 & (r < r_0) \\ \frac{1}{f_{\text{r}}}\rho_0 (r/r_0)^{q_{\text{radex}}} & (r_0 < r < R_{\text{max}}), \end{cases} \tag{3.5}$$

where r_0 denotes reference radius of 0.1 pc, or 0.05 pc (for G13 and G31); ρ_0 is the reference density at r_0. These values, together with R_{max} are taken from Equation 3.3 derived by RADEX modeling. Here f_{r} is a reduction factor applied to ρ_0. We manually adjusted f_{r} (Equation 3.5) and $X_{\text{mol}}(r)$ (Equation 3.4) in a trial-and-error manner to seek for better fits to the observational data. In the following we refer to q_{radex} as q_{dense} as this slope is fitted based on n(H$_2$) maps of CH$_3$OH RADEX modeling and retained as the slope of the dense gas profile in full radiative transfer `LIME` models. The best-fit model parameters T_{jump}, X_{out}, f_{inc} and f_{r} for this model (hereafter model B) are summarized in Table 3.7 (column B). Figure 3.12 shows a comparison between the CH$_3$OH line profiles reproduced from model B and the observations.

3.3.6 SMA 1.2 mm continuum analysis

The SMA 1.2 mm dust continuum images resolved two compact sources (separated by ~7.″2, ~0.15 pc) in G18, and resolved isolated compact sources in the rest of the samples (Figure 3.2). Hereafer we refer these compact sources as core structures. Before any further analyses, we based on the archival centimeter band data to subtract free-free contamination in G08b, G31, and G10, assuming optically thin condition (i.e., $S_\nu^{\text{free-free}} \propto \nu^{-0.1}$; for details see Appendix A.6). Then the core radius is defined as the area above 5σ emission contours of the 1.2 mm images. The core effective radius, peak intensity and integrated flux are listed in Table 3.1.

We assumed that dust emission in all cores is optically thin at 1.2 mm. Based on the OH5 opacity model (i.e., $\kappa_{1.2\text{mm}} = 0.81$ cm^{2}g^{-1}; Ossenkopf and Henning 1994), we converted the continuum intensity detected at >5σ to dust mass surface density, which was subsequently converted to gas mass surface density by assuming that the gas-to-dust mass ratio is 100. In these mass estimates, we assumed that dust temperature is identical to the gas temperature $T(r)$ which we derived (and refined, Equation 3.2) (c.f. Section 3.3.3, 3.3.5 and Section 3.3.7).

There is a subtlety in the way we applied $T(r)$, which is related to the assumption of the thermal and density structures of the cores. To gauge the uncertainty it yields, we compared two ways of applying $T(r)$. In the first, we defined a mean core gas temperature $\bar{T}_{\text{core}}$ by making averages of $T(r)$ within the core size. For each pixel, we then adopted a dust temperature which is equal to $min\{T(r = \ell)$, $\bar{T}_{\text{core}}\}$ when deriving N(H$_2$) where ℓ is the projected distance from the pixel to the 1.2 mm continuum peak (i.e., centers of the sources). Given that the projected radius ℓ is always smaller than the radius r, this approach still tends to overestimate the dust temperatures at small projected radii although it is alleviated. This in turns leads to underestimates of N(H$_2$). In a second approach, we assumed that the cores are spherically symmetric and optically thin. We used Abel transformation to convert the observed azimuthal averaged intensity profile of 1.2 mm emission to gas density $\rho(r)$ (for more details

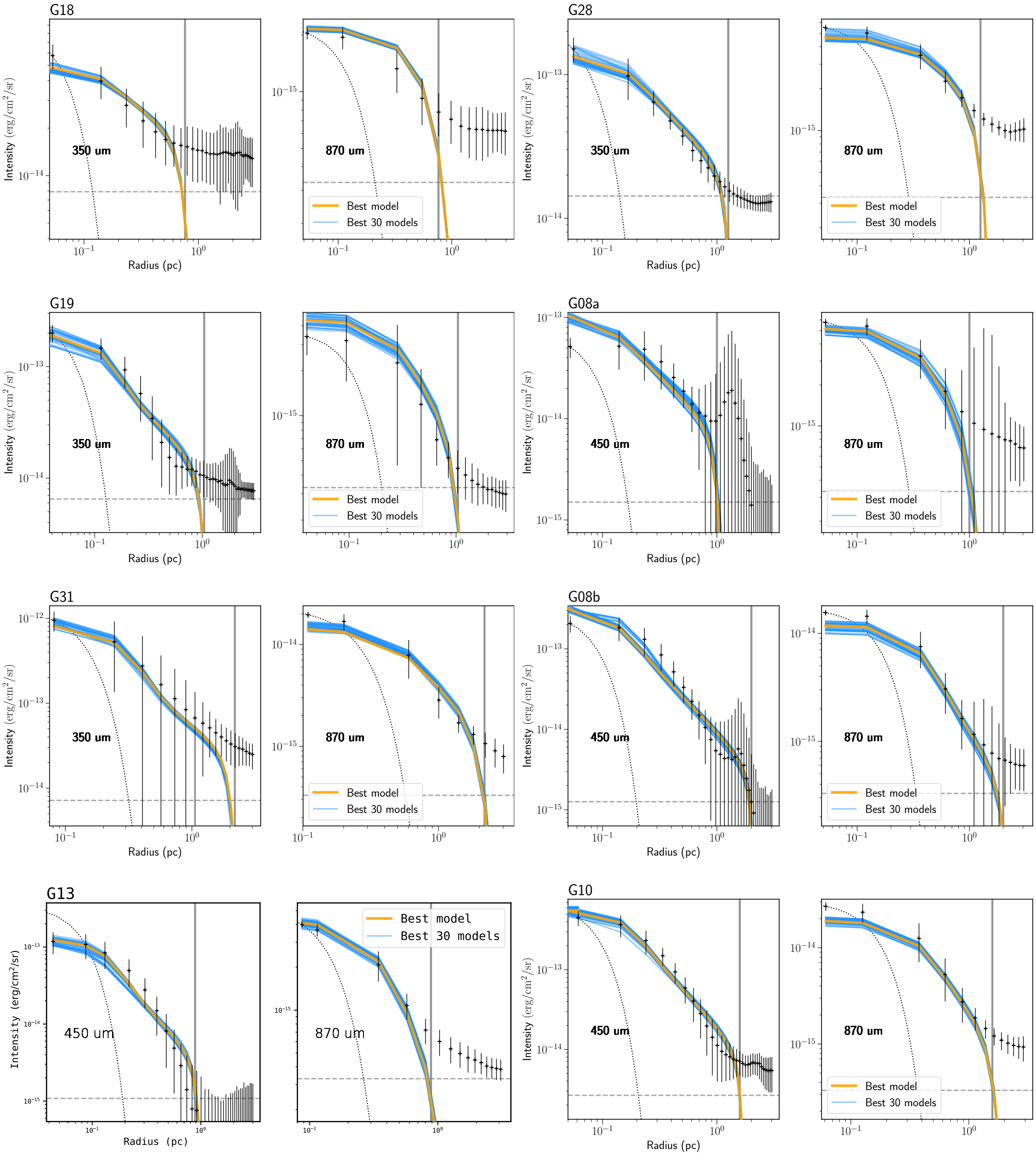

Figure 3.9: Radial intensity profile comparisons between observations and best-fit `RADMC-3D` models. Gray horizontal dashed lines indicate the noise level (3σ). Gray vertical lines indicate the clump radius used in the modeling. Dotted line indicates beam shape in each plot. For source G19, G08a, G13 and G31, model fit after re-adjusting T(r) is shown.

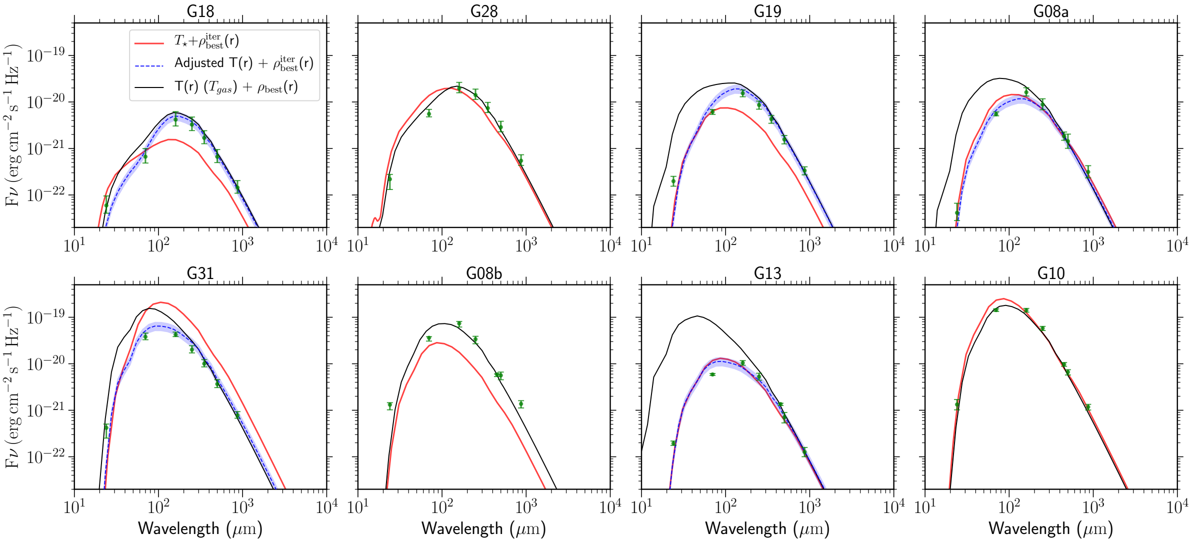

Figure 3.10: Comparison of SEDs of the best-fit `RADMC-3D` models with measured multi-wavelength fluxes for each source. Black line indicates the SED generated from assumed T(r) and the corresponding best density profile fits. Blue dashed line indicates the SED generated from adjusted T(r) and the re-iterated best density profile fits. Blue shaded regions indicates 20% difference around the blue dashed SED profile. Red line shows the SED generated by self-consistently calculating the dust temperature adopting a central heating ZAMS star plus the re-iterated best density profile.

see Roy et al. 2013), as

$$\rho(r) = -\frac{1}{\pi \kappa_\nu B_\nu[T(r)]} \int_r^{r_{\rm eff}} \frac{{\rm d}I_\nu}{{\rm d}b} \frac{{\rm d}b}{\sqrt{b^2 - r^2}}, \tag{3.6}$$

where $r_{\rm eff}$ is the core effective radius. We then integrated $\rho(r)$ over the line-of-sight to yield another version of N(H$_2$) map. The two versions of N(H$_2$) maps agree within a factor of 1.5-2. The average dust/gas temperatures within the core, two sets of mass estimates $M_{\rm core}$ and $M_{\rm core}^{\rm Abel}$, and average core density are summarized in Table 3.1.

3.3.7 Radiative transfer modeling of multi-wavelength continuum emission with `RADMC-3D`

We divided the 870 μm (using APEX/LABOCA), 450 μm (using JCMT/SCUBA-2), or 350 μm (using CSO/SHARCII or APEX/SABOCA) images (whenever available) of each clump into annuli which have intervals equal to half of the beam FWHM, and then (azimuthally) averaged the intensities in the annuli. When the intensity distribution is largely azimuthally asymmetric with respect to the clump center (e.g., when there is a bright adjacent core/clump or a bright external gas filament), we trimmed iteratively the contribution from those asymmetric (sub)structures before making the averages. In practice, at each radius we first derived the mean and standard deviation ($I_{\rm std}$) of the intensities and then masked the pixels at which the sum of the radial intensities deviates from the mean by more than 0.9 times the sum of radial $I_{\rm std}$.

We used radiative transfer models to invert these derived radial intensity profiles to radial dens-

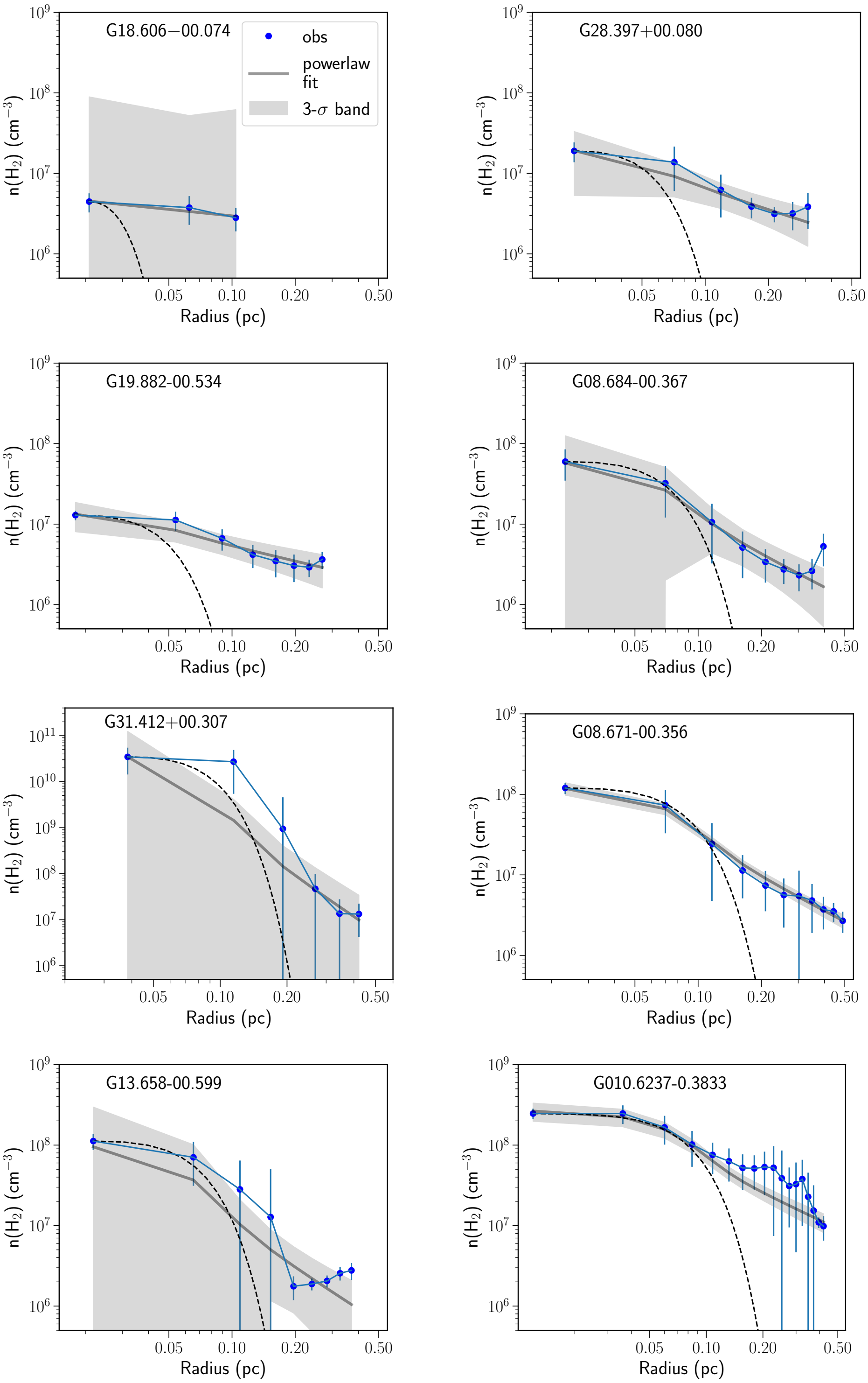

Figure 3.11: Azimuthal averaged n(H$_2$) radial profiles derived from n(H$_2$) maps shown in Fig. 3.8. Thick gray line indicates the best-fit single power-law model (beam convolution considered). Gray shadowed band indicates the 3σ confidence band of the best-fit model. The model parameters and 1σ errors are listed in Table 3.5.

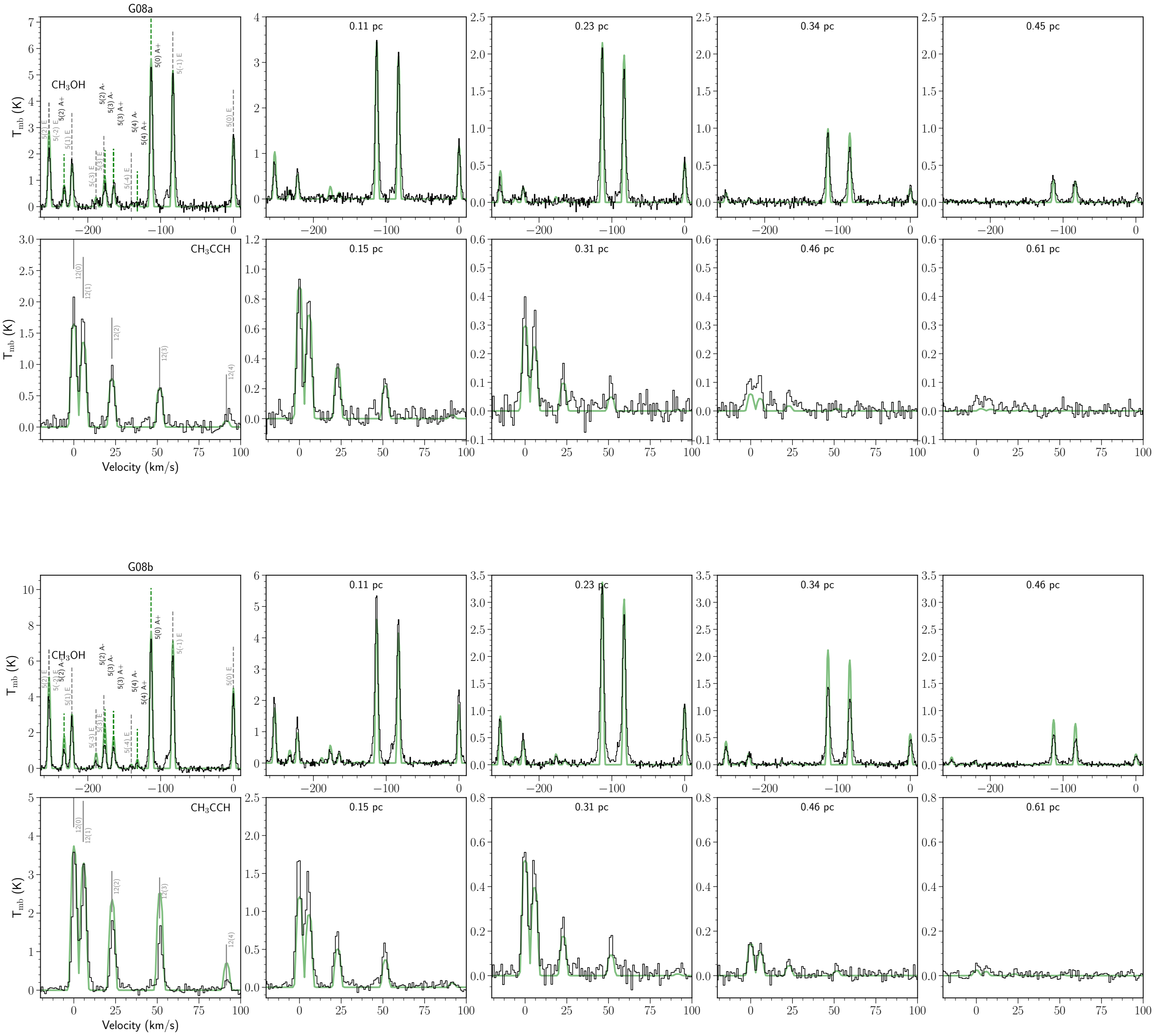

Figure 3.12: `LIME` modeling result of manually adjusting density model of piecewise power-law form, based on RADEX modeling derived n(H_2) result.

ity profiles. We employed the publicly available Monte Carlo radiative transfer code `RADMC-3D` (Dullemond et al. 2012). To find the simulated intensity profiles which match the observed ones, our modeling ergodically visited the parameter spaces of the assumed functional form for density (Equation 3.1, Sect. 3.3.5). We also let `RADMC-3D` generate the SEDs at 24, 70, 160, 250, 350, and 500 μm wavelengths and verified that they are broadly consistent with the aperture photometric measurements taken from the *Spitzer*/MIPS (Carey et al. 2009), *Herschel*/PACS, and *Herschel*/SPIRE images.

We assumed that dust opacity does not have spatial variation and quoted the opacity model from Ossenkopf and Henning (1994). Specifically, we quoted the column evaluated for the thin ice mantle coated dust which was coagulated for 10^5 years in an environment with 10^6 cm^{-3} gas density (hereafter OH5 model). This model has been successfully applied in the previous studies to explain the radial profiles of dust emission around high-mass embedded protostars (Mueller et al. 2002; Rolffs et al. 2011). The maximum grain size in the OH5 opacity model is under the Rayleigh limit such that the scattering opacity can be neglected in the modeling.

The hydrogen gas density profile ($\rho_{\rm bulk}(r)$) is described by the functional form of Equation 3.1. Using Monte Carlo radiative transfer to evaluate the temperature distributions (e.g., based on assumptions of heating sources and interstellar radiation field) is subject to a very large degree of freedom, which can be rather artificial. Instead, we adopted the radial gas temperature profile probed by the thermometers in Section 3.3.3, following the form of Equation 3.2.

We performed a simple single-component SED fitting to derive the overall mass of individual clumps ($M_{\rm sed}$) and used it as a prior for our subsequent modeling. Given that we only need to fit two free parameters ($\bar{\rho}$, q, c.f. Equation 3.1), the Markov chain Monte Carlo (MCMC) method has no clear advantage. Instead, for each observed molecular clump, we drew 10,000 samplers from the parameter space of q = 0.0-2.5, $\bar{\rho}$ = 10^3-10^6 cm^{-3} with a random process. The likelihood function of the clump total mass follows the truncated normal distribution:

$$ln\mathcal{L} = \begin{cases} -0.5(\frac{M-M_{\rm sed}}{3M_{\rm sed}})^2 & (0.2M_{\rm sed} \leq M \leq 5M_{\rm sed}) \\ -inf & (M < 0.2M_{\rm sed} \;\; or \;\; M > 5M_{\rm sed}) \end{cases} \tag{3.7}$$

We then ran `RACMC-3D` for each sampler and convolved the derived images with the corresponding Gaussian beams to compare with the multi-wavelengths observations. When summing the χ^2, we assumed that the observational data can have nominal ~20% errors, and adopted one standard deviation in the radial profile calculation as the uncertainty of the observational data. The χ^2 calculation follows,

$$\chi^2 = \sum_{\lambda}\sum_{r}\frac{(f_{\rm mod} - I_{\rm obs})^2}{I_{\rm std}^2 + (0.2I_{\rm obs})^2} \tag{3.8}$$

where $\sum\limits_{\lambda}$ and $\sum\limits_{r}$ denote summing over all wavelengths and sampled radii, respectively. $f_{\rm mod}$ stands for the model intensity at a certain radius.

Figure 3.9 compares the observed radial intensity profiles with the best-fit models. The fitted values of q and $\bar{\rho}$, the (pre-determined) clump radius, and overall clump mass, and the characteristic density determined from the best-fit model at 0.1 pc radius, are summarized in Table 3.6. The posterior probability distributions of $\bar{\rho}$-q are shown in Figure 3.13, with best-fit parameter set marked. In Figure 3.10 the observed multi-wavelength flux densities are compared with the SED generated from best-fit

`RADMC-3D` models.

It can be seen that the observed SEDs of source G19, G08a, G13 and G31 show large deviation from that of the best-fit models which were produced based on the assumed $T(r)$ profiles. For source G19, G08a and G13, the deviations are partially expected as these three source have overall smallest densities, from the clump center to outer region. It is likely that $T_{\rm rot}$ estimated from aforementioned thermometers is biased to the small proportion of the dense gas at each radius (clumpiness), while the temperature for the bulk gas at each layer, or the *average* gas temperature is smaller. In addition, for the intermediate-scale gas having densities $\lesssim 10^5$ cm^{-3}, which are mostly probed by CH_3CCH (12-11) and H_2CS lines in terms of gas temperature, the gas temperature being higher than dust temperature may also have an origin from turbulent heating, as under such gas densities thermal coupling between dust and gas is weaker (Pan and Padoan 2009). For G31, which is much denser in terms of bulk gas radially but shows the most prominent monolithic core in the center, the over-estimation of temperature likely originates from optical depth effect.

To refine $T(r)$ as guided by the observed SED shape, we retain the parametric form (Equation 3.2) as elaborated in Section 3.4.1, and only adjust the parameter $r_{\rm in}$ (Equation 3.2), scaled by a factor <1. Based on the adjustment, we regenerate SED profiles from `RADMC` modeling and find the best-fit rescaled $r_{\rm in}$, which are listed in Table 3.6 for the 5 sources. For these 5 sources, we then iterate the fitting of radial density profiles from `RADMC-3D` calculations, based on the adjusted temperature profiles $T(r)$. From Figure 3.13, the best-fit parameter set before and after adjusting $T(r)$ are shown together. Decreasing $r_{\rm in}$ in the temperature form, is equivalent to reduce the steepness and absolute value of temperature radial profile, which results in an increment of mean gas density and density profile slope in the radial intensity profile fits, as expected. As a further benchmark, we use `RADMC-3D` to self-consistently calculate the dust temperature. To convert the clump luminosity to a central stellar source, we use the stellar evolution models of solar metallicity from Choi et al. (2016) which give relations between luminosity, mass, radius and temperature for ZAMS to estimate the stellar $T_{\rm eff}$. The re-iterated best-fit density model is used to describe the envelope structure. The resultant SED is also shown in Figure 3.10.

3.3.8 Radiative transfer modeling of CH_3OH and CH_3CCH lines: benchmarking the results from one-component non-LTE/LTE models with `LIME`

The RADEX analysis of CH_3OH (5-4) lines in Section 3.3.4, with one-component non-LTE assumption, can be biased due to the mixed contribution along the LOS. On the other hand, the RADMC-3D modelings for dust continuum in Section 3.3.7 better represents the enclosed masses within certain radii by constraining $\rho_{\rm bulk}$, while they cannot provide constraint on the higher volume density internal structures. To refine our estimates of physical parameters, we build on these two efforts to conduct 3D radiation transfer forward modelings of CH_3OH (5-4) and CH_3CCH (12-11) lines. Specifically, we performed the non-LTE modeling for the excitation conditions using the `LIME` code (Brinch and Hogerheijde 2010) and then compared the synthetic spectra with the observed spectral cubes. The spatial distributions of CH_3OH (5-4) and CH_3CCH (12-11) line emission are rather extended such that they better characterize the majority of dense gas in the clumps. We focus on benchmarking the radial density profile of the dense gas ($\rho_{\rm dense}$). We fixed the gas temperature profiles ($T(r)$; Section 3.4.1) to what we obtained from Section 3.3.3 (and refined in Section 3.3.7), when constructing the input models. As $T(r)$ has been verified by full radiative transfer of dust continuuum by building SEDs, the CH_3CCH (12-11) modeling conducted here is further used as a sanity check that the assumed

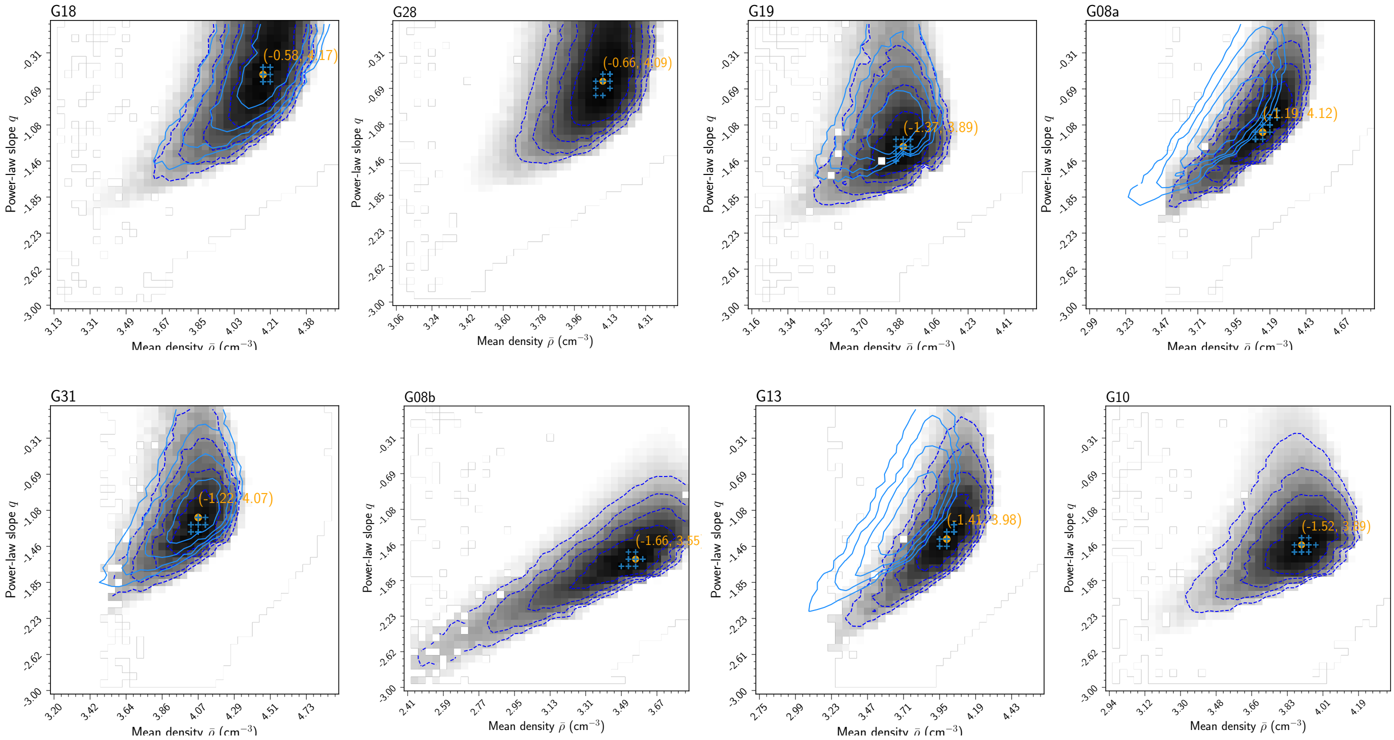

Figure 3.13: χ^2 converted probability distribution of the 10 000 parameter set of `RADMC-3d` models for all sources. Orange point indicates the best-fit model. Blue crosses mark the positions of the 30 best-fit models, so there could be overlaps between different parameter set due to the binning. For source G31, G13, G08a and G19, results before re-adjusting T(r) based on SED are shown additionally as light blue contours.

temperature profile can reproduce the line emission of this thermometer. We focus on benchmarking ρ_{dense} by `LIME` models.

The gas density radial profiles were initially specified to be the best fits from the modeling continuum intensity profiles, ρ_{bulk} (Equation 3.1, see details in Section 3.3.7). Based on this density model and temperature profile $T(r)$, we then experimented various assumptions of the abundance spatial variations of CH_3OH and CH_3CCH, motivated by the results of chemical network from Belloche et al. (2017) and Calcutt et al. (2019).

Based on the chemical network of Belloche et al. (2017), Calcutt et al. (2019) calculated the variation of gas-phase abundance of CH_3CCH as a function of warm-up time at different final densities which range from 10^7 to 10^{10} cm^{-3}. In these calculations, a two-stage physical evolution is assumed: a cold collapse stage is followed by a static warm-up stage which reaches a gas temperature of 400 K. The CH_3CCH abundance is significantly enhanced when the gas temperature reaches 30-40 K due to desorption of CH_4 to form CH_3CCH (i.e., dissociative recombination of larger hydrocarbons). The CH_3CCH abundance is significantly enhanced for another time when the gas temperature reaches 80-100 K, due to the direct desorption of CH_3CCH from the grain surface. Finally, the models with higher final gas density present systematically lower CH_3CCH abundance since in these high-density models CH_4 desorbs at slightly higher temperature (lower panel of Figure 3.14). Similarly, according

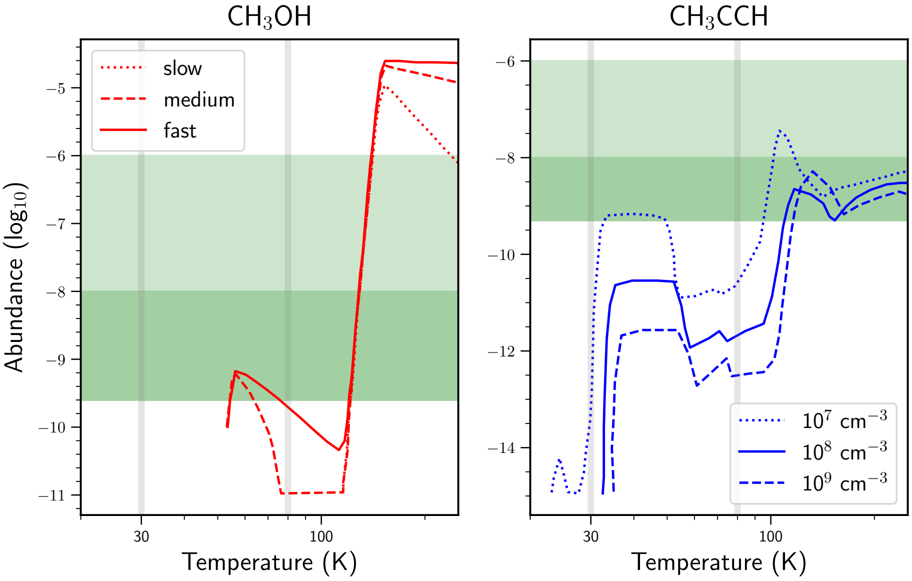

Figure 3.14: The abundance plot of CH_3OH and CH_3CCH from chemical models (lines) and the explored parameter space (filled) for the `LIME` modeling based on `RADMC-3D` density model. For CH_3OH the abundance profiles for different warm-up timescales are shown (Garrod et al. 2017); for CH_3CCH, abundance profiles of different final collapse densities are shown (Calcutt et al. 2019). The light green filled region indicate the lower abundance range explored by the `LIME` models, and the dark filled region the upper range. The vertical gray lines indicate the jump temperature of 30 and 80 K.

to the chemical model of Garrod et al. (2017), the abundance of CH_3OH experiences two significant enhancement at 30-40 K and 80-100 K gas temperatures (upper panel of Figure 3.14).

To mimic the abundance enhancement in the warm or luckwarm regions as described by these chemical models, we parameterized the CH_3OH and CH_3CCH abundance profiles as Equation 3.4. Again, we assumed that the A and E-type CH_3OH have the same abundance. The parameter ranges of $X_{\rm in}$ and $X_{\rm out}$ were chosen by referencing to $N_{\rm mol}$ for CH_3CCH and CH_3OH from XCLASS/RADEX modeling results (Section , 3.3.3-3.3.4) and the aforementioned chemical models. Figure 3.14 shows a comparison between the parameter space we explored and the chemical modeling results.

Presently, only the collisional coefficients of CH_3OH with para-H_2 are available, although it seems that only in hot shocked gas there is a significant difference between the thermal rate coefficients of collisions with ortho- and para-H_2 (Flower, Pineau des Forêts and Rabli 2010). Our non-LTE models were not affected by the uncertain collisional coefficients due to that we assumed a low ortho- to para-H_2 (OPR) abundance, such that the collisions with ortho-H_2 is negligible. Chemical models and observations towards early stage dense cores indeed indicate an OPR value of $\sim 10^{-3}$-10^{-2} (Flower, Pineau Des Forets and Walmsley 2006, cf. Troscompt et al. 2009), which is well below the equilibrium value of 3. In the post-shock gas, the OPR may remain low since the short timescale does not allow significant conversion from para-H_2 to ortho-H_2 (Leurini, Menten and Walmsley 2016).

When performing non-LTE modeling of CH_3CCH, the collisional rates of CH_3CN (Green 1986) were being substituted for those of CH_3CCH. This is a common approach since CH_3CCH and CH_3CN have similar molecular weights and configuration, while there is not yet published collisional rates for CH_3CCH. The collisional rates of CH_3OH were quoted from Rabli and Flower (2010) (c.f., Section

3.3.4).

To create the distributions of physical properties we adopted the `sf3dmodels` package (Izquierdo et al. 2018) to generate homogeneous grids in Cartesian coordinates, which are then interpolated onto the `LIME` input format of randomly generated set of points. We used the linear resolution of ~0.015-0.03 pc (depending on the source radius $R_{\rm clump}$, Table 3.6) as grid size which corresponds to better than 1/5 beam size for each source. On each grid, we specified a mean gas velocity using a random process to mimic the turbulent velocity field: the direction was uniformly sampled from the 4π solid angle while the magnitude of the velocity was drawn from a Gaussian distribution with σ =3.5 km s^{-1}. We additionally adopted a uniform Doppler broadening of 0.4 km s^{-1} ($\sigma_{\rm turb}$ = 0.4 km s^{-1}) to accommodate the unresolved (micro-)turbulence velocity. Therefore the intrinsic line-width for each grid is $\sigma_{\rm 1D} = \sqrt{\sigma^2_{\rm turb} + \sigma^2_{\rm thermal}}$, in which $\sigma_{\rm thermal}$ is determined by the assumed gas temperature. This yields linewidths which are comparable to the observed values.

We post-processed the output of `LIME` to match the angular and velocity resolutions of our observations, and then compared the annularly and beam averaged synthetic spectra with those from observed spectral cubes. For each observed clump, the best-fit model was taken as the one which has the least χ^2. The parameters of these best-fit chemical models were summarized in Table 3.7, column A.

We found that these initial models systematically underestimated the intensities of the higher K components of CH$_3$OH lines in the inner regions for all sources (Figure 3.16). There are some sources in which the intensities of the higher K components were underestimated also in the spectra at outer radii. This implies that, in general, the density profiles $\rho_{\rm bulk}$ derived from dust continuum modeling (Section 3.3.7) were not high enough to collisionally excite the high K levels of CH$_3$OH (e.g., gas may be concentrated to substructures of higher volume density). This was expected, as was revealed by the comparison to the $\rho_{\rm dense}$ derived by RADEX modeling: gas densities are 50-200 times larger than that of $\rho_{\rm bulk}$ derived by single-dish dust continuum. Therefore, we updated the radial density profile in the models according to the RADEX results $\rho_{\rm dense}$ (Section 3.3.4), following Equation 3.5. We manually adjusted the flexible parameters, which are the density scaling factor $f_{\rm n}$ (Equation 3.5) and that quantify the abundance profile of $X_{\rm mol}(r)$ in Equation 3.4, in a trial-and-error manner to seek for better fits to the observational data. Figure 3.15 demonstrates how the line ratios of CH$_3$OH K components vary with change in the gas density and molecular abundance while keeping a fixed overall molecular column density, as an example using the density model of G08b.

Our best-fit model parameters for all the clumps are summarized in Table 3.7, column B. In these results, $f_{\rm r}$ ranges from 1.5 to 5 in all the sources except G31, indicating RADEX results only moderately overestimated the gas densities. As mentioned in Section 3.3.9, the rather large $f_{\rm r}$ in G31 is due to the very high optical depth of its lower CH$_3$OH K components in the central region. In this case the CH$_3$OH (5-4) lines do not provide meaningful constraints for the RADEX modeling which was based on the assumption of moderate optical depth.

When spatially integrating Equation 3.5 with a spherical symmetric assumption, the resulting overall molecular gas masses ($M_{\rm mod}$) considerably exceed those derived based on modeling dust continuum emission, by integrating $\rho_{\rm bulk}$ (see Section 3.3.7). This implies that the dense gas structures traced by CH$_3$OH do not have spherically symmetric distributions. Instead, they are local gas concentrations that have small volume filling factors. To reconcile the mass difference, we defined $ff_{\rm dens} \equiv M_{\rm enc}/M_{\rm mod}$, where $M_{\rm enc}$ designates the enclosed molecular gas mass within 0.5 pc radius (a scale encompassing the CH$_3$OH emission entirely for all sources) derived from the dust continuum models following $\rho_{\rm bulk}$

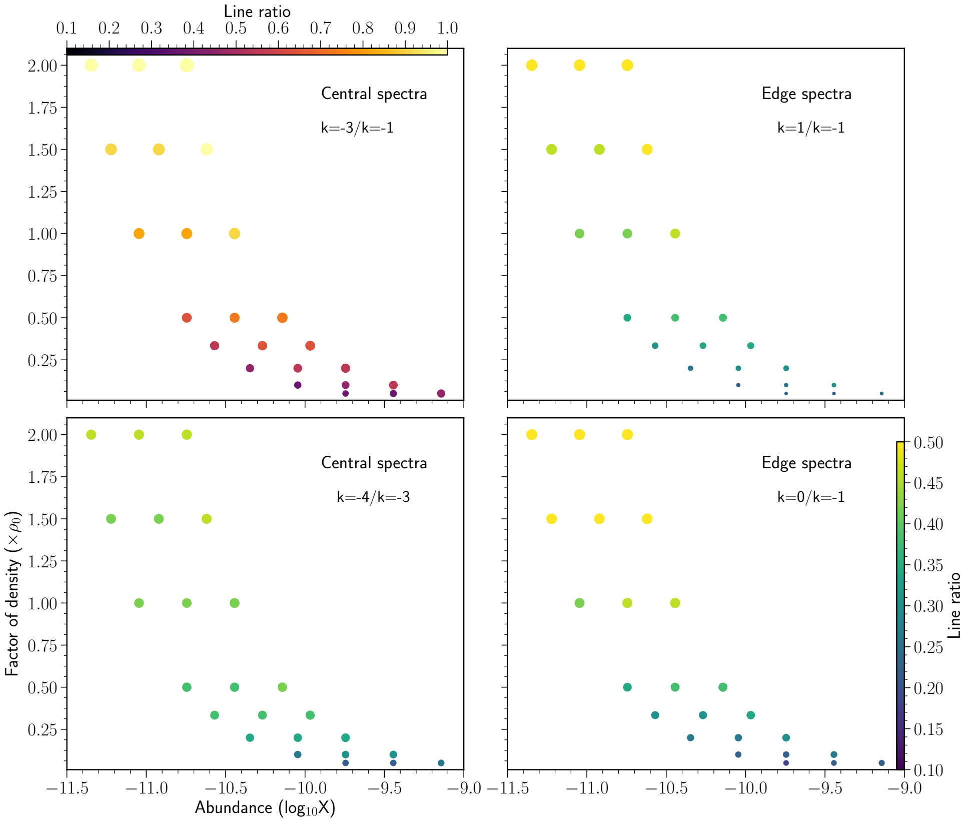

Figure 3.15: Line ratios of CH$_3$OH (5-4) K components from `LIME` models based on density profile of G08b (ρ_0 = f$_r\rho_{0.1pc}$, f$_r$ in Table 3.7 and $\rho_{0.1pc}$ in Table 3.5). Abundance value corresponds to outer abundance (X$_{out}$) as in Table 3.7. The central marker in horizontal y = 1 line corresponds to best-fit model in Table. 3.7 (column B). The comparison of observations with model spectrum is presented in Fig.3.12, top panel.

(Equation 3.1, Section 3.3.7). $ff_{\rm dens}$ can be regarded roughly as an upper limit of volume filling factor of the dense gas traced by CH_3OH. From the radiative transfer modeling point of view, to fit the observed line profiles, in the optically thin limit, varying the dense gas volume does not affect line intensity ratios, while the values of $X_{\rm mol}(r)$ can be adjusted accordingly such that the overall molecular column densities are not altered. We discuss the implications from the inferred volume filling factor of dense gas, and the dense gas mass fraction based on comparing $\rho_{\rm bulk}$ and $\rho_{\rm dense}$ in Section 3.4.5.

3.3.9 A comparison of the samples: density and temperature structure

We make a comparison of the fitted and refined $T(r)$ profiles (Equation 3.2) towards all sources (left panel of Figure 3.17). We can see that at 0.1 pc the resolved gas temperatures range from 30-80 K, and at 1 pc at around 20-30 K. It is also readily seen that temperature at a certain clump radius is not a monotonic function of source luminosity. Hot massive core G31 and source G13 have elevated temperature in the inner regions than their immediate more luminous sources in the rank. We discuss these temperature profiles in more detail in Section 3.4.1.

Comparing the derived radial gas density profile of the dense gas from CH_3OH modeling (here RADEX results are shown), we see that n(H_2) is several ~10^5 to 10^7 $\rm cm^{-3}$ at the ~0.2-0.3 pc projected radii (right panel of Figure 3.17). In the inner ~0.1 pc scale where the SMA identified continuum cores reside, n(H_2) ranges between several ~10^6 to 10^8 $\rm cm^{-3}$. There is exceptionally high n(H_2) at the center of G31. Although we have verify the high level of dense gas of this source by full radiative transfer modeling of CH_3OH lines, we caution that in this density regime CH_3OH (5-4) lines are becoming heavily optically thick. And the critical density is reached (e.g., n>$\rm n_{crit}$) such that the relative differences between the level populations do not serve as ideal densitometers anymore. Nonetheless, we can safely argue that the hot massive core G31 has much higher gas densities in its inner region than other sources in the sample, which is also reflected by the very monolithic nature of its central core from higher angular resolution observations (~2000 au, c.f., Beltrán et al. 2018). For source G10, notablthere is prominent higher gas densities at radii around its central at 0.1-0.4 pc than other sources, which is related to its flattened disk-like geometry. We discuss further on the density profile for individual clump in Section 3.4.2.

We compare the steepness of the radial gas density profiles ($q_{\rm bulk}$ and $q_{\rm dense}$, for $\rho_{\rm bulk}$ and $\rho_{\rm dense}$) as a function of source evolutionary stages as indicated by the clump luminosity to mass ratio L/M (Figure 3.18). There are strong correlations between the density power-law slopes with L/M, for both the dense gas component and the bulk gas structures. The slopes range from -0.6 to -1.7 for the bulk gas, and -0.25 to -1.7 for the dense gas for L/M from lower than 10 to 80 towards all sources. The correlation is stronger between the slope representing the bulk gas steepness and L/M. A similar evolutionary trend was reported by Beuther et al. (2002) based on the analyses of the 1.2 mm dust continuum emission towards a sample of massive clumps, for the bulk gas density structure. Comparably, other works on the density structures of massive clumps typically derived the power-law slopes ranging in -2.25--0.75 and peaking at -1.8--1.6 (Mueller et al. 2002, Beuther et al. 2002, van der Tak et al. 2000). In the early-stage sources (L/M < 20), the slopes we derived are relatively shallow (>-1.0) for both the bulk gas and dense gas radial profiles. We note that the slope derived for the dense gas profile of the early-stage source G18 is valid for a confined region of ~0.1 pc (just above the beam size) and is merely reflecting a pocket of dense gas rather compact and unresolved. Yet, for other early-stage sources, G28 and G19, the statistics are rather adequate, which show shallow slopes of ~-0.6. We note that different analysis methods could result in systematic biases in the derived

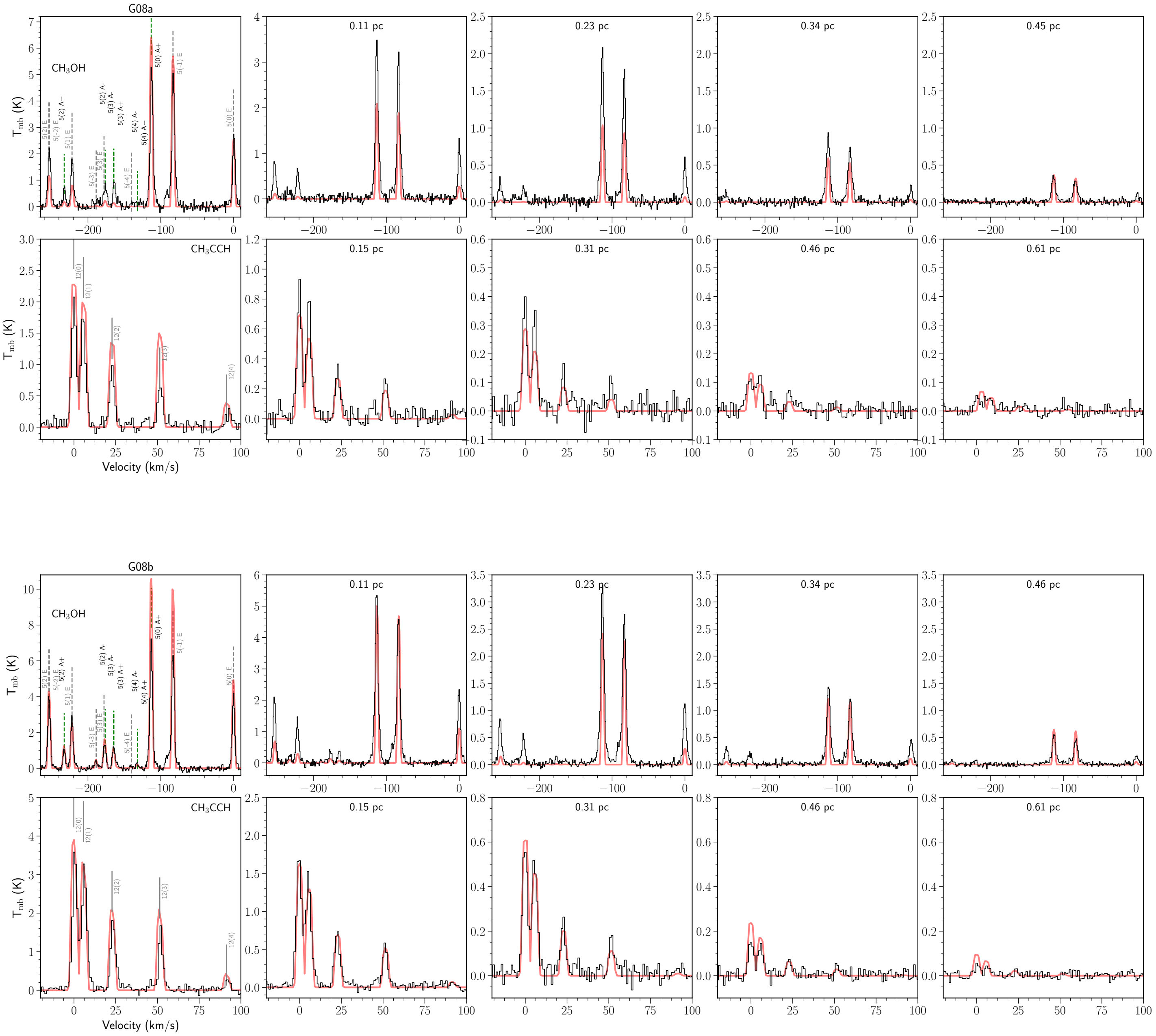

Figure 3.16: `LIME` modeling result based on best-fit density model from `RADMC-3D` continuum modeling. From *left* to *right*: annular beam-averaged spectra from the continuum center to the outer envelope. Considering the typical beam FWHM of our observations: the distance from the center of each annular region to the center of the source is marked on top of each spectra.

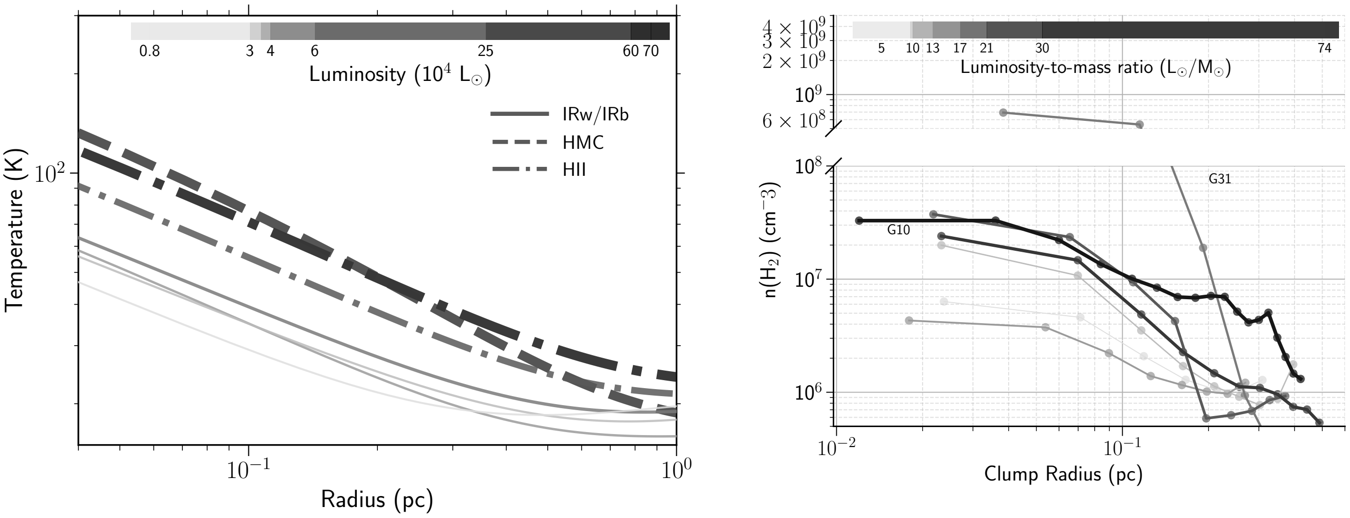

Figure 3.17: *Left panel:* The radial temperature profiles T(r) of all the target sources (Equation 3.2, refined T(r) is used for the relevant source). The thickness and the darkness of the lines increases with increasing luminosity. *Right panel*: The dense gas radial (azimuthally averaged) density profile of all the target sources, from hydrogen volume density maps derived by RADEX modeling of CH_3OH lines. The range of y axis is trimmed of range 1-5×10^8 to increase the contrast. For both panels, the luminosity and clump mass are calculated from `RADMC-3D` best-fit model (Table 3.6), representing the total quantities contributed from all the gas residing in the clumps.

density slope. In addition, in the analyses of dust continuum which were based on the optically thin assumption instead of relying on full radiative transfer models, the density and temperature profiles are degenerated. Moreover, close to the source center, the optically thin assumption for dust emission may also break down. Although qualitative comparison can be made, a careful gauge between different analysis conducted are necessary for a stringent comparison between different works. In Sect. 3.4.5 we make further discussions on the relation of density profiles of massive clumps with statistics on cloud structure, and elaborate on physical implications from comparing $\rho_{\rm bulk}$ and $\rho_{\rm dense}$.

3.3.10 Molecular linewidths and virial parameter

To understand the dynamic states of the target clumps, we examined how the linewidths and virial parameters vary with clump radii. Part of these analyses were based on the thermometer lines, CH_3CN, H_2CS and CH_3CCH. They primarily trace the dense gas close to the centers (0.1-0.4 pc) of the clumps. In addition, we examined the $C^{34}S$ (5-4) and $H^{13}CO^+$ (3-2) lines which can trace spatially more extended clump structures due to their lower excitation conditions. We performed single component Gaussian fits to the $C^{34}S$ (5-4) and $H^{13}CO^+$ (3-2) line cubes in a pixel-by-pixel manner to obtain the linewidth maps. For the analysis, we trimmed the pixels that have fitting errors of linewidth larger than 2 times the velocity channel widths ($\Delta FWHM$<2 km/s).

The virial parameter $\alpha_{\rm vir}$ characterizes an important aspect of the physical states of the molecular clumps. The ordinary definition of $\alpha_{\rm vir}$ (i.e., ignoring magnetic field; c.f., Bertoldi and McKee 1992)

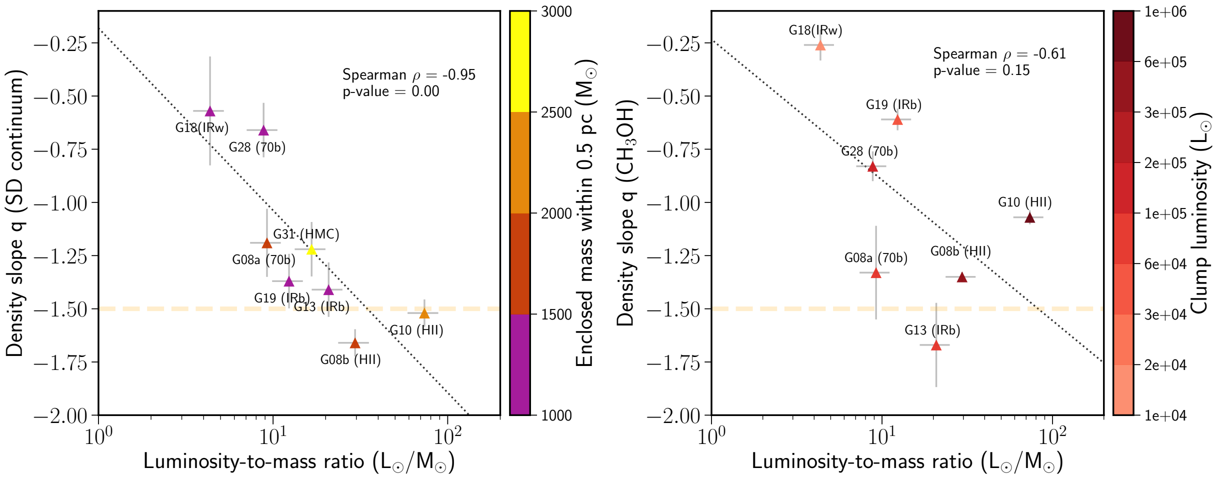

Figure 3.18: *Left panel:* Density power-law slope derived from continuum based on `RADMC-3D` modeling detailed in Section 3.3.7. The luminosity, clump mass and enclosed mass within 0.5 pc are calculated from `RADMC-3D` best-fit model, as listed in Table 3.6. *Right panel:* Density power-law slope derived from n(H_2) maps from CH_3OH RADEX modeling detailed in Sec. 3.3.4.

is

$$\alpha_{\rm vir} = a_1 \frac{2T}{|W|}, \tag{3.9}$$

where $T = \frac{3}{2} M_{\rm enc} \sigma_{\rm rms}^2$ is the kinetic energy, $W = -\frac{3}{5} a_1 \frac{G M_{\rm enc}^2}{R}$ is the gravitational potential energy, $M_{\rm enc}$ is the enclosed mass, and a_1 is a geometric factor which accounts for the inhomogeneity of the density distribution. For a spherical clump that has a $\propto r^{-q}$ radial gas density profile, $a_1 = \frac{1+q/3}{1+2q/5}$. With this definition, a source in energy equipartition (T∼$|W|$) has a critical virial parameter of $\alpha_{\rm cr} = 2a_1$. In a virialized source (2T∼$|W|$), it stands that $\alpha = a_1$ with $\alpha_{\rm vir}/\alpha_{\rm cr} = 0.5$. In the following we refer to the states of $\alpha_{\rm vir}/\alpha_{\rm cr} < 0.5$, ∼0.5-1 and >1 as sub-virial, virial and super-virial state, respectively.

When deriving $\alpha_{\rm vir}$, it is critical that the tracers observed for the measurement of $M_{\rm enc}$ and $\sigma_{\rm rms}$ are predominantly emanated from the same gas entity (Traficante et al. 2018). The mass tracer we adopted, which is the dust continuum emission, traces a broad range of gas volume density distributed in a wide range of radius. Our selected tracers to indicate linewidths, as the way the temperature profile is measured, show emission of progressively larger radii, which are complemented with two more extended tracers. We can now examine spatial variation of linewidths and $\alpha_{\rm vir}$ based on multiple tracers that cover distinct critical densities. We evaluated how $\alpha_{\rm vir}/\alpha_{\rm cr}$ varies with radius using the best-fit density models from the `RADMC-3D` continuum modeling (Section 3.3.7) to obtain $M_{\rm enc}$, a_1 and the linewidth maps from aforementioned tracers. Note that as compared with the SMA observations, the `RADMC-3D` models constrained by the coarser resolution single-dish continuum data systematically under-predicted the 1.2 mm fluxes in the inner radii. To avoid this bias, we adopt the $M_{\rm enc}$ as $M_{\rm core}^{\rm Abel}$ (Sect. 3.3.6) for the inner regions. We recall that $M_{\rm core}^{\rm Abel}$ is calculated by applying the derived $T(r)$ to SMA 1.2 mm continuum. We discuss the obtained radial profiles linewidth and virial parameter in Sect. 3.4.3.

3.3.11 Molecular abundance and abundance ratios

To facilitate the analysis on clump evolutionary stages, We derived the LOS integrated abundance maps ($N_{\rm mol}/N(\rm H_2)$) for some relevant molecular species for all sources. The bulk gas density profiles ($\rho_{\rm bulk}$(r), Sect. 3.3.5, and Section 3.3.7) were adopted and smoothed to the angular resolution of the specific line transition when deriving $N_{\rm mol}/N(\rm H_2)$. The calculation for $N_{\rm mol}$ of CH_3CCH, CH_3CN, H_2CS and CH_3OH are introduced in Sect. 3.3.3 and Section 3.3.4. The calculations of $N_{\rm mol}$ maps of CS/$C^{34}S$, SO, SO_2 and CCH lines were based on LTE assumption are detailed in Appendix A.8. We then derived the azimuthally averaged abundance profiles for each molecule. Naturally, the azimuthal averaging suppresses the contrast in the spatial variations of the abundance for the molecules that are enriched in the clump center or other localised regions (which reduces $N(\rm H_2$ to localised values than integration along the LOS extension). Nevertheless, this does not qualitatively change the overall radial trends as long as the abundance is increasing or decreasing with radius monotonically, with a steeper profile than that of the column density, while the latter is rather shallow, following $\Sigma \propto \rho r \propto \rho^{1+q} < \rho^{-0.7}$. Figures 3.19-3.20 show the relations between the source luminosity and the radial abundance variations of the carbon-chain and sulfur-bearing molecules, respectively.

From Figure 3.19 we can see that the abundances of CH_3OH, CH_3CCH and CH_3CN show similar behaviors. They appear largest in the hot massive cores G31; in the rest of the sources, the abundances of CH_3OH and CH_3CCH are in the range of several 10^{-9}-10^{-8}, while the abundances of CH_3CN are in the range of 10^{-10}-10^{-9}. These abundances are slightly positively correlated with the source luminosity. The abundances of CH_3CN and CH_3OH appear more tightly correlated with the source temperatures in the inner ~0.1 pc regions (see the insets in Figure 3.19). These trends are consistent with theoretical predictions that the de-sorption of these molecules from grain surface is more efficient with higher temperature. We note that these results cannot be obtained if the gas temperature distributions were derived based merely on the assumptions of bolometric luminosity instead of derived based on multi-transition observations of molecular lines, since the gas temperatures at certain radii do not increase monotonically with clump luminosity. This demonstrates the importance of measuring detailed temperature profiles when studying chemical evolution.

We observed a weak correlation of abundance of CH_3CCH and bulk gas temperature, which is reminiscent of the small variation of the CH_3CCH abundance towards massive clumps of various evolutionary stages reported by Giannetti et al. (2017) (see also Öberg et al. 2014). Other higher angular resolution observations of this species indicated a mixed behaviour of its spatial distribution, as to whether the emission coincides with the localised hot sources or appears offset to the continuum and more extended (Bøgelund et al. 2019, Öberg et al. 2014, Fayolle et al. 2015). Comparing rotational temperature maps of CH_3CCH (12-11), the temperatures of G13 and G31 in the core region is 20-30 K higher than those of G19, G08a and G08b. In addition, the higher J transitions CH_3CCH (14-13), (15-14) trace systematically higher temperatures in the core region in all sources. These evidence point to that the emission of CH_3CCH does have contribution from gas components which are residing inside or in the vicinity of hot cores. Except for the earliest stage source G18, the abundances of CCH appear enhanced at outer radii. The abundance of CCH measured for the inner ~0.1-0.2 pc regions is anti-correlated with the bolometric luminosity of the clump. These results are consistent with previous observations of shell-like CCH emission towards massive star-forming regions (Beuther et al. 2008, Jiang et al. 2015).

The abundance ratios of CCH, CH_3CCH and CH_3CN with CH_3OH in the clump center (0.1-0.15 pc) is shown in Figure 3.21. Normalisation by CH_3OH facilitates exploring chemical evolution or

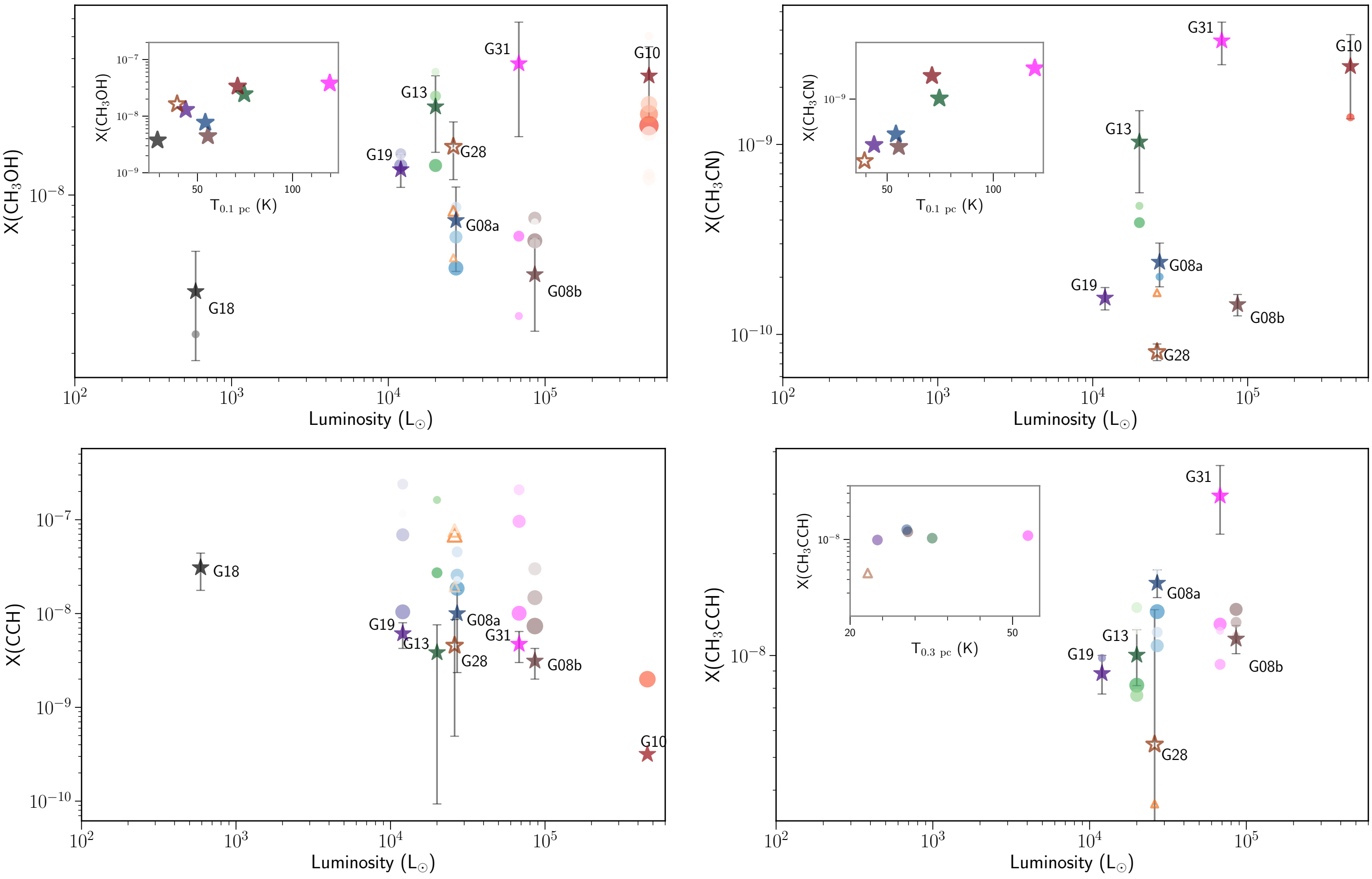

Figure 3.19: Abundance profiles of molecules CH_3OH, CH_3CN, CCH and CH_3CCH (whenever available) towards target sources. Markers are color-coded of relative distance to the continuum peak. Star represents the center position, other markers represent outer annulus: the larger and darker the marker, the closer it is to the continuum peak. X(CCH) for source G10 is taken from Jiang et al. (2015).The inset plots for CH_3CN shows the central abundance vs. gas temperature at 0.1 pc; for CH_3CCH shows the envelope abundance vs. gas temperature at 0.3 pc.

initial conditions by eliminating the effect of different desorption levels among sources. There are substantial variations of [CCH]/[CH_3OH] and [CH_3CN/CH_3OH] across clump L/M, while variations of [CH_3CCH/CH_3OH] are moderate.

The abundances of sulfur-bearing species in the central regions of the clumps also show correlation with temperatures (Figure 3.20). Comparing the relative abundance of $C^{34}S$ and H_2CS with respect to SO as a function of L/M (Figure 3.21, bottom panel), it seems there is a mixed behaviour: except source G13, the other sources show an increasing trend. On the other hand, for X(SO_2)/X(SO) there is a consistently increasing trend with source L/M. We discuss on the abundance variations further in Sect. 3.4.4 in a broader context, with comparisons to chemical modeling results.

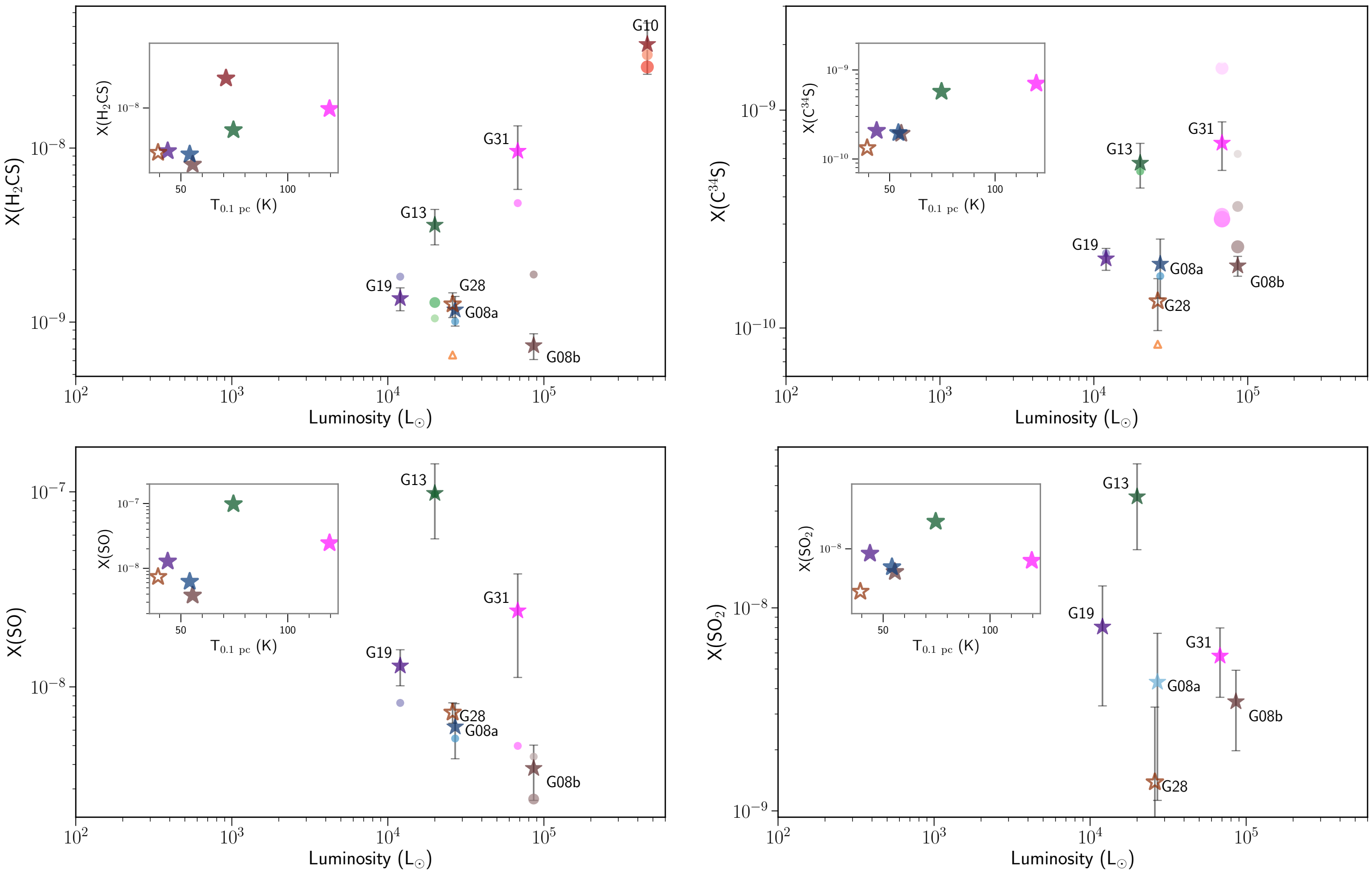

Figure 3.20: Same as Fig. 3.19, for H$_2$CS, C^{34}S and SO.

3.4 Discussion

3.4.1 Temperature structure and heating processes of massive star-forming clumps

The temperature measurement from multiple $T_{\rm rot}$ maps and the fitted and refined temperature profile $T(r)$ (Equation 3.2) are shown in Figure 3.22. The ∂ logT/∂log$R$ profiles are also summarized in the bottom right panel. Except for sources G13 and G31, the ∂ logT/∂log$R$ profiles asymptotes from -0.5 to zero from inner to outer radii. The levelling-off of the temperature at the outer radius of the clump is expected since all these massive star-forming clumps are immersed in intense interstellar radiation fields. At gas densities >$10^{4.5}$-10^5 cm^{-3}, thermal coupling between gas and dust can be quickly achieved due to collisions (Glover and Clark 2012; Goldsmith 2001). However, the $10^{4.5}$ cm^{-3} density threshold is not met in the outer layers of the sources which have lower masses. As we will explain below, the thermal decoupling between gas and dust is seen in some of these sources. The outer envelope dust temperature for all these sources flattens around 18-25 K. These values are consistent with an elevated infrared radiation field associated with these regions. Based on these temperatures, the scaling factors of the local ISRF (Mathis, Mezger and Panagia 1983) to characterise the radiation field surrounding these clumps are roughly $\gtrsim 10^{2.5}$-10^4 (estimated in the optically thick

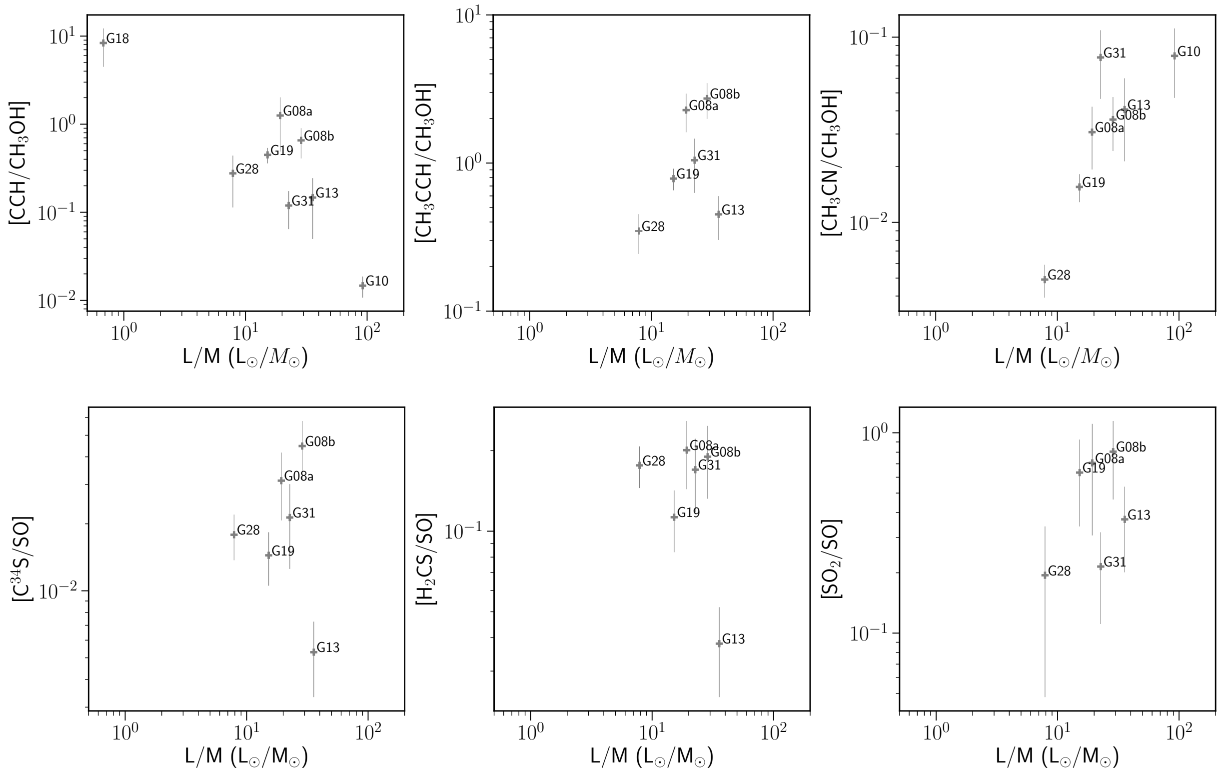

Figure 3.21: *Top:* Abundance ratios of carbon-chain molecules; *Bottom:*Abundance ratios of sulfur-bearing molecules at source center (beam averaged), shown against source L/M ratios.

limit, Krumholz 2014), which are typical values found in the vicinity of Galactic massive star-forming complexes (Binder and Povich 2018).

The $T(r)$ and $\partial\ \log T/\partial \log R$ in the inner regions may be approximated by the analytic temperature profile of thermally balanced dust grains distributed around a central heating point source (e.g. Adams 1991). Assuming optically thin and a submillimeter dust opacity spectral index (β), the model of Adams (1991) predicted that the radial temperature profile for dust grains in thermal balance around a central heating point source is proportional to $r^{-2/(4+\beta)}$. If β has no spatial dependence, then $\partial\ \log T/\partial \log R$ should be a constant of radius. In the diffuse interstellar medium β is around 1.8 (for a review see Hildebrand 1983), which yields the temperature slope of -~0.35. In high-density regions, β may become lower due to dust growth, resulting steeper temperature profile. The lower than 1.8 values of β have been reported by some previous observations towards Class 0-II young stellar objects, protostellar cores, and prestellar cores (e.g. Beckwith and Sargent 1991, Jørgensen et al. 2007, Bracco et al. 2017, and references therein). It should be caveated that the previous (sub)millimeter observations of dust growth might have systematically underestimated β values owing to underestimating optical depths (e.g., Li et al. 2017), neglecting the effect of dust scattering opacity (e.g., Liu 2019), and missing to consider the effects of temperature mixing when performing SED fittings (e.g. Juvela et al. 2018). From a modern point of views, by far, there might not yet be a solid evidence for the presence of β <1 on the spatial scales of molecular clumps.

In Figure 3.22, we also compare the observed temperature profiles with the centrally heating models evaluated for β =1 (i.e., $T = 2.70(\frac{L}{L_\odot})^{0.2}\ (\frac{R}{1\,\mathrm{pc}})^{-0.4}$; this is based on assumption of dust sublimation temperature of 1 100 K in the derivation Adams 1991, for more calculation details see their appendix), and with the simple expectation based on Stefan-Boltzmann law (T = $0.86(\frac{L}{L_\odot})^{0.25}\ (\frac{R}{1\,\mathrm{pc}})^{-0.5}$). We found that these profiles qualitatively agree with the measurements of $T(r)$ except for G13 and G31.

From Figure 3.22, it is seen that the temperature profiles of G13 and G31 are deviated from the form of a single power-law. Specifically, they show abrupt changes as well as elevated temperatures in the radius ranges of 0.1-0.3 pc and 0.1-0.5 pc, respectively. After we adjusted $T(r)$ (Section 3.3.7), G13 shows a less prominent temperature enhancement in the center while G31 still stands out. Beltrán et al. (2018) also noted the steep temperature profile of G31 within the central 0.1 pc. Their measurement consistently falls onto the functional form we fitted (i.e. the thick purple line in Figure 3.22) which was based on our independent measurements of T_{rot} on the larger spatial scales.

The rapid radial temperature decreases observed in G31 and G13 may be explained by their density profiles of the embedded dense gas structures (i.e., $\rho_{\mathrm{dense}}(r)$). In Figure 3.11, it can be seen that these two sources have most steeply decreasing $\rho_{\mathrm{dense}}(r)$. In addition, their central ~0.1 pc regions show high-density plateaus. The optically thin assumption of Adams (1991) may break down in the central region of the G31 and G13. Such a higher concentration of dense gas steepens the temperature distribution in the inner envelope according to $\propto \mathrm{r}^{-\frac{1-q}{4-\beta}}$, where q is the power-law index of radial density profile. This is closed to the diffusion approximation (e.g. Adams and Shu 1985, Rolffs et al. 2011), which effectively means that a higher optical depth gas would mimic the lower value of β in determining the temperature structure. The presence of flattened (protostellar) disks could also induce a steeper gradient (~-0.75) of temperature variations due to the gas heating by infall and accretion shocks (e.g. Lynden-Bell and Pringle 1974, Walch et al. 2009). Interestingly, hydrodynamic calculations of protostellar collapse demonstrate that a centrally flattened density profile results in a transitory phase of energetic accretion (Foster and Chevalier 1993, see also Henriksen, Andre and Bontemps 1997), which may be tentatively related to the elevated temperatures of G13 and G31.

Observations towards dense massive cores and envelopes of YSOs and discs generally find temperature slopes in the range of ~[-0.35,-0.5] (e.g. Palau et al. 2014, Beuther et al. 2007, Gieser et al. 2021). However, the exceptionally steep temperature profile of slope $\lesssim$-0.9 is seen towards 1 000-2 000 au of massive YSO object W3IRS4 (Mottram et al. 2020), similar to the result of G31 based on observations of similar spatial scale (Beltrán et al. 2018).

Strong radiative feedback has been invoked as a possible mechanism resisting over-fragmentation, which is prone to the formation of massive stars and dense environment (e.g. Krumholz, Klein and McKee 2012). When observed with ~2000 au resolution, source G31 consists of two cores with one of them dominating the emission (~60 times flux difference at 1 mm continuum, Beltrán et al. 2018). The elevated temperature in the inner 0.1 pc might have suppressed the fragmentation of the envelope structure of the main core, leaving with only one satellite core surrounding it. The highly concentrated dense gas structure of G13 traced by methanol lines (Figure 3.8) that does not extend further beyond its continuum emission (except to the west direction) may also indicate a featureless fragmentation; high resolution ($1''$) MIR imaging by Varricatt et al. (2018) reveal a binary system, although the mass contrast between the two YSO objects embedded is not as drastic as those of G31.

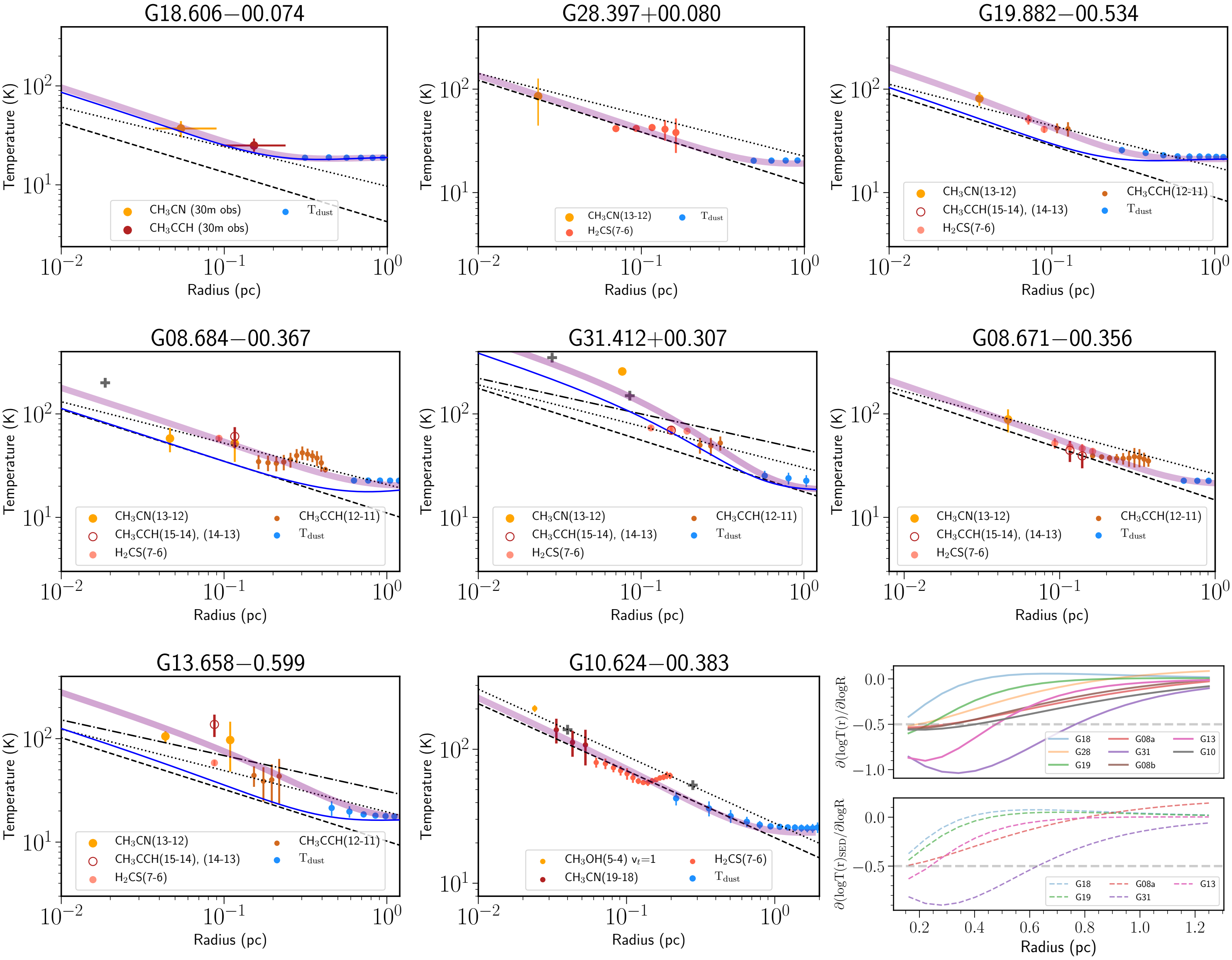

Figure 3.22: Derived azimuthal averaged temperature profile of the target sources. Error bars are showing the standard deviations for each annular average. Dashed and dotted show a radial temperature profile that follows $\propto L^{0.25} r^{-0.5}$ ($\beta = 0$), $L^{0.2} r^{-0.4}$ ($\beta = 1$) respectively (more details see texts). For G13 and G31, an additional radial temperature profile of $\propto L^{0.17} r^{-0.34}$ ($\beta = 1.8$) is shown (dashed dotted line). Whenever available, temperature measurement from higher angular resolution observations from previous work is included in the fits and in the plots as gray crosses. Thick purple line indicates the fitted temperature profile T(r) described in Sec. 3.4.1. Blue thin line indicates the adjusted temperature profile by varying $r_{\rm in}$ in T(r) expression to fit with dust SED profile (refined T(r), Section 3.3.7). Plot in the bottom right corner shows the first derivative in log-log scale of T vs. radius for all the sources, calculated from the fitted profile, thick purple and blue lines, for the upper and lower panel, respectively.

3.4.2 Density structure evolution: comparison with theoretical predictions

Figure 3.8 shows the n(H_2) maps which were derived based on the RADEX modeling for the CH_3OH lines (Section 3.3.4). In general, n(H_2) decreases radially with respect to the continuum center, although some sources appear notably asymmetric and present localised over-densities at large radii. We use single power-law forms (Equation 3.3) with parameters listed in Table 3.5, to describe the radial change of n(H_2) maps. Comparing the observed profile to the fitted single power-law form (Figure 3.11), it can be seen that there are higher density plateaus at the centers of G13 and G31, such that these two sources are better described by piece-wise power-law including a central density profile of slope ~0. Source G10 harbors even more dense gas at >0.1 pc radii as compared to its best-fit single power-law model, which is due to the highly flattened dense gas geometry of an edge-on rotational disk as revealed by gas kinematics (Liu 2017). In fact, for G10, the slope of dense gas profile $q_{\rm dense}$ is an average from two distributions: a geometrically flattened, high-density pseudo-disk with a slope shallower than -0.5, and an envelope of which the gas density decreases sharply (Figure 3.8) Clumps G28, G19 and G08a may also harbor high-density plateaus at the centers although they are not as significantly resolved as those in G10, G13 and G31.

We emphasize that the two set of power-law density slopes derived reflect clump gas in different density regimes: from single-dish continuum the slope represents density distribution of *averaged* (mass-weighted) bulk gas ($\bar{\rho}{\sim}10^{4.5}\ cm^{3}$) where the spherical symmetry might be a rather good approximation of source geometry, while the slope deduced from methanol emission is reflecting the truncated central dense gas portion ($\rho{\gtrsim}10^{6.5}\ cm^{-3}$) with an extension of 0.1-0.5 pc. This dense gas structure is likely highly fragmented and of reduced dimension due to the dominant role of self-gravity.

Figure 3.18 reveals the evolutionary trend of the radial density profiles of bulk gas and dense gas structures of the target massive clumps. Our results indicate that in the initial stage of massive clump evolution, gas may be less concentrated than the singular isothermal sphere (SIS, Shu 1977), and even the logatropic model (McLaughlin and Pudritz 1997). Observations towards low-mass cores at early stages generally found a density profile with a central plateau (e.g. Ward-Thompson, Motte and Andre 1999, Bacmann et al. 2002). Such density configuration is of reduced pressure gradient, in quasi-static models the additional support of magnetic field is required. The magnetic field and subsequent ambipolar diffusion may explain the existence and evolution of the shallower radial density profile of the gas, which is at an initial equilibrium stage (e.g. Mouschovias and Morton 1991). Alternatively, in an isothermal state, the incoherently converging compression wave from shocks propagating from outside-in can disrupt the centrally peaked density profile(Whitworth et al. 1996). Finally, hydrostatic model of a self-gravitating gas externally heated (e.g. Falgarone and Puget 1985) can also result in a similar density configuration. We also can not rule out the possibility that the shallower profiles actually reflect the underlying fragmentation is widely distributed within the clump and that the fragments do not show significant mass segregation (Sanhueza et al. 2019), whose imprints introduce a rather uniform density profile for the clumps.

Following definitions in Section 3.3.5, we denote the power-law slopes for the radial gas density of bulk gas and dense gas as $q_{\rm bulk}$ and $q_{\rm dense}$. In G18 and G28, both $q_{\rm bulk}$ and $q_{\rm dense}$ are shallower than -1 (Figure 3.17). This may be due to a combination of the heated gas profiles and a higher level of turbulence, which effectively slow down gravitational collapse at early stage (Figure 3.23; Section 3.4.3). Although these two sources have L/M $\lesssim$10 which are classified to be younger than or just reaching ZAMS phase (Molinari et al. 2008, Giannetti et al. 2017), it is likely the enhanced energy release of accretion associated with the massive star formation already introduces an observable temperature gradient (Figure 3.22).

The more evolved source G08a has a shallower overall distribution of gas (q_{bulk}~-1.2) than its dense gas component (q_{dense}~-1.3). Interestingly, source G19 displays an opposite relation between the two slopes (q_{bulk}~-1.4, q_{dense}~-0.6; Figure 3.18). Comparing the virial state of these two sources (Figure 3.23), it seems G19 is close to a global state of energy balance while G08a has excessive kinetic energy in the central 0.2 pc, possibly caused by energy transfer and induced motions from gravitational collapse (more in Section 3.4.3). If a steeper density profile corresponds to a more dominant role of gravitational collapse, then the kinematic differences inferred from line-widths are compatible with the relation between density slopes in local (dense gas regime) and global (bulk gas regime) scales for these two sources. We discuss this in more detail in Section 3.4.5.

The overall trend seen in right panel of Figure 3.17 can be qualitatively explained by the growing role of self-gravity in the evolution of gas dynamics in massive clumps. This is illustrated in hydrodynamic simulations of star-forming clouds with continuously driven turbulence (Lee, Chang and Murray 2015) that shows self-gravity plays the dominant role for all changes that happen with density structures over the scales up to >0.1 pc. Their results reveal that the power-law slopes around density peaks change from -1.3 to -1.55 before and after onset of star-formation till ±1/4 global free-fall timescale (t_{ff}). Separating the scales based on dominant mass contributor of gas or (forming) stars, Murray et al. 2017 demonstrate that close to the (proto)stars gas density profile has a slope of -1.5 (an attractor solution, see also Coughlin 2017) and in the outer envelope slope ranges from -1.6 to -1.8. These values are in quantitative agreement with the evolved sources in our sample. The three sources having bulk gas density slopes shallower than -1 (left panel of Figure 3.18) may reflect an initial condition close to constant-density core when gravitational collapse has not significantly altered the gas density profile, for both the bulk gas and dense gas structures (G18 and G28) or only the dense gas component (G19). The tendency of an initial flat inner density profile remaining flat over one t_{ff} determined by the gas central density is also discussed in Henriksen, Andre and Bontemps (1997), which is attributed to that the cloud center has the fastest growing velocity mode. The timescale is fleetingly short without further support of turbulence.

3.4.3 The kinematic state of clumps: radial profiles of molecular line-width and virial parameter

Based on the calculations in Section 3.3.10, Figure 3.23 shows the radial profiles of the molecular linewidths (ΔV = 2.355 σ_v) for individual species. We fitted a power-law to the radial linewidth profiles traced by thermometer lines (i.e. excluding the data points from $C^{34}S$ and $H^{13}CO^+$). In G08a, G31 and G13, the linewidth traced by these lines decrease radially with power-law indices of -0.40, -0.31, -0.56, respectively. Except for the sources G18 and G19, the linewidths on the extended regions traced by $C^{34}S$, $H^{13}CO^+$ are systematically larger than that traced by the thermometer lines.

In general, the linewidths variations do not seem to follow a monolithic radial change, which is in contrast to the $\sigma_{\mathrm{v}}^{1/2}$ law observed universally in giant molecular clouds and low-mass cores (i.e., Larson's first law; Larson 1981).

In high-mass star-forming regions, the observed line-widths are systematically larger, and σ_{v} may have a shallower power-law relation with scales (e.g. Plume et al. 1997, Caselli and Myers 1995). In addition, the virial equilibrium naturally infers that σ_{v} has a dependence on gas surface density, such that $\sigma_{\mathrm{v}} \propto (\Sigma R)^{0.5}$ (Heyer et al. 2009).

Moreover, recent 1D simulations incorporating gravitation-driven turbulence (i.e., adiabatic heating;

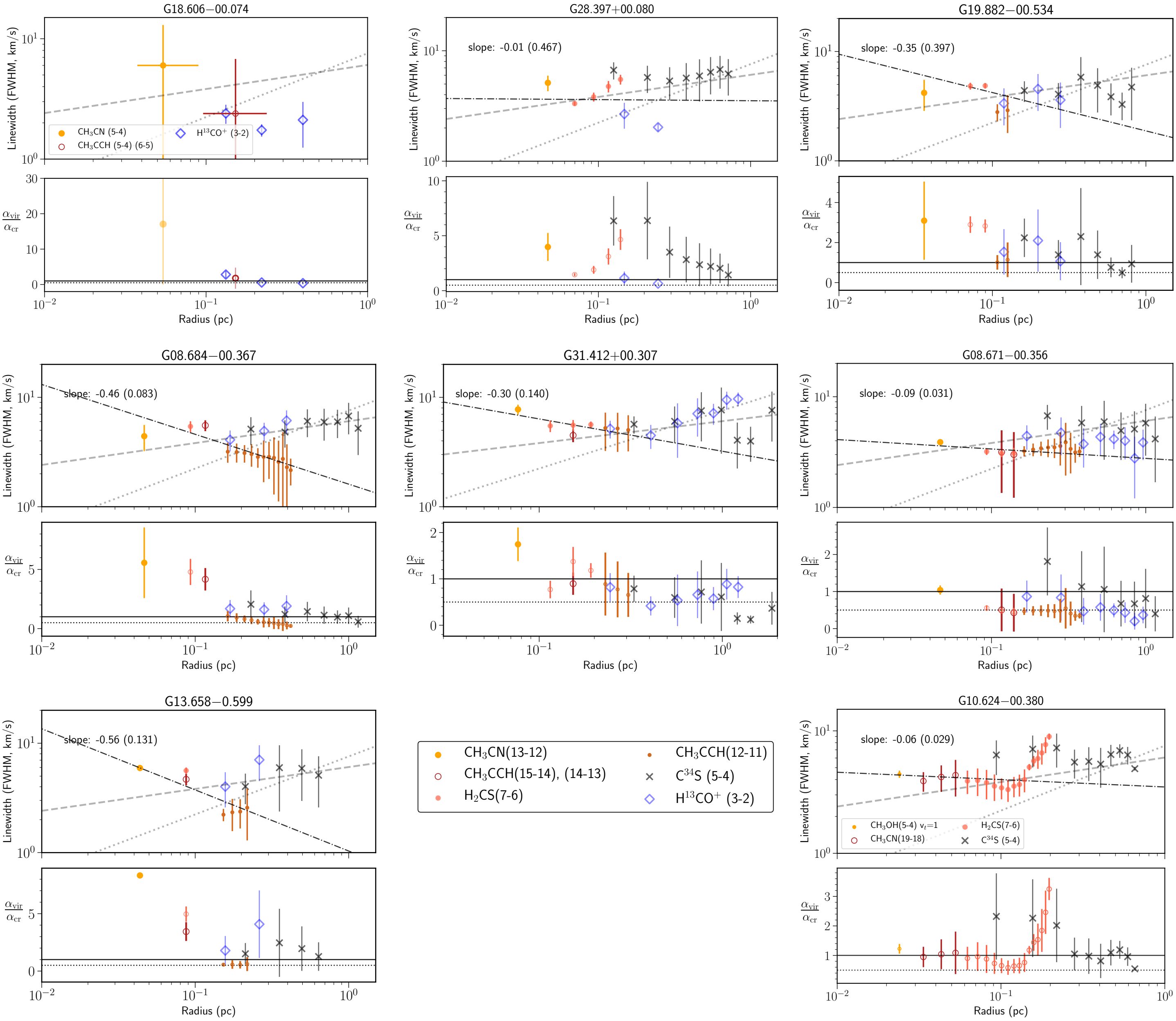

Figure 3.23: Derived averaged radial linewidth and virial parameter profiles. Dashed dotted line in each upper panel indicates the power-law fit to the linewidths from thermometer lines. In each upper panel, gray dotted line indicates relation found by Caselli and Myers (1995) of Orion low-mass cores scaled up by a factor 5, of $\Delta v/1\,\mathrm{km\,s^{-1}} = 7.5\ (\mathrm{r}/1\ \mathrm{pc})^{0.53}$; Gray dashed line shows a relation of $\Delta v/1\,\mathrm{km\,s^{-1}} = 6.0\ (\mathrm{r}/1\ \mathrm{pc})^{0.2}$. These two reference lines are identical in all plots. In each lower panel, the ratio between α_{vir} to critical virial parameter α_{cr} is shown; horizontal solid line and dotted line indicate ratio 1 (equipartition) and 0.5 (virial equilibrium), respectively. All plots except for G10 share the same legend shown in the middle panel of the last row, in which the color coding for the thermometer lines is the same as in Fig. 3.22.

c.f., Robertson and Goldreich 2012) found distinct relations between $\sigma_{\rm v}$ and spatial scales for star-forming clumps, due to the change of dominant turbulent driving mechanism from inner to outer regions (Murray and Chang, 2015). It has been found that $v_T \propto r^{-0.5}$ holds within the sphere enclosed by the stellar influence radius, which is defined as the radius where the enclosed gas mass is comparable (e.g., 1-3 times) to stellar mass (Murray and Chang 2015, Murray et al. 2017; see also Coughlin 2017, Xu and Lazarian 2020 for the analytic derivations).

As a rough estimate of the stellar influence radius, assuming the L_{bol} of each source is contributed solely from the luminosity of a single ZAMS star, adopting the stellar evolution model of Choi et al. (2016), the stellar mass $M_\star$ are estimated to be $12M_\odot$ for G19, 15-$16M_\odot$ for G08a, G13 and G28, $30M_\odot$ for G08b. Grave and Kumar (2009) fit radiative transfer accretion models of YSO to source G19 and G13 by building SED from near-infrared to submm, and their derived stellar masses are consistent with our rough estimates. For G10, previous observations suggest a stellar mass of $\sim 200M_\odot$ (Baobab Liu et al. 2010). We note that inferring stellar mass from luminosity assuming the sole contribution from a single star leads to a lower limit, as these clumps are forming a cluster of stars following the IMF. With the same total bolometric luminosity, this corresponds to a higher total stellar mass. Comparing with the central core masses we derived from 1.2mm continuum (Table 3.1), it seems we marginally resolved the influence radius (about half beam FWHM) for source G13, G08a and G10, but a bit further in the case of G08b. This may partially explain why in the inner region of G08b the observed linewidths do not decrease rapidly with radius. In G10, the observed linewidths have shallower variations with radius. This may be due to the presence of the ~0.2 pc scale edge-on rotational disc (Liu 2017), towards which gas settles into coherent rather than random motions.

For the early-stage clumps G18, G19, and G28, the bolometric luminosity is likely dominated by accretion energy. This leads to an overestimate of the stellar mass, such that in reality there is a more drastic difference between the embedded stellar mass and the gas mass at the scale probed, than our rough estimates. Therefore, it is likely that we do not see the decreasing trend of linewidths with radius in their inner regions due to the too coarse resolution to resolve the stellar influence radius. In addition, assuming turbulent velocity scales as the local infall velocity, Coughlin (2017) demonstrates that there is temporal steepening of radial profile of rms velocities, with gravitational field starting to dominate the dynamics of inflowing gas, which changes from $v_{\rm T} \propto r^{-0.2}$ to $v_{\rm T} \propto r^{-0.5}$. Hence, it may also be that early-stage clumps have a shallower inner slope that tend to flatten out, further smeared in coarser resolution measurements.

Exterior to the stellar influence radius, simulations found that $v_{\rm T} \propto r^{0.2}$ (see also Lee, Chang and Murray 2015). Compared to classical subsonic turbulence following Kolmogorov law ($v_{\rm T} \propto r^{1/3}$) or supersonic turbulence ($v_{\rm T} \propto r^{1/2}$), the shallower scaling relation between linewidth and spatial scale of the region beyond stellar influence radius, could be due to additional energy converted from (part of) gravitational collapse (Ballesteros-Paredes et al. 2011, Xu and Lazarian 2020) and/or kinetic energy of extended inflow gas transported by radial motions (Padoan et al. 2020). Klessen and Hennebelle (2010) demonstrate that the conversion efficiency to internal turbulence depends on the density contrast between accreting entity and inflow gas. These may explain why in the outer regions of G08a, G08b, G13 and G10, the observed linewidths rise with radius, having a power-law slope of $\gtrsim$0.2-0.3.

In light of the radial profiles of $\alpha_{\rm vir}$, it appears that our target clumps can be classified into three types, based on their $\alpha_{\rm vir}/\alpha_{\rm cr}$ ratios: sources G08b, G31 and G10 are in an overall virial to sub-virial state; G18, G08a and G13 show super-virial states in the centre and sub-virial states in outer envelope; G28 and G19 have uniform $\alpha_{\rm vir}$ fluctuating mostly above $\alpha_{\rm cr}$. To explain the observed super-virial states in the central regions of some of these clumps, it is required to introduce other line-broadening mechanisms.

The three sources that have large virial parameters in the centers have the lowest central core masses and densities (Table 3.1). If central cores are treated as a decoupled structure from clump envelope, the more massive and denser cores being more sub-virial is consistent with previous observations towards massive star-forming regions (e.g. Kauffmann, Pillai and Goldsmith 2013, Liu et al. 2015, Traficante et al. 2018). However, due to the insufficient angular resolution, the estimate of $\alpha_{\rm vir}$ in the clump center may suffer from larger uncertainties, e.g. there is possibly higher level of clumpiness with complex velocity structures that confuse the linewidth measurement. In addition, the $\alpha_{\rm vir}$ in the centermost is derived from linewidth of CH_3CN. CH_3CN has been shown to trace the interface of convergent flows in high-mass clumps (Csengeri et al. 2011, which is also enhanced in shocks (Bell et al. 2014) and associated with hot accretion flows (Liu et al. 2015).

Camacho et al. (2016) and Ballesteros-Paredes et al. (2018)) have shown that the observed high $\alpha_{\rm vir}$ may not be indicative of pressure confining or gas dispersal. Alternatively, for low column density clumps this picture might be due to highly dynamic externally driven gas accumulation. For high column density clumps it might be a result of neglecting the stellar mass or accreting materials outside the cores in contributing to the gravitational energy. The latter course may qualitatively explain the super-virial status in the center of the three sources G18, G08a and G13, which does not necessarily indicates halt of collapse. On the other hand, the inclusion of infall velocities to the observed linewidth may also cause the source which is undergoing collapse to appear seemingly unbound (e.g. Smith, Longmore and Bonnell 2009). Infall motions of dense cores that have large $\alpha_{\rm vir}$~5-8 are revealed by Cesaroni et al. (2019), inside a massive cluster-forming clump.

Giannetti et al. (2017) suggest that CH_3CCH is a reliable tracer for the kinematics of bulk gas structures in the massive clumps. From the $\alpha_{\rm vir}$ derived based on the CH_3CCH lines, it appears that all clumps are in sub-virial or virial status. But at smaller scales in the central region of the clumps, the gas can appear super-virial. Aside from the three clumps showing large $\alpha_{\rm vir}$ in the center, other clumps show an evolution of globally (for all radii) decreasing $\alpha_{\rm vir}$ with increasing L/M. Ballesteros-Paredes et al. (2018) and Camacho et al. (2020) investigated the evolution of $\alpha_{\rm vir}$ in molecular clouds based on numerical simulation. They showed that the gas structures may be initially assembled due to the large-scale turbulence. Afterwards, the assembled gas structures evolve from over-virial to sub-virial status, and finally approach energy equipartition, or further become super-virial after one $t_{\rm ff}$ due to gas expulsion. Our observations do not show such non-monolithic evolution of $\alpha_{\rm vir}$ with L/M. This is likely because that all target clumps remain in young evolutionary stages, which are prior to or in the stage of active star formation and have the gas mass dominates the mass budget.

3.4.4 Comparison with chemical models: carbon-chain molecules and sulfur-bearing species

The formation pathways of molecules and chemical rates are tightly influenced by gas temperature and volume density. In Section 3.3.11, we based on the molecular column densities of CH_3CCH, H_2CS, CH_3CN, ,CH_3OH, $C^{34}S$, CCH, SO and SO_2 to derive the molecular abundance distributions and abundance ratios between relevant species. We discuss comparisons between these results with predictions from chemical models in this section.

CH_3OH, CH_3CCH, CH_3CN, and CCH

CH_3CCH is designated as a 'cold molecule' (Bisschop et al. 2007), since it presents low excitation temperatures compared to other complex organic molecules (COMS) such as CH_3CN, CH_3OCH_3, etc. The formation pathways of CH_3CCH include cold gas phase reactions and grain-surface chemistry (Calcutt et al. 2019). The reactions in gas phase involve thermal desorption which requires only low temperature. Calcutt et al. (2019) suggested that CH_3CCH is a 'gateway' molecule which traces the interface between hot cores/corinos and colder envelope, and extends further out in the envelope. Inset in Figure 3.19 shows measured CH_3CCH abundance averaged from the outer region ($\gtrsim$0.1 pc) of the clumps with the gas temperature measured at 0.3 pc. These properties represent that of the bulk luke-warm gas. The small variation of CH_3CCH abundance across our sample indicates that it is not a sensitive molecule to trace the $\gtrsim$100 K thermal desorption of hot core regions. Its emission rather traces the more extended gas and is a good kinematic tracer for >0.1 pc gas structures within massive clumps (e.g. Giannetti et al. 2017). There is also not drastic radial change of the abundances of the other two COMs CH_3OH, CH_3CN for individual source (Figure 3.19). This is expected since our angular resolution is not sufficiently high to reveal the >100 K region (confined within 0.1 pc) where prominent abundance enhance of COMs is expected (Garrod et al. 2017).

The abundance profiles of CCH exhibit an increase towards the outer clump envelope for most the sources in the sample (Figure 3.19) and an overall decrease of abundance with clump luminosity. These results reflect that CCH is abundant at an early stage and then transformed to other molecules in the clump center (Beuther et al. 2002). The abundance of CCH in outer regions is maintained by reproduction from dissociated CO by external UV field. Similarly, in early-stage low-mass cores, CCH is also tracing more quiescent gas, e.g. the outer part of a circumbinary envelope (van Dishoeck et al. 1995).

We compare the abundance ratios between CCH, CH_3CN and CH_3CCH with CH_3OH in Figure 3.21. In low-mass star-forming cores, the ratio of [CCH]/[CH_3OH] is usually used to distinguish less evolved warm carbon-chain cores with hot corinos (e.g. Graninger, Wilkins and Oberg 2016). The strong anti-correlation of [CCH]/[CH_3OH] with L/M indicates that in the central region of massive clumps this ratio serves well as an evolutionary indicator. [CH_3CN]/[CH_3OH] has a tight correlation with L/M as well: except the hot massive core G31, the other sources show a clear monotonic increase of [CH_3CN]/[CH_3OH] with increasing L/M. This is consistent with the formation timescale of the two species: CH_3OH forms at early stages (10 K) on grain surfaces, primarily via successive hydrogenation of CO (e.g. Watanabe, Shiraki and Kouchi 2003), while the formation of CH_3CN appears late, through radiative association between HCN and CH_3^+ on grain surface as well as CH_3 with CN in gas phase (Nomura and Millar 2004).

Sulfur-bearing molecules

Time-dependent theoretical chemical models of sulfur-bearing species find that the evaporation of H_2S and subsequent chemical reactions in hot cores lead to an increasing abundance ratio of SO_2/SO (Wakelam, Hersant and Herpin 2011, Esplugues et al. 2014). At late stage of hot core evolution, H_2CS and CS are also drastically enhanced; together with SO_2, they become the the most abundant sulphur-bearing species. In shocked regions, similar trends along evolution are predicted (Wakelam et al. 2005, Esplugues et al. 2014). But observations seem to suggest opposite variations of X(CS)/X(SO) with source evolutionary stages (Li et al. 2015, Gerner et al. 2014, Herpin et al.

2009). Assuming the same ^{34}S/S isotopic ratio for our target clumps, we find similar result which is reflected by the feature in Figure 3.21 (left figure of bottom panel). In this context, therefore, it seems X(SO_2)/X(SO) is a more robust evolutionary indicator. We note that the temporal evolution of the abundance of sulfur-bearing species is highly dependent on the source physical structure (Wakelam et al. 2005, Wakelam, Hersant and Herpin 2011). Tailored chemical modeling for individual sources is required to disentangle such effect and pin down the evolutionary sequence across the sample.

3.4.5 Density structure: relation with cloud structure and implications for different dense gas conversions

In this section, we discuss how the radial density profiles of massive clumps (see Section 3.4.2) may be linked to statistics of parental cloud structures on large scales ($\gtrsim$10 pc). We also elaborate on the physical implications of the radial density profiles comparisons between bulk gas and dense gas structures, ρ_{bulk} and ρ_{dense}.

Gravoturbulence simulations for molecular clouds (e.g., Kritsuk, Norman and Wagner 2011, Lee, Chang and Murray 2015) showed that the cloud volume density probability distribution functions (ρ-PDF, p_{s}) have log-normal and power-law forms in the low- and high-density regimes, respectively. The log-normal form is attributed to the primordial and maintained supersonic turbulence, while the power-law tail is usually regarded as a sign of gravitational collapse. With these understandings, the PDF statistics are general methods to quantify and compare the physical states of molecular clouds. Gravitational contraction converts a fraction of low-density gas to high-density structures over a timescale comparable to the free-fall timescale (t_{ff}) of the mean density. With this process, the slope of the power-law tail s changes from s≈ -3 to s≈ -1.5--1 (e.g. Girichidis et al. 2014, Guszejnov, Hopkins and Grudić 2018), in a mean free-fall time. When the power-law tail of the ρ-PDF is dominated by a single gravitational bound massive clump which has a $\rho\,(r) \propto r^{q}$ density profile, there is the relation $s = 3/q$ (Federrath and Klessen 2013b). In other words, q is expected to evolve from ≈ -1 to -3--2 over a mean t_{ff}. Observational works usually constrain the column density probability distribution function (N-PDF, p_{η}) rather than ρ-PDF. In this case, the power-law slope of the N-PDF (s_N) can be related to the radial density profile of the molecular clump by $\frac{2}{1+q}$. Column density mapping towards Galactic massive star forming complexes yield power-law slopes for N-PDF ranging between ~-4 to -2 (Lin et al. 2017). The evolutionary trend of steepening density profiles (the bulk gas density profile) of the massive clumps resolved in this work is in general consistent with the prediction from cloud-scale statistics.

The cloud-scale (10 pc) dense gas fraction can be relatively well described by statistics of ρ/N-PDFs, which do not factor in features of spatial distribution. Within the ~1 pc scale clump structure, the spatial configuration of dense gas can be critical in determining the properties of final star clusters. We discussed the gas radial density profiles probed by dust emission and dense gas tracer (CH_3OH) separately in Section 3.4.2. Here we note again that dust emission is tracing *averaged* (mass-weighted) bulk gas structures ($\bar{\rho}$~$10^{4.5}$ cm^{3}) while CH_3OH emission probes dense gas regimes ($\rho \gtrsim 10^{6.5}$ cm^{-3}, up to several 10^{8} cm^{-3}) within the massive clumps. By relying on two density probes for different gas density regimes, we go beyond the self-similar solution of gravitational collapse by characterising the density configuration of massive clumps with two "layers" ρ_{bulk} and ρ_{dense}, each of which is described by a power-law form. The ρ_{dense} traced by CH_3OH from RADEX modeling (Section 3.3.4) is verified by full radiative transfer non-LTE models in Section 3.3.8, by introducing a volume filling factor ff_{dens} (Table 3.7) to spherical models. The low volume filling factor indicates that the dense gas is highly clumpy and may be organised into filament- or sheet-like structures, which is a natural outcome of supersonic turbulence and gravitational collapse. In general there seems to be a higher density contrast (decreasing ff_{dens}) with increasing L/M (as listed sequentially in Table 3.7, last column). While ff_{dens} provides an upper limit of the volume filling factor of high-density gas, we will make here some inferences for the dense gas mass fraction based on intuitive assumptions and references to numerical simulations. The aim is to establish the ratio of the bulk gas and dense gas density profiles, $\rho_{\text{bulk}}/\rho_{\text{dense}}$, as a measure of the dense gas fraction, and the radial profile of this ratio as an indicator of different star formation modes (or temporal variations of the SFE) for the massive clumps.

It is a well-known fact that there is a strong correlation between SFR and dense gas. Based on a gravo-turbulent fragmentation scenario, Padoan, Haugbølle and Nordlund (2012) and Padoan et al. (2017) derive an empirical relation between SFR per free-fall time ϵ_{ff} (the fraction of a cloud's mass that is converted to stellar mass over a free-fall time scale, Krumholz and McKee 2005) and α_{vir},

$$\epsilon_{\text{ff}} = \dot{M}/(M/t_{\text{ff}}) \propto \exp\left(-\alpha_{\text{vir}}^{1/2}\right) \tag{3.10}$$

In a hierarchical description of cloud structure in which gas density increases with decreasing scale, the conservation of $\dot{M}$ (or equivalently SFR) translates into

$$\epsilon_{\text{ff},1} M_{1,\text{tot}}/t_{\text{ff},\bar{\rho}_1} = \epsilon_{\text{ff},2} M_{2,\text{tot}}/t_{\text{ff},\bar{\rho}_2} \tag{3.11}$$

in which the number indices of 1 and 2 denote two adjacent levels in a hierarchy. We assume ρ_{bulk} represents the gas density of a lower-level structure in the hierarchy from which a higher level structure of gas density ρ_{dense} originates from. We further assume that only the dense gas ρ_{dense} participates in the star formation process. Then with a scale-invariant ϵ_{ff} (or equivalently scale-invariant α_{vir}), Equation 3.11 translates to $M_{\text{dense}} = M_{\text{tot}}(t_{\text{ff},\rho_{\text{dense}}}/t_{\text{ff},\rho_{\text{bulk}}})$. Substituting the free-fall timescale $t_{\text{ff}} \propto \rho^{-1/2}$ into the equation, we obtain,

$$M_{\text{dense}} \sim M_{\text{tot}}\left(\frac{\rho_{\text{bulk}}}{\rho_{\text{dense}}}\right)^{1/2}. \tag{3.12}$$

Naively, this relation means that at a certain scale, the closer the derived dense gas density is to the bulk gas density, the more mass fraction of the clump is occupied by the dense gas. We note that even without the assumption of scale-invariant ϵ_{ff}, considering only that the two set of densities are each the mass-weighted value in their respective density regimes, the mass fraction of dense gas to total clump gas is also largely determined by $\rho_{\text{bulk}}/\rho_{\text{dense}}$, when the ratio between density of bulk gas and gas not seen by CH_3OH is similar among sources and does not vary with scale.

Figure 3.24 shows the density profiles ρ_{dense} and ρ_{bulk}. This figure also shows the ratios between these two profiles, which provide measure of dense gas mass fraction (DGMF), i.e. $M_{\text{dense}}/M_{\text{tot}}$. We found that the DGMF in G19, G08b, and G10 decrease with radius, while it increases with radius in G28, G08a, and G13. Specifically, G19 shows an decreasing DGMF from 25% to 19%, G08b from 22% to 18% and G10 from 24% to 15%. For G28, DGMF increases from 15% to ∼17% at 0.1-0.2 pc. In G08a and G13, DGMF is ∼19% at their centers and achieve ∼22% at 0.2-0.3 pc radii.

Given these radial variations of DGMF, it might be indicative that among these 6 sources, G19 and G10 may be most efficiently converting gas into the dense gas regime, having a focused DGMF towards clump center. G08b exhibits a similarly high DGMF that changes slightly with scale, while early-phase clump G08a and the least massive G13 have DGMF peaking around the intermediate scales relative to the center. Another early-stage source G28 has the least DGMF overall and also shows an relatively invariant DGMF over scales. This trend is only partially reflected in the density profiles slopes of $\rho_{\rm bulk}$(r), which is generally regarded as a measure of dense gas concentration that directly inflates the SFR (e.g. Parmentier 2019). It is noteworthy that radial variations of the DGMF for individual source is compatible with the radial dependence of the virial parameter shown in Section 3.4.3 (Figure 3.23). These two measures are both indicative of the capability of the source in converting gas into the denser regime at different positions relative to the bottom of the clump's gravitational potential. It is straightforward to see that the three classes of increasing/flattened/decreasing DGMF as a function of radius, for a particular source, correspond to a shallower/similar/steeper dense gas profile ($q_{\rm dense}$) compared to that of its bulk gas ($q_{\rm bulk}$) on the basis of Eq.3.1, 3.3 and 3.12. In the non-homologously spherical collapse framework, the physical condition of an outer shell can be regarded as an earlier stage preceding the inner shell (e.g. Vázquez-Semadeni et al. 2019), then a radially-decreasing (increasing) DGMF corresponds to an accelerating (retarding) dense gas conversion and temporal increase (decrease) of SFE for a particular source.

The localised behavior of dense gas conversion may be causing the chaotic and scattered SFR vs. gas density relation, and such behavior goes beyond the self-similar solutions for collapsing clumps. The non-self-similar behavior is suggested to be relevant even for the spherical collapse as shown theoretically by Coughlin (2017), dependent on the initial conditions. The spatial variations of the DGMF may also reflect two competing gravitational collapses within these massive clumps: collapse towards the global potential center, and collapse of dense regions into ambient filaments, and the latter process is mostly induced by turbulence (Girichidis et al. 2011). The dominance of one or another process depends on the initial density profile and turbulence driving modes (Girichidis et al. 2011, Lomax, Whitworth and Hubber 2015).

We can also establish $\rho_{\rm bulk}/\rho_{\rm dense}$ as a measure of DGMF from another perspective, with a less strong assumption. In the framework of turbulent convergent flows, the gas density enhancement after a compressive shock has an inverse length scale relation following,

$$\rho_{\rm post}/\rho_0 \propto L_0/l_{\rm post} \sim \mathcal{M}_{\rm s}^2 \tag{3.13}$$

in which L_0 and $l_{\rm post}$ denote the length scales of the pre-shock and post-shock gas, and ρ_0 and $\rho_{\rm post}$ the gas densities, respectively. $M_{\rm s}$ denotes the sonic Mach number, $M_{\rm s} = \frac{\sigma_{\rm rms}}{c_{\rm s}}$. This shock jump condition is at the origin of the log-normal distribution of PDF. As Equation 3.13 links the gas length scale to density with an inverse relation, then the mass ratio of post-shock dense gas versus the pre-shock gas, may also be represented by a power-law form following $(\rho_0/\rho_{\rm post})^{-s}$ with slope s dependent on the assumed geometry. With a cylindrical geometry describing infinite filaments, the gas mass is $\propto \rho l^2$ with l denotes thickness (radius), with slope $s = 1$.

If the enhancement of gas density ($\rho_{\rm dense}$) as traced by CH_3OH is regarded as the result of compressive turbulence on the pre-shock gas that has a density represented by $\rho_{\rm bulk}$, the ratio $(\rho_0/\rho_{\rm post})$ still holds as a DGMF measure. Compared to Eq 3.12 ($s = 1/2$), the different scaling of $s = 1$ does not change the general trend of the radial change of this measure, but only to increase the contrast between outer layer and inner region.

In any case, the dense gas probed by CH_3OH does has contributions from shock entrainment, as suggested by locally increased $M_{\rm s}$ and the fact that CH_3OH is likely enhanced in shocked regions. On the other hand, we have already seen in Section 3.4.3 that gravitational collapse has altered the general scaling relation of $v_{\rm T}$ (hence $\mathcal{M}_{\rm s}$), which makes the slope s vary. A more stringent comparison

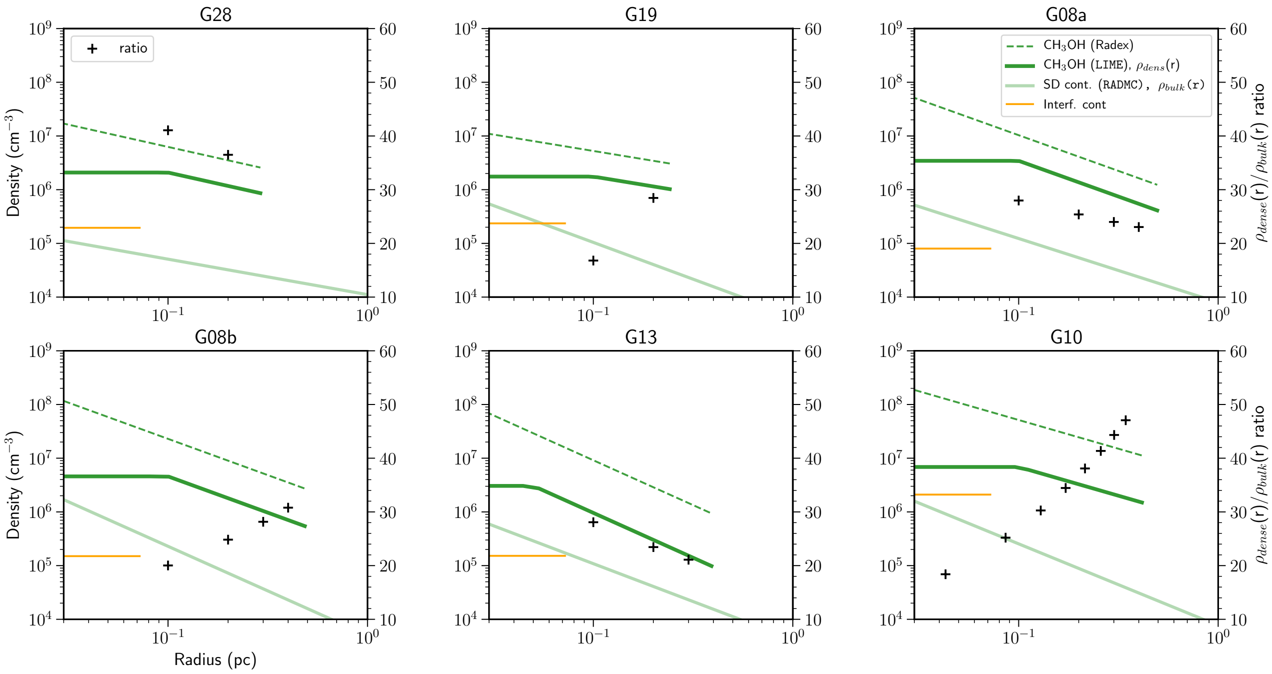

Figure 3.24: Comparison between gas density profiles derived by modeling continuum and CH_3OH line emission. The ratio between densities derived by CH_3OH `LIME` modeling ($\rho_{\rm dense}$) and continuum ($\rho_{\rm bulk}$) results are shown as pluses (following right y-axis). The density estimated by SMA 1.2 mm continuum observations representing the central core average density is shown as vertical orange line in each plot (Table 3.1).

of radial change of dense gas mass fraction to indicate the dense gas conversion efficiency would benefit from properly separating the part of dense gas associated with transient gas substructures with virialised cores and coherent flows, which is achievable with finer (both spectral and spatial) resolution observations.

3.5 Conclusions

The gas thermal properties are critical to the star-formation process. For massive star formation, the density structure of the nursery gas clumps may not be well predicted by previous hydrostatic equilibrium core models which are generally good representative of low-mass cores, due to a higher level of turbulence and gravitational collapse set at larger scales. We conduct an SMA and APEX line survey towards a sample of 8 massive star-forming clumps, in order to understand the evolution of temperature and density structure. The major findings are as follows:

1. Transitions of multiple molecular species (CH_3CN, CH_3CCH, H_2CS) of distinct critical densities, together with dust emission, provide a well sampling of the full gas temperature regime ($\gtrsim$200-20 K) over the clump scale. There is not a single power-law relation dependent only on source luminosity that could describe all the radial temperature variations in our sample. The elevated

temperature of a less luminous source may be related to the intermittency of accretion and shock-related activities.

2. CH_3OH line series are good density probe for massive clumps, selectively tracing density regimes of $\gtrsim 10^6$ cm^{-3}. Systematic steepening of density profiles along clump evolution, indicated by L/M, is revealed among the sample, from both continuum (bulk gas) and CH_3OH line (dense gas) modeling. The slopes change from >-1 to ~-1.5. The dense gas proportion becomes denser with increasing L/M, and the volume filling factor of which decrease corresponding to a higher density contrast.

3. The radial line-width profile traced by multiple lines displays a scale-dependent relation. Several sources, which have comparable stellar mass and gas content at the scale probed, have a central decreasing trend of $v_T \propto r^{-0.4}$ and a $v_T \propto r^{0.2}$ rise in the outer envelope, which may be tentatively related to conversion of gravitational energy to turbulence. On larger scale (0.2-0.5 pc) all clumps are close to a virial state ($\alpha_{vir}/\alpha_{cri}$~1), as indicated by CH_3CCH, $H^{13}CO^+$ lines. Small scale ($\lesssim$0.1 pc) virial parameters traced by CH_3CN and H_2CS can exceed equilibrium values for some of the sources, the origin of which needs to be studied with higher angular resolution. In general, seeing from overall scales, there is a trend of clump gas evolve from over-virial to sub-virial state with increasing L/M.

4. The abundance of CH_3OH, CH_3CN and H_2CS show better correlations with central temperature of the source than with source luminosity. Abundance ratios of [CCH]/[CH_3OH], [CH_3CN]/[CH_3OH] and [SO_2]/[SO] are in good correlation with clump L/M, and can be used as evolutionary indicators for massive star-forming clumps.

5. The evolutionary trend of the clump density profiles is compatible with cloud-scale diagnosis that frequently reveal the time-varying power-law tail of the density probability distribution function (PDF). In a hierarchical view, the radial variation of the dense gas mass fraction, which can be approximated by the density ratio between that representing the averaged bulk gas (dust continuum, no spatial filtering) and that probed by a high density tracer (CH_3OH) may be indicative of the efficiency of the source in converting and focusing dense gas to its gravitational center. The global/bulk gas density profile is a less distinct measure due to the fact that self-similar approximation is not adequately describing the clumpy gas structures within massive clumps.

In this work, we attempt to understand the role of self-gravity in shaping the gas structure with the evolution of massive clumps. Our results are based on $\lesssim$0.1 pc angular resolution observations, although a small dense gas (probed by CH_3OH lines) filling factor has been found, indicating a clumpy gas environment of higher density contrast along evolution, but the detailed fragmentation properties and their underlying morphology and kinematics remain unresolved. In any case, deduction of line-of-sight cloud geometry is difficult. With the unknown cloud thickness, the mass scale of the high-density gas regime remains highly uncertain.

Observations have broadly reveal transonic to subsonic line-widths associated with localised substructures in massive star-forming regions, the length scale of which is well above sonic scale, indicating an efficient turbulence dissipation process. Therefore, the detailed and more robust velocity line-width profiles require better resolved observations to disentangle multiple velocity components, and confusion from outflow activities, etc. In addition, while the scale-dependent line-width vs. radius relation is more indirect evidence (based on assumption that it mirrors radial infall velocity) of changing role of gravitational collapse in dominating gas dynamics, more direct evidence is measurement of infall velocities, or accretion rates as a function of radius. The latter will also be indispensable to distinguish different collapse models (e.g. Padoan et al. 2020). This calls for observations of multiple “infall tracers" sensitive to different gas density regimes, together with the thermal structure properly constrained.

References

Adams, F. C. and F. H. Shu (1985), *Infrared emission from protostars.*, Astrophys. J. **296** 655 (cit. on p. 120).

Adams, Fred C. (1991), *Asymptotic Theory for the Spatial Distribution of Protostellar Emission*, Astrophys. J. **382** 544 (cit. on pp. 119, 120).

Bachiller, R. and M. Pérez Gutiérrez (1997), *Shock Chemistry in the Young Bipolar Outflow L1157*, The Astrophysical Journal **487** L93, URL: `https://doi.org/10.1086%5C%2F310877` (cit. on p. 91).

Bacmann, A. et al. (2002), *The degree of CO depletion in pre-stellar cores*, Astron. Astrophys. **389** L6, arXiv: `astro-ph/0205154 [astro-ph]` (cit. on p. 122).

Ballesteros-Paredes, Javier et al. (2011), *Gravity or turbulence? - II. Evolving column density probability distribution functions in molecular clouds*, Mon. Not. R. Astron. Soc. **416** 1436, arXiv: `1105.5411 [astro-ph.GA]` (cit. on p. 125).

Ballesteros-Paredes, Javier et al. (2018), *Gravity or turbulence? - IV. Collapsing cores in out-of-virial disguise*, Mon. Not. R. Astron. Soc. **479** 2112, arXiv: `1710.07384 [astro-ph.GA]` (cit. on p. 126).

Baobab Liu, Hauyu et al. (2010), *The Decrease of Specific Angular Momentum and the Hot Toroid Formation: The Massive Clump G10.6-0.4*, Astrophys. J. **722** 262, arXiv: `1010.2255 [astro-ph.SR]` (cit. on pp. 84, 125).

Bate, Matthew R. (2009), *The importance of radiative feedback for the stellar initial mass function*, Mon. Not. R. Astron. Soc. **392** 1363, arXiv: `0811.1035 [astro-ph]` (cit. on p. 82).

Beckwith, Steven V. W. and Anneila I. Sargent (1991), *Particle Emissivity in Circumstellar Disks*, Astrophys. J. **381** 250 (cit. on p. 119).

Bell, T. A. et al. (2014), *Extended warm gas in Orion KL as probed by methyl cyanide*, Astron. Astrophys. **564**, A114 A114, arXiv: `1402.2842 [astro-ph.GA]` (cit. on p. 126).

Belloche, A. et al. (2017), *Rotational spectroscopy, tentative interstellar detection, and chemical modeling of N-methylformamide*, Astron. Astrophys. **601**, A49 A49, arXiv: `1701.04640 [astro-ph.GA]` (cit. on p. 108).

Beltrán, M. T. et al. (2018), *Accelerating infall and rotational spin-up in the hot molecular core G31.41+0.31*, Astron. Astrophys. **615**, A141 A141, arXiv: `1803.05300 [astro-ph.SR]` (cit. on pp. 112, 120).

Bergin, Edwin A. et al. (1994), *CH 3C 2H as a Temperature Probe in Dense Giant Molecular Cloud Cores*, Astrophys. J. **431** 674 (cit. on p. 91).

Bertoldi, Frank and Christopher F. McKee (1992), *Pressure-confined Clumps in Magnetized Molecular Clouds*, Astrophys. J. **395** 140 (cit. on p. 114).

Beuther, H. et al. (2002), *High-Mass Protostellar Candidates. II. Density Structure from Dust Continuum and CS Emission*, Astrophys. J. **566** 945, arXiv: `astro-ph/0110370 [astro-ph]` (cit. on pp. 82, 112, 127).

Beuther, H. et al. (2007), *Interferometric multi-wavelength (sub)millimeter continuum study of the young high-mass protocluster IRAS 05358+3543*, Astron. Astrophys. **466** 1065, arXiv: `astro-ph/0702560 [astro-ph]` (cit. on pp. 82, 120).

Beuther, H. et al. (2008), *Ethynyl (C_2H) in Massive Star formation: Tracing the Initial Conditions?*, Astrophys. J. Letters **675** L33, arXiv: `0801.4493 [astro-ph]` (cit. on p. 116).

Binder, Breanna A. and Matthew S. Povich (2018), *A Multiwavelength Look at Galactic Massive Star-forming Regions*, Astrophys. J. **864**, 136 136, arXiv: `1808.00454 [astro-ph.GA]` (cit. on p. 119).

Bisschop, S. E. et al. (2007), *Testing grain-surface chemistry in massive hot-core regions*, Astron. Astrophys. **465** 913, arXiv: `astro-ph/0702066 [astro-ph]` (cit. on p. 127).

Blake, Geoffrey A. et al. (1994), *Molecular Abundances and Low-Mass Star Formation. I. Si- and S-bearing Species toward IRAS 16293-2422*, Astrophys. J. **428** 680 (cit. on p. 91).

Bøgelund, Eva G. et al. (2019), *Molecular complexity on disc scales uncovered by ALMA. Chemical composition of the high-mass protostar AFGL 4176*, Astron. Astrophys. **628**, A2 A2, arXiv: `1906.06156 [astro-ph.SR]` (cit. on p. 116).

Bracco, A. et al. (2017), *Probing changes of dust properties along a chain of solar-type prestellar and protostellar cores in Taurus with NIKA*, Astron. Astrophys. **604**, A52 A52, arXiv: `1706.08407 [astro-ph.GA]` (cit. on p. 119).

Brinch, C. and M. R. Hogerheijde (2010), *LIME - a flexible, non-LTE line excitation and radiation transfer method for millimeter and far-infrared wavelengths*, Astron. Astrophys. **523**, A25 A25, arXiv: `1008.1492 [astro-ph.SR]` (cit. on p. 107).

Calcutt, H. et al. (2019), *The ALMA-PILS survey: propyne (CH_3CCH) in IRAS 16293-2422*, Astron. Astrophys. **631**, A137 A137, arXiv: `1909.13329 [astro-ph.SR]` (cit. on pp. 108, 109, 127).

Camacho, Vianey et al. (2016), *Energy Budget of Forming Clumps in Numerical Simulations of Collapsing Clouds*, Astrophys. J. **833**, 113 113, arXiv: `1609.09112 [astro-ph.GA]` (cit. on p. 126).

Camacho, Vianey et al. (2020), *Simultaneous evolution of the virial parameter and star formation rate in star forming molecular clouds*, arXiv e-prints, arXiv:2002.01594 arXiv:2002.01594, arXiv: `2002.01594 [astro-ph.GA]` (cit. on p. 126).

Carey, S. J. et al. (2009), *MIPSGAL: A Survey of the Inner Galactic Plane at 24 and 70 μm*, PASP **121** 76 (cit. on p. 106).

Caselli, P. and P. C. Myers (1995), *The Line Width–Size Relation in Massive Cloud Cores*, Astrophys. J. **446** 665 (cit. on pp. 123, 124).

Cesaroni, R. et al. (2019), *IRAS 23385+6053: an embedded massive cluster in the making*, Astron. Astrophys. **627**, A68 A68, arXiv: `1905.11257 [astro-ph.SR]` (cit. on p. 126).

Choi, Jieun et al. (2016), *MESA ISOCHRONES AND STELLAR TRACKS (MIST). I. SOLAR-SCALED MODELS*, The Astrophysical Journal **823** 102, URL: `https://doi.org/10.3847%2F0004-637x%2F823%2F2%2F102` (cit. on pp. 107, 125).

Contreras, Y. et al. (2013), *ATLASGAL - compact source catalogue: $330° < \ell < 21°$*, Astron. Astrophys. **549**, A45 A45, arXiv: `1211.0741 [astro-ph.GA]` (cit. on p. 97).

Coughlin, Eric R. (2017), *Spherically Symmetric Cold Collapse: The Exact Solutions and a Comparison with Self-similar Solutions*, Astrophys. J. **835**, 40 40, arXiv: `1611.09854 [astro-ph.GA]` (cit. on pp. 81, 123, 125, 130).

Csengeri, T. et al. (2011), *Convergent Flows and Low-velocity Shocks in DR21(OH)*, Astrophys. J. Letters **740**, L5 L5, arXiv: `1108.4451 [astro-ph.GA]` (cit. on p. 126).

Curry, Charles L. and Christopher F. McKee (2000), *Composite Polytrope Models of Molecular Clouds. I. Theory*, Astrophys. J. **528** 734, arXiv: `astro-ph/9908071 [astro-ph]` (cit. on p. 82).

Dullemond, C. P. et al. (2012), *RADMC-3D: A multi-purpose radiative transfer tool*, Astrophysics Source Code Library, ascl: `1202.015` (cit. on p. 106).

Esplugues, G. B. et al. (2014), *Modelling the sulphur chemistry evolution in Orion KL*, Astron. Astrophys. **567**, A95 A95, arXiv: `1406.2278 [astro-ph.SR]` (cit. on p. 127).

Falgarone, E. and J. L. Puget (1985), *A model of clumped molecular clouds. I - Hydrostatic structure of dense cores*, Astron. Astrophys. **142** 157 (cit. on p. 122).

Fayolle, Edith C. et al. (2015), *Complex organic molecules in organic-poor massive young stellar objects*, Astron. Astrophys. **576**, A45 A45, arXiv: `1501.03168 [astro-ph.SR]` (cit. on p. 116).

Federrath, Christoph and Ralf S. Klessen (2013a), *On the Star Formation Efficiency of Turbulent Magnetized Clouds*, Astrophys. J. **763**, 51 51, arXiv: `1211.6433 [astro-ph.SR]` (cit. on p. 82).

– (2013b), *On the Star Formation Efficiency of Turbulent Magnetized Clouds*, Astrophys. J. **763**, 51 51, arXiv: `1211.6433 [astro-ph.SR]` (cit. on p. 128).

Flower, D. R., G. Pineau Des Forets and C. M. Walmsley (2006), *The importance of the ortho:para H_2 ratio for the deuteration of molecules during pre-protostellar collapse*, Astron. Astrophys. **449** 621, arXiv: `astro-ph/0601429 [astro-ph]` (cit. on p. 109).

Flower, D. R., G. Pineau des Forêts and Djamal Rabli (2010), *Methanol line formation in outflow sources*, Mon. Not. R. Astron. Soc. **409** 29 (cit. on p. 109).

Foster, Prudence N. and Roger A. Chevalier (1993), *Gravitational Collapse of an Isothermal Sphere*, Astrophys. J. **416** 303 (cit. on p. 120).

Garrod, R. T. et al. (2017), *Exploring molecular complexity with ALMA (EMoCA): Simulations of branched carbon-chain chemistry in Sgr B2(N)*, Astron. Astrophys. **601**, A48 A48, arXiv: `1701.07160 [astro-ph.GA]` (cit. on pp. 109, 127).

Gerner, T. et al. (2014), *Chemical evolution in the early phases of massive star formation. I*, Astron. Astrophys. **563**, A97 A97, arXiv: `1401.6382 [astro-ph.SR]` (cit. on p. 127).

Giannetti, A. et al. (2017), *ATLASGAL-selected massive clumps in the inner Galaxy. V. Temperature structure and evolution*, Astron. Astrophys. **603**, A33 A33, arXiv: `1703.08485 [astro-ph.GA]` (cit. on pp. 83, 90, 91, 116, 122, 126, 127).

Gieser, C. et al. (2021), *The physical and chemical structure of high-mass star-forming regions. Unraveling chemical complexity with the NOEMA large program "CORE"*, arXiv e-prints, arXiv:2102.11676 arXiv:2102.11676, arXiv: `2102.11676 [astro-ph.GA]` (cit. on p. 120).

Girichidis, Philipp et al. (2011), *Importance of the initial conditions for star formation - I. Cloud evolution and morphology*, Mon. Not. R. Astron. Soc. **413** 2741, arXiv: `1008.5255 [astro-ph.SR]` (cit. on pp. 81, 130).

Girichidis, Philipp et al. (2014), *On the Evolution of the Density Probability Density Function in Strongly Self-gravitating Systems*, Astrophys. J. **781**, 91 91, arXiv: `1310.4346 [astro-ph.GA]` (cit. on p. 128).

Glover, Simon C. O. and Paul C. Clark (2012), *Is molecular gas necessary for star formation?*, Mon. Not. R. Astron. Soc. **421** 9, arXiv: `1105.3073 [astro-ph.GA]` (cit. on p. 118).

Goldsmith, Paul F. (2001), *Molecular Depletion and Thermal Balance in Dark Cloud Cores*, Astrophys. J. **557** 736 (cit. on p. 118).

Graninger, Dawn M., Olivia H. Wilkins and Karin I. Oberg (2016), *Carbon Chains and Methanol toward Embedded Protostars*, Astrophys. J. **819**, 140 140, arXiv: `1602.01472 [astro-ph.SR]` (cit. on p. 127).

Grave, J. M. C. and M. S. N. Kumar (2009), *Spitzer-IRAC GLIMPSE of high mass protostellar objects. II. SED modelling of a bona fide sample*, Astron. Astrophys. **498** 147, arXiv: `0901.2053 [astro-ph.SR]` (cit. on p. 125).

Green, Sheldon (1986), *Collisional Excitation of Interstellar Methyl Cyanide*, Astrophys. J. **309** 331 (cit. on p. 109).

Güsten, R. et al. (2006), *The Atacama Pathfinder EXperiment (APEX) - a new submillimeter facility for southern skies -*, Astron. Astrophys. **454** L13 (cit. on p. 84).

Guszejnov, Dávid, Philip F. Hopkins and Michael Y. Grudić (2018), *Universal scaling relations in scale-free structure formation*, Mon. Not. R. Astron. Soc. **477** 5139, arXiv: `1707.05799 [astro-ph.GA]` (cit. on p. 128).

Guszejnov, Dávid, Philip F. Hopkins and Xiangcheng Ma (2017), *Comparing models for IMF variation across cosmological time in Milky Way-like galaxies*, Mon. Not. R. Astron. Soc. **472** 2107, arXiv: `1702.04431 [astro-ph.GA]` (cit. on p. 82).

Guszejnov, Dávid, Mark R. Krumholz and Philip F. Hopkins (2016), *The necessity of feedback physics in setting the peak of the initial mass function*, Mon. Not. R. Astron. Soc. **458** 673, arXiv: `1510.05040 [astro-ph.SR]` (cit. on p. 82).

Hatchell, J. and F. F. S. van der Tak (2003), *The physical structure of high-mass star-forming cores*, Astron. Astrophys. **409** 589 (cit. on p. 82).

Helmich, F. P. and E. F. van Dishoeck (1997), *Physical and chemical variations within the W3 star-forming region. II. The 345 GHz spectral line survey.*, Astron. Astrophys. **124** 205 (cit. on p. 91).

Henriksen, R., P. Andre and S. Bontemps (1997), *Time-dependent accretion and ejection implied by pre-stellar density profiles.*, Astron. Astrophys. **323** 549, arXiv: `astro-ph/9701097 [astro-ph]` (cit. on pp. 120, 123).

Herpin, F. et al. (2009), *S-bearing molecules in massive dense cores*, Astron. Astrophys. **504** 853, arXiv: `0906.1122 [astro-ph.SR]` (cit. on p. 127).

Heyer, Mark et al. (2009), *Re-Examining Larson's Scaling Relationships in Galactic Molecular Clouds*, Astrophys. J. **699** 1092, arXiv: `0809.1397 [astro-ph]` (cit. on p. 123).

Hildebrand, R. H. (1983), *The determination of cloud masses and dust characteristics from submillimetre thermal emission.*, QJRAS **24** 267 (cit. on p. 119).

Hosokawa, Takashi and Kazuyuki Omukai (2009), *Evolution of Massive Protostars with High Accretion Rates*, Astrophys. J. **691** 823, arXiv: `0806.4122 [astro-ph]` (cit. on p. 83).

Izquierdo, Andrés F. et al. (2018), *Radiative transfer modelling of W33A MM1: 3D structure and dynamics of a complex massive star-forming region*, Mon. Not. R. Astron. Soc. **478** 2505, arXiv: `1804.09204 [astro-ph.GA]` (cit. on p. 110).

Jappsen, A. -K. et al. (2005), *The stellar mass spectrum from non-isothermal gravoturbulent fragmentation*, Astron. Astrophys. **435** 611, arXiv: `astro-ph/0410351 [astro-ph]` (cit. on p. 82).

Jiang, Xue-Jian et al. (2015), *SMA Observations of C_2H in High-mass Star-forming Regions*, Astrophys. J. **808**, 114 114, arXiv: `1507.04205 [astro-ph.SR]` (cit. on pp. 116, 117).

Jørgensen, Jes K. et al. (2007), *PROSAC: A Submillimeter Array Survey of Low-Mass Protostars. I. Overview of Program: Envelopes, Disks, Outflows, and Hot Cores*, Astrophys. J. **659** 479, arXiv: `astro-ph/0701115 [astro-ph]` (cit. on p. 119).

Juvela, Mika et al. (2018), *Herschel and SCUBA-2 observations of dust emission in a sample of Planck cold clumps*, Astron. Astrophys. **612**, A71 A71, arXiv: `1711.09425 [astro-ph.GA]` (cit. on p. 119).

Kainulainen, J. et al. (2009), *Probing the evolution of molecular cloud structure. From quiescence to birth*, Astron. Astrophys. **508** L35, arXiv: `0911.5648 [astro-ph.GA]` (cit. on p. 82).

Kauffmann, Jens, Thushara Pillai and Paul F. Goldsmith (2013), *Low Virial Parameters in Molecular Clouds: Implications for High-mass Star Formation and Magnetic Fields*, Astrophys. J. **779**, 185 185, arXiv: `1308.5679 [astro-ph.GA]` (cit. on p. 126).

Klessen, R. S. and P. Hennebelle (2010), *Accretion-driven turbulence as universal process: galaxies, molecular clouds, and protostellar disks*, Astron. Astrophys. **520**, A17 A17, arXiv: `0912.0288 [astro-ph.CO]` (cit. on p. 125).

Klessen, Ralf S. (2000), *One-Point Probability Distribution Functions of Supersonic Turbulent Flows in Self-gravitating Media*, Astrophys. J. **535** 869, arXiv: `astro-ph/0001379 [astro-ph]` (cit. on p. 82).

Klessen, Ralf S., Marco Spaans and Anne-Katharina Jappsen (2007), *The stellar mass spectrum in warm and dusty gas: deviations from Salpeter in the Galactic centre and in circumnuclear starburst regions*, Mon. Not. R. Astron. Soc. **374** L29, arXiv: `astro-ph/0610557 [astro-ph]` (cit. on p. 82).

Koda, Jin et al. (2011), *CO(J = 1-0) Imaging of M51 with CARMA and the Nobeyama 45 m Telescope*, Astrophys. J. Supp. **193**, 19 19, arXiv: `1102.3060 [astro-ph.IM]` (cit. on p. 88).

Kritsuk, Alexei G., Michael L. Norman and Rick Wagner (2011), *On the Density Distribution in Star-forming Interstellar Clouds*, Astrophys. J. Letters **727**, L20 L20, arXiv: `1007.2950 [astro-ph.GA]` (cit. on p. 128).

Kroupa, Pavel, Christopher A. Tout and Gerard Gilmore (1993), *The Distribution of Low-Mass Stars in the Galactic Disc*, Mon. Not. R. Astron. Soc. **262** 545 (cit. on pp. 82, 83).

Kroupa, Pavel et al. (2013), "The Stellar and Sub-Stellar Initial Mass Function of Simple and Composite Populations", *Planets, Stars and Stellar Systems. Volume 5: Galactic Structure and Stellar Populations*, ed. by Terry D. Oswalt and Gerard Gilmore, vol. 5 115 (cit. on p. 81).

Krumholz, Mark R. (2014), *DESPOTIC - a new software library to Derive the Energetics and SPectra of Optically Thick Interstellar Clouds*, Mon. Not. R. Astron. Soc. **437** 1662, arXiv: `1304.2404 [astro-ph.IM]` (cit. on p. 119).

Krumholz, Mark R., Richard I. Klein and Christopher F. McKee (2011), *Radiation-hydrodynamic Simulations of the Formation of Orion-like Star Clusters. I. Implications for the Origin of the Initial Mass Function*, Astrophys. J. **740**, 74 74, arXiv: `1104.2038 [astro-ph.GA]` (cit. on p. 82).

– (2012), *Radiation-hydrodynamic Simulations of the Formation of Orion-like Star Clusters. II. The Initial Mass Function from Winds, Turbulence, and Radiation*, Astrophys. J. **754**, 71 71, arXiv: `1203.2620 [astro-ph.SR]` (cit. on pp. 81, 120).

Krumholz, Mark R. and Christopher F. McKee (2005), *A General Theory of Turbulence-regulated Star Formation, from Spirals to Ultraluminous Infrared Galaxies*, Astrophys. J. **630** 250, arXiv: `astro-ph/0505177 [astro-ph]` (cit. on p. 129).

Kuiper, T. B. H. et al. (1984), *Methyl acetylene as a temperature probe for dense interstellar clouds.*, Astrophys. J. **276** 211 (cit. on p. 91).

Kurono, Yasutaka, Koh-Ichiro Morita and Takeshi Kamazaki (2009), *A Study of Combining Technique of Single-Dish and Interferometer Data: Imaging Simulations and Analysis*, PASJ **61** 873 (cit. on p. 88).

Larson, R. B. (1981), *Turbulence and star formation in molecular clouds.*, Mon. Not. R. Astron. Soc. **194** 809 (cit. on p. 123).

Larson, Richard B. (1969), *Numerical calculations of the dynamics of collapsing proto-star*, Mon. Not. R. Astron. Soc. **145** 271 (cit. on p. 81).

Lee, Eve J., Philip Chang and Norman Murray (2015), *Time-varying Dynamical Star Formation Rate*, Astrophys. J. **800**, 49 49, arXiv: `1406.4148 [astro-ph.SR]` (cit. on pp. 82, 123, 125, 128).

Lee, Yueh-Ning and Patrick Hennebelle (2019), *Stellar mass spectrum within massive collapsing clumps. III. Effects of temperature and magnetic field*, Astron. Astrophys. **622**, A125 A125, arXiv: `1812.05508 [astro-ph.GA]` (cit. on p. 81).

Leurini, S., K. M. Menten and C. M. Walmsley (2016), *Physical characteristics of bright Class I methanol masers*, Astron. Astrophys. **592**, A31 A31, arXiv: `1605.09406 [astro-ph.GA]` (cit. on p. 109).

Leurini, S. et al. (2004), *Methanol as a diagnostic tool of interstellar clouds. I. Model calculations and application to molecular clouds*, Astron. Astrophys. **422** 573 (cit. on pp. 83, 95).

Leurini, S. et al. (2007), *Methanol as a diagnostic tool of interstellar clouds. II. Modelling high-mass protostellar objects*, Astron. Astrophys. **466** 215 (cit. on pp. 83, 95).

Li, Jennifer I-Hsiu et al. (2017), *Systematic Analysis of Spectral Energy Distributions and the Dust Opacity Indices for Class 0 Young Stellar Objects*, Astrophys. J. **840**, 72 72, arXiv: `1704.06246 [astro-ph.SR]` (cit. on p. 119).

Li, Juan et al. (2015), *Sulfur-bearing Molecules in Massive Star-forming Regions: Observations of OCS, CS, H_2S, and SO*, Astrophys. J. **802**, 40 40, arXiv: `1501.06018 [astro-ph.SR]` (cit. on p. 127).

Li, Shanghuo et al. (2019), *Formation of Massive Protostellar Clusters—Observations of Massive 70 μm Dark Molecular Clouds*, Astrophys. J. **886**, 130 130, arXiv: `1909.08916 [astro-ph.GA]` (cit. on p. 82).

Lin, Yuxin et al. (2017), *Cloud Structure of Three Galactic Infrared Dark Star-forming Regions from Combining Ground- and Space-based Bolometric Observations*, Astrophys. J. **840**, 22 22, arXiv: `1704.06448 [astro-ph.GA]` (cit. on pp. 82, 128).

Liu, Hauyu Baobab (2017), *Interpreting observations of edge-on gravitationally unstable accretion flows. The case of G10.6-0.4*, Astron. Astrophys. **597**, A70 A70, arXiv: `1609.07296 [astro-ph.SR]` (cit. on pp. 122, 125).

– (2019), *The Anomalously Low (Sub)Millimeter Spectral Indices of Some Protoplanetary Disks May Be Explained By Dust Self-scattering*, Astrophys. J. Letters **877**, L22 L22, arXiv: `1904.00333 [astro-ph.SR]` (cit. on p. 119).

Liu, Hauyu Baobab, Qizhou Zhang and Paul T. P. Ho (2011), *An Overall Picture of the Gas Flow in a Massive Cluster-forming Region: The Case of G10.6-0.4*, Astrophys. J. **729**, 100 100, arXiv: `1101.3459 [astro-ph.SR]` (cit. on p. 84).

Liu, Hauyu Baobab et al. (2012), *The Origin of OB Clusters: From 10 pc to 0.1 pc*, Astrophys. J. **745**, 61 61, arXiv: `1110.1318 [astro-ph.SR]` (cit. on p. 84).

Liu, Hauyu Baobab et al. (2015), *ALMA Resolves the Spiraling Accretion Flow in the Luminous OB Cluster-forming Region G33.92+0.11*, Astrophys. J. **804**, 37 37, arXiv: `1505.04255 [astro-ph.SR]` (cit. on p. 126).

Lomax, O., A. P. Whitworth and D. A. Hubber (2015), *On the effects of solenoidal and compressive turbulence in pre-stellar cores*, Mon. Not. R. Astron. Soc. **449** 662, arXiv: `1502.04009 [astro-ph.SR]` (cit. on p. 130).

Lynden-Bell, D. and J. E. Pringle (1974), *The evolution of viscous discs and the origin of the nebular variables.*, Mon. Not. R. Astron. Soc. **168** 603 (cit. on p. 120).

Mathis, J. S., P. G. Mezger and N. Panagia (1983), *Interstellar radiation field and dust temperatures in the diffuse interstellar matter and in giant molecular clouds.*, Astron. Astrophys. **500** 259 (cit. on p. 118).

McLaughlin, Dean E. and Ralph E. Pudritz (1997), *Gravitational Collapse and Star Formation in Logotropic and Nonisothermal Spheres*, Astrophys. J. **476** 750, arXiv: `astro-ph/9609080 [astro-ph]` (cit. on pp. 81, 122).

Minh, Y. C. et al. (2011), *H_2CS in Outflows of the Massive Star-forming Core DR21(OH)*, Astrophys. J. Letters **737**, L25 L25 (cit. on p. 91).

Molinari, S. et al. (2008), *The evolution of the spectral energy distribution in massive young stellar objects*, Astron. Astrophys. **481** 345 (cit. on p. 122).

Molinari, S. et al. (2016), *Calibration of Evolutionary Diagnostics in High-mass Star Formation*, Astrophys. J. Letters **826**, L8 L8, arXiv: `1604.06192 [astro-ph.GA]` (cit. on p. 91).

Möller, T., C. Endres and P. Schilke (2017), *eXtended CASA Line Analysis Software Suite (XCLASS)*, Astron. Astrophys. **598**, A7 A7, arXiv: `1508.04114 [astro-ph.IM]` (cit. on p. 95).

Monsch, Kristina et al. (2018), *Dense Gas Kinematics and a Narrow Filament in the Orion A OMC1 Region Using NH_3*, Astrophys. J. **861**, 77 77, arXiv: `1806.01847 [astro-ph.GA]` (cit. on p. 88).

Motte, Frédérique, Sylvain Bontemps and Fabien Louvet (2018), *High-Mass Star and Massive Cluster Formation in the Milky Way*, ARA&A **56** 41, arXiv: `1706.00118 [astro-ph.GA]` (cit. on p. 81).

Mottram, J. C. et al. (2020), *From clump to disc scales in W3 IRS4. A case study of the IRAM NOEMA large programme CORE*, Astron. Astrophys. **636**, A118 A118 (cit. on p. 120).

Mouschovias, Telemachos Ch. and Scott A. Morton (1991), *Ambipolar Diffusion, Cloud Cores, and Star Formation: Two-dimensional, Cylindrically Symmetric Contraction. I. The Issues, Formulation of the Problem, and Method of Solution*, Astrophys. J. **371** 296 (cit. on p. 122).

Mueller, Kaisa E. et al. (2002), *The Physical Conditions for Massive Star Formation: Dust Continuum Maps and Modeling*, Astrophys. J. Supp. **143** 469, arXiv: `astro-ph/0207322 [astro-ph]` (cit. on pp. 82, 106, 112).

Müller, H. S. P. et al. (2001), *The Cologne Database for Molecular Spectroscopy, CDMS*, Astron. Astrophys. **370** L49 (cit. on p. 86).

Murray, Daniel W. et al. (2017), *Collapse in self-gravitating turbulent fluids*, Mon. Not. R. Astron. Soc. **465** 1316, arXiv: `1509.05910 [astro-ph.GA]` (cit. on pp. 81, 123, 125).

Murray, Norman and Philip Chang (2015), *Star Formation in Self-gravitating Turbulent Fluids*, Astrophys. J. **804**, 44 44, arXiv: `1407.6373 [astro-ph.SR]` (cit. on pp. 81, 125).

Myers, Philip C. (2015), *Characteristic Structure of Star-forming Clouds*, Astrophys. J. **806**, 226 226, arXiv: `1505.01124 [astro-ph.GA]` (cit. on p. 82).

Nomura, H. and T. J. Millar (2004), *The physical and chemical structure of hot molecular cores*, Astron. Astrophys. **414** 409, arXiv: `astro-ph/0311246 [astro-ph]` (cit. on p. 127).

Öberg, Karin I. et al. (2014), *Complex molecule formation around massive young stellar objects*, Faraday Discuss. **168** (0) 81, URL: `http://dx.doi.org/10.1039/C3FD00146F` (cit. on pp. 91, 116).

Offner, Stella S. R. et al. (2009), *The Effects of Radiative Transfer on Low-Mass Star Formation*, Astrophys. J. **703** 131, arXiv: `0904.2004 [astro-ph.SR]` (cit. on p. 81).

Ossenkopf, V. and T. Henning (1994), *Dust opacities for protostellar cores*, Astron. Astrophys. **291** 943 (cit. on pp. 101, 106).

Padoan, Paolo, Troels Haugbølle and Åke Nordlund (2012), *A Simple Law of Star Formation*, Astrophys. J. Letters **759**, L27 L27, arXiv: `1208.3758 [astro-ph.GA]` (cit. on p. 129).

Padoan, Paolo et al. (2017), *Supernova Driving. IV. The Star-formation Rate of Molecular Clouds*, Astrophys. J. **840**, 48 48, arXiv: `1702.07270 [astro-ph.GA]` (cit. on p. 129).

Padoan, Paolo et al. (2020), *The Origin of Massive Stars: The Inertial-inflow Model*, Astrophys. J. **900**, 82 82, arXiv: `1911.04465 [astro-ph.GA]` (cit. on pp. 81, 125, 133).

Palau, Aina et al. (2014), *Fragmentation of Massive Dense Cores Down to $\lesssim$1000 AU: Relation between Fragmentation and Density Structure*, Astrophys. J. **785**, 42 42, arXiv: `1401.8292 [astro-ph.GA]` (cit. on pp. 82, 120).

Pan, Liubin and Paolo Padoan (2009), *The Temperature of Interstellar Clouds from Turbulent Heating*, Astrophys. J. **692** 594, arXiv: `0806.4970 [astro-ph]` (cit. on p. 107).

Parmentier, G. (2019), *The Density Gradient Inside Molecular-gas Clumps as a Booster of Their Star Formation Activity*, Astrophys. J. **887**, 179 179, arXiv: `1911.04994 [astro-ph.GA]` (cit. on pp. 82, 130).

Passot, Thierry and Enrique Vázquez-Semadeni (1998), *Density probability distribution in one-dimensional polytropic gas dynamics*, PRE **58** 4501, arXiv: `physics/9802019 [physics.flu-dyn]` (cit. on p. 82).

Penston, M. V. (1969), *Dynamics of self-gravitating gaseous spheres-III. Analytical results in the free-fall of isothermal cases*, Mon. Not. R. Astron. Soc. **144** 425 (cit. on p. 81).

Pham, Duc Truong et al. (2006), *The Bees Algorithm - A Novel Tool for Complex Optimisation Problems* (cit. on p. 95).

Plume, Rene et al. (1997), *Dense Gas and Star Formation: Characteristics of Cloud Cores Associated with Water Masers*, The Astrophysical Journal **476** 730, URL: `https://doi.org/10.1086%5C%2F303654` (cit. on p. 123).

Qi, Chunhua (2003), "Initial Results from the Submillimeter Array", *SFChem 2002: Chemistry as a Diagnostic of Star Formation*, ed. by Charles L. Curry and Michel Fich 393 (cit. on p. 84).

Rabli, Djamal and D. R. Flower (2010), *The rotational excitation of methanol by molecular hydrogen*, Mon. Not. R. Astron. Soc. **406** 95 (cit. on pp. 97, 109).

Robertson, Brant and Peter Goldreich (2012), *Adiabatic Heating of Contracting Turbulent Fluids*, Astrophys. J. Letters **750**, L31 L31, arXiv: `1203.4815 [astro-ph.GA]` (cit. on p. 125).

Rolffs, R. et al. (2011), *Structure of evolved cluster-forming regions*, Astron. Astrophys. **527**, A68 A68 (cit. on pp. 82, 106, 120).

Roy, Arabindo et al. (2013), *Changes of Dust Opacity with Density in the Orion A Molecular Cloud*, Astrophys. J. **763**, 55 55, arXiv: `1211.6475 [astro-ph.GA]` (cit. on p. 103).

Sanhueza, Patricio et al. (2017), *A Massive Prestellar Clump Hosting No High-mass Cores*, Astrophys. J. **841**, 97 97, arXiv: `1704.08264 [astro-ph.GA]` (cit. on p. 82).

Sanhueza, Patricio et al. (2019), *The ALMA Survey of 70 μm Dark High-mass Clumps in Early Stages (ASHES). I. Pilot Survey: Clump Fragmentation*, Astrophys. J. **886**, 102 102, arXiv: `1909.07985 [astro-ph.GA]` (cit. on p. 122).

Sault, R. J., P. J. Teuben and M. C. H. Wright (1995), "A Retrospective View of MIRIAD", *Astronomical Data Analysis Software and Systems IV*, ed. by R. A. Shaw, H. E. Payne and J. J. E. Hayes, vol. 77, Astronomical Society of the Pacific Conference Series 433, arXiv: `astro-ph/0612759 [astro-ph]` (cit. on p. 84).

Schuller, F. et al. (2009), *ATLASGAL - The APEX telescope large area survey of the galaxy at 870 μm*, Astron. Astrophys. **504** 415, arXiv: `0903.1369` (cit. on p. 82).

Shirley, Yancy L. (2015), *The Critical Density and the Effective Excitation Density of Commonly Observed Molecular Dense Gas Tracers*, PASP **127** 299, arXiv: `1501.01629 [astro-ph.IM]` (cit. on p. 89).

Shu, F. H. (1977), *Self-similar collapse of isothermal spheres and star formation.*, Astrophys. J. **214** 488 (cit. on pp. 81, 122).

Smith, Rowan J., Steven Longmore and Ian Bonnell (2009), *The simultaneous formation of massive stars and stellar clusters*, Mon. Not. R. Astron. Soc. **400** 1775, arXiv: `0908.3910 [astro-ph.SR]` (cit. on p. 126).

Spaans, Marco and Joseph Silk (2000), *The Polytropic Equation of State of Interstellar Gas Clouds*, Astrophys. J. **538** 115, arXiv: `astro-ph/0002483 [astro-ph]` (cit. on p. 82).

Traficante, A. et al. (2018), *A possible observational bias in the estimation of the virial parameter in virialized clumps*, Astron. Astrophys. **619**, L7 L7, arXiv: `1811.00561 [astro-ph.GA]` (cit. on pp. 115, 126).

Troscompt, N. et al. (2009), *Constraining the ortho-to-para ratio of H_2 with anomalous H_2CO absorption*, Astron. Astrophys. **506** 1243 (cit. on p. 109).

Urquhart, J. S. et al. (2018), *ATLASGAL - properties of a complete sample of Galactic clumps*, Mon. Not. R. Astron. Soc. **473** 1059, arXiv: `1709.00392` (cit. on p. 82).

van der Tak, F. F. S. et al. (2007), *A computer program for fast non-LTE analysis of interstellar line spectra. With diagnostic plots to interpret observed line intensity ratios*, Astron. Astrophys. **468** 627, arXiv: `0704.0155 [astro-ph]` (cit. on p. 95).

van der Tak, Floris F. S. et al. (2000), *Structure and Evolution of the Envelopes of Deeply Embedded Massive Young Stars*, Astrophys. J. **537** 283, arXiv: `astro-ph/0001527 [astro-ph]` (cit. on pp. 82, 112).

van Dishoeck, Ewine F. et al. (1995), *Molecular Abundances and Low-Mass Star Formation. II. Organic and Deuterated Species toward IRAS 16293-2422*, Astrophys. J. **447** 760 (cit. on p. 127).

Varricatt, W. P. et al. (2018), *Discovery of two embedded massive YSOs and an outflow in IRAS 18144-1723*, Mon. Not. R. Astron. Soc. **480** 4231, arXiv: `1808.00230 [astro-ph.SR]` (cit. on p. 120).

Vázquez-Semadeni, Enrique et al. (2019), *Global Hierarchical Collapse In Molecular Clouds. Towards a Comprehensive Scenario*, arXiv e-prints, arXiv:1903.11247 arXiv:1903.11247, arXiv: `1903.11247 [astro-ph.GA]` (cit. on p. 130).

Wakelam, V., F. Hersant and F. Herpin (2011), *Sulfur chemistry: 1D modeling in massive dense cores*, Astron. Astrophys. **529**, A112 A112, arXiv: `1103.2860 [astro-ph.GA]` (cit. on pp. 127, 128).

Wakelam, V. et al. (2005), *Sulphur chemistry and molecular shocks: The case of NGC 1333-IRAS 2*, Astron. Astrophys. **437** 149, arXiv: `astro-ph/0503462 [astro-ph]` (cit. on pp. 127, 128).

Walch, S. et al. (2009), *Protostellar discs formed from rigidly rotating cores*, Mon. Not. R. Astron. Soc. **400** 13, arXiv: `0901.2127 [astro-ph.GA]` (cit. on p. 120).

Ward-Thompson, D., F. Motte and P. Andre (1999), *The initial conditions of isolated star formation - III. Millimetre continuum mapping of pre-stellar cores*, Mon. Not. R. Astron. Soc. **305** 143 (cit. on p. 122).

Watanabe, Naoki, Takahiro Shiraki and Akira Kouchi (2003), *The Dependence of H 2 CO and CH 3 OH Formation on the Temperature and Thickness of H 2 O-CO Ice during the Successive Hydrogenation of CO*, The Astrophysical Journal **588** L121, URL: `https://doi.org/10.1086%5C%2F375634` (cit. on p. 127).

Whitworth, A. P. et al. (1996), *Star formation and the singular isothermal sphere*, Mon. Not. R. Astron. Soc. **283** 1061 (cit. on p. 122).

Williams, J. P., L. Blitz and C. F. McKee (2000), "The Structure and Evolution of Molecular Clouds: from Clumps to Cores to the IMF", *Protostars and Planets IV*, ed. by V. Mannings, A. P. Boss and S. S. Russell 97, arXiv: `astro-ph/9902246 [astro-ph]` (cit. on p. 81).

Williams, S. J., G. A. Fuller and T. K. Sridharan (2005), *The circumstellar environments of high-mass protostellar objects. II. Dust continuum models*, Astron. Astrophys. **434** 257 (cit. on p. 82).

Xu, Siyao and Alex Lazarian (2020), *Turbulence in a Self-gravitating Molecular Cloud Core*, Astrophys. J. **890**, 157 157, arXiv: `2001.07721 [astro-ph.GA]` (cit. on p. 125).

CHAPTER 4

Massive star-forming clumps in W43-main: first results from NOEMA observations

The content of this chapter will be submitted to *Astronomy & Astrophysics*.

4.1 Background

The W43 molecular cloud is among the most prominent star-forming complexes in the galaxy, having a total gas mass of M~1×10^6 $M_\odot$, and a bolometric luminosity of more than 10^7 $L_\odot$ (Bally et al. 2010, Lin et al. 2016). It is located at a distance of 5.5 kpc at the intersection of the (near end) Galactic bar with the Scutum arm (Zhang et al. 2014). There is wide-spread low-velocity ($\lesssim$20 km s^{-1}) SiO emission detected towards W43, which is interpreted as a shock signature of large-scale colliding flows or merging filaments (Nguyen Luong et al. 2011). Such gas dynamics are caused by the special location of W43 in which orbit crowding induces violent interactions of gas streams. In addition, the HI filaments on ~200 pc scale show a velocity gradient towards W43 (Motte et al. 2014), consistent with the turbulent convergent flow model describing the transformation from atomic gas to molecular gas. These facts suggest a highly dynamical picture of the star formation process in this region. Particularly, W43 may be an ideal site for testing the *cloud-cloud* collision scenario for massive cluster formation (Inoue and Fukui 2013, Liow and Dobbs 2020).

Large-scale molecular lines and dust continuum surveys towards W43 reveal that it has a large amount of dense gas (Bally et al. 2010, Nguyen Luong et al. 2011, Motte, Schilke and Lis 2003). There are two sub-clouds: W43-main and W43-south. The W43-main is a “Z”-shaped filamentary cloud composed of two ridges (several pc long, elongated dense gas structures, Motte, Bontemps and Louvet (2018)). On the ~20 pc scale, observations of ^{13}CO (3-2) lines reveal two velocity components peaking at 82 km s^{-1} and 94 km s^{-1} that intersect at the western tips of the southern ridge, indicating cloud-cloud collisions (Kohno et al. 2021), in compliance with the origin of the wide-spread narrow-linewidth SiO emission. Adjacent to an extended HII region which surrounds a cluster of OB and Wolf-Rayet stars (Blum, Damineli and Conti 1999), the gas dynamics of W43-main may also be subject to strong stellar feedback mechanisms. There are a number of star-forming clumps inside W43-main, which are mostly infrared-dark, but some of them host UCHII regions. Particularly, the most massive clump, referred to as W43-MM1 (Figure 4.1), contains a gas mass of ~3000 $M_\odot$ with a spatial extent of 0.1-0.2 pc, representing the gas environment forming the most massive stars

(Sridharan et al. 2014,Louvet et al. 2014). ALMA observations achieving 0.01 pc resolution reveal that the underlying core population of W43-MM1 exhibits a top-heavy mass function (Motte, Bontemps and Louvet 2018), suggesting that direct mapping of the CMF to explain the origin of the IMF might not be adequate.

We aim to understand the physical properties, particularly of the extended gas structures at intermediate scale within the massive clumps of W43-main, with observations at moderate angular resolution of ~0.1 pc. Particularly, the highly turbulent cloud environment may introduce significant difference in the structure formation of the dense gas in the embedding clumps, compared to that associated with a "normal" molecular cloud, i.e. clouds that do not deviate much from the average Larson's linewidth-size relation. We conducted 3 mm observations with NOEMA and the IRAM 30m telescope towards 5 selected clumps identified on the 10 $''$ hydrogen column density map (Lin et al. 2016, Figure 4.1, Table 4.1), which are part of the southern ridge of the "Z"-shape W43-main complex. With multiple thermometers and densitometers, we constrain the detailed temperature and density structure of these clumps (Sect. 4.3.3). Concerning the gas dynamics associated with this particular region, we search for cloud colliding signatures at 0.1-1 pc scale (Sect. 4.3.4) which directly affect dense core and proto-cluster formation. Using multiple tracers from wide-band observations, we reveal multiple layers of dense gas structures and their velocity patterns (Sect. 4.3.5), and discover a population of cold dense cores whose properties are linked with parental clump and cloud dynamics (Sect. 4.3.7).

4.2 Observations and data reduction

The NOEMA pointed observations at 3 mm were taken between August to September 2019 with the D-array configuration in track-sharing mode. Nine antennas were used during the observations, covering a baseline range of 32-176 m. On-source observations were conducted in 20-30 minute intervals, which are interluded with observations on 1851+0035 as phase and amplitude calibrator. The adopted bandpass calibrators are 3C273, 3C454.3 and 3C345, and MWC349 was used as flux calibrator. The wide-band correlator PolyFix was used, which covers a simultaneous bandwidth of 31 GHz separated into 8 sidebands, with a fixed spectral resolution of 2 MHz (~ 6.2 km s^{-1} at 96 GHz). Multiple high-resolution spectral windows with 62.5 kHz (~ 0.2 km s^{-1}) channel spacing were placed to cover the molecular lines of interest.

We use the CLIC and MAPPING modules in the GILDAS software package [1] for calibration and imaging. The channels with line emission were identified by visual inspection with the IMAGER module and subtracted from the visibilities of low-resolution windows in in the full frequency range to form the continuum. Similarly, to extract line emission, the continuum level was fitted and removed from each of the high-resolution backend chunks. We cleaned the continuum and line cubes using the Hogbom algorithm (Högbom 1974) with natural weighting ($1/\sigma^2$, σ denotes the noise of the visibility) to maximize the point source sensitivity. The typical beam size is $4.''7$ at 96 GHz and varies with frequency in the wide-band dataset.

As a short-spacing complement to add extended molecular line emission, IRAM 30m observations towards these clumps were taken during November 2019 to June 2020 with the EMIR receiver. A region of $1.7'$ by $1.7'$ was mapped around each source with the on-the-fly observing mode. The focus was checked on Saturn every 4 hours and the pointing was determined every 1-1.5 hours on 1749+096

---

[1] http://www.iram.fr/IRAMFR/GILDAS/

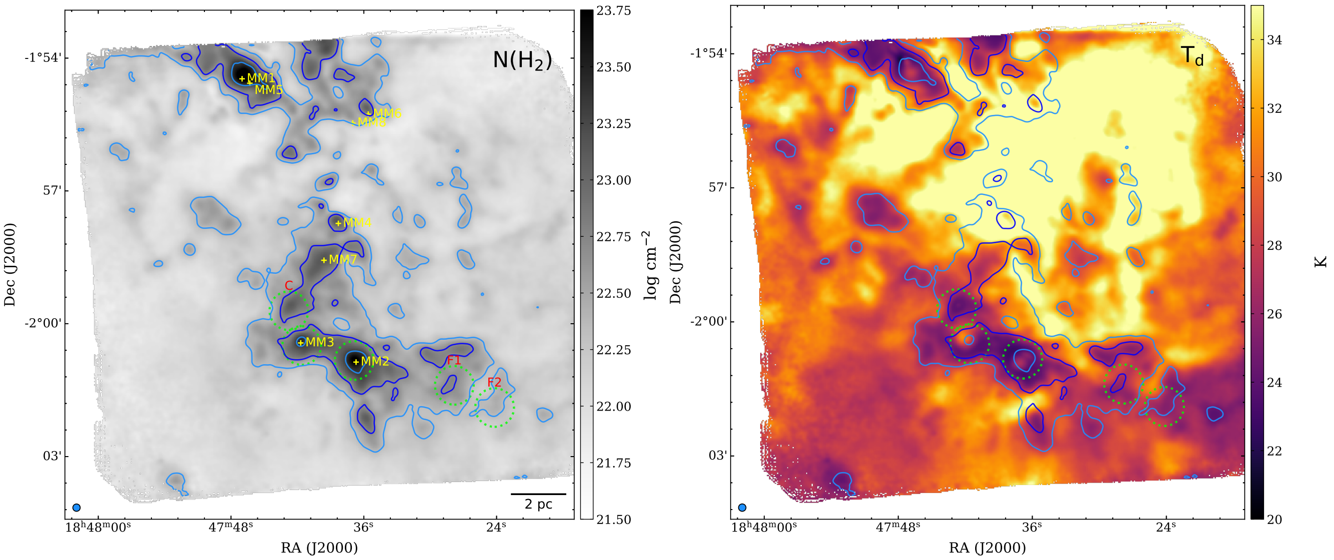

Figure 4.1: The molecular gas column density N(H$_2$) and dust temperature map T_d (truncated at 35 K for better contrast of the cold regions) of the W43-main molecular complex (10″ resolution, Lin et al. 2016). The three contour levels indicate column densities of 2.2×10^{22}, 5×10^{22}, and 2×10^{23} cm^{-3} (∼1 g cm^{-2}), respectively. The pointed observations towards the 5 selected clumps are shown in green circles of primary beam size (full-width half-maximum) at 96 GHz. In the *L*eft panel, the naming of the eight most massive clumps identified in Motte, Schilke and Lis (2003) based on BOLOCAM 1.1 mm survey are marked with yellow labels. Other target clumps are marked with red labels, following the names of C, F1 and F2.

or 1741-038. Data reduction follows the standard procedure with the CLASS module in GILDAS. The main beam efficiency ($\eta_{\rm mb}$[2]) was corrected to yield main-beam temperatures ($T_{\rm mb}$).

We used the short-spacing data from the 30m to generate pseudo-visibilities (task UVSHORT) which were added to the interferometry data. Joint imaging was then conducted to obtain combined spectral cubes; again we adopted the Hogbom cleaning algorithm to obtain the clean images.

Molecular lines of particular interest are listed in Table 4.3, which are all covered by the high-resolution chunks. For all these lines, we use the combined spectral cubes for the analysis.

4.3 Results

4.3.1 The 3 mm continuum

NOEMA 3 mm continuum maps of the 5 clumps are shown in Figure 4.2, overlaid on RGB maps of 8μm (Carey et al. 2009), 70μm (Molinari et al. 2010) and 5 cm. Clump MM2 and MM3 are resolved with one dominant compact source in the center. These two sources are slightly elongated along the north-south direction. For clump MM2, there is an adjacent substructure to the northwest of the central compact source. The location of this substructure coincides well with a series of condensations revealed by ALMA observations at 1.3 mm at 0.01-pc angular resolution (Cortes et al. 2019). For clump C and F2, there is no robust compact source detection towards the phase center. Clump F1

---

[2] https://publicwiki.iram.es/Iram30mEfficiencies

Table 4.1: Properties of the 5 target clumps in W43-main.

Source	R.A. (J2000)	Decl. (J2000)	Gas Mass^a (10^2 M$_\odot$)	Luminosity^a (10^3 L$_\odot$)	L/M (L$_\odot$/M$_\odot$)	Category	$V_{\rm LSR}$^{b} km s^{-1}
MM2	$18^{\rm h}47^{\rm m}36^{\rm s}.86$	-02°00′49.$^{\rm s}$8	38	58	15	70 μm bright	91.3
MM3	$18^{\rm h}47^{\rm m}41^{\rm s}.61$	-02°00′29.$^{\rm s}$5	19	51	26	UCHɪɪ	93.9
F1	$18^{\rm h}47^{\rm m}42^{\rm s}.77$	-01°59′42.$^{\rm s}$4	3.0	6.6	22	IR dark	89.5
F2	$18^{\rm h}47^{\rm m}27^{\rm s}82$	-02°01′23.$^{\rm s}$5	2.3	43	19	IR dark	85.5
C	$18^{\rm h}47^{\rm m}42^{\rm s}77$	-01°59′42.$^{\rm s}$4	7.6	12	16	IR dark	91.7

^{a}: Gas mass and luminosity are calculated above column density thresholds N$_{\rm thres}$: for MM2, MM3 and C, $N_{\rm thres}$ = 5×10^{22} cm^{-2}, for F1, $N_{\rm thres}$ = 4.5×10^{22} cm^{-2}, for F2, $N_{\rm thres}$ = 2.2×10^{22} cm^{-2}; the thresholds are chosen based on visual inspection of the N(H$_2$) and bolometric luminosity maps (derived from integrating SED profile) from Lin et al. 2016.

^{b}: The system velocities ($V_{\rm LSR}$) are with reference to Urquhart et al. (2018) based on finding the identical or nearest clumps.

Table 4.2: Source properties from 3 mm continuum emission.

Source	R.A.^{a} (J2000)	Decl.^{a} (J2000)	$F^b_{\rm int}$ (Jy)	$I^b_{\rm peak}$ (mJy arcsec^{-2})	Size^c (″)	$\sigma_{\rm rms}$ (mJy/beam)	Gas Mass ($M_\odot$)
MM2	$18^{\rm h}47^{\rm m}36^{\rm s}.80$	-02°00′54.$^{\rm s}$0	0.051	1.90	4.28	1.6	200
MM3^c	$18^{\rm h}47^{\rm m}41^{\rm s}.79$	-02°00′21.$^{\rm s}$7	0.463	7.40	7.75	1.6	900
F1	$18^{\rm h}47^{\rm m}27^{\rm s}.84$	-02°01′17.$^{\rm s}$0	0.029	0.24	7.93	0.4	350

Note– a: The coordinate corresponds to the position of the peak intensity.
b: The integrated intensity (above 5σ emission level) and peak intensity.
c: Radius R of the emission area A of >5σ, A = πR^2.
d: After subtraction of free-free emission.

exhibit a filamentary structure of ∼0.2 pc in width, extending up to ∼1.2 pc in length. We marked the three compact sources along the filament of F1 as F1-c0, F1-c1 and F1-c2 (Figure 4.2). The filament structure is only resolved partially, which truncates at the edge of the primary beam of our observations.

Clump MM3 is associated with an ultra-compact Hɪɪ (UCHɪɪ) region, which is the brightest UCHɪɪ in W43 (Bally et al. 2010). Assuming optically thin free-free emission, the intensity varies with frequency as $\nu^{-0.1}$. We re-scaled the VLA X-band (8.46 GHz) continuum[3] with (96/8.46)$^{-0.1}$. After convolution and regridding, the free-free contribution ($S_{\rm int\,free-free}$ = 0.24 Jy) to the 3 mm continuum was subtracted. The integrated flux, peak intensity and source size of the three clumps (MM2, MM3 and F1) extracted from 3 mm continuum are listed in Table 4.2. Assuming an average dust temperature of 30 K for MM2 and F1, and 100 K for MM3 (determined by the gas temperature in Sect. 4.3.3), and $\kappa_{100\,\rm GHz}$ = 0.245 cm^{-2} g^{-1}, a gas-to-dust ratio of 100, we derived 3 mm core masses, which are listed in Table 4.2.

---

[3] Obtained from NRAO archive: http://www.aoc.nrao.edu/ vlbacald/ArchIndex.shtml

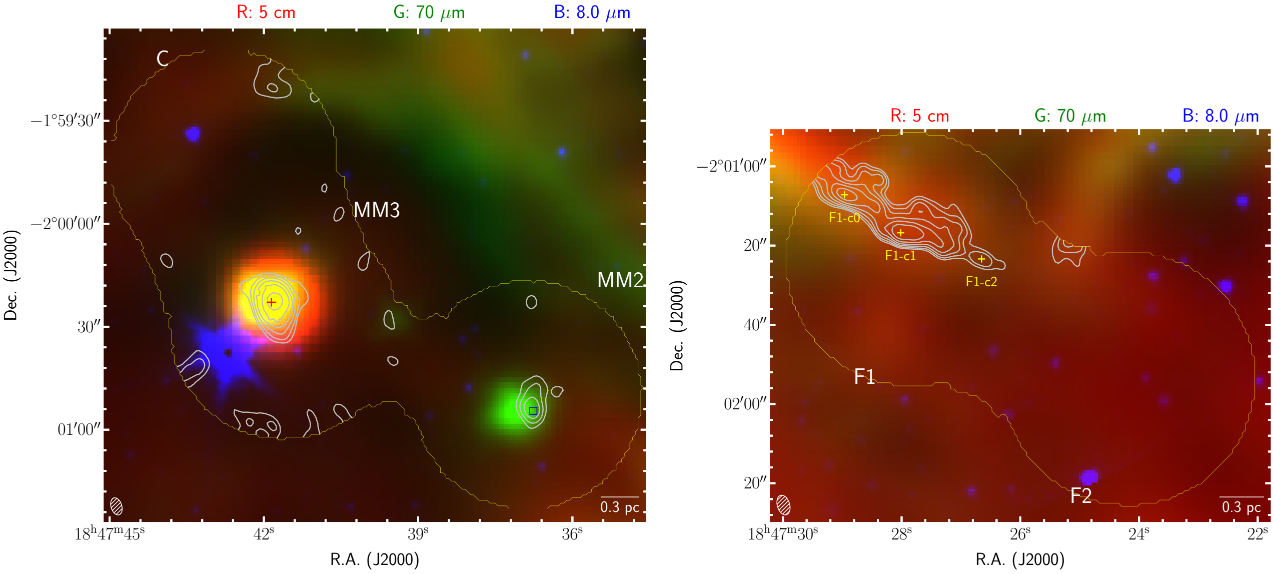

Figure 4.2: Three-color images of the clumps, where red is GLOSTAR 5 cm radio continuum, green is *H*erschel Hi-GAL PACS 70 μm, and blue is *S*pitzer 8.0 μm, overlaid with NOEMA 3 mm continuum contours. The beam of the 3 mm continuum is shown in the lower left corner. *L*eft: Target clump C, MM2 and MM3. The UCHII region (magenta cross) and OH maser (cyan square) are marked. Contour levels are logarithmic-spaced from $2\sigma_{\rm rms}$ ($\sigma_{\rm rms}$ = 1.6 mJy/beam) to 225.0 mJy/beam with 5 intervals. *R*ight: Target clump F1 and F2. Contour levels are logarithmic-spaced from $2\sigma_{\rm rms}$ ($\sigma_{\rm rms}$ = 0.4 mJy/beam) to 3.3 mJy/beam with 5 intervals. The three compact sources are marked with yellow filled circles.

4.3.2 Distribution of dense gas: multiple velocity components

There are multiple gas velocity components associated with the 5 clumps. To illustrate this, we present in Figure 4.5 and Figure 4.7 integrated intensity maps of the molecular lines CS(2-1), SO 2_3-1_2, $H^{13}CO^+$(1-0) and HC_3N (9-8) for the three clumps MM2, MM3, C in the north and two clumps F1, F2 in the south. The velocity intervals are chosen according to the line profiles of the averaged spectrum of CS (2-1) in the two regions. The average spectra towards the region containing clump MM2, MM3 and C, and region containing clumps F1 and F2, are shown in Figure 4.3-4.4. In these figures, the average spectra extracted towards the peak of each integrated intensity map of each velocity interval are also shown.

For the northern region, there are at least 3 velocity components peaking at velocity ranges of 80-92 km s^{-1}, 92-96 km s^{-1} and 96-108 km s^{-1}, respectively. Comparing the molecular gas distribution to the 3 mm continuum, source MM2 has peak line emission in good correlation with the continuum emission, while source MM3 has line emission peaking offset from the continuum, indicating strong absorption towards the densest UCHII region. Especially, the $H^{13}CO^+$ line shows absorption around 97-101 km s^{-1} at the continuum peak. We discuss the absorption feature further in Sect. 4.3.6. The strongest emission of these lines all coincide with clump MM2. Compared to $H^{13}CO^+$(1-0) and HC_3N (9-8), CS(2-1) and SO 2_3-1_2 show very extended emission in the 80-92 km s^{-1} (most red-shifted) range, prominent in the whole northwestern region within the primary beam. In this velocity range, towards clump C, the morphology of these two set of lines is also different, with CS(2-1) and SO

Table 4.3: Line parameters for the 3 mm molecular lines used in the analysis.

Transition	Rest frequency (GHz)	$E_{\rm up}$ (K)	$n_{\rm crit}$ [a] ($\rm cm^{-3}$)
HC_3N (9-8)	81.881	19.6	5.6×10^4 [b]
CS (2-1)	97.980	7.1	8.9×10^4
$H^{13}CO^+$ (1-0)	86.754	4.2	3.5×10^4
CH_3OH 2(1)-1(1) *E*	96.755	28.0	2.2×10^5
CH_3CCH 5(0)-4(0)	85.457	12.3	2.8×10^3
CH_3CCH 6(3)-5(3)	102.530	82.0	4.0×10^3
CCH $1_{2,2}$-$0_{1,1}$	87.407	4.2	9.3×10^3
SO 2(3)-1(2)	99.299	9.2	4.3×10^4
SiO (2-1)	86.846	6.3	4.8×10^4 [b]
H_2CS 3(0,3)-2(0,2)	103.040	9.9	3.0×10^4 [b]
H_2CS 3(2,1)-2(2,0)	103.051	62.6	1.1×10^4 [b]
NH_2D $1_{1,1}$-$1_{0,1}$	85.926	20.7	4.3×10^4 [b]

Note: a: The critical density $n_{\rm crit}$ is calculated assuming a gas kinetic temperature of 30 K with no optical depth correction. b: Based on calculation with collisional rates with para-H_2 (reference for HC_3N from Faure, Lique and Wiesenfeld 2016, for SiO from Balança et al. 2018, for H_2CS from Wiesenfeld and Faure 2013, for NH_2D from Daniel et al. 2014).

2_3-1_2 showing elongated structures roughly along the north-south direction, and $H^{13}CO^+$(1-0) and HC_3N (9-8) structures along the northwest-southeast direction. Clump MM3 hosts many sub-regions showing clumpy emission lying in the south of its 3 mm continuum, which are present in all lines of the velocity ranges 92-96 km s^{-1} and 96-108 km s^{-1}. Toward clump MM2 in the 92-96 km s^{-1} velocity range, the emission of CS (2-1) line is very weak compared to all the other lines, but appears again in the blue-shifted 96-108 km s^{-1} range, indicating absorption. In Figure 4.24, the spectra extracted towards the 3 mm continuum peak of MM2 and MM3 show the absorption dips. Comparing the emission morphology of the 3 velocity ranges, it seems the emission of the red-shifted velocity component and the blue-shifted one intersect at the location of clump MM3, and overlap at clump MM2. We discuss this feature in Sect. 4.3.4, which points to a possible cloud-cloud collision.

The southern region displays a velocity field of a higher complexity, showing at least 5 components, in velocity ranges of 76-82, 82-88, 88-93, 93-97.5 and 97.5-103.5 km s^{-1}. Clump F2 has dominant emission separated in two velocity ranges 76-82 km s^{-1} and 88-93 km s^{-1}, and appears rather compact in the $H^{13}CO^+$(1-0) and HC_3N (9-8) emission, while Clump F1 shows emission in 4 velocity ranges except 76-82 km s^{-1}. The morphology of the molecular line emission of clump F1 is quite complex, which seems to be composed of 3 parallel filamentary structures in the east-west direction in the velocity range of 88-93 km s^{-1}. Interestingly, from the integrated intensity maps of $H^{13}CO^+$(1-0) and HC_3N (9-8) in the velocity range 93-97.5 km s^{-1}, the filament associated with clump F1 is directed toward the northeast-southwest. Except for the core F1-c2, the filament seen in the 3 mm continuum of F1 appears mostly offset from the molecular gas emission. The peak emission of some of the integrated intensity maps is truncated at the edge of primary beam, due to the presence of an adjacent massive clump in the north of F1 (Figure 4.1). This also introduces some imaging defects (most apparent from the third panel from the left in Figure 4.7). Due to the limited spatial coverage, we cannot obtain a full picture of the dense gas distribution towards the southern region.

In Figure 4.6 and 4.8 we show additionally the channel maps of same velocity ranges of l-C_3H (9/2-7/2), CCH $1_{2,2}$-$0_{1,1}$, CH_3OH $5_{1,5}$-$4_{0,4}$, and $HOCO^+$ $4_{0,4}$-$3_{0,3}$ lines, and respective spectra in Figure 4.3 and 4.4. Especially for the G30.7 region containing clump MM2, MM3 and C, the extended l-C_3H (9/2-7/2) line emission appears only in the most blue-shifted velocity range (80-92 km s^{-1}, see also Figure 4.3), which is likely associated with the PDR surrounding the OB cluster in the north-west direction of W43-main. The extension of l-C_3H is even larger in region of clump F1 and F2, showing in a consistent blue-shifted velocity ranges (76-93 km s^{-1}). The l-C_3H line emission is present and appear compact with clump MM2, which may delineate a small PDR in the center of this relatively early-stage clump.

4.3.3 Gas temperature and density distribution from LTE and non-LTE modeling

To estimate the clump gas temperature and density, we adopted the CH_3CCH (6-5) and (5-4) ladders as main thermometers, and CH_3OH (2-1) A/E lines as densitometers. CH_3CCH is widely distributed in lukewarm gas of relatively evolved massive star-forming clumps (Molinari et al. 2016) to trace the bulk gas component. Whenever detected, we also use H_2CS (3-2) and CH_3CHCN (9-8) lines in the band which cover a range of upper energies allowing to derive rotational temperatures. The H_2CS and CH_3CCH emission (at comparable energy levels) cover similar spatial scales, while the emission of CH_3CHCN is confined to a centralized region of clump MM2. The line parameters of these transitions and the properties of the observed line emission are listed in Table 4.4.

To fit the observed line profiles, we utilised the XCLASS package to construct single-layer (isothermal) LTE models. For regions where multiple velocity components are seen from CH_3CCH and H_2CS lines, e.g. the central regions of clumps MM3, C, and F1 (Figure 4.9-4.10), we attempt to describe the line profiles with two independent gas components which do not radiatively interact with one another. Particularly, such decompositions yield for clump MM3 and C a narrow velocity component of hot gas and a broad velocity component of relatively cold gas (Figure 4.9). For clump F1, it seems there are more than two velocity components (Figure 4.10), but the sensitivity level is not high enough, especially for the higher K ladders, to ensure a robust identification. We therefore retain a two-component fit in this case.

We conducted pixel-based fits to obtain temperature maps ($T_{\rm rot}$) for each molecule. For each pixel the CH_3CCH and H_2CS lines are modelled by both one-component and two-component models. If the reduced χ^2 for the one-component model is 2 times larger than that of the two-component model, we adopt the two-component fit. For both the central region of clump C and MM3, two-component solutions fit better to the observed line profiles. Clump MM2 exhibit two-component velocity features around the region of the most prominent emission. The obtained maps of rotational temperature $T_{\rm rot1}$ and $T_{\rm rot2}$, line-width $\sigma_{\rm rms1}$ and $\sigma_{\rm rms2}$, and centroid velocity $V_{\rm c1}$ and $V_{\rm c2}$ are shown in Figure 4.11-4.20. After performing the fits, these maps are generated as follows: the velocity map by pixels where one-component model suffices is filled by one velocity from the two-component pixels, and the full map composes a more continuous velocity ($V_{\rm c1}$) map. This is done by calculating the median velocity of all adjacent single-component pixels and filling the periphery two-component pixels with

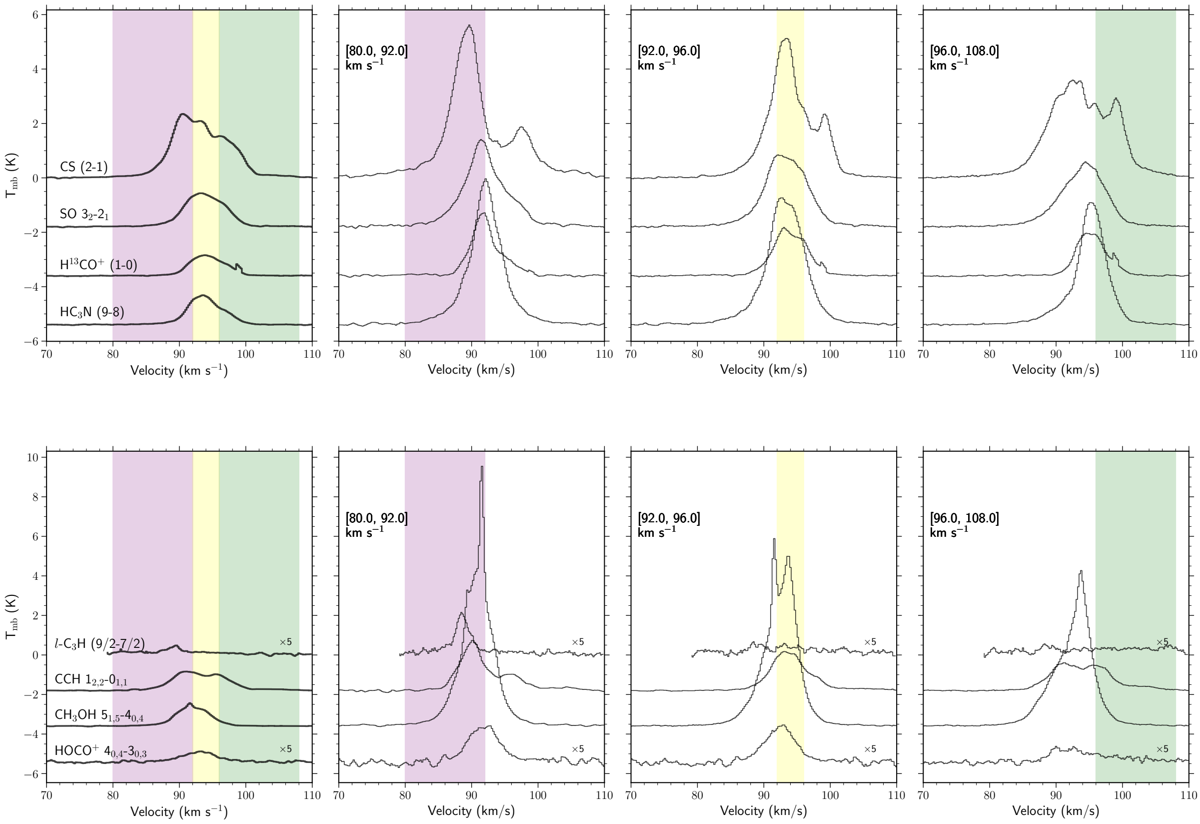

Figure 4.3: The spectra observed toward the region containing clumps MM2, MM3 and C. In the *left panel* the average spectra towards the full region of all three clumps are shown. The velocity components visually identified from averaged CS (2-1) spectrum are shown by filled regions, indicating their velocity ranges. In the other panels, average spectra towards region(s) of larger than 95% quantile of peak integrated intensity maps (the region within magenta contours shown in each panel of Figure 4.5) of respective velocity ranges are shown; each velocity range is indicated in the plot. The intensity of $HOCO^+$ and l-C_3H is artificially enlarged by 5 times for better comparison.

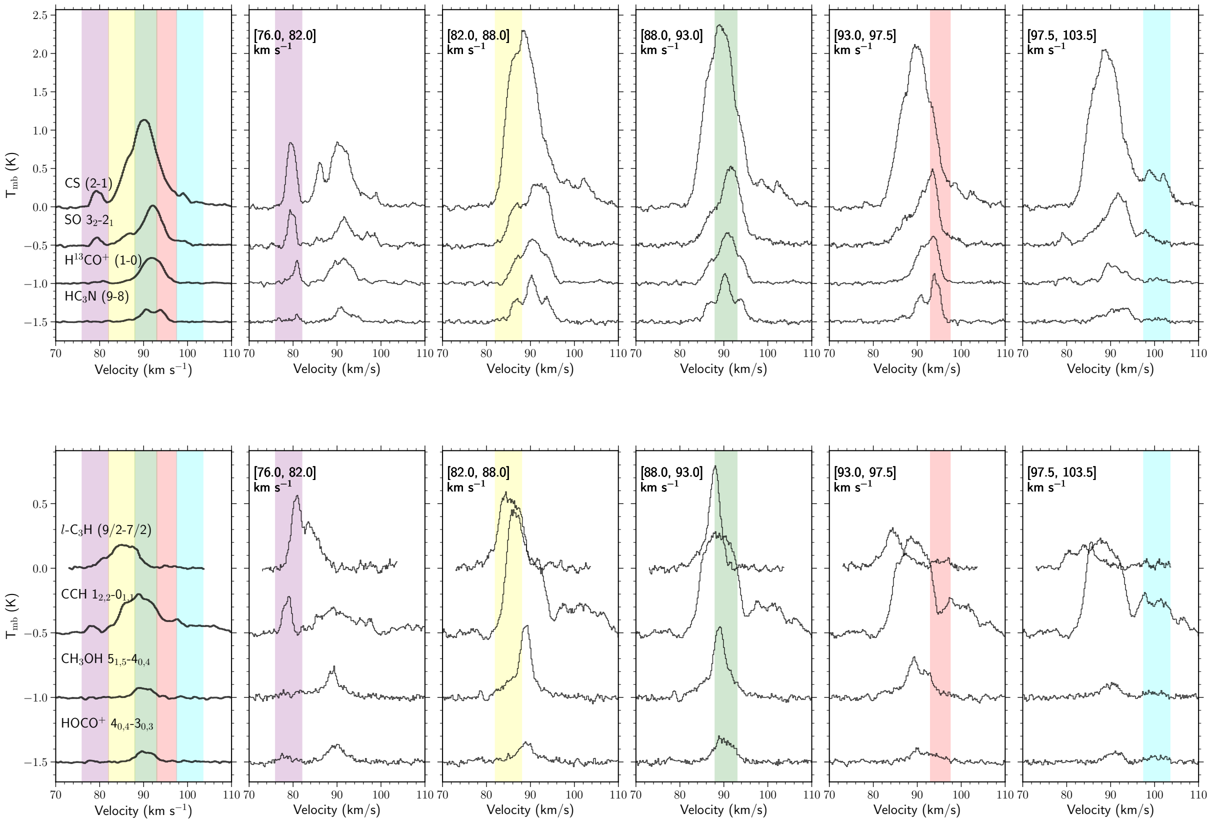

Figure 4.4: Same as Figure 4.3, but shows the spectra towards the region containing clumps F1 and F2.

one velocity of the two-component models that is closer to the median value. The procedure is done iteratively untill all pixels are filled. The other maps are generated correspondingly.

The derived gas rotational temperature maps from the thermometers are shown in Figure 4.11-4.13. The gas temperature distributions of CH_3CCH and H_2CS in general show similar features. Clump C has low temperature mostly lower than 25 K. Especially, one of the two gas components has temperature just above 10 K (right panel of Figure 4.11). Clump MM3 has an overall higher temperature (30-45 K) although its temperature distribution does not have a strong peaking (at the line emission peak). Clump MM2 shows a significantly higher temperature at the continuum peak, with the $T_{\rm rot}$ derived by CH_3CCH reaching $\gtrsim$50 K and that by CH_3CHCN of ~130 K. The difference between the two $T_{\rm rot}$ is expected as CH_3CCH emission is mostly contributed from extended gas of the colder clump envelope. The existence of CH_3CHCN and the derived high $T_{\rm rot}$ indicate the inner region of MM2 appears to be a hot-core like structure. Clump F1 and F2 have temperatures appearing rather uniform and below 25 K, showing similar level of temperature as clump C. Although in general the comparison of the overall temperature levels between the 5 clumps are positively correlated with their different luminosities, the high temperature towards central MM2 stands out, and MM2 presents a steeper temperature gradient at the probed scales (0.1-0.5 pc).

We conducted one-component Gaussian fits of CH_3OH (2-1) A/E lines (for each K component) for

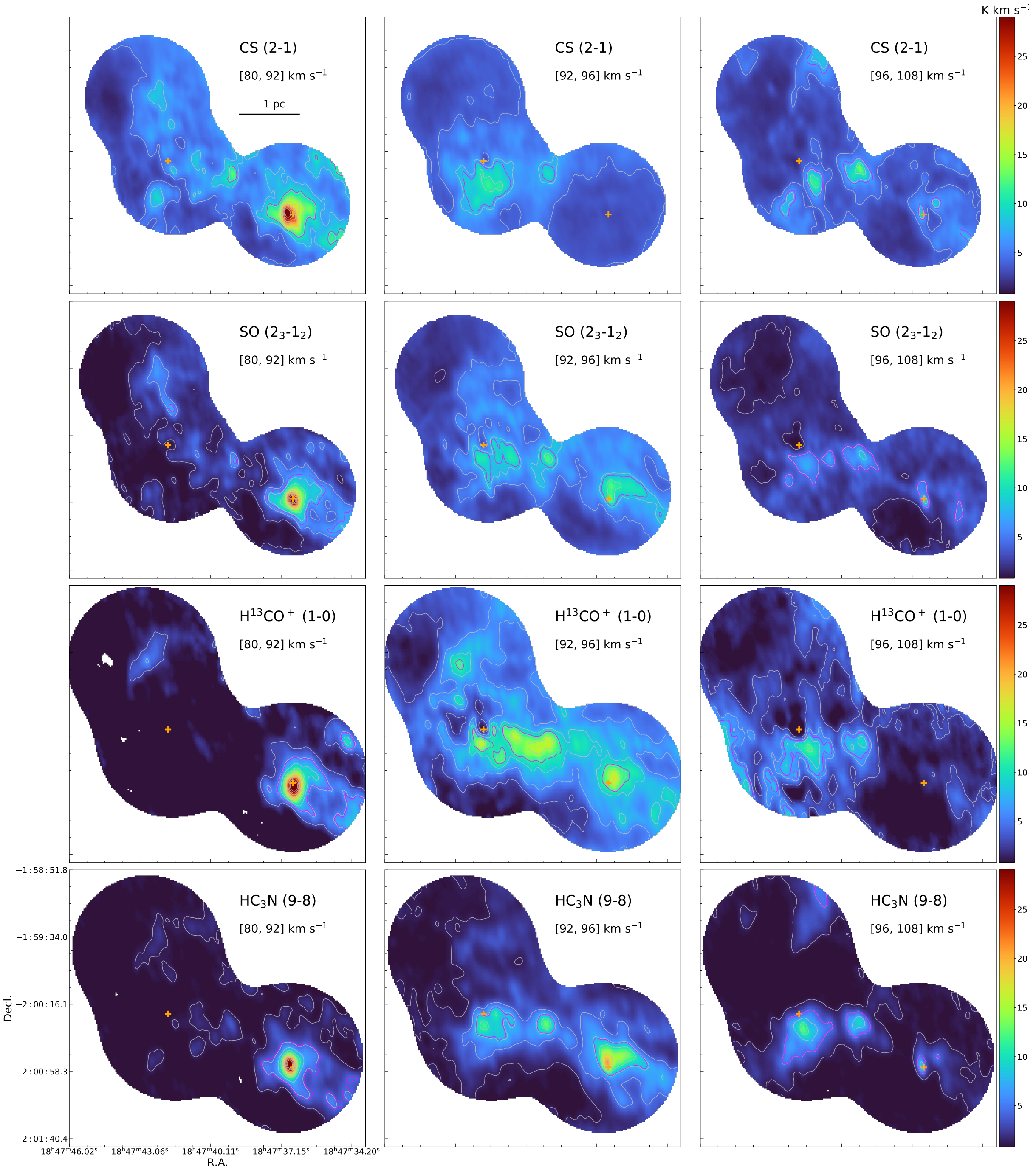

Figure 4.5: The integrated intensity maps of CS (2-1), SO (2_3-1_2), H^{13}CO$^+$ (1-0), and HC$_3$N (9-8). The velocity ranges for integration is indicated in each subplot, which are selected based on the present velocity components of the overall average spectrum of CS (2-1) line. The 3 mm continuum peaks of clump MM3 and MM2 are indicated as orange crosses. Contour levels starts from 1.6 K km s^{-1} to the peak integrated intensities of the [80, 92] km s^{-1} range with 8 uniform intervals. The peak integrated intensities are 76.4, 29.0, 12.5, 41.9 K km s^{-1} for CS (2-1), SO (2_3-1_2), H^{13}CO$^+$ (1-0), and HC$_3$N (9-8), respectively. The magenta contours indicate the level of 95% quantile in each integrated intensity map, within which the average spectrum is extracted and shown in Figure 4.3 (three panels in the right) of respective velocity range.

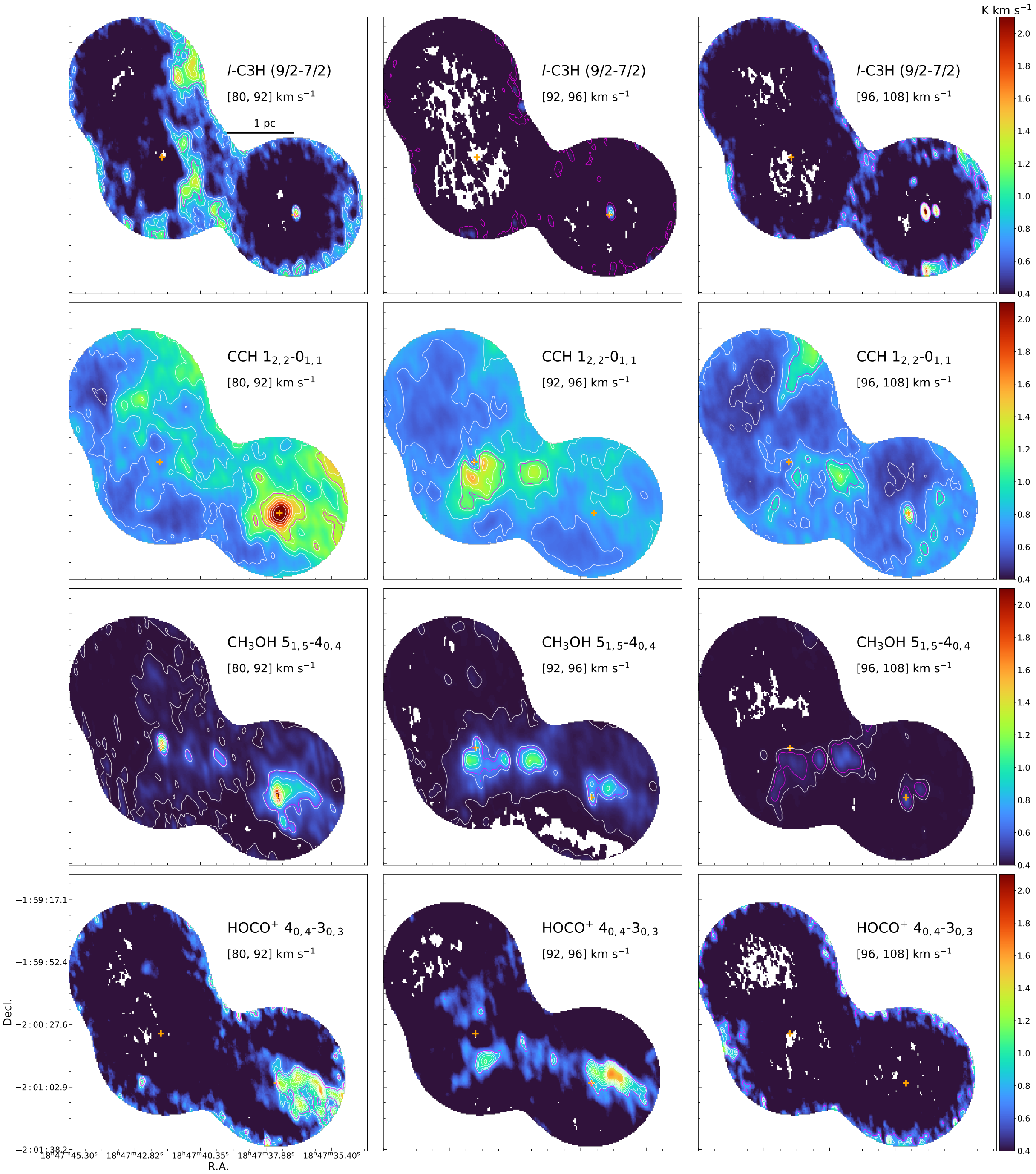

Figure 4.6: Same as Figure 4.5, but for molecular lines of *l*-C_3H (9/2-7/2), CCH $1_{2,2}$-$0_{1,1}$, CH_3OH $5_{1,5}$-$4_{0,4}$, and $HOCO^+$ $4_{0,4}$-$3_{0,3}$ lines. Contour levels starts from 0.8 K km s^{-1} for *l*-C_3H and $HOCO^+$, 1.2 K km s^{-1} for CCH and CH_3OH, to the peak integrated intensities of the [80, 92] km s^{-1} range with 8 uniform intervals. The peak integrated intensities are 2.7, 13.4, 95.0, 1.4 K km s^{-1} for *l*-C_3H (9/2-7/2), CCH $1_{2,2}$-$0_{1,1}$, CH_3OH $5_{1,5}$-$4_{0,4}$, and $HOCO^+$ $4_{0,4}$-$3_{0,3}$ lines, respectively.

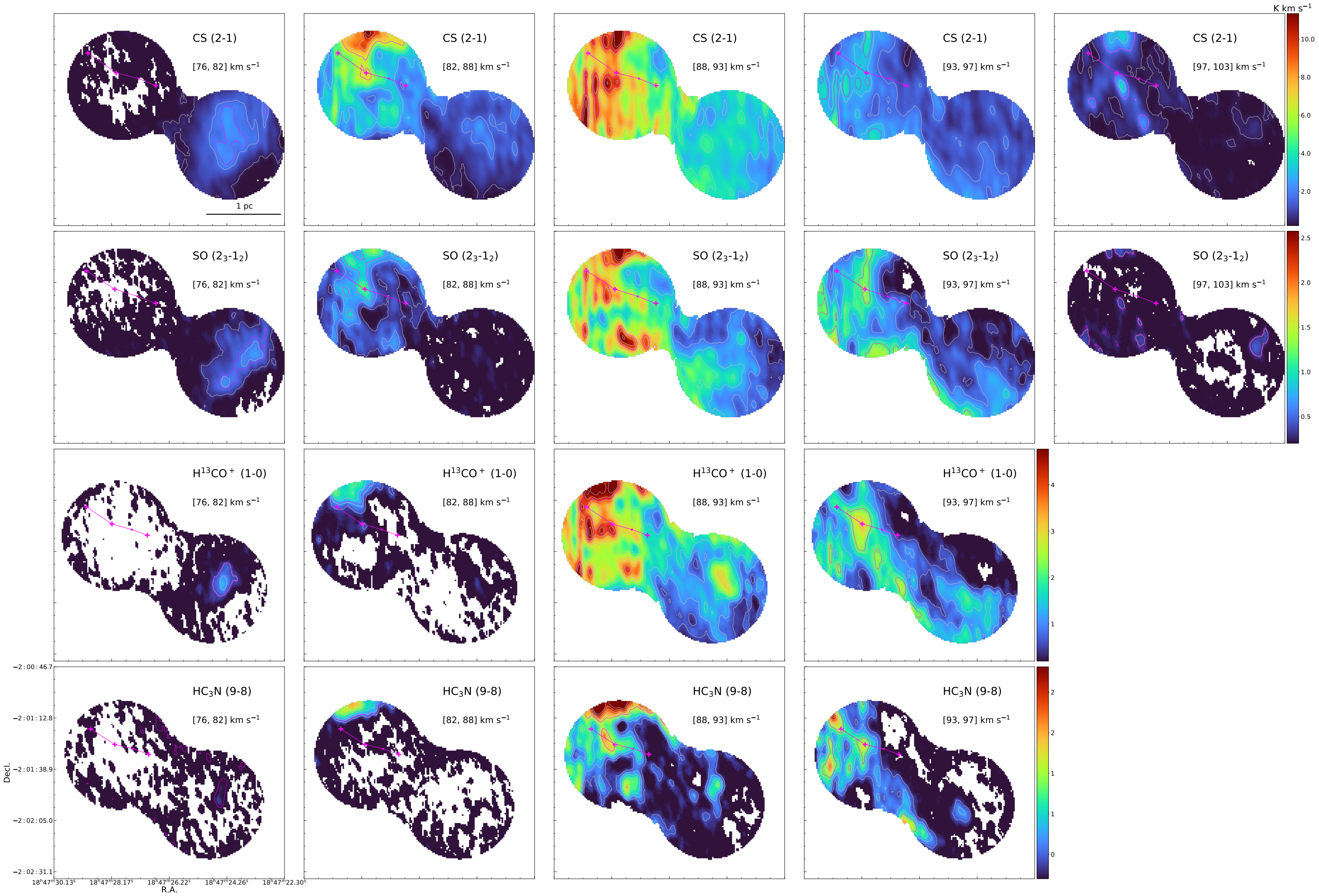

Figure 4.7: Same as Figure 4.5, but for the southern region containing clump F1 and F2. The 3 mm continuum peaks of clump F2 are indicated as orange crosses and linked with lines to indicate the filament ridge. Contour levels starts from 0.4 K km s^{-1} to the peak integrated intensities of the [88, 93] km s^{-1} range with 8 uniform intervals. The peak integrated intensities are 11.3, 4.8, 2.8, 2.6 K km s^{-1} for CS (2-1), SO (2_3-1_2), H^{13}CO$^+$ (1-0), and HC$_3$N (9-8), respectively. The magenta contours indicate the level of 95% quantile in each integrated intensity map, within which the average spectrum is extracted and shown in Figure 4.4 (five panels in the right) of respective velocity range. Integrated intensity maps of certain velocity range for some lines are trimmed if the emission is not significant.

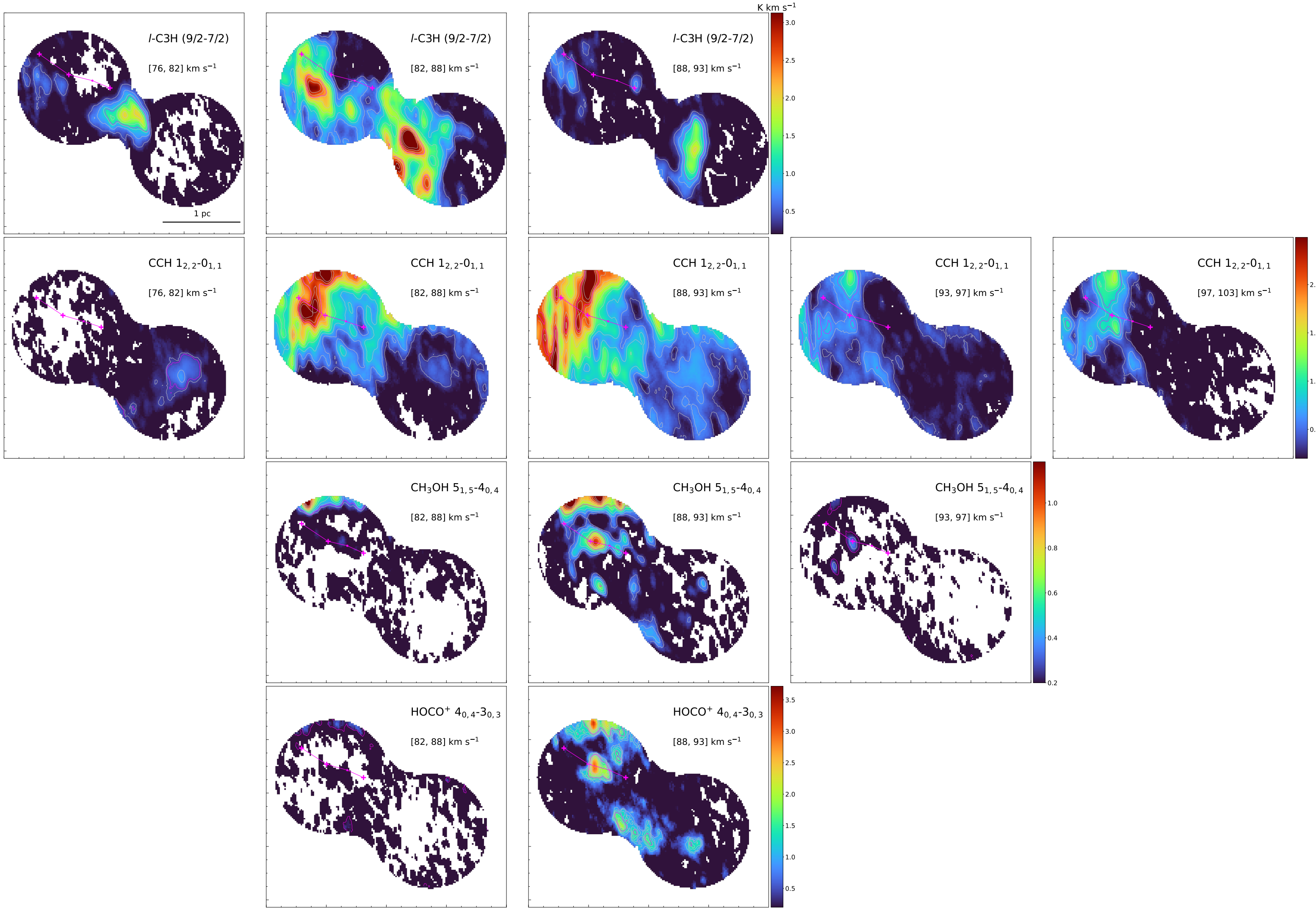

Figure 4.8: Same as Figure 4.7, but for molecular lines of *l*-C$_3$H (9/2-7/2), CCH $1_{2,2}$-$0_{1,1}$, CH$_3$OH $5_{1,5}$-$4_{0,4}$, and HOCO$^+$ $4_{0,4}$-$3_{0,3}$ lines. Contour levels starts from 0.4 K km s^{-1} to the peak integrated intensities of the respective velocity range with 8 uniform intervals. The peak integrated intensities are 3.1, 3.7, 2.5, 0.8 K km s^{-1} for *l*-C$_3$H (9/2-7/2), CCH $1_{2,2}$-$0_{1,1}$, CH$_3$OH $5_{1,5}$-$4_{0,4}$, and HOCO$^+$ $4_{0,4}$-$3_{0,3}$ lines, respectively.

each pixel, and then adopted RADEX modelling to construct hydrogen volume density (n(H_2)), and column density N_{CH_3OH} maps (assuming an A-to-E ratio of 1), with T_{kin} fixed to the one-component T_{rot} map derived from CH_3CCH lines (for available pixels). As already shown by the other molecular lines aforementioned, the CH_3OH (2-1) lines are likely also composed of more than 1 velocity component, but the confusion between different K ladders in this line series inhibits a robust multi-component Gaussian decomposition. The more uncertain decomposition of line intensities propagates to the RADEX modeling and will introduce a large bias in the parameter estimate of n(H_2) and N_{CH_3OH}. We therefore retain a one-component Gaussian fit of CH_3OH (2-1) lines. We will explore the possibility of guided Gaussian decomposition for such lines with the aid of other lines that show distinct velocity components in the future, to properly estimate the physical parameters of multiple velocity components.

The details of the MCMC RADEX modeling procedure follow that described in Chapter 3. The obtained parameter maps n(H_2), N_{CH_3OH} (A/E), centroid velocity V_c and linewidth σ_{rms} from one-component Gaussian fit, are shown in Figure 4.14 and 4.15 (right panel). The two most prominent localised dense gas enhance reside with clump MM2 and MM3, respectively. The maximum gas densities reach $\sim 10^7$ cm^{-3} and beyond. Within clump C, the gas densities also show increment around the peak emission but the density level ($10^{5.5}$-10^6 cm^{-3}) is close to the bulk gas density of MM2 and MM3. The central density enhancement ($\sim 10^{7.5}$ cm^{-3}) of MM2 coincides with the continuum peak and appears more extended towards the west-east direction, linking with an elongated density enhance ($\sim 10^{6.5}$ cm^{-3}) to the north which has a curved morphology. Cortes et al. 2019 resolved several cores northwest of the central cores in MM2, which lie close to the attaching region of the elongated density enhancement and the center. For MM3, the central density enhancement ($\sim 10^{6.5}$-10^7 cm^{-3}) is less prominent and less concentrated. It peaks slightly to the south of the continuum peak. There are several smaller pockets of dense gas enhance distributed in clump MM3, which are ~0.1-0.2 pc in size, remaining mostly unresolved. In Section 4.3.4, we compare the distribution of the dense gas enhance of clump MM2 and MM3 with velocity structures (linewidths and velocity field) of the CH_3OH (2-1) lines, and with velocity wings of SiO (2-1) and CH_3OH $5_{1,5}$-$4_{0,4}$ lines.

The n(H_2) map (Figure 4.15) of clump F1 presents enhance at the CH_3OH emission peak near F1-c1 and in the north (not fully covered by our observations, as can be seen from the unclosed contours in Figure 4.15), and also shows distributed density peaks at the edge of the extended CH_3OH emission. The maximum gas densities reach only $\lesssim 10^6$ cm^{-3}. The F1-c1 core has an averaged gas density of $10^{5.5}$ cm^{-3} and located at the CH_3OH emission peak. Clump F2 has gas densities mostly below 10^5 cm^{-3}.

4.3.4 The velocity field and linewidth distribution of the G30.7 region

Previous single-dish observations revealed wide-spread emission of SiO (2-1) throughout the ridges of W43-main, which is interpreted as arising from low-velocity shocks created by cloud collisions (Nguyen-Luong et al. 2013). However there is ambiguity as to whether the detected low-velocity SiO emission originates from outflows of embedded YSOs or cloud collisions. To search for cloud-cloud collision evidence and understand the gas dynamics at 0.1 pc scale, we present here the velocity fields measured by our high-angular resolution observations of the SiO (2-1) line, and examine the spatial correlations between the excessive line wings of SiO and dense gas pockets indicated in the n(H_2) map (Figure 4.14). We also make comparisons with the velocity field and linewidth seen by the thermometers CH_3CCH and H_2CS and the densitometers CH_3OH (2-1) line series.

The distribution of the SiO emission (integrated intensity map) is shown in the left panel of Figure

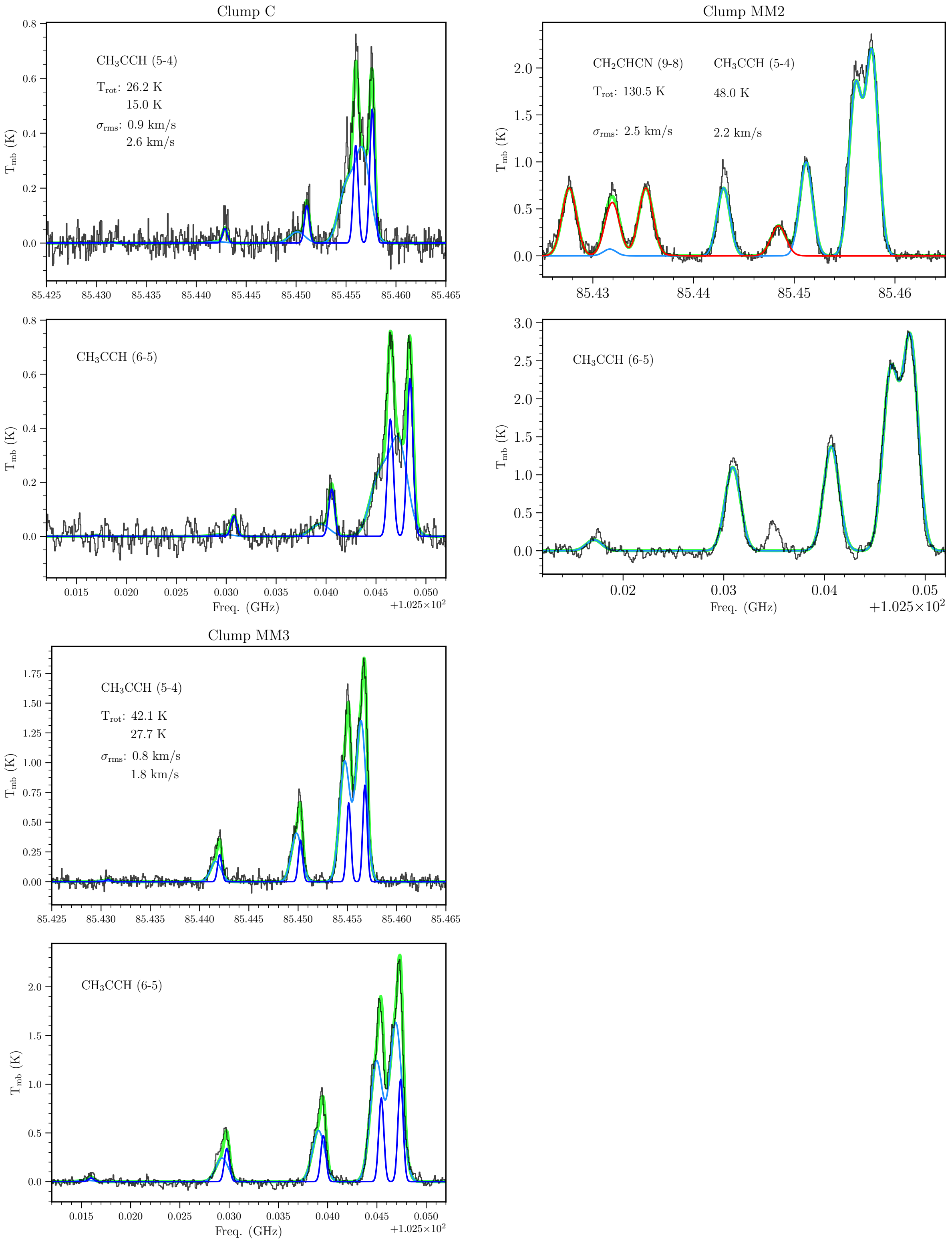

Figure 4.9: CH$_3$CCH spectra towards the peaks of the three clumps in the North: clump C, MM2, and MM3. For clump MM2, the CH$_2$CHCN emission is present and fitted (red line). In all plots, whenever there are more than one velocity component, both the composite line profile of the fits (green line) and individual fit (blue lines) are indicated.

Table 4.4: Information of lines used as thermometers.

			C		MM3		MM2		F1		F2	
Molecule	Transition	E_{up} (K)	T_{mb} (K)	ΔV (km s^{-1})	T_{mb} (K)	ΔV (km s^{-1})	T_{mb} (K)	ΔV (km s^{-1})	T_{mb} (K)	ΔV (km s^{-1})	T_{mb} (K)	ΔV (km s^{-1})
CH_3CCH	5(0)-4(0)	12.3	0.75	5.18, 2.36	1.80	1.88, 4.29	2.4	5.20	0.38	2.1, 0.6	0.20	1.5
	6(3)-5(3)	81.5	0.1		0.65		1.3		–		–	
H_2CS	3(1,3)-2(1,2)	22.9	0.65,0.62	3.41,3.20	3.0	2.33,5.19	5.50	4.20,11.70	0.20,0.12	2.18,5.69	0.10	2.0
	3(0,3)-2(0.2)[a]	9.89	0.60,0.40		1.78		3.80		0.15,0.08		0.08	
	3(2,2)-2(2,1)[a]	62.6										
	3(2,1)-2(2,0)	62.6	<0.05		0.20		1.0		<0.05		<0.05	
CH_2CHCN[b]	9(3,7)-8(3,6)	39.9					0.80	5.89				
	9(6,3)-8(6,2)	98.2					0.75					
	9(3,6)-8(3,5)	39.9					0.80					
	9(7,2)-8(7,1)	126.2					0.30					

Note: The peak intensity (T_{mb}) and corresponding line-width ($\Delta V = 2.355\sigma_{rms}$) are shown for each source. Whenever there are two velocity components, both line-widths are listed while the peak intensity is contributed from both components as a single value.

For CH_3CCH only two representative transitions are shown whilst for both (5-4) and (6-5) line series all the k ladders are used in the fits, whenever robustly detected.

a. The two lines blend with each other. The listed line parameters are contributed from both lines.

b. Vinyl Cyanide (CH_2CHCN) is only detected towards the center of clump MM2.

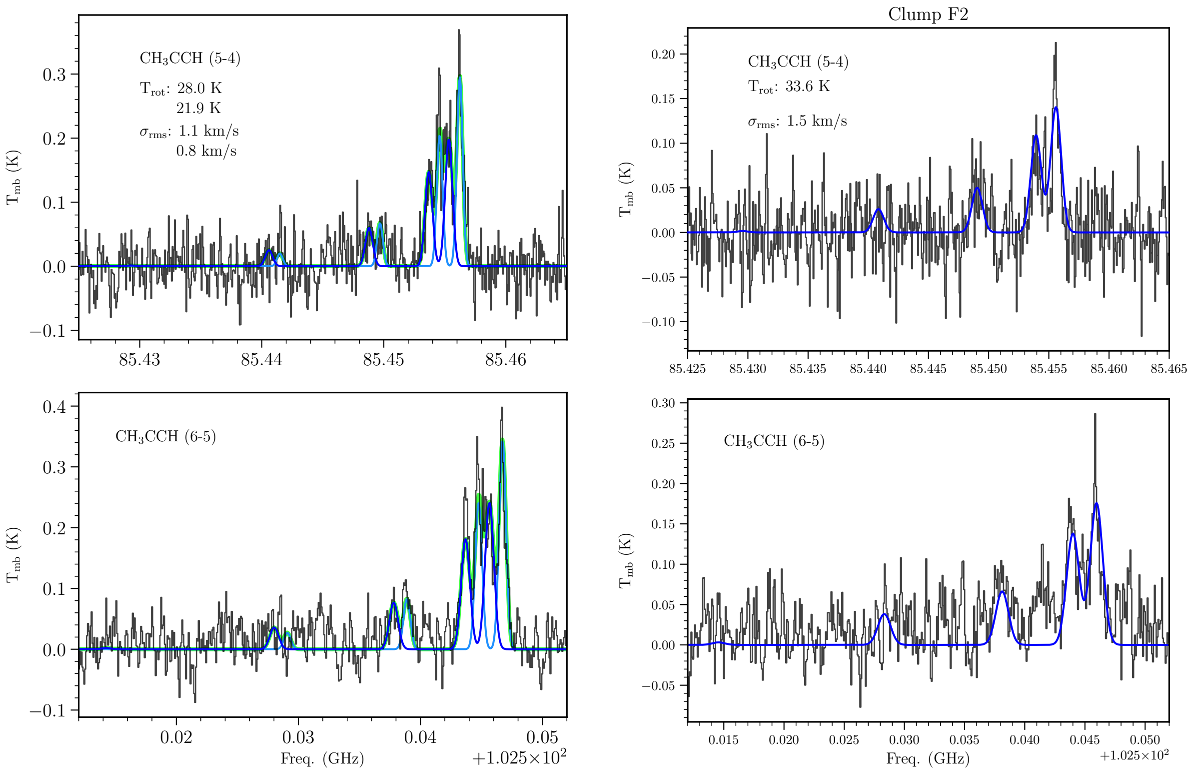

Figure 4.10: Same as Figure 4.9, but for the two clumps in the South, clump F1 and F2.

4.16. The two sub-regions showing the most intense SiO emission are located in the central region of clump MM2, and at the position of (35″, -10″) (Δα, Δδ) offset from MM2, respectively. The gas velocity field traced by SiO shows a pattern of complementary distribution: the velocity changes from blue-shifted to red-shifted and blue-shifted (compared to the $V_{\rm LSR}$ of MM3) again from north to south, covering clump C to MM3 and then MM2. A similar picture is also revealed in the integrated intensity maps of different velocity ranges from other lines shown in Figure 4.5. To illustrate this, we separated the blue-shifted and red-shifted velocity ranges and integrated the two velocity ranges individually for SiO. The separated integrated maps are overlaid together in Figure 4.16 (panel (b)). The distribution of the two parts present a “Y”-shaped structure. Particularly, the density enhance of clump MM3 (shown as colored contours) seems to follow the vertex region of the “Y” shape tightly. While the central region of clump MM2 lies in-between the two velocity parts and extends further to the north (by the curved elongated structure).

In the lower panel of Figure 4.16 the regions of density enhancement (>10^6 cm^{-3}, see contours in panel (a) of Figure 4.16 derived from the n(H_2) map presented in Figure 4.14), are shown together (as shaded regions) with the position-velocity (PV) cuts (each averaged over a width of 0.35 pc indicated in panel (b) of Figure 4.16) along the “Y"-shape structure, which are extracted from SiO (2-1) line and CH_3OH $5_{1,5}$-$4_{0,4}$ spectral cubes. The line wings of both lines are mostly within 8 km/s (terminal velocity) around the $V_{\rm LSR}$. Clearly, along the cuts, SiO lines show more spatially extended velocity wings compared to CH_3OH $5_{1,5}$-$4_{0,4}$, as seen especially from the ultra broad red-shifted wing at offset 1.0-2.4 pc from the PV cut of M, which also extends to a higher terminal velocity. The terminal

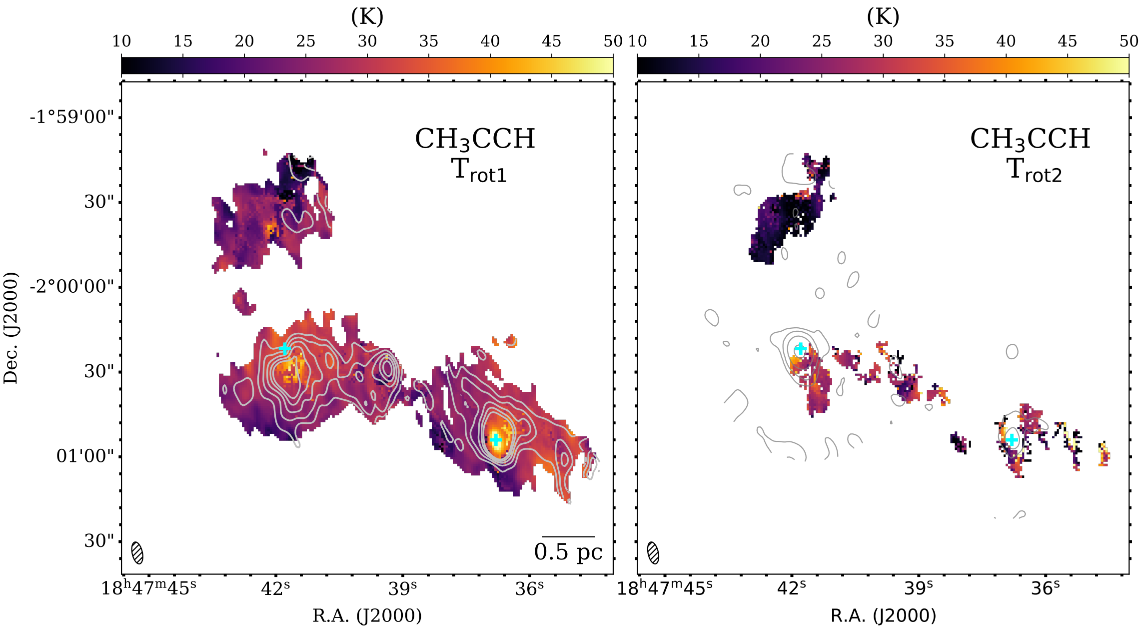

Figure 4.11: The rotational temperature maps derived by CH_3CCH (6-5) and (5-4) lines. The left and right panel show the temperatures from the two-component LTE models separately. In the left panel the contours represent integrated intensity map of CH_3CCH 5_2-4_2 line. The velocity range for integration is 80-100 km s^{-1}, and the contour levels are from 1.0 K km s^{-1} (5 σ) to 2 K km s^{-1} (0.3 times peak emission value of MM2) with 5 uniform intervals. In the right panel, the contours represent the 3 mm continuum emission, and are logrithmic-spaced from $2\sigma_{\rm rms}$ ($\sigma_{\rm rms}$ = 1.6 mJy/beam) to 225.0 mJy/beam with 5 intervals (same as Figure 4.2). In both plots, the cyan crosses indicate the position of the peak intensity of 3 mm emission.

velocities of SiO reach out to $V_{\rm LSR}\pm15$ km s^{-1} (as seen from the U cut and M cut, respectively). There are also a few prominent components that appear asymmetric in the SiO PV map, i.e. components with no counterparts in other velocity regime. These single components appear mostly blue-shifted (indicated by yellow rectangles) and do not have correspondingly excessive CH_3OH wings. It seems the central region of clump MM2 (offset 1.8-3.2 pc) around the continuum (illustrated as blue and purple shaded regions around the blue dotted line) coincides with double-peaked velocity wings, while the density enhance associated with the periphery of the continuum (UCHII region) in MM3 corresponds to a damp of velocity wing (as seen from the M cut of SiO PV map). The sub-regions of secondary density enhance (light-blue shaded regions) are mostly correlated with prominent line wings.

Along the PV cuts, we separate the region into 6 sub-regions (panel (b) of Figure 4.16) and plot the average spectra of SiO (2-1) and CH_3OH $5_{1,5}$-$4_{0,4}$ lines in Figure 4.17. We use a two-component Gaussian model to characterize the SiO (2-1) line profile. This leads to $\sigma_{\rm rms}$ of the narrow component ($\sigma_{\rm n}$) that ranges between 1.5-3.4 km s^{-1} with a mean value of ~1.7±1.5 km s^{-1}, and $\sigma_{\rm rms}$ for the broad component ($\sigma_{\rm w}$) between 3.0-7.4 km s^{-1} with a mean value of ~4.6±1.5 km s^{-1}. The majority of the centroid velocities of the narrow components is consistent with the peak velocity (velocity of intensity peak) of the SiO. The broad-component subtracted narrow line profiles are also shown in the figure, with the $V_{\rm LSR}$ of clump MM2 and MM3 indicated.

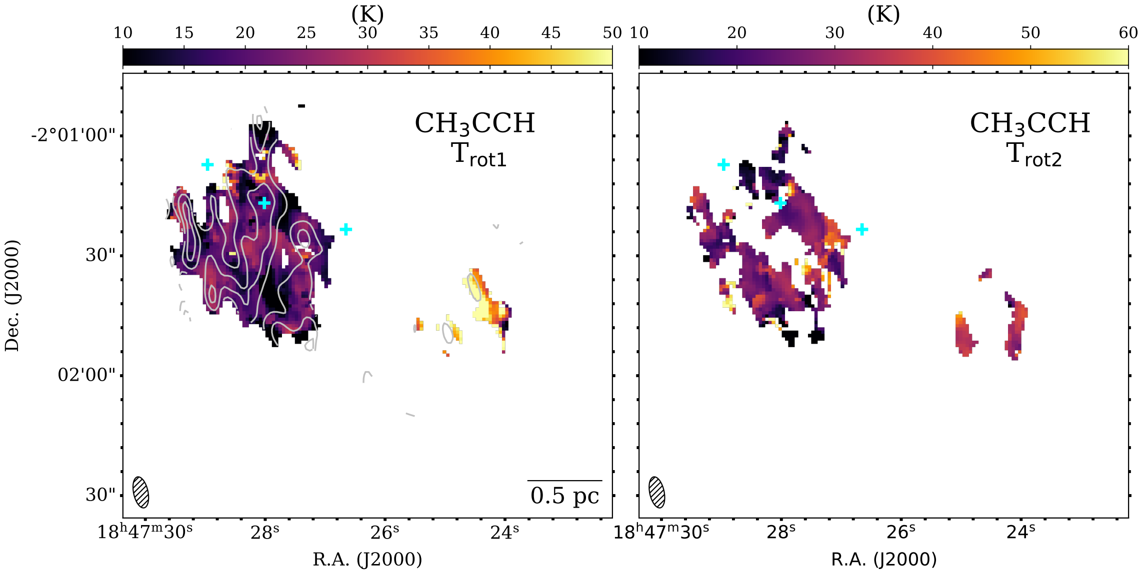

Figure 4.12: Same as Figure 4.11, but for the clump F1 and F2. In the left panel the contours represent integrated intensity map of CH_3CCH 5_2-4_2 line. The velocity range for integration is 75-105 km s^{-1}, and the contour levels are from 0.45 K km s^{-1} (3 σ) to 0.8 K km s^{-1} (0.9 times peak emission value of F1) with 3 uniform intervals. Cyan crosses mark the 3 cores from 3 mm continuum of F1 (as in Figure 4.2, right panel).

In Figure 4.14 lower panel and Figure 4.18-4.20, the derived centroid velocity and linewidth from the CH_3OH (2-1), and thermometers CH_3CCH and H_2CS lines are shown. In all the figures of centroid velocities, the velocity value of zero corresponds to the $V_{\rm LSR}$ (91.7 km s^{-1}) of clump C. From the centroid velocity indicated by one-component CH_3OH line fitting (Figure 4.14 lower panel), we can see that the overall velocity field of the three clumps also shows a complementary distribution of blue-, red- and blue-shifted pattern from north to south, with a relatively low maximum velocity difference ($\lesssim$10 km^{-1}). Although the two-velocity components fits of H_2CS lines (Figure 4.20) reveal that clump C has the most distinct (well separated and spatially most extended) two velocity components, appearing blue-shifted and red-shifted around its $V_{\rm LSR}$, the blue-shifted component dominates the emission at this region. From the centroid velocity of H_2CS line (Figure 4.20), we can also see that while clump MM3 shows a relatively uniform velocity field, MM2 has a slight velocity gradient of 1.5 km s^{-1} in the northwest to southeast direction, ranging from red-shifted to blue-shifted velocities, again reflecting the entangled gas components from the tail of the “Y”-shape velocity distribution seen by SiO (Figure 4.16).

From the linewidths of CH_3OH lines ($\sigma_{\rm rms}$) in Figure 4.14, we can see that the distributed dense gas pockets ($>10^6$ cm^{-3}, marked with green contours in the left panels) associated with clump MM3 show an increased linewidths compared to their ambient gas. The prominent density enhance in the center of MM2 and MM3 show different behavior of linewidths spatial variations from the outer ambient gas to the inner region. The one associated with MM2 has larger linewidths in the inner region, which are even increased towards the east-west direction. The other associated with MM3 shows a decrease in linewidths towards its center. Similar behavior of linewidths spatial variation is also seen in the linewidths of CH_3CCH and H_3CS (Figure 4.18, Figure 4.20). For the two velocity gas

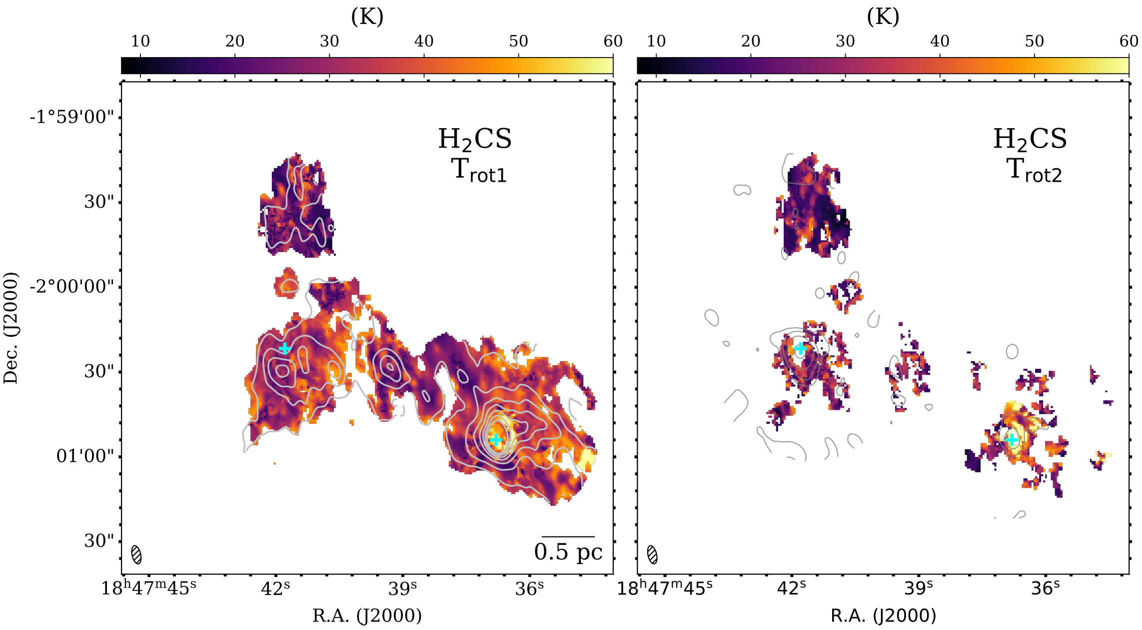

Figure 4.13: The rotational temperature maps derived by H_2CS (3-2) lines for clump MM2, MM3 and C. The left and right panel shows the temperatures from the two component LTE models separately. In the left panel the contours represent integrated intensity map of H_2CS 3(1,3)-2(1,2) line. The velocity range for integration is 80-100 km s^{-1}, and the contour levels are from 2.7 K km s^{-1} (6 σ) to 16.1 K km s^{-1} (0.5 times peak emission value of MM2) with 7 uniform intervals. In the right panel, the contours represent the 3 mm continuum emission, and are logrithmic-spaced from $2\sigma_{\rm rms}$ ($\sigma_{\rm rms}$ = 1.6 mJy/beam) to 225.0 mJy/beam with 5 intervals (same as Figure 4.2). In both plots, the cyan crosses indicate the position of the peak intensity of 3 mm emission.

components of Clump C, the redshifted component has systematically higher linewidths, and is of lower gas temperature, as indicated by result of CH_3CCH lines (Figure 4.11, Figure 4.18). The same trend is not reflected by the fitting result of H_2CS lines: the two velocity components have similar linewidths and the temperature difference is not systematic and large.

4.3.5 Velocity distribution comparison between SiO and other molecules: systematic velocity shift

In Figure 4.21 and Figure 4.22 we plot the PV cuts along U, M, L (Figure 4.16) for molecular lines CCH $1_{1,0}$-$0_{1,1}$, CH_3CCH 5(2)-4(2), HC_3N (9-8), $HC^{15}N$ (1-0), $H^{13}CO^+$ (1-0), SO 2_2-1_1, SO 2_3-1_2 in comparison to SiO (2-1) line. These transitions either show more extended emission than SiO, or show localised emission only coinciding with the density enhancements (as in Figure 4.16). The velocity peaks (velocity at the intensity peak) along the cuts are indicated with solid lines for each line.

For molecules that have extended emission, in general the velocity peaks of the CCH line coincide well with that of SiO along all three PV cuts, except the offset region of (0.8,2.4) pc in M cut where CCH appears more blue-shifted. The velocity peaks of SO 2_2-1_1 line, on the other hand, show a slightly red-shifted tendency along the cuts. The H_2CS line has a similar distribution as SO and is omitted here. The velocity shift between HC_3N and SiO is most obvious and almost everywhere

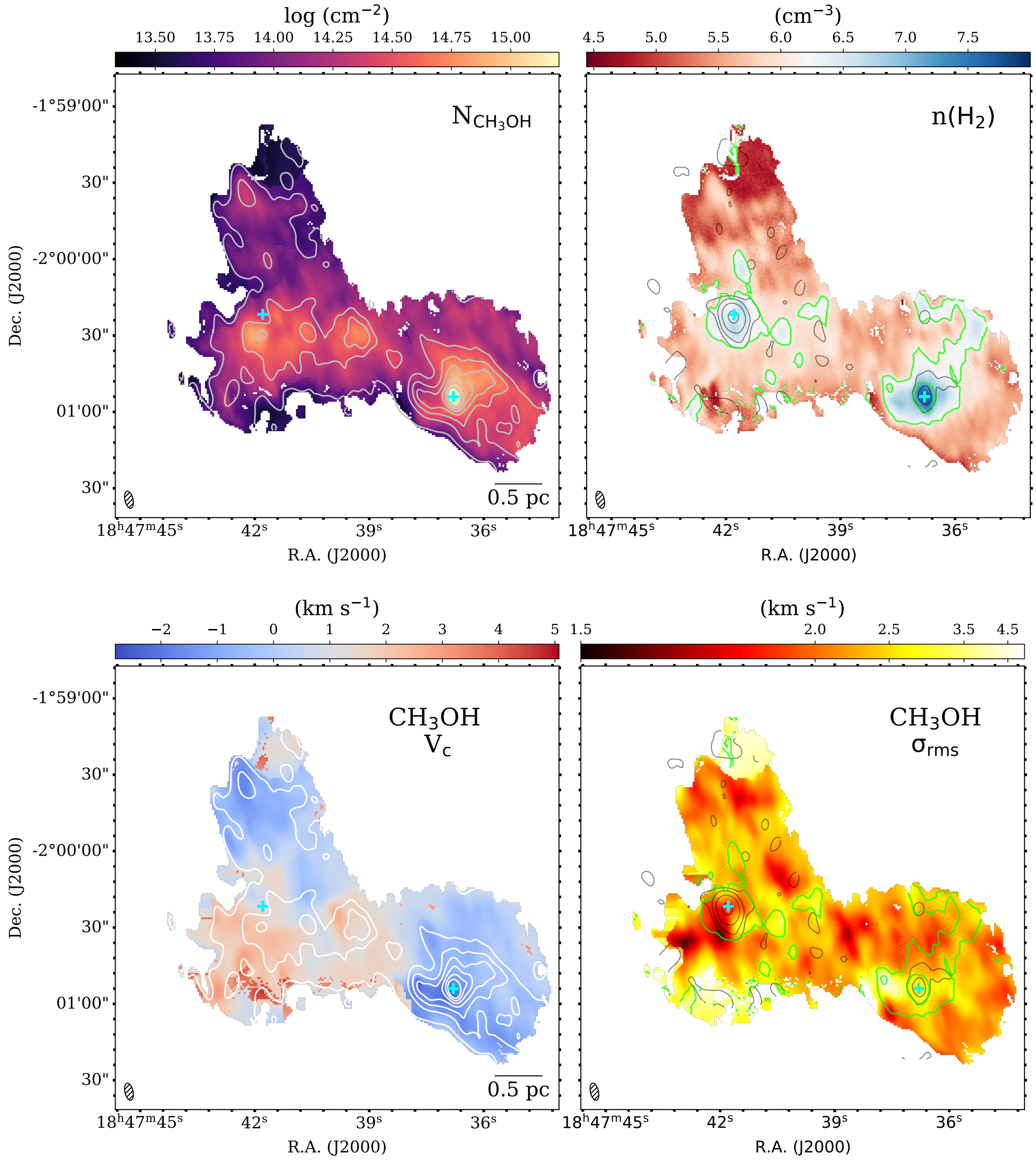

Figure 4.14: *Upper panel:* Derived CH_3OH column density (*E*-type) and hydrogen volume density distribution from RADEX modeling for clump MM2, MM3 and C. *Lower panel:* One-component Gaussian fit result of CH_3OH (2-1) line series. The centroid velocity (with respect to V_{LSR} = 91.7 km s^{-1}) and velocity dispersion ($\sigma_{rms} = \Delta V/2.355$) distribution. In left panels, the contours represent integrated intensity levels of CH_3OH *E*-type 2(0, 1)-1(0, 1) line. The velocity range for integration is 85-100 km s^{-1}, and the contour levels are from 1.3 K km s^{-1} (7 σ) to 37 K km s^{-1} (0.75 times peak emission value of MM2) with 7 uniform intervals. In right panels, the gray contours represent the 3 mm continuum emission, and are logrithmic-spaced from $2\sigma_{rms}$ (σ_{rms} = 1.6 mJy/beam) to 225.0 mJy/beam with 5 intervals (same as Figure 4.2). Cyan crosses mark the 3 mm continuum peak of MM2 and MM3. The green contours indicate n(H_2) levels of $10^{6.1}$ cm^{-3} and 10^7 cm^{-3}.

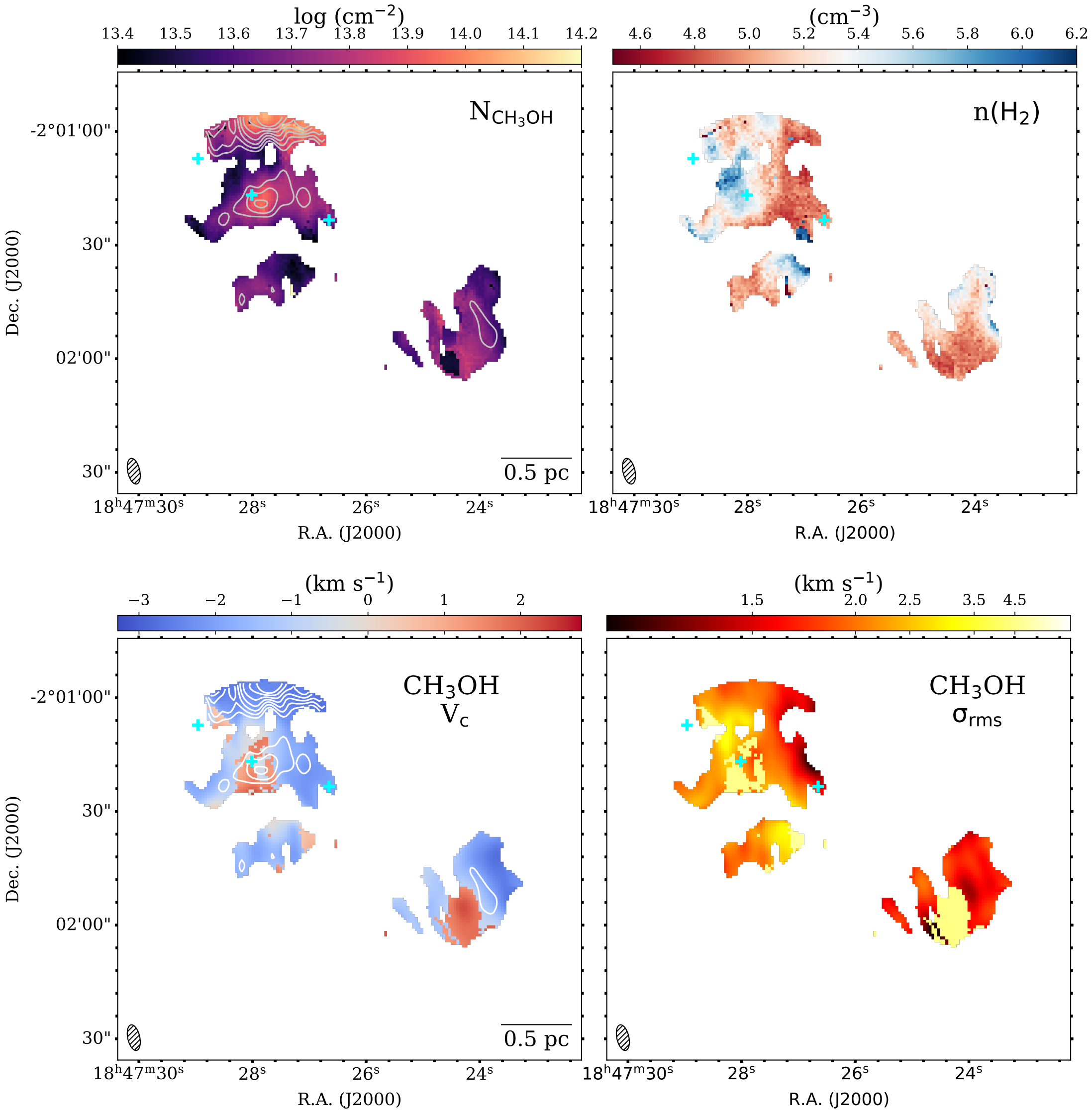

Figure 4.15: Same as Figure 4.14, but for the clumps F1 and F2. The centroid velocity is with respect to V_{LSR} = 85.5 km s^{-1} of clump F2. In left panels, the contours represent integrated intensity levels of CH_3OH E-type 2(0, 1)-1(0, 1) line. The velocity range for integration is 80-95 km s^{-1}, and the contour levels are from 1.2 K km s^{-1} (7 σ) to 2.6 K km s^{-1} (0.75 times peak emission value of F1) with 7 uniform intervals. Cyan crosses mark the 3 cores in 3 mm continuum of F1 (as in Figure 4.2, right panel).

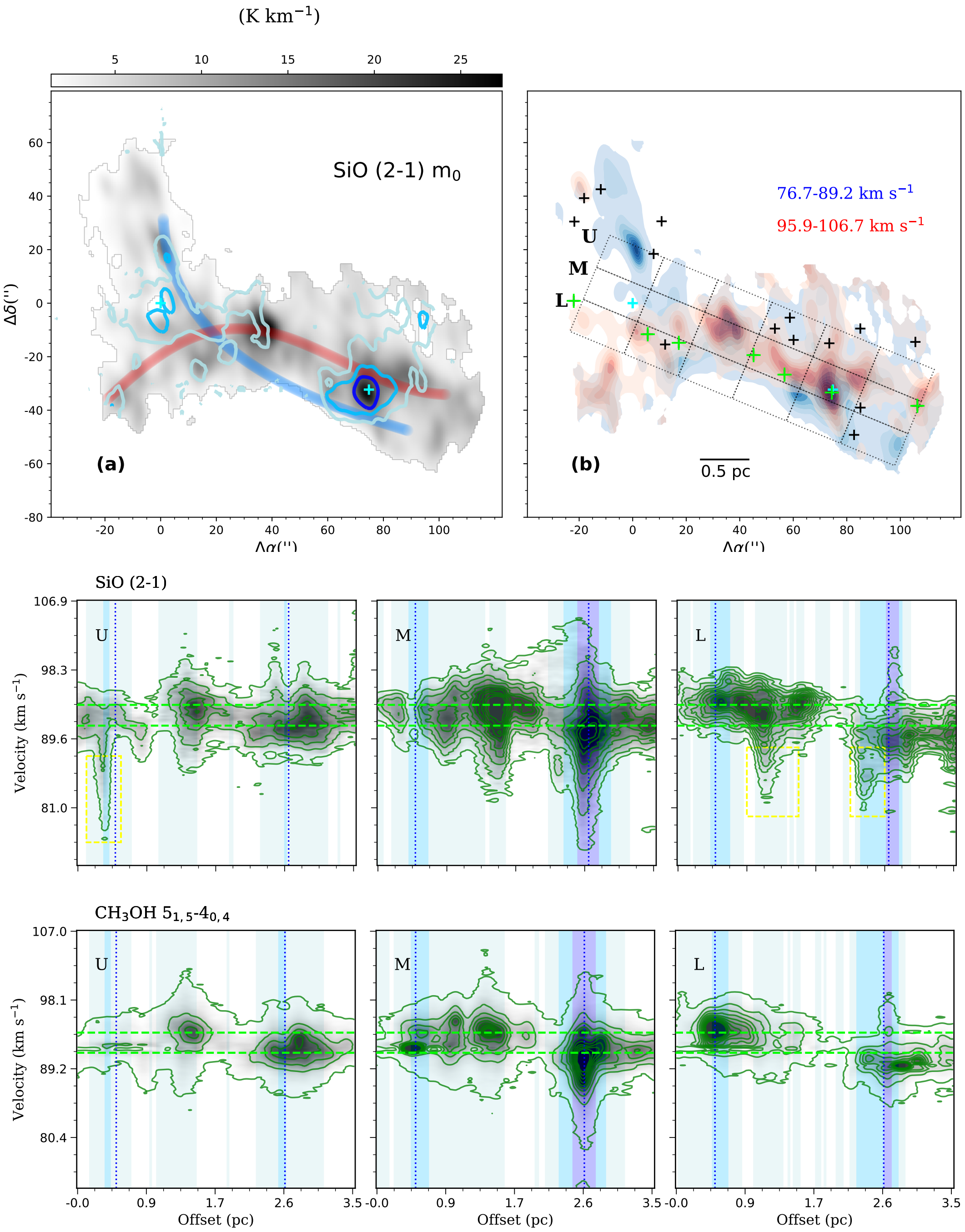

Figure 4.16: *Upper panel:* (a).The integrated intensity map of SiO (2-1) lines (76.7-106.7 km s^{-1}, gray scale) overlaid with the n(H$_2$) levels of 10^6, $10^{6.5}$, 10^7 cm^{-3} (in contours of light blue, blue and purple). The 3 mm continuum peak of clump MM2 and MM3 are indicated as crosses. The red and blue thick solid lines indicate the emission ridge of the blue-shifted and red-shifted parts shown in panel (b). (b). The integrated intensity maps of the SiO (2-1) blue-shifted and red-shifted velocity components. The integrated velocity ranges are indicated in the plot. The crosses in green and black indicate the NH$_2$D cores (Section 4.3.7): the green ones are cores with at least one velocity component of $\sigma_{\rm rms}$ 1 km s^{-1}. The three position-velocity cuts U, M, L are indicated as rectangles. For both panel (a) and (b), R.A. and Decl. offsets correspond to the 3 mm continuum peak of clump MM3. *Middle panel:* Position-velocity diagrams of SiO (2-1) line along the three cuts U, M and L. The color-shaded regions indicate the n(H$_2$) levels of 10^6, $10^{6.5}$, 10^7 cm^{-3} (in light blue, blue and purple), respectively. The system velocities $V_{\rm LSR}$ of clump MM2 and MM3 are indicated as green horizontal lines (93.9 km $^{-1}$ and 91.3 km $^{-1}$). The blue vertical lines indicate the position of the 3 mm continuum peak of MM2 and MM3. *Lower panel:* Position-velocity diagrams of CH$_3$OH $5_{1,5}$-$4_{0,4}$ line along the three cuts U, M and L. The shaded regions and the dotted and dashed lines follow the same definitions as in the middle panel.

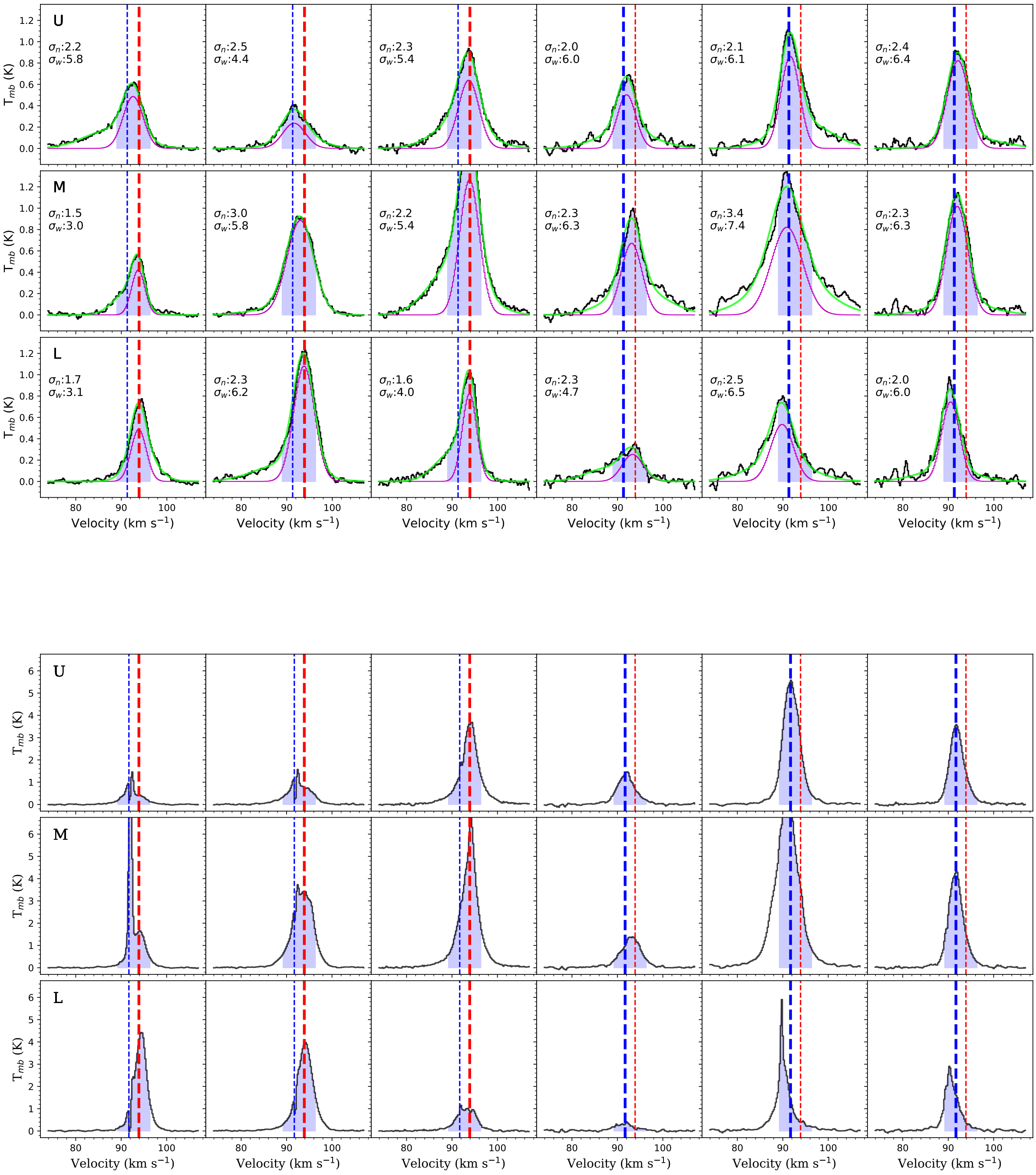

Figure 4.17: The average spectra of SiO (2-1) (upper panel) and CH_3OH $5_{1,5}$-$4_{0,4}$ (lower panel) along the three PV cuts U, M, L as in panel (b) of Figure 4.16. The spectra are arranged from northeast to southwest along the cuts. The blue and red dashed lines indicate the $V_{\rm LSR}$ of clump MM3 and MM2 (93.9 km s^{-1} and 91.7 km s^{-1}), with the thicker line corresponding to the $V_{\rm LSR}$ of either clump MM2 or MM3 at this position. The blue shaded regions indicate the line central velocity range from (91.3-2.5) km s^{-1} to (93.9+2.5) km s^{-1}, which is excluded from the integration of the intensity maps of panel (b) in Figure 4.16. In the upper plot, the two-component Gaussian fit to the SiO line is shown additionally, as green line. The broad-component subtracted spectrum (narrow-component line profile) is shown as magenta line. The velocity dispersion for the two components are indicated in the figure, in unit of km s^{-1}.

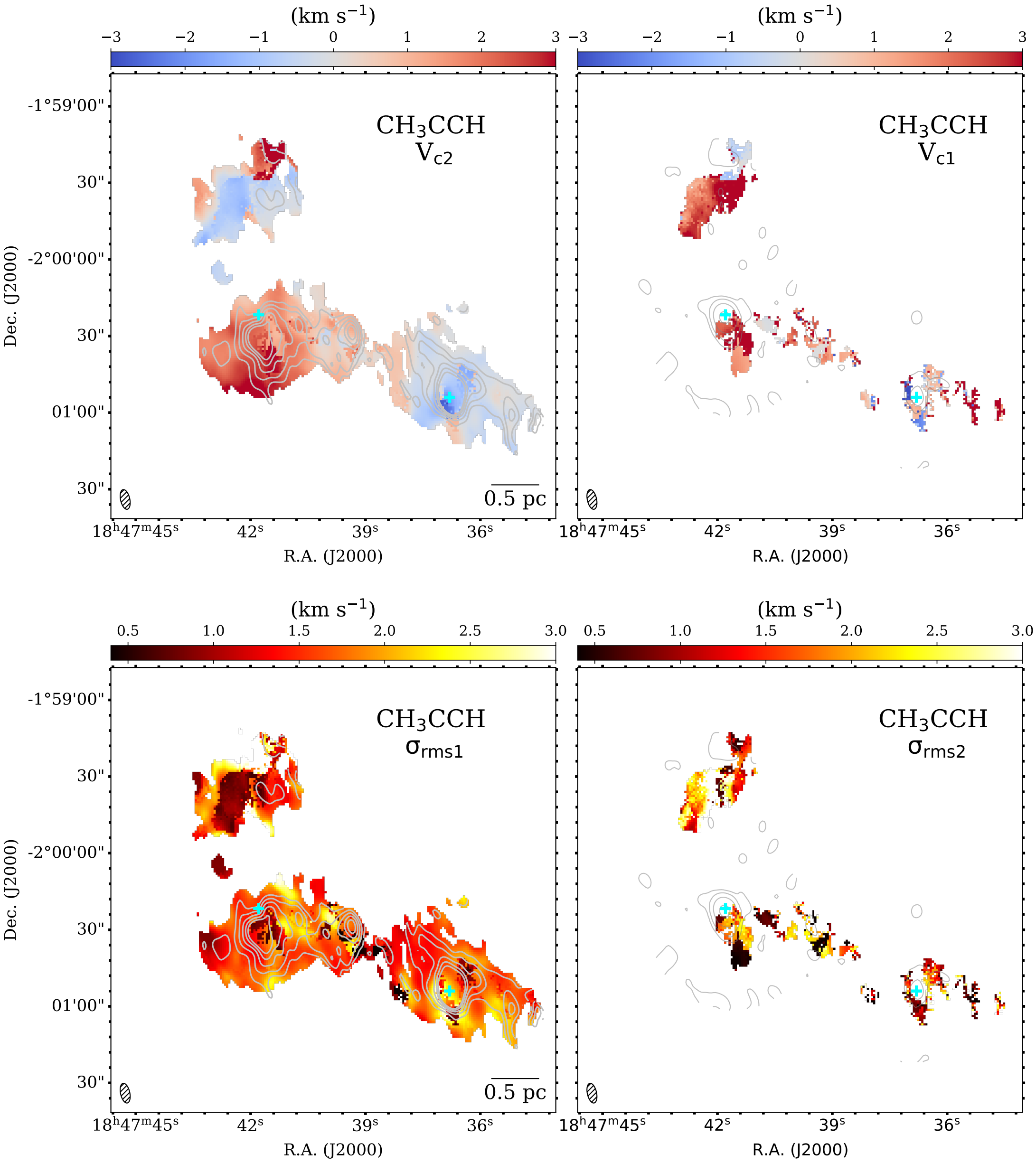

Figure 4.18: The centroid velocity and velocity dispersion distribution of the two-component Gaussian fits of CH_3CCH (6-5) and (5-4) line series for clump MM2, MM3 and C. The centroid velocity is with respect to V_{LSR} of clump F1 (85.5 km s^{-1}). The upper panel and lower panel shows the two components separately. In both upper and lower panel, the contours and crosses in left and right plot follow the same definitions as in Figure 4.11.

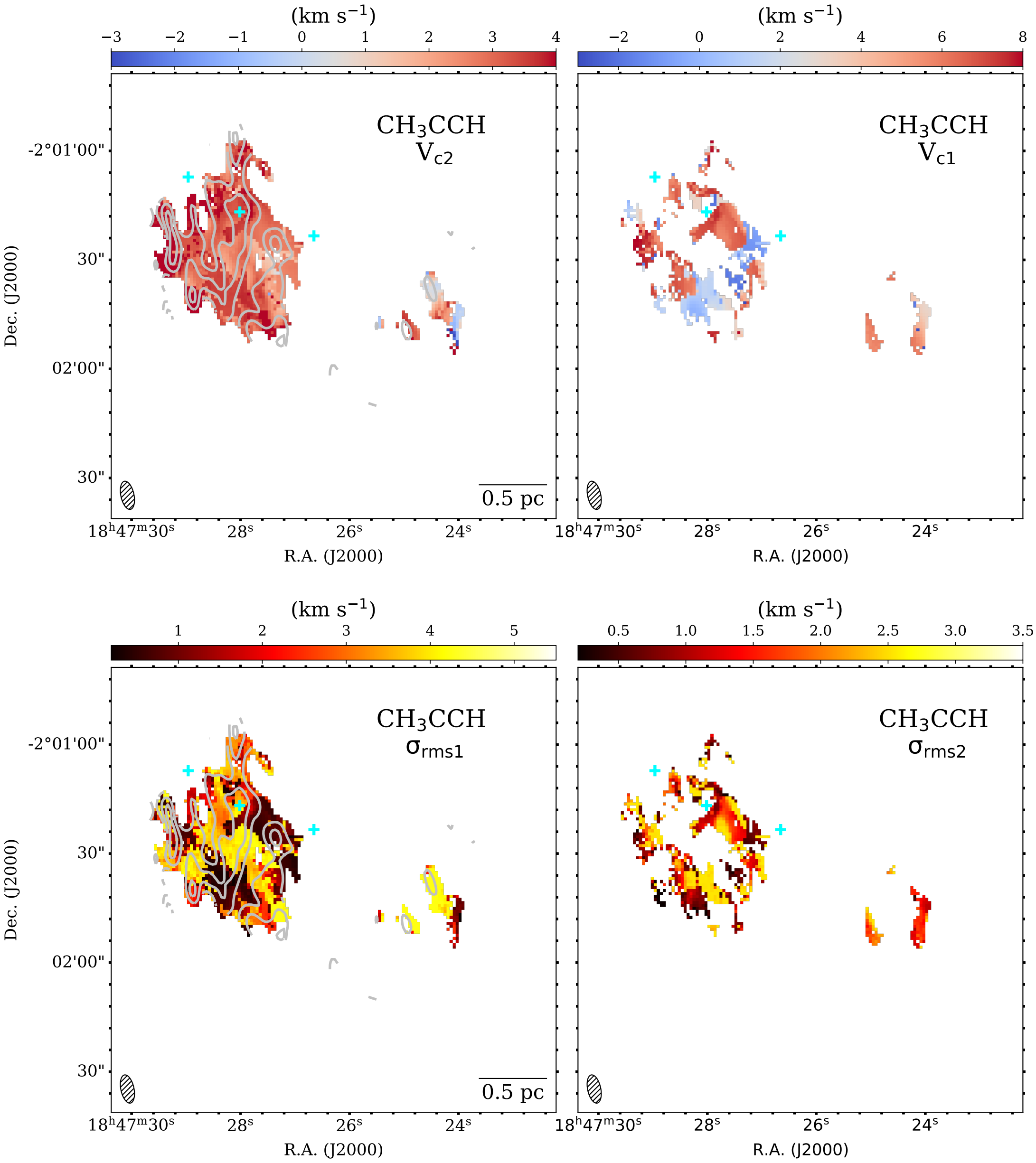

Figure 4.19: Same as Figure 4.18, but for the clump F1 and F2. In both upper and lower panel, the contours and crosses in left and right plot follow the same definitions as in Figure 4.12.

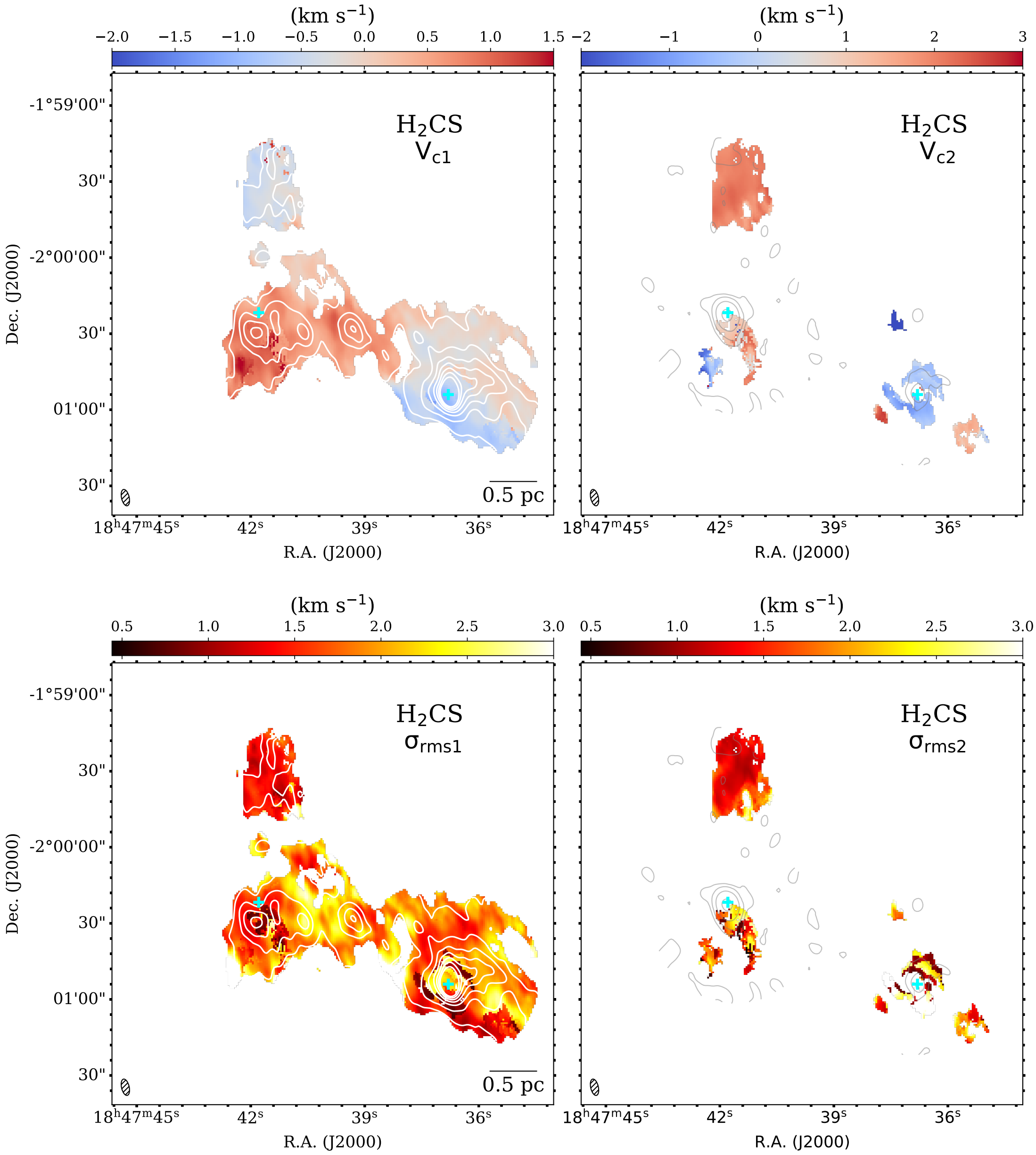

Figure 4.20: The centroid velocity and velocity dispersion distribution of the two-component Gaussian fits of H_2CS (3-2) line series. The upper panel and lower panel shows the two components individually. In both upper and lower panel, the contours and crosses in left and right plot follow the same definitions as in Figure 4.13.

except the offset region of (1.3, 2.0) pc in the M and L cut. The velocity differences reach up to ~2 km s^{-1} with the peak velocity of HC$_3$N appearing in the more red-shifted regime. The H^{13}CO$^+$ line shows a similar case as HC$_3$N. For the other three lines that have rather compact emission, CH$_3$CCH 5(2)-4(2) shows velocity peaks consistent with SiO, while HCN^{15} and SO 2_3-1_2 also appear to have velocity peaks mostly red-shifted.

From the PV maps of the CCH line, it is also clearly seen that at spatial offsets from clump MM2 in the L cut, there is a prominent red-shifted component which is not present in the SiO PV map, this component also exists in the HC$_3$N and H^{13}CO$^+$ PV map of cut L, but of lower spatial extension. The spectra of CCH line along the three PV cuts are shown in Figure 4.23. The two velocity components are seen both in the main line of CCH $1_{1,0}$-$0_{1,1}$, which is slightly optically thick with τ_m~0.5-2.5 in this region, and the least intense satellite line CCH $1_{1,1}$-$0_{1,1}$ which is optically thin (τ<0.5, more in Sect. 4.3.7). This suggests that the two-component line profile is not an optical depth effect. Also notably, from the CCH PV maps, there are several red-shifted wing components (~1.3 pc along U, M and L cut) reaching beyond 100 km s^{-1} (10 km s^{-1} around the $V_{\rm LSR}$) that do not all have clear counterparts in the PV maps of other lines.

The spatio-kinematic offsets between tracers have been suggested as an indication of cloud-cloud collision or merging for early-stage clouds (Henshaw et al. 2013, Bisbas et al. 2018). Broad bridging features in PV maps between two velocity components are also general evidence of cloud-cloud collisions (e.g. Haworth et al. 2015). The velocity difference between the two components is small in our case ($V_{\rm LSR}$ of 91.3 and 93.9 km s^{-1}), and the bridging feature is not significant in the velocity domain, but is spatially prominent towards all tracers that have extended emission. The two clumps MM2 and MM3 lying along the PV cuts may drive several outflows, which can be confused with the collision signatures. But the systematic peak velocity offsets between classes of tracers, and the asymmetric line wings in the PV maps which show peculiar "V"-shaped morphology (e.g. Takahira, Tasker and Habe 2014, Fukui et al. 2018), can all be seen as signs of cloud-cloud collision. The broader CCH lines and the additional further-away red-shifted velocity component around clump MM2 may reflect the relatively diffuse outer gas in the cloud merging process. This 0.1-1 pc scale gas kinematics are consistent with the larger scale ^{13}CO observations which show that a 82 km s^{-1} and a 94 km s^{-1} cloud are intersecting at this southern W43-main (Kohno et al. 2021). Our observations likely reveal dense gas tips of the compressed layer close to the large-scale red-shifted 94 km s^{-1} cloud.

4.3.6 Probing the infall motion of MM3: absorption of the H^{13}CO$^+$ (1-0) line

As already seen in Section 4.3.2, the H^{13}CO$^+$ line at the continuum peak (an UCHII region) of clump MM3 shows a negative absorption feature. In Figure 4.24, we plot spectra of different molecular species and the radio recombination lines H40α and H42α extracted towards the MM2 continuum peak ($\gtrsim$0.85I_{peak}, listed in Table 4.2). The same spectrum towards clump MM3 is shown as a comparison. It can be seen that the red-shifted absorption feature is also present in the HC^{15}N line, but less prominently. We calculate the peak opacity ($\tau_{\rm p}$) of the absorption line, as,

$$\tau_{\rm p} = \ln(1 - \frac{T_{\rm np}}{T_{\rm C}}), \qquad (4.1)$$

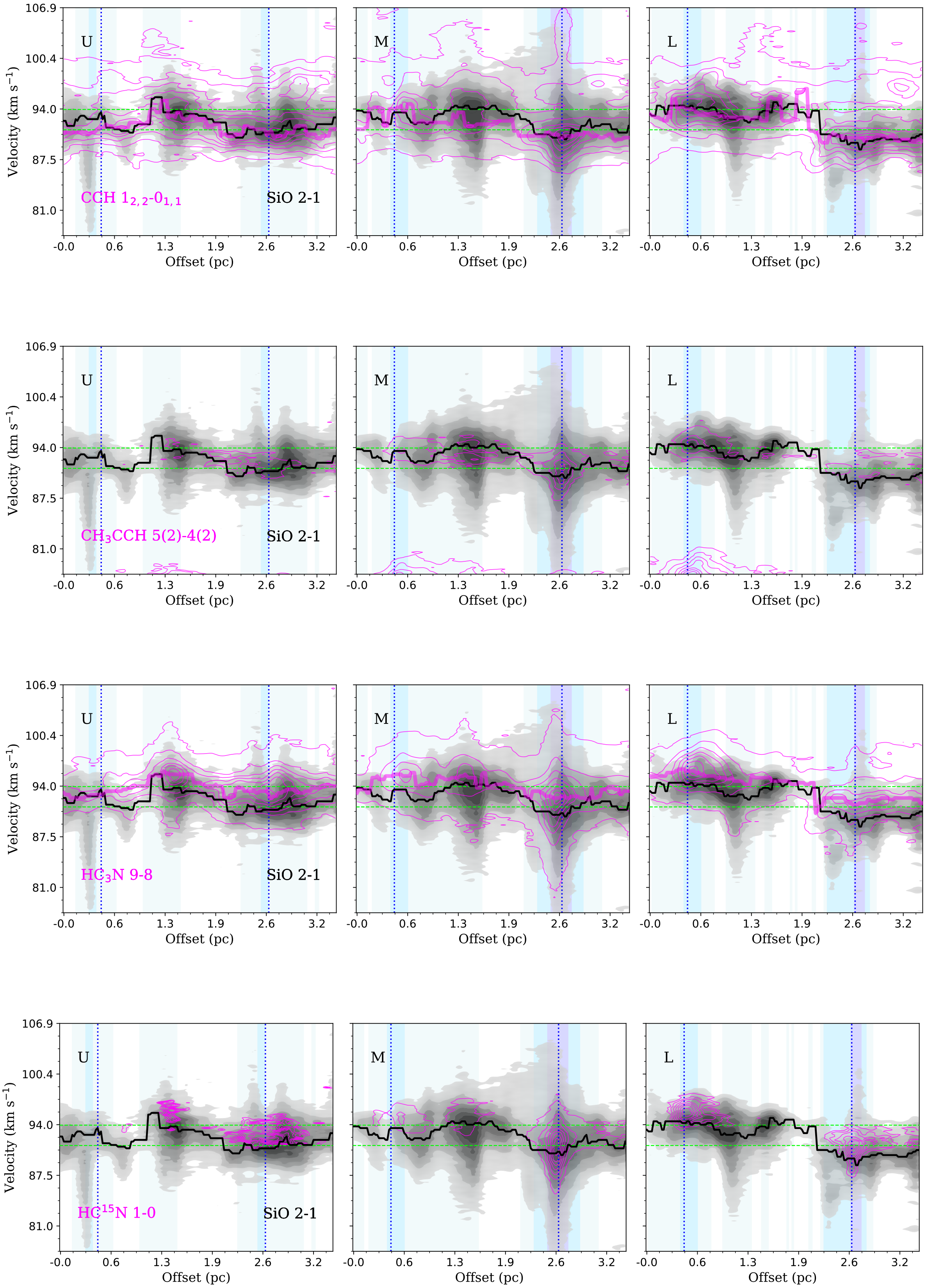

Figure 4.21: Position-velocity diagram for CCH $1_{2,2}$-$0_{1,1}$ and CH$_3$CCH 5(2)-4(2), HC$_3$N (9-8) and HC^{15}N (1-0) lines (from top to bottom, in magenta contours) in comparison to that of SiO (2-1) (gray filled contours), along the U, M, L cuts as illustrated in upper panel of Figure 4.16. The vertical dotted line and shaded regions follow those as in Figure 4.16. The peak velocity along the spatial offset for SiO (2-1) and the respective molecular line (that have extended emission) in each plot are indicated as black and magenta lines.

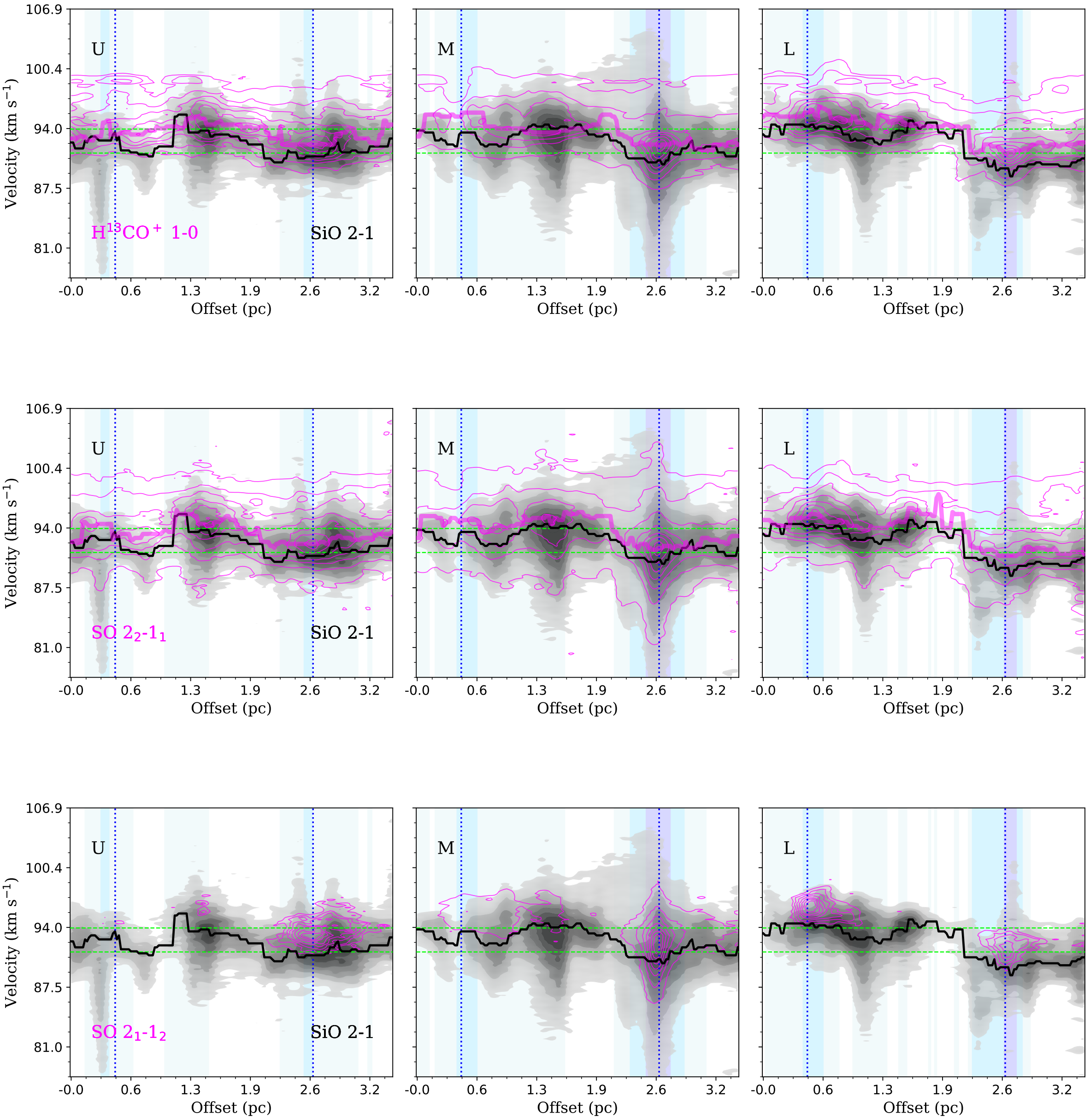

Figure 4.22: Same as Figure 4.21, but for H^{13}CO$^+$ (1-0), SO 2_2-1_1 and SO 2_3-1_2 (from top to lower bottom) lines.

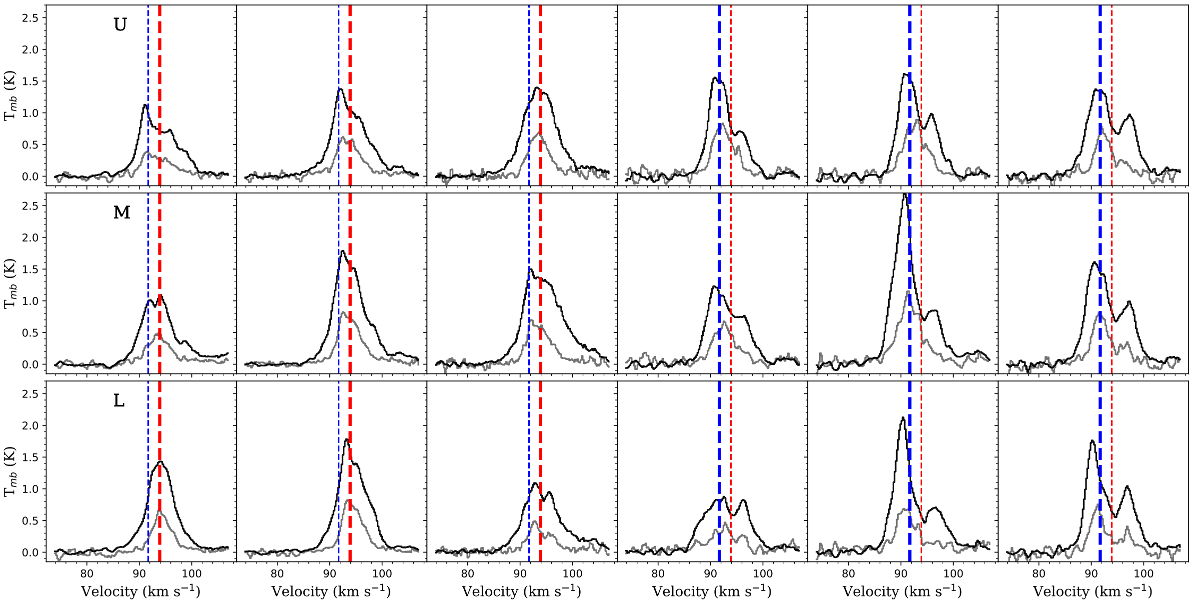

Figure 4.23: The average spectrum of the main line of CCH *hfs* component $1_{2,2}$-$0_{1,1}$ (black line) and the satellite line $1_{1,1}$-$0_{1,0}$ (gray line, the intensity is artificially enlarged by 3 times for comparison) along the three PV cuts U, M, L. From left to right, the spectra are arranged from northeast to southwest along the cuts. The blue and red dashed lines follow that in Figure 4.17.

in which $T_{\rm np}$ is the absolute minimum intensity of the absorption line, $T_{\rm C}$ is the continuum brightness plus the line emission contribution. We took an averaged continuum brightness temperature within 0.1 pc (~FWHM, same as line extraction in Figure 4.24) around the continuum peak, which yields 1.3 K. We obtain $\tau_{\rm p}$ for $H^{13}CO^+$ (1-0) line of 0.2, and for $HC^{15}N$ (1-0) of 0.03. The velocity at the minimum intensity of the absorption dip ($V_{\rm np}$) coincides with the peak velocity of the radio recombination lines H40α and H42α, indicating this infall signature is related to the gas layers located close to the UCHII region.

Assuming the infall velocity ($V_{\rm inf}$) as the velocity difference between the absorption dip and the systemic velocity of the clump, we have $V_{\rm inf}$ = $V_{\rm np}$-$V_{\rm LSR}$ = 4.5 km s^{-1}. The spherical uniform accretion rate can be described by,

$$\dot{M} = 4\pi r_{\rm inf}^2 m_{\rm H_2} n({\rm H_2}) V_{\rm inf} \tag{4.2}$$

where $r_{\rm inf}$ stands for the radius of the infalling region, $m_{\rm H_2}$ the hydrogen molecular mass and n(H_2) hydrogen volume density. Taking $r_{\rm inf}$ as the radius of the size of the UCHII region constrained from 3.5 and 6 cm radio continuum emission, of 0.075 pc, and the n_{H_2} as that averaged from the n(H_2) map derived by CH_3OH (2-1) lines (Section 4.3.3), of $10^{6.5}$ cm^{-3}, we obtain $\dot{M}$~7×10^{-2} M$_\odot$ yr^{-1}.

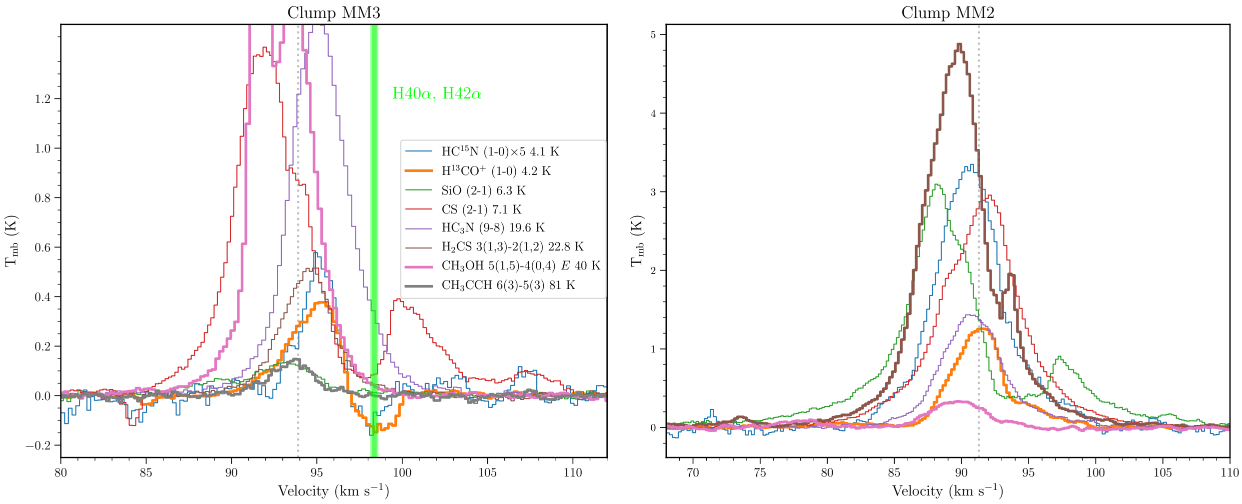

Figure 4.24: The spectra extracted towards the 3 mm continuum peak of clump MM3 and clump MM2. The system velocity $V_{\rm LSR}$ (Table 4.1) is indicated by the dotted vertical line. In the left panel, the peak velocity of H40α and H42α lines is shown as green vertical line.

4.3.7 Hyperfine fitting of NH_2D and CCH lines and NH_2D-traced cores

The NH_2D 1(1,1)-1(0,1) and CCH (1-0) lines are split into hyperfine (*hfs*) structures that allow to measure the exitation temperatures and optical depths of the lines. Similarly as for molecules presented earlier, we conduct one-component and two-component fits and choose the best-fit models.

In Figure 4.27 and Figure 4.31 the fitted excitation temperature $T_{\rm ex}$, total CCH column density $N_{\rm CCH}$, and the centroid velocity and linewidth of CCH (1-0) lines towards clump MM2, MM3 and C are shown. Figure 4.28 and Figure 4.32 show same maps towards clump F1 and F2. The emission of CCH is very extended especially in clump MM2 and MM3. Clump C has CCH emission mostly in the north-west region. For clump MM3, particularly, the CCH emission around the UCHII regions has a sharp decrease of emission in the north-east direction, exhibiting an arc-like morphology. This is consistent with previous observations and predictions that CCH in active star-forming regions is efficiently converted to other molecules (e.g. Beuther et al. 2008). The derived $N_{\rm CCH}$ ranges between $10^{15.5}$-$10^{16.5}$ cm^{-2}. The $T_{\rm ex}$ of CCH is mostly ~5-10 K, with local maxima reaching 25 K at the periphery of the central region of clump MM2 and at the intersection region of MM2 and MM3. Towards clump C, $T_{\rm ex}$ is also elevated in the region of most intense emission compared to the ambient region, but the enhance is not significant given the fitting errors. Comparing the linewidths ($\sigma_{\rm rms1}$ and $\sigma_{\rm rms2}$) to $T_{\rm ex}$, we again resolve, similarly as result of CH_3CCH lines, that the regions of high $T_{\rm ex}$ in clump MM2 and MM3 are displaying larger linewidths, while in clump C, $T_{\rm ex}$ and linewidths seem anti-correlated. The velocity field in the regions where CH_3CCH is detected has a generally consistent distribution with CCH. In other parts, notably, there are prominent red-shifted components reaching +8 km s^{-1} in the intersection region of clump MM2 and MM3, and in the southern part of MM2 (as illustrated also in Figure 4.21). As discussed in Sect. 4.3.5, these red-shifted components peaking at 96-98 km^{-1} represent an outer layer of the clouds in collisions.

In Figure 4.25 and Figure 4.29 the fitted parameters of the NH_2D 1(1,1)-1(0,1) lines towards clump MM2, MM3 and C shown. Figure 4.26 and Figure 4.30 show same maps towards clump F1 and

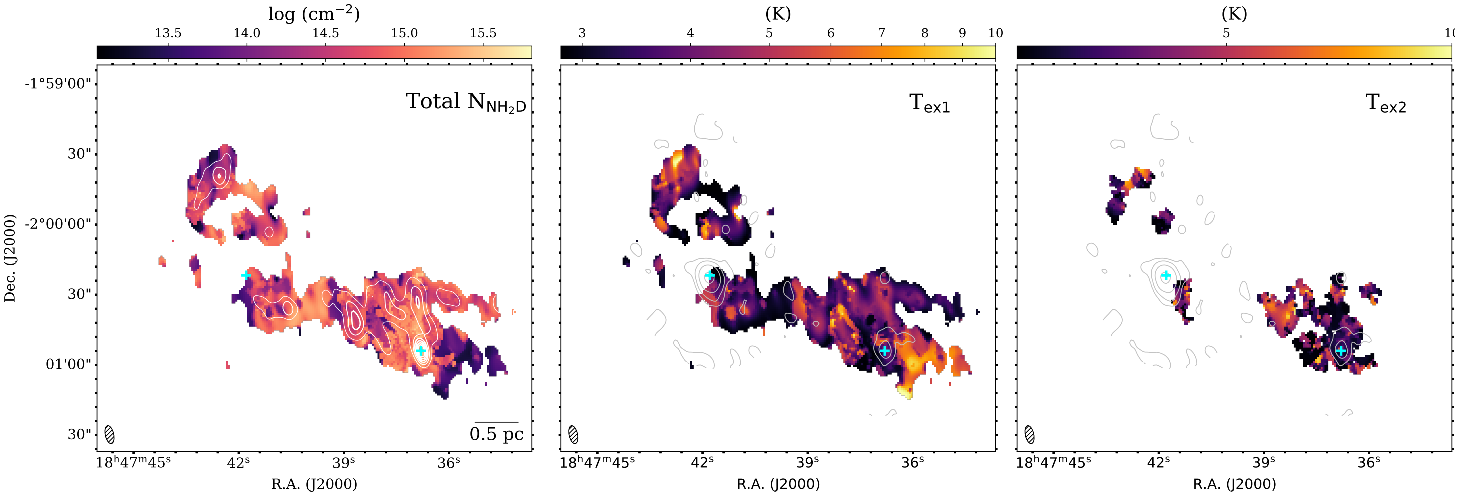

Figure 4.25: The total NH_2D column density and excitation temperatures from the two-component *hfs* fitting. White contours in the left panels represent the integrated intensity map of all *hfs* components of NH_2D line (80-115 km s^{-1}), from 1.8 K km s^{-1} (7 σ) to 10.2 K km s^{-1} (0.9 times the peak emission of MM2) with 6 uniform intervals. The gray contours, and crosses follow the same definitions as in Figure 4.13.

F2. The emission of NH_2D 1(1,1)-1(0,1) lines is rather localised, showing compact emission. The linewidths of NH_2D are smaller than that of CH_3CCH and H_2CS, indicating NH_2D is tracing more quiescent gas. In comparison to the 3 mm dust continuum, we see that only clump MM2 and core F1-c1 has strong emission of NH_2D. As can be seen in the integrated intensity map in Figure 4.35 (right panel), the NH_2D emission is mostly uncorrelated with the emission peak of the CH_3OH line and the localised density enhance seen from n(H_2) map. There are widely distributed gas pockets of compact NH_2D emission in MM2, lying mostly in the north and east direction. These regions have narrower linewidths ($\sigma_{\rm rms} \lesssim 0.5$ km s^{-1}), compared to the central core of MM2. In the south of the 3 mm continuum of clump MM3, NH_2D line has enhanced linewidths, which may be related to shocked gas. In some subregions of clump MM3 and MM2, the NH_2D line profile shows superposition of a narrow and a broad velocity component (see also Figure. 4.36, P4, P6, P9, P10, etc). For Clump C, we resolve for most regions two well-separated velocity components, both are of relatively narrow linewidths (see also Figure 4.36, P1-P3). Clump F2 is also mostly composed of two velocity components (see also Figure 4.37), and there is apparent increase of linewidths towards the edge of NH_2D emission.

To better characterise the localised emission of the NH_2D line, we run the dendrogram (Rosolowsky et al. 2008) algorithm on NH_2D spectral cube to extract physical parameters that define these NH_2D-traced subregions. We consider compact structures of peak emission larger than 5σ (the observational noise of NH_2D line) and are at least 3σ more significant than the emission of their lower level structures. The parameters of the extracted compact structures are listed in Table 4.5-4.6 and the locations are marked in Figure 4.35. Hereafter we refer to these compact structures as NH_2D cores. Average spectra towards all the identified cores are shown in Figure 4.36-4.37. We use one and two-component *hfs* fits to describe the observed line profiles. Based on the linewidths, these NH_2D cores can be classified into two categories, ones with broad-linewidth component of $\sigma_{\rm rms}>1$ km s^{-1}, and the others only having $\sigma_{\rm rms}<1$ km s^{-1} linewidth component (s). In clump MM2, MM3

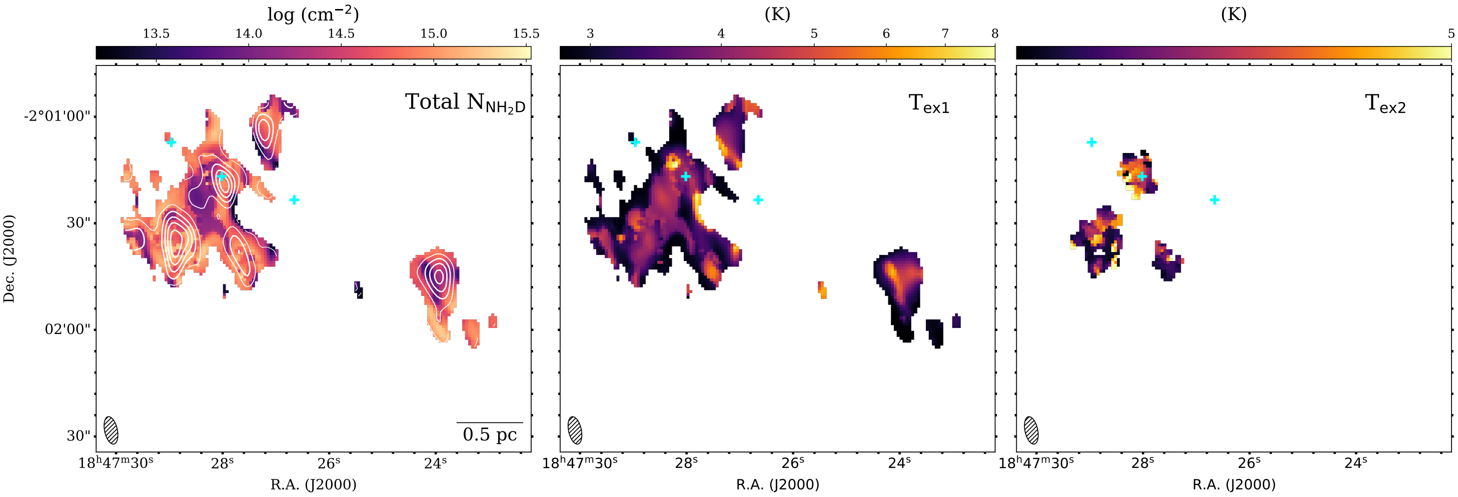

Figure 4.26: Same as Figure 4.25, but for the clump F1 and F2. White contours in the left panels represent the integrated intensity map of all *hfs* components of NH$_2$D line (75-110 km s^{-1}), from 1.0 K km s^{-1} (7 σ) to 3.6 K km s^{-1} (0.9 times the peak emission of F1) with 6 uniform intervals. Cyan crosses mark the 3 cores in 3 mm continuum of F1 (as in Figure 4.2, right panel).

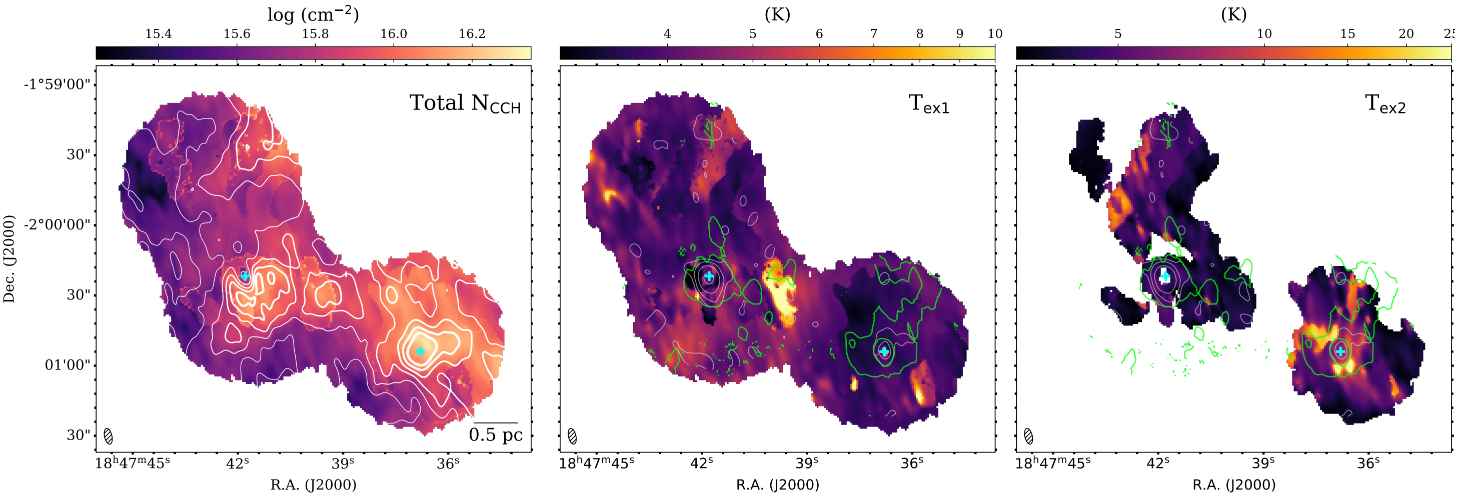

Figure 4.27: The total CCH column density and excitation temperatures from the two-component *hfs* fitting for clump MM2, MM3 and . White contours in the left panels represent the integrated intensity map of CCH $1_{1,1}$-$0_{1,1}$ line (85-100 km s^{-1}), from 3.3 K km s^{-1} (7 σ) to 9.8 K km s^{-1} (0.9 times the peak emission of MM2) with 6 uniform intervals. The gray and green contours, and crosses follow the same definitions as in Figure 4.13.

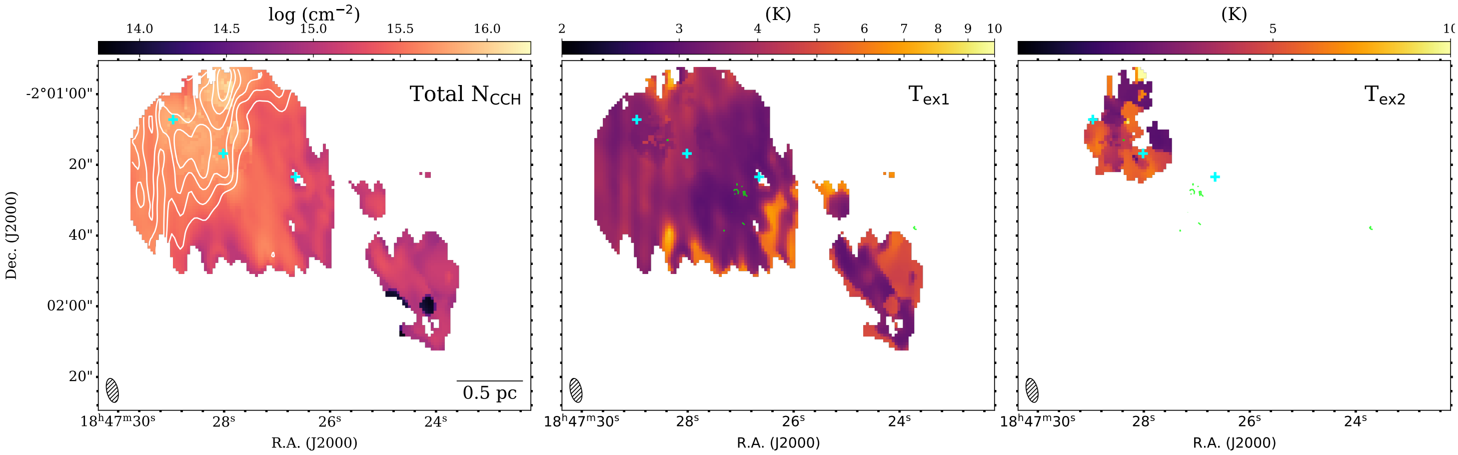

Figure 4.28: Same as Figure 4.27, but for clump F1 and F2. White contours in the left panels represent the integrated intensity map of CCH $1_{1,1}$-$0_{1,1}$ line (80-95 km s^{-1}), from 2.2 K km s^{-1} (7 σ) to 6.0 K km s^{-1} (0.9 times the peak emission of F1) with 6 uniform intervals.

and C, these cores are also indicated in Figure 4.16 (as green and black crosses). Towards this region, it seems all the cores of broad linewidths appear spatially correlated with the intersection region of the blue-shifted and red-shifted gas components of SiO (2-1) (Figure 4.16). Assuming a uniform density profile, the virial mass of NH$_2$D cores can be estimated by $M_{\rm vir} = \frac{5\sigma_{\rm rms}^2 R}{G}$, with $\sigma_{\rm rms}$ obtained from the *hfs* fits and taking R as the effective radius defined by core area from dendrogram extraction. The derived excitation temperature $T_{\rm ex}$ and the optical depth of the main line, and the $M_{\rm vir}$ (also individually for two component *hfs* fits) are also listed in Table 4.5-4.6.

We made comparison of the linewidths of the two velocity components of the NH$_2$D cores identified in clump MM2, MM3 and C, as shown in left panel of Figure 4.33. The two linewidths are weakly correlated, with a Spearman correlation coefficient of 0.47 (p-value = 0.05). With one exception, other cores have relatively large linewidth difference. We further make Core Velocity Dispersion (CVD(R)) calculation towards these cores, which is a statistical method to reveal the turbulence driving mode in molecular clouds by sampling the velocity field of density peaks (Qian et al. 2015, Xu 2020). A scaling relation of CVD(R) $\propto R^{1/3}$ and CVD(R) $\propto R^{1/2}$ point to Kolmogorov scaling and Burgers scaling, respectively, which correspond to solenoidal turbulent motions and compressive turbulent motions. We found the CVD(R) of the broad linewidths roughly follows CVD(R) $\propto r^{0.52}$, and that of narrow linewidths follows CVD(R) $\propto r^{0.64}$. These indicate the turbulent motions imprinted with these NH$_2$D cores are dominated by compressive driving mode, in the scale range of 0.1-4 pc.

As an assessment of fragmentation process, we made comparisons between the observed core separation (distance to each core's nearest neighbor), core virial mass and critical length and mass scale of Jeans fragmentation predictions, towards the region of clump MM2, MM3 and C. We adopt the clump envelope gas density and the turbulent linewidth (the broader velocity component) as one set of parameters, and core gas density and thermal linewidths as another, for Jeans fragmentation assessment. We regard these two parameter sets as representing roughly the properties of large-scale clump bulk gas, and in situ localised dense gas. The core densities are yielded from the CH$_3$OH derived n(H$_2$) maps, and the envelope density is adopted as a characteristic bulk gas density of 10^5 cm^{-3} for these clumps. Takahira et al. (2018) find that the core formation from cloud-cloud

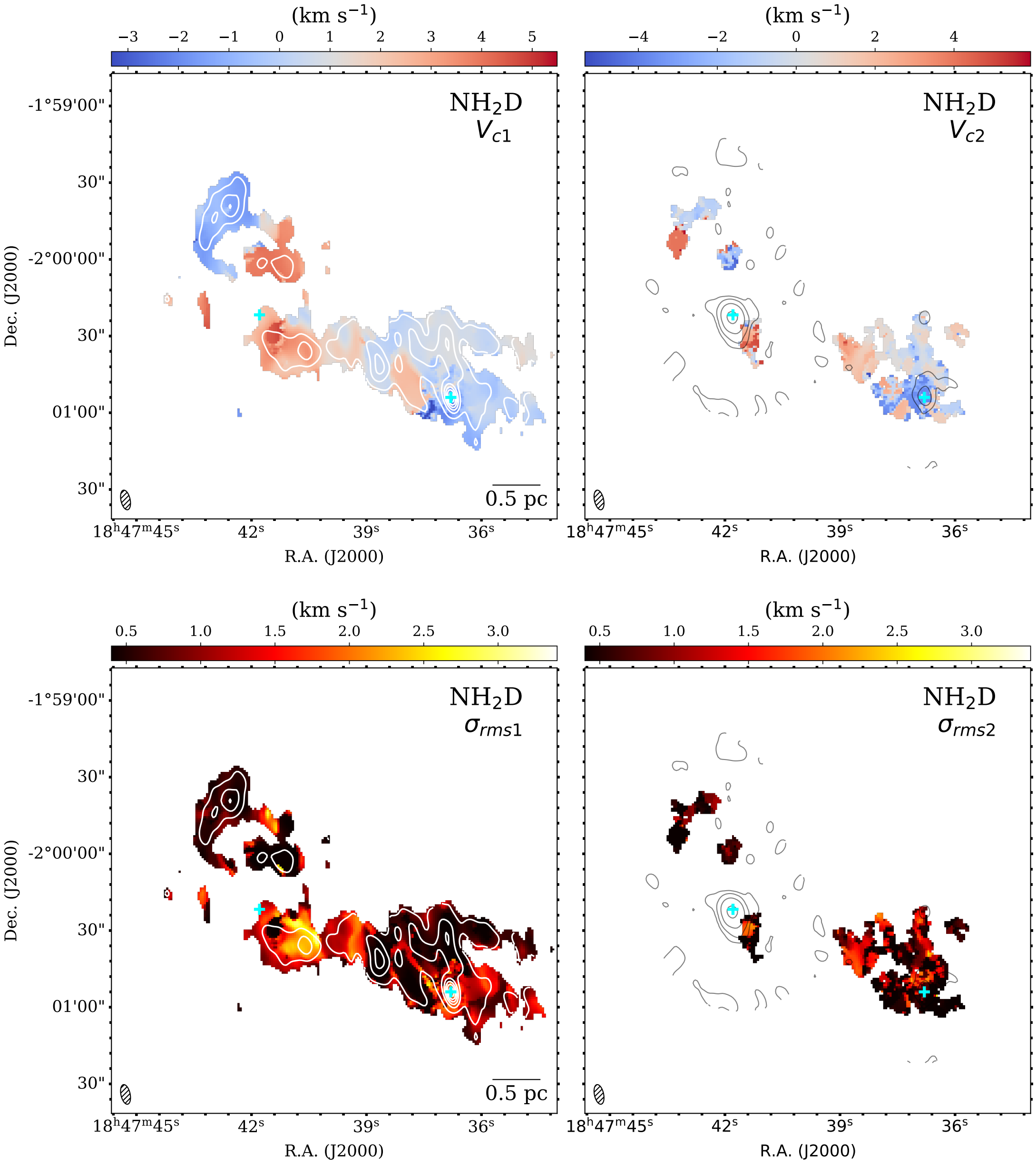

Figure 4.29: The centroid velocity and velocity dispersion distribution of the two-component Gaussian fits of NH$_2$D 1(1,1)-1(0,1) *hfs* lines for clump MM2, MM3 and C. The upper panel and lower panel show the two components separately. White contours in left panels follow same definitions as in Figure 4.25, representing the integrated intensity map of NH$_2$D. In both upper and lower panel, the gray contours, and crosses in left and right plot follow the same definitions as in Figure 4.13.

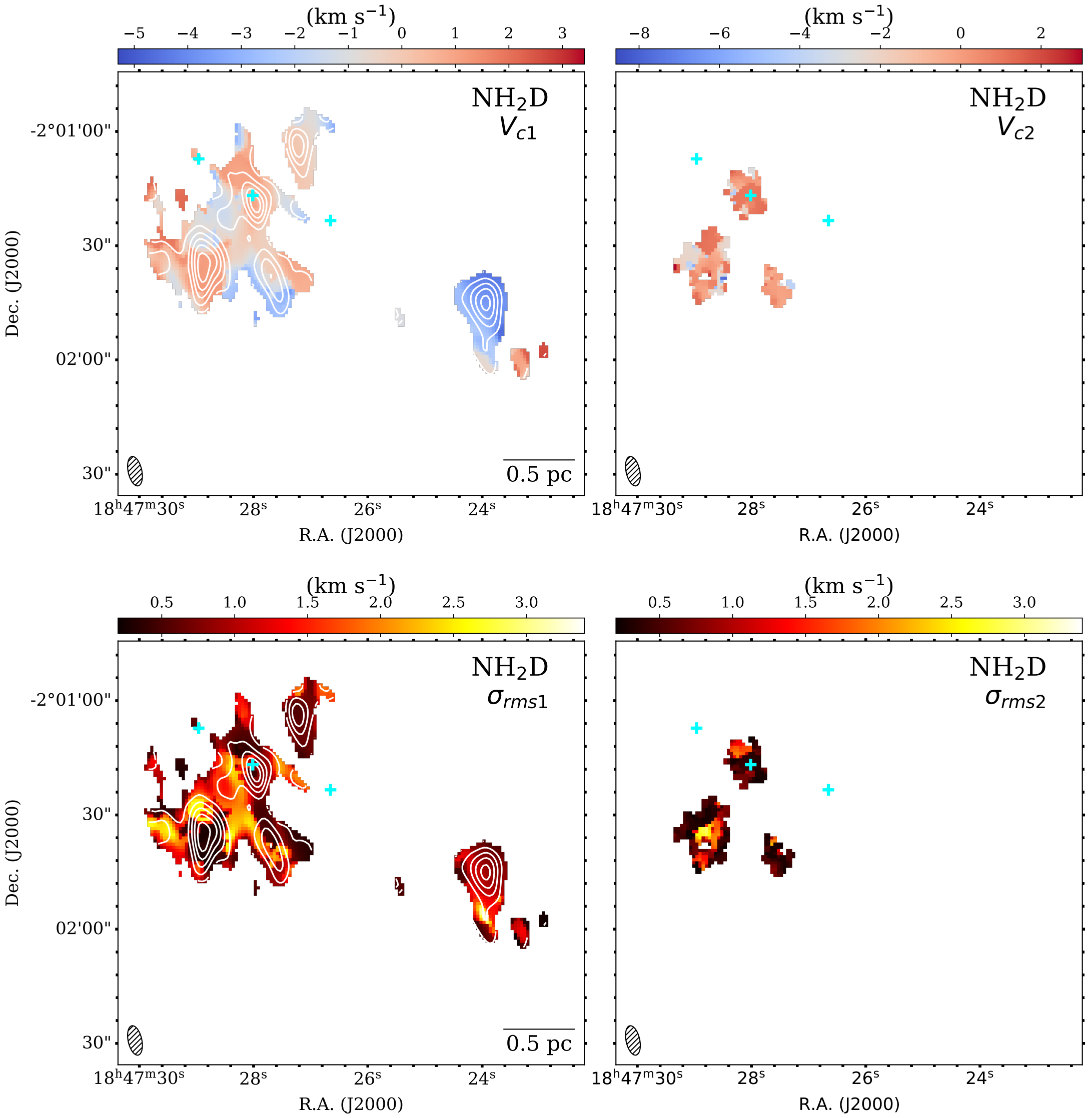

Figure 4.30: Same as Figure 4.29, but for the clump F1 and F2.

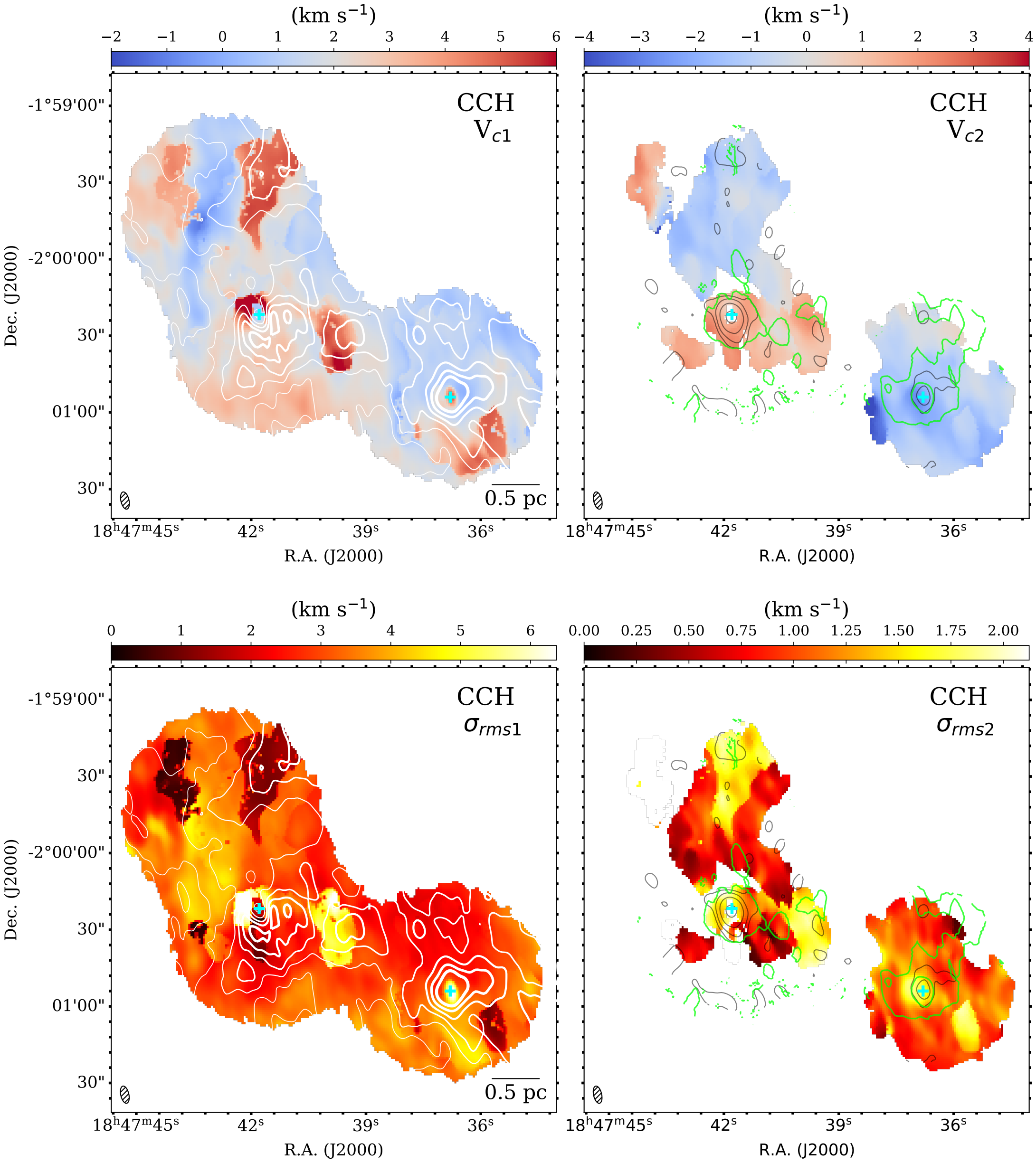

Figure 4.31: The centroid velocity and velocity dispersion distribution of the two-component Gaussian fits of CCH (1-0) *hfs* lines (ν~87.3 GHz) for clump MM2, MM3 and C. The upper panel and lower panel shows the two components individually. White contours in left panels follow same definitions as in Figure 4.27, representing the integrated intensity map of CCH. In both upper and lower panel, the gray and green contours, and crosses in left and right plot follow the same definitions as in Figure 4.13.

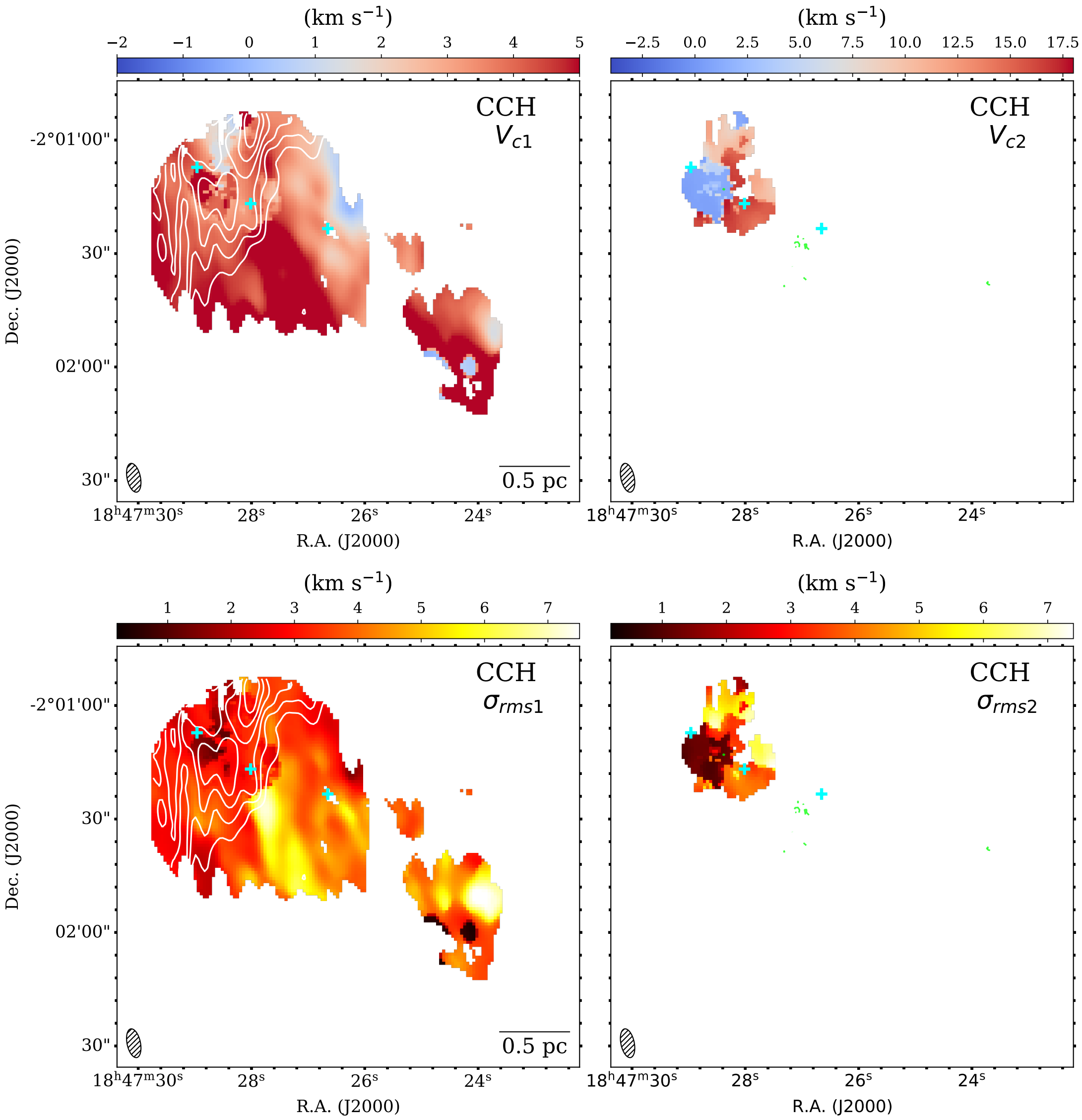

Figure 4.32: Same as Figure 4.31, but for the clump F1 and F2. White contours in left panels follow same definitions as in Figure 4.28, representing the integrated intensity map of CCH.

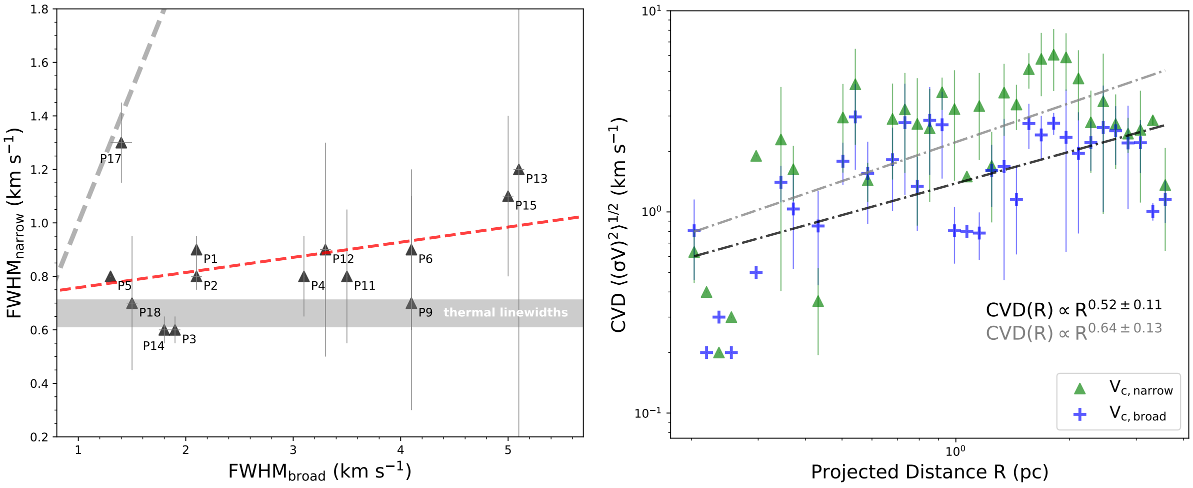

Figure 4.33: *L*eft: The relation between the narrow linewidths and broad linewidths of spectra of NH_2D cores residing in G30.7 of clump MM2, MM3 and C. The gray dashed line indicates equal linewidths, and the red dashed line indicates the linear fit between the linewidths, of $FWHM_{\rm narrow} = 0.05 FWHM_{\rm broad}$+0.70 (km s^{-1}). The shaded region indicates the thermal linewidths based on $T_{\rm rot}$ map derived by CH_3CCH lines (Section 4.3.3). *R*ight: The Core Velocity Dispersion (CVD) measurement for the broad (blue crosses) and narrow velocity components (green triangles), respectively. The fitted power-law relations are shown in gray and black lines, with parameters indicated in the plots.

collisions is dominated by accretion of shocked gas. Following their formulations, we calculate core formation timescale by adopting a characteristic accretion rate. The accretion rate is estimated by $\dot{M} = \pi r_{\rm acc}^2 \sigma_{\rm eff} \rho_{\rm acc}$, where $r_{\rm acc} = \frac{2GM_{\rm core}}{\sigma_{\rm eff}^2} + r_{\rm core}$, and $\rho_{\rm acc}$ is the average ambient gas density (within $r_{\rm acc}$ and excluding the core). Taking the $\rho_{\rm acc}$ from the n(H_2) map, and $M_{\rm core}$ as $M_{\rm vir}$, $\sigma_{\rm eff}$ as the $\sigma_{\rm rms}$ as that of the broad velocity component, we calculate core formation timescale as $t_{\rm form} = \frac{M_{\rm vir}}{\dot{M}}$. In left panel of Figure 4.34 we show the relation between the core mass and separation, and the ratio of the separations to the estimated critical Jeans lengths. In right panel of Figure 4.34, the comparison between core virial mass and core formation timescale, and the ratio of virial masses and critical Jeans masses are shown.

It can be seen that the observed separation between cores and the core mass do not particularly favor predictions of either turbulent fragmentation of the envelope, or thermal fragmentation of the in-situ dense gas. In general, the separations seem to be more close to predictions of turbulent fragmentation of the envelope, but the mass scales lie in-between the two scenarios. However, the core mass is taken to be the virial mass from linewidth of NH_2D, which may be several times underestimated (Pillai et al. 2011, Zhang et al. 2020), compared to dust mass. This will make the difference between the core mass and that of the turbulent fragmentation smaller, but still cannot single out this scenario. The formation timescale $t_{\rm form}$ of these NH_2D cores is weakly correlated with core mass, with a Spearman correlation coefficient of 0.37 (p-value ~ 0.1), ranging between 1×10^3-10^5 yr.

Table 4.5: Properties of dendrogram extracted NH_2D cores that reside in clump MM2, MM3 and C.

Core	R.A. (J2000)	Decl. (J2000)	R_{eff} [a] (pc)	ΔV [b] (km s^{-1})	V_c [b] (km s^{-1})	τ_m	T_{ex} (K)	$N_{NH_2D,20\,K}$ $\times10^{13}$ (cm^{-2})	M_{vir} [c] ($M_\odot$)
P0	$18^h47^m43^s.20$	$-02^\circ00'20.^s0$	0.10	1.0(0.2),4.5(1.8)	99.1(0.1),97.6(0.4)	1.4(0.2),0.1(0.0)	3.0(0.1),3.7(0.4)	0.7(0.2),1.1(0.6)	20.8
P1	$18^h47^m42^s.52$	$-01^\circ59'38.^s3$	0.13	1.1(0.2),1.1(0.0)	94.5(0.1),93.2(0.0)	0.3(0.3),0.9(0.0)	3.5(0.7),4.9(0.1)	0.7(0.2),4.5(0.2)	32.2
P2	$18^h47^m42^s.94$	$-01^\circ59'41.^s6$	0.10	0.8(0.1),2.1(0.1)	93.9(0.0),93.9(0.0)	1.2(0.1),0.1(0.2)	3.4(0.2),8.1(9.0)	1.3(0.2),3.0(0.5)	13.3
P3	$18^h47^m43^s.18$	$-01^\circ59'50.^s3$	0.16	1.9(0.0),0.8(0.1)	93.7(0.0),98.7(0.0)	0.3(0.1),0.3(0.3)	4.8(0.6),3.4(0.9)	2.9(0.2),0.5(0.1)	21.0
P4	$18^h47^m40^s.58$	$-02^\circ00'35.^s7$	0.08	3.1(0.3),0.8(0.0)	96.2(0.1),99.8(0.0)	1.1(0.1),2.1(0.0)	3.2(0.1),3.6(0.0)	3.2(0.4),2.2(0.1)	11.5
P5	$18^h47^m40^s.92$	$-02^\circ00'36.^s3$	0.12	1.3(0.0),0.8(0.0)	96.1(0.0),99.8(0.0)	1.4(0.1),1.7(0.0)	3.4(0.1),3.6(0.1)	2.2(0.1),1.9(0.1)	15.6
P6	$18^h47^m41^s.35$	$-02^\circ00'32.^s4$	0.12	0.9(0.0),4.1(0.6)	99.4(0.0),97.2(0.1)	0.5(0.1),0.3(0.3)	4.2(0.4),3.5(0.9)	1.5(0.1),2.1(0.4)	19.9
P7	$18^h47^m41^s.21$	$-02^\circ00'02.^s4$	0.11	0.9(0.0)	98.4(0.0)	1.9(0.0)	3.5(0.0)	2.1(0.1)	18.6
P8	$18^h47^m41^s.01$	$-01^\circ59'50.^s2$	0.07	1.3(0.1),0.4(0.1)	98.2(0.1),98.1(0.0)	1.3(0.2),0.1(0.9)	3.1(0.1),6.1(27.7)	1.2(0.3),0.4(0.2)	2.4
P9	$18^h47^m38^s.72$	$-02^\circ00'40.^s2$	0.10	4.1(0.8),0.7(0.0)	96.5(0.2),95.1(0.0)	0.1(0.6),1.9(0.0)	5.0(13.0),4.3(0.1)	2.4(0.9),3.4(0.2)	10.1
P10	$18^h47^m37^s.95$	$-02^\circ00'47.^s5$	0.11	3.9(1.2),0.8(0.0)	96.9(0.2),97.0(0.0)	0.1(1.2),0.9(0.1)	4.2(16.4),4.2(0.3)	1.4(1.0),2.2(0.2)	15.3
P11	$18^h47^m36^s.83$	$-02^\circ00'35.^s8$	0.15	1.0(0.0)	95.6(0.0)	1.3(0.0)	4.8(0.1)	5.0(0.1)	32.2
P12	$18^h47^m37^s.72$	$-02^\circ00'34.^s6$	0.09	0.8(0.3),1.1(0.0)	93.5(0.1),95.2(0.0)	1.3(0.4),1.2(0.1)	2.9(0.1),4.5(0.1)	0.4(0.2),4.6(0.2)	11.6
P13	$18^h47^m37^s.81$	$-02^\circ00'26.^s2$	0.13	1.3(0.1),0.8(0.2)	95.1(0.0),93.5(0.1)	0.9(0.1),2.9(0.1)	3.8(0.2),2.9(0.0)	2.9(0.2),0.4(0.1)	17.1
P14	$18^h47^m38^s.19$	$-02^\circ00'30.^s3$	0.09	1.8(0.1),0.4(0.1)	95.1(0.1),94.6(0.0)	1.2(0.1),0.9(0.4)	3.6(0.1),3.3(0.4)	3.8(0.3),0.5(0.2)	3.0
P15	$18^h47^m36^s.77$	$-02^\circ00'54.^s2$	0.08	1.1(0.1),5.0(0.6)	90.9(0.1),92.8(0.1)	2.9(0.0),1.1(0.1)	3.1(0.1),3.8(0.2)	1.5(0.2),11.7(1.9)	20.5
P16	$18^h47^m36^s.05$	$-02^\circ00'59.^s9$	0.12	2.3(0.2)	94.9(0.1)	0.1(0.1)	6.9(4.0)	2.5(0.3)	134.0
P17	$18^h47^m36^s.21$	$-02^\circ01'10.^s0$	0.12	1.4(0.3),1.3(0.2)	95.1(0.2),93.5(0.1)	0.1(0.5),0.6(0.2)	5.4(13.4),3.8(0.5)	1.0(0.3),1.7(0.3)	43.3
P18	$18^h47^m36^s.06$	$-02^\circ00'30.^s3$	0.11	0.9(0.2),1.0(0.0)	91.4(0.1),95.0(0.0)	2.3(0.2),1.1(0.1)	2.9(0.0),4.1(0.2)	0.4(0.1),3.0(0.2)	19.0
P19	$18^h47^m34^s.63$	$-02^\circ00'59.^s2$	0.10	2.1(1.5),3.7(6.2)	95.6(0.3),93.8(4.3)	0.1(1.1),0.1(1.7)	4.6(20.3),4.2(24.0)	1.0(2.7),1.4(2.8)	96.8
P20	$18^h47^m34^s.68$	$-02^\circ00'35.^s3$	0.07	0.7(0.3),2.0(0.6)	95.9(0.1),95.7(0.2)	2.4(0.3),1.6(0.3)	3.0(0.2),3.1(0.2)	0.5(0.4),1.7(0.9)	7.3

a: R_{eff} is the effective radius of the core area, i.e. $\pi R_{\mathrm{eff}}{}^2$ = Area.

b: ΔV and V_c are the FWHM linewidth and centroid velocity from Gaussian line profile, listed for two-component fits and one-component fit accordingly.

c: For the two-component fits, M_{vir} is calculated using the narrower linewidth.

Table 4.6: Properties of dendrogram extracted NH_2D cores that reside in clump F1 and F2.

Core	R.A. (J2000)	Decl. (J2000)	$R_{\rm eff}{}^{a}$ (pc)	ΔV^{b} (km s^{-1})	$V_{\rm c}{}^{b}$ (km s^{-1})	$\tau_{\rm m}$	$T_{\rm ex}$ (K)	$N_{\rm NH_2D,20\,K}$ $\times10^{13}$ (cm^{-2})	$M_{\rm vir}{}^{c}$ ($M_{\odot}$)
SP0	$18^{\rm h}47^{\rm m}23^{\rm s}.95$	-02°01′45.″0	0.21	1.2(0.2),1.9(0.3)	87.2(0.1),88.4(0.2)	3.8(0.0),0.1(0.4)	2.9(0.1),4.9(7.6)	0.6(0.3),1.1(0.3)	62.5
SP1	$18^{\rm h}47^{\rm m}27^{\rm s}.18$	-02°01′03.″6	0.12	1.4(0.0),0.7(0.1)	91.6(0.0),87.9(0.0)	1.1(0.1),1.6(0.1)	3.6(0.1),3.0(0.1)	2.5(0.1),0.5(0.1)	12.2
SP2	$18^{\rm h}47^{\rm m}28^{\rm s}.00$	-02°01′19.″6	0.10	1.0(0.0),3.5(0.4)	92.6(0.0),91.8(0.1)	0.8(0.1),0.1(0.3)	3.9(0.2),4.5(5.5)	1.8(0.1),1.6(0.4)	21.6
SP3	$18^{\rm h}47^{\rm m}27^{\rm s}.21$	-02°01′38.″0	0.12	1.1(0.1)	92.5(0.0)	1.0(0.1)	3.3(0.1)	1.3(0.1)	30.0
SP4	$18^{\rm h}47^{\rm m}27^{\rm s}.59$	-02°01′41.″3	0.18	0.8(0.1),6.0(2.6)	91.7(0.0),90.6(0.1)	0.8(0.3),0.1(1.1)	3.0(0.1),3.9(11.4)	0.3(0.1),1.7(1.3)	24.4
SP5	$18^{\rm h}47^{\rm m}28^{\rm s}.86$	-02°01′35.″6	0.14	0.7(0.0),6.4(4.1)	92.8(0.0),92.1(0.2)	1.4(0.1),0.1(1.6)	3.7(0.1),4.0(19.4)	1.7(0.1),2.0(2.4)	14.4
SP6	$18^{\rm h}47^{\rm m}29^{\rm s}.64$	-02°01′33.″5	0.10	0.8(0.1),5.5(3.5)	93.3(0.0),91.9(0.3)	0.6(0.3),0.6(1.1)	3.3(0.4),3.0(0.7)	0.6(0.2),1.8(1.7)	13.5

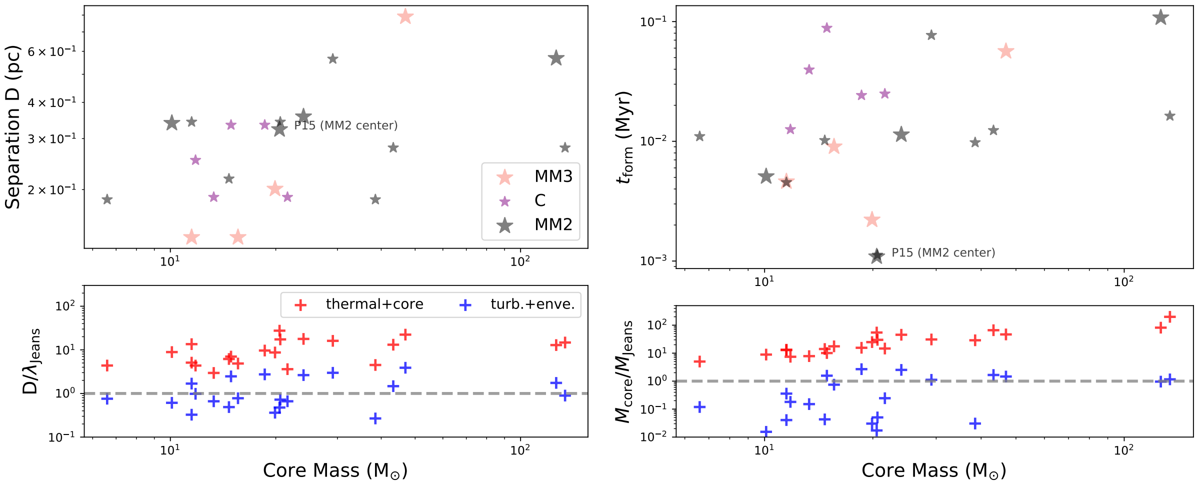

Figure 4.34: *L*eft: The relation of mass of NH_2D cores in G30.7 and their separation (to the nearest neighbor) (upper panel); the ratio between the separation and the critical length scale estimated from Jeans fragmentation (lower panel). *R*ight: The relation of mass of NH_2D core and formation timescale (upper panel). The ratio between the separation and the critical mass scale estimated from Jeans fragmentation (lower panel). The plots in right panel share the same labels as in the legend of the left panel. In both upper plots, the cores that have $\sigma_{\rm rms} > 1$ km s^{-1} in at least one velocity component is shown as enlarged markers.

4.4 Summary

We conducted 3 mm NOEMA and IRAM 30m observations towards massive clumps in W43-main molecular complex, with the primary goal of constraining the physical structures. The clumps are residing in highly turbulent environment, which are of different evolutionary stages. Our results are summarized as follows:

- The distribution of dense gas around the three clumps MM2, MM3 and C shows multiple velocity components. A main filamentary structure is linking clump MM2 and MM3 which extend ~3 pc in length, which is a zoom-in view of the southern tail of the “Z”-shaped W43-main cloud. Overall the velocity field of clump C, MM2 and MM3 shows a complementary picture, changing from blue-shifted to red-shifted and blue-shifted again.

- We derive the rotational temperature maps using H_2CS (3-2) and CH_3CCH (6-5), (5-4), and C_2H_3CN (9-8) lines as thermometers with LTE modeling, and the hydrogen volume density maps based on non-LTE modeling of CH_3OH (2-1) line series. The gas temperatures of clump MM3 show the most centrally peaked profile, reaching 130 K in the clump center and leveling to 30 K at radius of 0.3 pc. Clump MM3 has temperatures of ~40-50 K at the peak of the line emission, offset from the peak of 3mm continuum emission. There are two distinct velocity components towards clump C, one with bulk temperature 25-35 K and one with $\lesssim$20 K, as traced by CH_3CCH. The two rotational temperatures derived by H_2CS show a less contrast, which may indicate H_2CS is mostly tracing the lower density, shocked envelope gas surrounding CH_3CCH emission.

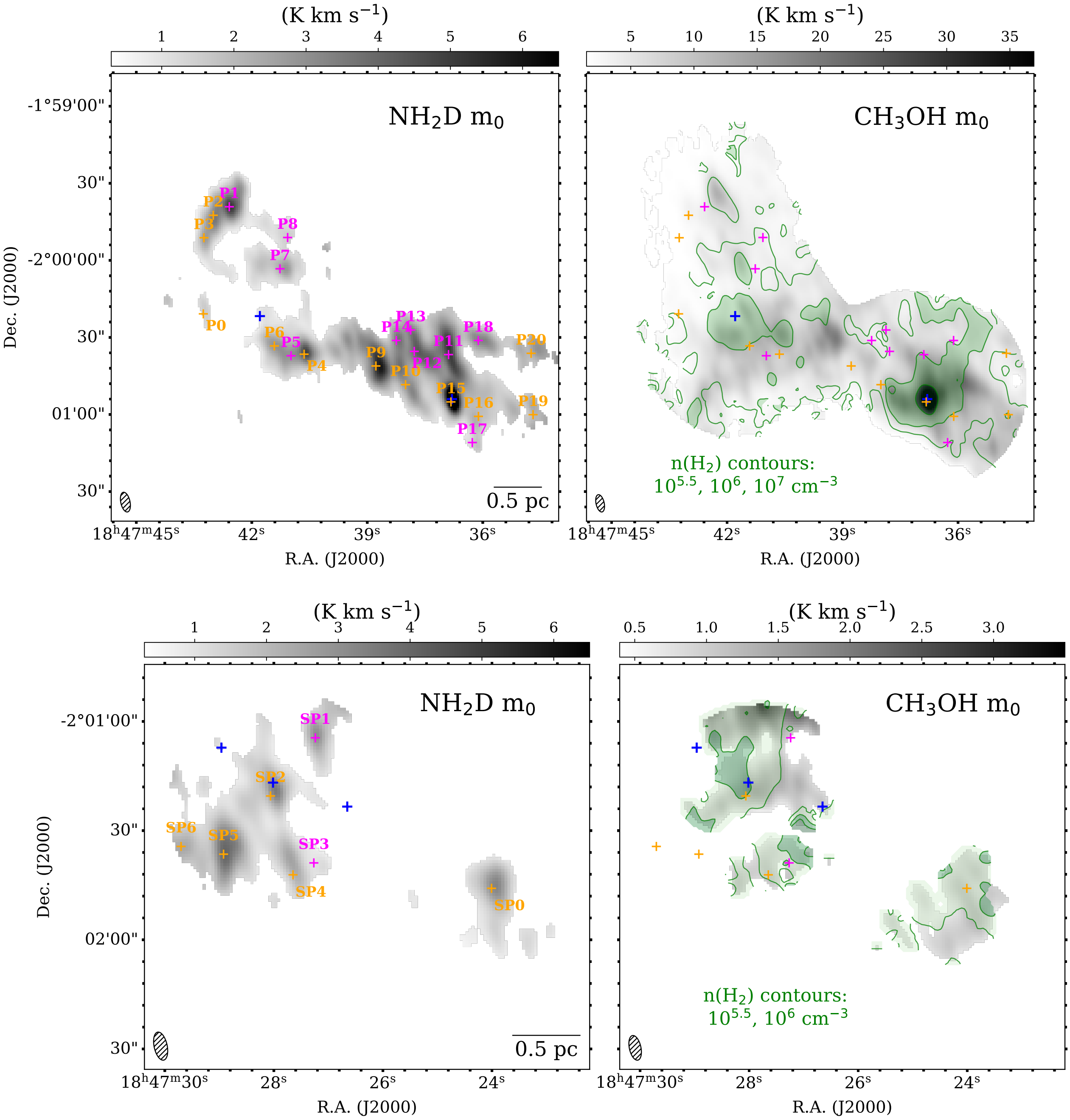

Figure 4.35: *Upper left:* The integrated intensity map of NH_2D line emission of clump MM2, MM3 and C (colorscale, of velocity range 80-115 km s^{-1}) marked with locations of NH_2D cores by colored crosses: the orange crosses indicate the cores which have a $\sigma_{\rm rms}$>1 km s^{-1} velocity components. *Upper right*: The integrated intensity map of CH_3OH 2(0,1)-1(0,1) line (colorscale, of velocity range 85-100 km s^{-1}) overlaid by contours of n(H_2) map (green). In both plots, the blue crosses mark the position of the peak intensity of the 3 mm continuum of clump MM2 and MM3. *Lower panels:* same as upper panels, but for the clump F1 and F2. In both plots, the blue crosses mark the position of the 3 cores in 3 mm continuum of clump F1 (as in Figure 4.2, right panel).

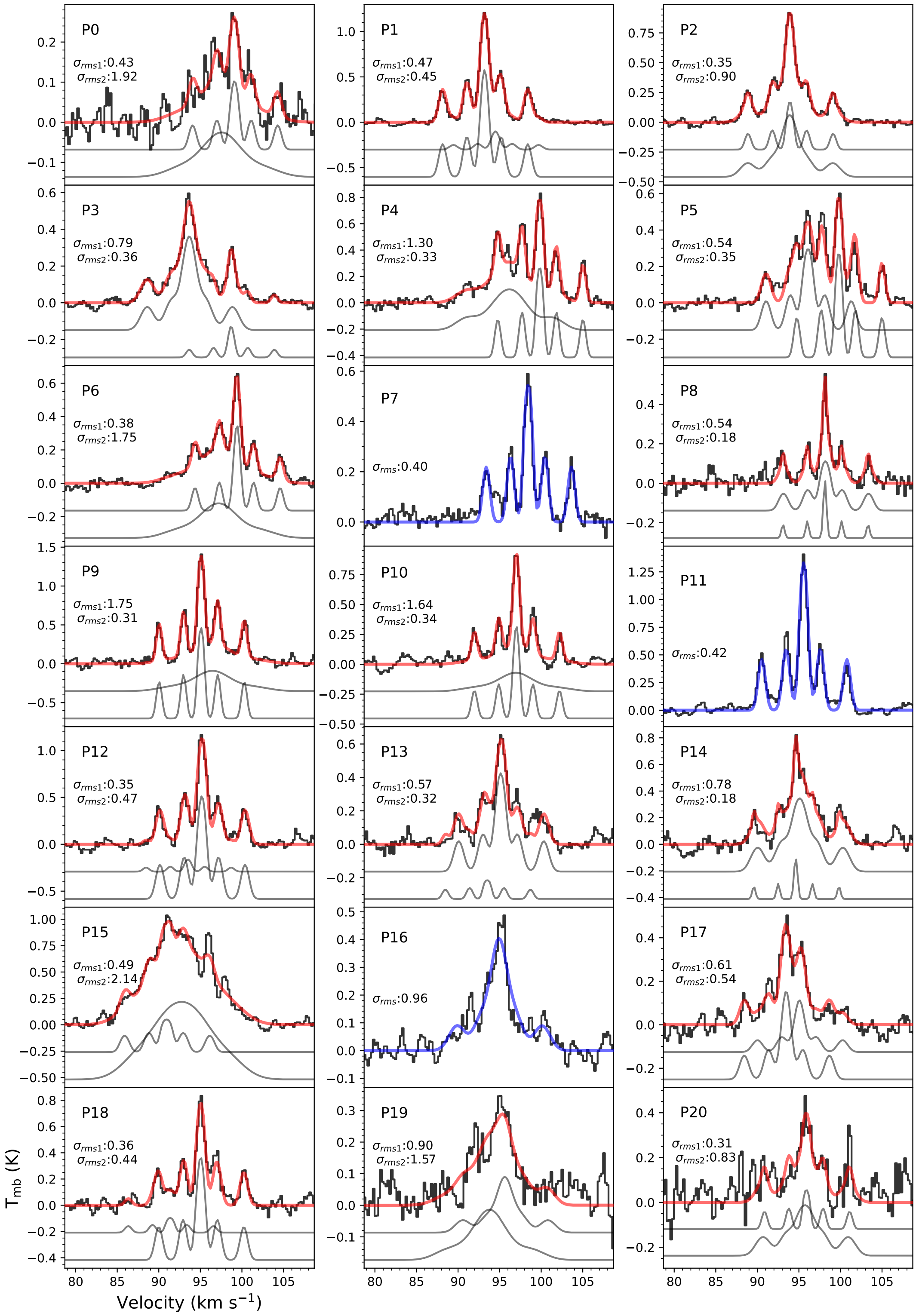

Figure 4.36: The NH_2D spectra of the dendrogram identified cores in clump MM2, MM3 and C. For cores that a single *hfs* component suffices to fit the line profile, the model is shown as blue line, whereas two-component *hfs* fits are shown as red (sum) line and gray lines (manually offseted from zero level) for the two components, separately. The core names are denoted as Pn with n of integers between [0, 20] (Figure. 4.35, upper panels).

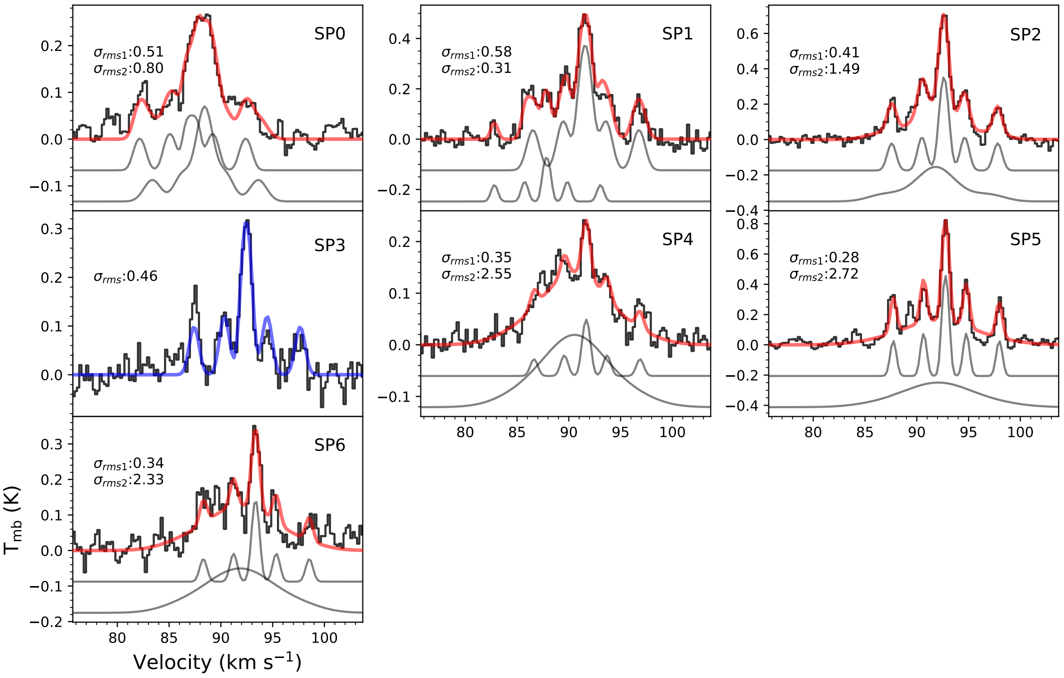

Figure 4.37: Same as Figure 4.36, but for NH_2D spectra for cores residing in clump F1 and F2. The core names are denoted as SPn with n of integers between [0, 7] (Figure. 4.35, lower panels).

- The position-velocity maps of SiO (2-1) and CH_3OH $5_{1,5}$-$4_{0,4}$ along the main filament show multiple double-wing velocity profiles, of linewidths $\lesssim$8 km s^{-1}. The line wings present in CH_3OH $5_{1,5}$-$4_{0,4}$ all have counterparts in SiO (2-1) profiles, while SiO (2-1) exhibit additionally single blue-shifted line wings, exhibiting V-shape structure, which reach terminal velocities of $\gtrsim$10 km s^{-1} around the $V_{\rm LSR}$. Although there is possible confusion from outflowing gas driven by embedded forming clusters, we attribute the relatively narrow-wing, spatially extended and highly asymmetric SiO line emission as signatures of cloud collisions, consistent with previous observations on larger scale cloud structure of W43-main. The double-peaked CCH (1-0) lines is additional evidence suggesting merging clouds, by tracing the outer less dense gas layer.

- We find systematic velocity shifts between the peak velocities of HC_3N, $H_{13}CO^+$, $HC^{15}N$ with respect to SO, H_2CS, and to SiO, CH_3OH, along the main filament. The peak velocities of SiO are most consistent with that of CH_3OH, CCH and CH_3CCH. The peak velocities of SO and H_2CS are systematically red-shifted by 1 km s^{-1} compared to SiO. HC_3N, $H^{13}CO^+$ and HCN are further red-shifted, reaching 2 km s^{-1} difference of peak velocities compared to SiO. The distinct and systematic layering between these tracers is another evidence of cloud collisions and merging.

- Towards the UCHII region of clump MM3, $H^{13}CO^+$ (1-0) and $HC^{15}N$ (1-0) line show negative absorption dips peaking at the centroid velocity of H40α and H42α lines. We calculate an infall rate based on the velocity difference of the absorption dip and V_{LSR} and gas densities derived from CH_3OH lines, of 7×10^{-2} $M_\odot$ yr^{-1}, which is at the high end of accretion rates of high-mass star-forming regions from previous works.

- We discover a population of NH_2D cores which can be categorised into two classes: those that lie close to the main filament that show colliding features, having broad velocity components of $\sigma_{\mathrm{rms}} > 1$ km s^{-1}, and the others that are further away from the main filament that only have narrow velocity component of σ_{rms}~0.5 km s^{-1}, which are in the range of transonic (~$2c_{\mathrm{s}}$) to subsonic ($\lesssim c_{\mathrm{s}}$) linewidths as estimated from T_{rot} derived by CH_3CCH lines. The cores located close to the main filament may represent evolutionary stages still prior or in the stage of turbulence dissipation. The virial masses of these NH_2D cores range from 3 to 100 $M_\odot$. The Core Velocity Dispersion analysis of the centroid velocity of the broader velocity component of these cores points to a turbulent environment dominated by compressive driving mode. The existence of these cores may hint at a new generation of stars being formed in the post-shock gas compressed by cloud collisions. The formation timescales of these cores roughly scale with their masses, and the fragmentation properties are more close to turbulent fragmentation of envelope gas, than to the in-situ fragmentation of dense gas.

References

Balança, Christian et al. (2018), *Rotationally inelastic collisions of SiO with H_2*, Mon. Not. R. Astron. Soc. **479** 2692 (cit. on p. 150).

Bally, J. et al. (2010), *Herschel observations of the W43 "mini-starburst"*, Astron. Astrophys. **518**, L90 L90, arXiv: `1005.4092 [astro-ph.GA]` (cit. on pp. 145, 148).

Beuther, H. et al. (2008), *Ethynyl (C_2H) in Massive Star formation: Tracing the Initial Conditions?*, Astrophys. J. Letters **675** L33, arXiv: `0801.4493 [astro-ph]` (cit. on p. 176).

Bisbas, Thomas G. et al. (2018), *The inception of star cluster formation revealed by [C II] emission around an Infrared Dark Cloud*, Mon. Not. R. Astron. Soc. **478** L54, arXiv: `1803.00566 [astro-ph.GA]` (cit. on p. 172).

Blum, R. D., A. Damineli and P. S. Conti (1999), *The Stellar Content of Obscured Galactic Giant H II Regions. I. W43*, Astron. J. **117** 1392, arXiv: `astro-ph/9812070 [astro-ph]` (cit. on p. 145).

Carey, S. J. et al. (2009), *MIPSGAL: A Survey of the Inner Galactic Plane at 24 and 70 μm*, PASP **121** 76 (cit. on p. 147).

Cortes, Paulo C. et al. (2019), *The Seven Most Massive Clumps in W43-Main as Seen by ALMA: Dynamical Equilibrium and Magnetic Fields*, Astrophys. J. **884**, 48 48, arXiv: `1907.12994 [astro-ph.GA]` (cit. on pp. 147, 158).

Daniel, F. et al. (2014), *Collisional excitation of singly deuterated ammonia NH_2D by H_2*, Mon. Not. R. Astron. Soc. **444** 2544, arXiv: `1408.5757 [astro-ph.GA]` (cit. on p. 150).

Faure, Alexandre, François Lique and Laurent Wiesenfeld (2016), *Collisional excitation of HC_3N by para- and ortho-H_2*, Mon. Not. R. Astron. Soc. **460** 2103, arXiv: `1605.03786 [astro-ph.GA]` (cit. on p. 150).

Fukui, Yasuo et al. (2018), *Formation of the young compact cluster GM 24 triggered by a cloud-cloud collision*, PASJ **70**, S44 S44, arXiv: `1706.05768 [astro-ph.GA]` (cit. on p. 172).

Haworth, T. J. et al. (2015), *Isolating signatures of major cloud-cloud collisions - II. The lifetimes of broad bridge features*, Mon. Not. R. Astron. Soc. **454** 1634, arXiv: `1509.00859 [astro-ph.GA]` (cit. on p. 172).

Henshaw, J. D. et al. (2013), *Complex, quiescent kinematics in a highly filamentary infrared dark cloud*, Mon. Not. R. Astron. Soc. **428** 3425, arXiv: `1210.6835 [astro-ph.SR]` (cit. on p. 172).

Högbom, J. A. (1974), *Aperture Synthesis with a Non-Regular Distribution of Interferometer Baselines*, Astron. Astrophys. Supp. **15** 417 (cit. on p. 146).

Inoue, Tsuyoshi and Yasuo Fukui (2013), *Formation of Massive Molecular Cloud Cores by Cloud-Cloud Collision*, Astrophys. J. Letters **774**, L31 L31, arXiv: `1305.4655 [astro-ph.GA]` (cit. on p. 145).

Kohno, Mikito et al. (2021), *FOREST unbiased Galactic plane imaging survey with the Nobeyama 45 m telescope (FUGIN). VI. Dense gas and mini-starbursts in the W 43 giant molecular cloud complex*, PASJ **73** S129, arXiv: `2001.10693 [astro-ph.GA]` (cit. on pp. 145, 172).

Lin, Y. et al. (2016), *Cloud Structure of Galactic OB Cluster-forming Regions from Combining Ground- and Space-based Bolometric Observations*, Astrophys. J. **828**, 32 32, arXiv: `1606.07645` (cit. on pp. 145–148).

Liow, Kong You and Clare L. Dobbs (2020), *The role of collision speed, cloud density, and turbulence in the formation of young massive clusters via cloud-cloud collisions*, Mon. Not. R. Astron. Soc. **499** 1099, arXiv: `2009.07857 [astro-ph.GA]` (cit. on p. 145).

Louvet, F. et al. (2014), *The W43-MM1 mini-starburst ridge, a test for star formation efficiency models*, Astron. Astrophys. **570**, A15 A15, arXiv: `1404.4843 [astro-ph.SR]` (cit. on p. 146).

Molinari, S. et al. (2010), *Clouds, filaments, and protostars: The Herschel Hi-GAL Milky Way*, Astron. Astrophys. **518**, L100 L100, arXiv: `1005.3317` (cit. on p. 147).

Molinari, S. et al. (2016), *Calibration of Evolutionary Diagnostics in High-mass Star Formation*, Astrophys. J. Letters **826**, L8 L8, arXiv: `1604.06192 [astro-ph.GA]` (cit. on p. 151).

Motte, F., P. Schilke and D. C. Lis (2003), *From Massive Protostars to a Giant H II Region: Submillimeter Imaging of the Galactic Ministarburst W43*, Astrophys. J. **582** 277, eprint: `astro-ph/0208519` (cit. on pp. 145, 147).

Motte, F. et al. (2014), *The formation of the W43 complex: constraining its atomic-to-molecular transition and searching for colliding clouds*, Astron. Astrophys. **571**, A32 A32, arXiv: `1404.4404 [astro-ph.GA]` (cit. on p. 145).

Motte, Frédérique, Sylvain Bontemps and Fabien Louvet (2018), *High-Mass Star and Massive Cluster Formation in the Milky Way*, ARA&A **56** 41, arXiv: `1706.00118 [astro-ph.GA]` (cit. on pp. 145, 146).

Nguyen Luong, Q. et al. (2011), *W43: the closest molecular complex of the Galactic bar?*, Astron. Astrophys. **529**, A41 A41, arXiv: `1102.3460 [astro-ph.SR]` (cit. on p. 145).

Nguyen-Luong, Q. et al. (2013), *Low-velocity Shocks Traced by Extended SiO Emission along the W43 Ridges: Witnessing the Formation of Young Massive Clusters*, Astrophys. J. **775**, 88 88, arXiv: `1306.0547 [astro-ph.GA]` (cit. on p. 158).

Pillai, T. et al. (2011), *Probing the initial conditions of high-mass star formation. II. Fragmentation, stability, and chemistry towards high-mass star-forming regions G29.96-0.02 and G35.20-1.74*, Astron. Astrophys. **530**, A118 A118, arXiv: `1105.0004 [astro-ph.GA]` (cit. on p. 184).

Qian, Lei et al. (2015), *A New Method for Constraining Molecular Cloud Thickness: A Study of Taurus, Perseus, and Ophiuchus*, Astrophys. J. **811**, 71 71, arXiv: `1508.04220 [astro-ph.GA]` (cit. on p. 179).

Rosolowsky, E. W. et al. (2008), *Structural Analysis of Molecular Clouds: Dendrograms*, Astrophys. J. **679** 1338, arXiv: `0802.2944 [astro-ph]` (cit. on p. 177).

Sridharan, T. K. et al. (2014), *Hot Core, Outflows, and Magnetic Fields in W43-MM1 (G30.79 FIR 10)*, Astrophys. J. Letters **783**, L31 L31, arXiv: `1312.2561 [astro-ph.GA]` (cit. on p. 146).

Takahira, Ken, Elizabeth J. Tasker and Asao Habe (2014), *Do Cloud-Cloud Collisions Trigger High-mass Star Formation? I. Small Cloud Collisions*, Astrophys. J. **792**, 63 63, arXiv: `1407.4544 [astro-ph.GA]` (cit. on p. 172).

Takahira, Ken et al. (2018), *Formation of massive, dense cores by cloud-cloud collisions*, PASJ **70**, S58 S58, arXiv: `1706.08656 [astro-ph.GA]` (cit. on p. 179).

Urquhart, J. S. et al. (2018), *ATLASGAL - properties of a complete sample of Galactic clumps*, Mon. Not. R. Astron. Soc. **473** 1059, arXiv: `1709.00392` (cit. on p. 148).

Wiesenfeld, L. and A. Faure (2013), *Rotational quenching of H_2CO by molecular hydrogen: cross-sections, rates and pressure broadening*, Mon. Not. R. Astron. Soc. **432** 2573, arXiv: `1304.4804 [astro-ph.SR]` (cit. on p. 150).

Xu, Siyao (2020), *Projected velocity statistics of interstellar turbulence*, Mon. Not. R. Astron. Soc. **492** 1044, arXiv: `1911.00521 [astro-ph.GA]` (cit. on p. 179).

Zhang, B. et al. (2014), *The Parallax of W43: a Massive Star-forming Complex near the Galactic Bar*, Astrophys. J. **781**, 89 89, arXiv: `1312.3849 [astro-ph.GA]` (cit. on p. 145).

Zhang, Chuan-Peng et al. (2020), *Probing the initial conditions of high-mass star formation. IV. Gas dynamics and NH_2D chemistry in high-mass precluster and protocluster clumps*, Astron. Astrophys. **638**, A105 A105, arXiv: `2004.13946 [astro-ph.GA]` (cit. on p. 184).

CHAPTER 5

Discussion and outlook

In this thesis, intermediate-scale ($\lesssim$0.1-0.2 pc) gas structures of massive star-forming clumps have been systematically investigated towards a carefully selected sample of regions. The physical resolution roughly corresponds to the Jeans length determined by characteristic properties of massive clumps (of gas densities on average of 10^5 cm^{-3} and temperatures of 30 K). We made an effort to increase the dynamical range of the data, by combining data on both small and large spatial scales, in order to robustly probe extended gas structures within massive clumps. We are limited by our angular resolution and sensitivity to directly relate the properties of this extended gas component with those of underlying core populations, which are expected to have a smaller, but wide range of length scales (below thousands of AU to $\lesssim$0.1 pc) and masses. Nonetheless, the results we present provide important missing links between existing higher angular resolution observations towards massive star-forming regions that are able to resolve cores at/below the thousands of AU scale, and the unbiased single-dish surveys of the galactic plane that yield statistical properties at $\gtrsim$pc scale for massive clumps and their parental giant molecular clouds.

In Chapter 2, based on surveying a large sample of massive clumps with dust emission, we found limited fragmentation, and most of the clumps appear centrally concentrated, following a density profile of $r^{-1.5}$, which is determined by the column density contrast between the central cores and their parental clumps. The number of fragments is positively correlated with clump density, but appears lower than predictions of Jeans fragmentation at the 0.1 pc scale. At around this scale (~0.1-0.2 pc), we also do not find a significant difference in mass scales between quiescent cores and star-forming ones identified using MIR and 70 μm compact source association. However, the quiescent cores appears to be more extended and hence less dense on average. To better distinguish between core evolutionary stages, it is necessary to unveil the kinematics of gas structures below the ~0.1 pc scale. Intriguingly, we discover a tight correlation between the mass of clumps and that of their most massive child cores. This correlation indicates that the clump gas reservoir is highly relevant for gas accumulation process for underlying massive cores, which indirectly corroborates the importance of extended accretion or inflow beyond the core scale for massive star formation.

In Chapter 3 we step further into understanding the physical structure of massive clumps. We target a carefully selected sample, which spans an evolutionary sequence, to investigate the density and thermal structure evolution using spectroscopic surveys. We establish a continuous distribution of gas temperature and density at 0.1-1 pc scales, from the central most massive core to extended envelope gas that contributes the bulk of mass for massive clumps. Based on the 0.1 pc angular resolution observations, we find that the gas temperature profiles of the relatively evolved massive clumps ($L/M \gtrsim 10$), seem to be mostly compatible with the central heating models describing a single illuminating object surrounded by spherically symmetric gas envelopes. This may indicate that the forming (massive) stars in the center of the massive clumps decisively shape the thermal properties of the extended gas, such that the fragmentation process of cores distributed in the outer parts of clumps can be predictable (if they follow Jeans fragmentation) without specific measurement of gas temperatures. Yet our continuum sensitivity is insufficient to detect the possibly existing cores of lower masses >0.1 pc from the clump center, and thus cannot *directly* link the clump thermal and density properties to the fragmentation properties. The tight correlation between the clump evolutionary stage indicated by L/M and the steepness of the gas density profiles of the bulk gas structures, suggests that the global evolution of massive clumps can be relatively well described by models of self-gravitating turbulent gas spheres and have temporally varying global SFR (e.g. Murray et al. 2017, Parmentier 2019). Meanwhile, based on our obtained dense gas profiles that show a weaker evolutionary trend, it seems that the localised density enhancements can be more prone to the detailed gas dynamics associated with individual source and may hint to competing collapse processes, either towards the clump centers or the ambient dense structures.

In Chapter 3 we also demonstrate that combining single-dish dust continuum and interferometric observations of a dense gas densitometer can diagnose the spatially varying dense gas mass fraction, which can be linked to the temporally varying SFE/SFR and different star-formation modes. This may be an important characteristic to categorize massive star-forming clumps. Here we note that multi-layer gas structures with different density regimes can be a more realistic description of massive clumps, where self-similar solutions applicable to a single collapsing object may not suffice due to the highly hierarchical and clumpy distribution of dense gas pockets, as induced by enhanced turbulence or/and prevailing gravitational collapse. We investigate the radial variation of linewidths and $\alpha_{\rm vir}$ using multiple tracers that reflect the dynamical state of the clumps. We reveal a scale-dependent linewidth-radius relation, marking the transition to gravitational collapse in driving the gas motions at smaller scale. This result again suggests a gravo-turbulent collapse picture for massive clumps, in which the linewidths showing turbulent motions are dominated by infall velocities. The radial variations of $\alpha_{\rm vir}$ shows a decreasing trend with clump L/M, and are compatible with the radial variations of the dense gas fraction. These indicate the evolution of massive clumps follow a comprehensive evolutionary track: the massive clumps can be quantified by temporal variations of energy balance, which reflects gas dynamics driving dense gas conversion and subsequent star formation.

In Chapter 4, we analyze the physical structure of 5 massive clumps residing in the W43-main molecular complex, which has a highly turbulent environment in which clouds are colliding and merging. These 5 clumps represent an early evolutionary sequence. Their temperature structures show mostly rather uniform profiles at 0.1 pc resolution, and may represent clumps of evolutionary stages that host distributed heating sources before their central merging, in contrast to most of the targets studied in Chapter 3. We discovered a sample of early-stage cores which are traced by compact NH_2D emission. The formation of these cores is likely triggered by cloud collisions on a shorter timescale, which is deduced from the cores' centroid velocity statistics reflecting dominant compressive turbulent motions (CVD method, Qian et al. 2015). In addition, the cores belong to two distinct categories as defined by the presence or non-presence of broader linewidths, which likely correspond to cores before or after turbulence dissipation, respectively. Besides these more quiescent cores, the localised density enhancements probed by CH_3OH, likely representing shock processed warmer dense gas pockets, are tightly correlated with regions showing collision signatures. These suggest cloud collisions aiding in dense gas conversion which accelerates star formation. This chapter, compared to Chapters 2 and 3, shows that including the influence of large-scale gas dynamics is also important for our systematic understanding of the formation of massive clumps and their underlying cores.

We intend to extend this line of works to statistically larger, statistically significant samples, with data of higher angular resolution and sensitivity. Particularly, improved continuum sensitivity is a necessity for probing core populations at the low-mass end. However, it has long been known that multiplicity of star-forming clumps can exist well below 1000 AU ($0.''2$ at 5 kpc) (Preibisch et al. 1999); therefore very high angular resolution observations may be needed that can only be obtained towards smaller samples, making statistically significant conclusions difficult. Indeed, understanding the hierarchical multi-scale nature of massive star-forming regions might be more critical. We will combine dissecting the gas multi-scale kinematics with detailed measurements of gas densities across multiple density regimes, which is achievable with the strategies presented in Chapter 3 and 4.

Following the results in this thesis, there are several immediate aspects that are relevant and worth further investigations. While our results suggest a correlation between the masses of clumps and their most massive child core at 0.1 pc scales, such a correlation is missing in higher angular resolution observations resolving scales of thousands of AU, as revealed by ALMA observations towards early-stage clumps (Sanhueza et al. 2019). It therefore is necessary to unveil the substructures of the ~0.1 pc cores that we resolved in Chapter 2. Confronting such multi-scale results with theoretical models will be important. Particularly, the *global hierarchical collapse* model predicts the generation of new cores to happen in existing ones. The break down of the correlation between core and clump mass may point to a critical scale beyond which the extended accretion stops contributing to the final stellar mass compared to the initial core mass. The mass origin of OB stars is an essential question to be answered in the realm of massive star formation. While it seems that the isolated massive star formation scenarios can be almost ruled out (at least as a general formation avenue, however, see Csengeri et al. 2019), it is critical to understand, across the evolutionary sequence of massive clumps, the mass partition of the cores forming massive stars and their sibling low-mass cores.

It will also be interesting to examine the radial linewidth and $\alpha_{\rm vir}$ relations towards the scale close to and within prestellar cores in a statistical manner. The (spherically averaged) radial profile of linewidths is shown to monotonically increase in the framework of the *inertial inflow* model, exhibiting a scaling relation shallower than that predicted by supersonic turbulence. This represents essential evidence for compressive turbulent motions dominating the mass accumulation process. In the *global hierarchical collapse* model, the velocity profile of prestellar cores also exhibits characteristic patterns: infall/radial velocity increases linearly with radius and remains subsonic within the core boundary, and has a slightly decreasing profile in the surrounding envelope/background gas. The velocity dispersion follows a similar profile, which peaks at the core's envelope. At later stages, however, in concordance with the gravo-turbulent model suggests and consistent with some of our observations for massive clumps at 0.1 pc resolution, a scale-dependent velocity profile appears. This reflects the conversion of accelerated gravitational collapse to turbulent kinetic energy at the bottom of the potential well, which transitions to a (close-to) subsonic velocity scaling at larger scales. Such evolutionary distinctive velocity dispersion profiles can be used to diagnose the evolutionary stages of cores in combination with other evolutionary signposts. The systematic diagnosis of core evolutionary stages has relied heavily on searching for MIR counterparts, dating outflow timescales and chemical content. Adding such a kinematic analysis, which is made possible by using multiple tracers, will complete the picture of core evolution.

We emphasize that looking at the relation between the properties (usually a set of single *averaged* parameters without continuous mapping) of the bulk gas component of massive clumps and the underlying localised cores, as most of previous works did, provides a rather static view of the dense gas fraction/core formation efficiency. On the other hand, a tomographic view of different gas density regimes, can potentially trace the evolution of the progressively condensing gas flows and/or contracting ambient envelopes surrounding localised cores, providing a temporal diagnosis of the mass accumulation process. As in the self-similar collapse scenario, the outer gas layer can be regarded as representing an earlier evolutionary stage. Existing massive star formation scenarios predict different trends of temporal variations of the accretion rate onto the massive stars (Section 1.2). While direct measurements of the accretion rates can be difficult, the spatial variation of the dense gas mass fraction may be used as an alternative gauge to estimate the dense gas conversion efficiency.

In Chapter 2 and 3, due to the limited angular resolution, we have not systematically analyzed the specific kinematics of the probed dense gas structures, which requires resolving the gas geometry in greater detail. Due to the role of supersonic turbulence in condensing gas structures in addition to self-gravity, some of the dense gas components can rather be transient structures that disperse eventually, and thus do not contribute to the final cluster mass. This is a common drawback when linking the unresolved dense gas fraction to the ability/fertility of star formation. To this end, it is also advantageous to conduct higher velocity resolution observations of the selected thermometers and densitometers, to identify coherent or characteristic gas structures, i.e. filamentary flows, rotating toroids, outflowing gas, etc, in order to characterize the gravitational boundedness of dense gas.

Since extended accretion and inflow along filaments towards cores is suggested to be a critical ingredient for massive star formation, kinematic studies have focused on searching for velocity gradients along filaments, referred to as fibres and striations. But it has been shown that the line-of-sight (LOS) confusion can bias such an analysis by creating false velocity coherent structures (Zamora-Avilés, Ballesteros-Paredes and Hartmann 2017, Clarke et al. 2018) in PPV space, as LOS velocities are a density weighted quantity. Combining the density estimates from multiple densitometers may help distinguish sub-structures that are tangled up in velocity space, and facilitate estimates of the accretion/inflow rate and its spatial variations.

For our understanding of the birth of massive stars, the definition of a core is also critical. From the observational side, this definition can sometimes be ambiguous due to the uncertain boundaries and projection effects. It has also been shown that coarser angular resolution maps can systematically overestimate masses of cores by including gas from their ambient envelopes, or merging several cores into a single structure. Observationally, the flux distribution, mostly from the continuum, defines the cores, i.e., regions showing a density contrast or gradient with respect to the envelope or background gas. Interferometers are less sensitive to extended structures, hence they enhance the contrast allowing to easier separate the small scale cores. However, ideally, core boundaries should correspond to a spatial change of $\alpha_{\rm vir}$ or linewidth, sometimes referred to as where “transition to coherence” occurs (Goodman et al. 1998). When extracting core structures from the output of numerical simulations, a precise value of $\alpha_{\rm vir}$ can be obtained to define core boundaries (Gong and Ostriker 2011, Padoan et al. 2020). For the analysis of observational data, a similar attempt will require measurements of $\alpha_{\rm vir}$ and linewidths continuously from within the core to the ambient envelope gas, which is made possible again by adopting multiple tracers to constrain the gas density profiles (or with gas density profiles determined from continuum). The definition of cores by their density gradients and measurements of the aforementioned velocity profiles as well as $\alpha_{\rm vir}$ variations can be a two-way test for understanding core structure.

Quantifying the behavior of turbulence associated with massive star-forming regions is also critical.

We measured turbulent motions using centroid velocities of NH_2D cores in Chapter 4, based on the CVD method (Qian et al. 2015), which has been applied to study the velocity statistics imprinted by discrete density peaks of cores. With a similar concept, the structure function of the (projected) velocity maps can identify the critical turbulence scales, and in turn provide a constraint of the cloud thickness (Xu 2020), which helps to constrain the cloud geometry and to corroborate measurements of the dense gas fraction. A continuous mapping of velocity correlation functions with multiple density tracers can be tested, which may even provide a picture of the 3D structure of the gas distribution. This can be an important analysis for understanding the impact of the initial condition on massive star formation, and the fertilities of massive star-forming regions.

It may also be enlightening to look at other statistics of turbulent motions associated with massive star-forming regions. Theoretical works demonstrate that turbulence and its mode mixing have significant impact on the final properties of star clusters (Federrath and Klessen 2012), which is at play in combination with the clouds' initial density profiles (Girichidis et al. 2011, Lomax, Whitworth and Hubber 2015). Brunt and Federrath (2014) propose an approach in which the fraction of solenoidal and compressible modes is analyzed. It is applicable to the observed 2D projected moment maps, and has been used to interpret data for Orion B (Orkisz et al. 2017). This line of work can be extended to more distant early-stage massive clumps and clouds. The density selectivity of multiple densitometers can help to gauge the density-velocity correlation which needs to be decoupled beforehand in this approach. Moreover, as simulations show that compressive turbulence accelerates the onset of star formation and boosts SFE compared to that dominated by the solenoidal mode (e.g. Federrath et al. 2016), observational correlations between the fraction of the turbulence driving modes (being incompressible or compressible) and dense gas mass fraction are to be systematically examined. This is especially relevant for understanding massive clumps residing in extreme environments such as the central molecular zone or cloud-cloud intersection regions such as the W43 complex. Particularly, in the *inertial-inflow* model, the inertial compressive motions from the extended gas (up to 10 pc) are essential for mass accumulation towards massive stars. Systematic measurement of turbulence driving modes together with the dense gas fraction will shed light on such formation models.

In Chapter 3 and Chapter 4, one main science goal has been determining the clump temperature structure at 0.1 pc scales. We found that some sources show clear deviations from a single heating model. The origin and occurrence of such deviations remains to be resolved for a statistically large sample, to see if it is caused by the geometry or (fragmented) substructure of the dense gas, and how they shape the formation of widely distributed cores. This effect is missed by simple radiative transfer approximations based on a central heating source, which are routinely adopted to ease the computing burden instead of solving for full radiative transfer. Observationally, it is also hard to separate the energy budget into accretion luminosity and stellar intrinsic luminosity, while the absolute scale and impact of the former is theoretically highly uncertain and shown to be an important factor governing fragmentation and mass distribution of cores (Urban, Martel and Evans 2010, Hennebelle et al. 2020). In light of this, measuring the detailed temperature structure of early-stage sources may provide constraints on accretion luminosity.

We will consider more realistic gas geometries in radiative transfer models in future works constrained by higher angular resolution observations. Throughout Chapter 3 we have effectively made simplifying assumptions on the geometry, using a spherical structure to describe the underlying gas of massive clumps in radiative transfer modelings. This is a natural choice, given the limited angular resolution of our data. The spherical gas geometry represents the most dynamic gravitational collapse compared to flattened or filamentary configurations. However, the level of radiative feedback can be drastically different in asymmetric density structures, as attenuation of radiation through optically thin gas is more efficient. For example, the existence of non-uniform lower density regions due to outflow cavities or asymmetric density distributions can greatly reduce the impact of radiative heating (Cunningham et al. 2011, Rosen et al. 2016). Moreover, disk-mediated accretion has a similar effect (Mathew and Federrath 2020). These complexities have to be considered when analysing higher angular resolution observations at <0.1 pc. At the 0.1 pc scale we probed, it is likely that for the relatively evolved clumps we analysed, the luminosity centers of forming stars have merged to create a heating environment that can be approximated well by a central heating model, modulated by a different steepness of spherical gas density profiles. For massive clumps in still earlier stages, how the more distributed heating, mainly induced by accretion energy, affects the early-stage fragmentation process remains to be investigated.

The temporal evolution of the CMF may have a dependence on the heated gas structures and properties of turbulent motions. Simulations have shown that the higher Mach number leads to a lower median mass and a wider mass distribution of core populations (Gong and Ostriker 2011). In contrast, the radiative heating from massive stars may introduce a top-heavy CMF, by suppressing excessive fragmentation of low-mass objects (Krumholz, Klein and McKee 2011). Comparing CMFs across an evolutionary sample of massive clumps, and clumps in different molecular environments is an important follow-up of our current works. For example, in Chapter 4, due to the special environment of cloud collisions, the core formation timescale can be estimated based on an accretion-dominated scenario adoptable for colliding clouds, and is found to be lower for the former category of cores. In this context, within a single clump, the evolution of the CMF can be deduced. However, the low number of cores recovered by our coarse resolution observations inhibits a robust CMF determination. We shall conduct such an analysis for a larger sample of prestellar cores, to understand the progressive core generation within massive clumps.

In this thesis it is not attempted to comprehensively understand the clumps' chemical content to the degree that it could serve as a diagnostic. In Chapter 3 we adopt several pairs of molecular species that are chemically relevant, only to use their abundance ratios to facilitate sequencing the evolutionary stage of the clumps under study. Based on a more detailed chemical analysis, chemo-physical modeling of massive star forming clumps can constrain timescales of relevant physical processes (Gieser et al. 2021). Previous works have mainly focused on understanding the hot massive core stage and the very early cold phase when clump gas is characterised by high deuteration. Recent observations have revealed that COM chemistry is not only relevant in the hot-core stage, but is generally present across massive star-forming regions of various evolutionary stages (e.g. Fayolle et al. 2015, Coletta et al. 2020, Law et al. 2021). Towards warmer sources, the cold gas relic, as traced by enhanced emission of deuterated molecules (e.g. Guzmán et al. 2018, Redaelli et al. 2021), can carry important implications on the gas dynamical history. Investigations of the evolution of the chemical content of massive star-forming regions, using both higher angular resolution to disclose the detailed structured chemical distribution, and intermediate-scale resolution to distinguish the impact of large-scale cloud environment, are necessary for a full understanding of chemical processes. This in turn will aid the understanding of physical processes in massive star formation.

In the era of ALMA, several large programs on the topic of massive star formation are underway, which are delivering promising data sets with high angular resolution towards large samples that will allow investigating the physical and chemical structure of massive star-forming regions in unprecedented detail. The ALMA-IMF large program (PI: F. Motte, Louvet 2019) puts a special emphasis on measuring CMFs towards the most prominent massive star-forming sites in the Galaxy.

For example, the pioneer studies of W43-main MM1 have shown that the CMF of massive clumps in certain cloud environments can appear top-heavier than the canonical IMF. Such results have important implications on the origin of stellar mass and question the direct mapping from the CMF to the invariant IMF. The ALMAGAL program (PI: S. Molinari) targets a much larger sample ($>$ 1000) of massive clumps in vastly different galactic environments, aiming at drawing an evolutionary picture of clump structures at $\lesssim$1000 au. Illuminating the fragmentation properties and gas dynamics, especially the infall motions, and the role of filaments in the massive star formation process are all essential goals of these programs. The large datasets also call for more advanced data analysis and computing methods, for an efficient exploitation of such versatile resources. We expect considerable progress in the understanding of the massive star formation process in the next decade, based on such new datasets, refined modeling and systematic comparison with simulations. The modeling efforts and data analysis methods presented in this thesis are first steps in addressing the physical properties on a large range of spatial scales in massive star-forming sites and developing more efficient and systematic techniques that can be used for future data sets.

References

Brunt, C. M. and C. Federrath (2014), *An observational method to measure the relative fractions of solenoidal and compressible modes in interstellar clouds*, Mon. Not. R. Astron. Soc. **442** 1451, arXiv: `1405.1285 [astro-ph.GA]` (cit. on p. 199).

Clarke, S. D. et al. (2018), *Synthetic* $C^{18}O$ *observations of fibrous filaments: the problems of mapping from PPV to PPP*, Mon. Not. R. Astron. Soc. **479** 1722, arXiv: `1806.08564 [astro-ph.GA]` (cit. on p. 198).

Coletta, A. et al. (2020), *Evolutionary study of complex organic molecules in high-mass star-forming regions*, Astron. Astrophys. **641**, A54 A54, arXiv: `2006.15413 [astro-ph.GA]` (cit. on p. 200).

Csengeri, T. et al. (2019), *Search for high-mass protostars with ALMA revealed up to kilo-parsec scales (SPARKS). II. Complex organic molecules and heavy water in shocks around a young high-mass protostar*, Astron. Astrophys. **632**, A57 A57 (cit. on p. 197).

Cunningham, Andrew J. et al. (2011), *Radiation-hydrodynamic Simulations of Massive Star Formation with Protostellar Outflows*, Astrophys. J. **740**, 107 107, arXiv: `1104.1218 [astro-ph.SR]` (cit. on p. 200).

Fayolle, Edith C. et al. (2015), *Complex organic molecules in organic-poor massive young stellar objects*, Astron. Astrophys. **576**, A45 A45, arXiv: `1501.03168 [astro-ph.SR]` (cit. on p. 200).

Federrath, C. et al. (2016), *The Link between Turbulence, Magnetic Fields, Filaments, and Star Formation in the Central Molecular Zone Cloud G0.253+0.016*, Astrophys. J. **832**, 143 143, arXiv: `1609.05911 [astro-ph.GA]` (cit. on p. 199).

Federrath, Christoph and Ralf S. Klessen (2012), *The Star Formation Rate of Turbulent Magnetized Clouds: Comparing Theory, Simulations, and Observations*, Astrophys. J. **761**, 156 156, arXiv: `1209.2856 [astro-ph.SR]` (cit. on p. 199).

Gieser, C. et al. (2021), *The physical and chemical structure of high-mass star-forming regions. Unraveling chemical complexity with the NOEMA large program "CORE"*, arXiv e-prints, arXiv:2102.11676 arXiv:2102.11676, arXiv: `2102.11676 [astro-ph.GA]` (cit. on p. 200).

Girichidis, Philipp et al. (2011), *Importance of the initial conditions for star formation - I. Cloud evolution and morphology*, Mon. Not. R. Astron. Soc. **413** 2741, arXiv: `1008.5255 [astro-ph.SR]` (cit. on p. 199).

Gong, Hao and Eve C. Ostriker (2011), *Dense Core Formation in Supersonic Turbulent Converging Flows*, Astrophys. J. **729**, 120 120, arXiv: `1101.2650 [astro-ph.SR]` (cit. on pp. 198, 200).

Goodman, Alyssa A. et al. (1998), *Coherence in Dense Cores. II. The Transition to Coherence*, Astrophys. J. **504** 223 (cit. on p. 198).

Guzmán, Andrés E. et al. (2018), *Chemistry of the High-mass Protostellar Molecular Clump IRAS 16562-3959*, Astrophys. J. Supp. **236**, 45 45, arXiv: `1804.06544 [astro-ph.GA]` (cit. on p. 200).

Hennebelle, Patrick et al. (2020), *What is the role of stellar radiative feedback in setting the stellar mass spectrum?*, arXiv e-prints, arXiv:2010.03539 arXiv:2010.03539, arXiv: `2010.03539 [astro-ph.GA]` (cit. on p. 199).

Krumholz, Mark R., Richard I. Klein and Christopher F. McKee (2011), *Radiation-hydrodynamic Simulations of the Formation of Orion-like Star Clusters. I. Implications for the Origin of the Initial Mass Function*, Astrophys. J. **740**, 74 74, arXiv: `1104.2038 [astro-ph.GA]` (cit. on p. 200).

Law, Charles J. et al. (2021), *Subarcsecond Imaging of the Complex Organic Chemistry in Massive Star-forming Region G10.6-0.4*, Astrophys. J. **909**, 214 214, arXiv: `2101.07801 [astro-ph.GA]` (cit. on p. 200).

Lomax, O., A. P. Whitworth and D. A. Hubber (2015), *On the effects of solenoidal and compressive turbulence in pre-stellar cores*, Mon. Not. R. Astron. Soc. **449** 662, arXiv: `1502.04009 [astro-ph.SR]` (cit. on p. 199).

Louvet, Fabien (2019), “ALMA-IMF Large program, toward the understanding of the origin of the IMF”, *ALMA2019: Science Results and Cross-Facility Synergies* 8 (cit. on p. 200).

Mathew, Sajay Sunny and Christoph Federrath (2020), *Implementation of stellar heating feedback in simulations of star cluster formation: effects on the initial mass function*, Mon. Not. R. Astron. Soc. **496** 5201, arXiv: `2007.01875 [astro-ph.GA]` (cit. on p. 200).

Murray, Daniel W. et al. (2017), *Collapse in self-gravitating turbulent fluids*, Mon. Not. R. Astron. Soc. **465** 1316, arXiv: `1509.05910 [astro-ph.GA]` (cit. on p. 196).

Orkisz, Jan H. et al. (2017), *Turbulence and star formation efficiency in molecular clouds: solenoidal versus compressive motions in Orion B*, Astron. Astrophys. **599**, A99 A99, arXiv: `1701.00962 [astro-ph.GA]` (cit. on p. 199).

Padoan, Paolo et al. (2020), *The Origin of Massive Stars: The Inertial-inflow Model*, Astrophys. J. **900**, 82 82, arXiv: `1911.04465 [astro-ph.GA]` (cit. on p. 198).

Parmentier, G. (2019), *The Density Gradient Inside Molecular-gas Clumps as a Booster of Their Star Formation Activity*, Astrophys. J. **887**, 179 179, arXiv: `1911.04994 [astro-ph.GA]` (cit. on p. 196).

Preibisch, Thomas et al. (1999), *Multiplicity of the massive stars in the Orion Nebula cluster*, New Astron. **4** 531 (cit. on p. 197).

Qian, Lei et al. (2015), *A New Method for Constraining Molecular Cloud Thickness: A Study of Taurus, Perseus, and Ophiuchus*, Astrophys. J. **811**, 71 71, arXiv: `1508.04220 [astro-ph.GA]` (cit. on pp. 196, 199).

Redaelli, E. et al. (2021), *Identification of prestellar cores in high-mass star forming clumps via* H_2D^+ *observations with ALMA*, arXiv e-prints, arXiv:2104.06431 arXiv:2104.06431, arXiv: `2104.06431 [astro-ph.GA]` (cit. on p. 200).

Rosen, Anna L. et al. (2016), *An unstable truth: how massive stars get their mass*, Mon. Not. R. Astron. Soc. **463** 2553, arXiv: `1607.03117 [astro-ph.SR]` (cit. on p. 200).

Sanhueza, Patricio et al. (2019), *The ALMA Survey of 70 µm Dark High-mass Clumps in Early Stages (ASHES). I. Pilot Survey: Clump Fragmentation*, Astrophys. J. **886**, 102 102, arXiv: `1909.07985 [astro-ph.GA]` (cit. on p. 197).

Urban, Andrea, Hugo Martel and II Evans Neal J. (2010), *Fragmentation and Evolution of Molecular Clouds. II. The Effect of Dust Heating*, Astrophys. J. **710** 1343, arXiv: `0912.3819 [astro-ph.GA]` (cit. on p. 199).

Xu, Siyao (2020), *Projected velocity statistics of interstellar turbulence*, Mon. Not. R. Astron. Soc. **492** 1044, arXiv: `1911.00521 [astro-ph.GA]` (cit. on p. 199).

Zamora-Avilés, Manuel, Javier Ballesteros-Paredes and Lee W. Hartmann (2017), *Are fibres in molecular cloud filaments real objects?*, Mon. Not. R. Astron. Soc. **472** 647, arXiv: `1708.01669 [astro-ph.GA]` (cit. on p. 198).

APPENDIX A

Supporting information

Appendix A.1-A.4 are supplementary materials for Chapter 2. In Appendix A.1 all the observed SABOCA maps are shown. Appendix A.2 elaborates on the 70 μm flux rescaling method we use for SED fitting. The dendrogram results for benchmarking the *Gaussclumps* source extraction method is shown in Appendix A.3. All the available MALT90 spectra for the identified massive prestellar cores are shown in Appendix A.4.

Appendix A.5-A.9 are supplementary materials for Chapter 3. Appendix A.5 gives a general description of our selected target massive clumps, based on previous studies. In Appendix A.6 the data information of the centimeter continuum used for free-free emission subtraction is presented. Appendix A.7 gives the detailed procedure of the MCMC RADEX modeling of CH_3OH lines. The LTE analysis for sulfur-bearing lines are summarized in Appendix A.8. The comparisons between the one-component LTE result and the LIME modeling results, and the observed line profiles of all the target sources not shown in main text are presented in Appendix A.9.

A.1 SABOCA maps

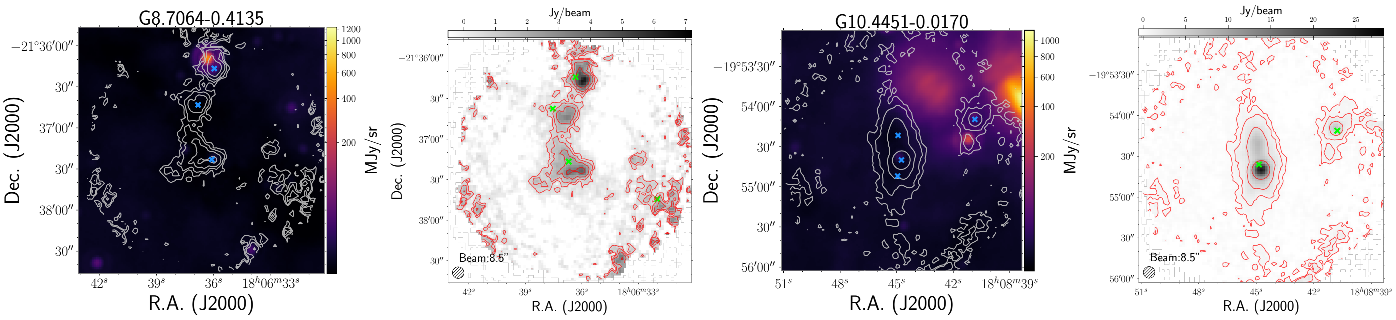

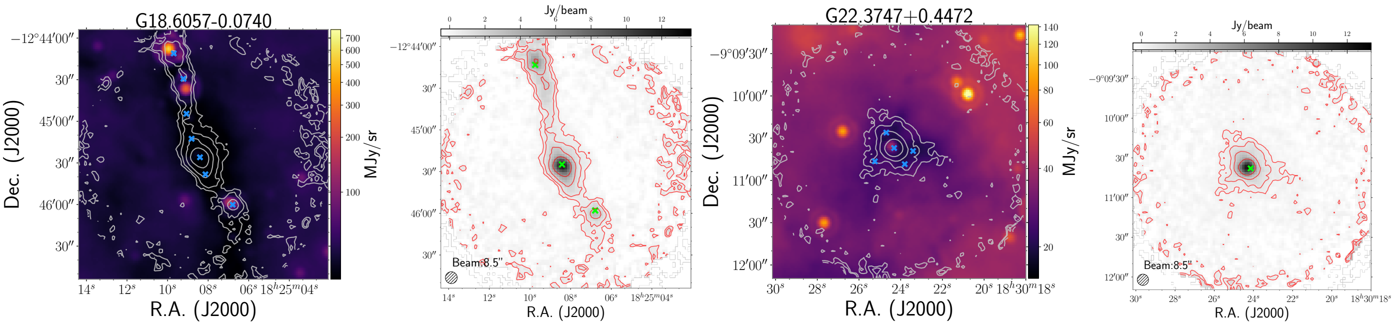

Figure A.1: SABOCA 350 μm and 24 μm emission from Spitzer/MIPS emission maps of target sources. Contour levels start at $5\times\sigma$ and show 5 uniformly spaced intervals on a logarithmic scale up to peak flux density of each field of 350 μm flux. The green crosses show the position of ATLASGAL sources. Coloured images show the 24 μm emission from Spitzer/MIPS on a logarithmic scale, contours are the same as in the top panel of the 350 μm emission. red crosses mark the positions of the compact sources identified in the SABOCA maps. The target name from the ATLASGAL Gaussclumps catalog is given in each plot.

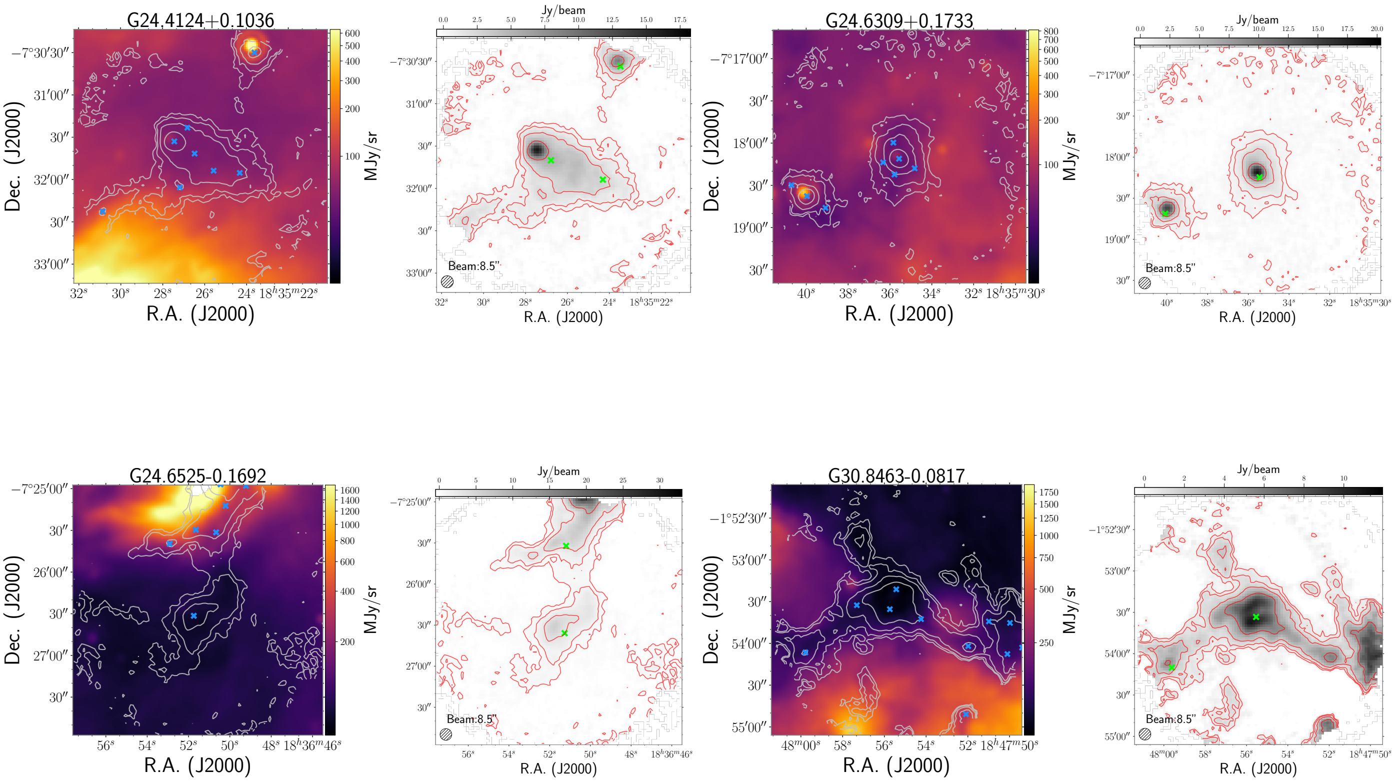

Figure A.2: Continued.

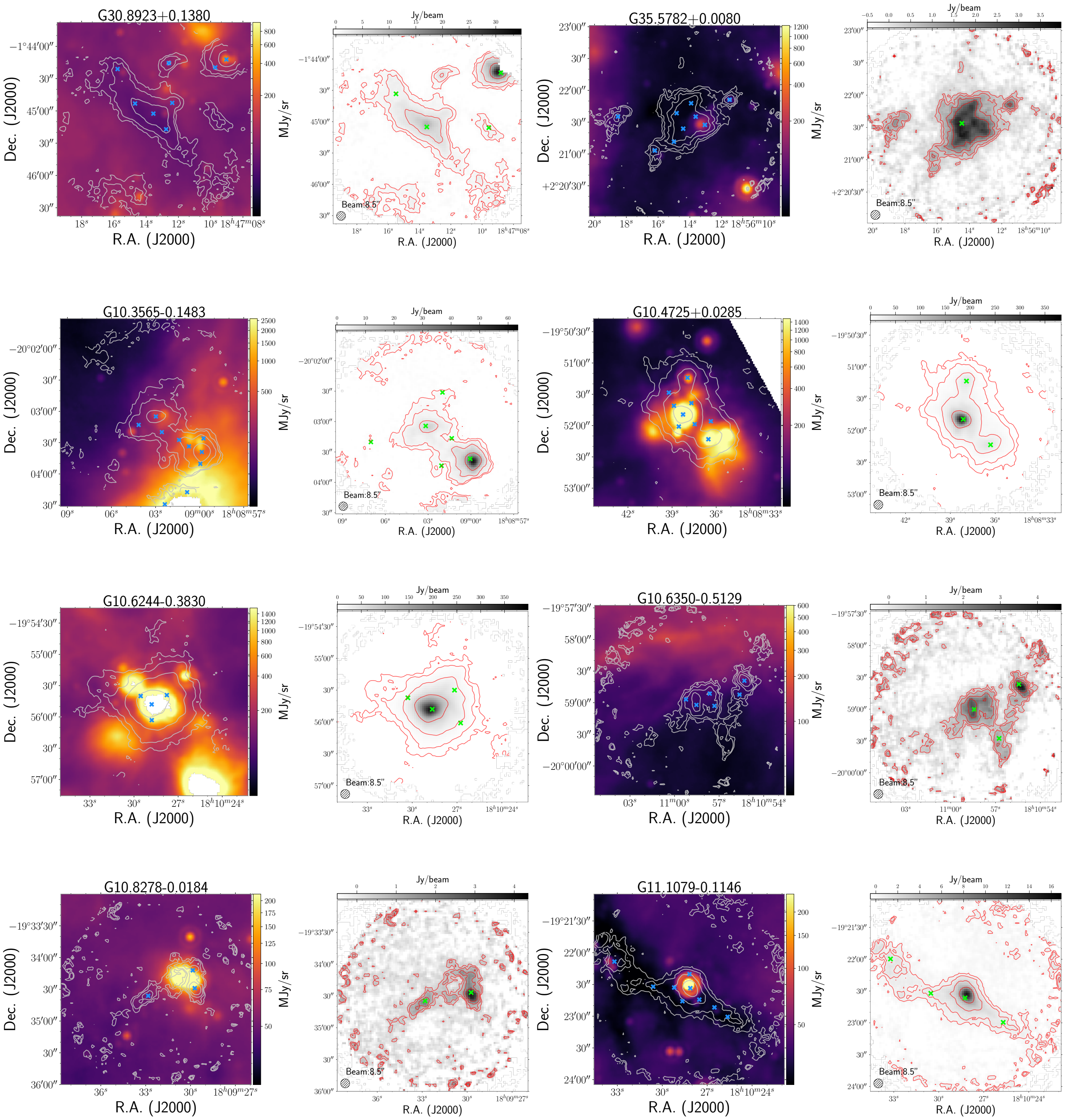

Figure A.3: Continued.

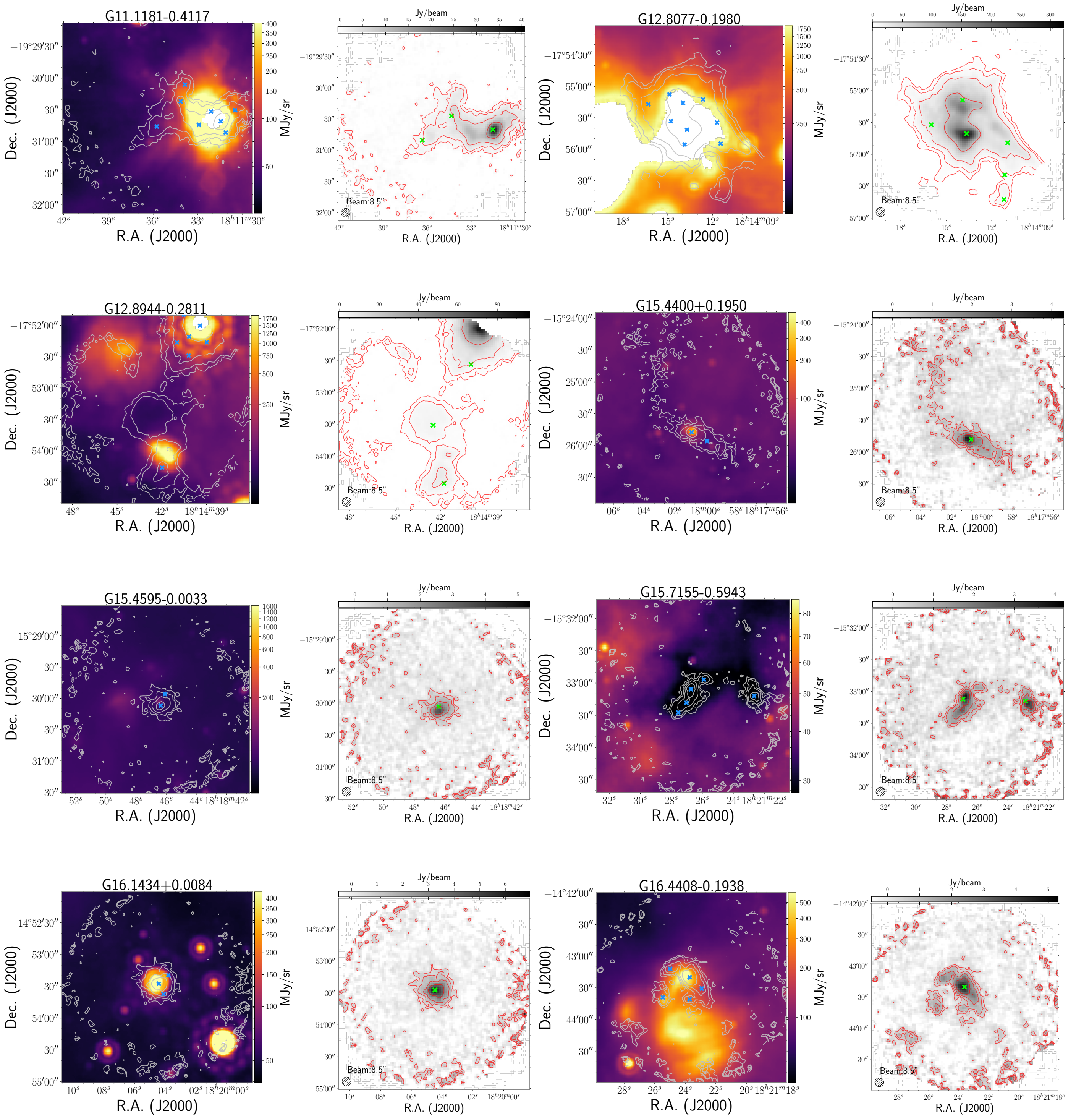

Figure A.4: Continued.

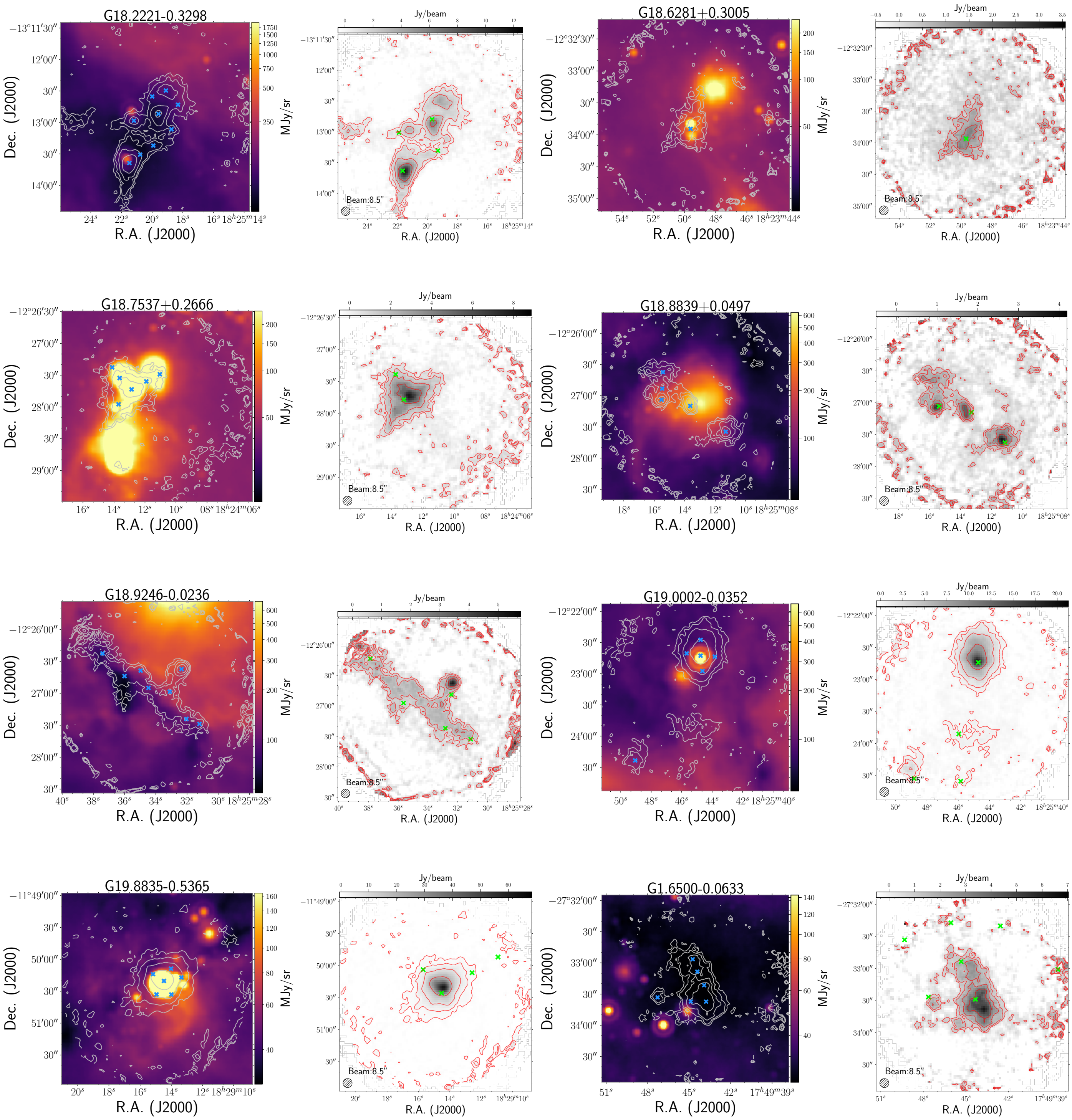

Figure A.5: Continued.

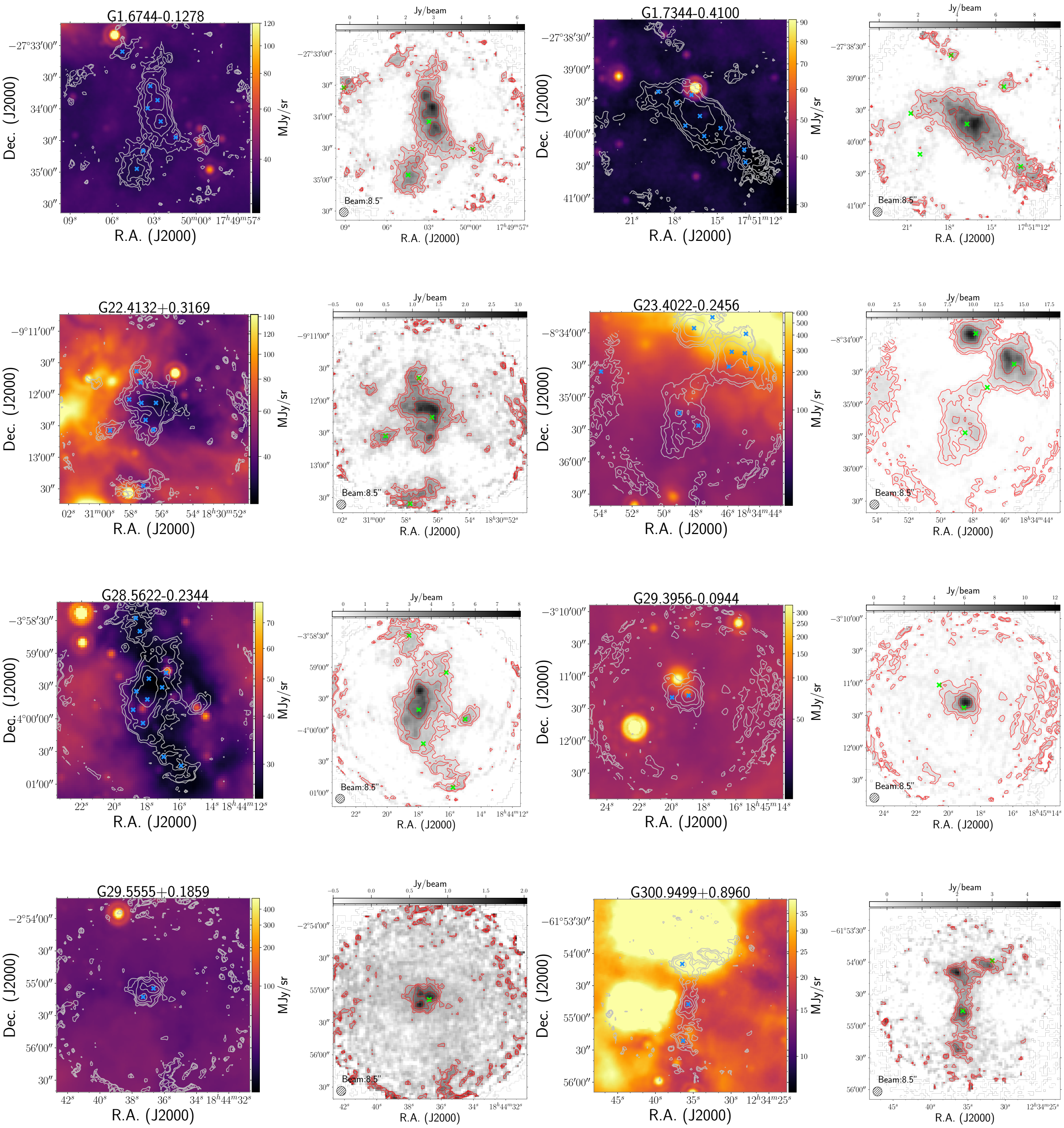

Figure A.6: Continued.

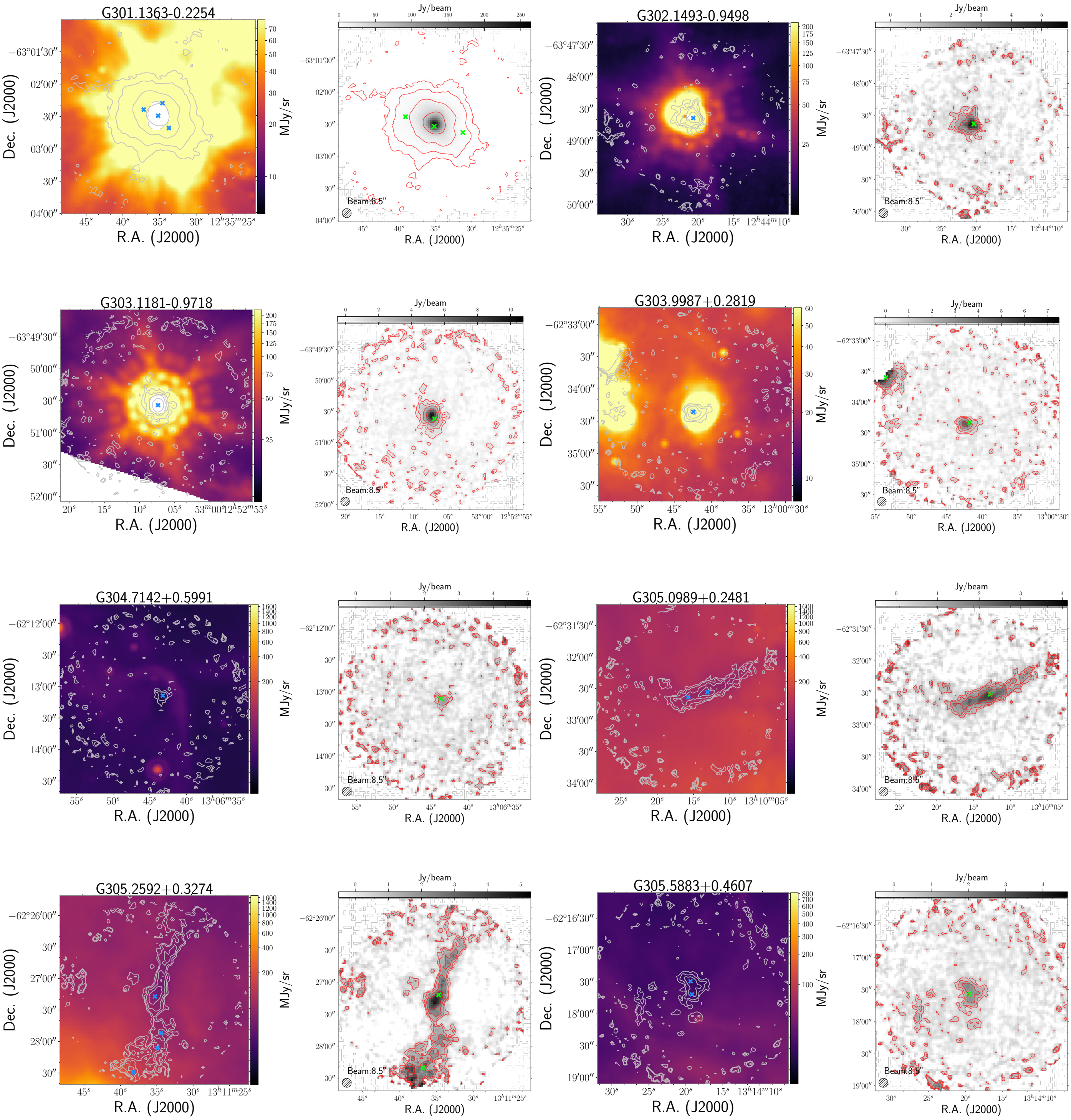

Figure A.7: Continued.

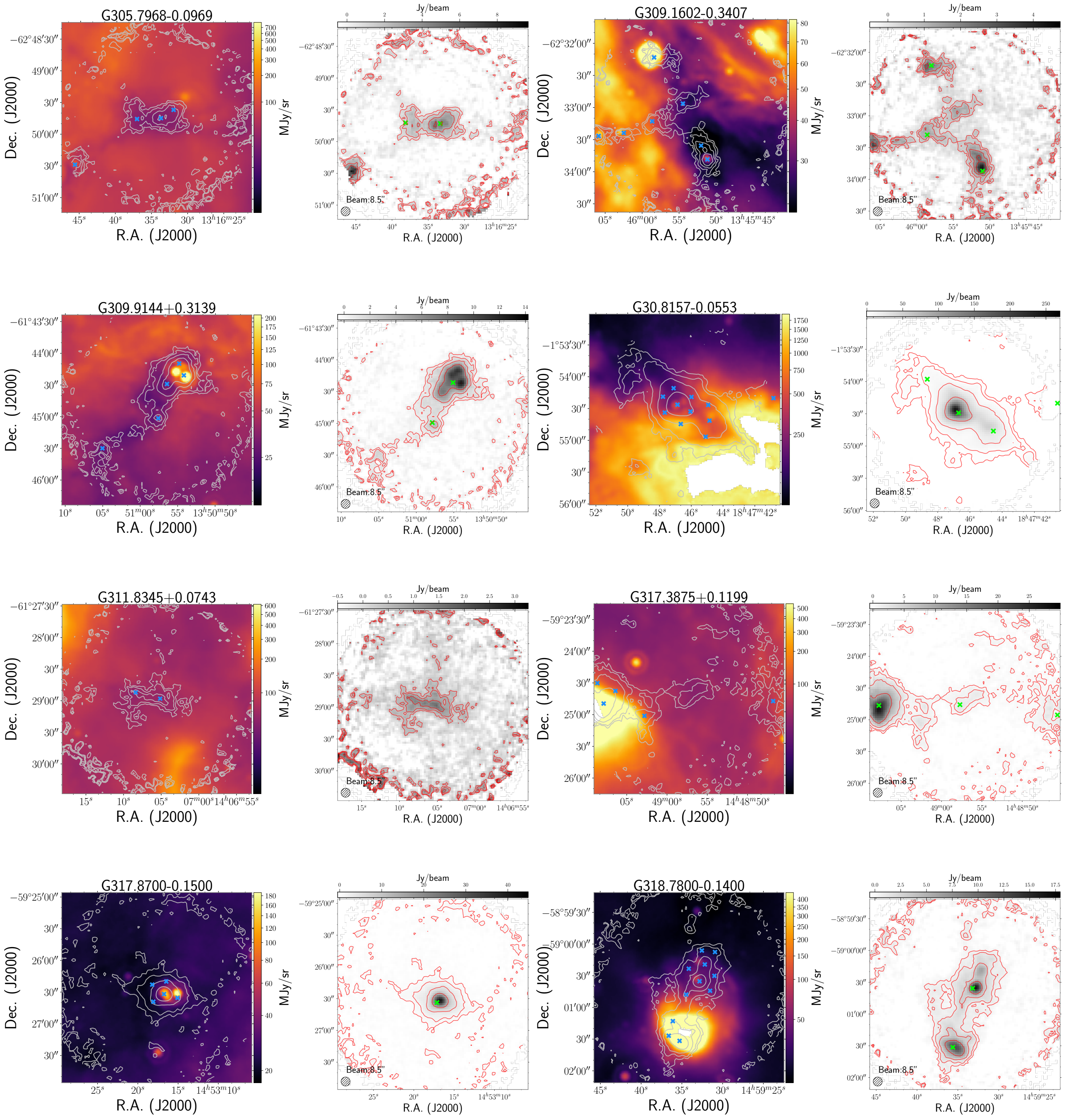

Figure A.8: Continued.

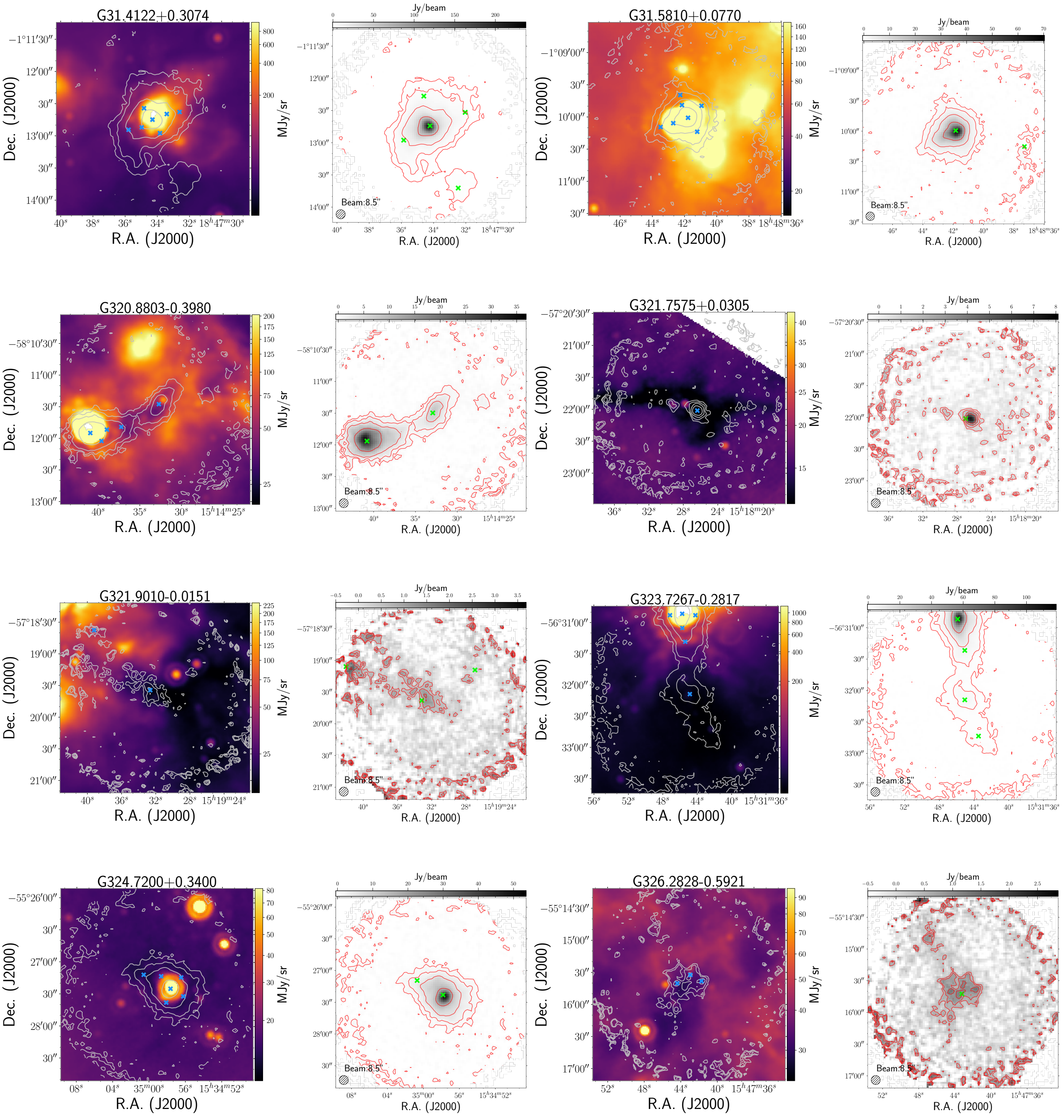

Figure A.9: Continued.

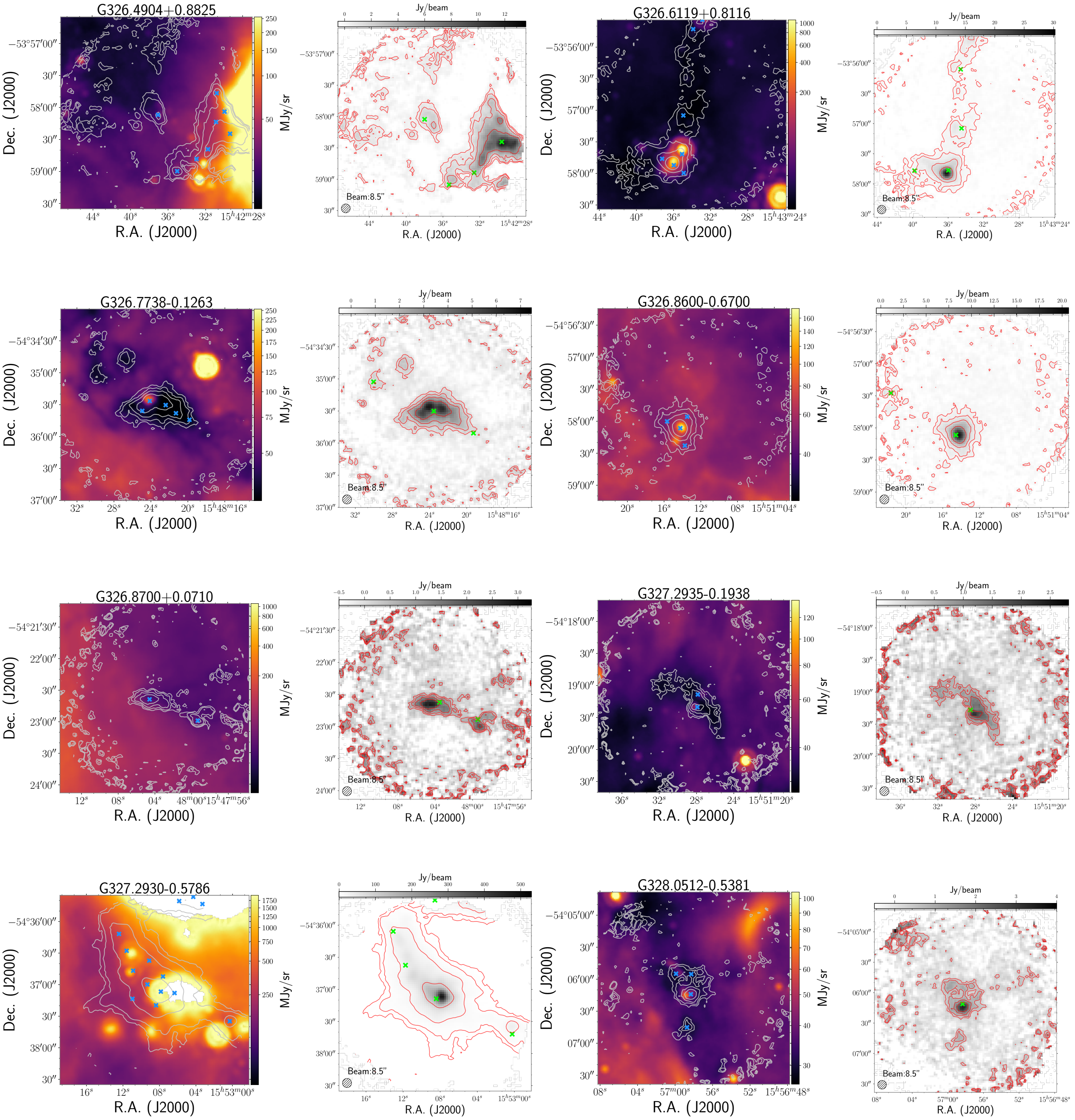

Figure A.10: Continued.

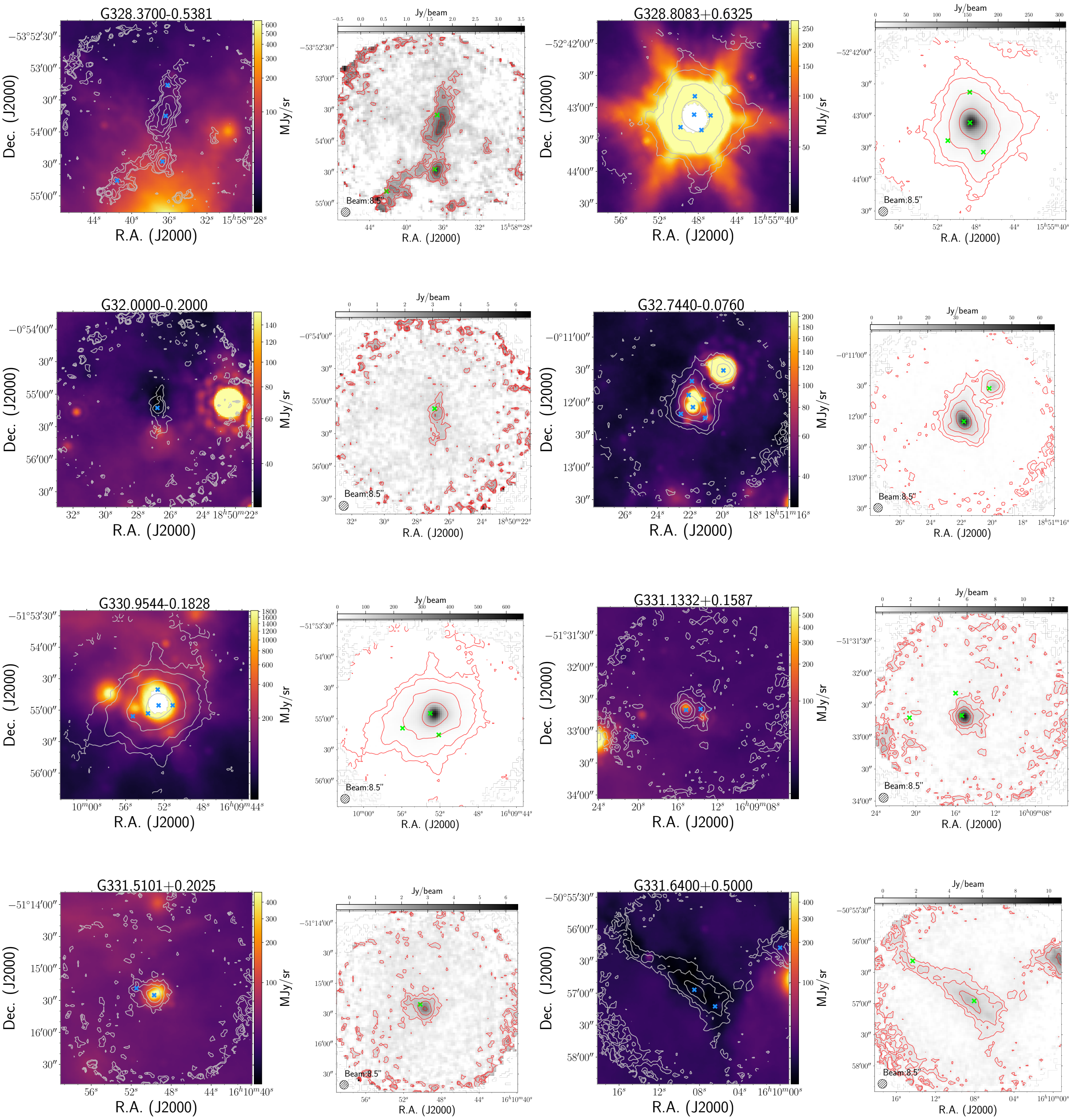

Figure A.11: Continued.

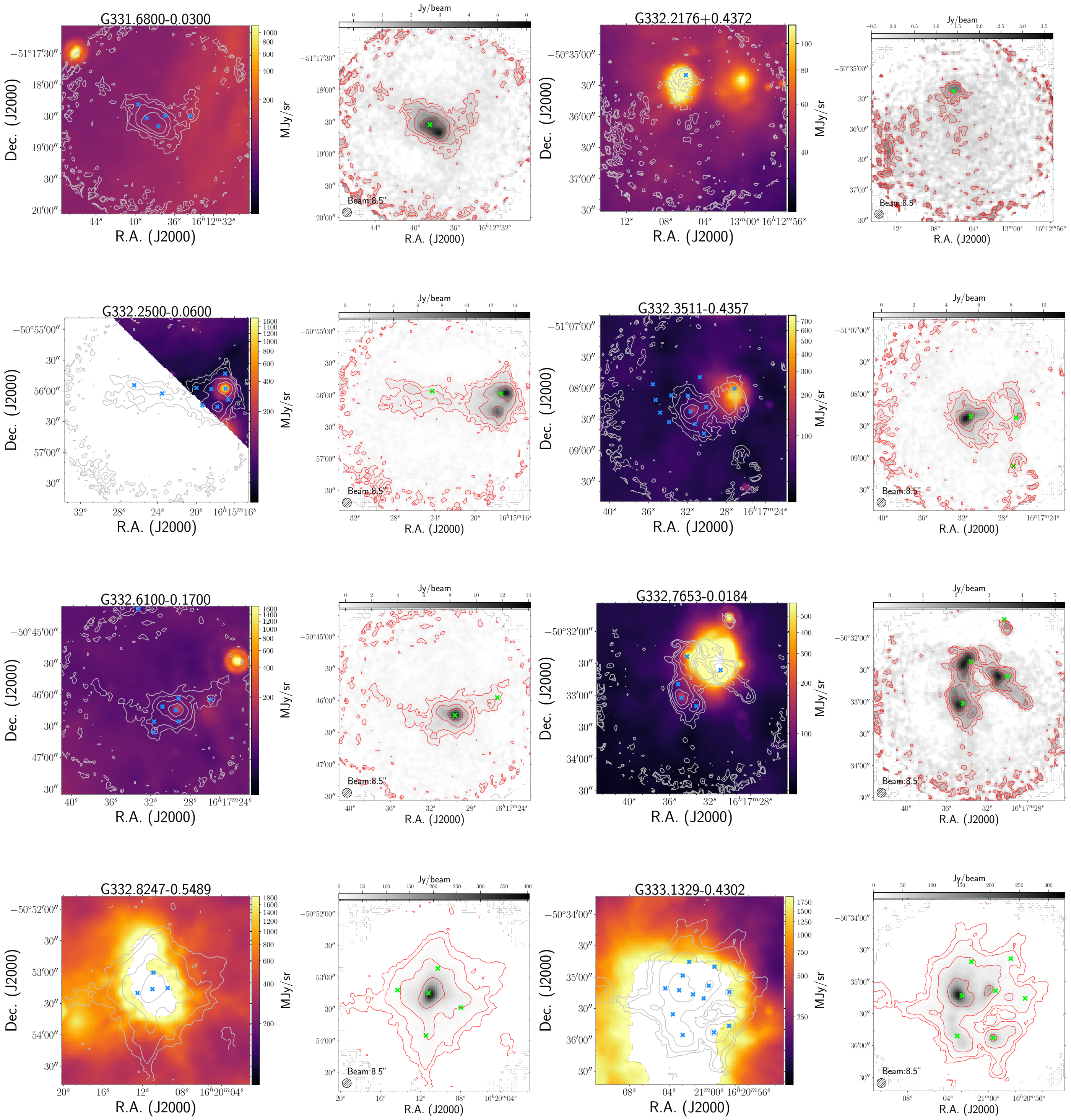

Figure A.12: Continued.

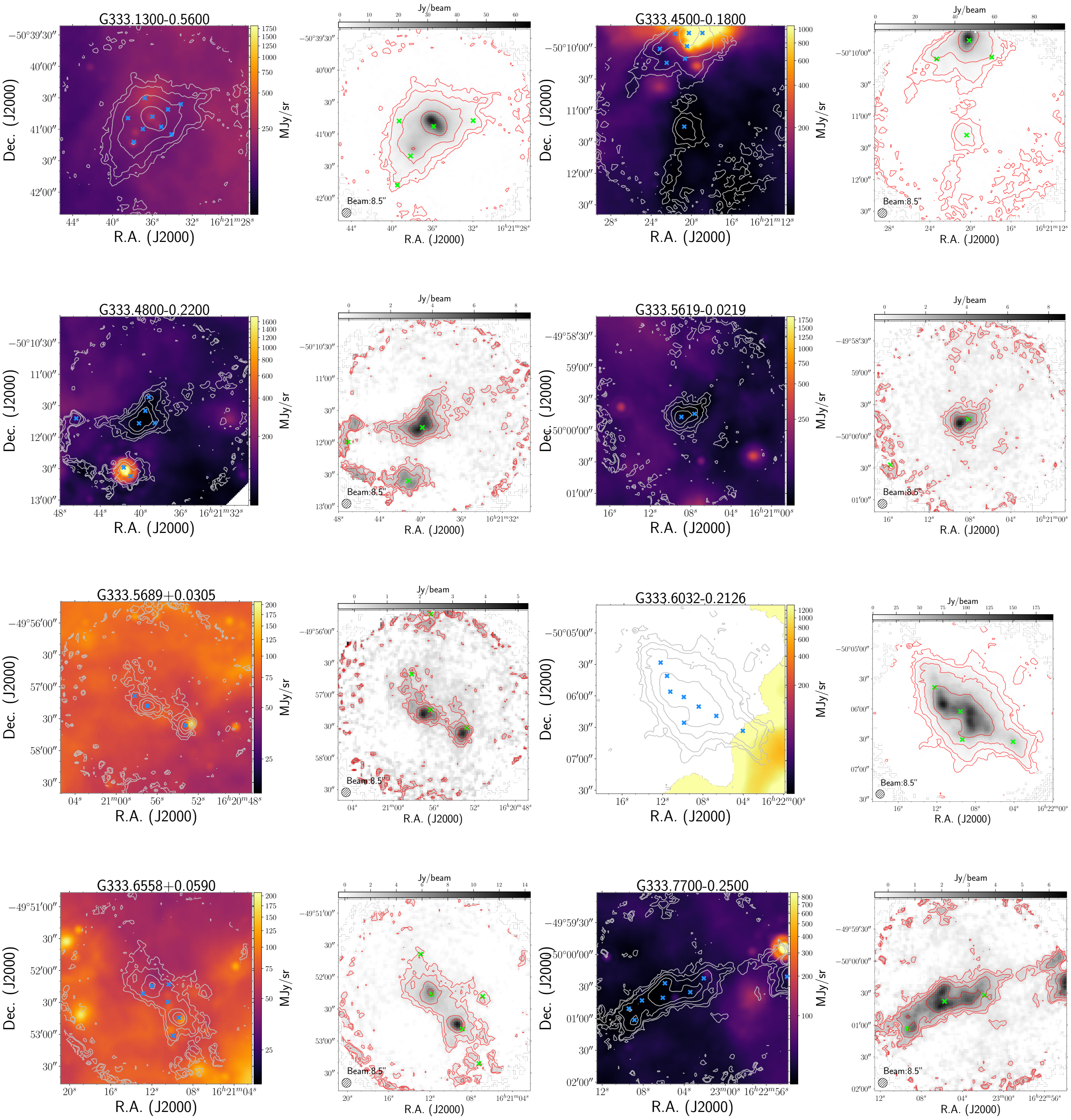
G333.1300-0.5600

G333.4500-0.1800

G333.4800-0.2200

G333.5619-0.0219

G333.5689+0.0305

G333.6032-0.2126

G333.6558+0.0590

G333.7700-0.2500

Figure A.13: Continued.

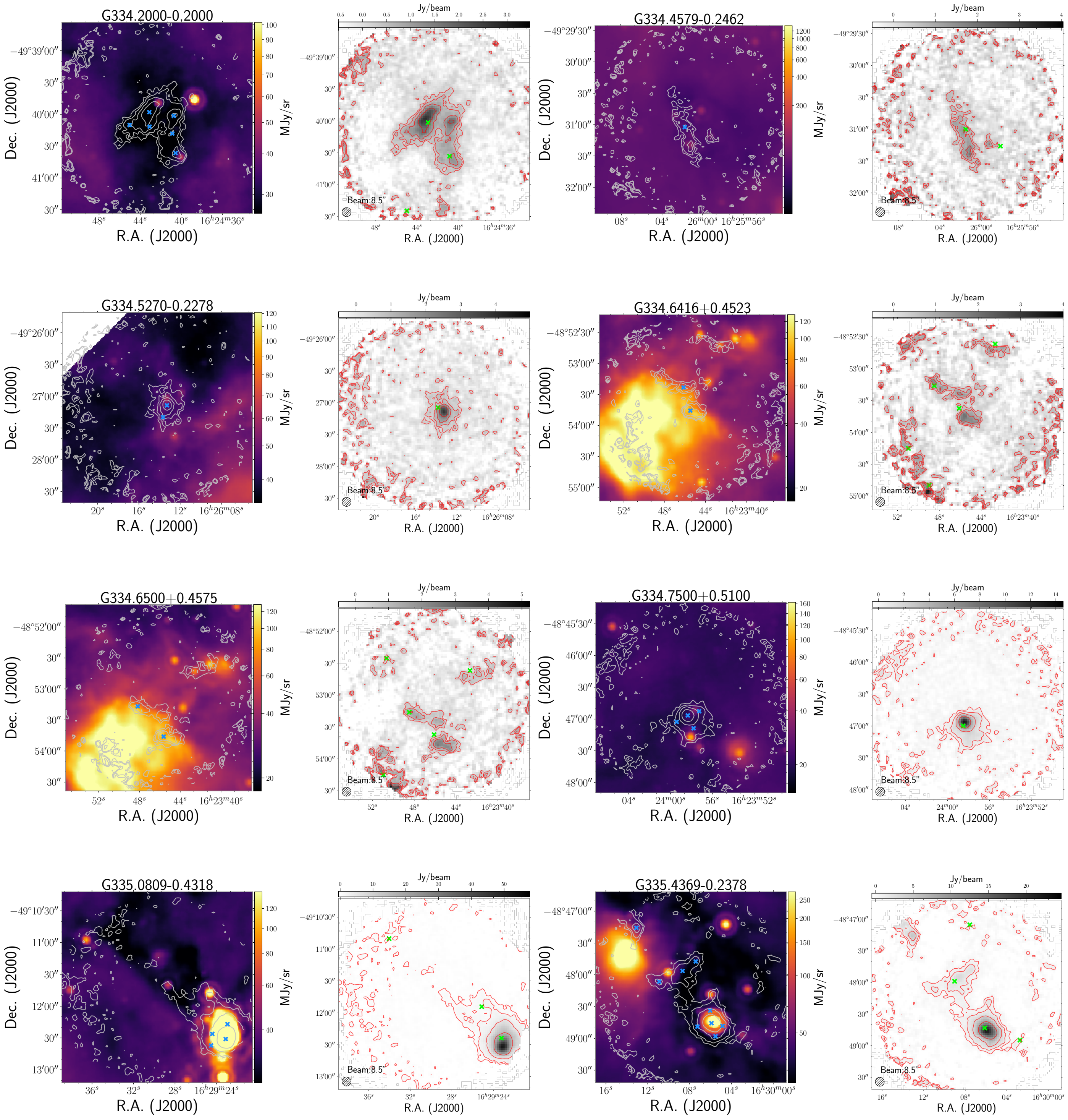

Figure A.14: Continued.

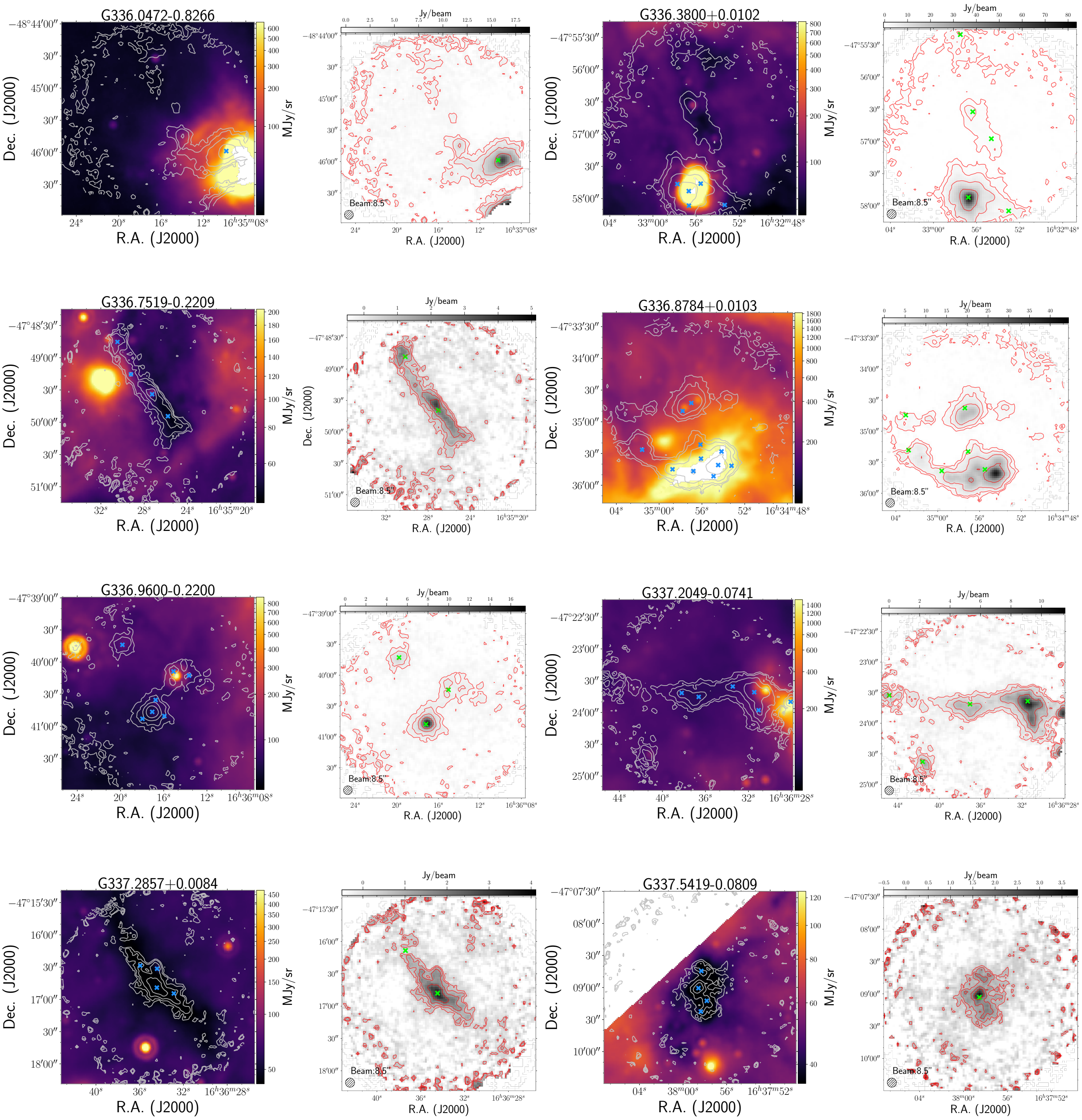

Figure A.15: Continued.

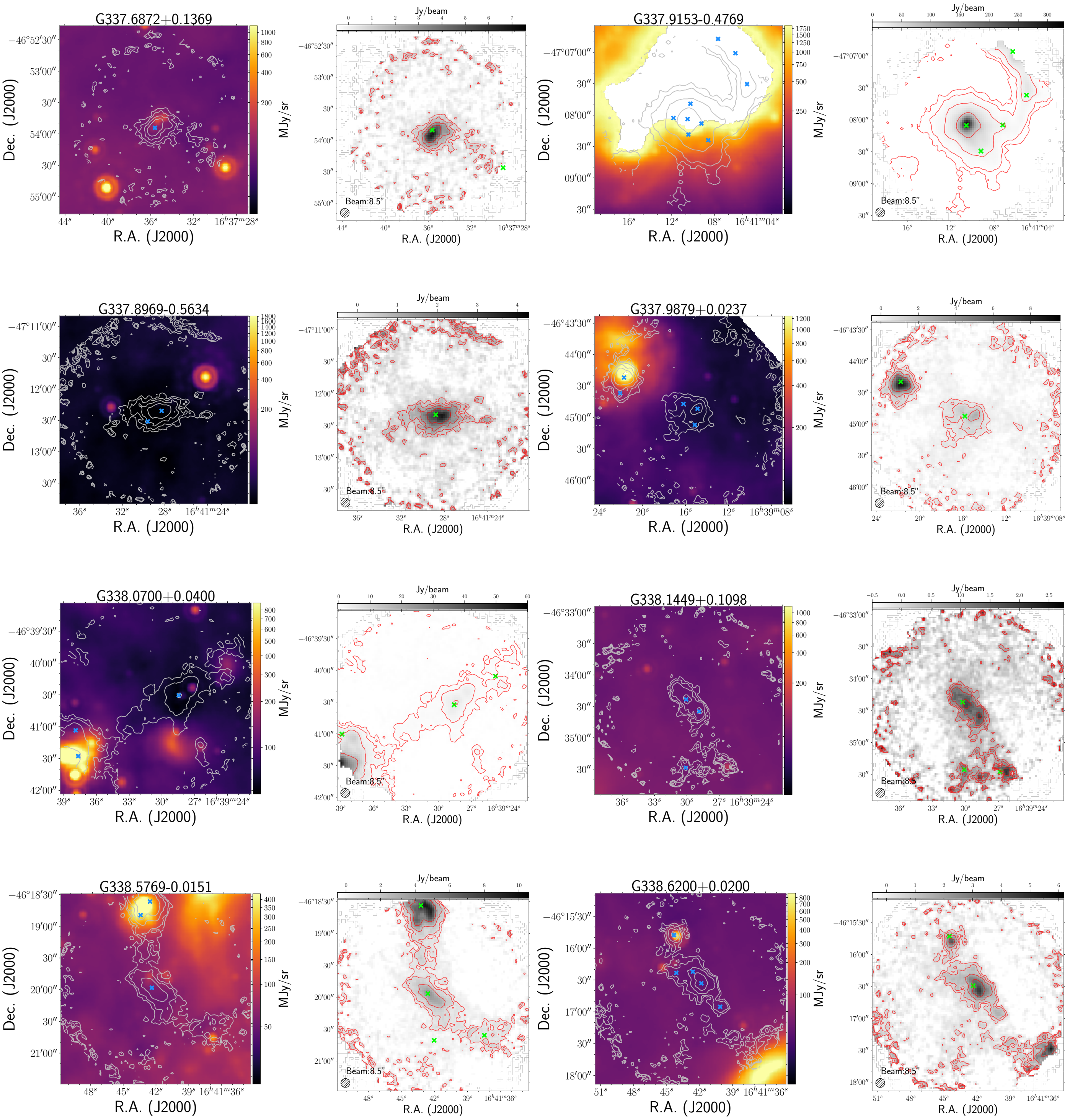

Figure A.16: Continued.

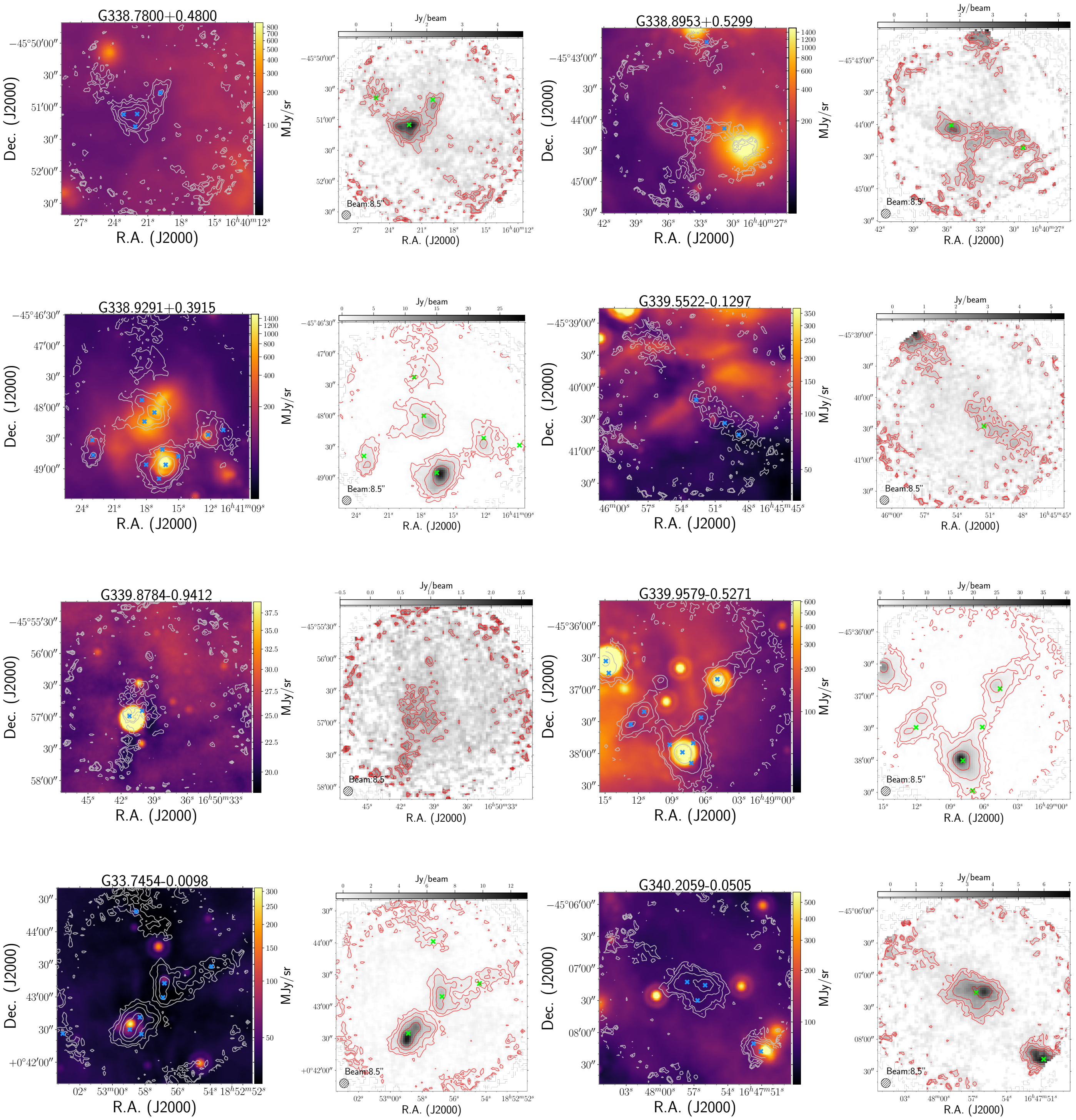

Figure A.17: Continued.

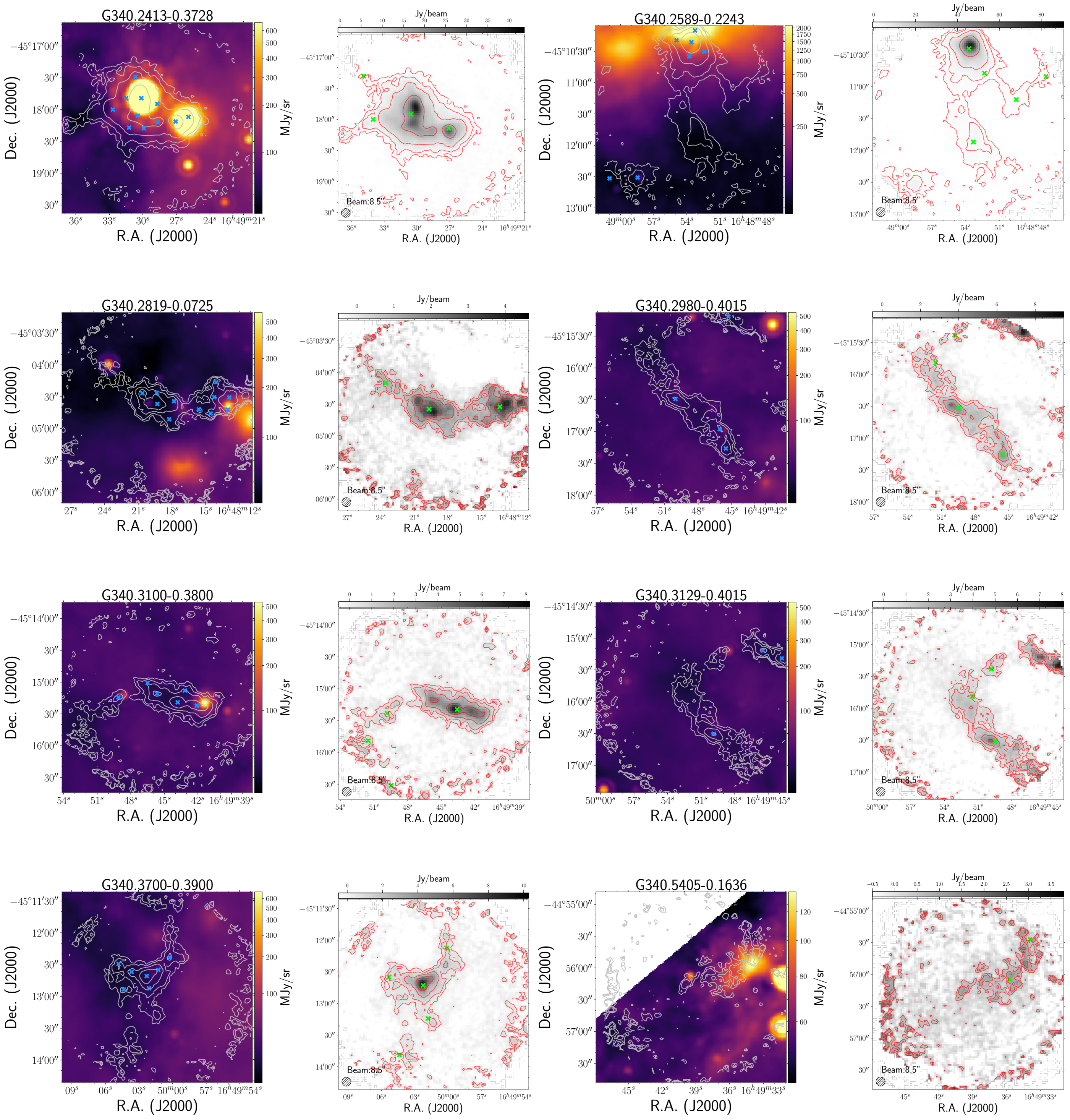

Figure A.18: Continued.

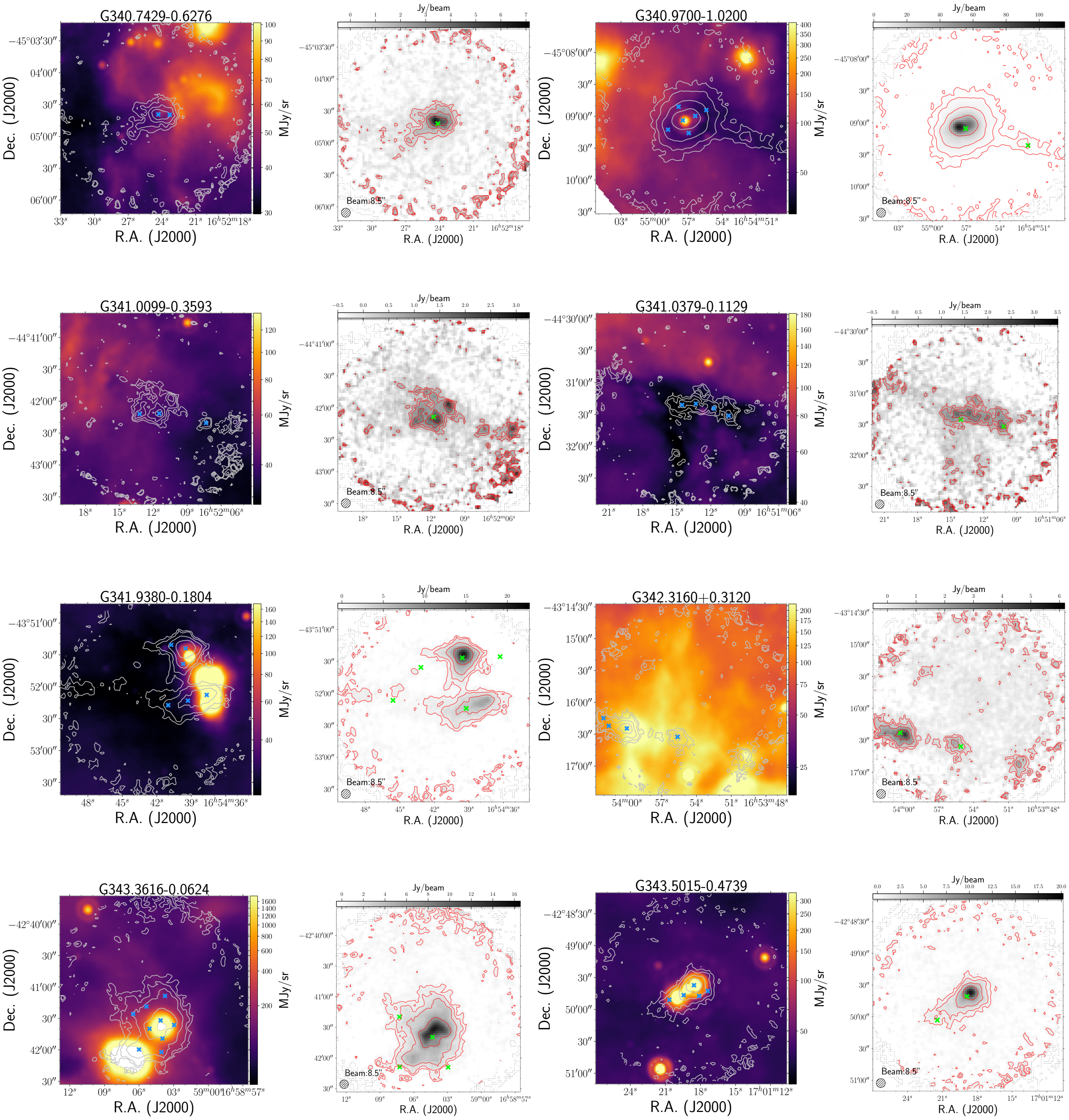

Figure A.19: Continued.

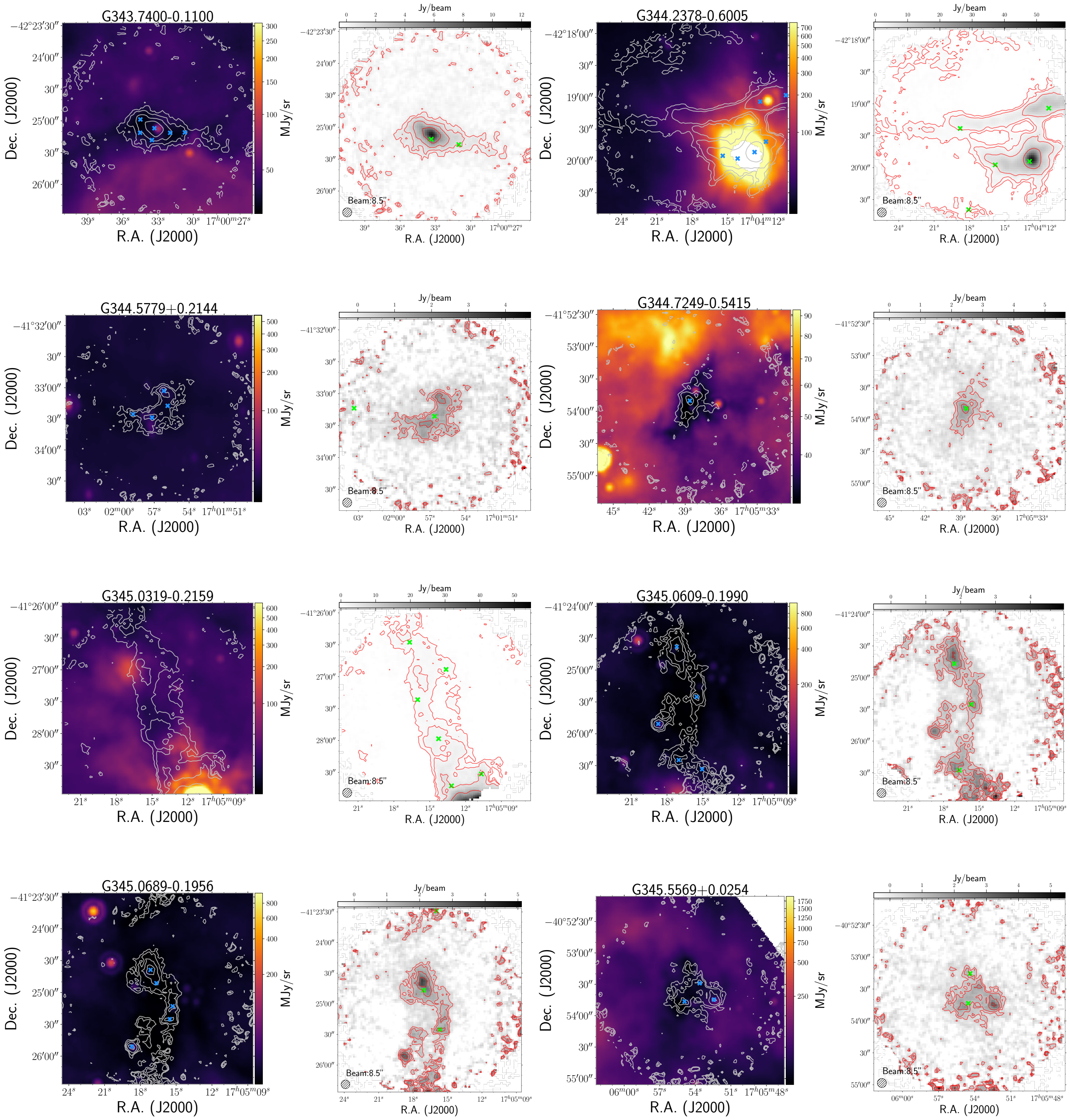

Figure A.20: Continued.

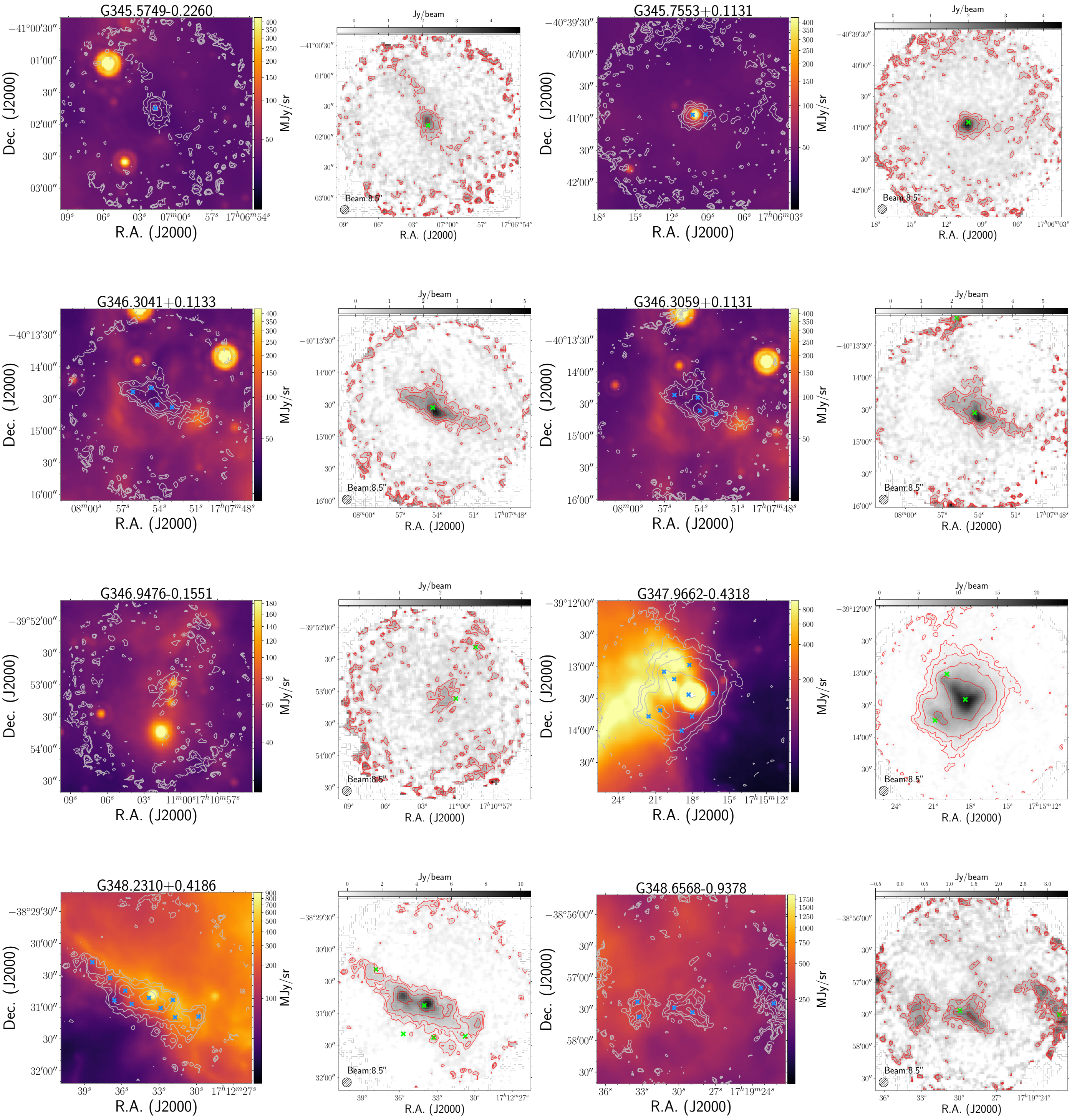
G345.5749-0.2260

G345.7553+0.1131

G346.3041+0.1133

G346.3059+0.1131

G346.9476-0.1551

G347.9662-0.4318

G348.2310+0.4186

G348.6568-0.9378

Figure A.21: Continued.

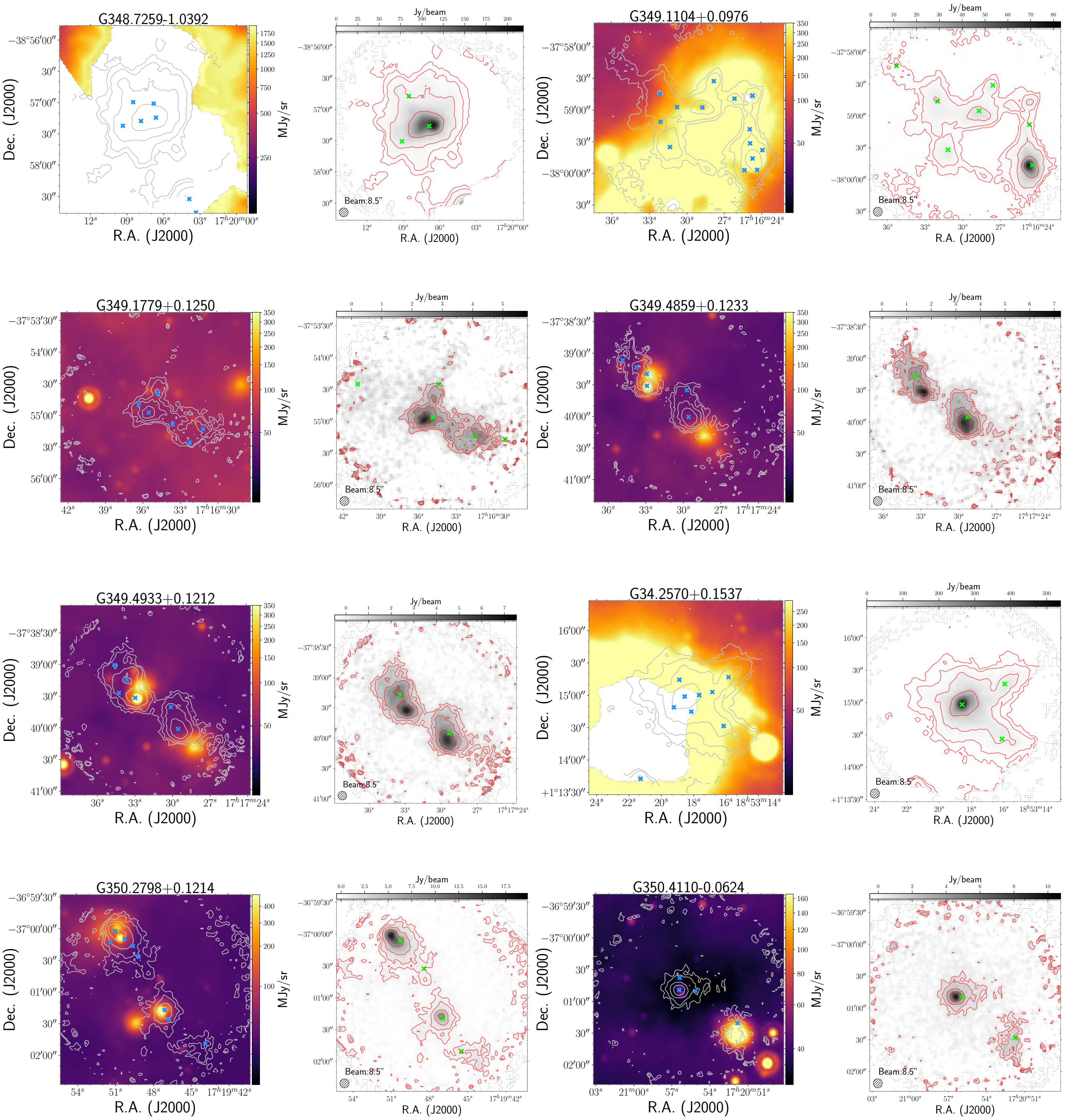

Figure A.22: Continued.

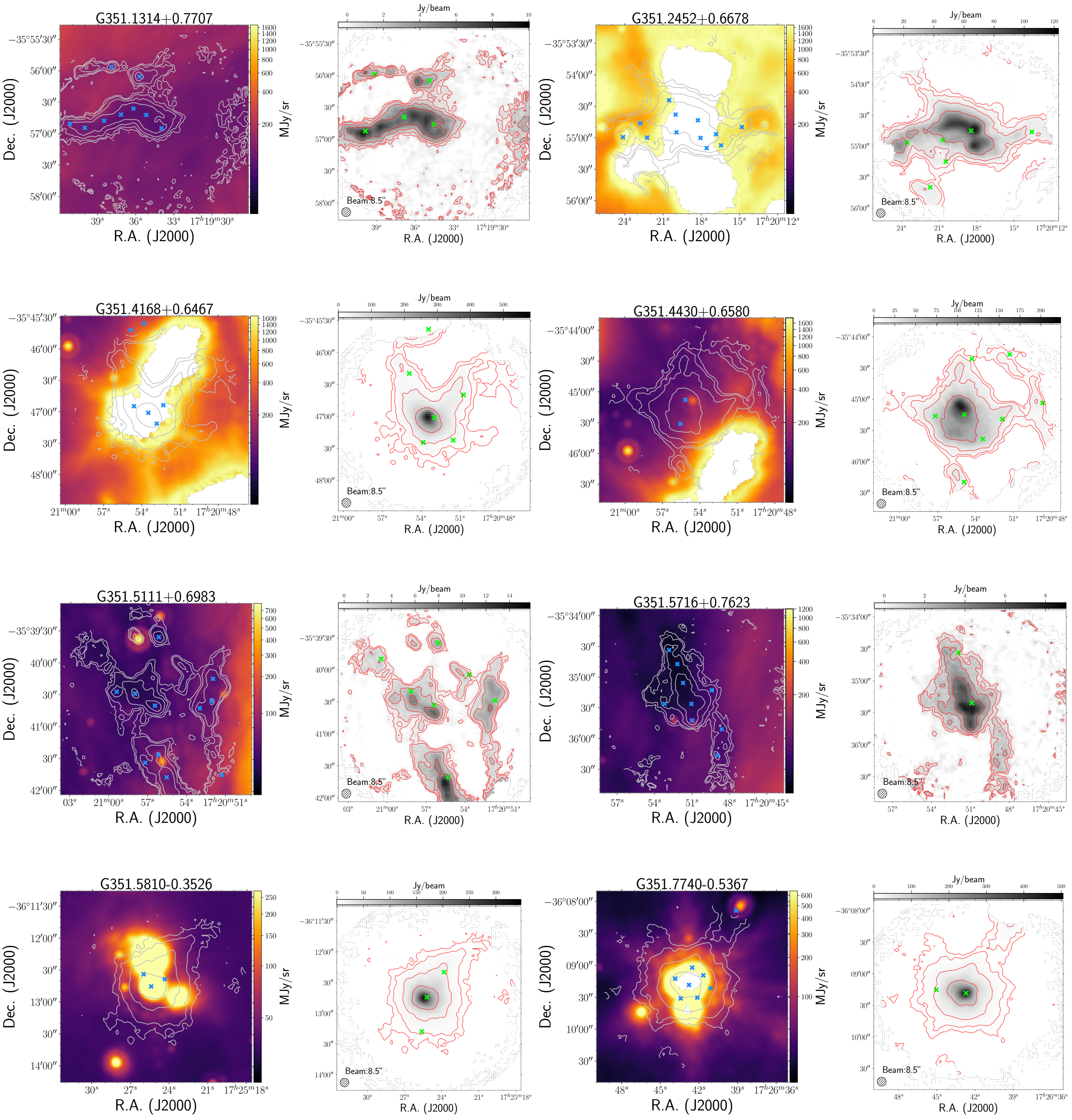

Figure A.23: Continued.

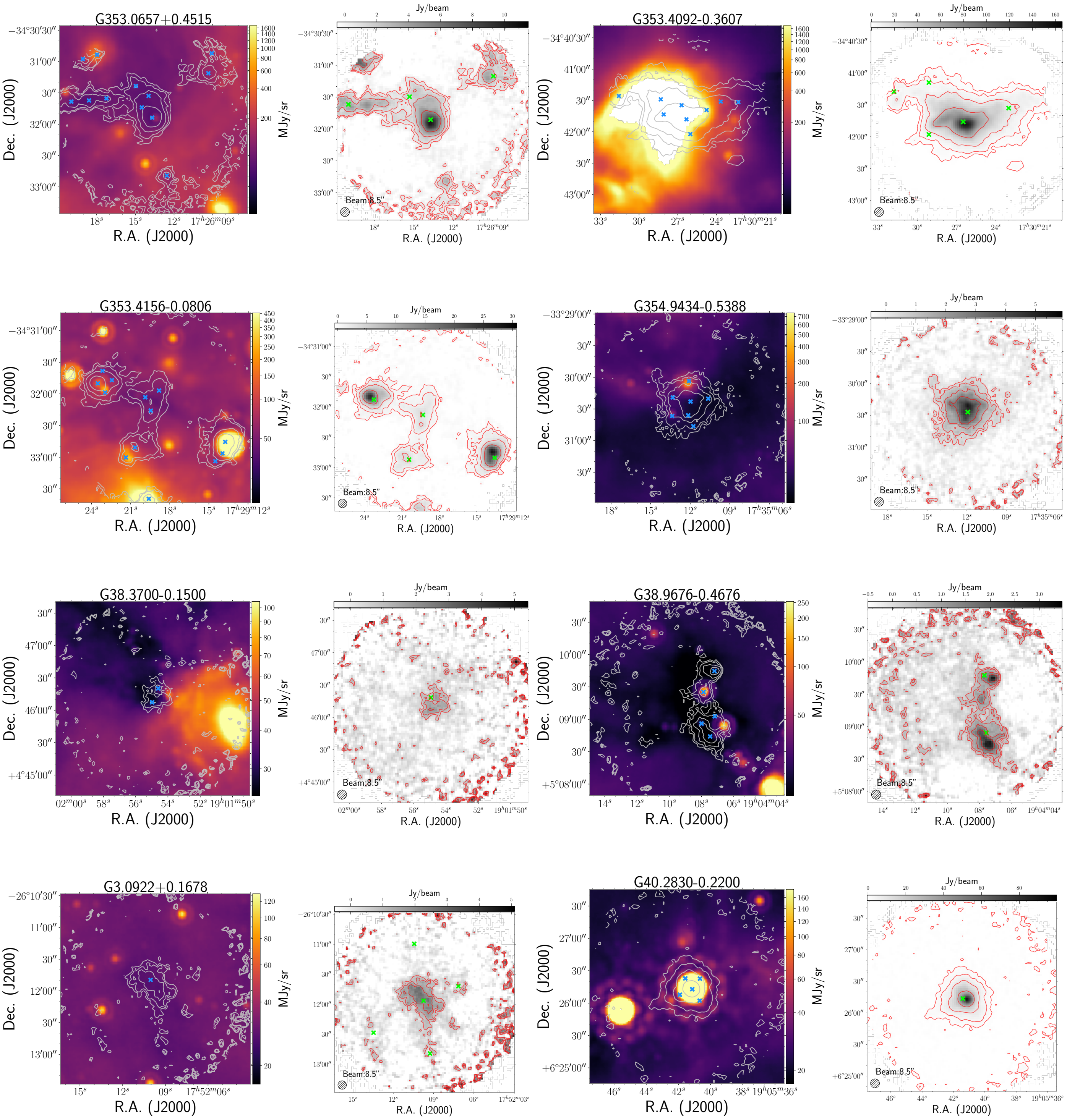

Figure A.24: Continued.

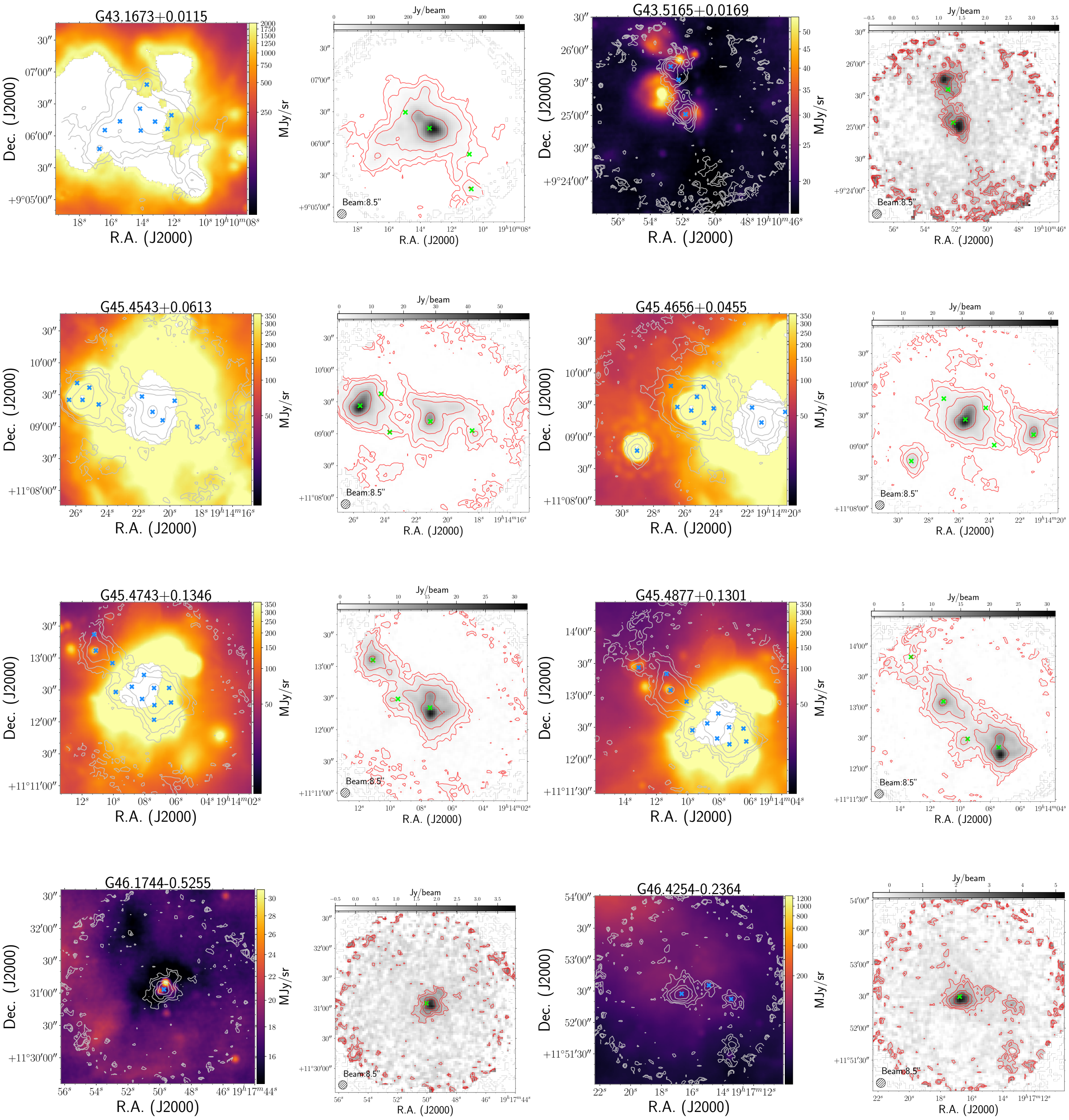

Figure A.25: Continued.

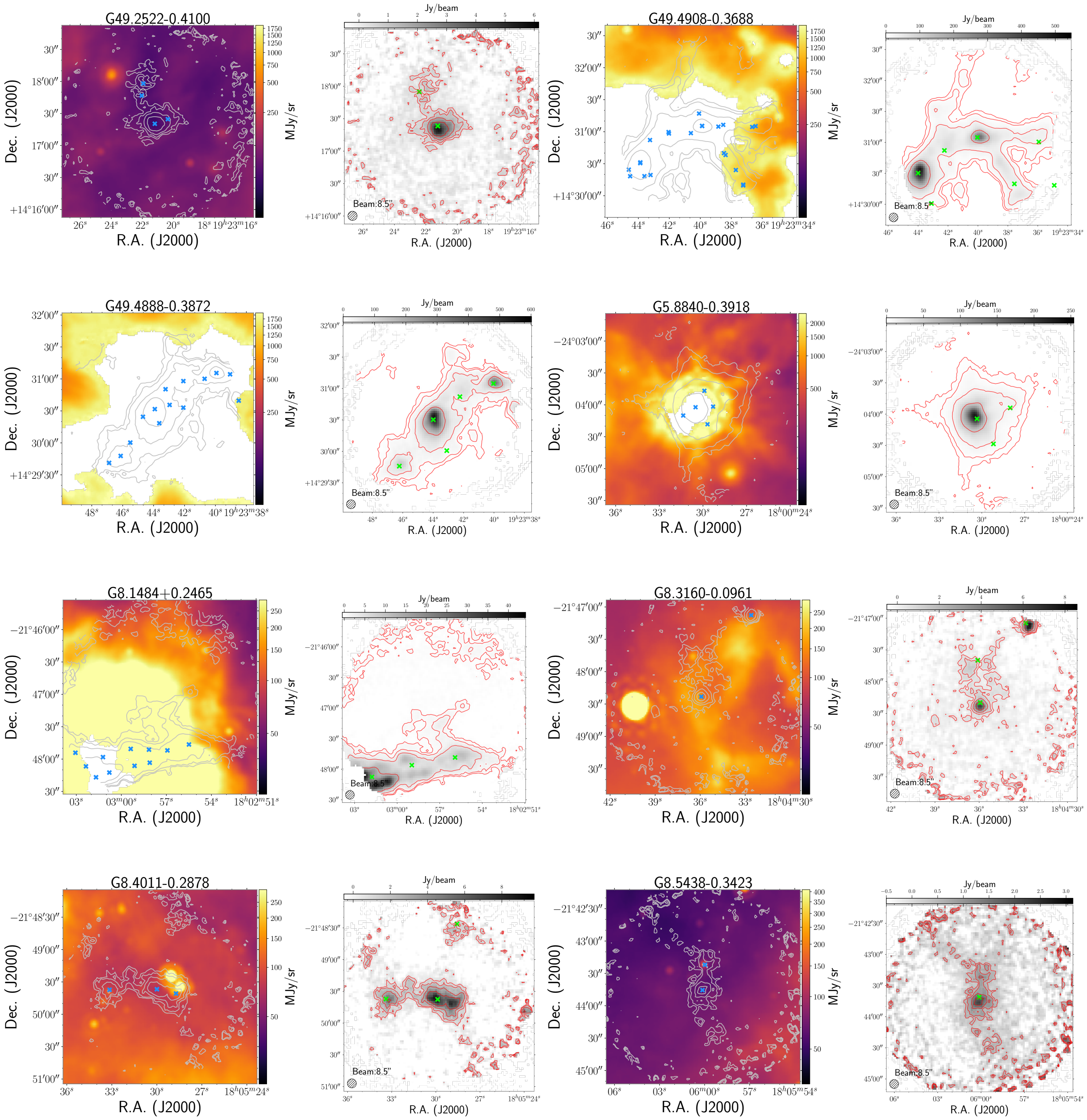
G49.2522-0.4100

G49.4908-0.3688

G49.4888-0.3872

G5.8840-0.3918

G8.1484+0.2465

G8.3160-0.0961

G8.4011-0.2878

G8.5438-0.3423

Figure A.26: Continued.

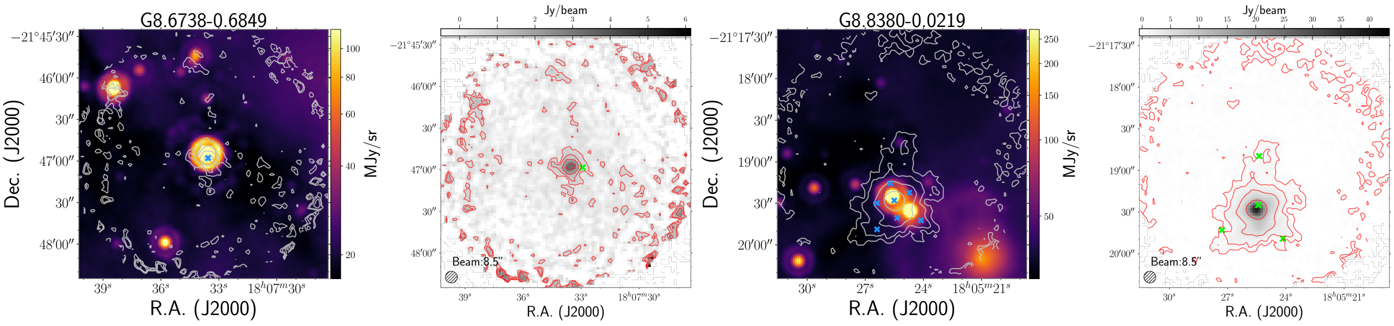

A.2 The 70 μm scaling factor and the comparison between the 25″ and 10″ $N(\mathrm{H_2})$ and T_d maps

The method we adopt for the 10″ resolution SED fit is based on the assumption that the SED at longer wavelengths 160, 250, 350 and 870 μm fluxes represent the cold component of gas which dominate the bulk of mass (envelope of cores) at the scale we are probing. Thus the predicted 70 μm fluxes from this SED compared to the observed fluxes provide a correction factor to account for the hot gas component, which otherwise would bias the derived T_d to a higher value and hence underestimate the gas column density.

In Fig. A.27, we present 25″ and 10″ resolution column density and dust temperature maps for two fields, for source G10.8278-0.0184 (left panel) and G12.7914-0.1958 (right panel). In the column density and dust temperature maps, the identified SABOCA cores are marked and labeled with number. The corresponding SED curves for the pixels of these core positions are shown in Fig. A.28. We denote the difference between the derived column density and temperature, $N(\mathrm{H_2})$ and T_d from the unscaled 70 μm flux and that from the scaled 70 μm as $\Delta N(\mathrm{H_2})$ and ΔT_d. In Fig. A.29 we present the 2d histogram of the pixels in the 10″ derived maps of G10.8278-0.0184, in terms of their 70 μm scaling factor, f with $\Delta N(\mathrm{H_2})/N(\mathrm{H_2})$ and $\Delta T_\mathrm{d}/T_\mathrm{d}$, with the color scale indicating the pixel fractions. The anti-correlation between scaling factor with $\Delta T_\mathrm{d}/T_\mathrm{d}$ reflects the increase of the dust temperature of these relatively cold sources (<20 K), i.e. core 2 in source G10.8278-0.0184 (left panel of Fig. A.27), is correlated with the increase of the 70 μm flux fraction from the bulk gas component, representing a gradual warm-up process of the envelope. The values of $\Delta T_\mathrm{d}/T_\mathrm{d}$ are within 30%, depending on the absolute value of the rescaling factor f. $\Delta N(\mathrm{H_2})/N(\mathrm{H_2})$ has a more tight relation to the rescaling factor f, close to a linear relation of $\Delta N(\mathrm{H_2})/N(\mathrm{H_2}) = 0.5f$-0.45.

Scaling down the 70 μm flux according to cold component extrapolated 70 μm flux is not equivalent to fixing temperature to the coarser resolution temperature map. As we can see from the left panel of Fig. A.27, the enhanced temperatures of larger than ~25 K, i.e. for core 1 and 3 and their adjacent region, are better resolved in the 10″ temperature map. In addition, we can now compare the derived fragment mass to the clump mass on a common basis to avoid an overestimate of temperature due to the inclusion of 70 μm map in the higher resolution fits.

We also show cases in which the scaling factors are larger than 1, i.e. cores 2, 7, 9 in source G12.7914-0.1958 (right panel of Fig. A.27). This is due to external heating by the nearby mid-infrared bright object, therefore along the line-of-sight there is a mixture of hot and cold dust with the hot component not well-shielded due to its relatively low density cold component. In this case the 4 band

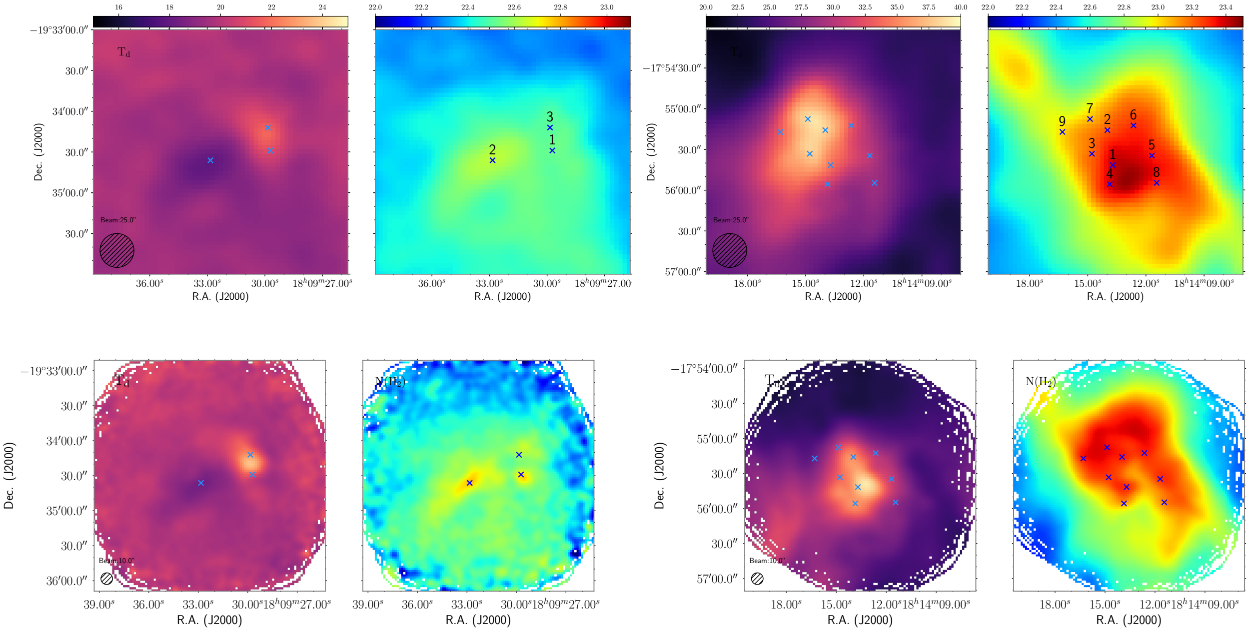

Figure A.27: 25″ and 10″ column density and dust temperature maps for source G10.8278-0.0184 and G12.7914-0.1958. The corresponding SED curves for the positions marked by red crosses with number labels are given in the subplots of Fig. A.28 with same number labels in red.

fits probe a temperature close to the hot dust and a column density close to the cold component, thus giving a predicted 70 μm flux higher than the observations. These sources should be intrinsically hotter, for which the inclusion of 70 μm flux into the SED would better constrain the T_d and $N(\mathrm{H_2})$. Thus for these sources, we use directly the unscaled PACS 70 μm fluxes in the high resolution fit.

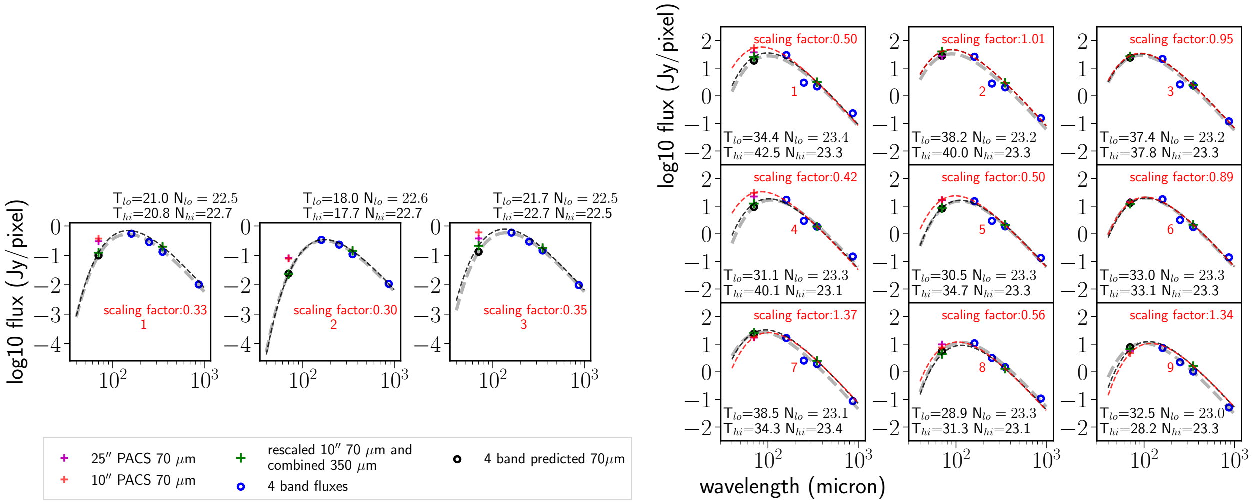

Figure A.28: Example SED curves for pixels in Fig. A.27. The gray dashed line represents the 4 band fitted SED curve for the 25″ resolution maps and the black dashed line represents the 2 band fitted SED curve for the 10″ resolution maps after rescaling 70 μm fluxes. Red and magenta crosses mark the fluxes from smoothed 10″ and 25″ PACS 70 μm maps, respectively. Red circles represent 25″ fluxes for 4 band fits, and black circles extrapolated 25″ 70 μm flux from the 4 band fits. In the right panel, the additional red dashed line in each subplot represents the 2 band fitted SED curve for the 10″ resolution maps from unscaled 70 μm fluxes.

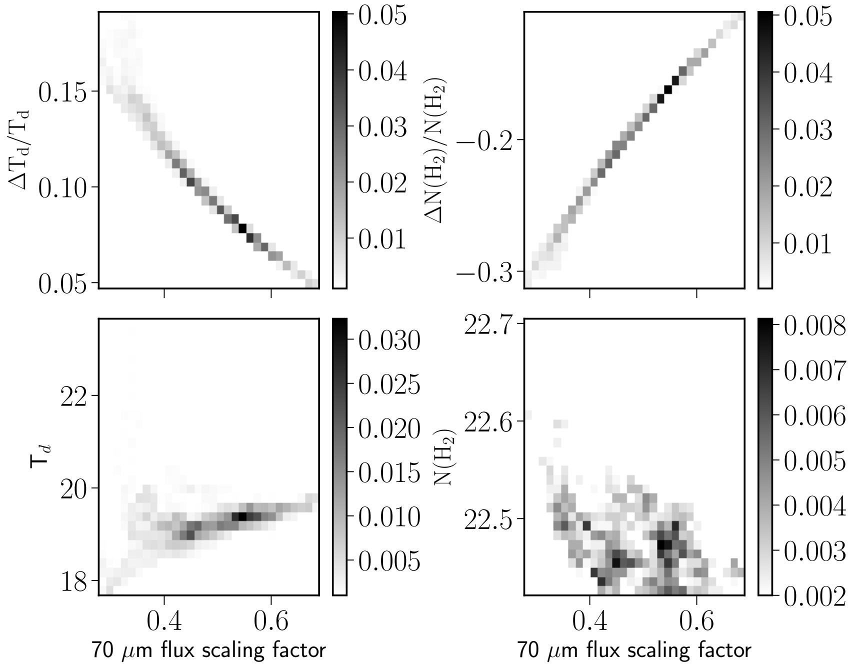

Figure A.29: 2-dimensional distribution of 70 μm flux scaling factors with derived T_d, $N(H_2)$ and $\Delta N(H_2)/N(H_2)$, $\Delta T_d/T_d$ for pixels in 10″ derived maps, of source G10.8278-0.0184.

A.3 Fragmentation analysis: a comparison with Dendrogram results

In this paper we use *Gaussclumps* to identify the compact sources in the SABOCA emission maps. *Gaussclumps* is a non-hierarchical source extraction method, which assumes that cloud structures are composed of multiple Gaussian sources which can overlap. In contrast, another widely-used source extraction method, `dendrogram`, is a hierarchical source identification method, which is discreet in the sense that a given emission area (or pixel) can only belong to a single structure, no overlap is allowed among the structures (of same level). We explore here the dendrogram representation of the cloud structure seen in the SABOCA maps, and compare these results with *Gaussclumps*.

There are several parameters to control the dendrogram source extraction, `min_value, min_delta and min_npix`, representing the minimum threshold, the minimum significance of a structure compared to its merging level, and the minimum size of a structure. Similarly as we did with *Gaussclump*, we set the `min_value` to 3 times the rms of the SABOCA map, and `min_npix` as the number of pixels corresponding to beam size. For `min_delta`, we set this to zero, as an attempt to pick up the maximum number of sources as well as to be consistent with *Gaussclump*, which does not have a similar control parameter.

We run `dendrogram` on the SABOCA emission maps and apply the extracted structures to the $10''$ column density maps in order to derive the physical properties of these structures. We define the size scale of the structures extracted by `dendrogram` as the geometrical mean of the area, similarly, assuming this size scale is representative of the scale of the line-of-sight dimension, the average gas density ($\rho_{\rm clump}$) is estimated. For the analysis, we only include structures that have closed contours within the map. We find that the relatively small FOV of the SABOCA maps provide an incomplete view of the structures at the lowest contours, especially for those showing a filamentary structure. Therefore, requiring a closed contour for the first structure is a condition that strongly limits our statistics.

With `dendrogram`, we define the fragmentation level as the number of leaves residing within the lowest parental structure (branch or trunk) on the map. Isolated leaves without any parental structures are omitted. For example in Fig. A.30, source G19.8835−0.5363 appears to be an isolated structure, while source G334.2000−0.2000 has 3 leaves (1 blue, 2 red) residing in the lowest branch (outer green contour) which gives one statistic. In general, compared to *Gaussclump*, `dendrogram` picks up in addition numerous structures with irregular morphology, i.e. the magenta leaves at the edge of G333.7700−0.2500; the number of leaves is smaller than number of compact sources identified by *Gaussclump* with the average size appears larger. The differences are intrinsically linked with their different ways of defining structures. Although a systematic comparison between these two methods is beyond the scope of this paper, here we benchmark the analysis in Sec. 2.5.3 to see whether the choice of source extraction method causes systematic differences in the results.

In Fig. A.31 the fragmentation level is compared with the clump properties, similarly as in Fig. 2.14. We again find a correlation between the fragmentation level with the parental clump mass, with a Spearman correlation coefficient of 0.42 (p-value<0.001), although we have smaller statistics here. We again define the specific fragmentation level as number of fragments normalised by clump size, as $N_{\rm mm}/R_{\rm clump}$. There is no correlation between specific fragmentation level with clump L/M ratio, with Spearman correlation coefficient of 0.018. Finally, comparing the fragmentation level with the Jeans fragmentation prediction, we find a Spearman correlation coefficient of 0.30 of specific fragmentation level with clump gas density (p-value~0.05). As for the comparison of fragmentation level with number of Jeans mass predicted by clump dust temperature and gas density, a Spearman correlation coefficient of 0.48 is found (p-value~0.003). Assuming a fragmentation temperature of 20 K, the Spearman correlation coefficient is 0.44 (p-value<0.001). These results are broadly consistent with Fig. 2.14 in Sec. 2.5.3. The relation of mass of the most massive fragment with clump L/M and clump mass are also compatible with Fig. 2.15, despite the drastic difference in the contrast of surface densities between the most massive fragment and their parental clump as in the right panel of Fig. 2.15 and Fig. A.32. We size-coded the data points in the right panel of Fig. A.32 according to the size difference between the most massive fragment and its parental clump. It is obvious that the large scatter of the two surface density values is related to the relative size difference defining the parent and child structures, which together lead again to the tight correlation between the mass of the most massive fragment and the parental clump mass. We therefore conclude that the source extraction method and the way we define the fragmentation level by allocating sources in a non-hierarchical way do not affect the analysis results within the scope of this work.

A.4 MALT90 spectra towards the massive pre-stellar cores

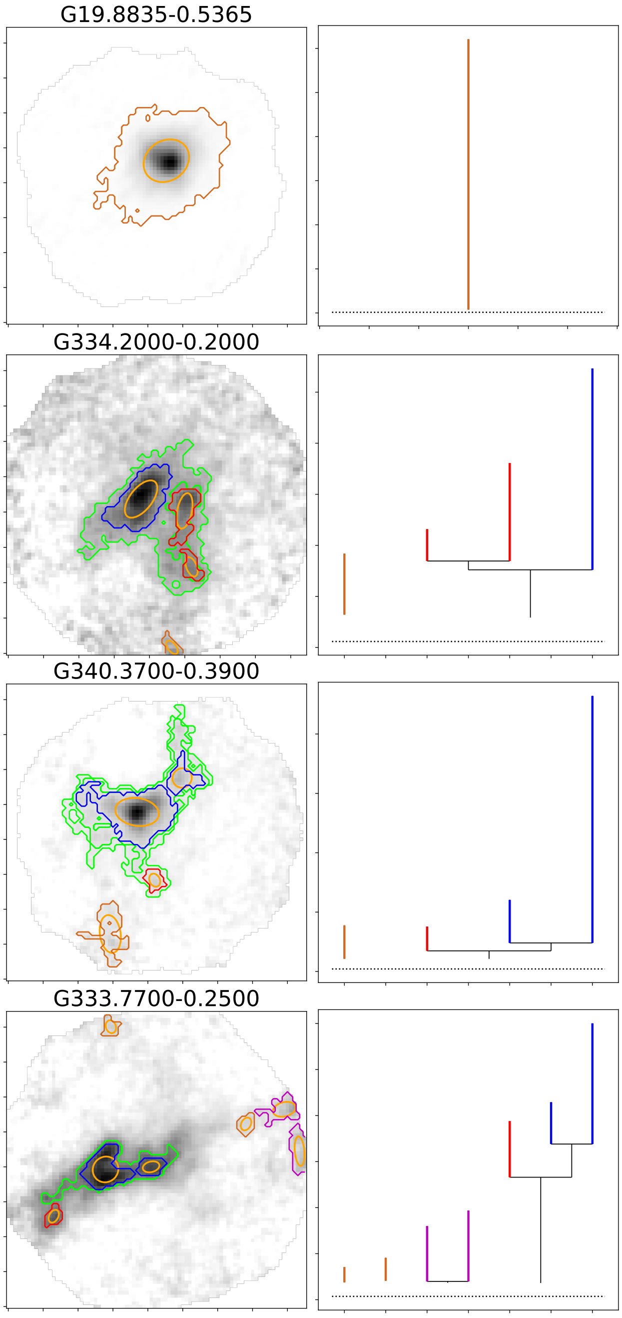

Figure A.30: Dendrogram source extraction results of four sources. *Left*: Dendrogram identified multi-level structures overlaid on the SABOCA emission map. Leaves originating from same top branch structures are marked with same color (in red, blue, cyan or magenta) as contour lines. Leaves with brown color are isolated leaf structures, i.e. with no parental structure present in the emission map. Orange ellipses are the corresponding schematic ellipse calculated based on the weight of intensity. Branches that do not intersect with the map edge, i.e. with closed contours as defined in the texts, are marked with lime contour lines. *Right*: Dendrogram tree plot representation of the left panel. Similarly, leaves from same top branch are marked with same color as in left panel. Horizontal dotted line indicates the 3σ threshold we use for minimum level as input parameter of dendrogram identification.

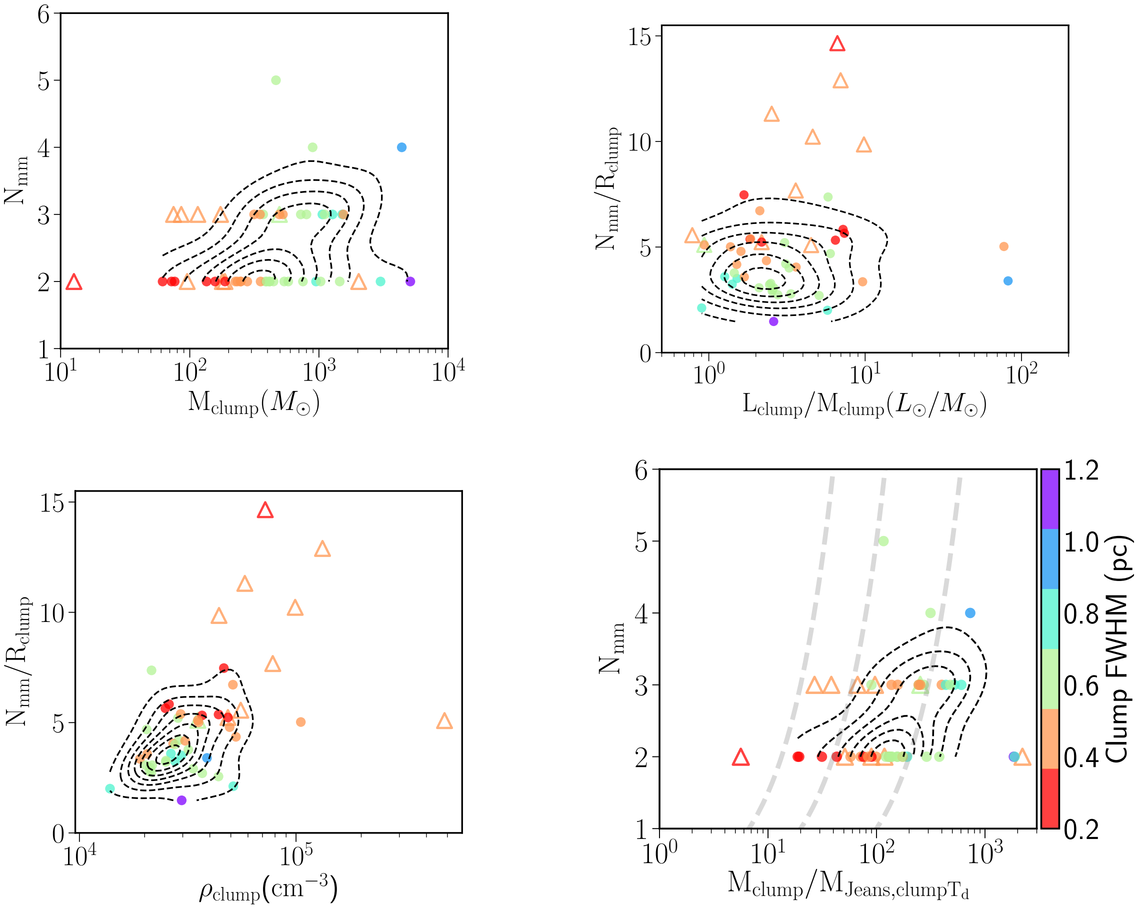

Figure A.31: Fragmentation level as a function of clump properties of sources located at a distance in 2-4 kpc (dots) and 1-2 kpc (triangles). In each plot, data points are color-coded according to the clump size. Dashed contours show the distribution of sources at 2-4 kpc from Gaussian kernel density estimation. *Upper left*: Number of fragments as a function of clump mass. *Upper right*: Specific fragmentation level (normalised by parent structure size) as a function of the clump's luminosity-to-mass ratio. *Lower left*: Specific fragmentation level as a function of the clump's density. *Lower right*: Number of fragments as a function of predicted number of fragments based on Jeans fragmentation scenario. Gray dashed lines mark the lines of N_{mm} = 0.15/0.05/0.01×$M_{clump}/M_{Jeans\,clump\,T_d}$.

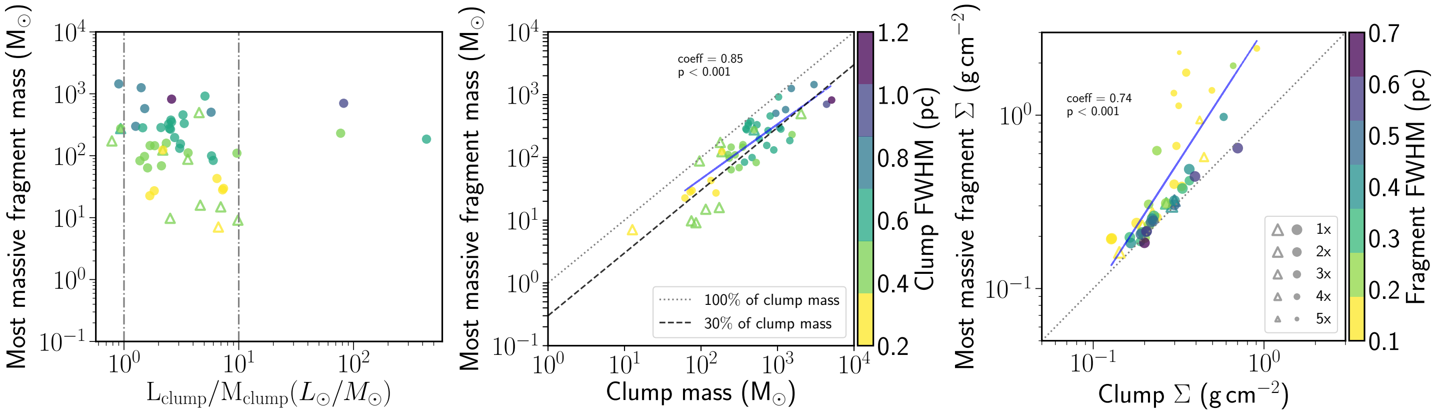

Figure A.32: *Left*: Most massive fragment mass as a function of clump properties for sources at a distance 2-4 kpc (dots) and 1-2 kpc (triangles). *Left*: Mass of the most massive fragment as a function of clump luminosity-to-mass ratio. Vertical lines mark the luminosity-to-mass ratio of 1 and 10. *Middle*: Mass of the most massive fragment mass as a function of clump mass. Gray lines show the 30% and 100% proportion of clump mass; blue line shows the result of a linear fit on logarithmic scale to sources in 2-4 kpc distance range of $M_{\rm fragments} = 0.87 \log M_{\rm clumps} - 0.21$. Left and middle plots share the same color bar, with clumps color coded according to their sizes. *Right*: Surface density of the most massive fragment as a function of clump surface density. Gray line marks the line of equality; the blue line shows the result of a linear fit to sources in 2-4 kpc distance range of $\log\Sigma_{\rm fragments} = 1.51 \log\Sigma_{\rm clumps} + 1.13$. The different sizes of markers correspond to the size ratios between the parental clump size and most massive fragment size, as indicated in the legend, i.e. the smaller the size of a marker, the larger size difference between fragment and its parental clump, up to a factor of 5.

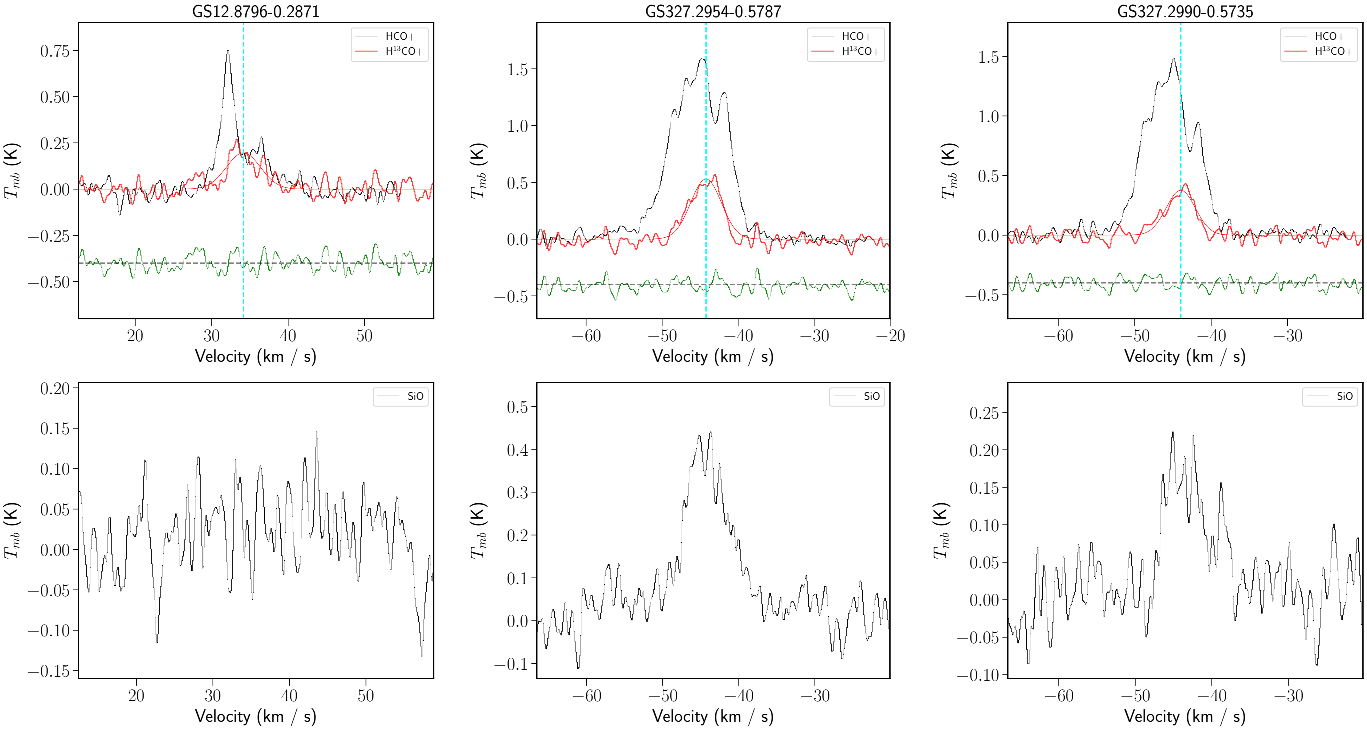

Figure A.33: MALT90 spectra towards the >100 $M_\odot$ quiescent cores at < 5 kpc. The source names are shown in the title. $HCO^+/H^{13}CO^+$ and SiO lines are plotted in the top and bottom panels, respectively. The V_{LSR} is indicated with a vertical line in the $HCO^+/H^{13}CO^+$ plot. The residual of the $H^{13}CO^+$ fit is shown in green, offset by -0.4 K.

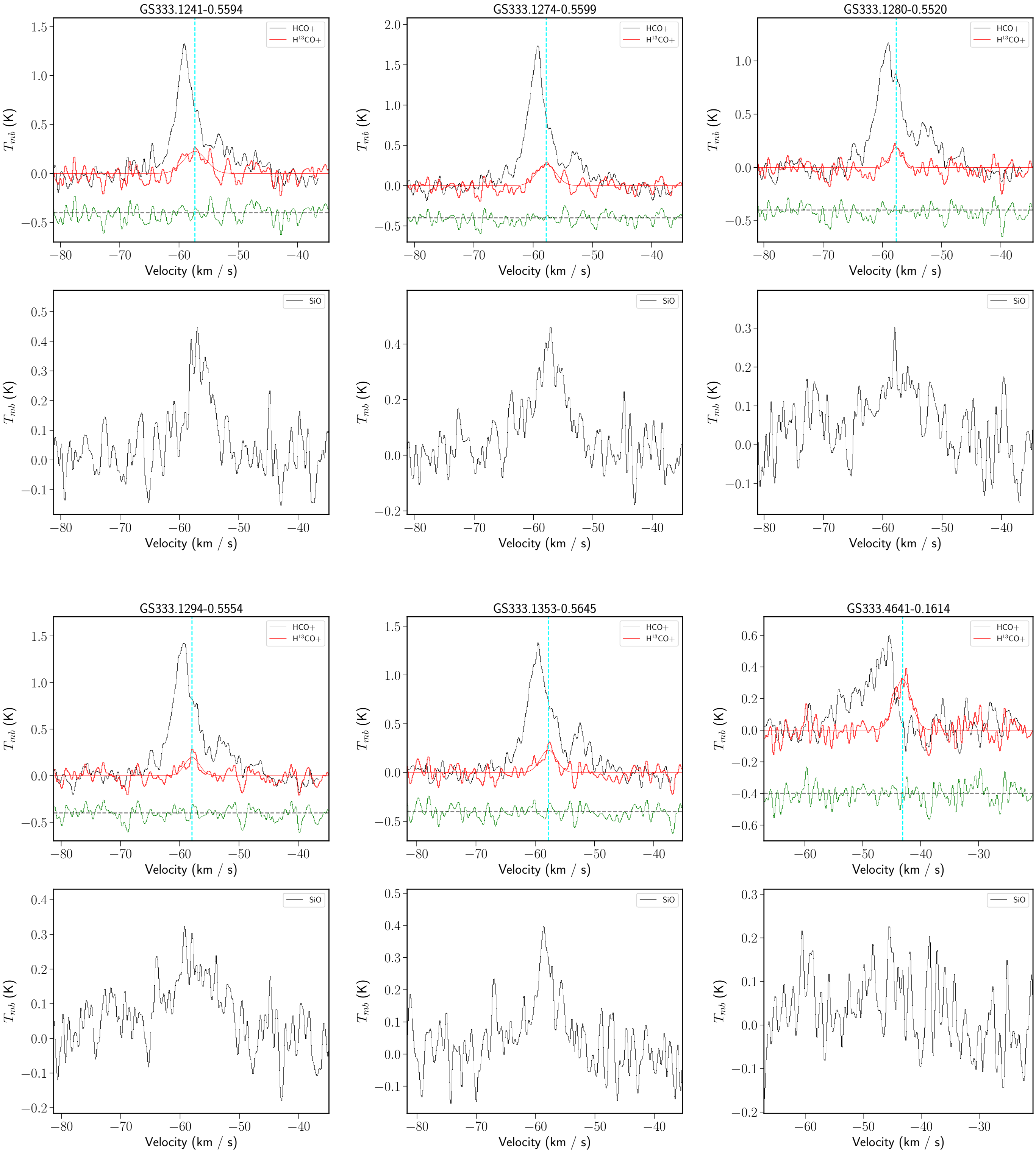

Figure A.34: Continued.

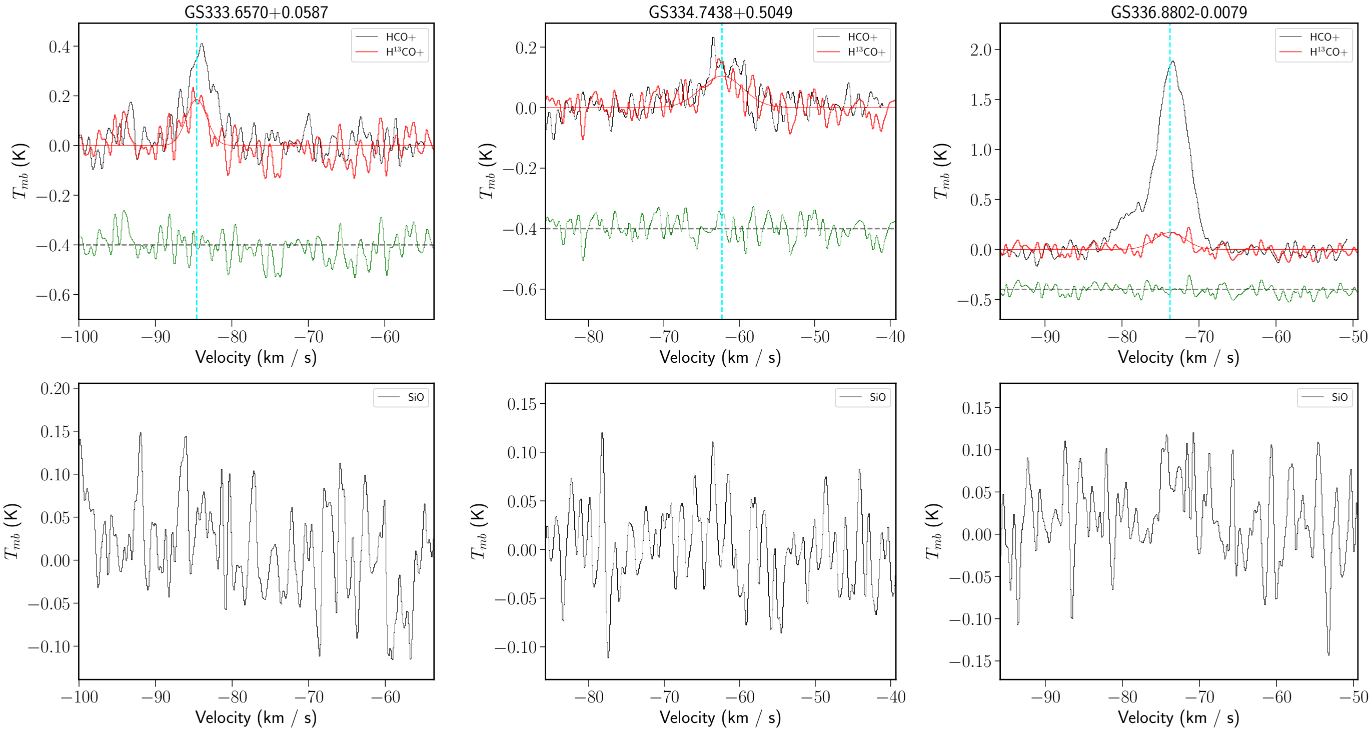

Figure A.35: Continued.

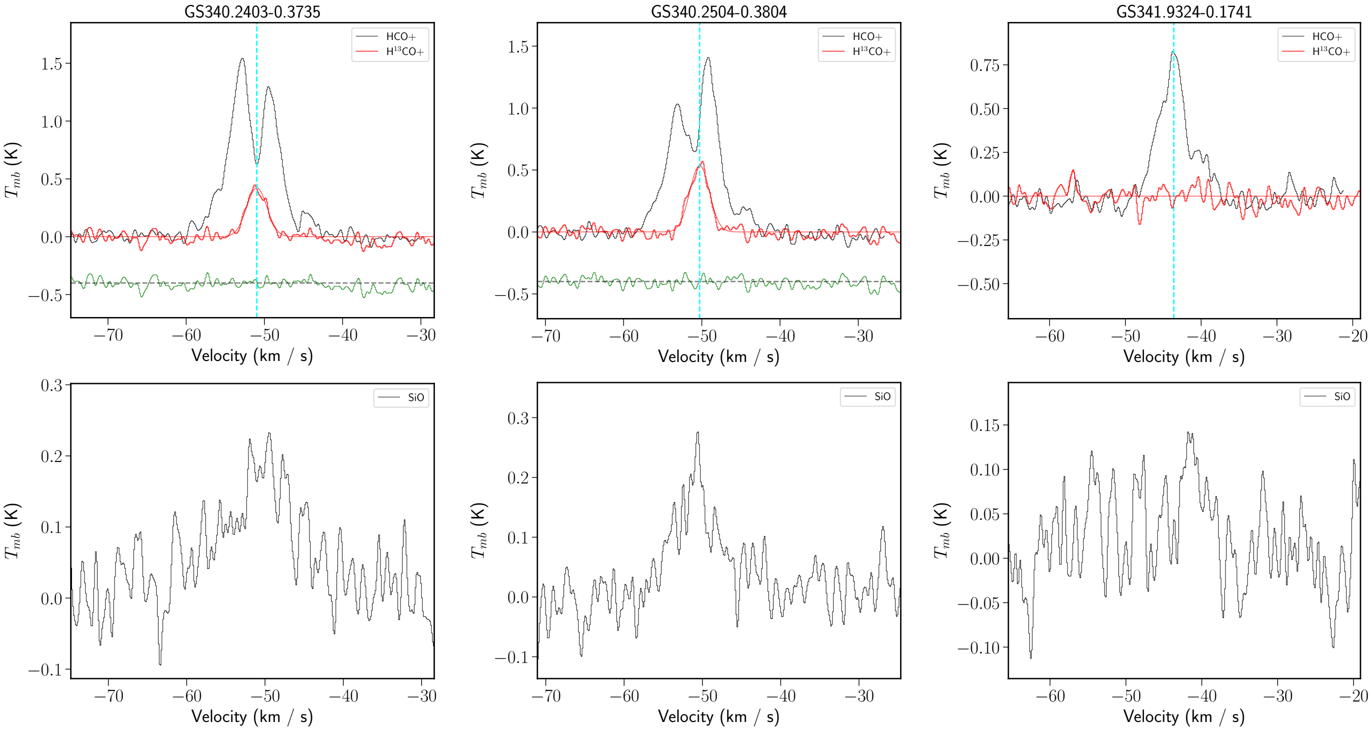

Figure A.36: Continued.

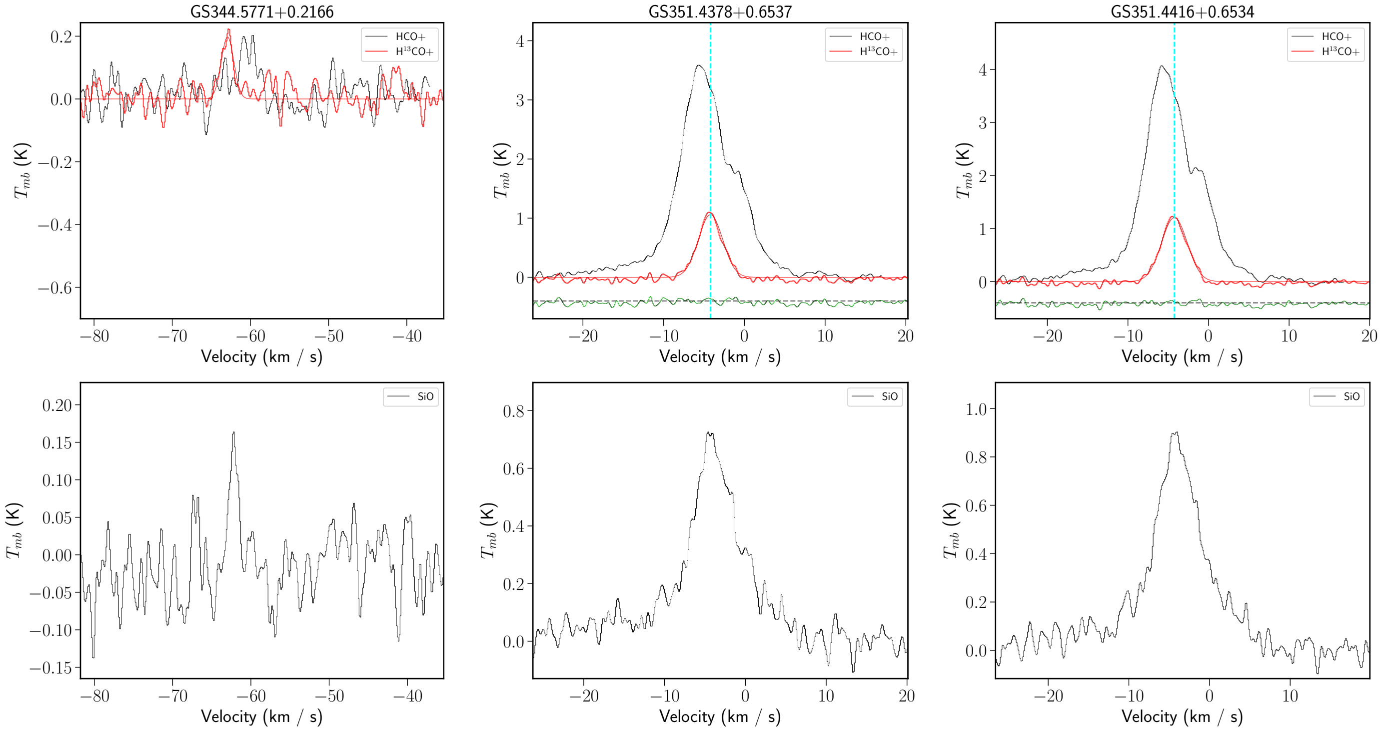

Figure A.37: Continued.

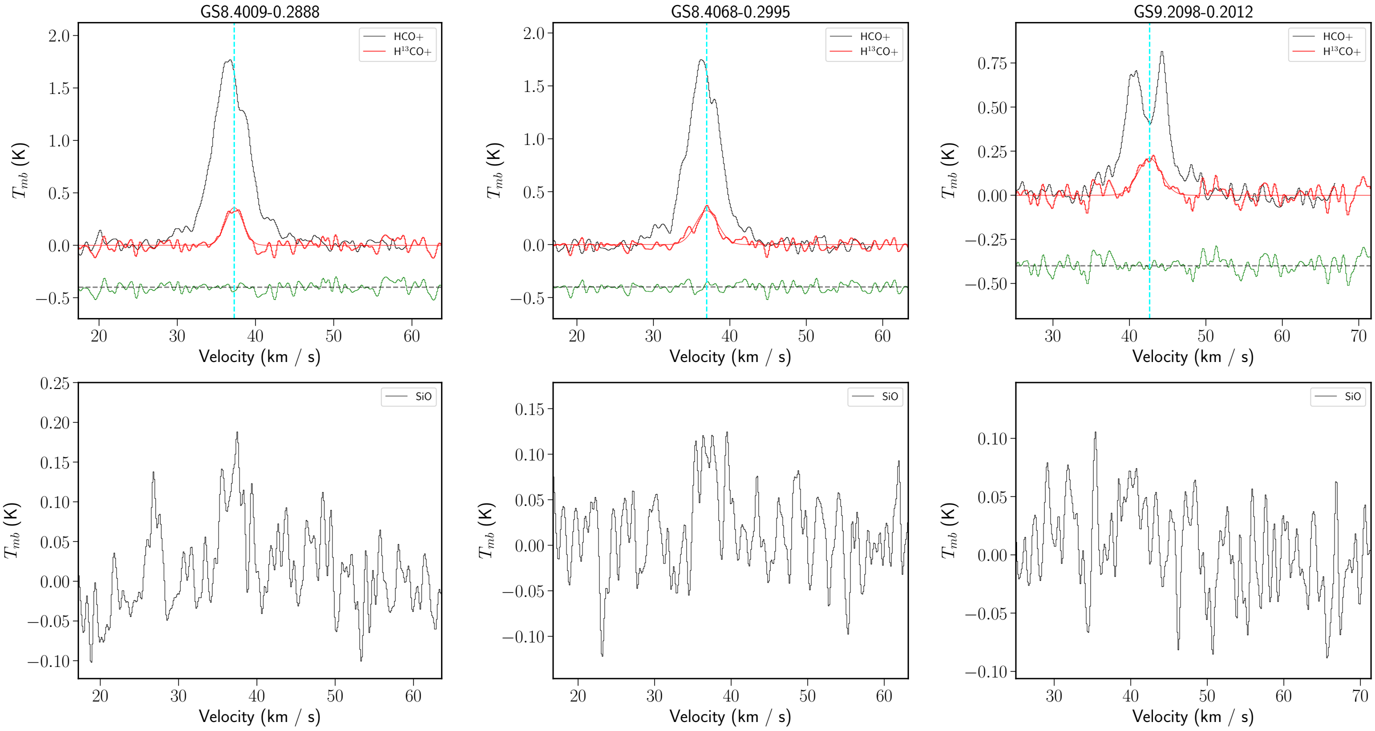

Figure A.38: Continued.

A.5 Target sources

A.5.1 G19.882-00.534

G19.882-00.534 (IRAS 18264–1152), is classified as an extended green object (EGO, Cyganowski et al. 2008), located at 3.7 kpc with luminosity of $>10^4$ $L_\odot$. Most prominent features of this source are the high-velocity outflow (Qiu et al. 2007, Leurini et al. 2014) and the high level of maser activities (among a sample of 56 high-mass star-forming region, Rodríguez-Garza et al. 2017). The outflow is oriented in a east-west direction, showing enhanced H_2 near-infrared emission as well (Varricatt et al. 2010). Sensitive 7 mm and 1.3 cm observations resolved the source into a triple system, consisting of two optically HII or dust emitting sources, and a thermal jet or a partially optically thick HII region (Zapata et al. 2006).

A.5.2 G08.684-00.366 and G08.671-00.356

The two massive star-forming clumps are parts of IRAS 18032-2137 star-forming cloud located at 4.8 kpc (Purcell et al. 2006). Multiple water, methanol and hydroxide masers are detected towards both sources (Hofner and Churchwell 1996, Caswell 1998, Gómez et al. 2010). G08.671-00.356 ($\sim$ 9000 $L_\odot$) is a UCHII region (Wood and Churchwell 1989), while G08.684-00.366 ($\sim$ 3000 $L_\odot$) is a less evolved relatively infrared weak source, lying 1 $'$ offset in the north-eastern direction. Strong SiO emission towards G08.684-00.366 indicates star formation already takes place in this source (Harju et al. 1998). Previous SMA observations resolve the source into 3 dense cores accompanied by extended outflow components traced by CO (2-1) emission; the core masses are around several to ten solar masses, a small fraction of the total clump mass (Longmore et al. 2011).

A.5.3 G10.624-00.380

G10.624-00.380 is an extremely luminous and massive ($>10^5$ $L_\odot$, $\sim$5000 $M_\odot$) OB cluster forming clump in the galaxy, located at 4.95 kpc (Sanna et al. 2014). Previous high angular resolution submm and centimeter observations reveal the clump in the central 0.6 pc is a flattened rotating system (Keto, Ho and Haschick 1988; Keto, Ho and Reid 1987,) where multiple UCHII regions are deeply embedded (Ho and Haschick 1986, Sollins et al. 2005); the clump is fed by the converging flows from ambient filamentary clouds (Liu, Zhang and Ho 2011; Liu et al. 2012). Within the HII region, absorption lines indicate that the gas accretion continues despite the ionising and radiative pressure (Keto 1990). Overall, the clumps seems to be in an global collapsing state with a rotating Toomre-unstable disk-like structure in the center (Liu 2017).

A.5.4 G13.658-00.599

G13.658-00.599 (IRAS 18144-1723) is a molecular clump having a luminosity of $>10^4$ $L_\odot$ at 3.7 kpc. It is associated with multiple water and methanol masers (Gómez-Ruiz et al. 2016). H_2 image shows a bowshock feature $18''$ offset in the west from the center of the IRAS emission, which seems to originate from an extended K-band continuum source associated with the IRAS source (Varricatt et al. 2010). The bowshock feature is surrounded by multiple 44 GHz methanol masers (Gómez-Ruiz et al. 2016), indicating it is likely caused by outflow activities. Deep mid-infrared imaging reveals that the central source hosts two YSOs separated by $\sim$ 10000 au, and are of different evolutionary

Table A.1: Information of the centimeter continuum data collected from NRAO archive.

Source	Freq. (GHz)	Resolution ($''$)	Obs. Date	Integrated flux (Jy)
G31	43.3	1.62	2001-11-26	0.42
G08b	8.5	0.85	2005-02-28	0.99
G10	23.8	0.09	2002-02-01	3.55

stages; outflow traced by CO(3-2) line coincides well with the H_2 emission, and is likely caused by the younger source in formation (Varricatt et al. 2018).

A.5.5 G31.412+00.307

G31.412+00.307 is a well-known hot massive core (HMC) that has been extensively studied by both single-dish and interferometry observations (e.g. Cesaroni et al. 1994,Beltrán et al. 2004, 2018, Rivilla et al. 2017), a source showing great chemical richness. It is located at a kinematic distance of 7.9 kpc (Churchwell, Walmsley and Cesaroni 1990), and of luminosity $\gtrsim 10^5$ $L_\odot$. The central hot core structure is massive and compact (~500 $M_\odot$ of ~8000 au in size, Cesaroni et al. 2011, Beltrán et al. 2004). There is an ultra-compact HII region $5''$ away from the core (Churchwell, Walmsley and Cesaroni 1990). The kinematic features consistently support a rotating core experiencing infall motions (Cesaroni et al. 2011, Wyrowski et al. 2012). Recent ALMA observations of higher angular (~1700 au) resolution indicate both the rotation and infall speed up towards the center, and the core is composed of a main core of size ~5300 au and a satellite core of much smaller mass (Beltrán et al. 2018). The overall monolithic feature of source G31 makes it an ideal source for understanding the high mass star formation scenario in light of gas mass origin and evolution.

A.6 Subtraction of free-free emission from the SMA 1.2 mm continuum

We use centimeter radio continuum data retrieved from the NRAO data archive[1] for the Very Large Array (VLA) for sources G08b, G31 and G10, to estimate the free-free emission contribution to the 1.2 mm flux. Given potential time variability of centimeter emission, we select the latest observed data product, basic information of which is listed in Table A.1.

Assuming that the dust emission and free-free emission are both optically thin, and that the dust emissivity has a spectral index $\beta = 1.0$, then the relation of $S_\nu \propto \nu^{2+\beta}$ and $S_\nu \propto \nu^{-0.1}$ describe the variation of the two emission components, respectively, as a function of frequency. The free-free emission at 1.2 mm can then be solved for by simultaneous equations of total flux contributed and related from these scaling relations, at two considered frequencies. The centimeter data was smoothed and regridded to match the 1.2 mm data and subtraction was done in a pixel-by-pixel basis.

---

[1] http://www.aoc.nrao.edu/ vlbacald/ArchIndex.shtml

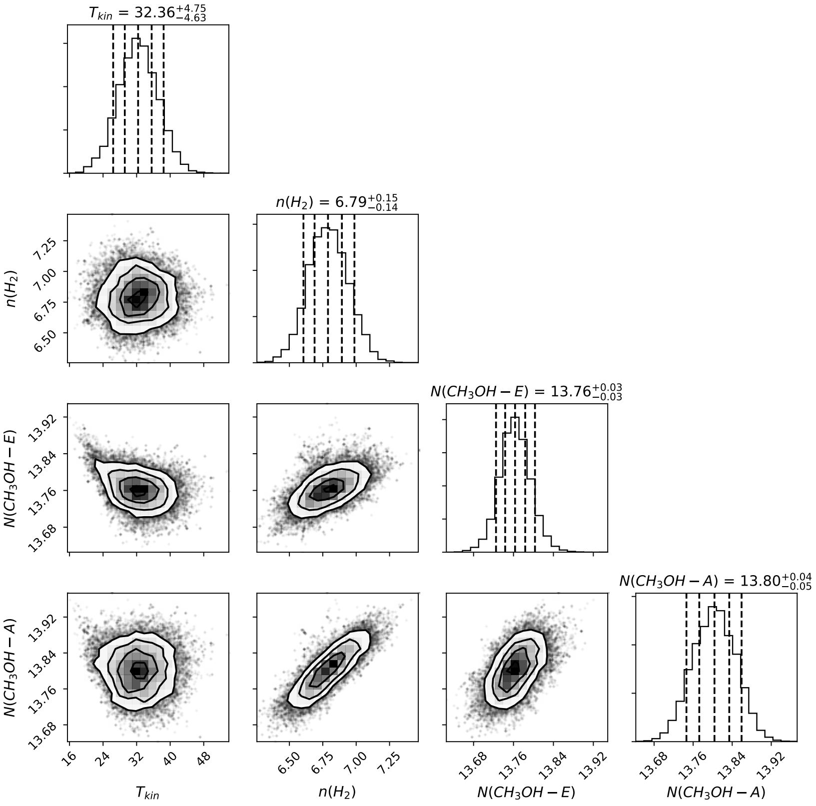

Figure A.39: Posterior distribution of parameters from MCMC RADEX fitting of CH_3OH (5-4) line series. The column densities of A/E type are velocity averaged value (log cm^{-2}/km s^{-1}).

A.7 RADEX modeling of CH_3OH lines: the MCMC procedure

For both E-type and A-type CH_3OH, we generated RADEX model grids in the column density (N/Δv) range from 10^{12} to 10^{18} cm^{-2} (with 60 logarithmically spaced uniform intervals), in the density range from 10^4 to 10^9 cm^{-3} (with 100 logarithmically spaced uniform intervals), and in the kinetic temperature range between 10−200 K (with 80 uniform intervals). The external radiation field was taken to be the cosmic background of 3 K. We used a linear interpolator to estimate the line intensities for parameters in between the intervals to better constrain the parameters and to allow for a continuous examination of parameter space. Nevertheless, the accuracy of the best-fit parameters remains limited by the resolution of the grid.

We fit the A- and E−CH_3OH (5-4) (v_t = 0) line profiles with Gaussian models pixel-by-pixel for all the sources. We assumed that the line width is identical for all the K components and for A and E types. We also took into consideration that the HNCO $11_{0,11} - 10_{0,10}$ line is blended with the CH_3OH $5_{-1} - 4_{-1}$ E line ($\delta V \sim 8.44$ km s^{-1}) and removed the contribution from this HNCO line by fitting an additional Gaussian component of which the line-width and amplitude are free parameters.

We employ the Markov Chains Monte Carlo (MCMCs) method with an affine invariant sampling algorithm[2] (emcee, Foreman-Mackey et al., 2013) to perform the pixel-by-pixel fitting. Our prior assumption for each pixel adopted the temperature $T_{\rm rot}$ predicted from the temperature profiles in Section 3.3.3, which means that for $T_{\rm kin}$ we assumed a normal distribution centering at $T_{\rm rot}$ and with a standard deviation of 5 K. For the other parameters, the priors were assumed to be uniform distributions. We use a likelihood distribution function which takes into account observational thresholds; the formulas follow,

$$P \propto \prod_i p_i \prod_j p_j \tag{A.1}$$

where p_i stands for probabilities of the ith data that is a robust detection and p_j the jth data that gives a constrain by an upper limit; we adopt the normal distribution as likelihood function,

$$p_i \propto \exp\,[-\frac{1}{2}(\frac{f_i^{\rm obs} - f_i^{\rm model}}{\sigma_i^{\rm obs}})^2]\Delta f_i \tag{A.2}$$

$$p_j \propto \int_{-\infty}^{f_{lim,j}^{\rm obs}} \exp\,[-\frac{1}{2}(\frac{f_j - f_j^{\rm model}}{\sigma_j})^2]df_j \tag{A.3}$$

As the starting points (initialization) for the chains, we chose the parameter set corresponding to a global χ^2 minimum calculated between the grid models and the observed values. We also employed the "burn-in" phase in the MCMC chains and several resets of the starting-points to ensure the final chains are reasonably stable around the maximum of the probability density. An example posterior distribution of the fitted parameters is shown in Figure A.39. The obtained n(H_2) maps and column density maps of CH_3OH for all sources are shown in Figure 3.8 and Figure A.40, respectively.

A.8 LTE analysis for other lines

CS/C^{34}S (5-4)

Transitions of CS are tracers for dense gas. Our spectral setup covered the J=5-4 transition of CS and its rare isotopologue, C^{34}S, for the 7 sources. For G10, the data we utilized only covered the C^{34}S (5-4) line. In the observed sources, the CS line and the 1.2 mm continuum emission trace similar structures. The CS line images additionally revealed some spatially more extended structures.

Assuming that CS and C^{34}S trace gas of identical temperature and linewidth, the optical depth of the C^{34}S line can be estimated by

$$\frac{W_{\rm CS}}{W_{\rm C^{34}S}} = \frac{[1-\exp{(-R\tau_{\rm C^{34}S})}]}{[1-\exp{(-\tau_{\rm C^{34}S})}]}, \tag{A.4}$$

where $W_{\rm CS}$ and $W_{\rm C^{34}S}$ are the integrated line intensities, and $R = 22.6$ is our assumed ^{34}S/^{32}S abundance ratio. The CS line, as expected, is broader than the C^{34}S line, and shows self-absorption profiles in most of the cases. These are two effects canceling out each other when estimating $\tau_{\rm C^{34}S}$ since our derivation was based on the integrated intensity ratios. We found that $\tau_{\rm C^{34}S}$ ranges from less than 0.1 to 0.25 in most of the sources, while it reaches 0.3-0.45 in G08b and reaches as high as 0.9 in G31.

---

[2] Detailed description of the method can be found in the emcee documentation.

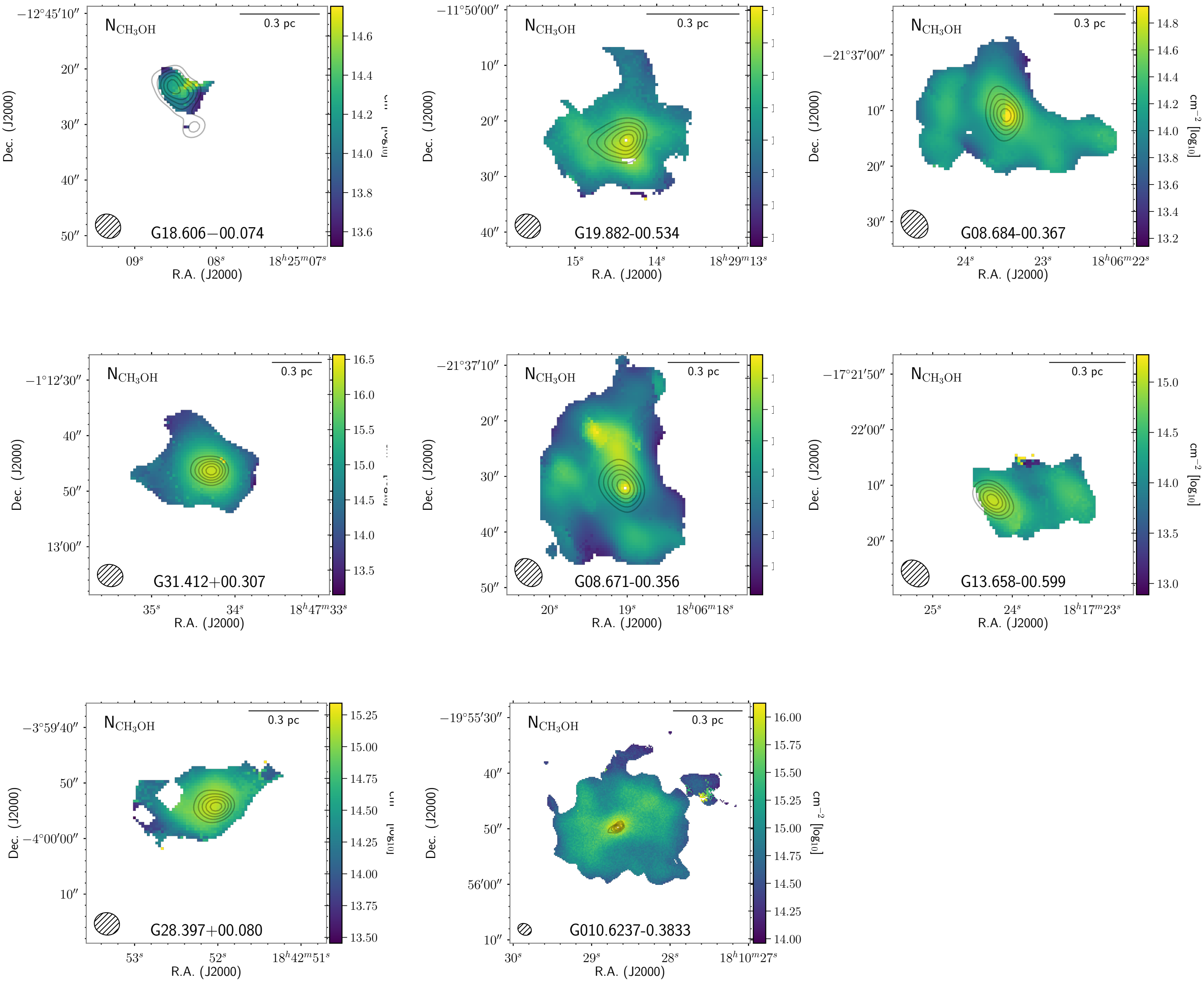

Figure A.40: CH_3OH derived N_{CH_3OH} maps from RADEX modeling of all target sources.

Assuming a beam filling factor $f = 1$, a lower limit of the excitation temperature ($T_{\rm ex}$) can be estimated from the brightness temperature of $C^{34}S$,

$$J(T_{\rm b}) = \left[J(T_{\rm ex}) - J(T_{\rm bg})\right]\left[1 - \exp\left(-\tau_{\rm C^{34}S}\right)\right]. \tag{A.5}$$

Since the $n_{\rm crit}$ of CS is higher than the thermometers except CH_3CN used in Sect. 3.3.3, and that there is more extended cold envelope gas contributing to the emission of CS line, as expected, the derived $T_{\rm ex}$ is in general lower than the $T_{\rm rot}$ profiles derived from the observations of multiple transition of the other molecular thermometers (see Sect. 3.3.3). The derived $T_{\rm ex}$ is <10 K in G18, in the range of 20-30 K in most of the other sources, and reaches ~45 K at the emission peak of G31.

Under LTE assumption, the overall column densities of the $C^{34}S$ ($N_{\rm C^{34}S}$) then can be estimated based on evaluating the partition functions, adopting $T_{\rm ex}$. The derived $C^{34}S$ column densities are in the range of 4.4×10^{12} - 5.0×10^{14} $\rm cm^{-2}$.

In an alternative approach, we assumed that the $T_{\rm ex}$ of $C^{34}S$ is the same with the $T_{\rm rot}$ measured from the other molecular thermometers, and then directly solved for $\tau_{\rm C^{34}S}$ based on an LTE assumption. The $N_{\rm C^{34}S}$ derived this way is 1.1-1.5 times larger for warmer sources except for G18. In G18, the $N_{\rm C^{34}S}$ derived with this approach is ~10 times smaller than the derivation based on the $CS/C^{34}S$ intensity ratio. This is due to the dependence between $N_{\rm C^{34}S}$ and $T_{\rm ex}$ under LTE assumption: $N_{\rm C^{34}S}$ drops significantly below ~30 K and rises only slowly for larger values of $T_{\rm ex}$.

A.8.1 CCH (3-2)

The hyperfine line components of CCH resulting from electron-nucleus interactions allow for an direct measure of the CCH line optical depth. We adopted a fitting procedure similar to that described in Estalella (2017), adopting relative line intensities from LTE predictions. From hyperfine line fitting, we derived excitation temperature and optical depth in a pixel-by-pixel basis, and then used these to estimate the CCH column densities. We found that the optical depth of the main line, $\tau_{\rm m}$~0.1 in extended regions, but can become optically thick at high column densities in localized regions. In most of the sources, $\tau_{\rm m}$ reaches up to ~3. But in G18, $\tau_{\rm m}$ reaches ~10 at the center, which is close to the upper limit in our fitting procedure. The column density of CCH ranges between 1.2×10^{14} - 6×10^{15} $\rm cm^{-2}$ across the emission region for all the sources. In general, the CCH column density distribution shows porosity over extended regions (~0.2-0.3 pc) except G18, and is systematically larger in outer regions, resembling a ring-like structure, especially for clump G08b and G31. The central region of the hot massive core G31 is almost completely devoid of CCH emission. Jiang et al. (2015) present high-angular resolution CCH observation towards clump G10 together with other 3 more evolved high-mass clumps than our sample, which also exhibit ring-like distributions.

A.8.2 SO and SO_2

Our spectral setup covered three SO lines (Table 3.4) which have similar upper level energies $E_{\rm up}$. These three lines were detected in all clumps except G18. The resolved SO intensities were spatially compact and were confined within where 1.2 mm continuum emission was detected.

The SO_2 14(0,14)-13(1,13) ($E_{\rm up}$~94 K) line was detected in the all clumps except G18 and G28; in G28, a lower excitation transition SO_2 3(2,2)-2(1,1) (E_{up}~15 K) was marginally detected.

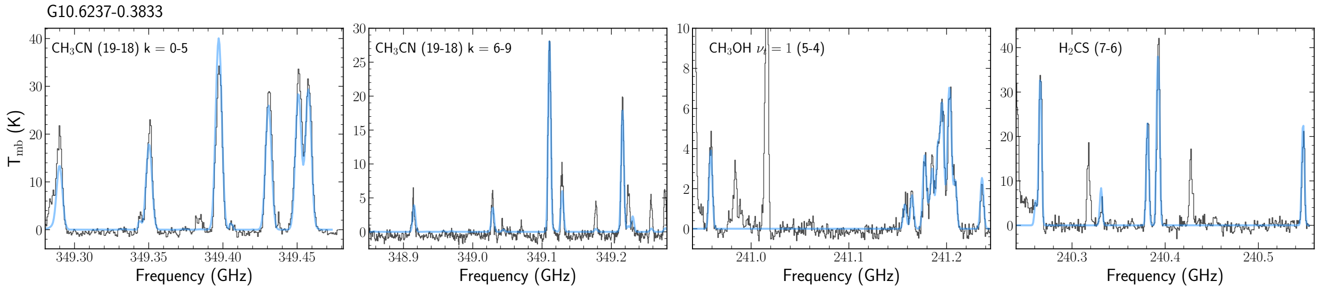

Figure A.41: Same as Figure 3.5, but for source G10.

These SO and SO$_2$ transitions are likely thermalized given that the emission closely follows the extension of the central core, which are of relatively high critical densities (Table 3.4). We cannot directly derive the excitation temperatures of the SO and SO$_2$ molecules owing to not covering multiple transitions, or owing to that the covered transitions have similar $E_{\rm up}$. Therefore, we adopted the gas temperature derived from the thermometer lines (Section 3.3.3) when estimating their column densities, assuming LTE condition.

A.9 Comparison between observed spectra and modeling results

The following panels include XCLASS fitting result of G10 (Sec. 3.3.3), and `LIME` modeling results for the other sources (except that of source G08a and G08b which are shown in Sec. 3.3.8).

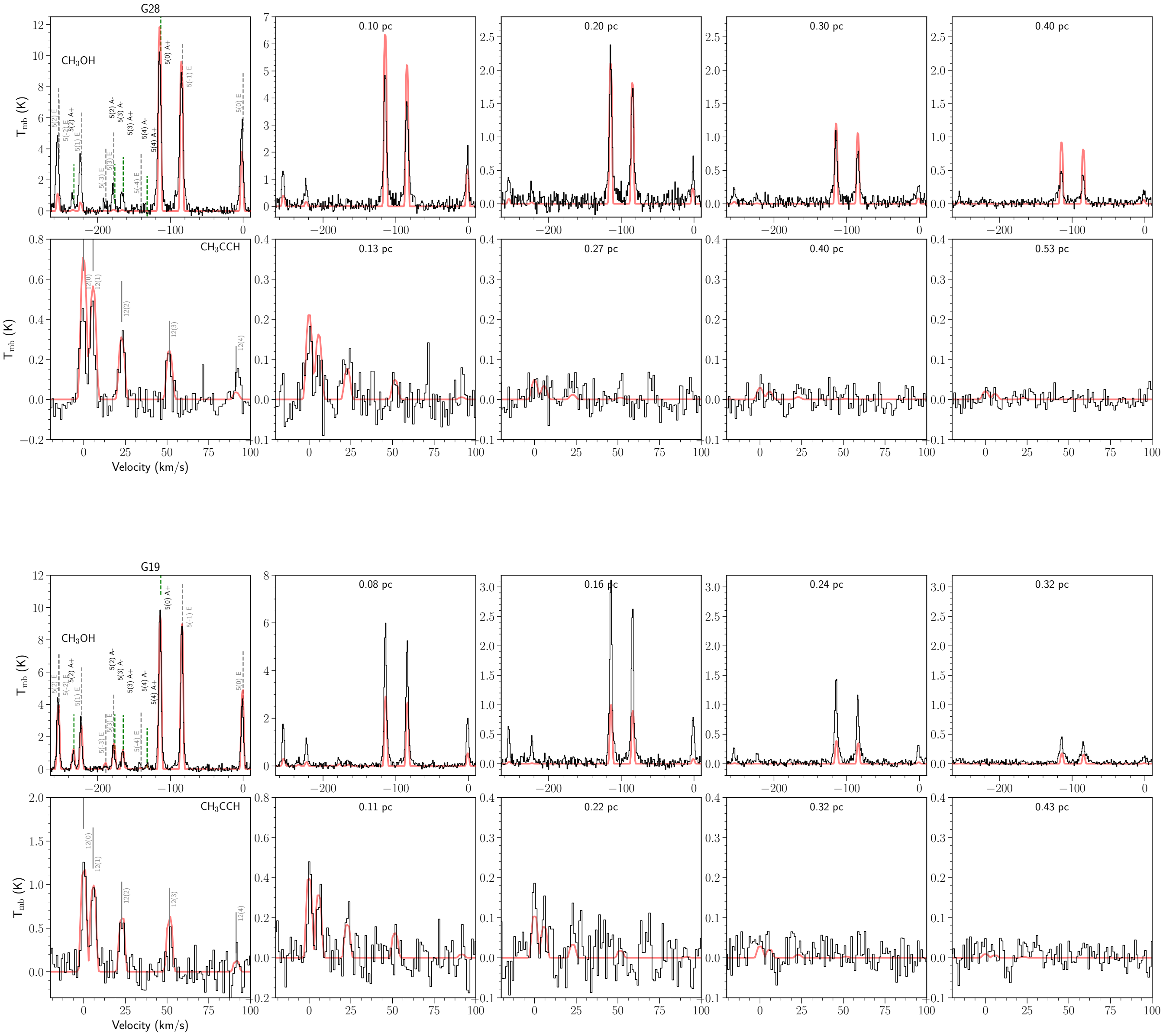

Figure A.42: Same as Figure 3.16, for other target sources.

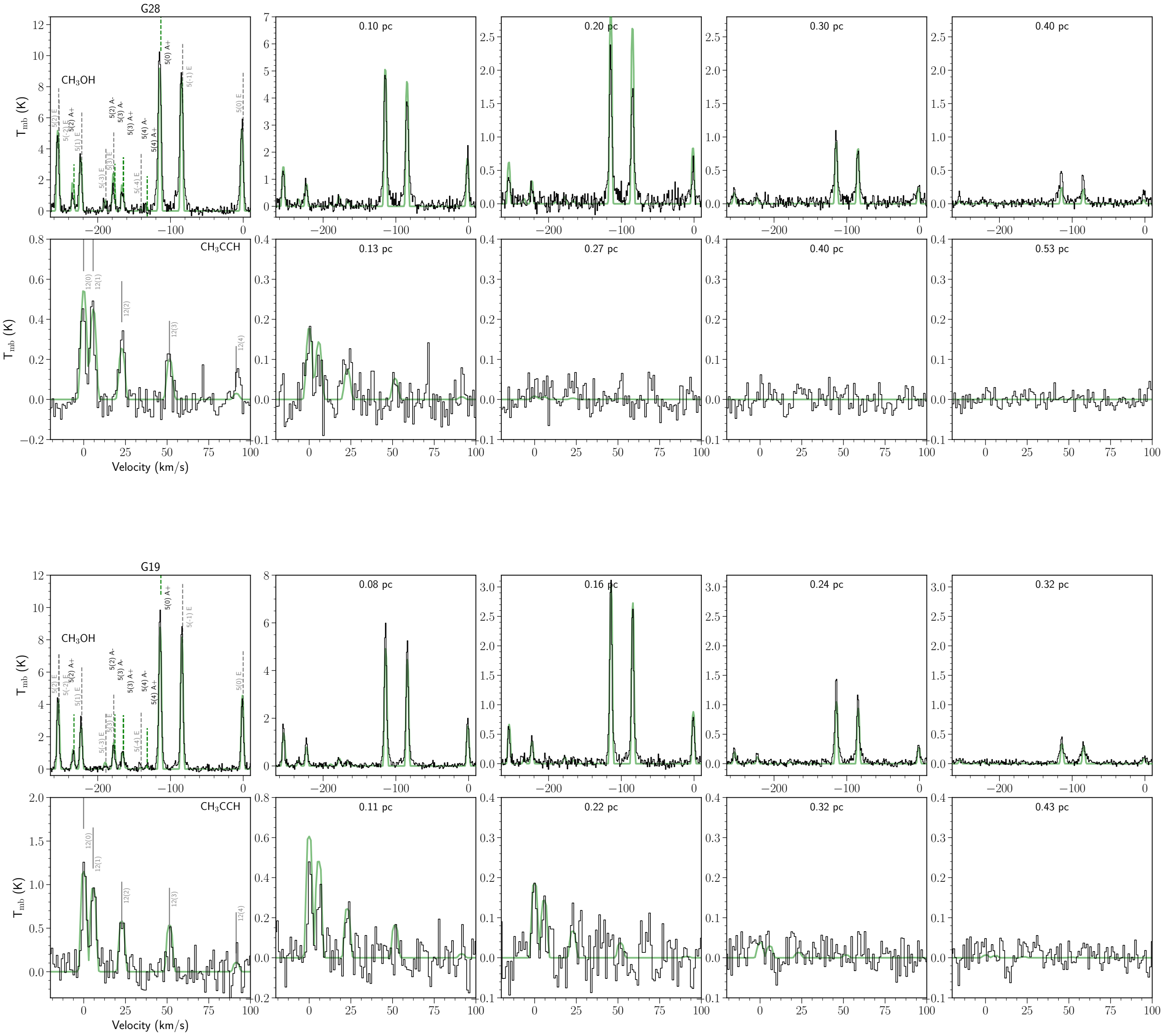

Figure A.43: Same as Figure 3.12, for other target sources.

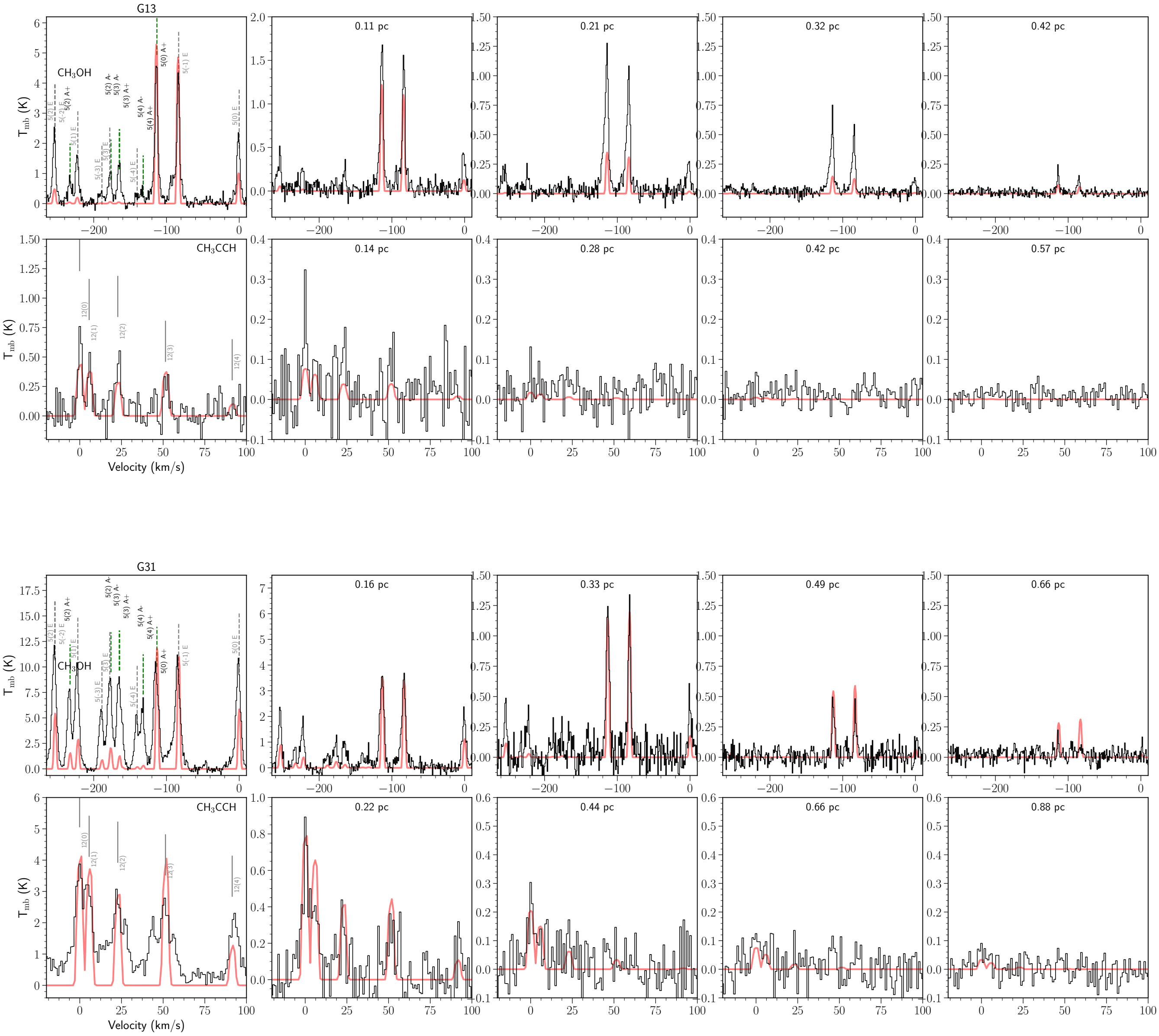

Figure A.44: Same as Figure 3.16, for other target sources.

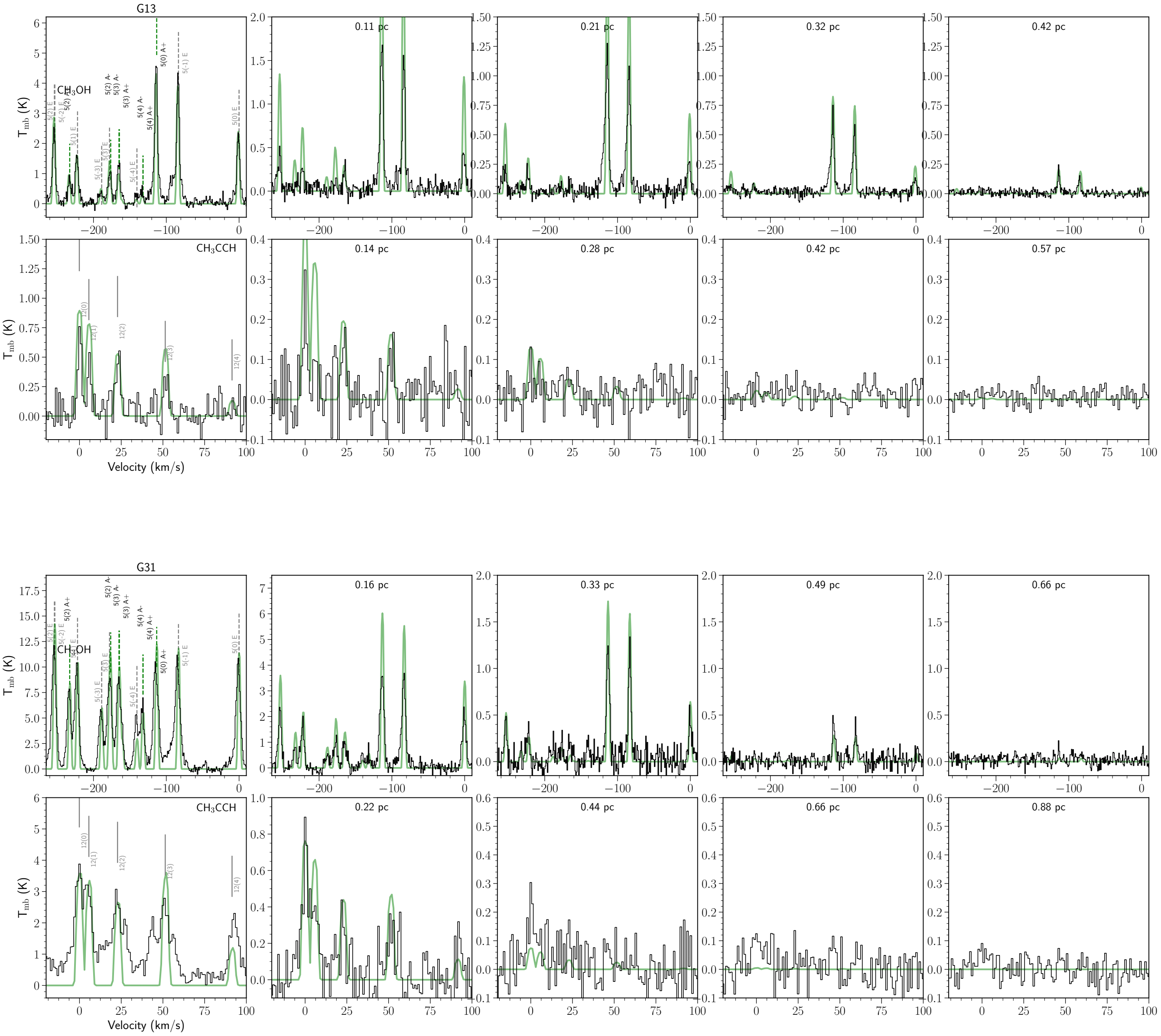

Figure A.45: Same as Figure 3.12, for other target sources.

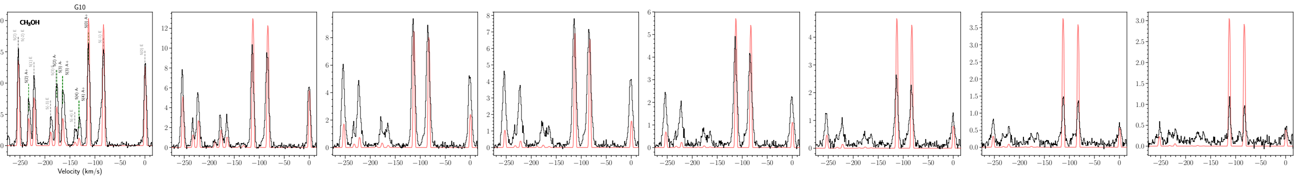

Figure A.46: Same as Figure 3.16, for other target sources.

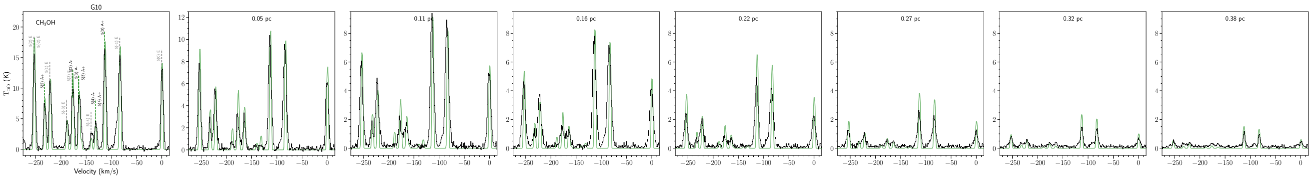

Figure A.47: Same as Figure 3.12, for other target sources.

References

Beltrán, M. T. et al. (2004), *Rotating Disks in High-Mass Young Stellar Objects*, Astrophys. J. Letters **601** L187, arXiv: `astro-ph/0312495 [astro-ph]` (cit. on p. 246).

Beltrán, M. T. et al. (2018), *Accelerating infall and rotational spin-up in the hot molecular core G31.41+0.31*, Astron. Astrophys. **615**, A141 A141, arXiv: `1803.05300 [astro-ph.SR]` (cit. on p. 246).

Caswell, J. L. (1998), *Positions of hydroxyl masers at 1665 and 1667 MHz*, Mon. Not. R. Astron. Soc. **297** 215 (cit. on p. 245).

Cesaroni, R. et al. (1994), *A Massive Young Embedded Object Associated with the UC H II Region G31.41+0.31*, Astrophys. J. Letters **435** L137 (cit. on p. 246).

Cesaroni, R. et al. (2011), *Dissecting a hot molecular core: the case of G31.41+0.31*, Astron. Astrophys. **533**, A73 A73, arXiv: `1107.2849 [astro-ph.SR]` (cit. on p. 246).

Churchwell, E., C. M. Walmsley and R. Cesaroni (1990), *A survey of ammonia and water vapor emission ultracompact HII regions*, Astron. Astrophys. **83** 119 (cit. on p. 246).

Cyganowski, C. J. et al. (2008), *A Catalog of Extended Green Objects in the GLIMPSE Survey: A New Sample of Massive Young Stellar Object Outflow Candidates*, Astron. J. **136** 2391, arXiv: `0810.0530 [astro-ph]` (cit. on p. 245).

Estalella, Robert (2017), *HfS, Hyperfine Structure Fitting Tool*, PASP **129** 025003, arXiv: `1608.04088 [astro-ph.IM]` (cit. on p. 250).

Foreman-Mackey, Daniel et al. (2013), *emcee: The MCMC Hammer*, PASP **125** 306, arXiv: `1202.3665 [astro-ph.IM]` (cit. on p. 248).

Gómez, Laura et al. (2010), *A Catalog of* CH_3OH 7_0-6_1 A^+ *Maser Sources in Massive Star-forming Regions. II. Masers in NGC 6334F, G8.67-0.36, and M17*, Astrophys. J. Supp. **191** 207, arXiv: `1010.1566 [astro-ph.GA]` (cit. on p. 245).

Gómez-Ruiz, A. I. et al. (2016), *A Catalog of Methanol Masers in Massive Star-forming Regions. III. The Molecular Outflow Sample*, Astrophys. J. Supp. **222**, 18 18, arXiv: `1601.01084 [astro-ph.GA]` (cit. on p. 245).

Harju, J. et al. (1998), *A survey of SiO emission towards interstellar masers. I. SiO line characteristics*, Astron. Astrophys. **132** 211 (cit. on p. 245).

Ho, P. T. P. and A. D. Haschick (1986), *Molecular Clouds Associated with Compact H II Regions. III. Spin-up and Collapse in the Core of G10.6-0.4*, Astrophys. J. **304** 501 (cit. on p. 245).

Hofner, P. and E. Churchwell (1996), *A survey of water maser emission toward ultracompact HII regions.*, Astron. Astrophys. **120** 283 (cit. on p. 245).

Jiang, Xue-Jian et al. (2015), *SMA Observations of* C_2H *in High-mass Star-forming Regions*, Astrophys. J. **808**, 114 114, arXiv: `1507.04205 [astro-ph.SR]` (cit. on p. 250).

Keto, E. R. (1990), *Radiative Transfer Modeling of Radio-Frequency Spectral Line Data: Accretion onto G10.6-0.4*, Astrophys. J. **355** 190 (cit. on p. 245).

Keto, Eric R., Paul T. P. Ho and Aubrey D. Haschick (1988), *The Observed Structure of the Accretion Flow around G10.6-0.4*, Astrophys. J. **324** 920 (cit. on p. 245).

Keto, Eric R., Paul T. P. Ho and Mark J. Reid (1987), *Gravitational Collapse in Molecular Cloud Cores around Ultracompact H II Regions: Two Candidates*, Astrophys. J. Letters **323** L117 (cit. on p. 245).

Leurini, S. et al. (2014), *SiO excitation from dense shocks in the earliest stages of massive star formation*, Astron. Astrophys. **570**, A49 A49, arXiv: `1409.4181 [astro-ph.GA]` (cit. on p. 245).

Liu, Hauyu Baobab (2017), *Interpreting observations of edge-on gravitationally unstable accretion flows. The case of G10.6-0.4*, Astron. Astrophys. **597**, A70 A70, arXiv: `1609.07296 [astro-ph.SR]` (cit. on p. 245).

Liu, Hauyu Baobab, Qizhou Zhang and Paul T. P. Ho (2011), *An Overall Picture of the Gas Flow in a Massive Cluster-forming Region: The Case of G10.6-0.4*, Astrophys. J. **729**, 100 100, arXiv: `1101.3459 [astro-ph.SR]` (cit. on p. 245).

Liu, Hauyu Baobab et al. (2012), *The Origin of OB Clusters: From 10 pc to 0.1 pc*, Astrophys. J. **745**, 61 61, arXiv: `1110.1318 [astro-ph.SR]` (cit. on p. 245).

Longmore, S. N. et al. (2011), *Is Protostellar Heating Sufficient to Halt Fragmentation? A Case Study of the Massive Protocluster G8.68-0.37*, Astrophys. J. **726**, 97 97, arXiv: `1011.1442 [astro-ph.SR]` (cit. on p. 245).

Purcell, C. R. et al. (2006), *A CH_3CN and HCO^+ survey towards southern methanol masers associated with star formation*, Mon. Not. R. Astron. Soc. **367** 553, arXiv: `astro-ph/0512589 [astro-ph]` (cit. on p. 245).

Qiu, Keping et al. (2007), *High-Resolution Imaging of Molecular Outflows in Massive Young Stars*, Astrophys. J. **654** 361, arXiv: `astro-ph/0609285 [astro-ph]` (cit. on p. 245).

Rivilla, V. M. et al. (2017), *Formation of ethylene glycol and other complex organic molecules in star-forming regions*, Astron. Astrophys. **598**, A59 A59, arXiv: `1608.07491 [astro-ph.GA]` (cit. on p. 246).

Rodríguez-Garza, C. B. et al. (2017), *A Catalog of 44 GHz Methanol Masers in Massive Star-forming Regions. IV. The High-mass Protostellar Object Sample*, Astrophys. J. Supp. **233**, 4 4, arXiv: `1709.09773 [astro-ph.GA]` (cit. on p. 245).

Sanna, A. et al. (2014), *Trigonometric Parallaxes to Star-forming Regions within 4 kpc of the Galactic Center*, Astrophys. J. **781**, 108 108, arXiv: `1312.3181 [astro-ph.GA]` (cit. on p. 245).

Sollins, Peter K. et al. (2005), *Spherical Infall in G10.6-0.4: Accretion through an Ultracompact H II Region*, Astrophys. J. Letters **624** L49, arXiv: `astro-ph/0410604 [astro-ph]` (cit. on p. 245).

Varricatt, W. P. et al. (2018), *Discovery of two embedded massive YSOs and an outflow in IRAS 18144-1723*, Mon. Not. R. Astron. Soc. **480** 4231, arXiv: `1808.00230 [astro-ph.SR]` (cit. on p. 246).

Varricatt, Watson P. et al. (2010), *A near-IR imaging survey of intermediate- and high-mass young stellar outflow candidates*, Mon. Not. R. Astron. Soc. **404** 661, arXiv: `1001.2708 [astro-ph.SR]` (cit. on p. 245).

Wood, Douglas O. S. and Ed Churchwell (1989), *The Morphologies and Physical Properties of Ultracompact H II Regions*, Astrophys. J. Supp. **69** 831 (cit. on p. 245).

Wyrowski, F. et al. (2012), *Terahertz ammonia absorption as a probe of infall in high-mass star forming clumps*, Astron. Astrophys. **542**, L15 L15, arXiv: `1203.3406 [astro-ph.GA]` (cit. on p. 246).

Zapata, Luis A. et al. (2006), *In Search of Circumstellar Disks around Young Massive Stars*, Astron. J. **131** 939, arXiv: `astro-ph/0510761 [astro-ph]` (cit. on p. 245).

List of Figures

List of Tables

Acknowledgements

I would first like to thank my thesis advisor Dr. Friedrich Wyrowski. He has consistently helped and supported me in my projects, and during the many times of proposal preparations. He always steered me in the right direction in each and many discussions we had. He guided me through my first observation run at APEX telescope. It was a valuable experience, and an important start for becoming a well-rounded observer. I still clearly remember the day he interviewed me, which started the whole journey of my PhD life. He is a great mentor whose patience and professional attitude have always steered me in the right direction.

I would also like to thank Dr. Timea Csengeri, who helped me with great commitment, especially in my first project, when I started up at MPIfR and was trying to adapt to everything in a foreign country. Without her caring words and timely encouragement I would not have a smooth transition to settle down here. I sincerely thank my first supervisor, Prof. Dr. Karl Menten, who has always been supportive, and a strong source of motivation to me. His thoughtful and inspiring suggestions, with detail-oriented comments on my works constantly remind me of the traits I should be pursuing as a scientific researcher.

I am gratefully indebted to Dr. Hauyu Baobab Liu for his constant help and input to my works, and the many restorative, morale-boosting conversations we had. He had been a great mentor during my Master's years and has been a dearest friend since then.

I would also like to thank my collaborators: Dr. James Urquhart and Dr. Dario Colombo who contributed a lot to my research. The many discussions with them, and their passionate participation have stimulated me a great deal along the path. I would also like to acknowledge Prof. Dr. Pavel Kroupa at the University of Bonn, who is the second supervisor and reader of this thesis, and I am very grateful to his insightful suggestions during the TAC meetings and paper preparations.

I really appreciate the office hours with my caring, interesting and hard-working officemates, all the casual talks with whom are such relaxing intervals that I look forward to each day.

Finally, I must express my profound gratitude to my parents and my old friends, for providing me with unfailing support and encouragement throughout the years. I appreciate the companion of Mr. Buckwheat the British shorthair, who has been there since last Christmas and who always strikes me with his great concentration, curiosity and vivid life. During the lockdown period, the little one has contributed a lot to keep me mentally healthy.

This accomplishment would not have been possible without them. It has been a long journey full of unforgettable moments and delightful scenery, and I am sincerely grateful.